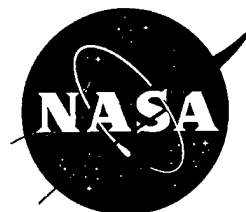DOT/FAA/AR-97/2, II

Proceedings of the

FAA-NASA Symposium on the Continued Airworthiness of Aircraft Structures

FAA Center of Excellence in Computational Modeling of Aircraft Structures
Atlanta, Georgia
August 28-30, 1996

July 1997

19971117 095

NOTICE

This document is disseminated under the sponsorship of the U.S. Department of Transportation in the interest of information exchange. The United States Government assumes no liability for the contents or use thereof. The United States Government does not endorse products or manufacturers. Trade or manufacturer's names appear herein solely because they are considered essential to the objective of this report.

1. Report No. DOT/FAA/AR-97/2, II	2. Government Accession No.	3. Recipient's Catalog No.
4. Title and Subtitle PROCEEDINGS OF THE FAA-NASA SYMPOSIUM ON THE CONTINUED AIRWORTHINESS OF AIRCRAFT STRUCTURES		5. Report Date July 1997
		6. Performing Organization Code
7. Author(s) Compiled by Catherine A. Bigelow, Ph.D.		8. Performing Organization Report No.
9. Performing Organization Name and Address Federal Aviation Administration NASA Langley Research Center Airport and Aircraft Safety Materials Division Research and Development Division Hampton, VA 23681 William J. Hughes Technical Center Atlantic City International Airport, NJ 08405		10. Work Unit No. (TRAIS)
		11. Contract or Grant No.
12. Sponsoring Agency Name and Address U.S. Department of Transportation Federal Aviation Administration Office of Aviation Research Washington, DC 20591		13. Type of Report and Period Covered Proceedings August 28-30, 1996
		14. Sponsoring Agency Code AAR-400

15. Supplementary Notes

Edited by Catherine A. Bigelow, Ph.D, Federal Aviation Administration, William J. Hughes Technical Center

16. Abstract

This publication contains the fifty-two technical papers presented at the FAA-NASA Symposium on the Continued Airworthiness of Aircraft Structures. The symposium, hosted by the FAA Center of Excellence for Computational Modeling of Aircraft Structures at Georgia Institute of Technology, was held to disseminate information on recent developments in advanced technologies to extend the life of high-time aircraft and design longer-life aircraft. Affiliations of the participants included 33% from government agencies and laboratories, 19% from academia, and 48% from industry; in all 240 people were in attendance.

Technical papers were selected for presentation at the symposium, after a review of extended abstracts received by the Organizing Committee from a general call for papers.

17. Key Words Corrosion, Crack detection, Nondestructive inspection, Residual strength, Fatigue, Crack growth		18. Distribution Statement Document is available to the public through the National Technical Information Service, Springfield, Virginia 22161	
19. Security Classif. (of this report) Unclassified	20. Security Classif. (of this page) Unclassified	21. No. of Pages 346	22. Price

Form DOT F1700.7 (8-72)   Reproduction of completed page authorized

CONTENTS

Volume I

Volume II

v

EXECUTIVE SUMMARY

The Federal Aviation Administration (FAA) and the National Aeronautics and Space Administration (NASA) jointly sponsored the Symposium on Continued Airworthiness of Aircraft Structures in Atlanta, Georgia, August 28-30, 1996. The Symposium was hosted by the FAA Center of Excellence for Computational Modeling of Aircraft Structures at Georgia Institute of Technology.

Technical papers were selected for presentation at the symposium, after a review of extended abstracts received by the Organizing Committee from a general call for papers. Keynote addresses were given by Dr. George L. Donohue, Associate Administrator of Acquisition and Research of the Federal Aviation Administration, and Dr. Robert W. Whitehead, Associate Administrator for Research and Acquisition, National Aeronautics and Space Administration.

Full-length manuscripts were requested from the authors of papers presented; these paper are included in the proceedings.

The members of the Conference Organizing Committee are as follows:

> Chris C. Seher, Conference Chairman, Federal Aviation Administration
> Charles E. Harris, Conference Co-Chairman, NASA Langley Research Center
> Satya N. Atluri, Georgia Institute of Technology
> Amos W. Hoggard, Douglas Aircraft Company
> Roy Wantanabe, Boeing Commercial Airplane Group
> John W. Lincoln, US Air Force
> Thomas Swift, Federal Aviation Administration
> Aubrey Carter, Delta Airlines
> Jerry Porter, Lockheed Martin Aerospace
> Catherine A. Bigelow, Federal Aviation Administration
> James C. Newman, NASA Langley Research Center
> Andres Zellweger, Federal Aviation Administration

Approximately 240 people attended the conference. The affiliations of the attendees included 33% from government agencies and laboratories, 19% from academia, and 48% from industry.

Chris C. Seher
FAA Technical Center

FATIGUE-LIFE PREDICTION METHODOLOGY USING SMALL-CRACK THEORY AND A CRACK-CLOSURE MODEL

J. C. Newman, Jr. and E. P. Phillips
NASA Langley Research Center
Hampton, Virginia, USA

M. H. Swain
Lockheed Engineering and Sciences Company
Hampton, Virginia, USA

ABSTRACT

This paper reviews the capabilities of a plasticity-induced crack-closure model to predict fatigue lives of metallic materials using "small-crack theory" for various materials and loading conditions. Crack tip constraint factors, to account for three-dimensional state-of-stress effects, were selected to correlate large-crack growth rate data as a function of the effective-stress-intensity factor range (ΔK_{eff}) under constant-amplitude loading. Some modifications to the ΔK_{eff} -rate relations were needed in the near-threshold regime to fit measured small-crack growth rate behavior and fatigue endurance limits. The model was then used to calculate small- and large-crack growth rates and to predict total fatigue lives for notched and unnotched specimens made of two aluminum alloys, a titanium alloy, and a steel under constant-amplitude and spectrum loading. Fatigue lives were calculated using the crack-growth relations and microstructural features like those that initiated cracks for the aluminum alloys and steel for edge-notched specimens. An equivalent-initial-flaw-size concept was used to calculate fatigue lives in other cases. Results from the tests and analyses agreed well.

INTRODUCTION

On the basis of linear-elastic fracture mechanics (LEFM), studies on small cracks (10 µm to 1 mm) have shown that small cracks grow much faster than would be predicted from large-crack data (Pearson [1], Ritchie and Lankford [2], Miller and de los Rios [3]). This behavior is illustrated in Figure 1, where the crack-growth rate, da/dN or dc/dN, is plotted against the linear-elastic stress-intensity factor range, ΔK. The solid (sigmodal) curve shows typical results for large cracks in a given material and environment under constant-amplitude loading. The solid curve is usually obtained from tests with large cracks. At low growth rates, the threshold stress-intensity factor range, ΔK_{th}, is usually obtained from load-reduction (ΔK-decreasing) tests. Some typical results for small cracks in plates and at

331

Constant-Amplitude Loading
R=Constant

$S_1 < S_2 < S_3$

Large Crack

Small Crack

S_3

$\frac{da}{dN}$, $\frac{dc}{dN}$

Small Crack

Small Crack

S_2

S_1

Large Crack

(ΔK Decreasing Test)

Steady State

ΔK_{th}

ΔK
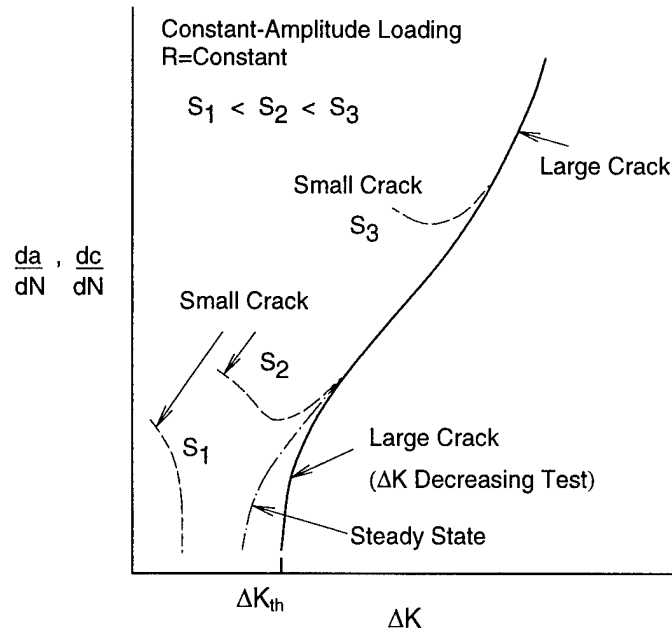
Figure 1. Typical Fatigue-Crack Growth Behavior for Small and Large Cracks.

notches are shown by the dashed curves. These results show that small cracks grow at ΔK levels below the large-crack threshold and that they also grow faster than large cracks at the same ΔK level above threshold. Small-crack effects have been shown to be more prevalent in tests which have compressive loads such as negative stress ratios (Zocher [4], Newman and Edwards [5,6]). Over the past decade, various studies on small- or short-crack growth behavior in metallic materials have led to the realization that fatigue life of many materials is primarily crack growth from microstructural features such as inclusion particles, voids or slip-band formation. Concurrently, improved fracture-mechanics analyses of some of the crack tip shielding mechanisms such as plasticity-induced crack closure and analyses of surface- or corner-crack configurations (Raju and Newman [7,8]) have led to more accurate crack-growth and fatigue-life prediction methods. Thus, small-crack theory is the treatment of fatigue as a crack-propagation process from a microdefect (or crack) to failure.

During the last decade, research on small- or short-crack effects have concentrated on three possible explanations for the behavior of such cracks. They are plasticity effects, metallurgical effects, and crack closure. All of these features contribute to an inadequacy of LEFM and the use of the ΔK-concept to correlate fatigue-crack growth rates. Some of the earliest small-crack experiments were conducted at high stress levels which were expected to invalidate LEFM methods. Nonlinear or elastic-plastic fracture mechanics concepts, such as the J-integral and an empirical length parameter (El Haddad et al. [9]), were developed to explain the observed small-crack effects. Recent research on the use of ΔJ as a crack-driving parameter suggest that plasticity effects are small for many of the early and more recent small-crack experiments (Newman [10]). But the influence of plasticity on small-crack growth and the appropriate crack-driving parameter is still being debated.

332

Small cracks tend to initiate in metallic materials at inclusion particles or voids, in regions of intense slip, or at weak interfaces and grains. In these cases, metallurgical similitude breaks down for these cracks (which means that the growth rate is no longer an average taken over many grains), see Leis et al. [11]. Thus, the local crack growth behavior is controlled by metallurgical features. If the material is markedly anisotropic, the local grain orientation will strongly influence the growth rate. Crack-front irregularities and small particles or inclusions affect the local stresses and, therefore, the crack growth response. For large cracks, all of these metallurgical effects are averaged over many grains, except in very coarse-grained materials. LEFM and nonlinear fracture mechanics concepts are only beginning to explore the influence of metallurgical features on stress-intensity factors, strain-energy densities, J-integrals, and other crack-driving parameters.

Very early in small-crack research, fatigue-crack closure (Elber [12]) was recognized as a possible explanation for rapid small-crack growth rates (see Nisitani and Takao [13]). Fatigue-crack closure is caused by residual plastic deformations left in the wake of an advancing crack. Only that portion of the load cycle for which the crack is fully open is used in computing an effective stress-intensity factor range (ΔK_{eff}) from LEFM solutions. A small crack initiating at an inclusion particle, a void, or at a weak grain does not have the prior plastic history to develop closure. Thus, a small crack may not be closed for as much of the loading cycle as a larger crack. If a small crack is fully open, the stress-intensity factor range is fully effective and the crack-growth rate will be greater than steady-state, crack-growth rates. (A steady-state crack is one in which the residual plastic deformations and crack closure along the crack surfaces are fully developed and stabilized under steady-state loading.) Small-crack growth rates are also faster than steady-state behavior because these cracks may initiate and grow in weak microstructure. In contrast to small-crack growth behavior, the development of the large-crack threshold, as illustrated in Figure 1, has also been associated with a rise in crack-opening load as the applied load is reduced (Minikawa and McEvily [14] and Newman [15]). Thus, the steady-state, crack-growth behavior may lie between the small-crack and large-crack threshold behavior, as illustrated by the dash-dot curve.

The purpose of this paper is to review the capabilities of a plasticity-induced, crack-closure model (Newman [16,17]) to correlate large-crack growth rate behavior and to predict fatigue lives in two aluminum alloys, a titanium alloy, and a steel under various load histories using small-crack theory. Test results from the literature on 2024-T3 and 7075-T6 aluminum alloys, Ti-6Al-4V titanium alloy, and 4340 steel under constant-amplitude loading were analyzed with the closure model to establish an effective stress-intensity factor range (ΔK_{eff}) against crack-growth rate relation. The ΔK_{eff}-rate relation and some micro-structural features were used with the closure model to predict total fatigue lives on notched specimens made of aluminum alloys and steel under various load histories. An equivalent-initial-flaw-size (EIFS) concept (Rudd et al. [18]) was used to calculate fatigue lives for unnotched and notched aluminum and titanium alloys. The load histories considered were constant-amplitude loading over a wide range in stress ratios, FALSTAFF (van Dijk et al. [19]), Gaussian (Huck et al. [20]), TWIST (deJonge et al. [21]), Mini-TWIST (Lowak et al. [22]) and Felix/28 (Edwards and Darts [23]) load sequences. The crack configurations used

in these analyses were through-crack configurations, such as middle-crack and compact tension specimens, and three-dimensional crack configurations, such as a corner crack in a bar or a surface crack at a circular hole or semicircular edge notch. Comparisons are made between measured and calculated or predicted fatigue lives on various unnotched and notched specimens.

CRACK AND NOTCH CONFIGURATIONS ANALYZED

The large-crack, ΔK-rate data for the two aluminum alloys and the steel were obtained from middle-crack tension specimens and the data for the titanium alloy was obtained from compact tension and corner crack in a bar specimens. The data for the 2024-T3 alloy was obtained from Hudson [24], Phillips [25], and Dubensky [26], whereas the data for the 7075-T6 alloy was obtained from Phillips and Deng (see Refs. 27 and 28). The data for the 4340 steel was obtained from Swain et al. [29]. The data for the Ti-6Al-4V alloy was obtained from Raizenne [30], Mom and Raizenne [31], and Powell and Henderson [32].

The fatigue specimens analyzed are shown in Figure 2. They were

(a)   the uniform stress ($K_T = 1$) unnotched specimen,
(b)   the circular-hole ($K_T = 3$) specimen,
(c)   the single-edge-notch tension (SENT, $K_T = 3.15$ or 3.3) specimen, and
(d)   the double-edge-notch tension (DENT, $K_T = 3.1$) specimen.

Here the stress concentration factor, K_T, is expressed in terms of the remote (gross) stress, S, instead of the net-section stress.
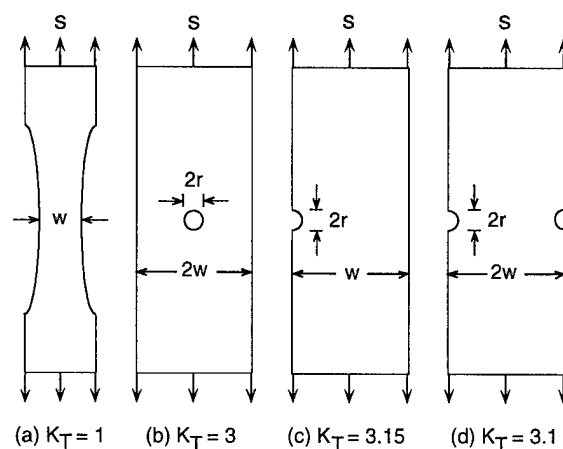
Figure 2. Fatigue Specimens Analyzed With Small-Crack Theory.

PLASTICITY-INDUCED CRACK-CLOSURE MODEL

The crack-closure model (Newman [16]) was developed for a central through crack in a finite-width specimen subjected to remote applied stress. The model was later extended to a through crack emanating from a circular hole and applied to the growth of small cracks (Newman [15]). The model was based on the Dugdale [33] model, but it was modified to leave plastically deformed material in the wake of the crack. The details of the model are given elsewhere and will not be presented here. One of the most important features of the model, however, is the ability to model three-dimensional constraint effects. A constraint factor, α, is used to elevate the flow stress ($\alpha\sigma_0$) at the crack tip to account for the influence of stress state. The flow stress σ_0 is the average between the yield stress and ultimate tensile strength. For plane-stress conditions, α is equal to unity (original Dugdale model), and for simulated plane-strain conditions, α is equal to 3. Although the strip-yield model does not model the correct yield-zone pattern for plane-strain conditions, the model with a high constraint factor is able to produce crack-surface displacements and crack-opening stresses quite similar to those calculated from an elastic-plastic finite element analysis of crack growth and closure for a finite-thickness plate (Blom et al. [34]). In conducting fatigue-crack growth analyses, the constraint factor α is used as a fitting parameter to correlate crack-growth rate data against ΔK_{eff} under constant-amplitude loading for different stress ratios. However, tests conducted under single-spike overloads seem to be more sensitive to state-of-stress effects and may be a more appropriate test to determine the constraint factor.

Effective Stress-Intensity Factor Range

For most damage tolerance and durability analyses, the linear-elastic analyses have been found to be adequate. The linear-elastic effective stress-intensity factor range developed by Elber [12] is given by

$$\Delta K_{eff} = (S_{max} - S'_0) \sqrt{(\pi c)} \, F(c/w) \qquad (1)$$

where S_{max} is the maximum stress, S'_0 is the crack-opening stress, and F is the boundary-correction factor. However, for high stress-intensity factors, proof testing, and low-cycle fatigue conditions, the linear-elastic analyses are inadequate and nonlinear crack-growth parameters are needed. To account for plasticity, a portion of the Dugdale cyclic-plastic-zone length (ω) has been added to the crack length, c. The cyclic-plastic-zone corrected effective stress-intensity factor [10] is

$$(\Delta K_p)_{eff} = (S_{max} - S'_0) \sqrt{(\pi d)} \, F(d/w) \qquad (2)$$

where d = c + ω/4 and F is the cyclic-plastic-zone corrected boundary-correction factor. Herein, the cyclic-plastic-zone corrected effective stress-intensity factor range will be used in the fatigue-life predictions unless otherwise noted.

Constant-Amplitude Loading

As a crack grows in a finite-thickness body under cyclic loading (constant stress range), the plastic-zone size at the crack front increases. At low stress-intensity factor levels, plane-strain conditions should prevail but as the plastic-zone size becomes large compared to sheet thickness, a loss of constraint is expected. This constraint loss has been associated with the transition from flat-to-slant crack growth. Schijve [35] has shown that the transition occurs at nearly the same crack-growth rate over a wide range in stress ratios for an aluminum alloy. This observation has been used to help select the constraint-loss regime (see Ref. 36).

Newman [17] developed crack-opening stress equations for constant-amplitude loading from crack-closure model calculations for a middle-crack tension specimen. These equations give crack opening stress as a function of stress ratio (R), maximum stress level (S_{max}/σ_o), and the constraint factor (α). These equations are used to develop the baseline ΔK_{eff} -rate relations that are used in the life-prediction code FASTRAN-II [37] to make crack-growth and fatigue-life predictions.

LARGE-CRACK GROWTH BEHAVIOR

To make life predictions, ΔK_{eff} as a function of the crack-growth rate must be obtained for the material of interest. Fatigue crack-growth rate data should be obtained over the widest possible range in rates (from threshold to fracture), especially if spectrum load predictions are required. Data obtained on the crack configuration of interest would be helpful but it is not essential. The use of the nonlinear crack tip parameters is only necessary if severe loading (such as low-cycle fatigue conditions) are of interest. Most damage-tolerant life calculations can be performed using the linear elastic stress-intensity factor analysis with crack-closure modifications.

Under constant-amplitude loading, the only unknown in the analysis is the constraint factor, α. The constraint factor is determined by finding (by trial and error) an α value that will correlate the constant-amplitude fatigue crack-growth rate data over a wide range in stress ratios, as shown by Newman [17]. This correlation should produce a unique relationship between ΔK_{eff} and crack-growth rate. In the large-crack-growth threshold regime for some materials, the plasticity-induced closure model may not be able to collapse

the threshold (ΔK-rate) data onto a unique ΔK_{eff}-rate relation because of other forms of closure. Roughness- and oxide-induced closure (see Ritchie and Lankford [2]) appear to be more relevant in the threshold regime than plasticity-induced closure. This may help explain why the constraint factors needed to correlate crack-growth rate data in the near threshold regime are lower than plane-strain conditions. The constraint factors are 1.7 to 2 for aluminum alloys, 1.9 to 2.2 for titanium alloys, and 2.5 for steel. However, further study is needed to assess the interactions between plasticity-, roughness- and oxide-induced closure in this regime. If the plasticity-induced closure model is not able to give a unique ΔK_{eff}-rate relation in the threshold regime, then high stress ratio (R $\geq$ 0.7) data may be used to establish the ΔK_{eff}-rate relation.

In the following, the ΔK_{eff}-rate relation for two aluminum alloys, a titanium alloy, and a steel will be presented and discussed. A detailed description will be given for one material but similar procedures were used to establish the relationships for all materials used in this study.

Aluminum Alloy 2024-T3

The large-crack results for 2024-T3 aluminum alloy are shown in Figure 3 for data generated by Hudson [24], Phillips [25], and Dubensky [26]. This figure shows the elastic ΔK_{eff} (eqn. 1) plotted against crack-growth rate. The data collapsed into a narrow band with several transitions in slope occurring at about the same rate for all stress ratios. Some large differences were observed at high R-ratios in the high-rate regime. These tests were conducted at extremely high remote stress levels (0.75 and 0.95 of the yield stress). Even elastic-plastic analyses, such as equation 2, were unable to collapse the data along a unique curve in this regime. From a high-cycle fatigue standpoint, however, this discrepancy has very little influence on total life. The elastic-plastic fracture criterion (Two-Parameter Fracture Criterion, TPFC; see Ref. 39) used in the analysis ($K_F = 267$ MPa$\sqrt{m}$; m = 1) predicted failure very near to the vertical asymptotes of the test data, see the vertical dashed and dotted lines for R = 0.7 and 0.5 (at 0.75 and 0.95 of yield), respectively. Similar vertical lines (not shown) would also indicate failure at the other R ratios. Lower R ratios would fail at higher values of ΔK_{eff}. For these calculations, a constraint factor (α) of 2.0 was used for rates less than 1E-07 m/cycle (start of transition from flat-to-slant crack growth) and α equal to 1.0 was used for rates greater than 2.5E-06 m/cycle (end of transition from flat-to-slant crack growth). For intermediate rates, α was varied linearly with the logarithm of crack-growth rate (see Ref. 37). The values of α and rate were selected by trial and error and from analyses of crack growth under spectrum loading (see Ref. 38). The constraint-loss regime (α = 2 to 1) has also been associated with the flat-to-slant crack-growth behavior.

Reference 38 developed an expression to predict the location of the flat-to-slant crack-growth regime and the effective stress-intensity factor at transition is by

$$(\Delta K_{eff})_T = 0.5 \, \sigma_o \, \sqrt{B} \tag{3}$$

Figure 3. Effective Stress-Intensity Factor Range Against Crack-Growth Rate for Large Cracks in 2024-T3 Aluminum Alloy Sheet.

For the 2024-T3 alloy sheet, $(\Delta K_{eff})_T = 10.2$ MPa$\sqrt{m}$. The width of the constraint-loss regime, in terms of rate or ΔK_{eff}, is a function of thickness but this relationship has yet to be developed. In the low crack-growth rate regime, near and at threshold, tests and analyses [14,15] have indicated that the threshold develops because of a rise in the crack-opening stress-to-maximum-stress ratio due to the load-shedding procedure. In the threshold regime then, the actual ΔK_{eff} -rate data would lie at lower values of ΔK_{eff} because the rise in crack-opening stress was not accounted for in the current analysis. For the present study, an estimate was made for this behavior on the basis of small-crack data [5] and it is shown by the solid line below rates of about 2E-09 m/cycle. The baseline relation shown by the solid line (see Table 1) will be used later to predict fatigue lives under constant-amplitude and spectrum loading.

Table 1. Mechanical, Fracture, and Baseline Crack-Growth (ΔK_{eff}-Rate) Properties.

2024-T3		7075-T6		Ti-6Al-4V		4340 Steel	
B = 2.3 mm		B = 2.3 mm		B = 10-13 mm		B = 5.1 mm	
σ_{ys} = 360 MPa		σ_{ys} = 520 MPa		σ_{ys} = 860 MPa		σ_{ys} = 1410 MPa	
σ_u = 490 MPa		σ_u = 575 MPa		σ_u = 960 MPa		σ_u = 1510 MPa	
E = 72000 MPa		E = 72000 MPa		E = 115000 MPa		E = 207000 MPa	
K_F = 267 MPa√m		K_F = 50 MPa√m		K_F = 54 MPa√m		K_F = 170 MPa√m	
m = 1.0		m = 0.0		m = 0.0		m = 0.0	
ΔK_{eff} MPa√m	dc/dN m/cycle	ΔK_{eff} MPa√m	dc/dN m/cycle	ΔK_{eff} MPa√m	dc/dN m/cycle	ΔK_{eff} MPa√m	dc/dN m/cycle
0.8	1.0E-11	0.9	1.0E-11	1.0	1.0E-11	3.2	1.0E-11
1.05	1.0E-10	1.25	1.0E-09	2.5	1.0E-10	3.75	5.0E-10
2.05	2.0E-09	3.0	1.0E-08	4.4	1.0E-09	5.2	2.0E-09
4.0	8.0E-09	4.0	6.3E-08	8.0	1.0E-08	7.3	7.0E-09
7.7	1.0E-07	10.0	1.0E-06	12.8	1.0E-07	14.0	5.0E-08
13.5	1.0E-06	14.8	1.0E-05	25.0	1.0E-06	50.0	6.5E-07
23.0	1.0E-05	23.0	1.0E-04	54.0	2.0E-05	108.0	1.0E-04
36.0	1.0E-04						
85.0	1.0E-02						
α	dc/dN m/cycle	α	dc/dN m/cycle			α	dc/dN m/cycle
2.0	1.0E-07	1.8	7.0E-07	α = 1.9		2.5	5.0E-07
1.0	2.5E-06	1.2	7.0E-06			1.2	2.5E-05

Aluminum Alloy 7075-T6

The large-crack results for 7075-T6 aluminum alloy are shown in Figure 4 for data generated at two different laboratories and at three stress ratios (Phillips and Deng, see Ref. 27). The data collapsed into a narrow band, again, with several transitions in slope occurring at about the same rate for all stress ratios. These data demonstrate why a table-lookup ΔK_{eff}-rate curve is needed to fit crack-growth rate data over many orders of magnitude in rate. Some differences were observed in the near threshold regime. For these calculations, a constraint factor α of 1.8 was used for rates less than 7E-07 m/cycle and α equal to 1.2 for rates greater than 7E-06 m/cycle. Again, the values of α and rate were selected by trial and error. For this sheet alloy, the constraint-loss regime occurs near $(\Delta K_{eff})_T$ = 13.1 MPa√m. In the threshold regime, an estimate was made to fit small-crack growth rate behavior (see Ref. 28) and it is shown by the solid line below a rate of about 2E-09 m/cycle. The baseline relation shown by the solid line (see Table 1) will be used later to predict small-crack growth rates and fatigue lives under constant-amplitude and spectrum loading.

Figure 5 shows the ΔK_{eff} -rate data for small corner cracks (open symbols) in 10-mm-thick Ti-6Al-4V titanium alloy (Raizenne [30]). In these tests, the initial defect size was a 250-μm quarter-circular, electrically discharged, machined notch in a square bar under tension. The dashed line shows the results of analyses on additional corner-crack data from Reference 31. The solid symbols show the results from 13-mm-thick compact specimens (Powell and Henderson [32]) tested over a wide range of R ratios and down to much lower rates than the corner-crack tests.
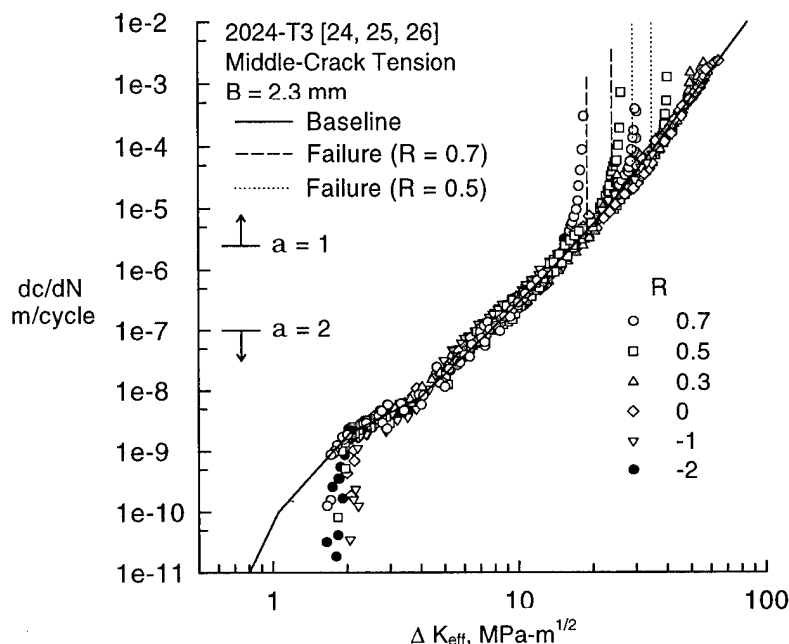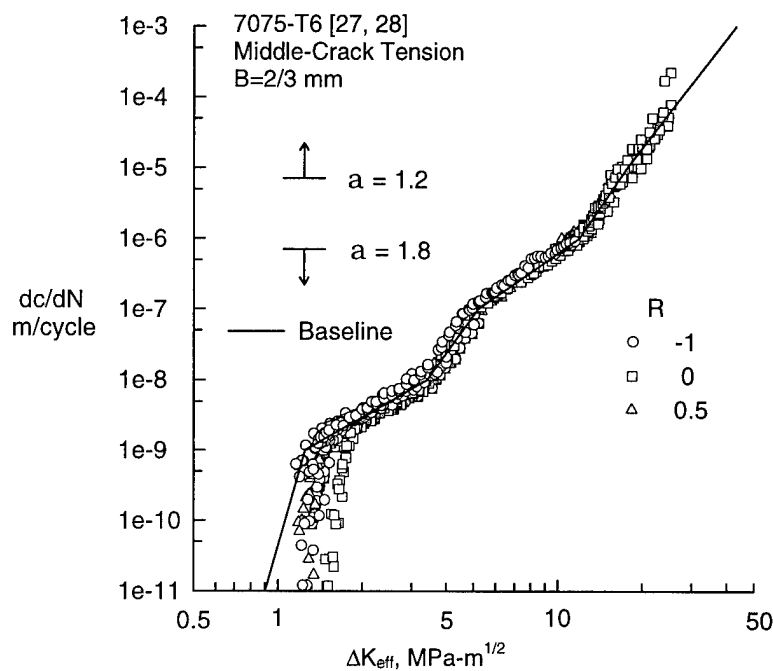

Figure 4. Effective Stress-Intensity Factor Range Against Crack-Growth Rate for Large Cracks in 7075-T6 Aluminum Alloy Sheet.

For the thick material, the loss of constraint occurs near a $(\Delta K_{eff})_T$ value of about 50 MPa$\sqrt{m}$, which is beyond the current test data. A constraint-loss regime would occur in this material but the fracture toughness $K_F = 54$ MPa$\sqrt{m}$ (m = 0; LEFM). Thus, the specimens will fracture before the constraint loss is activated. Consequently, a constant constraint factor was used over the complete ΔK_{eff} range. The data correlated quite well with a constant constraint factor of 1.9. The baseline relation (solid line) fit to the corner-crack results in the midregion, and the compact results in the low-rate regime (see Table 1) will be used later to predict fatigue lives for 3.5-mm-thick double-edge notched tension specimens.

The constraint-loss regime for the thinner titanium alloy would occur at a $(\Delta K_{eff})_T$ value of about 27 MPa$\sqrt{m}$. Because only constant-amplitude loading will be considered later, the constant constraint relationship with $\alpha = 1.9$ will also be used for the thinner alloy.
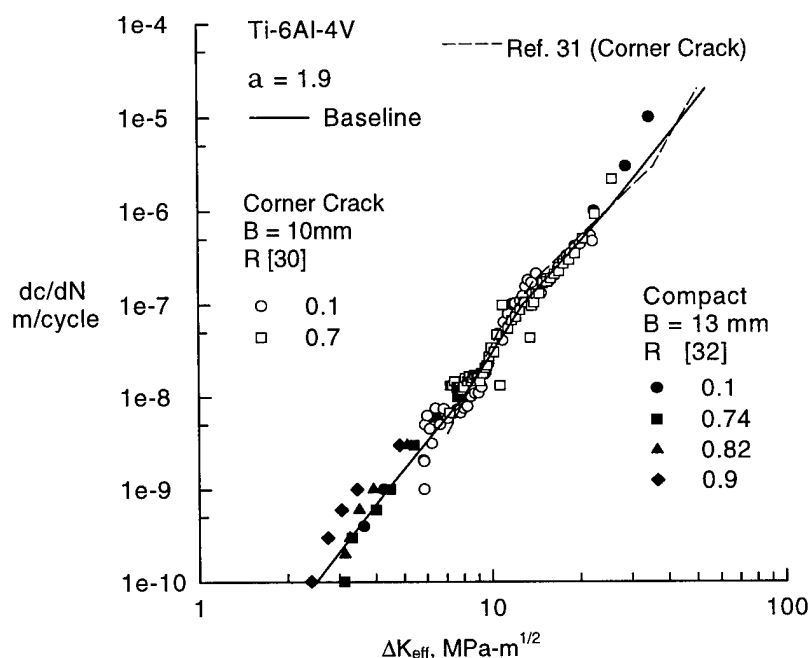
Figure 5. Effective Stress-Intensity Factor Range Against Crack-Growth Rate for Large Corner and Through Cracks in Ti-6Al-4V Titanium Alloy.

Steel 4340

The large-crack results for the 4340 steel are shown in Figure 6 for data generated at two different laboratories and at four stress ratios (see Swain et al. [29]). For these calculations, a constraint factor α of 2.5 was used for rates less than 5E-07 m/cycle and α equal to 1.2 for rates greater than 2.5E-05 m/cycle. Again, the values of α and rate were selected by trial and error. For this material and thickness, the constraint-loss regime occurs near $(\Delta K_{eff})_T = 52$ MPa$\sqrt{m}$, which corresponds closely to the sharp change in growth rates at about 1E-06 m/cycle. The data collapsed into a fairly tight band, in the midrate regime, but some differences were observed in the near threshold regime. For the high-strength steel, small- and large-crack data tended to agree in the near threshold regime (see Ref. 29). The baseline relation shown by the solid line (see Table 1) will be used later to predict fatigue lives under constant-amplitude and spectrum loading.
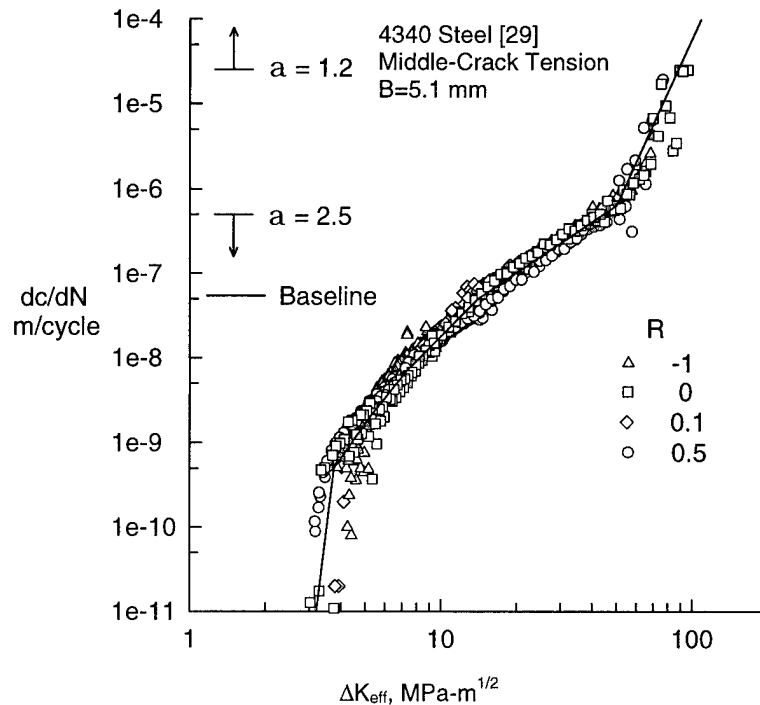
Figure 6. Effective Stress-Intensity Factor Range Against Crack-Growth Rate for Large
Cracks in 4340 Steel.

SMALL-CRACK GROWTH RATE BEHAVIOR

Earlier work by Pearson [1] on fatigue-crack initiation and growth of small cracks
from inclusion particles in two aluminum alloys (BS L65 and DTD 5050) set the stage for the
development of the small-crack theory. His results are shown in Figure 7, as the dashed curve,
along with additional small- and large-crack data from Lankford [40] on 7075-T6 aluminum
alloy. Pearson concluded that cracks of about the size of the average grain-size, grew several
times faster than large cracks at nominally identical ΔK values. The open symbols and dash-
dot curve show the large-crack data and the development of the large-crack threshold at about
3 to 4 MPa$\sqrt{m}$. The light solid lines show measured small-crack growth rates, from small
surface cracks, with growth at ΔK levels as low as 1.5 MPa$\sqrt{m}$. Some general observations,
by Lankford [40], was that the minimum in da/dN occurred when the crack depth, a, was
about the minimum dimension of the pancake grain (subsurface grain boundary) and that the
magnitude of the lower rates was controlled by the degree of microplasticity in the next grain
penetrated by the crack. If the next grain is oriented like the first, then no deceleration will
occur, as indicated by the uppermost small-crack curves in Figure 7.

342
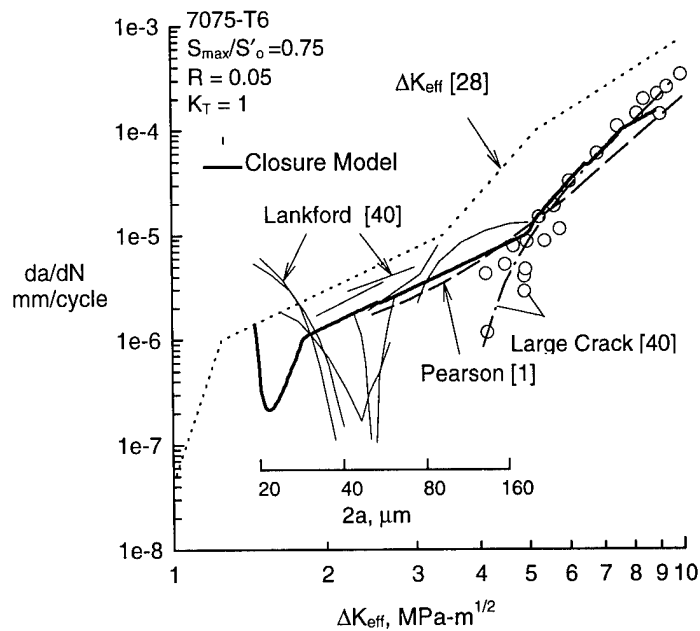
Figure 7. Measured and Predicted Small- and Large-Surface Crack-Growth Rates in an
Aluminum Alloy.

At this stage, it would be of interest to compare the test results from Pearson and
Lankford with the small-crack growth predictions made from the crack-closure model. The
ΔK_{eff}-rate relation for the 7075-T6 alloy [27,28] is shown as the dotted lines. These results
were generated from large-crack data for rates greater than about 2E-06 mm/cycle. The
results are quite different from those shown for the Pearson-Lankford large-crack data. The
reason for this discrepancy is unknown. The lower section of the ΔK_{eff}-rate relation (below
2E-06 mm/cycle) was estimated on the basis of small-crack data, also generated in Reference
28. The ΔK_{eff}-rate relation is closure free and this is the starting point for all small cracks
because these cracks are assumed to be fully open on the first cycle. The results of an
analysis of the test specimen used by Lankford is shown by the heavy solid curve. The initial
defect was selected as a 10 μm radius semicircular surface crack, so that the 2a dimension (on
the surface) would be 20 μm. As the small crack grew, the closure level increased much
faster than the ΔK level and a rapid decrease in rates was calculated. This rapid drop is a
combination of the closure transient and the sharp change in slope of the ΔK_{eff}-rate curve at
about 1E-06 mm/cycle. At about 30 μm, the crack-opening stresses from the model had
nearly stabilized (apparent by the fact that the heavy solid line is parallel to the dotted line).
Also, the effects of plasticity on the crack-driving force, like equation 2, is quite small
considering that the applied stress level was 0.75 times the flow stress (see Figure 6 in Ref.
10). The predicted results for the small-crack growth rates are in excellent agreement with
Pearson's data and agree with Lankford's data which do not exhibit a grain-boundary

343

influence. Interestingly, the small-crack analysis shows a single dip in the small-crack curve, similar to the single dip observed in some of Lankford's small-crack data. Would the grain-boundary interaction always occur at the same crack length (40 μm)? Why aren't there other dips, or small indications of a dip, in the rate curve at 80, 120, or 160 μm? Further study is needed to help resolve these issues. The following section will review the use of small-crack theory to predict or calculate fatigue life for unnotched and notched specimens under various load histories.

FATIGUE-LIFE PREDICTIONS

At this point, all of the elements are in place to assess small-crack theory—a total fatigue-life prediction methodology based solely on crack propagation from microstructural features. In this approach, a crack is assumed to initiate and grow from a microstructural feature on the first cycle. The crack-closure model and the baseline ΔK_{eff}-rate curve are used to predict crack growth from the initial crack size to failure. The final crack size was calculated from the fracture toughness of the material, except where noted. Comparisons are made with fatigue tests conducted on unnotched tension, circular-hole tension, and single- or double-edge notch tension specimens. Results are presented for two aluminum alloys, a titanium alloy, and a high-strength steel under either constant-amplitude or spectrum loading.

Aluminum Alloy 2024-T3

Grover et al. [41] conducted fatigue tests on flat ($K_T = 1$) dog-bone specimens (Figure 2a) made of 2024-T3 aluminum alloy under R = 0 and -1 loading. The specimens were electro-polished but no information on crack-initiation sites was available. Thus, in the analyses it was assumed that cracks initiated as quarter-circular corner cracks. A comparison of experimental and calculated fatigue lives is shown in Figure 8. Various initial crack sizes were selected by trial and error to find the best value to fit the test data. Analyses with a 20-μm initial crack size fit the test data quite well for both R ratios. Results for each R ratio approached the flow stress σ_0 (average of the yield stress and ultimate tensile strength) for high applied stress levels. Some discrepancies were observed for both R = 0 and -1 analyses at applied stress levels above the yield stress. These discrepancies were expected because the closure model does not account for strain-hardening effects but uses an average flow stress. To fit fatigue limits, a value of $(\Delta K_{eff})_{th}$ of 0.8 MPa$\sqrt{m}$ was needed for the 20-μm initial crack.
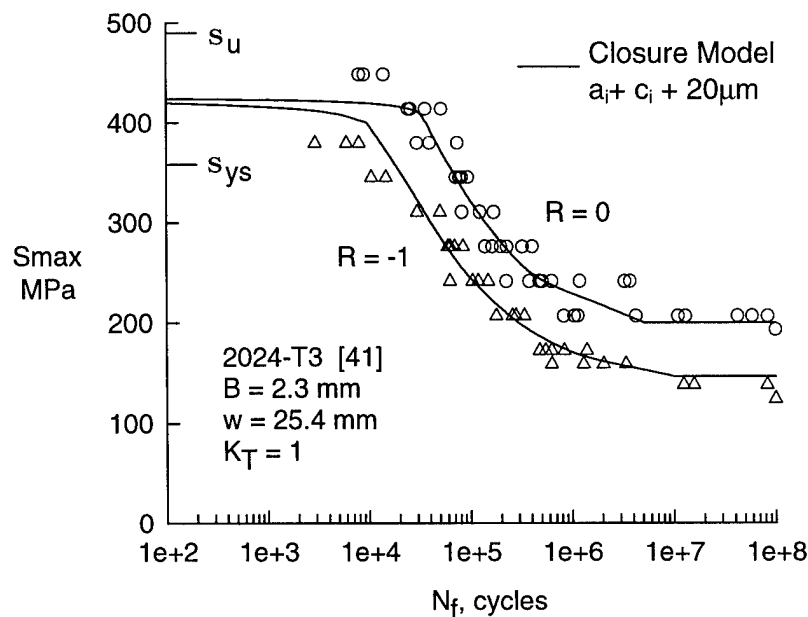
Figure 8. Measured and Calculated Fatigue Lives for 2024-T3 Aluminum Alloy Unnotched
Specimens.

Landers and Hardrath [42] determined the fatigue lives of 2024-T3 aluminum alloy
specimens with a central hole (Figure 2b). The results for specimens with a hole radius of
1.6 mm are shown in Figure 9. Predicted results, as shown by the curves, were made using
an initial semicircular crack size (6 μm) that had an equal area to the average inclusion-
particle sizes that initiated cracks [5]. Results from the elastic-plastic analyses (eqn. 2)
agreed fairly well with the test data, but the elastic analyses (eqn. 1) over-predicted fatigue
life at the high stress levels. The elastic-plastic analyses tended to underpredict lives for R =
0 and slightly over-predict lives for R = -1. The influence of stress ratio on fatigue limits was
predicted quite well using a value of $(\Delta K_{eff})_{th}$ of 0.8 MPa$\sqrt{m}$ (determined from the
unnotched specimens, Figure 8). The smaller initial crack size for a notched specimen
compared to that for the unnotched specimen (20 μm) is probably due to a much smaller
volume of material under the stress that caused failure.

Comparisons of experimental and predicted fatigue lives for 2024-T3 single-edge
notch tension (SENT) specimens (Figure 2c) under the FALSTAFF [19], Gaussian [20], and
TWIST [21] load sequences are shown in Figure 10. The specimens were cycled until a
crack had grown across the full thickness, that is $2a_f$ = B. The predictions were made using
the same initial crack size used for the previous constant-amplitude predictions (6 μm). The
predicted lives, again, agreed well with the test data. For these conditions, however, the
elastic and elastic-plastic analyses showed very little difference.

345

Figure 9. Measured and Calculated Fatigue Lives for 2024-T3 Aluminum Alloy Circular-Hole Specimens.
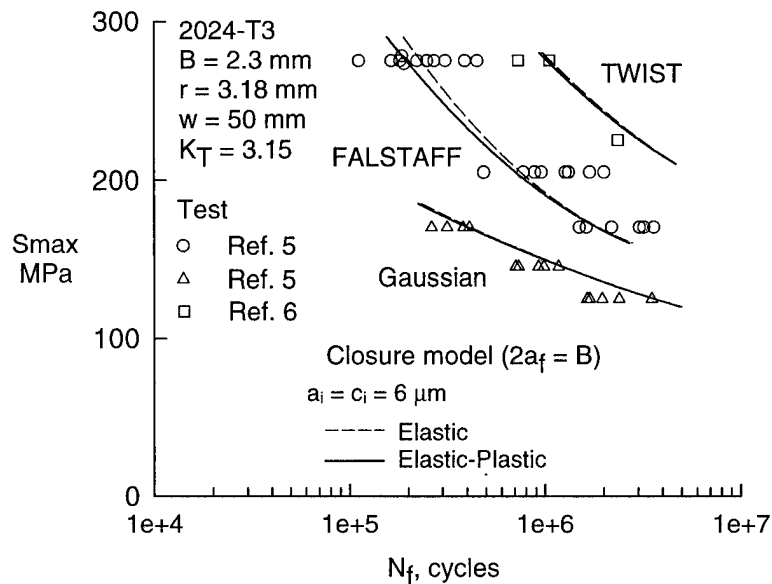
Figure 10. Measured and Predicted Fatigue Lives for 2024-T3 Aluminum Alloy SENT Specimens Under Various Spectrum Loading.

Again, Grover et al. [41] conducted fatigue tests on flat dog-bone specimens made of 7075-T6 aluminum alloy. The specimens were also electropolished. In the analyses it was assumed that cracks initiated as quarter-circular corner cracks at a specimen edge. A comparison of experimental and calculated fatigue lives is shown in Figure 11. Similar to the 2024-T3 alloy, a 20-μm initial crack size fit the mean of the test data at R = 0 quite well. The 20-μm initial crack size was also able to predict the behavior of 7075-T6 fatigue specimens tested at R = -1 (not shown).
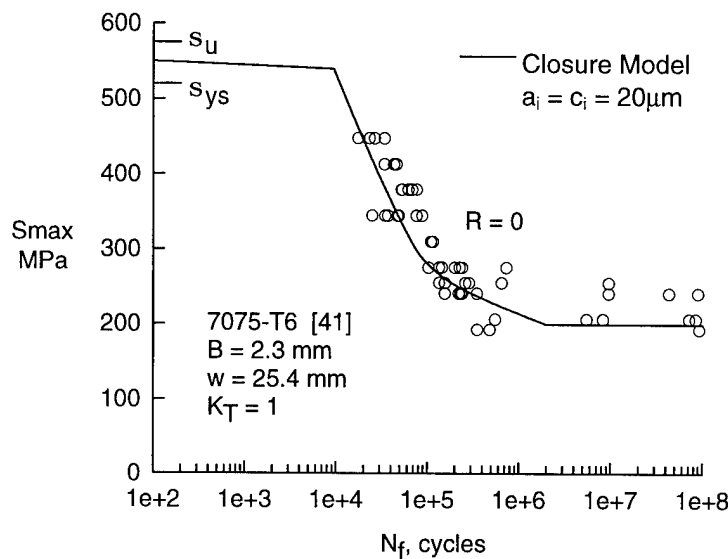
Figure 11. Measured and Calculated Fatigue Lives for 7075-T6 Aluminum Alloy Unnotched Specimens.

The results of fatigue tests conducted on 7075-T6 specimens with a hole radius of 0.8 mm are shown in Figure 12 (symbols). Predicted results were, again, made using an initial semicircular crack size (6 μm) that had an equal area to the average inclusion-particle sizes that had initiated cracks [27,28]. Results from the elastic-plastic analyses (eqn. 2) agreed fairly well with the test data. Again, the analyses tended to underpredict for R = 0 and slightly over-predict for R = -1, which is similar to the trends observed for the 2024-T3 specimens (Figure 9). The reason for these discrepancies is unknown, but it may be related to assuming a mathematical surface crack on the first cycle instead of a crack initiating from an inclusion-particle cluster or void (see Bowles and Schijve [43]). The fatigue limits were predicted quite well using a value of $(\Delta K_{eff})_{th}$ of 0.75 MPa$\sqrt{m}$ with the 6-μm initial crack.

Experimental and predicted results for fatigue tests conducted on 7075-T6 specimens under the Mini-TWIST wing spectrum are shown in Figure 13. These tests were conducted

on SENT specimens [27,28] that were cycled to failure. The predictions were made using an initial semicircular defect size that was close to the average inclusion-particle sizes where cracks initiated. The predicted lives were in good agreement with the test results.
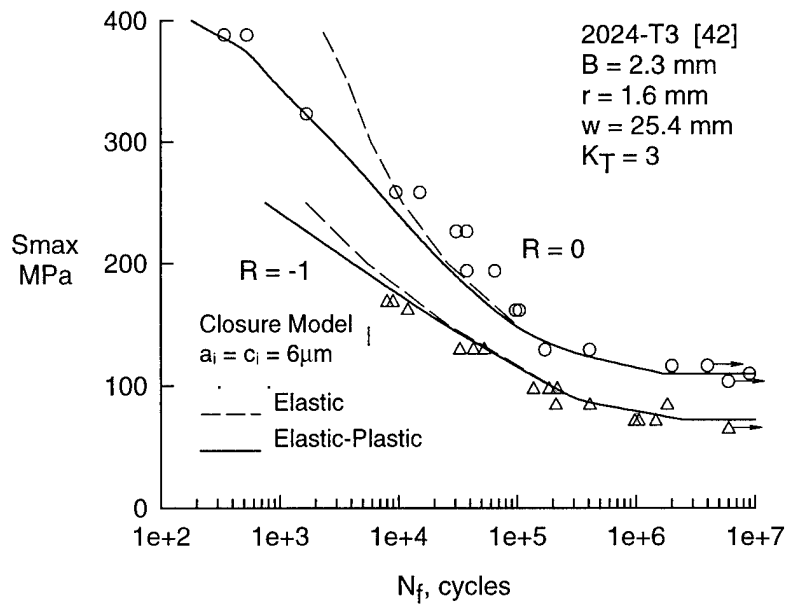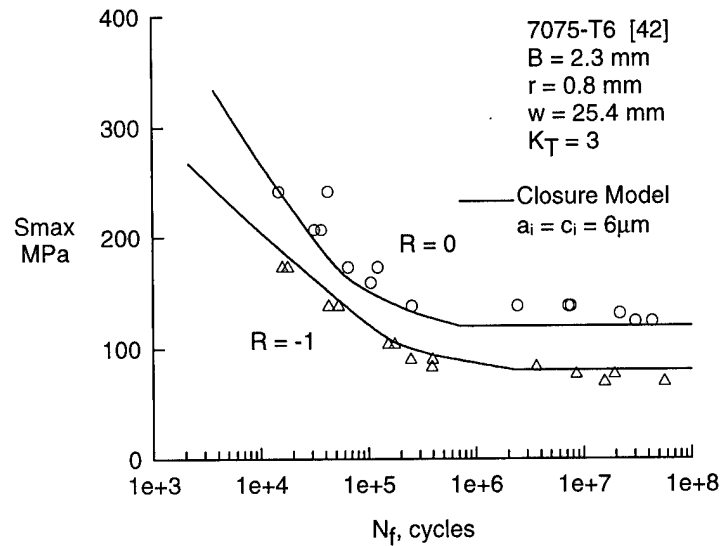

Figure 12. Measured and Calculated Fatigue Lives for 7075-T6 Aluminum Alloy Circular-Hole Specimens.
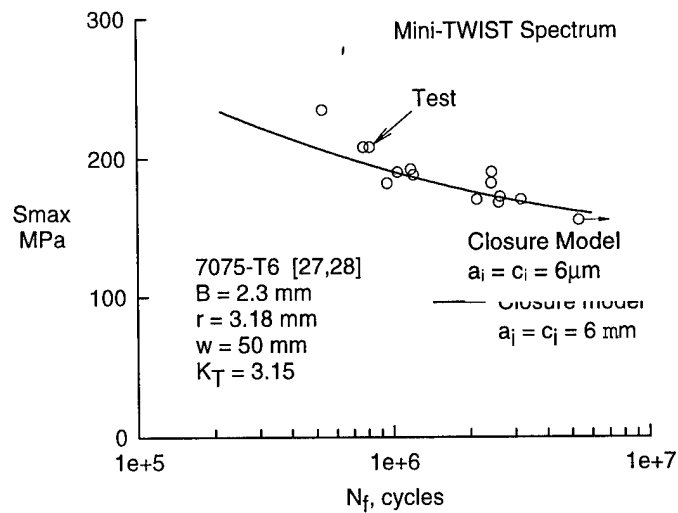
Figure 13. Measured and Predicted Fatigue Lives for 7075-T6 Aluminum Alloy SENT Specimens Under Mini-TWIST Spectrum Loading.

Fatigue tests were conducted on Ti-6Al-4V titanium alloy double-edge notch tension (DENT) specimens (Figure 2d) in the AGARD Engine Disc Cooperative Test Programme (Ref. 31). These results (symbols) are shown in Figure 14 for two fan disc forgings. To make fatigue-life calculations, the baseline ΔK_{eff} -rate relation, shown in Figure 5, was used to calculate the life of the titanium specimens. Because no information on crack-initiation behavior was given in Reference 31, life calculations were made on initial crack sizes that would bound the experimental data, like the equivalent-initial-flaw size (EIFS) concept [18]. The solid curves show the calculations for an initial semicircular surface crack of a_i = 2 and 20 μm at the notch root. The solid symbol on the stress axis denotes where the net-section stress is equal to the ultimate tensile strength. Because of the notch configuration, notch strengthening is expected and the upper plateau is an estimate for the maximum net-section stress. In a microstructural analysis, Wanhill and Looije [44] found that the primary α-grains were about 10 μm in diameter and the transformed and aged β-grains were about 20 μm in diameter for these fan disc materials. Using a 10 μm flaw in the analysis, the predicted behavior would fit the mean of the test data very well. Further study is needed on these materials to see if cracks of these sizes would be present early in life or to see if the baseline curve (Figure 5) is appropriate for small cracks. For low ΔK_{eff} values, small cracks in the titanium alloys may grow faster than large cracks, as observed by Lanciotti and Galatolo (Ref. 45).
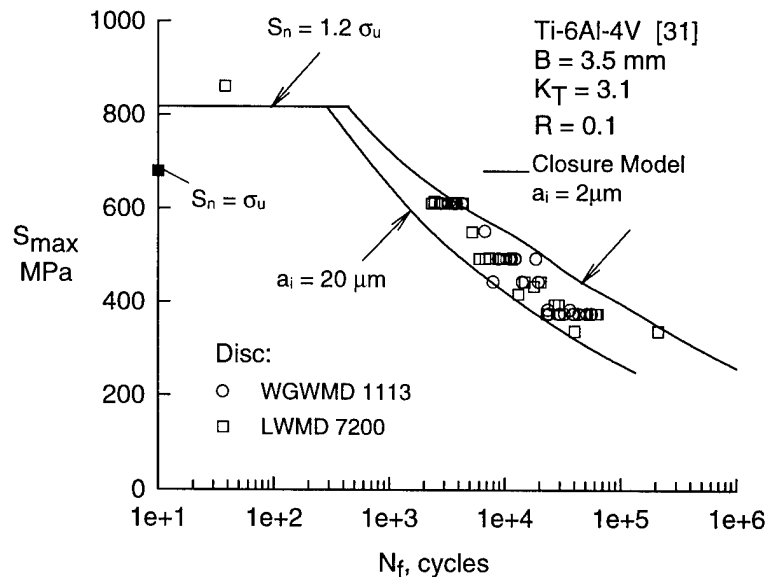
Figure 14. Measured and Calculated Fatigue Lives for Ti-6Al-4V Titanium Alloy DENT Specimens.

Swain et al. [29] conducted fatigue and small-crack tests on 4340 steel single-edge notch tension specimens. These tests were conducted under both constant-amplitude and spectrum loading. Inspection of fatigue surfaces showed that in each case a crack had initiated at an inclusion particle defect. The initiation site was either at a spherical (calcium-aluminate) or a stringer (manganese sulfide) inclusion particle. Examination of initiation sites for over 30 fatigue cracks produced information on the distribution of crack initiation site dimensions. The spherical particle defects range in size from 10 to 40 μm in diameter. The stringer particles were typically 5 to 20 μm in the thickness direction and range up to 60 μm in the width direction. The median values of the defect dimensions measured were $a_i = 8$ μm and $c_i = 13$ μm. An equivalent area (semicircular) defect is 10 μm. This initial defect size will be used later to predict fatigue lives.

Figure 15 shows test data (symbols) obtained from notched specimens tested at three stress ratios. Using a 10-μm initial semicircular surface crack located at the center of the notch and the baseline crack-growth relation (Figure 6), predicted fatigue lives are shown by the solid curves. A small-crack effective threshold, $(\Delta K_{eff})_{th}$, of 3.2 MPa√m was used to predict the endurance limits quite accurately. For the 4340 steel, the large- and small-crack thresholds were the same.
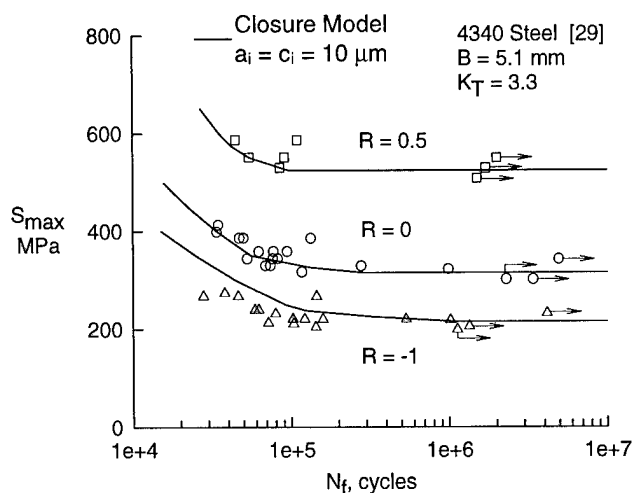
Figure 15. Measured and Predicted Fatigue Lives for 4340 Steel SENT Specimens.

The results of fatigue life tests under the Felix/28 load sequence are shown in Figure 16 as symbols. The type of defect that initiated the fatigue failures are identified. Predictions of total fatigue life under the Felix/28 load spectrum were made using the closure model by calculating the number of cycles necessary to grow a crack from the assumed initial defect

size (10 μm), located at the center of the notch root, to failure. The predicted results agreed well with the test data.
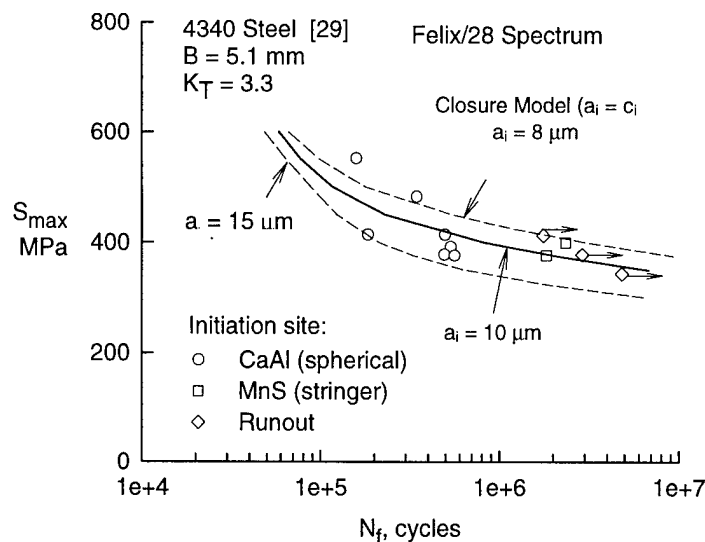
Figure 16. Measured and Predicted Fatigue Lives for 4340 Steel SENT Specimens Under Felix/28 Spectrum Loading.

CONCLUDING REMARKS

A plasticity-induced crack-closure model was used to correlate large-crack growth rate data on two aluminum alloys, a titanium alloy, and a steel under constant-amplitude loading for a wide range of stress ratios. A constraint factor, which accounts for three-dimensional state-of-stress effects, was used in determining the effective stress-intensity factor range against rate relations. Comparisons made between measured and predicted small-crack growth rates for an aluminum alloy showed that the closure model could predict the trends that were observed in the tests. Using the closure model and some microstructural features, such as inclusion-particle sizes, a total fatigue-life prediction method was demonstrated. Calculated and predicted fatigue lives for unnotched and notched specimens made of two aluminum alloys compared well with test data under constant-amplitude and spectrum loading. Calculated fatigue lives for a Ti-6Al-4V titanium alloy were bounded by using initial crack sizes of 2 and 20 μm in the life-prediction method. Similarly, predicted fatigue lives for notched specimens made of a high-strength steel also compared well with test data under constant-amplitude and spectrum loading.

351

ACKNOWLEDGMENT

NOMENCLATURE

a	Crack length in thickness (B) direction, mm
a_i	Initial defect or crack length in B-direction, mm
b	Defect or void half height, mm
B	Specimen thickness, mm
c	Crack length in width (w) direction, mm
c_i	Initial defect or crack length in w-direction, mm
F	Boundary-correction factor
K_F	Elastic-plastic fracture toughness in TPFC, MPa$\sqrt{m}$
m	Fracture toughness parameter in TPFC
N	Number of cycles
N_f	Number of cycles to failure
R	Stress ratio (S_{min}/S_{max})
r	Notch or hole radius, mm
S	Applied stress, MPa
S'_o	Crack-opening stress, MPa
S_{max}	Maximum applied stress, MPa
S_{min}	Minimum applied stress, MPa
w	Specimen width or half width (see Figure 2), mm
α	Constraint factor
ΔK	Stress-intensity factor range, MPa$\sqrt{m}$
ΔK_{eff}	Effective stress-intensity factor range, MPa$\sqrt{m}$
$(\Delta K_{eff})_T$	Effective stress-intensity factor range, MPa$\sqrt{m}$
$(\Delta K_{eff})_{th}$	Small crack ΔK_{eff} threshold, MPa$\sqrt{m}$
ΔK_{th}	Large crack ΔK threshold, MPa$\sqrt{m}$
ρ	Plastic-zone size, mm
σ_o	Flow stress (average of σ_{ys} and σ_u), MPa
σ_{ys}	Yield stress (0.2 percent offset), MPa
σ_u	Ultimate tensile strength, MPa
ω	Cyclic-plastic-zone size, mm

REFERENCES

1.   Pearson, S., "Initiation of Fatigue Cracks in Commercial Aluminum Alloys and the Subsequent Propagation of Very Short Cracks," Engineering Fracture Mechanics, Vol. 7, No. 2, 1975, pp. 235-247.

2.   Ritchie, R. O. and Lankford, J., eds., Small Fatigue Cracks, The Metallurgical Society, Inc., Warrendale, PA, 1986.

3.   Miller, K. J. and de los Rios, E. R., eds., The Behaviour of Short Fatigue Cracks, European Group on Fracture, Publication No. 1, 1986.

4.   Zocher, H., ed., Behaviour of Short Cracks in Airframe Components, AGARD CP-328, 1983.

5.   Newman, J. C., Jr. and Edwards, P. R., "Short-Crack Growth Behaviour in an Aluminum Alloy - An AGARD Cooperative Test Programme," AGARD R-732, 1988.

6.   Edwards, P. R. and Newman, J. C., Jr., eds., Short-Crack Growth Behaviour in Various Aircraft Materials, AGARD Report No. 767, 1990.

7.   Raju, I. S. and Newman, J. C., Jr., "Stress-Intensity Factors for a Wide Range of Semi-Elliptical Surface Cracks in Finite-Thickness Plates," Engineering Fracture Mechanics, Vol. 11, No. 4, 1979, pp. 817-829.

8.   Newman, J. C., Jr. and Raju, I. S., "Stress-Intensity Factor Equations for Cracks in Three-Dimensional Finite Bodies," ASTM STP 791, Vol. I, 1983, pp. 238-265.

9.   El Haddad, M., Dowling, N., Topper, T., and Smith, K., "J Integral Application for Short Fatigue Cracks at Notches," International Journal of Fracture, Vol. 16, 1980, pp. 15-30.

10. Newman, J. C., Jr., "Fracture Mechanics Parameters for Small Fatigue Cracks," Small Crack Test Methods, ASTM STP 1149, J. Allison and J. Larsen, eds., 1992, pp. 6-28.

11. Leis, B., Kanninen, M., Hopper, A., Ahmad, J., and Broek, D., "Critical Review of Fatigue Growth of Short Cracks," Engineering Fracture Mechanics, Vol. 23, 1986, pp. 883-898.

12. Elber, W., "The Significance of Fatigue Crack Closure," Damage Tolerance in Aircraft Structures, ASTM STP 486, 1971, pp. 230-242.

13. Nisitani, H. and Takao, K. I., "Significance of Initiation, Propagation and Closure of Microcracks in High Cycle Fatigue of Ductile Materials," Engineering Fracture Mechanics, Vol. 15, No. 3, 1981, pp. 455-456.

14.   Minakawa, K. and McEvily, A. J., "On Near-Threshold Fatigue-Crack Growth in Steels and Aluminum Alloys," Proceedings of the International Conference on Fatigue Thresholds, Vol. 2, 1981, pp. 373-390.

15.   Newman, J. C., Jr., "A Nonlinear Fracture Mechanics Approach to the Growth of Small Cracks," Behaviour of Short Cracks in Airframe Components, H. Zocher, ed., AGARD CP-328, 1983, pp. 6.1-6.26.

16.   Newman, J. C., Jr., "A Crack-Closure Model for Predicting Fatigue-Crack Growth under Aircraft Spectrum Loading," Methods and Models for Predicting Fatigue Crack Growth under Random Loading, J. Chang and C. Hudson, eds., ASTM STP 748, 1981, pp. 53-84.

17.   Newman, J. C., Jr., "A Crack-Opening Stress Equation for Fatigue Crack Growth," International Journal of Fracture, Vol. 24, 1984, R131-R135.

18.   Rudd, J., Yang, J., Manning, S., and Garver, W., "Durability Design Requirements and Analysis for Metallic Airframes," Design of Fatigue and Fracture Resistant Structures, ASTM STP 761, P. R. Abelkis and C. M. Hudson, eds., 1982, pp. 133-151.

19.   van Dijk, G. and deJonge, J., "Introduction to a Fighter Loading Standard for Fatigue Evaluation—FALSTAFF," NLR MP 75017 U, Nationaal Lucht-en Ruimtevaartlaborium, 1975.

20.   Huck, M., Schutz, W., Fischer, R., and Kobler, H. G., "A Standard Random Load Sequence of Gaussian Type Recommended for General Application in Fatigue Testing," IABG Report No. TF-570 or LBF Report No. 2909, Germany, 1976.

21.   deJonge, J. B., Schutz, D., Lowak, H., and Schijve, J., "A Standardized Load Sequence for Flight Simulation Tests on Transport Aircraft Wing Structures (TWIST)," NLR TR-73029 U, Nationaal Lucht-en Ruimtevaartlaborium, Netherlands, 1973.

22.   Lowak, H., deJonge, J. B., Franz, J., and Schutz, D., "Mini-TWIST—A Shortened Version of TWIST," LBF Report No. TB-146, Laboratorium fur Betriebsfestigkeit, Germany, 1979.

23.   Edwards, P. R. and Darts, J., "Standardized Fatigue Loading Sequences for Helicopter Rotors (Helix and Felix) - Part 2: Final Definition of Helix and Felix," RAE Technical Report 84085, 1984.

24.   Hudson, C. M., "Effect of Stress Ratio on Fatigue-Crack Growth in 7075-T6 and 2024-T3 Aluminum Alloy Specimens," NASA TN D-5390, 1969.

25.   Phillips, E. P., "The Influence of Crack Closure on Fatigue-Crack Growth Thresholds in 2024-T3 Aluminum Alloy," ASTM STP 982, 1988, pp. 505-515.

26. Dubensky, R. G., "Fatigue Crack Propagation in 2024-T3 and 7075-T6 Aluminum Alloys at High Stress," NASA CR-1732, March 1971.

27. Newman, J. C., Jr., Wu, X. R., Swain, M. H., Zhao, W., Phillips, E. P., and Ding, C. F., "Small-Crack Growth Behavior in High-Strength Aluminum Alloys - A NASA/CAE Cooperative Program," 18th Congress International Council of Aeronautical Sciences, Beijing, PRC, September 1992, pp. 799-820.

28. Newman, J. C., Jr., Wu, X. R., Venneri, S. L., and Li., C. G., "Small-Crack Effects in High-Strength Aluminum Alloys - A NASA/CAE Cooperative Program," NASA Reference Publication 1309, 1994.

29. Swain, M. H., Everett, R. A., Newman, J. C., Jr., and Phillips, E. P., "The Growth of Short Cracks in 4340 Steel and Aluminum-Lithium 2090," AGARD R-767, P. R. Edwards and J. C. Newman, Jr., eds., 1990, pp. 7.1-7.30.

30. Raizenne, M. D., "AGARD SMP Sub-Committee 33 Engine Disc Test Programme Fatigue-Crack Growth Rate Data and Modeling Cases for Ti-6Al-4V, IMI-685 and Ti-17," LTR-ST-1785, National Research Council, Canada, 1990.

31. Mom, A. J. A. and Raizenne, M. D., eds., AGARD Engine Disc Cooperative Test Programme, AGARD Report No. 766, 1988.

32. Powell, B. E. and Henderson, I., "The Conjoint Action of High and Low Cycle Fatigue," AFWAL-TR-83-4119, 1983.

33. Dugdale, D. S., "Yielding of Steel Sheets Containing Slits," Journal of Mechanics and Physics of Solids", Vol. 8, No. 2, 1960, pp. 100-104.

34. Blom, A. F., Wang, G. S., and Chermahini, R. G., "Comparison of Crack Closure Results Obtained by 3-D Elastic-Plastic FEM and Modified Dugdale Model," Proceedings 1st International Conference on Computer Aided Assessment and Control of Localized Damage, Portsmouth, England, 1990, pp. 57-68.

35. Schijve, J., "Significance of Fatigue Cracks in Micro-Range and Macro-Range," Fatigue Crack Propagation, ASTM STP 415, 1967, pp. 415-459.

36. Newman, J. C., Swain, M. H., and Phillips, E. P., "An Assessment of the Small-Crack Effect for 2024-T3," Small Fatigue Cracks, R. Ritchie and J. Lankford, eds., 1986, pp. 427-452.

37. Newman, J. C., Jr., "FASTRAN II—A Fatigue Crack Growth Structural Analysis Program," NASA TM 104159, 1992.

38. Newman, J. C., Jr., "Effects of Constraint on Crack Growth under Aircraft Spectrum Loading," Fatigue of Aircraft Materials, A. Beukers et al., eds., Delft University Press, 1992, pp. 83-109.

39.   Newman, J. C., Jr., "Fracture Analysis of Various Cracked Configurations in Sheet and Plate Materials," ASTM STP 605, 1976, pp. 104-123.

40.   Lankford, J., "The Growth of Small Fatigue Cracks in 7075-T6 Aluminum," Fatigue of Engineering Materials and Structures, Vol. 5, 1982, pp. 233-248.

41.   Grover, H. J., Hyler, W. S., Kuhn, P., Landers, C. B., and Howell, F. M., "Axial-Load Fatigue Properties of 24S-T and 75S-T Aluminum Alloy as Determined in Several Laboratories," NACA TN-2928, 1953.

42.   Landers, C. B. and Hardrath, H. F., "Results of Axial-Load Fatigue Tests on Electropolished 2024-T3 and 7075-T6 Aluminum Alloy Sheet Specimens with Central Holes," NACA TN-3631, 1956.

43.   Bowles, C. Q. and Schijve, J., "The Role of Inclusions in Fatigue Crack Initiation in an Aluminum Alloy," International Journal of Fracture, Vol. 9, No. 2, 1973, pp. 171-179.

44.   Wanhill, R. J. H. and Looije, C. E. W., "Fractographic and Microstructural Analysis of Fatigue Crack Growth in Ti-6Al-4V Fan Disc Forgings," AGARD Engine Disc Cooperative Test Programme, T. Pardessus, E. Jany, and M. D. Raizenne, eds., AGARD Report 766 (addendum), 1993, pp. 2.1-2.88.

45.   Lanciotti, A. and Galatolo, R., "Short Crack Observations in Ti-6Al-4V Under Constant-Amplitude Loading", Short-Crack Growth Behaviour in Various Aircraft Materials, P. R. Edwards and J. C. Newman, Jr., eds., AGARD R-767, 1990, pp. 10.1-10.7.

FULL-SCALE GLARE FUSELAGE PANEL TESTS[1]

Roland W. A. Vercammen and Harold H. Ottens
National Aerospace Laboratory (NLR)
Amsterdam, The Netherlands

SUMMARY

A GLARE fuselage panel, representative of the crown section of the Fokker 100 fuselage just in front of the wing, has been tested in the curved fuselage panel test facility that was recently commissioned at the National Aerospace Laboratory (NLR). Panels are loaded by internal air pressure resulting in tangential stresses in the panel and by axial loading representative of both the cabin pressure and the fuselage bending due to taxiing and gust loading. A fatigue test was performed in which 180,000 flights (two lifetimes) were simulated. After the fatigue test no damage was observed. The fatigue test was followed by static tests to limit load and to ultimate load. Finally the panel was loaded to failure at 1.32 ultimate load. This paper will describe the test setup in some detail, demonstrate the obtained uniform strain distribution in the panel, show the fatigue loads applied at high test frequency, and present the results of the GLARE fuselage panel tests which proof that the use of GLARE leads to a substantial weight reduction without affecting the fatigue or static strength.

INTRODUCTION

In fuselage design studies there will always be the necessity to test components in a realistic way. The fuselage panel test facility developed and built at the National Aerospace Laboratory (NLR) (fig. 1) offers the possibility to test fuselage skin sections, with curvatures ranging from panels of relatively small aircraft like the Fokker 50 to panels from relatively large aircraft like the Airbus A300, at a high fatigue testing speed (ref. 1). The fatigue test loads simulate flight simulation loading conditions by loads in circumferential direction caused by cabin pressurization and axial loads representative of both the cabin pressure and the fuselage bending due to taxiing and gust loading. The new fuselage panel test facility has also the possibility to perform static strength and residual strength tests.

In order to verify the applicability of GLARE A[2] as a fuselage skin material Fokker designed and built a Fokker 100 fuselage panel with a GLARE A skin and GLARE N

---

stringers, representative of the crown section just in front of the wing. GLARE A as skin material is weight favorable compared to GLARE C when the amount of necessary doublers for countersunk riveting is restricted to only doublers in the axial lapjoints. In the frame-skin attachments no doublers were required as the frames were connected to the stringers by means of cleats instead of to the skin by means of castellations as is normally done by Fokker. Applying cleats led to a panel design with a threefold test objective:

- Verification of the applicability of GLARE A as a fuselage skin material for loading conditions which are representative of the crown section of the Fokker 100 fuselage.

- Generation of test evidence on the static strength and fatigue behavior of rigid stringer-frame attachments in the GLARE fuselage.

- Determining the deterioration of the static strength of the GLARE skin after two times the design life (2 × 90,000 flights).

The overall panel dimensions are 1210 mm × 3030 mm containing five aluminum frames with a pitch of 500 mm, seven stringers with a pitch of 147 mm, seven stringers couplings and a longitudinal riveted lap joint in the panel center (fig. 2). One of the frames is a Z-shaped frame, the others are C-shaped frames. A complete top section made of GLARE A with GLARE N stringers and rigid stringer-frame attachments has a weight that is 63 percent of the current Fokker 100 design in aluminum (ref. 2).

TEST FACILITY

Fuselage skins of most aircraft are subjected to biaxial loads, owing to bending and pressurization of the fuselage. In evaluating damage tolerance properties of candidate fuselage structures and materials, it is highly desirable that curved structures are tested under biaxial loading conditions. For this purpose one generally uses a barrel test setup. This is a full-size cylindrical pressure vessel consisting of several interconnected fuselage panels. A barrel test setup, however, has some features which make it less flexible and therefore less attractive for studies not directly related to a particular aircraft design. The radius of curvature is fixed, a large number of panels have to be tested simultaneously and the test frequency is rather low. In addition, barrel tests are expensive due to the large number of panels and the long testing time. The panel test facility at NLR was developed to avoid the aforementioned disadvantages. In the curved fuselage panel test facility, which has flexibility with regard to panel diameter, panel width, and panel length, a single fuselage panel can be tested at a relatively high testing speed.

---

[2] GLARE A=GLARE 3-2/1-0.3: 2×(0.3 mm 2024 sheet) + (0.25 mm cross-ply glass prepreg)
   GLARE N=GLARE 1-3/2-0.3: 3×(0.3 mm 7475 sheet) + 2×(0.25 mm UD glass prepreg)
   GLARE C=GLARE 3-3/2-0.2: 3×(0.2 mm 2024 sheet) + 2×(0.25 mm cross-ply glass prepreg)

The major components of the test facility are the main frame, the pressure chamber, and the load introduction systems (fig. 1). The main frame is a very stiff steel structure. It consists of heavy bottom and top beams and two vertical main columns. A pyramidal shaped frame, which houses the hydraulic actuator, is mounted above the top beam and two auxiliary vertical columns. The panel is mounted in the frame such that the center of gravity of its cross section is in the working line of the actuator. The height of the test facility is about 7.2 m; the width is about 4.5 m. The pressure chamber is formed by a seal and base structure connected to a transport system. The base structure of the pressure chamber is formed by a stiffened base plate and two support beams which are bolted to the vertical columns of the main structure. The base plate has a large central hole for air supply. At the front side the base plate has curved wooden blocks around the edges which form the side walls of the pressure chamber. An inflatable inner seal is mounted on the wooden blocks and the pressure chamber is closed by the panel. In order to accomplish an air-tight seal without net radial force acting on the panel edges, an inflatable outer seal is mounted at the outside of the panel just opposite the inner seal. The outer seal is bonded on the reaction frame, which consists of an open rectangular steel frame with curved wooden blocks. With the transport system the pressure chamber can easily be shifted aside during the test, which significantly improves the inspectability of the test panel. The chamber pressurization, axial loads, and seal pressurization are regulated by a control system.

Pressurization of the fuselage panel is reacted to the test frame leading to tangential stresses in the skin and normal stresses in the frames. The ratio of the stresses in the skin and frames is determined and can be adjusted by the stiffness ratio of the skin-to-testframe and frame-to-testframe connections. The tangential stresses in the skin are taken out by bonded glass fibers. The loads in the frames are transferred to steel rods. Therefore the ends of the panel frames are locally reinforced. The wooden blocks have several holes through which the panel frame tensile rods are guided. The openings between the panel frame tensile rods and the hole edges are sealed air-tight with silicone rubber collars. In axial direction the panel ends are loaded by rods which are connected to the panel ends by steel brackets. At these axial panel ends the stringers are ended and the stringers loads are taken by a gradually increased skin thickness (fig. 2). This makes it possible to seal directly on the skin of the panel.

The advantages of using unidirectional glass fibers is that the loads are very evenly introduced over the length of the panel (ref. 3). Therefore hardly any distance is required for stress redistribution, i.e., the stress distribution is uniform at a very small distance from the panel edge. In addition, the use of unidirectional fibers does not result in local stiffening of the panel edges in axial direction. The length of the glass fiber sheets was chosen sufficiently large to limit the rotation of the fibers at the upper side of the panel owing to axial elongation of the panel. The small rotation that occurs during the test does not significantly alter the load transfer through the panel. The glass fibers are bonded to steel tangential plates. Because of their large width, the tangential plates act more or less as hinges. The outward movement of the panel due to pressurization is therefore nearly radial and will not result in a significant change in the shape of the panel from circular to oval. The tangential clamping

system was designed such that the angle between tangential plates and the vertical column was adjustable to allow for a large range of panel diameters to be tested.

PANEL LOADS

The GLARE panel is designed for the Fokker 100 loads in the crown section at Fuselage Station 14911. The axial loading sequences of the fatigue spectrum are derived from the spectrum applied in the Fokker 100 full-scale test (ref. 4). The axial load is written as

$$F_{axial} = a_1 \times M_y + a_2 \times \Delta p$$

with

F_{axial} = axial load in fuselage panel
M_y = bending moment at Fuselage Station 14911
Δp = cabin pressure
$a_{1,2}$ = Fuselage Station dependent constants

The spectrum consists of 36 repeating testblocks of 5000 flights. Each testblock of 5000 flights is subdivided in four subblocks of 1250 flights. Three subblocks are exactly equal; the fourth block is equal but for one severe flight. Within this spectrum eight flight types with different gust loading severity have been defined. Figure 3 shows the axial loading and frequency per 5000 flights for these typical eight flight types. Each flight has five segments: ground, initial climb, climb/descent, cruise, and approach. During the ground segments the cabin pressure Δp = zero, during the cruise segment $\Delta p = \Delta p_{max}$. In case of climb/descent the cabin pressure varies between zero and Δp_{max}.

The fatigue test is followed by static tests. The GLARE panel is subjected to one limit load case, two ultimate load cases, and a failure strength test. These static load cases are intended to demonstrate that after two times the design life (2 × 90,000 flights) and possible undetectable cracks in the GLARE skin the residual strength is still sufficient to carry limit and ultimate load. The limit load case equals cabin pressure $\Delta p = \Delta p_{max}$ plus limit load bending moment. The first ultimate load case is the cabin pressure ultimate load case: $\Delta p = 2 \times \Delta p_{max}$. The second ultimate load case equals 1.5 × [cabin pressure $\Delta p = \Delta p_{max}$ plus limit load bending moment]. The second ultimate load case is followed by the failure strength test at $\Delta p = \Delta p_{max}$ by increasing the axial load until failure of the panel.

STRAIN DISTRIBUTION

At fastening of a test panel, the length of each axial tensile rod and frame loading rod can be adjusted with nut keys such that over the panel width and length a uniform strain or stress distribution is achieved when the panel is loaded. The amount of load that is taken out of the panel frames also depends on the stiffness of the rods. The rods are therefore panel

dependent parts and have load cells incorporated. The nut keys and the output of the load cell in each panel frame can be used for proper adjustments.

The strain distribution in the middle of the panel, obtained by using the glass fibers, frame loading rods in tangential direction, and tensile rods at the reinforced, nonstiffened panel ends in axial direction, is shown in figures 4 and 5. These graphs visualize a smooth distribution of the axial and tangential strain levels and a uniform tangential strain distribution within 100 mm of the panel edges loaded with glass fibers. Strain level variations at the gauges R13a, R14c, and R16a are due to the lap-joint, radius differences of panel halves, and stringer couplings. The tangential strain distribution over the panel length is given in figure 6. Over the panel width the influence of the stringers run-outs and skin reinforcements are negligible after the first frame (fig. 7).

At constant bending moment ($Fax_{bending}$ = constant), the radial expansion of the panel increased due to raising cabin pressure. When, at constant cabin pressure ($Fax_{\Delta p}$ = constant), the axial force was raised the radial expansion of the panel decreased. The panel displaced inwards to the pressure chamber to resist the increasing tangential contraction due to the Poisson's ratio effect due to the axial extension. The increase of the tangential contraction and the displacement of the panel inwards led to a decrease of the tangential strains in the skin.

FATIGUE TEST

During the fatigue test the defined 180,000 flights were applied. The testing frequency was about 10,000 flights per 24 hours. The axial loads had an accuracy of 0.5 percent, the chamber pressure reproduced within 3 percent. The panel was inspected by eddy current at the axial lap joint and stringer run-outs and checked visually at the stringer couplings, doubler run-outs, stringers at the connection with the cleats, frames at the connection with the cleats, and load introduction points of the frames. In accordance with the lifetime predictions (ref. 2) no cracks or damages were found.

STATIC TESTS

The fatigue test was followed by static tests. The first static load case was the limit load test. For this load case, figure 7 gives the axial strain levels from station zero till the fourth frame. Clearly visible is the pillowing of the skin. The lower axial strains in the second and third bay are caused by the stringer couplings and the difference in stiffnesses of the frames. During this limit load test the panel extended linearly, and no permanent deformations took place. Some results of the first ultimate load case at $2 \times \Delta p$ are visualized in figure 5. Figure 5 shows the tangential strain levels in the middle of the panel. The axial strain levels are less than 20 percent of the tangential levels. Like during the limit load, test

pillowing occurred and the panel expanded linearly without permanent deformations. After the $2 \times \Delta p$ ultimate load case, the second ultimate load test was applied. No final failure occurred and the strain distribution was, except for plasticity which occurred above limit load, conformed to the distribution during the limit load test. Conclusion: the ultimate load tests showed sufficient residual strength of the GLARE panel after two lifetimes of fatigue loading.

To determine the deterioration of the panel after two lifetimes of fatigue loading, the first few load steps of the limit load and ultimate load tests were compared with reference tests performed before the fatigue test. The deterioration of strain levels in the axial direction was a small fixed value of 50 μstrain caused by settling of the brackets, doublers, and rivets. In the tangential direction negligible differences (≤ 1.0 percent) were noticed.

After the second ultimate load test, the cabin pressure was fixed at $\Delta p = \Delta p_{max}$ and the panel was axially loaded to failure. The axial strains are visualized in figure 8. Failure occurred at an axial load of 770 kN, i.e., $1.32 \times$ axial ultimate load. This axial load is 15 percent higher than the theoretically expected axial failure load (ref. 2). The skin failed between the third and fourth frame at the cross section of the last rivets of the stringers couplings (fig. 9). Conclusion: in the crown section of the Fokker 100, GLARE A as fuselage skin material and GLARE N as stringer material are applicable. The skin, lap joint, and rigid stringer frame attachments (cleats) had enough fatigue and static strength.

CONCLUSIONS

The new full-scale fuselage panel test facility operated correctly. The load introduction in the panel in axial and tangential direction was uniform and realistic fatigue loads due to cabin pressure and fuselage bending could be applied at high frequency (10,000 flights per 24 hours).

The conclusions with regard to the Fokker GLARE panel are:

- No cracks were found in lap joints, cleats, stringers, skin, frames, and stringer couplings after the two lifetimes fatigue test (inspection was done visually and by eddy current).

- The panel as a whole did not permanently deform at limit load.

- In both ultimate load test cases, no failure occurred.

- Final failure occurred at $1.32 \times$ axial ultimate load, which is 15 percent higher than theoretically expected.

- GLARE A can be used as fuselage skin material in the crown section of the Fokker 100. GLARE N can be applied as stringer material.

- The rigid stringer-frame attachments (cleats) are applicable in the crown section of the Fokker 100 fuselage.

Because of the excellent fatigue behavior with sufficient static strength and a weight reduction of 37 percent, the designed GLARE panel proved the feasibility of GLARE as a fuselage material.

REFERENCES

1. De Jong, G. T.; Elbertsen, G. A.; Hersbach, H. J. C.; and van der Hoeven, W.: Development of a full-scale fuselage panel test methodology, NLR contract report CR 95361 C, May 1995 (Restricted).

2. Wit, G. P.: Fuselage top panels tests (GLARE A), Stress Office Technical Data Sheet T.D. No avb7226, March 1995.

3. De Jong, G. T.; Botma, J.; and Ottens, H. H.: Stress analysis of the load introduction concept for the fuselage panel test facility, NLR report CR 95142 C, May 1995 (Restricted).

4. Jongebreur, A. A.; Louwaard, E. P.; and van der Velden, R. V.: Damage tolerance test program of the Fokker 100, ICAF Doc. 1490, Pisa, May 1985.
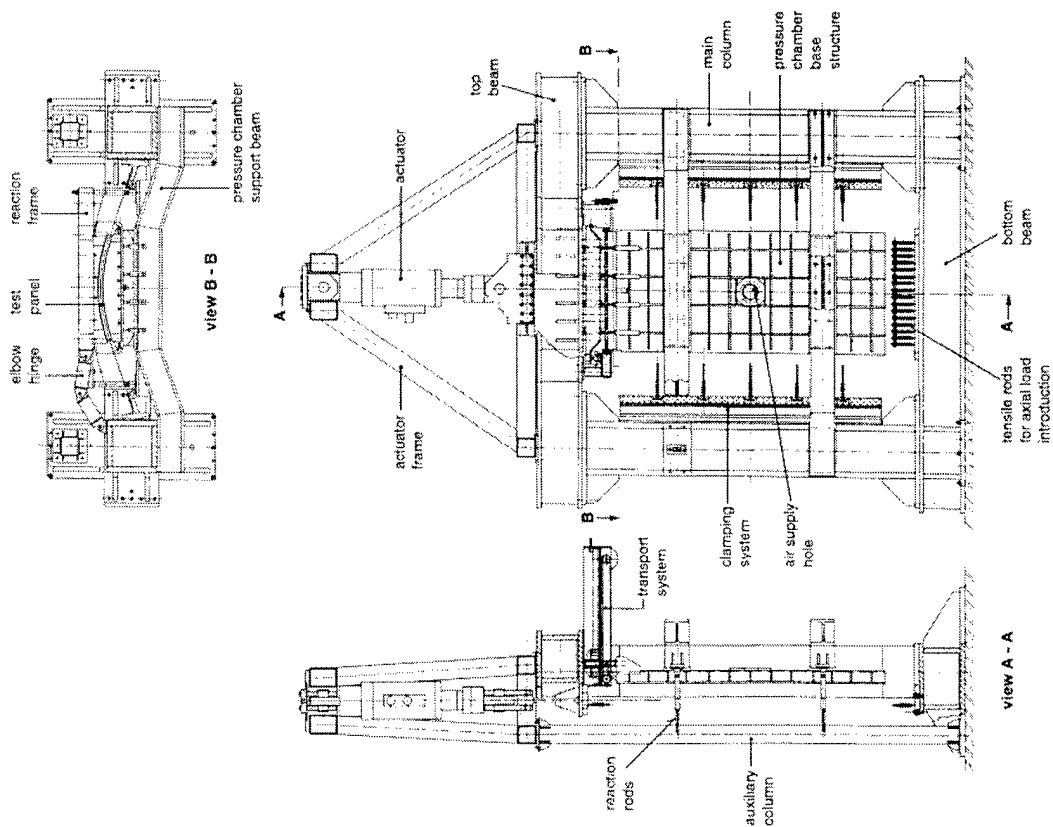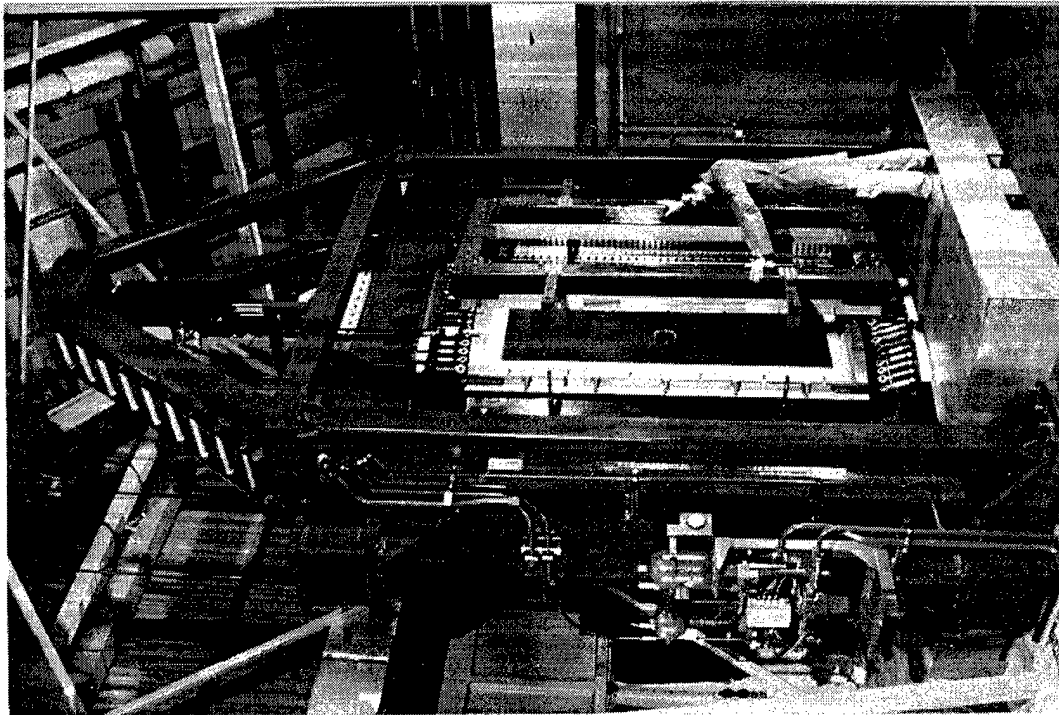
Figure 1. Fuselage panel test facility at NLR.
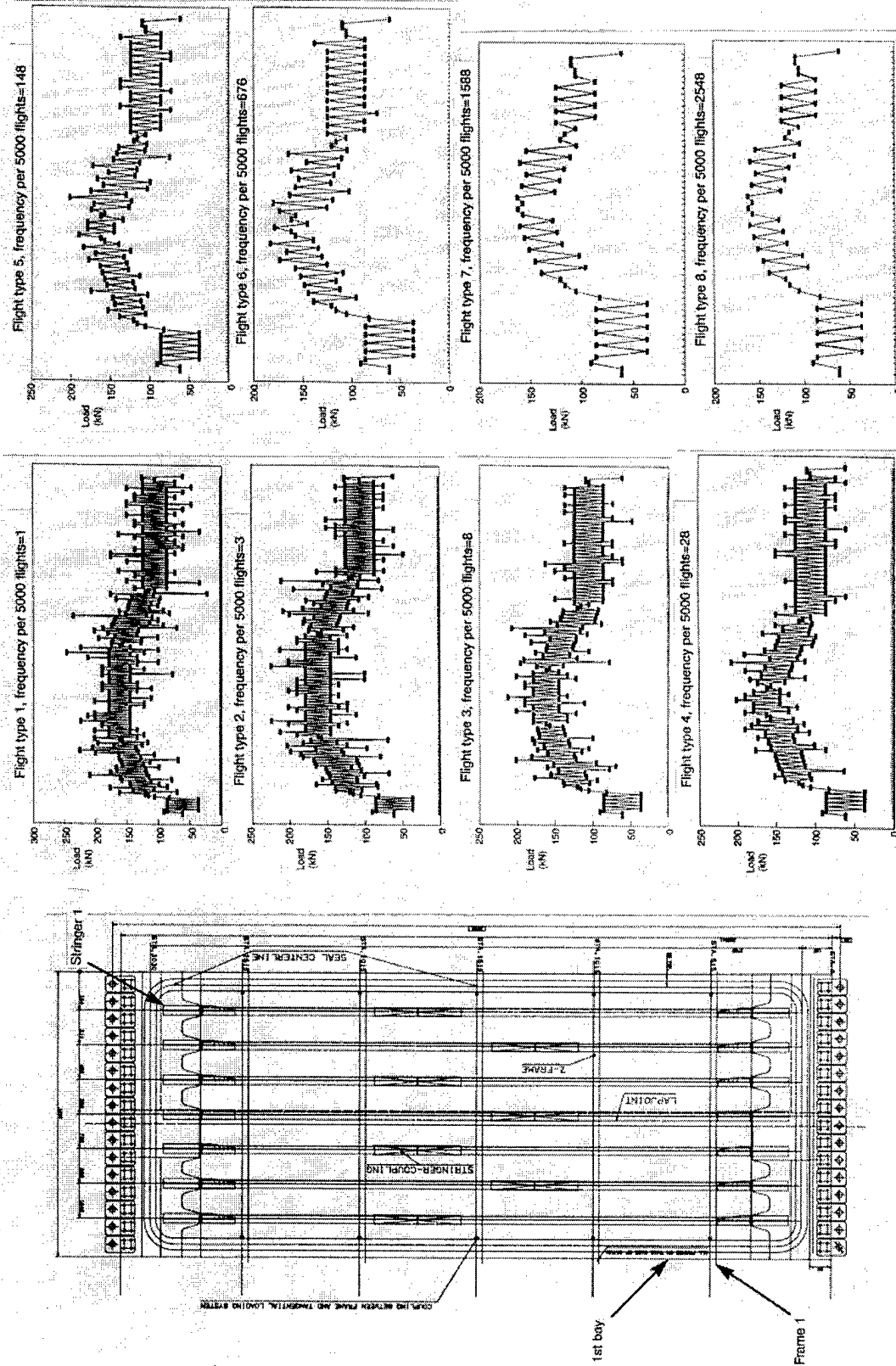
Figure 3. Axial load on the GLARE panel for the eight flight types.

Figure 2. GLARE panel.
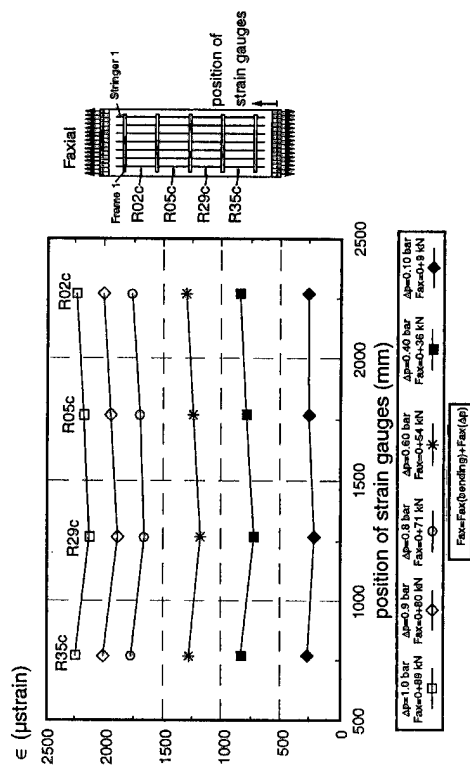
Figure 4. Axial strains during the Limit Load test, in the middle of the panel.
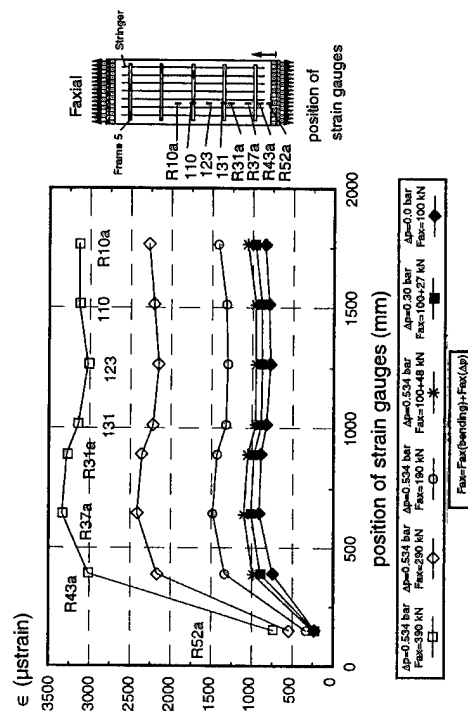
Figure 5. Tangential strains during 1st Ultimate Load test, in middle of the panel.

Figure 6. Tangential strains during 1st Ultimate Load test, over the panel length.

Figure 7. Axial strains during Limit Load test, between bottom and 4th frame.

crack

Figure 9. Inside of the panel after failure.

Figure 8. Axial strains during 2^d Ultimate Load test, between bottom and 4th frame.

A GRAPHIC USER INTERFACE (GUI) FRONT-END FOR PARAMETRIC SURVEY AND ITS APPLICATION TO COMPOSITE PATCH REPAIRS OF METALLIC STRUCTURE

H. Kawai, H. Okada, and S. N. Atluri
FAA Center of Excellence for
Computational Modeling of Aircraft Structures
Georgia Institute of Technology
Atlanta, GA 30332-0356

SUMMARY

A graphical user interface (GUI) front-end program Parametric Survey (ParS) has been developed on Microsoft Windows NT and Windows 95. It supports the parametric survey of analyses. In a parametric survey, a series of analyses of the same kind are performed with different input parameter sets, and multiple output parameter sets are collected. The data are visualized as charts which show the relationship between input and output parameters. Using ParS, a user can perform a parametric survey effectively through its automation of analyses and visualization functionality.

ParS is applied to a composite patch repair problem of aircraft fuselage. In this problem, a crack exists in a pressurized fuselage of an aircraft. Analyses for the effectiveness of the adhesive bonded composite repair were carried out. Some results of the analyses are presented.

INTRODUCTION

A Graphical User Interface (GUI) front-end program ParS (Parametric Survey) has been developed on Microsoft Windows NT and Windows 95 operating systems. It supports parametric survey of analyses. Figure 1 describes the typical sequences of a parametric survey.

An analysis, such as a simulation of structural mechanics, fluid dynamics, chemical reaction, or molecular dynamics requires a huge number of input data and generates a huge amount of output data. When an engineer has to solve more specific problems, such as cracks in aircraft fuselage or a flow field behind a car, these analyses are represented typically by a few key input and output parameters from the engineer's point of view. For example, in the case of the structural integrity analysis for an aircraft fuselage (with cracks), one needs to specify a few key input parameters such as the length of the crack, size of the fuselage model, and material properties. Other input data for the analysis program can be generated

369
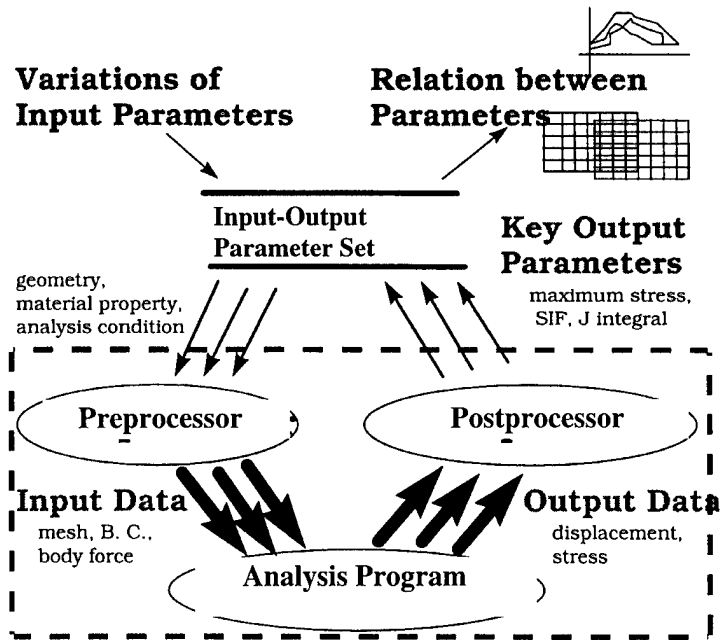
Figure 1. Parametric Survey.

automatically using a special purpose preprocessor. After the analysis is performed using a special purpose postprocessor, one can collect the key output parameters, such as displacement at specific points, stress-intensity factors, and J integral values, from output data generated from the analysis program (Figure 2).
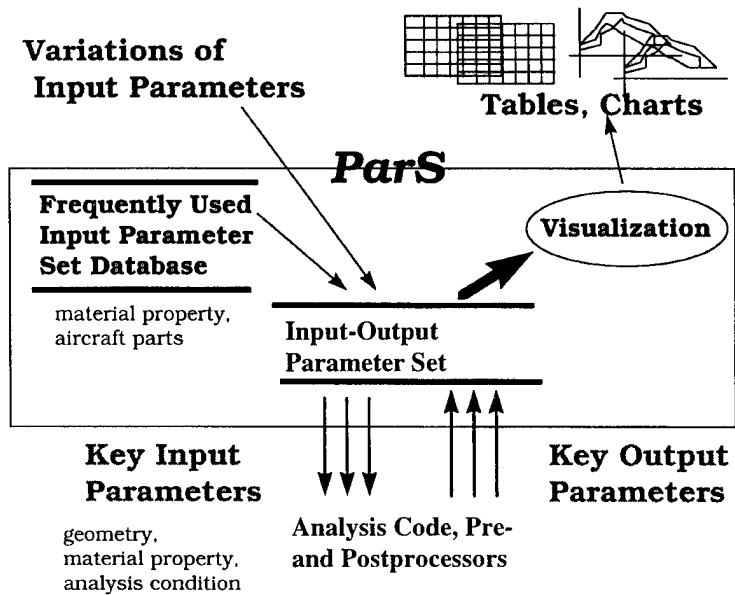
Figure 2. Schematic View of ParS.

In a parametric survey, a series of analyses of the same kind are performed with different input parameter sets. For each input parameter, variations may be specified, such as the minimum and maximum values of the variation and its interval of steps. After the parametric survey is finished, multiple output parameter sets are collected. These data are visualized later as tables or charts which show the relationship between the input and output parameters. Using ParS, a user can perform parametric survey effectively through its automation of analyses and visualization functionality.

Automatic Execution of Multiple Analyses for Parametric Survey

After specifying the values of input parameters, a single analysis is performed and one set of output parameters is obtained. With each input parameter, the user can specify variations of the parameter value such as minimum value, maximum value, and division count. In this case, multiple analyses are performed automatically with different values of the input parameter. When multiple input parameters are specified, the number of analyses carried out is a product of counts of all the input parameters which are changed. Collected output parameters can be displayed in a separate window in a table format.

Database of Input Parameter Set

Certain input parameters are grouped as a parameter set. If some specific values of input parameter sets are used frequently in a specific problem, the user may register these data into a database of the input parameter set. For example, in the case of structural analysis, input parameters such as Young's modulus and Poisson's ratio are grouped as a set of material properties, and specific values of each material such as iron and aluminum may be stored in an input parameter set database. The user can create his or her own database of input parameter sets. The user can refer to values of the input parameter sets later when the user specifies values of input parameters for analyses.

Visualization Method Using Line Chart and Table

After the output parameters are collected for a parametric survey, the relation between an input parameter and an output parameter can be visualized as a table or a line chart. The user can add multiple curves on a chart. A curve on the chart represents a set of data points which are pairs of output and input parameter values. When more than two input parameters are changed in the parametric survey, one input parameter is specified as the X-axis parameter, and the values of the other input parameters have to be fixed. In this case, ParS extracts a relevant portion of data for the curve from all the output parameter data of the parametric survey.

The developed system is very general so that many kinds of parametric surveys can be performed. The system accepts any type of analysis which has one or few input parameters and one or few output parameters.

ParS can call one or many external programs sequentially from itself as separate processes. Any kind of analysis programs, pre- and postprocessors which are executed in noninteractive mode can be accepted. Input and output parameters are transferred between ParS and external programs as text files. Both ParS and external programs are executed using Microsoft Windows NT or Windows 95 operating systems.

APPLICATION OF ParS TO PATCH PROBLEMS

We applied ParS to a composite patch repair problem of an aircraft fuselage [1]. In this problem, a crack exists in a pressurized fuselage of an aircraft. Analysis for the effectiveness of adhesive bonded composite repair is carried out. In this case, only a local region near the patch, which is extracted from the fuselage skin, is analyzed as a two-dimensional problem. This local analysis is divided into two stages. The first stage is the evaluation of stresses in the adhesive and the patch. The second stage is the calculation of stress-intensity factors using the finite element alternating method (FEAM). In this case, we assumed that the geometry of the problem is symmetric. The geometry model is described in Figure 3.
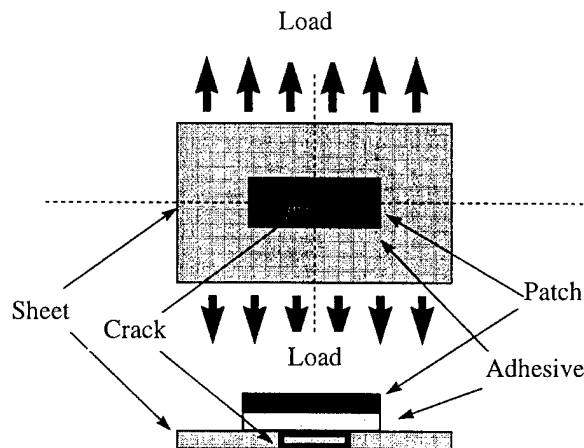
Figure 3. Composite Patch Repair Problem.

We selected several key input and output parameters, which are shown in Figure 4. As input parameters, geometry property, sheet material properties, patch, adhesive, and load are considered. Databases for the sheet material properties and patch are prepared. For example, boron epoxy, carbon epoxy, Al 2024-T3, and GLARE are supplied as sheet material properties. As output parameters, stress-intensity factors, especially K_I, are obtained in patched cases and unpatched cases. Note that input parameters related to patch and adhesive have no meaning in the case of unpatched analyses.

372

Input Parameters	Output Parameters
Geometric Parameters sheet width, height, thickness, patch width, height, thickness, adhesive thickness, crack length **Sheet Material Properties** Young's modulus, Possion's ratio **Patch Material Properties** Young's modulus, Possion's ratio, shear modulus **Adhesive Material Properties** shear modulus **Analysis Condition** load	**Stress-Intensity Factor** K_I, unpatched K_I, patched

Figure 4. Input and Output Parameters for Patch Problem.

In Figure 5, the system configuration of the patch problem is shown. We assume the system is configured in a Microsoft Windows environment. The system is composed of three executable files: ParS.EXE, MAKE_DATA.EXE, and PANMD.EXE.

Variations of Input Parameters ↘ ↗ **Tables, Charts**

ParS.EXE

Crack Length, Geometry & Material of Sheet, Patch, Adhesive
(as Key Input Parameters)

Stress Intensity Factors
(as Key Output Parameters)

MAKE_DATA.EXE
(as Preprocessor)

PANMD.EXE
Finite Element Alternating Method Code Customized for Patch Problem
(as Analysis Code and Postprocessor)
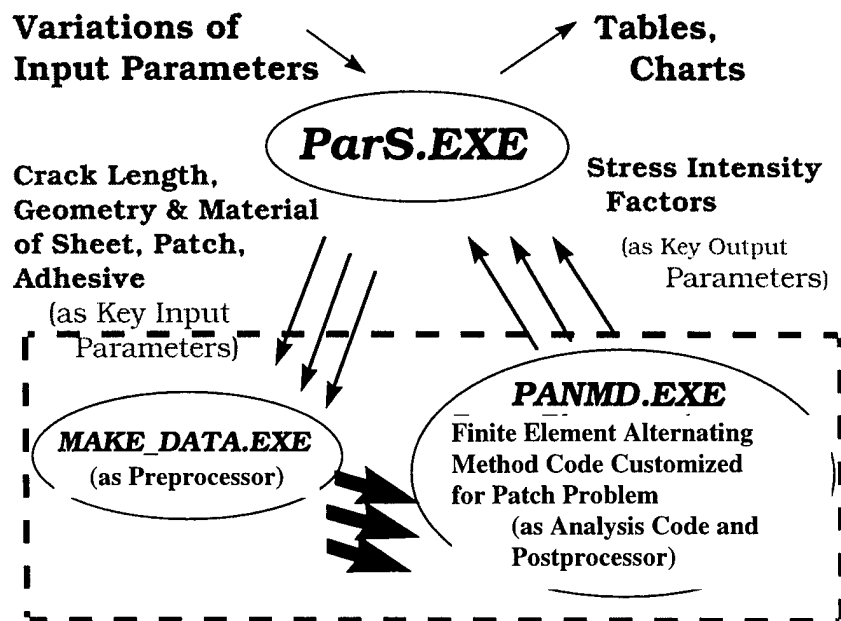
Figure 5. System Configuration for Patch Problem on Microsoft Windows.

ParS.EXE works as a GUI front end in Microsoft Windows. It controls the analyses for a parametric survey carried out by MAKE_DATA.EXE and MANMD.EXE which produces tables and line charts for visualization of results.

PANMD.EXE is an executable file of the FEAM analysis code customized for this patch problem. It accepts mesh data, geometry information of a crack, material properties, and analysis conditions for the problem. PANMD.EXE behaves not only as an analysis code but also as a postprocessor. It then produces stress-intensity factors directly at two end points of the crack. ParS.EXE extracts only relevant output parameters from an output file generated from PANMD.EXE.

MAKE_DATA.EXE works as a preprocessor for PANMD.EXE. It accepts key input parameters specified by ParS.EXE and then produces an input file for PANMD.EXE.

All the communications between these processes are carried out by text files. Both MAKE_DATA.EXE and PANMD.EXE must perform without any input from the user, because these routines are executed multiple times automatically by ParS.EXE during a parametric survey.

ParS.EXE is developed as a general purpose parametric survey tool and can be adapted to any other problems. All the dependent knowledge specific to the patch problem is isolated. They are

1. Name of the problem (e.g., Composite patch repairs).

2. Description of each input and output parameter such as a name, unit type, acceptable range of values, and a default value (e.g., Patch width is the input parameter, unit type is inches, default value is 3 inches).

3. Names of executable files and text files for analysis code, pre- and postprocessors (e.g., MAKE_DATA, PANMD).

4. Structure of predefined input parameter set databases and each data entry in the databases (e.g., Sheet material database where each entry is composed of two input parameters, Young's Modulus and Poisson's ratio).

Figures 6, 7, and 8 show actual screen images of ParS running on Microsoft Windows NT. In Figure 6, input parameters of patch material property are specified. Each parameter value can be specified directly through a text field in the dialog box Edit PS in Figure 6 or referred from the patch material database, as shown in Figure 7.

In Figure 8, the input parameters, the length of the crack, and the type of patch material are changed, and a series of patch analyses are performed. The parameter on the X-axis in the chart is the length of the crack, and the parameter on the Y-axis is the stress-intensity factor (K_I) for the patched and unpatched.

In the cases above, one execution of a patch analysis required about 30 seconds on a personal computer (PC) with a Pentium 66 MHz processor. It typically takes from 10 to 30 minutes to obtain the data shown in Figure 8.
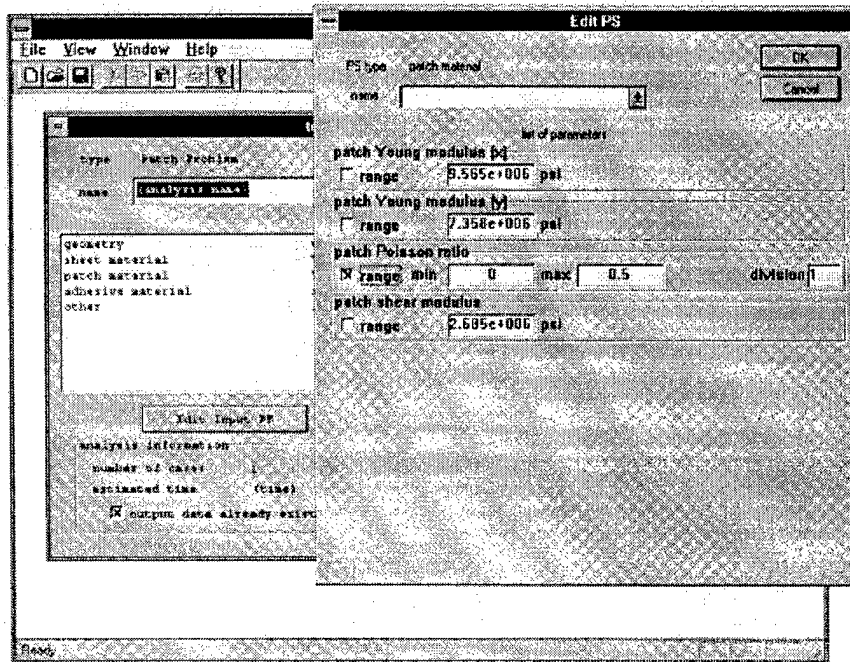
Figure 6. Input of Patch Material Properties.
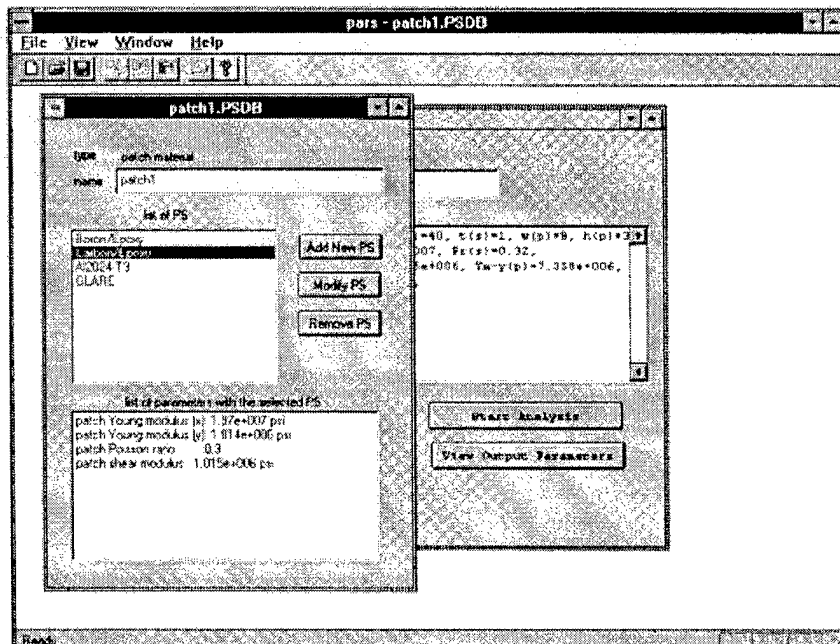
Figure 7. Access to Patch Material Database.

375
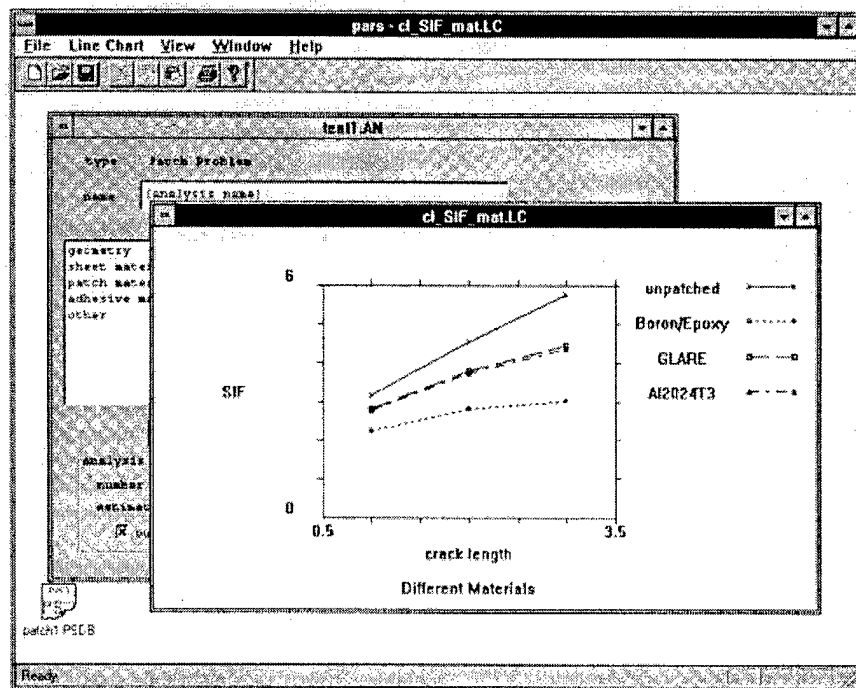
Figure 8. Result Visualization With Different Patch Materials.

SUMMARY

A GUI front-end tool for parametric survey, ParS, has been developed on Microsoft Windows to include

1. Automation of multiple analyses for parametric survey,
2. A database of frequently used input parameter sets, and
3. Visualization using table and line charts.

The system was successfully applied to a problem of composite patch repair of an aircraft fuselage.

REFERENCES

1. Nagaswamy, V., Pipkins, D. S., and Atluri, S. N.: An FEAM Based Methodology for Analyzing Composite Patch Repairs of Metallic Structures, ASME Structural Integrity in Aging Aircraft, vol. 47, pp. 273-300.

376

IMPLEMENTATION AND APPLICATION OF A
LARGE-ROTATION FINITE ELEMENT FORMULATION IN
NASA CODE ZIP2DL[1]

Xiaomin Deng
Department of Mechanical Engineering
University of South Carolina
Columbia, SC

J. C. Newman, Jr.
NASA Langley Research Center
Hampton, VA

SUMMARY

Recent stable tearing tests conducted on ARCAN specimens at the NASA Langley Research Center indicate that stable crack growth is accompanied by large specimen rotation at the point of loading due to the overall deformation of the specimen. To analyze these tests with proper accounting of the large rotation effects, a total Lagrangian large-deformation finite element formulation has been implemented in a new NASA crack-growth simulation code, ZIP2DL, as an extension of the original NASA code, ZIP2D. This new code has been applied to a number of crack growth tests on ARCAN specimens using a CTOD fracture criterion, where the critical CTOD value is determined experimentally. Results so far suggest that small-deformation simulations underestimate the load predicted by large-deformation simulations by almost a constant amount, with a relative error of about 6% at the peak load. It appears that by adjusting CTOD within the experimental scatter band, the load against crack-growth curve from a large-deformation simulation can be made to agree with test data over a large range of crack growth, and a major portion of the curve can also be reproduced by a small-deformation simulation with a different CTOD value.

INTRODUCTION

In this paper we discuss the development and application of a new elastic-plastic finite element code for mixed-mode crack growth simulation under plane stress, plane strain, or mixed state of stress conditions. This new code, named ZIP2DL, is an extension of the existing NASA code ZIP2D [1, 2], and, in particular, has the ability to handle large-deformation kinematics based on a total Lagrangian finite element formulation. This code has been successfully applied to simulate stable crack growth experiments conducted on

---

[1] Work done under a grant to the University of South Carolina, NAG-1-1664.

ARCAN specimens at the NASA Langley Research Center [3], and to analyze and understand the effect of large specimen rotation at the point of loading on crack-growth simulation under small-deformation conditions, especially on the load against crack growth curve for both mode I and mixed-mode cases. In the following, we will first outline the finite element formulation, then present the results of some verification studies, and finally discuss in some detail the findings from our ARCAN test simulations.

FINITE ELEMENT FORMULATION

Consider a body undergoing an arbitrary deformation. Suppose that at the current time t the body occupies a domain Ω with boundary Γ (the *current configuration*) and that at an initial time t_0 it occupies a domain Ω_0 with boundary Γ_0 (the *reference configuration*). Further, suppose that a material particle is described by its position X at t_0 and position $x=x(X, t)$ at t, and the displacement of the particle at t relative to its position at t_0 is $u=u(X, t)$, so that $x(X, t)=X+u(X, t)$. Following conventions in the literature [3, 4]), we now define our stress and strain measures. The *deformation gradient tensor* F is defined by

$$F = x\vec{\nabla} = 1 + u\vec{\nabla}, \quad \text{or} \quad F_{iJ} = \frac{\partial x_i}{\partial X_J} = \delta_{iJ} + \frac{\partial u_i}{\partial X_J} \tag{1}$$

where 1 is the second-order identity tensor. The *Green-Lagrange strain tensor* E is given by

$$E = \frac{1}{2}\left(F^T \cdot F - 1\right) = \frac{1}{2}\left[u\vec{\nabla} + \vec{\nabla}u + \left(\vec{\nabla}u\right)\cdot\left(u\vec{\nabla}\right)\right] \tag{2}$$

where superscript "T" denotes transposition. Let σ be the (symmetric) *Cauchy stress tensor*, then the symmetric *second Piola-Kirchhoff stress tensor*, S, can be defined by

$$S = JF^{-1} \cdot \sigma \cdot \left(F^{-1}\right)^T \tag{3}$$

where J is the *Jacobian* and is given by $J=\det F$, which is the determinant of F.

The *Principle of Virtual Work* at time $t+\Delta t$ is given by

$$\int_{\Omega_0} S(t + \Delta t):\delta E d\Omega_0 = \delta W(t + \Delta t) \tag{4}$$

where on the left-hand side is the *internal virtual work* stated in the reference configuration; δW is the *external virtual work* done by external forces (e.g., boundary surface tractions) on δu, and δu and δE are, respectively, the *virtual displacement vector* and the *associated virtual strain tensor*. It is worth noting that δu and δE are not related to each other by simply replacing u and E in Eq. 2 with δu and δE, respectively. Their relationship will be given later. To develop an iterative finite element algorithm we express the value of any quantity at

time $t+\Delta t$ as the sum of its value at time t and its increment at time t, so that we can write, for the stress tensor, displacement vector and strain tensor in the preceding equations,

$$S(t+\Delta t) = S + \Delta S, \ u(t+\Delta t) = u + \Delta u, \ E(t+\Delta t) = E + \Delta E \qquad (5)$$

where the strain tensor increment ΔE is related to the displacement vector increment Δu as follows:

$$
\begin{aligned}
\Delta E &= \Delta\varepsilon + \Delta\varepsilon^* + \Delta\varepsilon^{**}, \\
\Delta\varepsilon &= \frac{1}{2}\left[(\Delta u)\vec{\bar{\nabla}} + \vec{\nabla}(\Delta u)\right], \\
\Delta\varepsilon^* &= \frac{1}{2}\left[\vec{\nabla}u\cdot(\Delta u)\vec{\bar{\nabla}} + \vec{\nabla}(\Delta u)\cdot u\vec{\bar{\nabla}}\right], \\
\Delta\varepsilon^{**} &= \frac{1}{2}\vec{\nabla}(\Delta u)\cdot(\Delta u)\vec{\bar{\nabla}}
\end{aligned}
\qquad (6)
$$

Similarly, the virtual displacement vector and virtual strain tensor can be written as

$$
\begin{aligned}
\delta u &= \delta\Delta u, \ \delta E = \delta\varepsilon + \delta\varepsilon^* + \delta\varepsilon^{**}, \\
\delta\varepsilon &= \frac{1}{2}\left[(\delta\Delta u)\vec{\bar{\nabla}} + \vec{\nabla}(\delta\Delta u)\right], \\
\delta\varepsilon^* &= \frac{1}{2}\left[\vec{\nabla}u\cdot(\delta\Delta u)\vec{\bar{\nabla}} + \vec{\nabla}(\delta\Delta u)\cdot u\vec{\bar{\nabla}}\right], \\
\delta\varepsilon^{**} &= \frac{1}{2}\left[\vec{\nabla}(\Delta u)\cdot(\delta\Delta u)\vec{\bar{\nabla}} + \vec{\nabla}(\delta\Delta u)\cdot(\Delta u)\vec{\bar{\nabla}}\right]
\end{aligned}
\qquad (7)
$$

Substitution of Eqs. 5-7 into Eq. 4 leads to

$$\int_{\Omega_0}\left[\Delta S\!:\!\delta E + S\!:\!\delta\varepsilon^{**}\right]d\Omega_0 = \delta W - \int_{\Omega_0} S\!:\!\left(\delta\varepsilon + \delta\varepsilon^*\right)d\Omega_0 \qquad (8)$$

A generalization of the Hooke's law to arbitrarily large deformation cases is given by

$$S = C\!:\!E \quad \text{or} \quad \Delta S = C\!:\!\Delta E \qquad (9)$$

where C is the conventional fourth-order elasticity tensor. To apply the theory of plasticity, we note that, when measured in the reference configuration Ω_0, the tensors E and S are invariant under arbitrary rigid-body rotations. As such, they can be used in place of the engineering strain and stress measures in small-strain constitutive equations under general large-rotation and small-strain deformation conditions. For example, a generalization of an incremental theory of plasticity (e.g., the J_2 flow theory of plasticity used in the current study) to large-deformation (rotation) but small-strain cases can be written as

$$\Delta S = C:\left(\Delta E - \Delta E^P\right) \quad \text{or} \quad \Delta S = C^{el-pl}:\Delta E \tag{10}$$

where ΔE^P is the plastic strain increment tensor and C^{el-pl} is the fourth-order elastic-plastic tangent modulus tensor. An approach for elastic-plastic computation under large-rotation and small-strain conditions is to substitute the first equation in (10), move the plasticity induced nonlinear term to the right-hand side of the equation as an equivalent body force, and drop all higher-order nonlinear terms related to $\Delta\varepsilon^{**}$ and $\delta\varepsilon^{**}$, so that

$$\int_{\Omega_0}\left(\Delta\varepsilon + \Delta\varepsilon^*\right):C:\left(\delta\varepsilon + \delta\varepsilon^*\right)d\Omega_0 = \delta W - \int_{\Omega_0} S:\left(\delta\varepsilon + \delta\varepsilon^*\right)d\Omega_0 + \int_{\Omega_0}\Delta E^P:C:\left(\delta\varepsilon + \delta\varepsilon^*\right)d\Omega_0 \tag{11}$$

Equation 11 can be viewed as an extension of the initial stress method [6] to large-rotation and small-strain deformation problems and can be properly termed an *initial-stress based total Lagrangian finite element formulation*. The resulting nonlinear finite element matrix equation is as follows:

$$\left([K^1]+[K^2]\right)\{\Delta U\} = \{f\}+\left\{f^P\right\} \tag{12}$$

where $\{\Delta U\}$ is the vector of unknown nodal displacement increments; $[K^1]$ is the constant stiffness matrix for a linearly elastic, small-deformation problem; $[K^2]$ is the contribution to the stiffness matrix from the nonlinear large-deformation kinematics, which depends on the current state of deformation; $\{f\}$ is a vector of unbalanced nodal forces due to external loads and interal stresses and is zero at equilibrium; and $\{f^P\}$ is a vector of nodal forces due to plastic strain increments and is zero for a converged solution. Alternatively, an approach based on the tangent-stiffness method [7] is to use the second equation in (10) and keep the plastic nonlinear term on the left-hand side of the equation to obtain

$$\int_{\Omega_0}\left(\Delta\varepsilon + \Delta\varepsilon^*\right):C^{el-pl}:\left(\delta\varepsilon + \delta\varepsilon^*\right)d\Omega_0 = \delta W - \int_{\Omega_0} S:\left(\delta\varepsilon + \delta\varepsilon^*\right)d\Omega_0 \tag{13}$$

This is a *classical tangent-stiffness based total Lagrangian finite element formulation*. The resulting nonlinear finite element matrix equation is given by

$$\left([K^1]+[K^2]+[K^3]\right)\{\Delta U\} = \{f\} \tag{14}$$

where $[K^3]$ is the contribution to the stiffness matrix due to plasticity while other quantities have the same meaning as those in Eq. 12. It is noted that the effect of plasticity is treated as a stiffness contribution in Eq. 14 instead of a force contribution as in Eq. 12.

The above two formulations have been implemented in ZIP2DL under plane stress, plane strain and mixed state of stress conditions. (In a mixed state of stress analysis, plane-strain conditions are imposed around the crack tip while plane-stress conditions are imposed elsewhere [10]). Four- and eight-noded quadrilateral isoparametric elements and three-noded

triangular elements are provided. The resulting nonlinear finite element equations, Eqs. 12 and 14 are solved with either the standard or the modified Newton-Raphson iteration method. Convergence of the finite element solution is monitored and controlled by checking a norm (measure) of the total incremental nodal force vector (the out-of-balance force or force increment) on the right-hand side of Eq. 12 or 14 and its inner product (the energy increment) with the nodal displacement increment vector $\{\Delta U\}$. Stress integration of the incremental plasticity theory is accomplished by the use of a modified tangent-prediction radial-return algorithm and algorithms for subincrementation and prevention of numerical negative plastic flow [8]. With regard to crack growth simulation, the following strategy is used. Cracks are identified by finite element node pairs along existing crack surfaces and their prospective crack growth paths. The two nodes of a node pair on a unbroken crack growth path are initially tied together by two mutually perpendicular rigid springs. Crack growth is achieved through a crack tip nodal release procedure that unzips the crack tip node pair. In this nodal release procedure, the fracture criterion is checked at the end of every loading step and crack growth step. When the criterion is met, the stiffness of the two rigid springs that tie the crack tip node pair together will be reduced monotonically to zero in a number of iterations, at the end of which the crack will have grown by an amount equal to the size of the element ahead of the crack in the direction of the crack path.

VERIFICATION STUDIES

A number of verification studies have been conducted to ensure the reliability, efficiency and accuracy of ZIP2DL. While the results of all verification studies are excellent, only some of them will be reported here. In the first example, the problem of uniaxial elastic stretching under both plane stress and plane strain conditions is studied. As shown in Figure 1, a rectangular element is stretched uniformly in one direction in its plane by an original uniform stress σ_0 (the first Piola-Kirchhoff stress, which equals the load divided by the original, undeformed loading area). Visually, the finite element solutions are identical to the exact solutions (these and later exact solutions are obtained by the authors in the course of this study). In the second example, a square element is loaded uniformly in two perpendicular directions in its plane (see Figure 2) and the strains in these two directions are calculated as a function of the original applied uniform stress σ_0. Again it is seen that the finite element solutions for both plane stress and plane strain appear to be identical to the exact solutions. Both elastic cases involve large displacement and large strain. In the third example, to investigate the applicability of ZIP2DL to large-rotation problems, the rigid-body rotation of a square element around one of its corner points is modeled. As shown in Figure 3, the square element is made to rotate about its only pinned point at node 3 by specifying the displacement of node 2 as a function of the rotation angle θ. The displacements of node 1 and node 4 are then solved with ZIP2DL and compared with the exact solutions in Figure 3, where u and v are the horizontal and vertical displacements, respectively, and subscripts 1 and 4 refer to the node numbers. The agreement is again excellent. In the above examples, it takes about four iterations to get convergence after each load step. (As a reference, a data point in Figures 1-3 represents a solution at one load step).
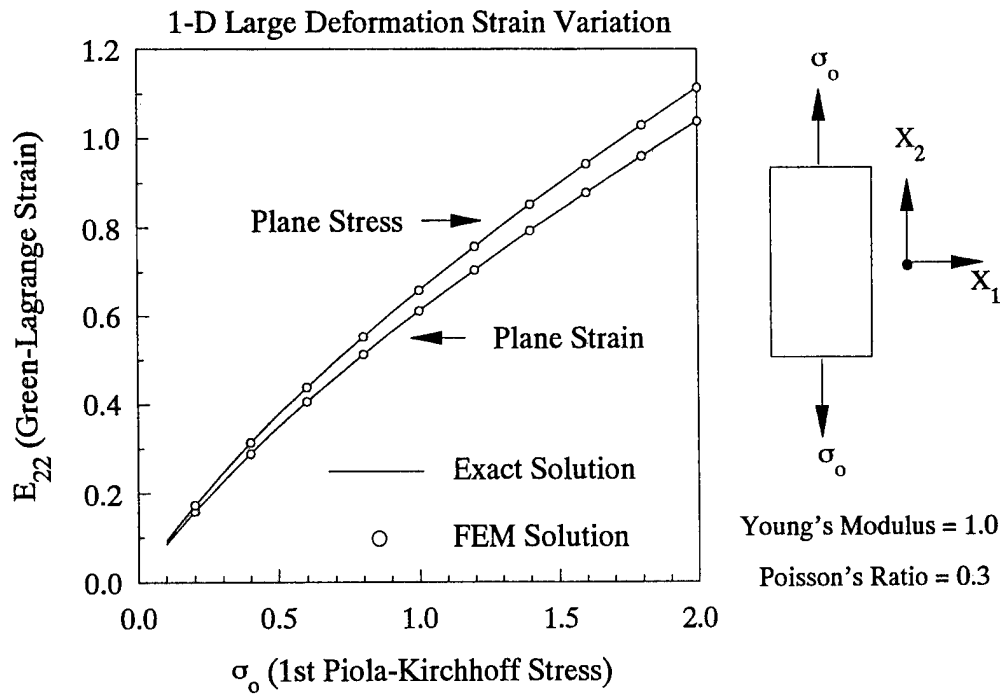
Figure 1. A Comparison of Exact and ZIP2DL Solutions for a Uniaxial Elastic Stretching Problem.
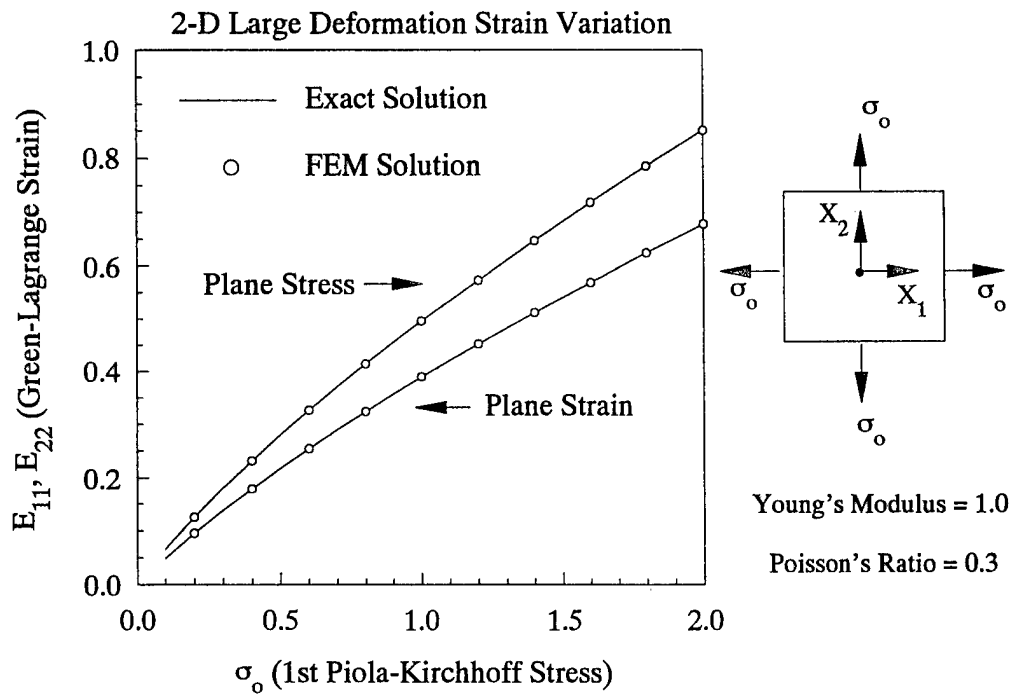
Figure 2. A Comparison of Exact and ZIP2DL Solutions for a Biaxial Elastic Stretching Problem.
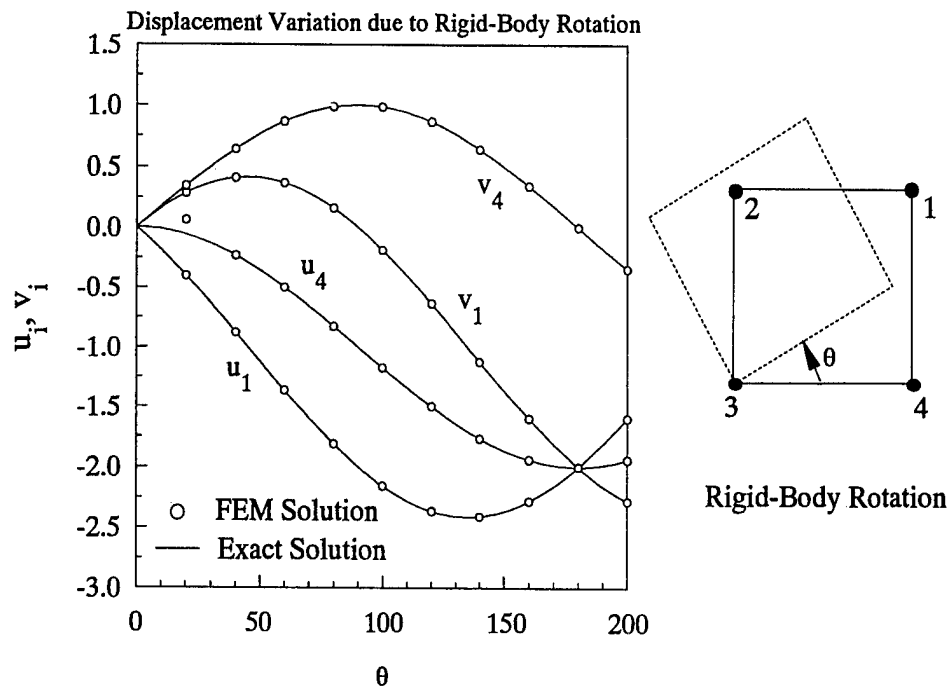
Figure 3. A Comparison of Exact and ZIP2DL Solutions for a Rigid-Body Rotation Problem.
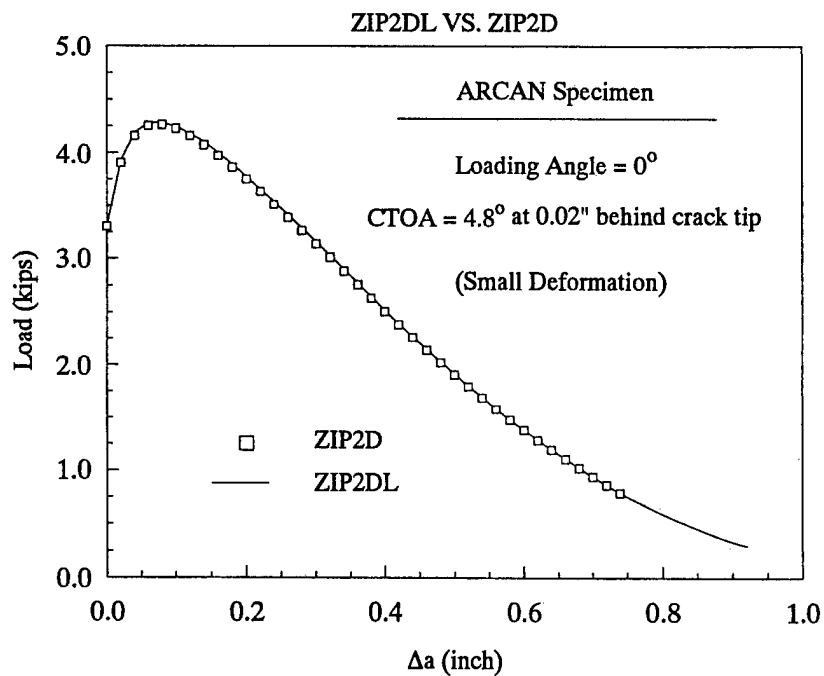
Figure 4. A Comparison of Exact and ZIP2D and ZIP2DL Crack-Growth Predictions for an ARCAN Test.

The accuracy of ZIP2DL in elastic-plastic calculations has been tested extensively. Here in the final example, we compare ZIP2DL against the established NASA code ZIP2D for an ARCAN test (refer to the next section for a description of the test and modeling details). This test case involves elastic-plastic stable crack growth in a 2024-T3 aluminum sheet specimen under mode I, displacement controlled loading. The comparison between small-deformation plane stress predictions of the two codes for the load against crack increment (change in crack length) curve is very satisfactory, as shown in Figure 4. It takes about six iterations to get convergence after each load step and after the completion of each nodal release procedure.

RESULTS AND DISCUSSIONS

So far a limited number of mode I and mixed-mode crack growth tests conducted on ARCAN specimens have been simulated using ZIP2DL. Results presented here pertain to the mode I case and those for the mixe-mode cases are given separately in this volume [9]. A schematic of the ARCAN specimen and its fixture is shown in Figure 5, where loading in the $0°$ direction corresponds to mode I loading. The specimen is made of 2024-T3 aluminum and the fixture is made of a steel. Both materials are assumed to obey the J_2 flow theory of plasticity. The effective stress-strain curves for the materials are obtained experimentally from uniaxial tension tests and are approximated as piece-wise linear curves. Plane stress is assumed.
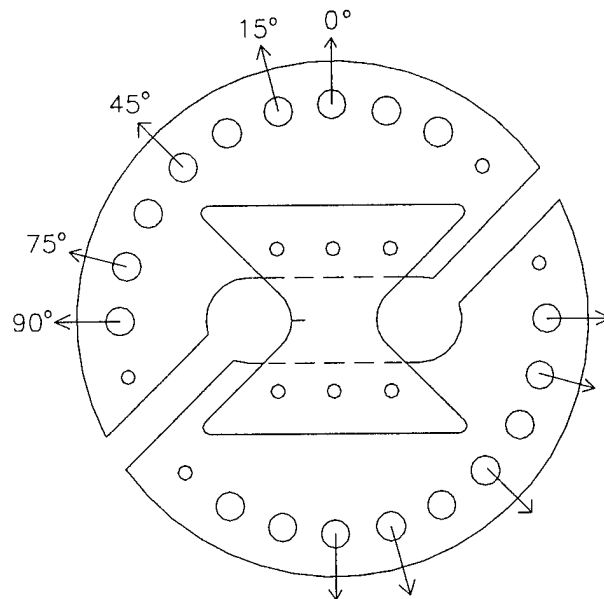
Figure 5. A Schematic of the ARCAN Test Fixture and Specimen Containing a Single-Edge Crack.

The finite element mesh is composed of three-noded triangular (constant-strain) elements, as shown in Figure 6. A uniform, fine mesh surrounds the single-edge crack and along its growth path (Figure 6b). A vertical displacement is specified at the second center-line node from the top and the corresponding node at the bottom is fixed. The specified displacement increases monotonically from zero until crack growth is completed. Crack growth is initiated and continued when the two nodes of a node pair at a fixed distance behind the crack tip are displaced relative to each other by an amount equal to a critical CTOD value, which in this study had been obtained experimentally at the NASA Langley Research Center in an earlier study [3]. Specifically, the current study has used CTOD values measured at 0.04 inch behind the crack tip for a TL-oriented specimen with a 0° loading angle (see [3] for a description of the specimen orientation). The equivalent CTOA value is found to be 4.8° with a ±1° scatter. Two meshes of different refinement are used to check for element size dependence. One mesh consists of 1416 nodes and 2514 elements, with a 0.02-inch uniform element size around the crack path. A finer mesh is composed of 2772 nodes and 5064 elements, with a 0.01-inch uniform near-tip element size. As shown in Figure 7, these two meshes lead to nearly identical load against crack growth curves, implying that the coarser mesh is adequate. The coarser mesh is chosen for later calculations because it requires less computer time.

(a)   (b)
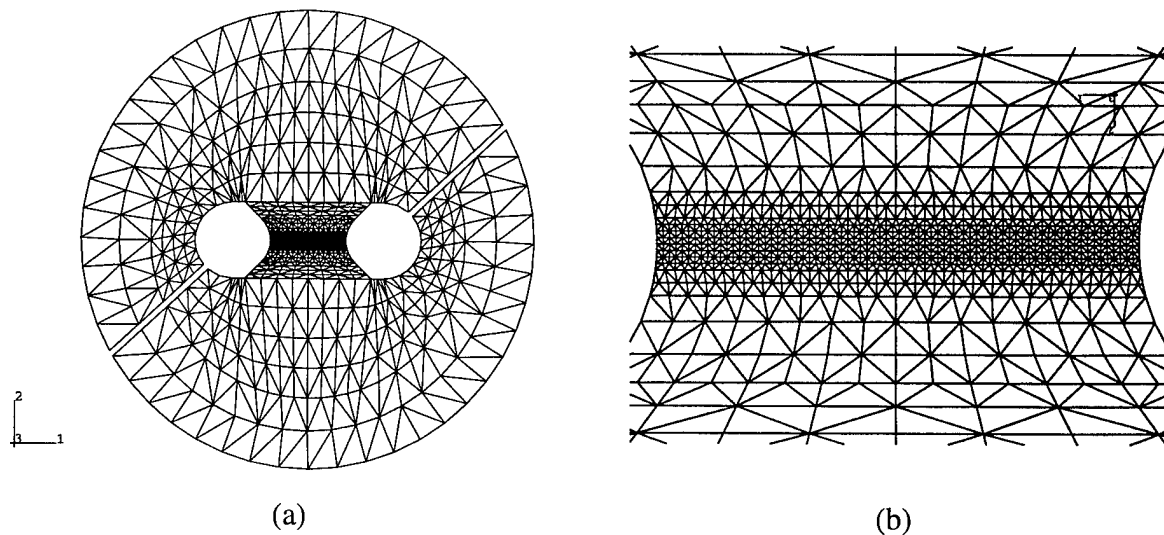
Figure 6. Finite Element Mesh used in Mode I ARCAN Test Simulations: (a) Global Mesh, (b) Refined Local Mesh Along Crack Growth Path.
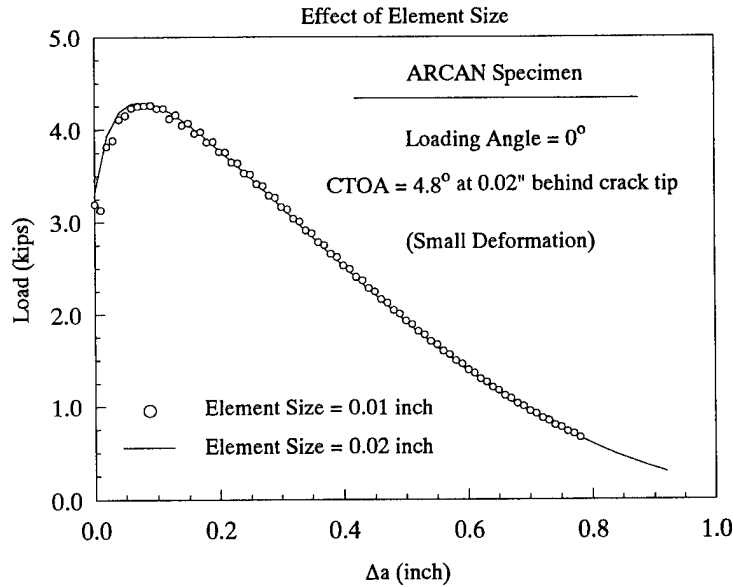
Figure 7. Effect of Finite Element Size Con Crack Growth Simulation.

Figure 8 shows a comparison between two small-deformation crack growth simulation predictions. In one simulation a CTOA of 4.8° is specified at 0.02 inch behind the crack tip while in the other the CTOA is specified at 0.04 inch behind the crack tip. In the early stage of crack growth the latter prediction oscillates and is different from the former prediction by a fairly small amount. It is seen however that these two predictions tend to approach each other after the peak load as crack growth continues. Because the enforcement of CTOA at 0.02 inch behind the crack tip leads to a smoother simulation curve, it will be used in all later simulations.
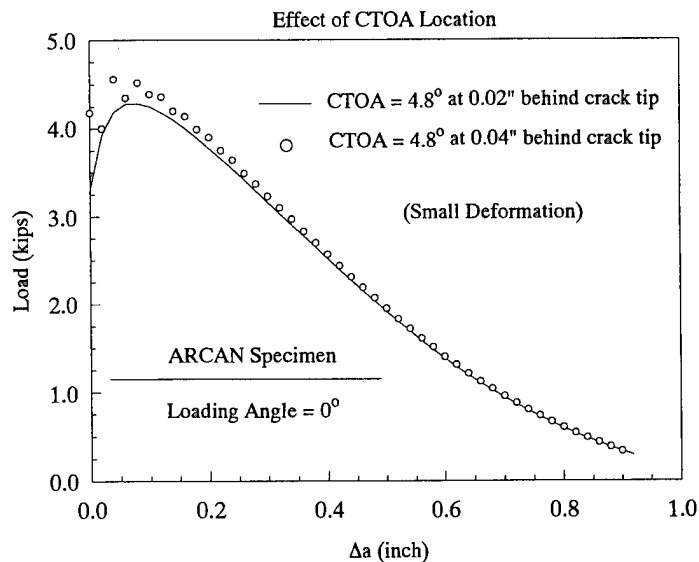
Figure 8. Effect of Critical CTOA Location on Crack Growth Simulation.

386

The effect of large specimen rotation at the point of loading on the crack growth behavior can be seen from the comparison shown in Figure 9. When a CTOA of 4.8° is specified at 0.02 inch behind the crack tip the relative difference between the predicted fracture loads with and without consideration of large rotation is about 6% at the peak load. Another case shown in Figure 9 is for a CTOA of 4.5° specified at 0.02 inch behind the crack tip. It is clear from these two cases that the load predicted by a small-deformation simulation consistently underestimates that predicted by a corresponding large-deformation simulation by almost a constant amount. Further, it is seen that by adjusting the CTOA value (or equivalently, the CTOD value) within the scatter band (±1°) of the experimental CTOA measurement, a large portion of the load against crack growth curve can be made to shift upwards or downwards by a large margin. This observation seems to suggest that the load against crack growth curve predicted by a large-deformation simulation can be reproduced, perhaps except near the end of crack growth (see Figure 9), by a small-deformation simulation by using a larger CTOA value. Further study is needed to confirm this speculation.
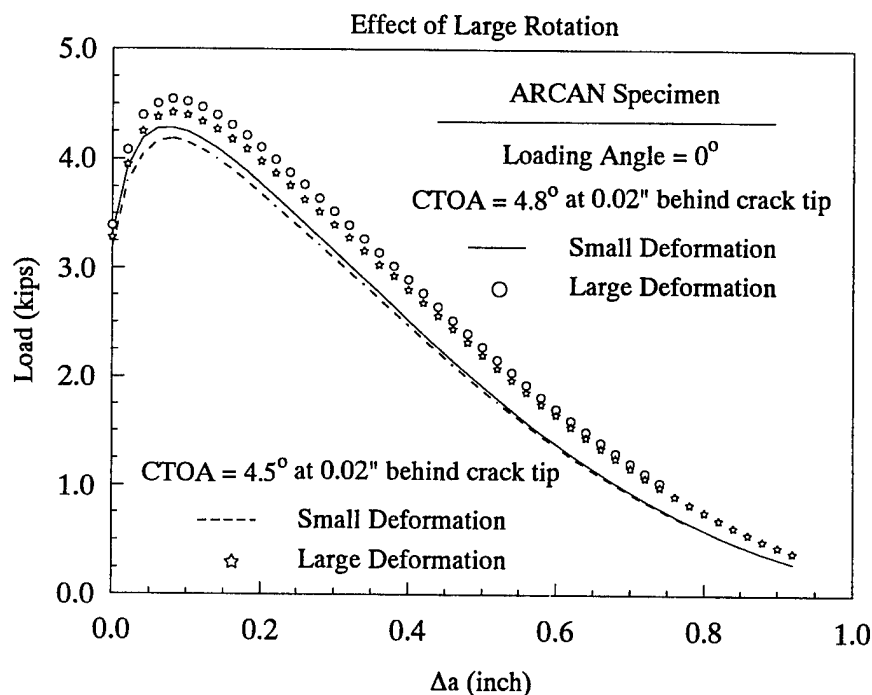
Figure 9. Effect of Large Specimen Rotation on Crack Growth Simulation.

A comparison of computer simulation results with experimental measurement is shown in Figure 10, where the test data are for a TL oriented 2024-T3 aluminum ARCAN specimen (see [3] for a description of the specimen orientation). The critical CTOA value of 4.5° used in this comparison is close to the mean value (4.8°) of the test data obtained in [3] which contains a scatter band of ±1°. At this CTOA value the small-deformation result agrees with the test data at and immediately following the peak load while the large-deformation result agrees with the test data along the rest of the crack growth curve. From an

earlier observation, it appears that the large-deformation curve can be made to follow a major portion of the test data by matching the test data at the peak load by lowering the CTOA a few tenths of a degree. It will be worthwhile to see if this matched CTOA value can be used in mixed-mode crack growth and still produce simulation results with good agreement with corresponding test data. Small-deformation, mixed-mode simulations so far (see [9] for detail) indicate a very good possibility in that respect.
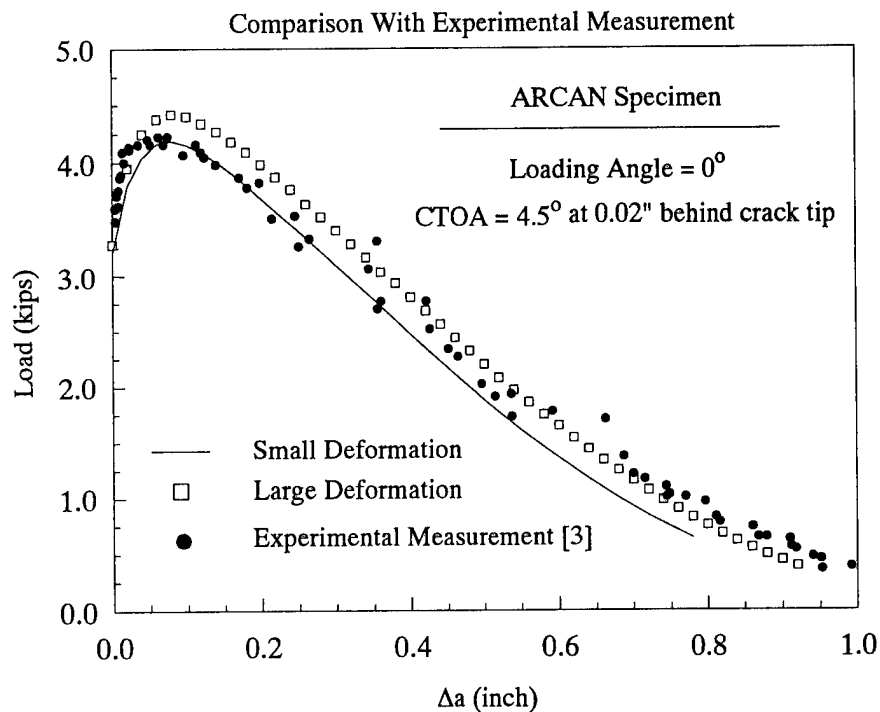
Figure 10. A Comparison of ZIP2DL Predictions With Experimental Measurement [3].

Finally, it is noted that the above simulations require about six iterations for convergence after each load step and nodal release procedure if the tangent-stiffness approach (see Eq. 14) is used and about 12 iterations if the initial-stress approach (see Eq. 12) is used. The advantage of the initial-stress approach is that, when used for small-deformation simulations, the stiffness matrix does not need to be updated except during crack tip nodal release, thus it can lead to big savings in computer time.

ACKNOWLEDGEMENTS

REFERENCES

1. Newman, J.C., Jr.: Finite-Element Analysis of Fatigue Crack Propagation Including the Effects of Crack Closure. Ph.D. Thesis, Virginia Polytechnic Institute, Blacksburg, VA, 1974.

2. Newman, J.C., Jr.: User guide for ZIP2D. NASA Langley Research Center, Hampton, Virginia, modified April 2, 1996.

3. Amstutz, B.E.; Sutton, M.A.; Dawicke, D.S.; and Boone, M.L.: Effects of Mixed-Mode I/II Loading and Grain Orientation on Crack Initiation and Stable Tearing in 2024-T3 Aluminum. *Fatigue and Fracture Mechanics: 27th Volume, ASTM STP 1296*, R. S. Piascik, J.C. Newman, Jr., and N.E. Dowling, Eds, American Society for Testing and Materials, Philadephia, 1995.

4. Malvern, L.E.: *Introduction to the Mechanics of a Continuous Medium*. Prentice-Hall, Englewood Cliffs, New Jersey, 1969.

5. Bathe, K.-J.: *Finite Element Procedures*. Prentice-Hall, Englewood Cliffs, New Jersey, 1996.

6. Zienkiewicz, O.C.; Valliappan, S.; and King, I.P.: Elasto-Plastic Solutions of Engineering Problems: Initial Stress Finite Element Approach. *International Journal for Numerical Methods in Engineering*, Vol. 1, 1969, pp. 75-100.

7. Marcal, P.V.: A Stiffness Method for Elastic-Plastic Problems. *Int. J. Mech. Sci.*, Vol. 7, 1965, pp. 220-238.

8. Deng, X.; and Rosakis, A.J.: Negative Plastic Flow and its Prevention in Elasto-Plastic Finite Element Computation. *Finite Element in Analysis and Design*, Vol. 7, 1990, 181-191.

9. Sutton, M.A.; Zhao, W.; Dawicke, D.S.; Deng, X.; and Newman, J.C., Jr.: Numerical Investigations into the Viability of CTOD as a Fracture Parameter for Mixed-Mode I/II Tearing of Thin Aluminum Sheets. FAA-NASA Symposium on Continued Airworthiness of Aircraft Structures, 1996.

10. Newman, J.C.; Booth, B.C.; and Shivakumar, K.N.: An Elastic-Plastic Einite-Element Analysis of the J-Resistance Curve Using a CTOD Criterion. *Fracture Mechanics: Eighteenth Symposium, ASTM STP 945*, D. T. Read and R. P. Reed, Eds., American Society for Testing and Materials, Philadephia, 1988.

IMPLICATIONS OF CORROSION PILLOWING ON THE STRUCTURAL INTEGRITY OF FUSELAGE LAP JOINTS*

Nicholas C. Bellinger and Jerzy P. Komorowski
Structures, Materials, and Propulsion Laboratory
Institute for Aerospace Research
National Research Council Canada
Ottawa, Ontario, Canada

SUMMARY

Finite element techniques were used to determine the effect that pillowing, caused by the presence of corrosion products, has on fuselage lap joints. The stress caused by the internal pressure and riveting process was taken into account while the fuselage curvature was ignored. The results indicate that as the pillowing (i.e. thickness loss) increases, the stress in the joint increases. Also, these results suggest that the volume of corrosion products present within a joint is the main parameter governing the increase in stress and not the percent thickness loss. For example, if a joint contains 5% thickness loss in each skin, although the total thickness loss is only 5%, the volume of corrosion products is equivalent to a 10% thickness loss in one skin. A preliminary fracture mechanics analysis carried out on a single crack located just beyond the rivet head suggests that the crack edge along the faying surface would grow more rapidly along the rivet row forming a semielliptical crack front with a very high aspect ratio. This type of crack is more difficult to detect during visual inspection.

INTRODUCTION

Concern has grown as to the possible effects corrosion might have on the structural integrity of fuselage lap joints. Environmental attack can lead to early crack initiation, enhanced crack growth rates (corrosion fatigue), thickness loss (increased stresses), and intergranular and stress corrosion cracking and pitting (stress risers). Present maintenance guidelines allow for a maximum thickness loss of 10% within a single skin before repairs must be made to a joint (ref. 1). However, in a previous study carried out at the National Research Council Canada (NRCC), the volumetric increase associated with corrosion by-products was found to be approximately 6.5 times greater than the volume of parent material lost (ref. 2). This large volumetric increase results in local deformations (pillowing) which can affect the structural integrity of fuselage lap joints.

Finite element techniques along with a mathematical model (ref. 3) were used to simulate the presence of corrosion products within a fuselage lap joint. The stress resulting from the internal pressure (hoop stress), the prestress caused by the rivet fastening process and the reduction in thickness caused by the material loss were all taken into account while the curvature of the fuselage was ignored. The results indicated that the stress in the area of the rivets increases significantly due to the presence of corrosion pillowing. A fracture mechanics analysis was also carried out on a single crack of a length just beyond the rivet head to help assess the structural integrity implications of corrosion pillowing.

FINITE ELEMENT MODEL

A typical lap joint configuration was chosen for this study and consisted of two skins (outer and inner) of equal thickness, 1.14 mm (0.045 in), fabricated from Al 2024-T3. The skins were joined using three rows of rivets with a 25.4 mm (1.0 inch) spacing. Each rivet had a nominal shank diameter of 3.96 mm (0.156 inch) and a rivet head diameter of 5.8 mm (0.232 inch). A hat-section stringer was attached to the middle rivet row through the hat crown as shown in Figure 1. Three finite element models were generated to simulate the different loads that are present within a corroded joint. These loads were; 1) hoop stress caused by the internal pressure, 2) prestress caused by the riveting process and, 3) stress due to corrosion pillowing. To save computation time and storage space only three rivets were modeled as shown in Figure 2. The rivet/skin interaction was simulated using nonlinear gap elements.

Stress Analysis

All models were generated using the first-order brick elements available in the NISA finite element package. It was assumed for the hoop stress model that some of the load transfer would be due to friction under the rivet heads which was simulated by merging the nodes in these areas. A pressure was applied along a skin edge to simulate the hoop stress while the opposing edge was fixed in all directions. For the prestress model, all the nodes were merged to prevent the skins from penetrating, and a pressure was applied to the rivet heads to simulate the riveting process. To model the corrosion pillowing, a three-stage process was used; 1) a 6.89 kPa (1 psi) pressure was initially applied to the faying surfaces and the resulting volume determined, 2) given a specified thickness loss in one skin, the volume required to accommodate the corrosion products was calculated using a previously derived formula (ref. 3-4), and 3) assuming a linear relationship between the applied pressure and volume due to the incompressibility of the corrosion products, the pressure necessary to obtain the required volume was calculated and then reapplied to the faying surfaces (ref. 4). The finite element analysis was then rerun and the resulting displacements obtained.

Fracture Mechanics Analysis

To carry out the fracture mechanics analysis, the stress model for each loading case was modified. Second-order elements (i.e., elements with mid-side nodes) were generated in the area of the critical rivet row (upper row). For this preliminary study, a straight-fronted through crack perpendicular to the hoop stress loading was assumed to be present on one side of the rivet hole just beyond the rivet head, see Figure 3. The mid-side nodes for the elements surrounding the crack tip were moved to the quarter point to simulate the stress singularity at this location. Load transfer by friction under the rivet heads was ignored. The resulting quarter-point and corner nodal displacements were then used in an equation developed by Kuang and Chang (ref. 5) to calculate the Mode I stress intensity factor:

$$K_1 = \frac{1}{4} \sqrt{\frac{2\pi}{L}} E \left(\frac{8v_1 - v_2}{3} \right) \tag{1}$$

where v_1 is the displacement for the quarter-point node perpendicular to the crack face, v_2 is the corresponding displacement for the corner node and L is the length of the crack tip element. Plane stress conditions were assumed to exist ahead of the crack front.

RESULTS AND DISCUSSION

Stress Analysis

To determine the resultant stress which would occur from a combination of the three loading cases, the nodal displacements obtained from each case were added together and the analysis rerun. A plot of the stress in the vicinity of the upper rivet row in the outer skin and the lower rivet row in the inner skin (which are the critical locations in terms of cracking for the respective skins) is shown in Figure 4. As can be seen from this figure, the stress in the vicinity of the rivet holes increases as the pillowing increases. A comparison was also made between the increase in stress caused by an equivalent thinning of the outer skin and that caused by pillowing, Figure 5. This comparison clearly shows that pillowing has a greater influence on the stress in a joint as compared to the effective thickness loss alone.

The maximum stress for small amounts of corrosion occurred at the upper rivet row away from the hole approximately 45° to the hoop stress loading which was verified by experimental tests (ref. 6) carried out on accelerated corroded multisite damage specimens, Figure 4. However this maximum stress location can shift thus causing another rivet row to become critical. Since, for this analysis, a constant thickness loss was assumed to be present throughout the joint, the maximum stress shifted to the lower rivet row in the upper skin when the thickness loss was greater than 6%. It should be emphasized that this row is not critical for this particular joint configuration in the absence of corrosion. Since corrosion is a

random process, the shift in maximum stress raises concerns as to the possibility that given the location of the corrosion and the severity of the pillowing, the maximum stress in a joint could occur in other skins, particularly in the second or third layers causing premature cracking. Some corroded lap joints obtained from retired aircraft were disassembled, cleaned and inspected using X-ray techniques. These images showed cracks in the area of maximum pillowing, Figure 7. The first image, Figure 7a, shows numerous cracks present in the four rivet holes which surround the area of maximum pillowing in the outer skin. This joint had a maximum thickness loss of 14% in some of the pits which is greater than the maximum allowable of 10%. However, given that corrosion was only present in this area of the joint and the skin thickness was approximately 1.78 mm (0.070 inch), it is highly unlikely that this damage would have been detected under normal maintenance procedures. The other image, Figure 7b, shows cracks that are present in the inner skin at the upper rivet row (which is not critical for this skin). This joint had a maximum thickness loss of less than 10% in the inner skin.

Fracture Mechanics Analysis

To calculate the Mode I stress intensity factor, the nodal displacements for the three loading cases were added together and substituted into Equation (1). The results were non-dimensionalized with respect to the hoop stress, σ_h, and plotted against percentage thickness loss, Figure 8. As can be seen from this figure, the stress intensity factors for the different crack edges diverge as the thickness loss increases. The stress intensity factor for the edge of the crack located on the inner (faying) and outer surfaces of the outer skin are approximately equal when no corrosion is present indicating that both crack edges would grow at about the same rate. However, as the thickness loss increases and thus the pillowing, the stress intensity factor for the crack edge along the outer surface decreases while the crack edge on the inner surface increases. This is understandable since the bending in the skin caused by the pillowing produces a compressive stress in the rivet area on the outer surface while a high tensile stress is present on the faying surface. The difference in the stress intensity factor for the two surfaces suggests that the crack edge on the faying surface would grow faster than the crack on the outer surface causing a semielliptical crack front with a high aspect ratio. In fact, this is the situation that is present in the joints shown in Figure 7. The majority of the cracks present in these joints have not yet penetrated the outer surface although some of the crack lengths are greater than 6.3 mm (0.25 inch) on the faying surface. This raises concerns as to the possible effect that corrosion pillowing might have in a multisite or wide spread fatigue damage scenario. Swift (ref. 7) proposed that after a predetermined number of flight hours, special inspections be carried out on aging aircraft in specific areas to decrease the probability of failure caused by multisite damage. Since corrosion pillowing can significantly increase the stress in fuselage lap joints, cracks could initiate prematurely thus making it necessary to inspect for multisite damage earlier than was previously thought, see Figure 9. To complicate the situation even more, once initiated, the cracks would grow along the faying surface resulting in high aspect ratio cracks which are difficult to detect. This in turn would

decrease the probability of detecting multisite damage in the presence of corrosion and thus increase the probability of premature failure.

CONCLUSIONS

The results from this study can be summarized as follows:

- The stress in a fuselage lap joint increases as the pillowing caused by the corrosion by-products increases.

- Depending on the location of the corrosion and severity of the pillowing, the maximum stress in a joint could shift to other skins (i.e., second or third layers) causing premature crack initiation.

- The increase in the stress intensity factor for the crack edge on the faying surface and the subsequent decrease on the opposite side suggests that a crack would grow more rapidly in the direction of the row of rivets than through the skin toward the outer surface resulting in a semielliptical crack front with a high aspect ratio.

- The high aspect ratio cracks would make detection difficult thus decreasing the probability of detection and increasing the risk of premature failure.

- One of the main factors influencing the structural integrity of a lap joint is the volume of corrosion products present in the vicinity of a rivet hole and not the percentage thickness loss in each skin. For example, take a joint which has 7% thickness loss in each skin. Although this joint would be considered to have a total of 7% corrosion and could continue to fly without being repaired, the maximum stress present in the joint is equivalent to a single skin containing 14% thickness loss which would have to be repaired.

REFERENCES

1. Thompson, J. G.: Subsurface Corrosion Detection in Aircraft Lap Splices Using a Dual Frequency Eddy-Current Inspection Technique. Materials Evaluation, v 51, n 12, Dec. 1993, pp. 1398-1401.

2. Krishnakumar, S.; Komorowski, J. P.; and Sproule I.: "Chemical Characterization of Corrosion Products in Fuselage Lap Joints." LTR-ST-1952, November 1993.

3. Bellinger, N. C.; Krishnakumar, S.; and Komorowski, J. P.: Modelling of Pillowing Due to Corrosion in Fuselage Lap Joints. CAS Journal, Vol. 40, No. 3, September 1994, pp. 125-130.

4. Bellinger, N. C.; Komorowski, J. P.; and Krishnakumar, S.: Numerical Modelling of Pillowing Due to Corrosion in Fuselage Lap Joints. LTR-ST-2005, April 1995.

5. Beres, W.: NSIFS Postprocessor for Displacement-Based Stress Intensity Factor Extraction from NISA II Calculation Results. ST-727, October 17, 1994.

6. Wakeman, R. B.: Interaction of Multiple Site Fatigue Damage and Corrosion in Fuselage Lap Splices. Master's Thesis, Carleton University, Ottawa, Canada, to be published.

7. Swift, T.: Widespread Fatigue Damage Monitoring - Issues and Concerns. NASA CP 3274, FAA/NASA International Symposium on Advanced Structural Integrity Methods for Airframe Durability and Damage Tolerance, Sept. 1994, pp. 829-870.
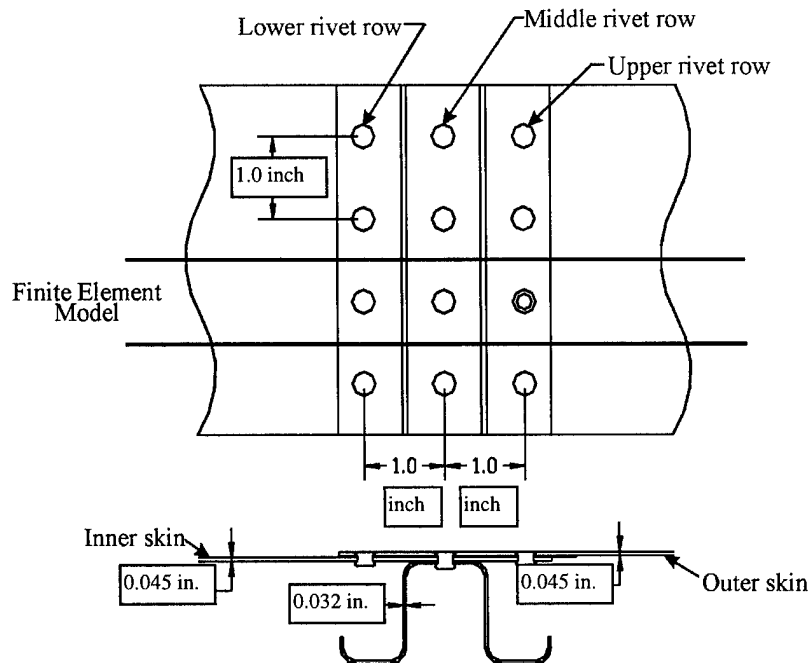
Figure 1. Lap Joint Configuration.
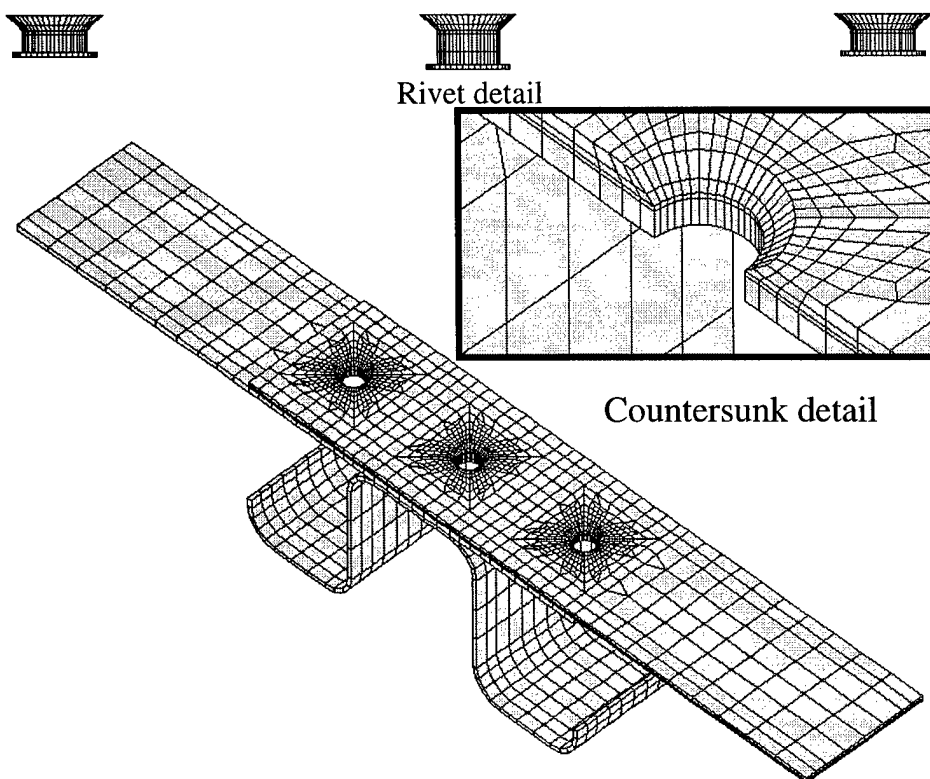
Figure 2. Stress Analysis Finite Element Model.

(a) Critical Rivet Row Detail   (b) Boundary Line Plot Showing Crack.
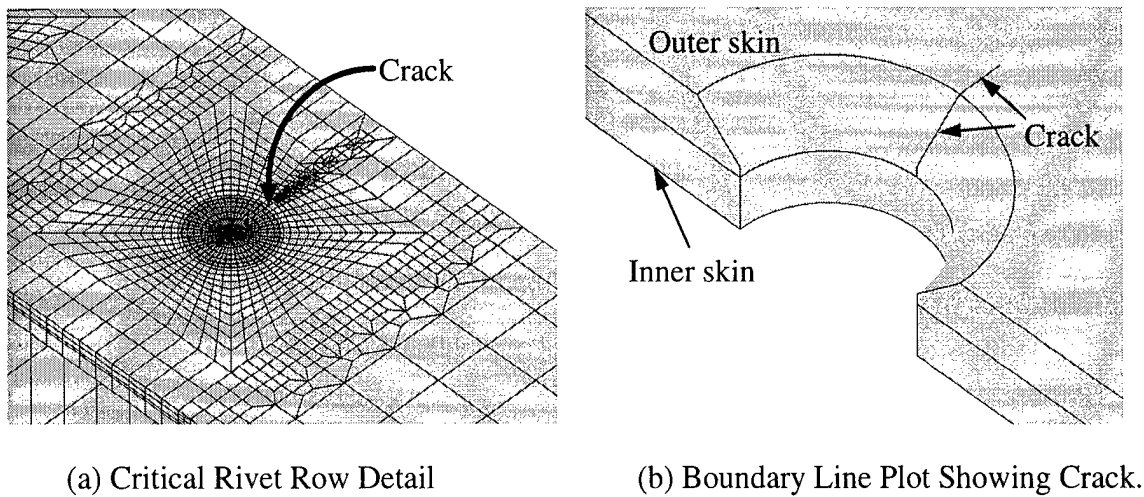
Figure 3. Fracture Mechanics Finite Element Model.
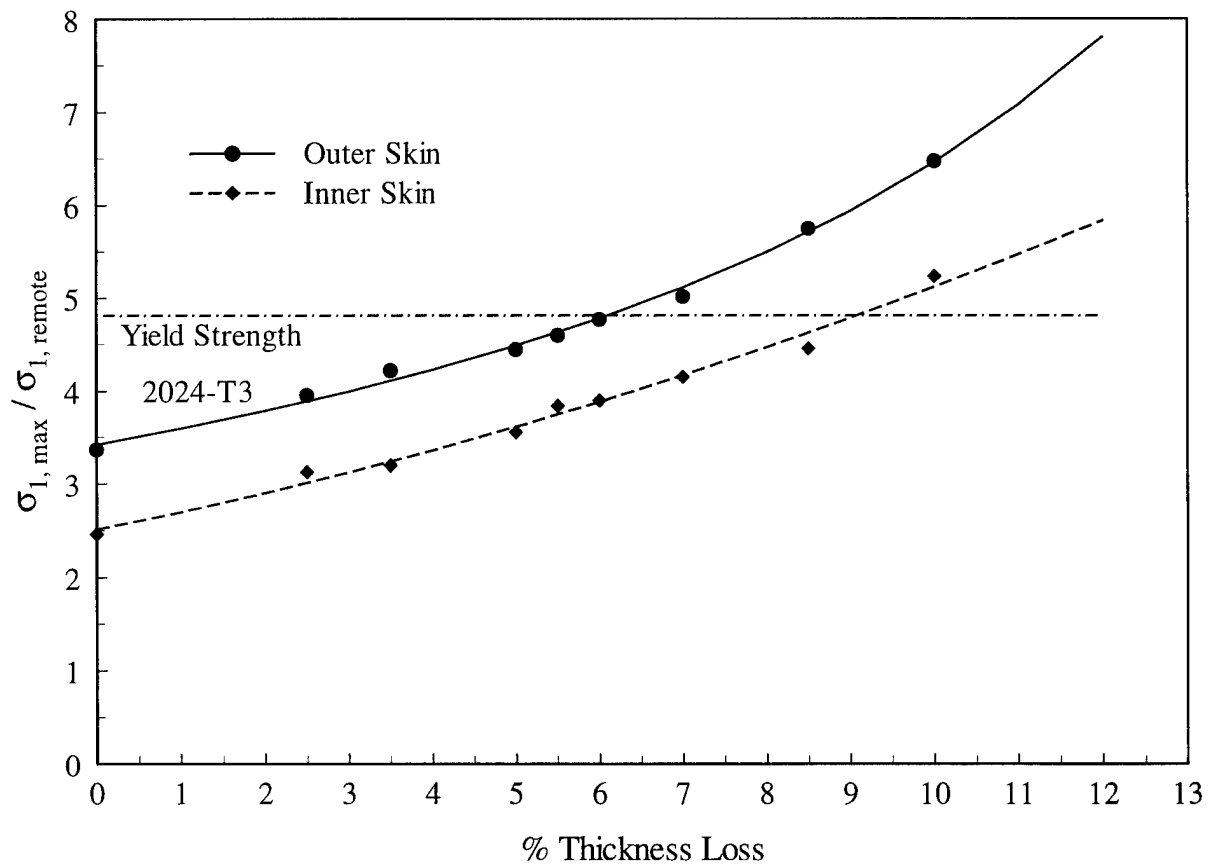
Figure 4. Effect of Increased Corrosion Pillowing on Critical Rivet Row of Respective
Skins.
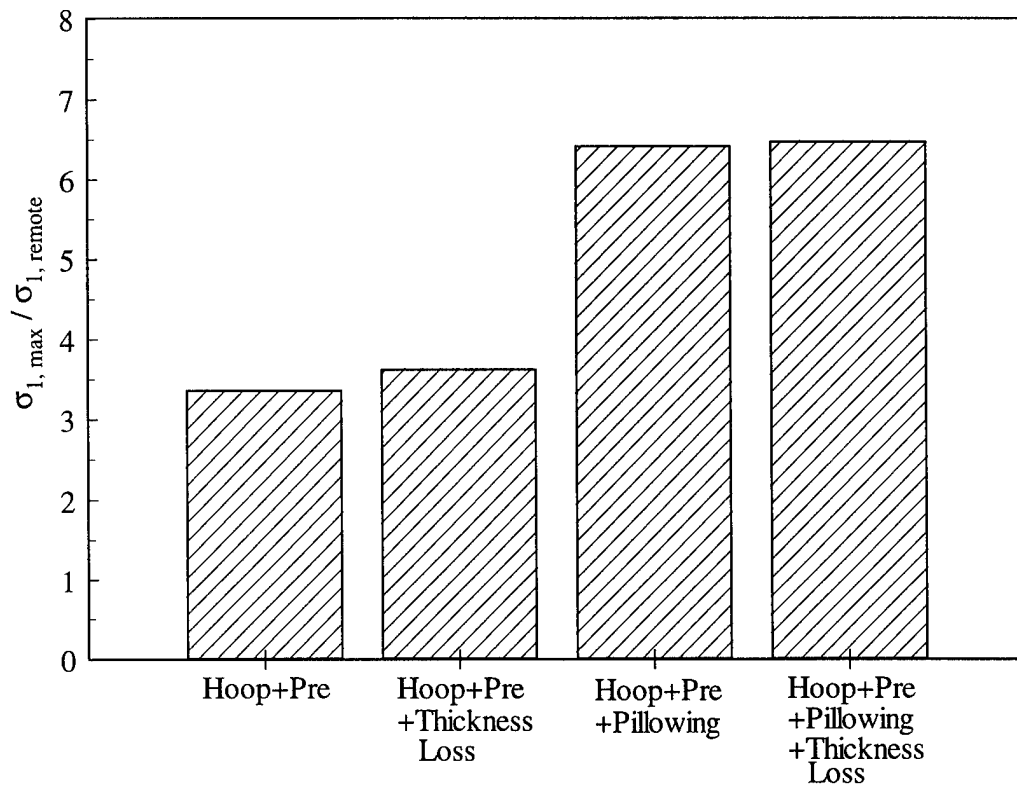
Figure 5. Effect on Stress Caused by Reduction of Outer Skin Thickness as Compared to Pillowing (10% thickness loss).
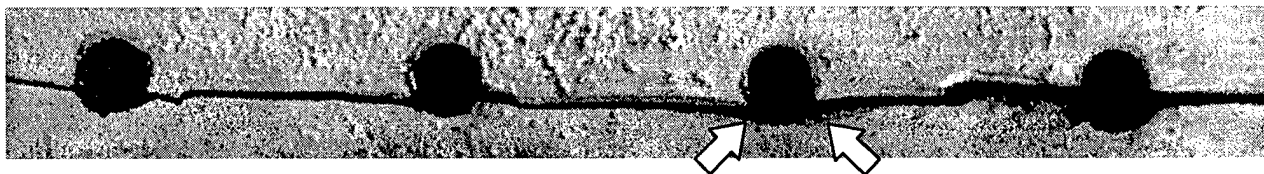
(a) Crack Located in Upper Rivet Row in Precorroded Specimen. Arrows Indicate Crack Initiation Sites.

(b) Maximum Principal Stress Location Obtained From Finite Element Analysis.

Figure 6. Comparison of Crack Initiation Sites in Multisite Damage Specimens and Maximum Principal Stress Location.
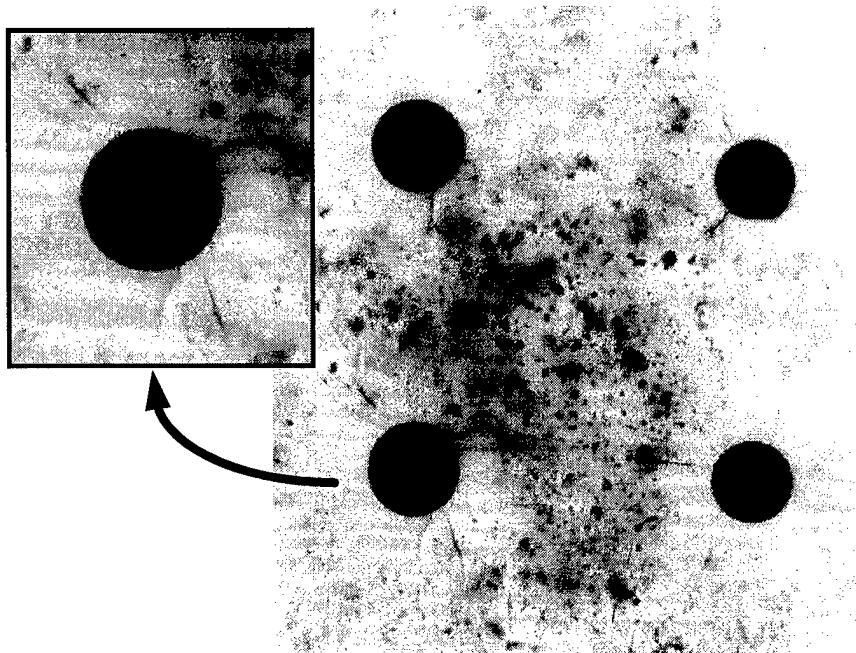
(a) Cracks in Area of Maximum Pillowing in Outer Skin.
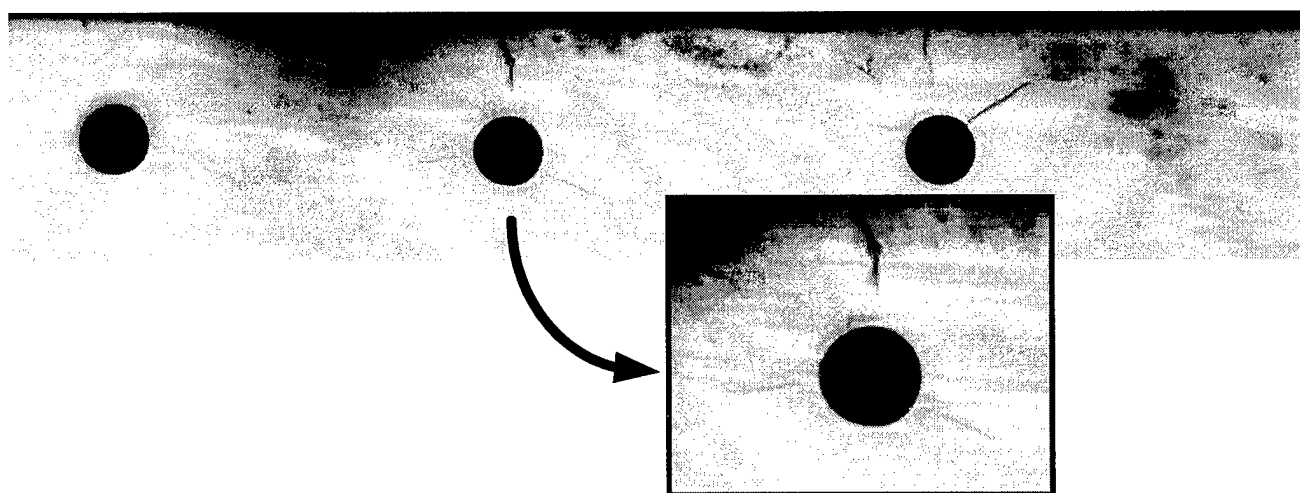
(b) Cracks in Area of Maximum Pillowing in Inner Skin.

Figure 7. X-Ray Images of Retired-Fuselage Lap Joints.
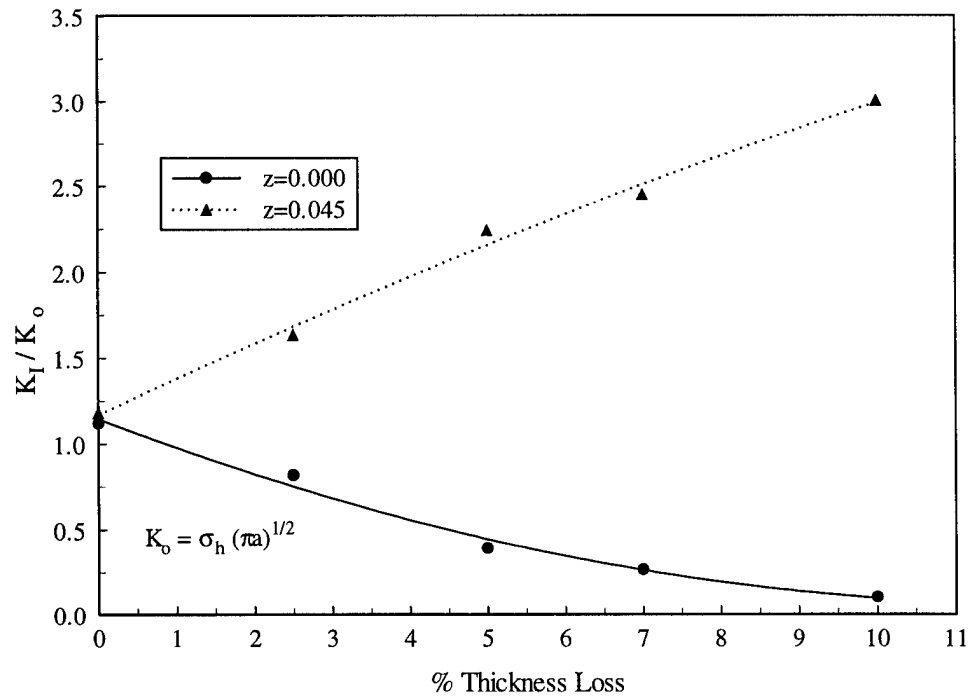
Figure 8. Nondimensional Stress Intensity Plot of Outer Skin (z=0.000) and Inner Skin (z=0.045) Crack Edges Where σ_h is the Applied Hoop Stress in Plate and a is the Crack Length From the Center of the Rivet Hole.

Chart labels: K_I / K_o (vertical axis); % Thickness Loss (horizontal axis); legend z=0.000, z=0.045; $K_o = \sigma_h \, (\pi a)^{1/2}$
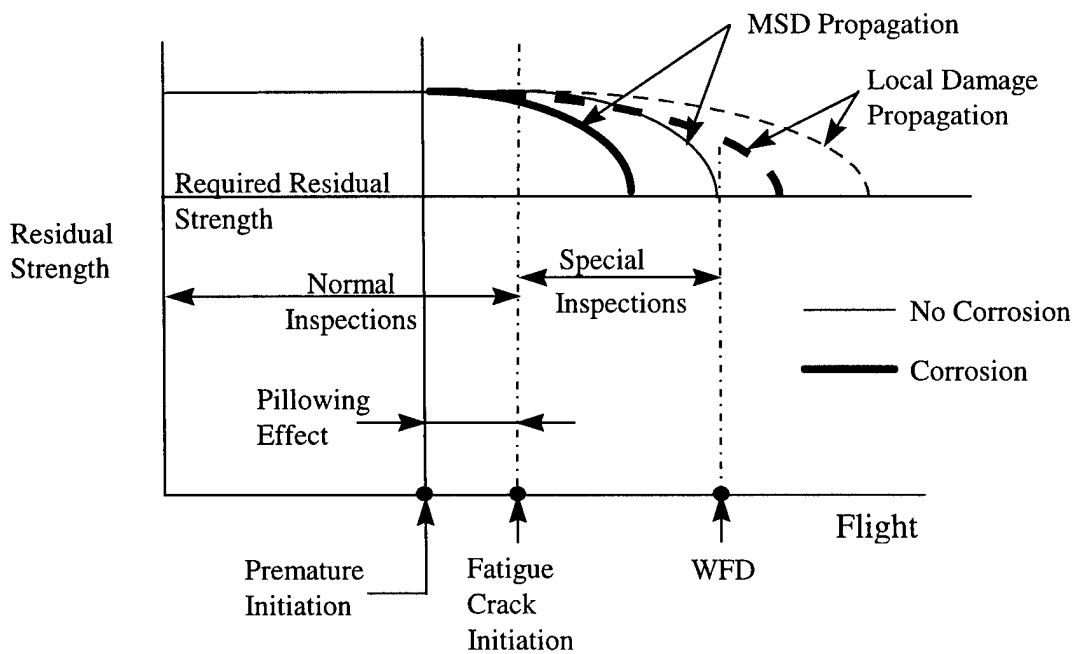
Figure 9. Implications of Corrosion Pillowing on Structural Integrity of Fuselage Lap Joints. Graph Modified From Reference 7.

IMPROVED NONDESTRUCTIVE INSPECTION TECHNIQUES FOR AIRCRAFT INSPECTION

Don Hagemaier and Dwight Wilson
McDonnell Douglas Aerospace
Long Beach, California

ABSTRACT

Through the use of an Integrated Product Team approach and new inspection techniques incorporating the latest in imaging capabilities and automation, the costs of some manpower intensive tasks can now be drastically reduced. Also, through the use of advanced eddy current techniques, the detectable size of cracks under flush-head fasteners can be reduced while maintaining a reliable inspection.

Early in this decade, the Federal Aviation Administration (FAA) William J. Hughes Technical Center and the National Aeronautics and Space Administration (NASA) Langley Research Center formulated an aging aircraft research plan. The unique aspect about the research is that it is driven by the aircraft manufacturers and airlines in order to center only on those areas in which help is needed and to keep it focused. Once developed, the manufacturer works with the FAA Aging Aircraft Nondestructive Inspection Validation Center at Sandia National Laboratories, the airline, and the researcher to transfer technology to the field.

This article first describes the evaluation and results obtained using eddy-current technology to determine the minimum detectable crack size under installed flush-head fasteners. Secondly, it describes the integrated efforts of engineers at McDonnell Douglas Aerospace and Northwest Airlines in the successful application of mobile automated scanner (MAUS) eddy-current C-scanning of the DC-10 circumferential and axial crown splices. The eddy-current C-scanning greatly reduced the man-hour effort required for the existing radiographic inspection. Thirdly, it describes the use of a novel ultrasonic technique coupled to a scanner and graphics for the detection and quantification of corrosion thinning and stress corrosion cracking of the DC-9 lower wing tee cap. This successful effort resulted from a rather large integrated task team. It also results in a vast man-hour savings over the existing internal visual inspection.

INTRODUCTION

The nondestructive inspection (NDI) portion of the FAA National Aging Aircraft Research Program (NAARP) predicates that improvements must be made to existing

inspection techniques and devices so as to provide more reliable detection capabilities. In June 1988, the First International Conference on Aging Airplanes was held in Arlington, Virginia. As a result of the recommendations from the 1988 conference, an FAA National Aging Aircraft Research Plan (NAARP) was completed in 1989. Jointly with NASA Langley Research Center, the FAA William J. Hughes Technical Center has directed and sponsored nondestructive inspection research and development (R&D) programs to assure aircraft safety. Considerable work has been done in laying the groundwork for an active program to develop new and improved NDI methods and techniques for in-service inspection of aircraft structures. What follows is a description of three activities which advanced the state of the art for NDI technologies and provided increased reliability through smaller detectable flaw sizes and a great savings in man-hours needed to perform the required inspections.

Although the FAA NAARP was initiated in 1989, the manufacturers, operators, and regulators have been studying the question of how to assure the structural integrity of aging aircraft since 1978. Accordingly, about 1983, the Douglas Aircraft Company (DAC) and the operators established an Industry Steering Committee (ISC) to oversee the development of Supplemental Structural Inspection Documents (SSIDs) for each of its aircraft models. Since that time, DAC has produced SSIDs for the DC-3, DC-6, DC-8, DC-9, and DC-10 aircraft models. Through the FAA-NASA program, new and improved NDI techniques have been developed which can replace or become an alternate means of compliance for an existing SSID inspection. This is the case for two of the inspections described below.

EDDY-CURRENT DETECTION OF SHORT CRACKS UNDER INSTALLED FASTENERS

It is a known fact that aluminum aircraft fuselage skins can develop small fatigue cracks after an extended period of service due to the numerous pressurization cycles. Usually, the outer skin is countersunk to provide for assembly with flush-head fasteners. The sharp edge in the skin, caused by the countersink, provides a high stress concentration for fatigue crack generation (see Figure 1). Numerous small cracks may be generated along a particular row of fasteners. When this happens, they are generally referred to as multiple-origin fatigue cracks. The small cracks continue to grow with time and at some point they can join up causing failure of the skin and rapid decompression of the aircraft cabin. Hence, there exists a need to detect them at the smallest size possible.

Many high-frequency eddy-current inspection techniques have been developed to detect fatigue cracks, which extend beyond the periphery of installed flush-head fasteners, in aluminum fuselage skins. However, until recently, the shortest crack that could be reliably detected was 2.54 mm (0.10 inch) in length. Damage tolerance (stress) engineers were unhappy with that figure and requested that improved eddy-current techniques be developed to detect fatigue cracks on the order of 1.25 mm (0.050 inch) in length. Cracks of this length barely extend beyond the fastener head which makes them difficult to detect.
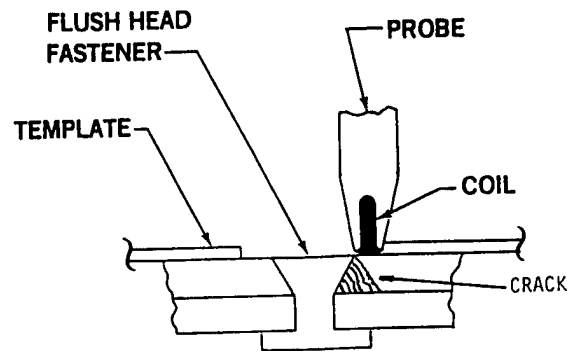
Figure 1. Short Fatigue Crack Under Flush-Head Fastener.

In order to prove that certain improved eddy-current equipment or probes could detect the flaw size goal, fatigue cracks and electrical discharge machine (EDM) notches were fabricated into countersunk fuselage skin panels. The cracks and notches ranged from 0.635 mm (0.025 inch) to 2.54 mm (0.10 inch) in length (see Figure 2). This particular study program was funded by NASA Langley Research Center with Dr. William Winfree as the Technical Director.
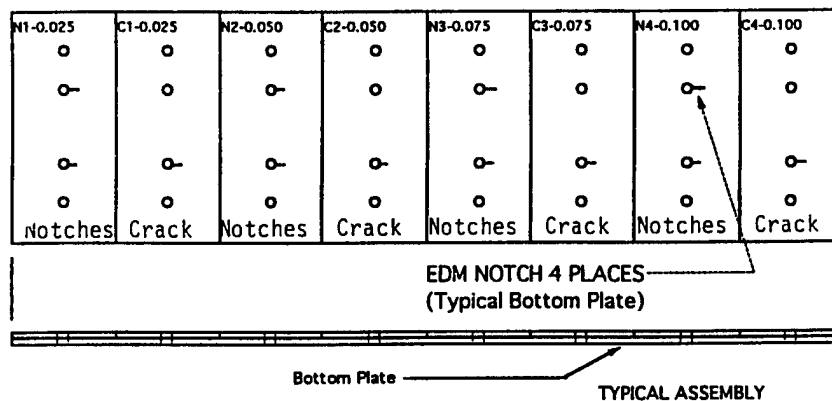
Figure 2. Typical Notched/Cracked Test Panel.

A variety of existing equipment was evaluated for this program and is fully described in Reference 1. Instruments used in this study were the pulsed eddy-current Nortec Eddyscan 30, the Hocking FastScan, the Northrop low-frequency eddy-current array (LFECA), and the Rohman Elotest with minirotor and GK Engineering probe. Typical results for a 1.25-mm (0.050-inch) crack under a flush-head aluminum rivet is shown in Figure 3(a) for the Eddyscan 30, in Figure 3(b) for the Elotest B1 with mini rotor, and in Figure 3(c) for the LFECA. There were 32 rivet sites in the test panel with 4 cracks and 4 EDM notches. Figure 4 shows the total results for the 32 test sites with the LFECA and Table 1 compares the

405

signal-to-noise ration (SNR) for the flawed sites to the unflawed sites. Figure 5 shows the CRT responses for the cracks in the test panel using the Hocking FastScan. Table 2 shows the results for the four instruments' ability to detect first layer cracks and second layer notches under both flush-head aluminum rivets and steel fasteners.

A. Eddyscan 30   B. Elotest   C. LFECA
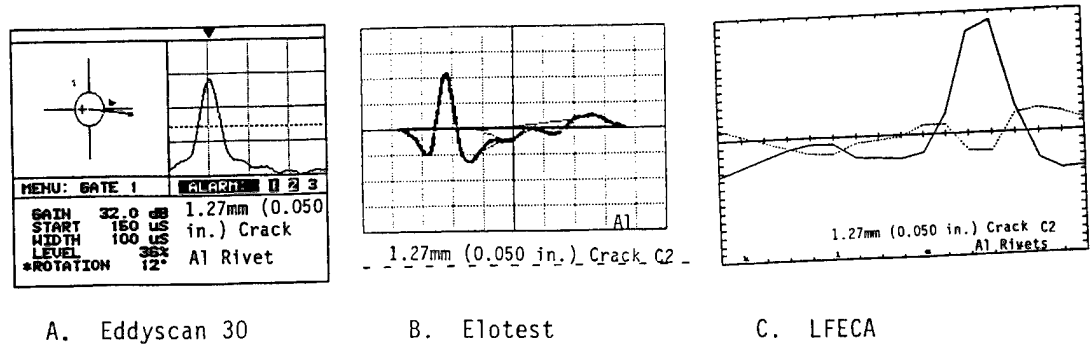
Figure 3. Detection of 1.27-mm (0.050-in.) Crack Under Flush-Head Aluminum Fastener.
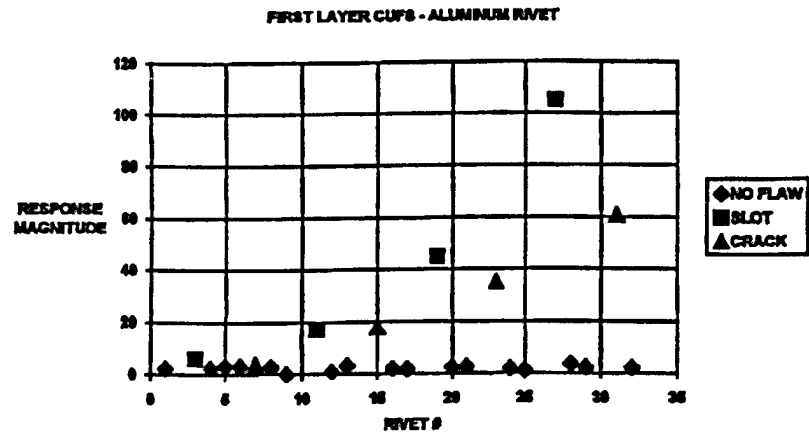
Figure 4. Response Magnitude for First Layer CUFS With Aluminum Rivets

Table 1. SNR for First Layer CUFS With Aluminum Rivets.

FLAW SIZE (mm)	SLOT or CRACK	SNR (dB)
0.635	Slot	5.0
0.635	Crack	1.5
1.27	Slot	14.0
1.27	Crack	14.7
1.90	Slot	22.6
1.90	Crack	20.5
2.54	Slot	30.0
2.54	Crack	25.0

406
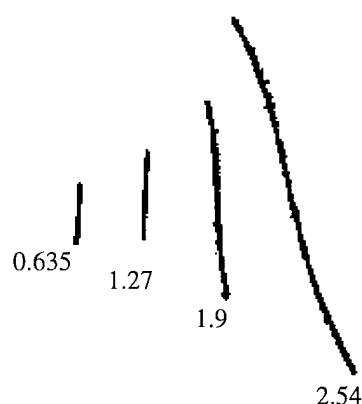
Figure 5. Hocking FastScan Results for Cracks Under Flush-Head Rivets (Millimeters)

Table 2. Eddy-Current Flaw Detectability Under Flush-Head Fasteners

Detectability for Cracks Under Aluminum Rivets, 1st. Layer

Nortec 30 Eddyscan   1.0 mm (0.040 in.)
Northrop LFECA   1.0 mm
Hocking FastScan   1.0 mm
GE Engineering/Elotest   1.0 mm

Detectability for Cracks Under Steel Fasteners, 1st. Layer

Nortec 30 Eddyscan   1.27 mm (low SNR)
Northrop LFECA   1.27 mm (0.050 in.)
Hocking FastScan   1.27 mm
GE Engineering/Elotest   1.90 mm (0.075 in.)

Detectability for Notches Under Aluminum Rivets, 2nd. Layer

Nortec 30 Eddyscan   1.27 mm (0.050 in.)
Northrop LFECA   1.27 mm
Hocking FastScan   1.27 mm
GE Engineering/Elotest   1.90 mm (0.075 in.) manual probe only

Detectability for Notches Under Steel Fasteners, 2nd. Layer

Nortec 30 Eddyscan   1.27 mm (low SNR)
Northrop LFECA   1.27 mm (0.050 in.)
Hocking FastScan   1.27 mm
GE Engineering/Elotest   1.90 mm (0.075 in.) manual probe only

The DC-10 SID program requires an inspection of the fuselage skins, finger doublers, and longerons around the longitudinal and transverse splices on the crown of the aircraft (Figure 6). This splice consists an exterior doubler, fuselage skin, finger doubler, and longeron (Figure 7). Fatigue cracks must be detectable in the longitudinal and transverse direction in the skin and finger doubler. Only cracks in the transverse direction must be detected in the longerons.
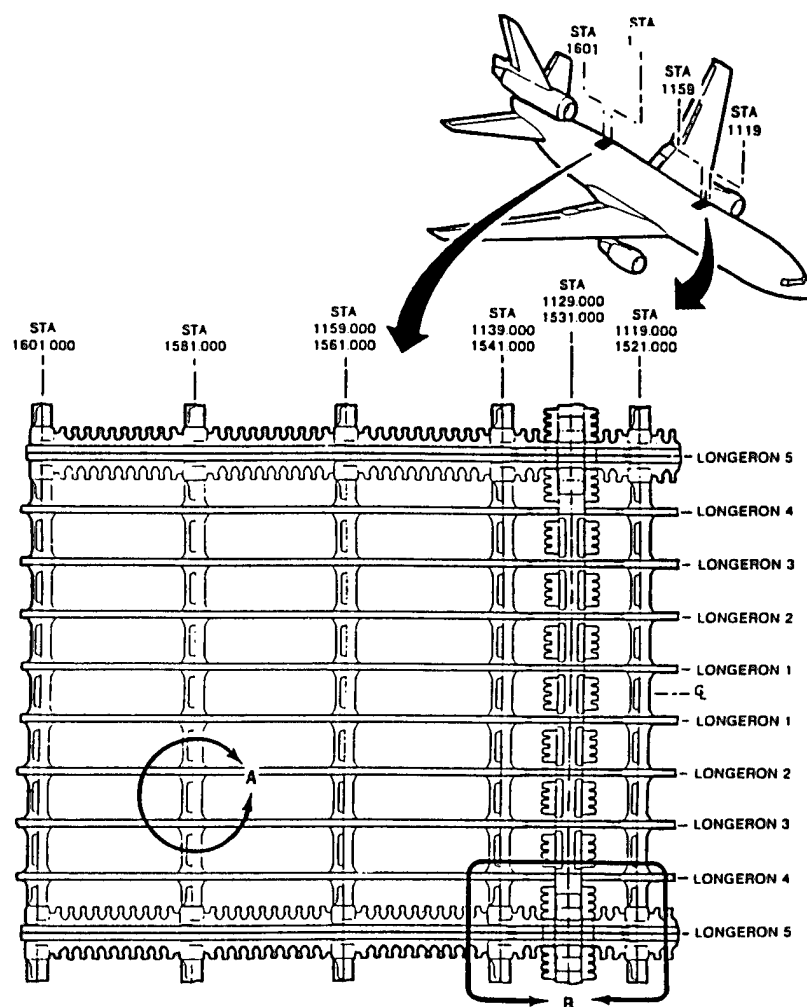
Figure 6. Inspection Areas.

Two NDI methods were originally selected for evaluation of the splices: eddy-current and x-ray radiography. Radiography, in general, is a difficult technique to apply in this application due to the multiple layers of material and geometric features in the splices. In theory, eddy-current was the preferred method to try; however, the underlying geometry in the splices also created interpretation problems when using conventional eddy-current

technology. Several types of sensors were evaluated before the investigator concluded that the underlying structure was too complex for a manual eddy-current inspection. Hence, the radiographic procedure was developed for the Supplemental Inspection Document (SID) inspection with an additional manual eddy-current inspection for cracks in the external doubler and internal finger doubler.
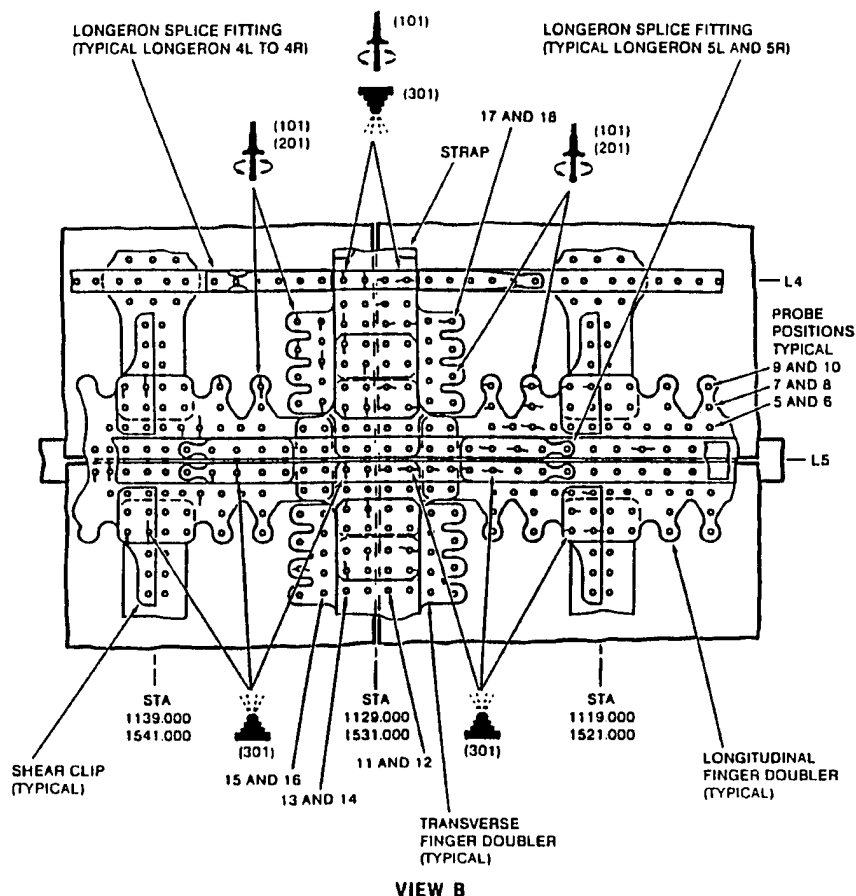
Figure 7. Crack Location and Orientation in Skin and Finger Doubler, Longitudinal and Transverse Splice.

The current radiographic procedure requires a two-sided access to the splices. Removal of the interior of the aircraft to provide access can take up to 110 labor hours. The actual radiographic inspection takes about 100 labor hours to complete and requires 98 radiographs. In addition, this inspection is usually limited to off-shift periods because of the radiation hazard to unprotected workers.

During a demonstration of the MAUS II eddy-current C-scan system in September 1993, it was recognized that the MAUS (Figure 8) was a potential alternative for the radiographic inspection. It was hoped that the C-scan image would provide enough additional information, relating sensor signals to the geometry features in the structure, in

order to detect cracks. An integrated product team was established between personnel from Northwest Airlines and McDonnell Douglas Aerospace-East & West.
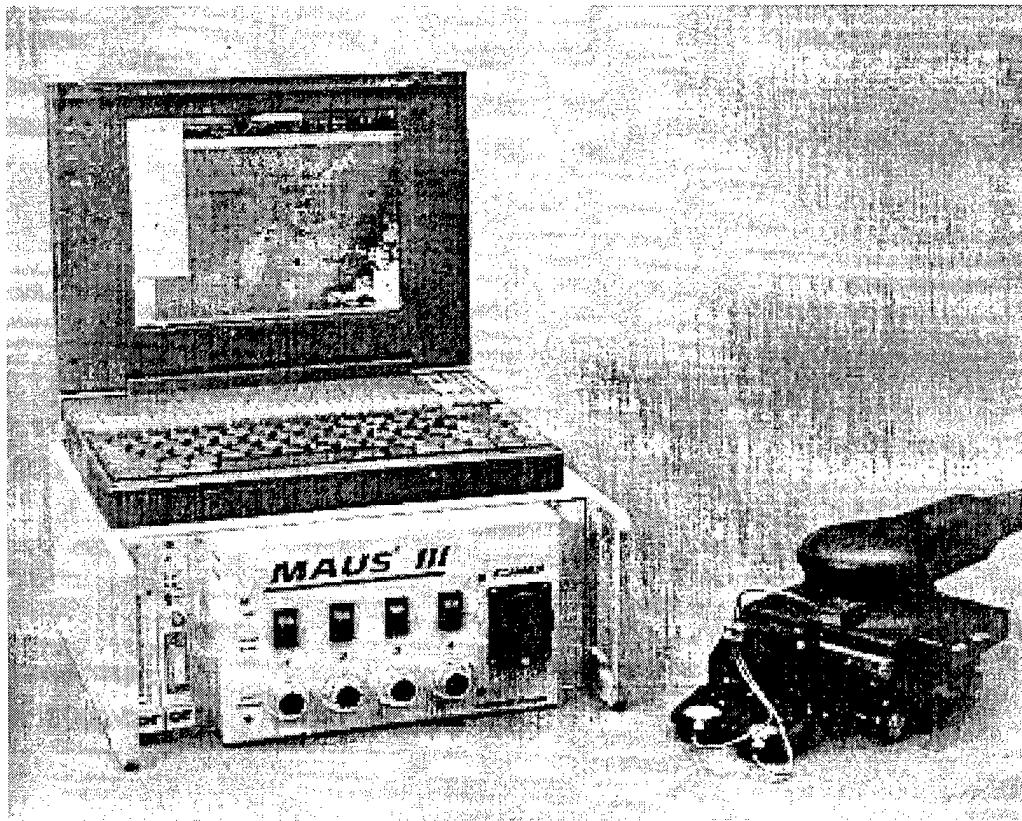
Figure 8. Mobile Automated Scanner (MAUS III).

A splice joint standard with notches in the four layers and in two directions was fabricated. Tests using this standard indicated that the operating frequency of the MAUS needed to be lower than 1 kHz to detect cracks in the longerons and a special scanner fixture was needed to avoid problems when scanning across the external doubler.

Many trials were made, using a variety of sensors, both in the laboratory and on-aircraft. A special vacuum cup holding and scanning fixture was fabricated by GK Engineering. This allowed the inspection to be performed by one technician, in about four hours, after the fixture was installed. The procedure was performed in two scans, operating a single sensor at different frequencies. One scan at 3.5 kHz inspected the external doubler, skin, and finger doubler below the skin. The second scan was performed at 600 Hz to detect cracks in the longerons and finger doubler thicker sections. In general, the data repeatability was excellent and the procedure was finalized in June 1996. Figure 9 shows a typical MAUS eddy-current C-scan image of the crown splice. Finally, this documentation has been submitted to the FAA for consideration as an alternate means of compliance for the SID through the yearly revision process. The cost savings between the MAUS eddy-current and x-ray inspections amount to about 95% man-hour savings plus the cost of the x-ray film.

410

Notch in Longeron

* - Notch from fastener to edge

Notch in Skin

Skin/Doubler

Skin/Doubler/Longeron

Skin/Doubler

Notch in Doubler

Notch in Doubler

Skin/Doubler area collected at 3.5 KHz,
Skin/Doubler/Longeron area collected at 600 Hz
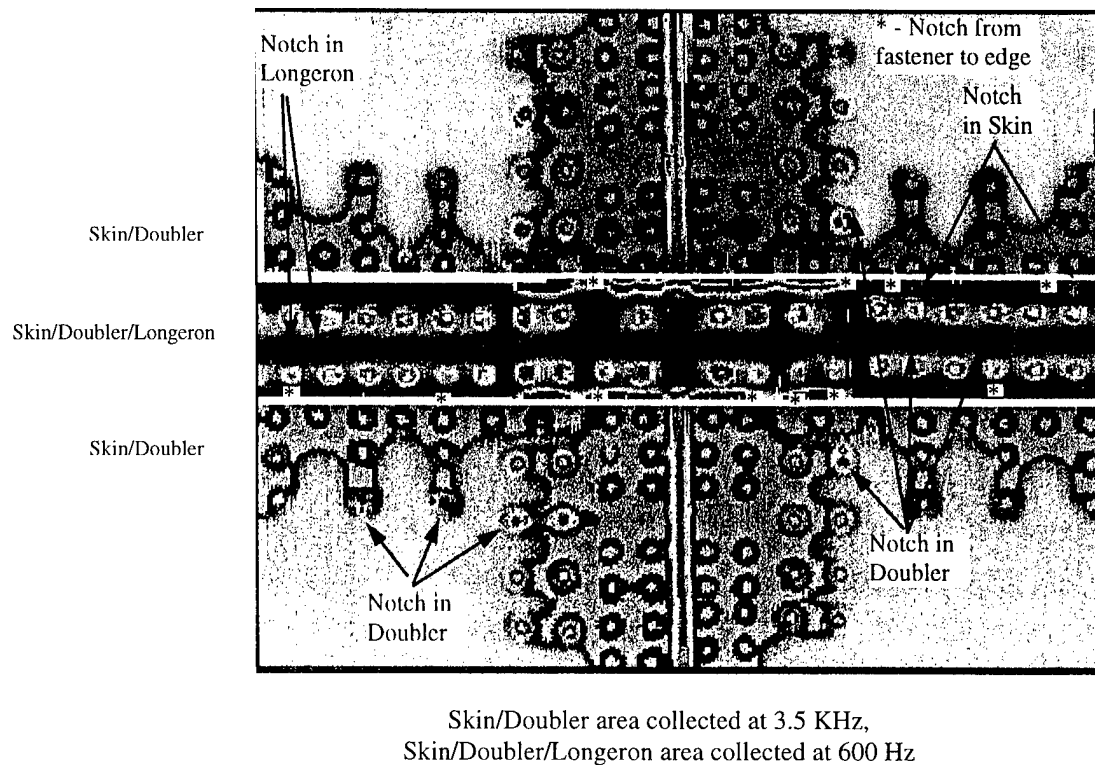
Figure 9. C-Scan Images of Notches in DC-10 Crown Skin Joint Standard.

STA
Y=484.000

STA
Y=585.000

A

A
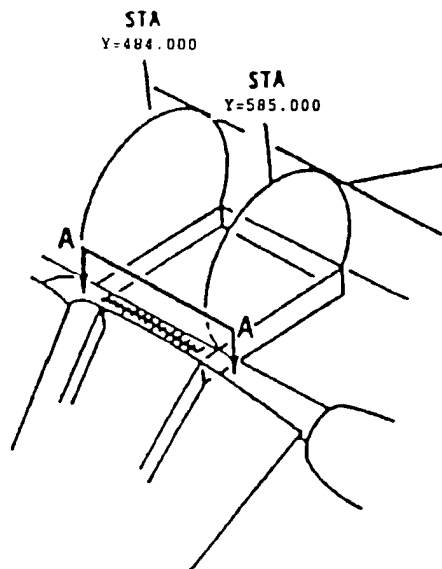
Figure 10. Inspection Area With Respect to Wing and Fuselage.

411

From the start of the FAA NAARP program, every effort was made to direct the efforts of the FAA Center for Aviation Systems Reliability (CASR) investigators to solutions of actual inspection and maintenance challenges identified in the field. It was evident that a successful project required a significant level of synergism between participants from CASR, maintenance facilities, and aircraft manufacturers.

The current procedure to inspect for exfoliation corrosion and stress corrosion cracks of the lower tee cap requires entry into the fuel tank for visual inspection. Figure 11 illustrates a typical cross section of the tee cap which connects the wing center box to the outer wing. Typical areas of exfoliation corrosion and stress corrosion are also illustrated in Figure 11. The inner and outer wing stringers are joined by bolts which extend through the tee cap. A layer of faying surface sealant is used between the lower skin and horizontal leg of the tee cap to make the structure fuel-leak free as well a corrosion inhibitor. The faying surface sealant allows transmission of the ultrasonic beam to the tee cap for corrosion and crack detection.

View Looking Down
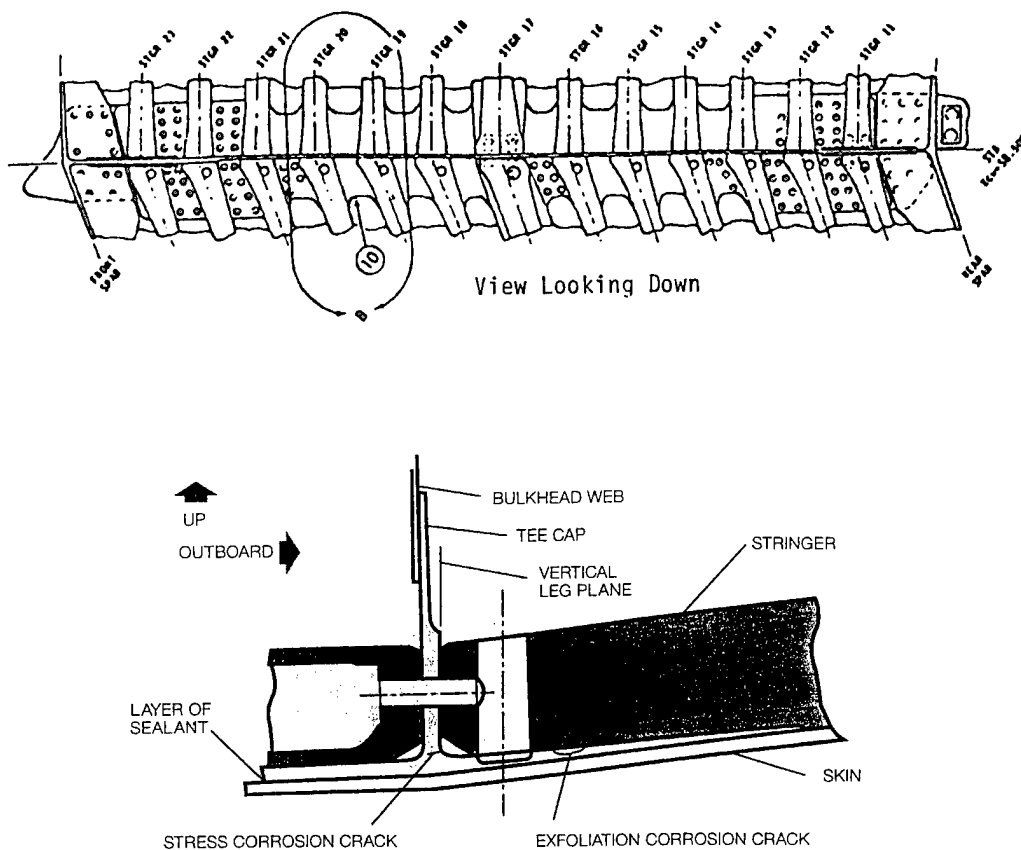
Figure 11. DC-11 Lower Wing Skin and Tee Cap and Stringers.

In the 2nd layer ultrasonic technique, developed by Drs. Jan Achenbach and Igor Komsky at Northwestern University, two wedge-mounted transducers are used in a pitch-catch configuration as shown in Figure 12. With carefully selected wedge angles, transducer spacing, and operating frequency, maximum penetration in the second layer tee cap can be achieved. Transducer 1 generates ultrasonic signals in both layers. One signal propagates in the top layer and, after reflection by the sealant, is received by Transducer 2. Another signal penetrates through the sealant and, after being reflected either by the bottom of the second layer or by corrosion spots, is received by Transducer 2. Times of flight (the time it takes for the sound to travel back and forth) of both waves is used for material loss characterizations.
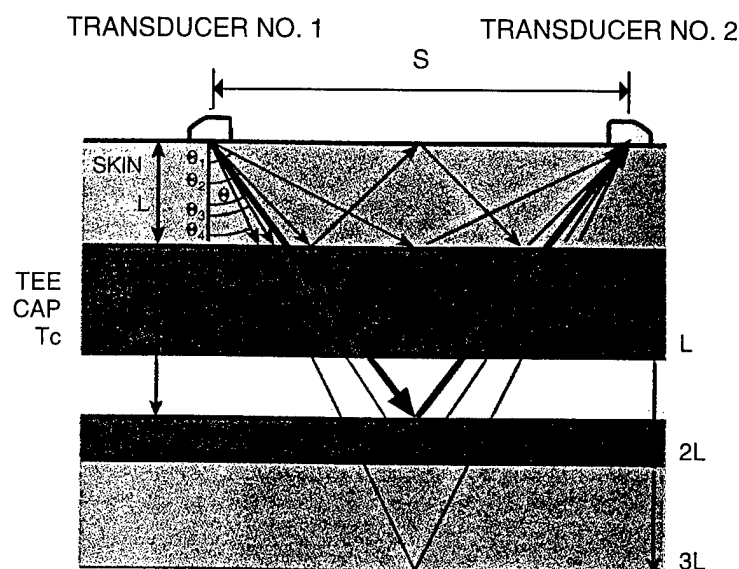
Figure 12. Second Layer Ultrasonic Inspection. Soundpaths Penetrate the Skin and Tee Cap at Various Depths to Reveal Material Loss Due to Corrosion.

By linking the pitch-catch transducers and signal output to an imaging system, C-scans can be produced which indicate the degree of thinning or cracking. Northwest Airlines personnel fabricated typical flawed standards from 7075-T6 machined plate stock. The two plates were bonded with PRC-1422 sealant and clamped together using Hi-Lok fasteners. To simulate corrosion in the tee cap inner surface, spot faces were machined to controlled depths. To simulate stress corrosion cracks, EDM notches were added at the radius of the tee horizontal and vertical legs. Similar standards were fabricated from scrapped DC-9 wing sections. Figure 13 shows a C-scan recording showing two spot faced areas of 4% and 7% thinning and an actual corroded area with 7% thinning in the tee cap inner surface.

Spot Face Exfoliation Spot Face
7% Loss Corrosion 4% Loss
7% Loss
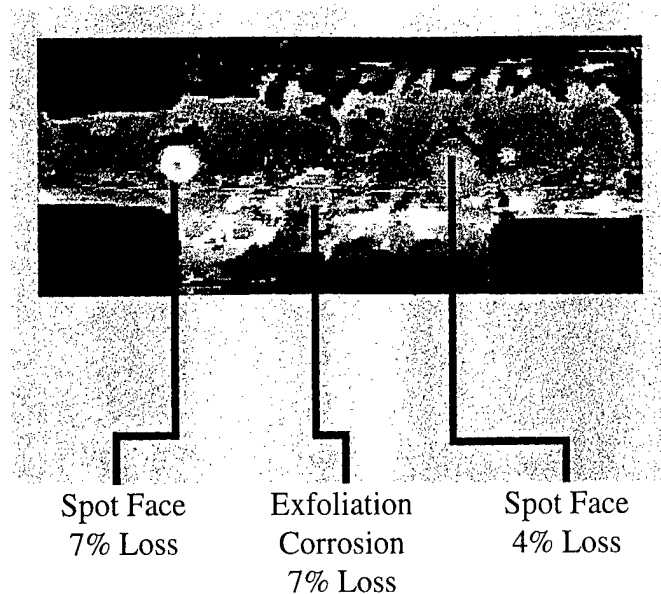
Figure 13. Second Layer Ultrasonic C-Scans Can Reveal Small Amounts of Material Loss

The Service Bulletin work-hour estimate for visual inspection, without repair, is 376 man-hours per aircraft. The total number of hours needed from preparation of the aircraft through functional check is estimated to be quite a bit more than this. The ultrasonic inspection of the fourth aircraft, using the new technique, was done in less than 48 man-hours. This represents a tremendous cost savings to the affected operators. The procedure has been approved, by the FAA, as an Alternate Means of Compliance to the Service Bulletin internal visual inspection.

The DC-9 wing box inspection team was recently awarded the McDonnell Douglas Aerospace 1995 Silver Eagle and Model of Excellence awards.

SUMMARY

The development and implementation of acceptable maintenance and inspection programs for both new and aging aircraft is complicated and entails many aspects. The process of developing these inspections has evolved from those in which each program was operator unique to a sophisticated relationship of interdependence between operators, regulatory agencies, researchers, and NDI equipment and aircraft manufacturers. By taking the concepts of integrated product teams to the next logical step and including the university, the regulator, and the customer, the aircraft manufacturer can now offer drastic inspection cost savings.

ACKNOWLEDGMENT

REFERENCES

1. Hagemaier, D.: "Eddy Current Detection of Short Cracks Under Installed Fasteners," 1995 ATA NDT Forum, Hartford, Connecticut.

2. Jappe, W., Johnson, M., and Wood, N.: "The Transition Process from Emerging NDT Technology to Production Inspection Application." 1995 ATA NDT Forum, Hartford, Connecticut.

3. Komsky, I. N., Achenbach, J. D., Andrew, G., Grills, R., Register, J., Linkert, G., Hueto, G. M., Steinberg, A., Ashbaugh, M., Moore, D. G., and Weber, H.: "An Ultrasonic Technique to Detect Corrosion in DC-9 Wing Box From Concept to Field Application," Materials Evaluation, July 1995, pp. 848-852.

IMPROVING THE DAMAGE TOLERANCE OF BONDED STRUCTURES VIA ADHESIVE LAYER BARRIERS

Dr. John C. Brewer
Volpe National Transportation Systems Center
Cambridge, MA 02142-1093

ABSTRACT

Modern aircraft possess numerous applications for structural adhesive bonding. Continued airworthiness of these applications requires tolerance of undetected damage such as debonding. A serious concern is that a partial debond could grow unstably across the entire bond. For example, composite patch repairs of structural cracks can be extremely effective at retarding crack growth, yet they need a damage tolerant bonding mechanism that maintains the patch's utility even after partial bond failure. Analysis is presented that shows that a composite patch on a cracked aluminum sheet will still be effective even if a large portion of the bonded area has debonded, as long as the remaining bonded region is stable and the patch still provides a viable load path around the crack. A method is proposed which enhances the damage tolerance of a bond with barriers that divide the adhesive layer into discrete regions. The barriers are inserted into the adhesive bond layer before curing and make uninterrupted contact with both adherends, thereby forming separate zones of adhesive. The barriers may be constructed of a nonstick material and may be slightly thicker than the nominal adhesive layer. If a local debond were to grow to a barrier, the debond front should preferentially travel along the lower energy bond between the adhesive and the barrier rather than through the adhesive or along an adhesive/adherend interface. The barriers should prevent the extension of the debond from one region to the next. Since most load is transferred in a boundary region near the edge of a bond, dividing the bond into several regions should make it sufficiently redundant to withstand locally unstable debond growth.

INTRODUCTION

Any evaluation of aircraft structural integrity must consider the long-term ability to withstand reasonably expected loads after damage has occurred. Prudent engineering principles suggest the use of redundant structures and redundant joining methods. The Federal Aviation Administration requires that transport category aircraft be "damage tolerant." That is, they must be

"evaluated to ensure that should serious fatigue, corrosion, or accidental damage occur within the operational life of the airplane, the remaining structure can withstand reasonable loads without failure or excessive structural deformation until the damage is detected." [1]

The above definition recognizes that not all structural damage is immediately detectable. Structural redundancy and inspection must be used to assure that components with insidious damage can tolerate expected loads until the damage is found and repaired.

The damage tolerance regulations apply not only to virgin aircraft structure but also to repairs of affected aircraft. In practical terms, aircraft repairs should also be quick, durable, and relatively inexpensive. Some aircraft, mostly military, have used bonded composite patches to repair structural cracks. A patch has two beneficial effects. First, it provides an alternate load path. Patches are primarily unidirectional such that the fibers bridge the crack. Much of the load is transferred out of the plane of the damaged component. Second, a patch enforces a virtual limit to the maximum crack opening. Both of these results limit the stress intensity factor at the crack tip which in turn limits the crack extension in each cycle. Patches are designed to keep the crack size well below its critical value during the remaining economic life of the aircraft. Boron/epoxy patches have been used most often because of their high stiffness and the ability to monitor crack size through the patch using eddy-current technology.

Currently, the application of composite patches to aircraft is generally limited to cracks small enough that they will not, over the course of several inspection periods, grow to a critical size for the largest expected lifetime load. In this way, even if the patch were somehow completely ineffective, the damage could be monitored and repaired via another method long before operational safety was jeopardized. Patches applied to small cracks could economically extend the component lifetime.

This paper describes a method that may help to achieve structural redundancy and damage tolerance requirements in bonded structures. The method is conceptually general enough to be applied to bonded joints in any vehicle or infrastructure application.

DAMAGE TOLERANCE OF COMPOSITE PATCHES

The application considered here is a structural plate with a crack that is repaired with a unidirectional fiber composite patch. The crack is assumed to be perpendicular to the principal loading direction. The fibers of the patch are aligned with the load. The arrangement is illustrated in Figure 1. An undamaged patch restrains the opening of the crack, virtually arresting it.

The patch is applied to the structure with an adhesive. Two aspects of the damage tolerance of these patches will be considered here: (1) the ability of a patch that is only partially bonded to effectively restrain the opening of the crack in the plate and (2) the ability of the patch to resist debonding under cyclic loading, even in cases where debonding has started.

Intuition can sometimes mislead people into believing that load is transferred uniformly across the adhesive layer in a bonded joint. Most load is transferred in a boundary region near the edge. In the central region, the bonded parts have similar displacement (and therefore strain) fields. Therefore, the majority of the adhesive's ability to transfer load is kept in reserve.
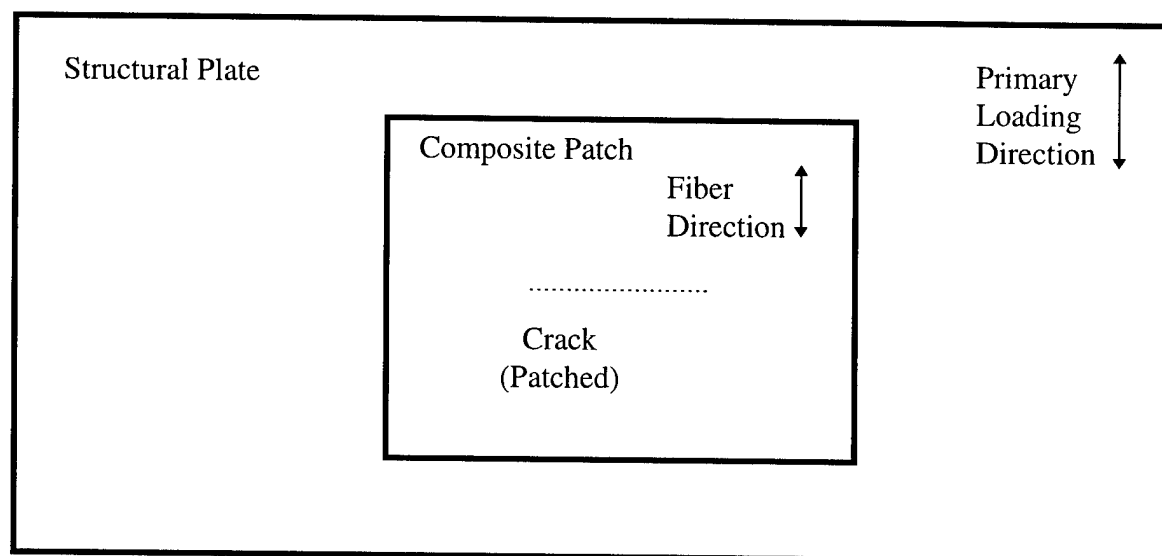
Figure 1. Schematic of Structural Application.

ADHESIVE LAYER BARRIERS FOR DAMAGE TOLERANCE

A patch will be tolerant of debond damage if debonds are arrested while the patch is still highly effective. Small debonds should not seriously degrade the adequacy of the patch. An appropriate inspection program could virtually assure that the debond would be detected and repaired before the crack approached critical size, so long as the debond growth were slow and predictable. Ultrasonic testing or a "tap test" can find debonds that extend over a significant fraction of the adhesive region. If a boron/epoxy patch is used, the crack size can also be monitored using eddy-current technology. Thus, damage can be detected and repaired.

Theoretically, debond fronts can grow rapidly or even unstably. An unstable debond might be stopped if the adhesive layer were divided into several discrete, unconnected regions. One method would be to separate the adhesive area into disparate regions by introducing gaps. Unfortunately, most adhesives have a low-viscosity phase of the cure during which there is a great deal of flow. Under the pressure applied during the bond cure, the adhesive regions could run together, resulting in a continuous adhesive layer capable of sustaining a debond completely across the patch.

419

As an alternative, it is proposed to insert physical barriers to separate the regions of the adhesive layers. A smooth nonstick-type surface would be a good candidate in that it should provide a low interfacial strength between the barrier and the adhesive. Thus, as a debond follows the lowest energy path along the adhesive/adherend interface, it should be arrested at the barrier as shown in Figure 2.
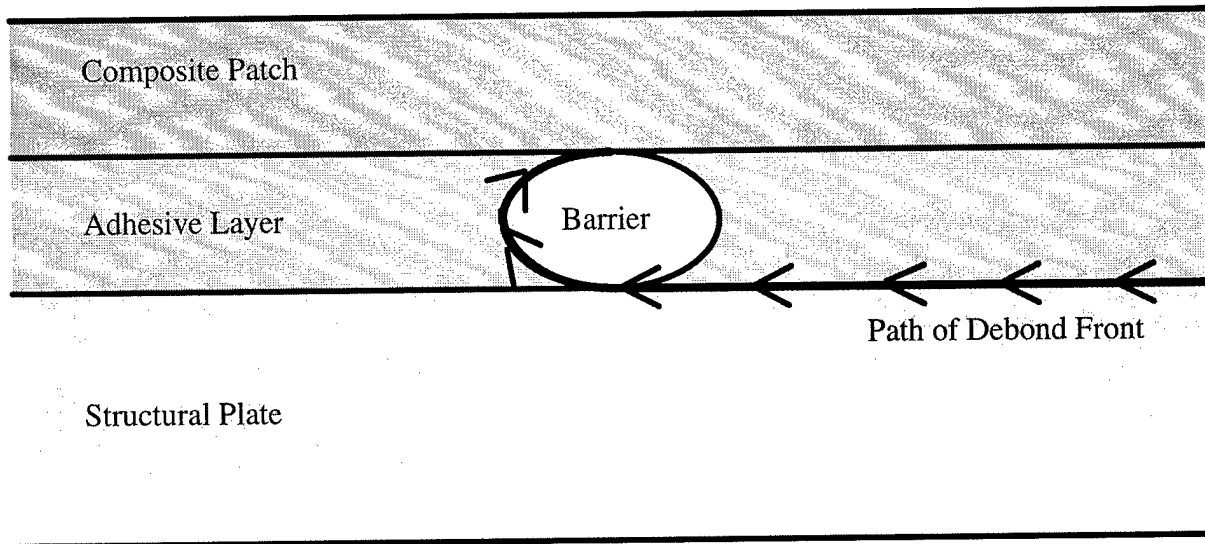
Figure 2. Debond Arrest Mechanism of Adhesive Barriers.

ANALYSIS

A finite element analysis of a square untapered boron/epoxy patch on a cracked aluminum sheet was performed to quantify the effectiveness of partially bonded patches [2]. The commercially available code ANSYS was employed. The elements used were 20-node quadratic "brick" elements. One layer of elements was used for each of the three materials. Quarter symmetry was used for computational efficiency. Eight hundred and twenty five elements were used. A typical mesh is shown in Figure 3.

The elements surrounding the crack tip were singular elements formed by collapsing one face of a 20-node element onto a line and locating the side nodes of the adjacent edges one quarter of the distance to the far face. The resulting element has the $r^{-1/2}$ singularity observed at crack tips, where r is the distance from the crack tip. The stress intensity factor is estimated from the displacement of the nodes of these elements along the crack face.
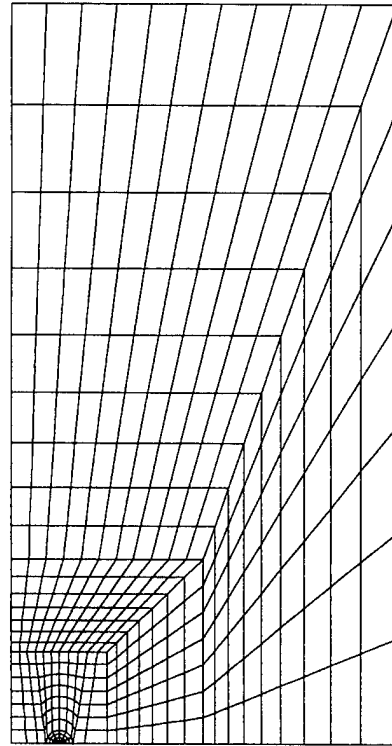
Figure 3. Typical Finite Element Mesh.

The adhesive was assumed to have debonded in rectangular regions as shown in Figure 4. The cases of intact adhesive layers directly over the crack were contrasted with those of intact adhesive layers at the edges of the patch. The ratio of patch width to crack width was 4:1. The material parameters are given in Table 1.
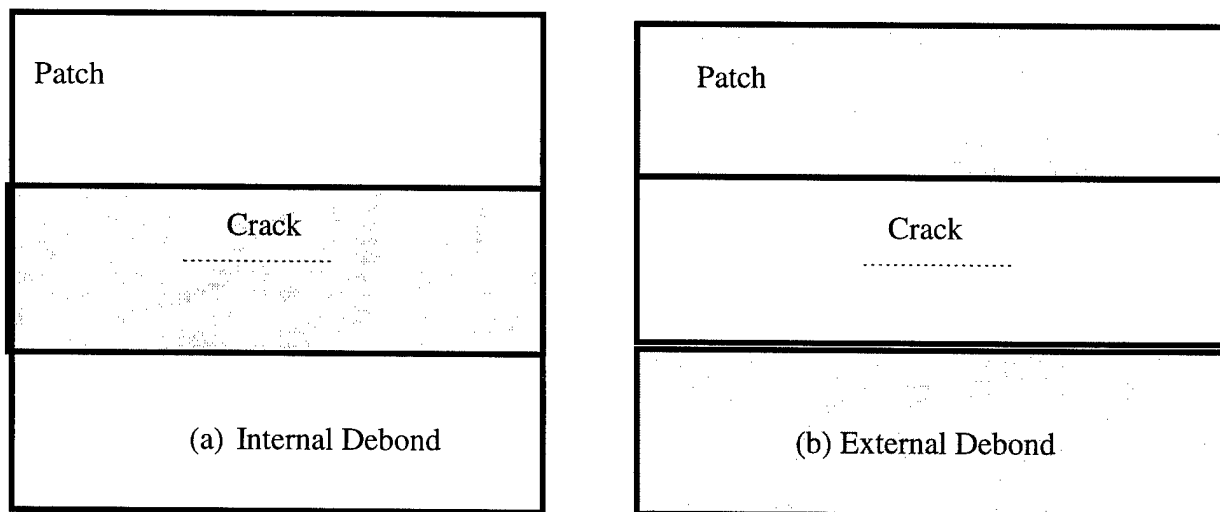
Note: Shaded region indicates debond.

Figure 4. Assumption of Rectangular Debonds.

Table 1. Material Parameters For Finite Element Analysis.

	Aluminum	Adhesive	Boron/Epoxy
Layer Thickness	0.036″	0.004″	0.020″
Longitudinal Modulus	10.3 msi	0.23 msi	30.2 msi
Transverse Modulus	10.3 msi	0.23 msi	3.8 msi
Major Poisson's Ratio	0.32	0.35	0.16

Note: msi = 10^6 lbs/in^2

The fibers were oriented parallel to the uniaxial loading. The results are shown in Figure 5. They show that, if the adhesive is intact directly over the crack, the state of the outer areas is less crucial in reduction of the stress intensity factor. In contrast, when the adhesive is intact at the edges of the patch and not over the crack, increasing the total bonded area can be beneficial. Nonetheless, even small bonded regions at the edges will produce a significant decrease in stress intensity factor. Since crack growth in each cycle is roughly proportional to the stress intensity factor raised to the fourth power, the increase in life is substantial.
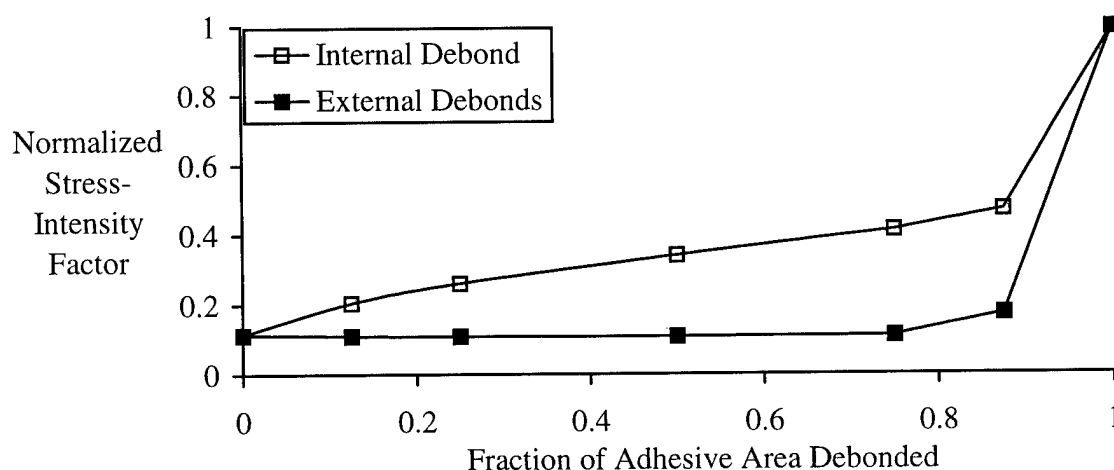
Figure 5. Effect of Debonded Area on Calculated Stress-Intensity Factor.

Experimental verification of these analyses was performed in a related study [3]. Aluminum specimens 6 inches wide with 1.0 inch (nominal) cracks were cycled at 16000 psi for 40,000 cycles. Of the six specimens, two were unpatched, two were patched with specimens with an internal debond, and two patched with patches with an external debond. The patches were unidirectional graphite/epoxy with approximately the same stiffness as the uncracked aluminum. The experiments showed that unpatched specimens failed in fewer than 6600 cycles while the patched specimens showed no more than 22% growth over 40,000 cycles. The scatter in the limited number of specimens made it difficult to assess experimentally whether the internal or external debonds were more severe.

Further experiments in that study [3] were intended to demonstrate the capability of the barriers to arrest debond growth and show that the barriers were unlikely to be the source of damage. Unfortunately, the results were inconclusive because the loading was insufficient to produce significant growth over 40,000 cycles. The study produced no evidence, however, that the barriers would not work. For example, none of the 64 barriers on the eight test specimens initiated a detectable debond over 40,000 cycles.

DISCUSSION AND CONCLUSIONS

The analyses show that partially debonded patches could still effectively reduce crack growth in aircraft structures. Thus, if adhesive layer barriers are shown to be capable of stabilizing debond damage, they could allow the patch to retard crack growth longer and more effectively. This, in turn, allows the structure to better tolerate the initial damage from the crack. In this way, adhesive layer barriers may improve the damage tolerance of patches.

This technology may have other applications. Many nonaerospace vehicles and structures would benefit from an adhesive bonding technology that arrests debonds, thereby enabling partial failure modes that can be detected via inspection. This may be economically preferable to the cost of designing and constructing more redundant structures.

As adhesive layer barriers are an immature technology, they cannot be recommended for use in safety critical applications until an appropriate data base has been generated. Further work is needed to confirm that rapidly growing debonds can be arrested or retarded.

REFERENCES

1.   Federal Aviation Administration Advisory Circular 25.571-1A, March 1986.

2.   Brewer, John C.: "Effectiveness of Composite Patches with Partial Debonds," Volpe Center Report LTR-FA4D8-9401, Letter report to the Federal Aviation Administration Technical Center, November 1993.

3.   Brewer, John C., and McManus, Hugh L.: "Adhesive Layer Barriers to Provide Damage Tolerance of Bonded Structures," Proceedings of the Eleventh Annual Advanced Composites Conference and Exposition, Dearborn, MI, November 6-9, 1995, pp. 133-143.

IN SEARCH OF THE HOLY GRAIL
THE DETERMINISTIC PREDICTION OF DAMAGE

Digby D. Macdonald and Jose Magalhaes
The Pennsylvania State University
Center for Advanced Materials
517 Deike Building
University Park, PA 16802
USA

ABSTRACT

The development of fatigue and corrosion fatigue damage, and of other forms of localized corrosion damage, in aircraft structures is generally described in terms of damage tolerance methods in which the fatigue data are incorporated as empirical crack growth rate/stress intensity (range) correlations, and the corrosion information is either ignored or is included on an ad hoc basis. However, the prediction of corrosion damage in other industries (e.g., the electric power industry) is gradually yielding to determinism, which allows much more robust predictions of failure times to be made. In this paper, we review the deterministic methods and explore the prospects for developing similar techniques for predicting failures in aircraft structures.

INTRODUCTION

The prediction of service-induced damage (pitting, fatigue, corrosion fatigue, and general corrosion) in aircraft structures is currently made on the basis of empirical and semi-empirical methods in which laboratory data (e.g., da/dN vs. ΔK for cyclic crack growth) are used to estimate metal loss and crack extension rates under preselected conditions. These predictions are then combined with periodic in-service inspections, within the framework of the damage tolerance philosophy, to assess and track the progression of damage. While the fracture mechanics basis for this procedure is well-developed, the corrosion aspects are incorporated on an ad hoc basis, with the result that our ability to predict the evolution of damage as a function of operating conditions is poor.

In this paper, a detailed analysis is presented of methods that have been developed in other areas of science and engineering (e.g., in the nuclear power industry) for deterministically predicting corrosion damage, with particular emphasis on the prospects of applying these techniques to aircraft. These methods appeal to the natural laws (conservation of charge, Faraday's law, etc.) for their predictive rigor and provide an opportunity for accurate damage prediction, provided that future operating conditions can be envisioned and specified. In the general case, which will be emphasized, the progression of damage is

425

described as arising from a progressive nucleation/growth/death process. Thus, for a single event (e.g., a pit or crack), these three phases occur sequentially, each of which is amenable to deterministic modeling, but for an ensemble of events, the extent of damage develops collectively in a parallel manner. This scenario is most effectively described in terms of a damage function, which is the distribution in the damaging parameter (e.g., pit or crack length) as a function of exposure conditions and observation time. The damage function provides a convenient mathematical basis for defining "failure time," "service life," "corrosion allowance," "probability of failure," and many other such terms and concepts that enter into life prediction for complex engineering structures.

THE TEMPORAL DEVELOPMENT OF DAMAGE

The development of damage, regardless of the details of the processes involved, is best described as a progressive nucleation/growth/death process. Such processes are characterized by the nucleation of new damage as existing damage grows and dies, with the result that the damage is distributed. The most convenient way of expressing damage is in the form of a damage function,[1] which is a histogram of frequency versus depth for a given observation time (t_1, t_2, or t_3), as shown in Figure 1. These functions display the general trends that are seen in experimental damage functions as well as those that are predicted theoretically, including:

1. The total damage, as represented by the area, increases with increasing observation time.

2. The upper extreme of the damage function extends to greater depths with increasing observation time.

3. The distribution may be multimodal only if more than one nucleation phenomenon is present and only then if the kinetics of nucleation are temporally separated.

For most purposes, we are interested in estimating failure times, and DFA (Damage Function Analysis) allows us to do that by specifying a failure criterion. In many cases, this criterion will be a critical dimension (L_{crit}, Figure 1), corresponding perhaps to the thickness of a pipe wall or to an acceptable "corrosion allowance". However, the criterion may be less (physically) direct. For example, in specifying failure for systems that exhibit stress corrosion cracking or corrosion fatigue, it is necessary to specify a critical stress intensity factor, K_I, such that $K_I > K_{IC}$, where K_{IC} is the fracture toughness, corresponding to conditions for unstable (fast) fracture. In this case, the failure criterion is a function of other system parameters, including stress and geometry. Thus, with reference to Figure 1, L_{crit} will decrease as the stress is made larger, so that damage that was subcritical at one stress level may become supercritical at another. This is clearly an important issue for aircraft, where wide ranges of stress are experienced during operation.

Returning again to Figure 1, it is important to note that the most damaging events (defined here as being the deepest) are generally the first to nucleate and/or the last to die,

426

and the least damaging events are those that are last to nucleate and/or the first to die. In any event, a deterministic prediction of the evolution of damage, and hence estimation of the failure time, must address all three constitutive phenomena; nucleation, growth, and death. These phenomena must be described in a manner that recognizes their serial relationships for a single event (birth → growth → death) but that they occur in parallel for an ensemble of events.

The Nucleation of Damage

The initial fundamental event in the nucleation of localized corrosion damage (e.g., that due to pitting, stress corrosion cracking, and corrosion fatigue) is passivity breakdown and the eventual establishment of a highly nonuniform current distribution within microscopic dimensions of the nucleation point. As a result of an intensive effort over the past decade to develop an understanding of the breakdown of passive films, we have derived theoretical distribution functions for passivity breakdown that are in good agreement with experiment[2-6]. We derived these distribution functions from our point defect model (PDM) for the growth and breakdown of passive films by assuming that breakdown occurs when a critical concentration of cation vacancies accumulates locally at the metal/passive-film interface such that decohesion occurs between the barrier layer and the metal substrate. Subsequently, localized dissolution and/or mechanical instability leads to rupture of the film.[2] We further assumed that the breakdown sites are normally distributed with respect to the diffusivity of cation vacancies within the film.[3-5] The full derivation of these distribution functions can be found in the literature.[2-6]

From the PDM,[2] the breakdown voltage and the induction time for a single pit nucleation site on the surface are given by

$$V_c = \frac{4.606 RT}{\chi \alpha F} \log\left[\frac{J_m}{J^o \hat{u}^{-\chi/2}}\right] - \frac{2.303 RT}{\alpha F} \log(a_x) \tag{1}$$

and

$$t_{ind} = \xi'\left[\exp\left(\frac{\chi \alpha F \Delta V}{2RT}\right) - 1\right]^{-1} + \tau \tag{2}$$

respectively, where χ is the film stoichiometry $\left(MO_{\chi/2}\right)$, α is the dependence of the potential drop across the film/solution interface on applied voltage, a_x is the activity of halide ion in the solution, τ is a relaxation time ($\tau \sim 0$), $\Delta V = V - V_c$, V is the applied voltage (or the corrosion potential under open circuit conditions), $J^o = \hat{a}D$, and the parameters $\hat{a}, u$, and J_m are defined in the original derivation[2].

Assuming that the breakdown sites are normally distributed in terms of the cation vacancy diffusivity,

$$\frac{dN}{dD} = \frac{1}{\sqrt{2\pi}\sigma_D} \exp\left[-(D-\bar{D})^2 / 2\sigma_D^2\right] \tag{3}$$

where $\bar{D}$ is the mean diffusivity and σ_D is the standard deviation, the PDM yields the distributions in the breakdown voltage and induction time:[3-6]

$$\frac{dN}{dV_c} = -\frac{\hat{\gamma}\bar{D}}{\sqrt{2\pi}\sigma_D} \cdot e^{-(D-\bar{D})^2 / 2\sigma_D^2} \tag{4}$$

and

$$\frac{dN}{dt_{ind}} = \left[\frac{\xi u^{\chi/2}}{\sqrt{2\pi}\sigma_D \hat{a}}\right] e^{-(D-\bar{D})^2 / 2\sigma_D^2} \cdot \frac{e^{-\hat{\gamma}V}}{a_x^{\chi/2}\left(t_{ind} - \tau\right)^2} \tag{5}$$

where $\hat{\gamma} = \chi F \alpha / 2RT$. Equations 4 and 5 contain four important system parameters; $\bar{D}$ and σ_D, which describe the transport properties of cation vacancies in the passive film, and α and β, which appear in the expression for the dependence of the potential drop across the film/solution interface on applied voltage and pH, i.e., $\phi_{f/s} = \alpha V + \beta pH + \phi_{f/s}^o$, where $\phi_{f/s}^o$ is a constant. All four parameters can be determined by independent experiment: $\bar{D}$ from electrochemical impedance spectroscopy, σ_D from passivity breakdown induction time measurements,[2] and α and β from film growth data, some of which exists in the literature.

The Growth of Damage

The growth of damage due to localized corrosion is an electrochemical phenomenon, and any model that purports to be deterministic must conserve charge and obey Faraday's law, which are the two governing natural laws.[7-13] Accordingly, with reference to Figure 2, the conservation of charge requires that $\int_S i\, dS = 0$, where i is the current density on surface element dS, with the integral being evaluated over the entire surface, including the crevice internal and external surfaces, where anodic (metal oxidation) and cathodic (e.g., oxygen reduction) reactions predominate, respectively. Thus, solution of Laplace's (or more strictly, Poisson's) equation for the appropriate boundary conditions, subject to the constraint imposed by $\int_S i\, dS = 0$, yields the potential and current distributions within the system. Knowledge of the current density (i_t) at the crevice base (pit or crack) therefore yields the extension rate according to Faraday's law as $dL/dt = \bar{M} i_t / 2\rho_m \bar{z} F$, where $\bar{M}$ and $\bar{z}$ are the composition-averaged (for alloys) atomic weight and oxidation number, respectively, ρ_m is the density of the alloy, and F is Faraday's constant. Differentiation between pit growth and crack growth is accomplished by noting that, in the latter, the oxidation current density is strain-rate dependent. It is important to note that even though all of the mechanistic details in these "coupled environment" models may not be correct, they are deterministic in the global sense and hence, in principle, are capable of providing for robust prediction.

Death

Perhaps the most difficult phenomenon to deal with in localized corrosion is the death of an individual event (pit or crack), principally because most attention has been focused on nucleation rather than on describing the ultimate fate of a crevice. However, it is now known that two quite distinct "death" phenomena need to be defined: (i) prompt repassivation, and (ii) delayed repassivation. Prompt repassivation occurs when the crevice nucleus that is produced by passivity breakdown fails to attain conditions that permit sustained growth. The necessary conditions for transition from metastable to stable pitting for stainless steels have been expressed in terms of a pit stability product (PSP)[14-17] as[14] $0.6 mA/cm > i a > 0.3 mA/cm$, where i is the current density at the pit nucleus surface of radius a (hemispherical geometry). The lower limit is imposed by the need to establish sufficiently aggressive conditions that pit growth is sustained, whereas the upper limit is defined by the solubility of the salt. Average lifetimes for metastable pits depend on the properties of the substrate and the environment but are typically less than one second.

The second death phenomenon, "delayed repassivation," is responsible for the death of stable pits, i.e., the repassivation of those pits that satisfy Equation 12, over much longer times. The kinetics and mechanisms of this process are poorly defined or understood, but numerous causes might be postulated, including changes in the properties of the environment (pH, corrosion potential, flow velocity, etc.). At the present time, delayed repassivation appears to be best described as a first order decay process, $-dN/dt = k_r N$, where N is the number of active (surviving) pits, and k_r is the rate constant. No theory currently exists that allows one to calculate k_r from first principles; instead, the best that can be done at the moment is to fit the model to experimentally determined damage functions for well-controlled conditions. This is clearly an unsatisfactory state of affairs, and a major effort is needed to define the kinetics and mechanisms of delayed repassivation.

At this point, it is worth noting that Equation 5 strictly yields the number of breakdown events per unit time and does not address the fate of these events once breakdown has occurred. However, Williams et al.[18] have found that the number of surviving pits (after prompt repassivation) is proportional to the number of metastable breakdown events. Thus, to a good (first) approximation, we may write, $(dN/dt)_{surviving} = \Phi(dN/dt)$, where Φ is the "differential survival probability," which is related (in an as yet unknown way to the PSP), and dN/dt is given by Equation 5. As is the case for k_r, the theory of prompt repassivation is not well developed, although the general characteristics of the phenomenon have been explored in the phenomenological sense,[18,19] and physical models have been forwarded to account for the PSP.[14] Again, a major effort is required to develop a sound mechanistic basis for estimating Φ.

For any given set of conditions, Equation 5 predicts that, in the absence of death, the cumulative number of surviving pits is as shown schematically in Figure 3.[1] If the observation time is t_{obs}, and an increment in time, Δt_i, is chosen such that $\sum_{i=1}^{M} \Delta t_i < t_{obs}$, then the ΔN_i pits that nucleate in that interval will have grown to a depth of h_i. Thus, by moving the time increment from $t = t_{obs}$ to $t = 0$, corresponding to depths of $h = 0$ to $h = h_{max}$, we are able to construct a damage function of the type shown in Figure 1. Moving t_{obs} to higher values therefore yields a family of damage functions that extend to increasing depths. Thus, in order to determine the failure time, t_{obs} is increased until $h_{max} = L_{crit}$. For systems that exhibit repassivation, the fate of the pits that nucleate within Δt_i must be followed through to t_{obs}, and the number that repassivate within Δt_j where $j > i$ after growing to a depth of h_i^j must be counted in the population, thereby greatly distorting the damage function. Because the events that nucleate first are most susceptible to repassivation, but yet are the most damaging (because they grow to the greatest depth), delayed repassivation can have a profound effect on the calculated failure time. However, ignorance of delayed repassivation yields a conservative criterion for failure, in that the smallest failure time is calculated.

EXAMPLES OF THE PREDICTION OF DAMAGE

In order to illustrate application of the concepts discussed above, three specific cases are discussed: (i) stress corrosion cracking of low-alloy steel disks in low-pressure steam turbines in nuclear and fossil-fired power plants; (ii) pitting of stainless steels in condensing heat exchangers, and (iii) pitting of carbon steel in pure water. In each case, required chemical (e.g., pH, conductivity, chloride activity) and electrochemical (e.g., corrosion potential) parameters have been estimated using well-established, deterministic models, which will not be discussed here.

Stress Corrosion Cracking in Low-Pressure Steam Turbines[20,21]

In this case, damage, in the form of pits that transform into stress corrosion cracks and ultimately into unstable mechanical fracture, nucleates and develops beneath thin electrolyte films. This phenomenon has been responsible for the catastrophic failure of many steam turbines, resulting in enormous loss to the electrical power utilities. Examination of turbine disks after short exposure times has shown them to contain pits and short cracks, so that it is reasonable to assume that pit nucleation is rapid and that failure is dominated by growth. In that case, it is necessary only to predict the trajectory of localized corrosion from the nucleation of a pit to the onset of rapid mechanical overload fracture in order to estimate the

failure time. This has been done by estimating the crevice (pit or crack) growth rate and, hence, by estimating the increase in crevice length for a given time increment, Δt_i. At each iteration, the stress intensity factor is calculated and compared with K_{ISCC} (critical stress intensity factor for the initiation of a crack from a pit) and K_{IC} (fast mechanical overload fracture). Thus, if $K_I < K_{ISCC}$, crevice growth is due to pitting, but for $K_{ISCC} < K_I < K_{IC}$, crevice growth occurs by SCC. The SCC initiation time is determined by summing Δt_i such that $K_I < K_{ISCC}$, whereas the total failure time is the sum of Δt_i for $K_I < K_{IC}$.

Figure 4 shows a typical trajectory in the development of damage for a single event. The event is assumed to begin as a flaw (subsequent to passivity breakdown) of 5- x 10^{-5}-cm radius and 1- x 10^{-3}-cm length, with the other conditions of chemistry ([NaCl], [HCl], [O_2]) and thickness (h) of the thin electrolyte film on the disk surface, and the (tensile) stress in the disk, being given in the caption. The crevice initially grows as a pit with the pit growth rate decreasing with increasing pit length (and hence with increasing K_I). When $K_I > K_{ISCC}$, the pit transforms into a crack and the crevice growth rate increases rapidly in the Stage I region of the classical CGR versus K_I correlation before reaching a plateau in the Stage II region. Once $K_I > K_{IC}$, catastrophic failure occurs.

The concentration of oxygen in the electrolyte film (and hence in the steam) and the temperature have significant impact on both the SCC initiation and failure times. However, while the failure time decreases by a factor of about five on increasing the temperature from 97°C (exit of turbine) to 180°C (entrance), increasing the oxygen concentration a thousand-fold (1 ppb to 1 ppm) results in a decrease in the predicted failure time by less than a factor of three. On the other hand, changing the composition of the electrolyte film (and hence the conductivity) from that of a dilute solution to that of a concentrated solution is predicted to have an enormous impact on the failure time (Figure 6). Furthermore, by decreasing the stress from 300 MPa to 100 MPa, we predict that the failure time can be increased by an order of magnitude. These predictions are in excellent agreement with experiment and field observations and point to the need to prevent the formation of concentrated electrolyte films on the disk surface as being the most effective way of preventing turbine failure. This requires close control of the steam temperature and pressure to ensure that the Wilson line lies downstream of the low pressure turbine.

Pitting of Condensing Heat Exchangers[22]

As a result of the quest for higher efficiency in gas-fired heat exchangers for domestic and industrial heating, designs have evolved in which the temperature of the flue gas at the exit has steadily decreased. Furthermore, operation by on/off cycling allows the condenser temperature to fall below the dew point of the flue gas, thereby resulting in the formation of a highly corrosive (pH = 1-3, high [Cl⁻]), thin electrolyte layer on the stainless steel condenser tube surface. Calculated damage functions, excluding delayed repassivation effects, are shown in Figure 7 for times ranging from 4.32 x 10^6s (~7 weeks) to 5.19 x 10^7s (~1.65 years) together with the critical dimension. The distributed nature of the damage function is clearly

evident, and the failure time is estimated to be 11.4 months for this particular case. In a completely independent (and blind) study, Stickford et al. (see Ref. 22) measured failure times in an instrumented furnace, and their experimental data and our predictions are compared in Figure 8. Where comparison is possible (two highest chloride concentrations) good agreement is obtained. Note that the input in our calculations were fundamental electrochemical parameters, the chloride concentration, the flue gas composition, and the duty cycle.

Pitting of Carbon Steel in Pure Water

The pitting of carbon steel in pure oxygenated water is a recurring problem in many industries, including the electrical power industry. Examples of differential and integral damage functions for two different repassivation rates are shown in Figures 9 and 10. The differential damage function gives the number of pits within each depth increment (Figure 9), whereas the integral damage function (Figure 10) yields the remaining pits as the surface is milled away one depth increment at a time. This latter damage function was defined because that is the function that is normally determined experimentally. The impact that delayed repassivation has on both the differential and integral damage functions is gleaned from a comparison of Figures 9 and 10. Thus, a ten-fold increase in k_r, implying more intense repassivation, leads to a substantial decrease in the maximum pit depth. In this particular case, repassivation is so intense that all of the pits are dead at the observation time of two years, so that if the critical dimension were greater than the maximum pit depth, failure would never occur unless the pits reactivated.

POSSIBLE APPLICATION TO AIRCRAFT STRUCTURES

To our knowledge, this type of analysis has never been applied to aircraft structures. However, great commonality exists between the systems discussed above (particularly steam turbines and condensing heat exchangers) and aircraft in that the physical configurations (airfoils in aircraft and turbines) and chemical environments are somewhat similar. Thus, aircraft corrosion generally occurs under thin electrolyte films that condense onto the hydrophilic (AlOOH) surface. Furthermore, the oxygen content of these films is easily calculated, the necessary electrochemical parameters for metal dissolution, hydrogen evolution, and oxygen reduction are known or are readily measured, and the stress state in various critical components (e.g., wing spars) are known or can be calculated using finite element techniques. Also, extension of the crevice growth model to consider cyclic loading is possible, so that failure due to corrosion fatigue could be accommodated. Finally, the measurement of important properties of the metal/environment (thin electrolyte film) system, such as time of wetness versus duty cycle, conductivity, and the corrosion potential, could be made using on-board instrumentation and sensors so that realistic duty cycles for mechanical, chemical, and electrochemical parameters could be used as inputs to a deterministic model for predicting the evolution of damage in aircraft structures.

ACKNOWLEDGMENTS

REFERENCES

1. Macdonald, D. D. and Urquidi-Macdonald, M.: *Corrosion*, vol. 48, no. 5, 1992, p. 354.

2. Lin, L. F., Chao, C. Y., and Macdonald, D. D.: *J. Electrochem. Soc.*, vol. 128, 1981, p. 1194.

3. Macdonald, D. D. and Urquidi-Macdonald, M.: *Electrochem. Acta*, vol. 31, 1986, p. 1079.

4. Macdonald, D. D. and Urquidi-Macdonald, M.: *J. Electrochem. Soc.*, vol. 134, 1987, p. 41.

5. Macdonald, D. D. and Urquidi-Macdonald, M.: *J. Electrochem. Soc.*, vol. 136, 1989, p. 961.

6. Macdonald, D. D.: *J. Electrochem. Soc.*, vol. 139, 1992, p. 3434.

7. Macdonald, D. D. and Urquidi-Macdonald, M.: *Corros. Sci.*, vol. 32, 1991, p. 51.

8. Macdonald, D. D. and Urquidi-Macdonald, M.: *Proc. 5th Intl. Symp. Environ. Degrad. Mat. in Nucl. Power Systs.--Water Reactors*, ANS, LaGrange Park, IL, 1992, p. 345.

9. Macdonald, D. D. and Urquidi-Macdonald, M.: *CORROSION/92*, paper no. 87, Houston, TX.

10. Macdonald, D. D., Urquidi-Macdonald, M., and Lu, P.-C.: *CORROSION/94*, paper no. 246, Baltimore, MD.

11. Lu, P.-C.: Ph.D. Dissertation, The Pennsylvania State University, 1994.

12. Macdonald, D. D. and Yeh, T.-K.: *Nucl. Sci. Eng.*, vol. 121, 1995, p. 468.

13. Yeh, T.-K.: Ph.D. Dissertation, The Pennsylvania State University, 1994.

14. Pistorius, P. C. and Burstein, G. T.: *Phil. Trans. R. Soc. London A.*, vol. 341, 1992, p. 531.

15.   Frankel, G. S., Stockert, L., Hunkeler, F., and Bohni, H.: *Corros. Sci.*, vol. 43, 1987, p. 429.

16.   Galvale, J. R.: *J. Electrochem. Soc.*, vol. 123, 1976, p. 464.

17.   Galvale, J. R.: *Corros. Sci.*, vol. 21, 1981, p. 551.

18.   Williams, D. E., Stewart, J., and Balkwill, P. H.: *Corros. Sci.*, vol. 36, 1994, p. 1213.

19.   Shibata, T., and Takeyama, T.: *Corrosion*, vol. 33, 1977, p. 243.

20.   Liu, C. and Macdonald, D. D.: *Proc. of Fossil Plant Maintenance Conference*, EPRI, July 28-August 1, 1996, Baltimore, MD.

21.   Macdonald, D. D. and Liu, C.: *Proc. of 12th Intl. Corros. Congr.*, vol. 5A, 1993, p. 3446.

22. Macdonald, D. D., Liu, C., Urquidi-Macdonald, M., Stickford, G., Hindin, B., and Agrawal, A. K.: *Corrosion*, vol. 50, 1994, p. 761.
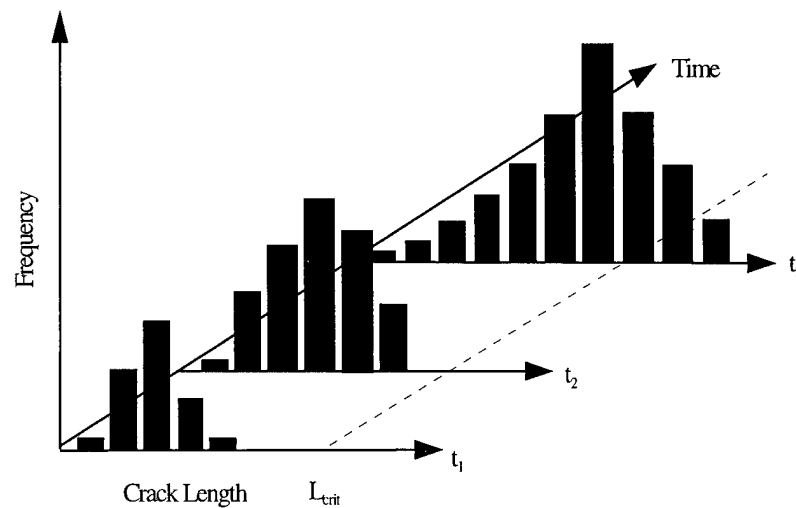
Figure 1. Schematic Damage Functions for Three Exposure Times (t_1, t_2, t_3). The Broken Line Represents a Critical Dimension (L_{crit}) Defined in Engineering Terms (e.g., Pipe Wall Thickness, Corrosion Allowance, or Crack Length for the Onset of Fast Fracture).
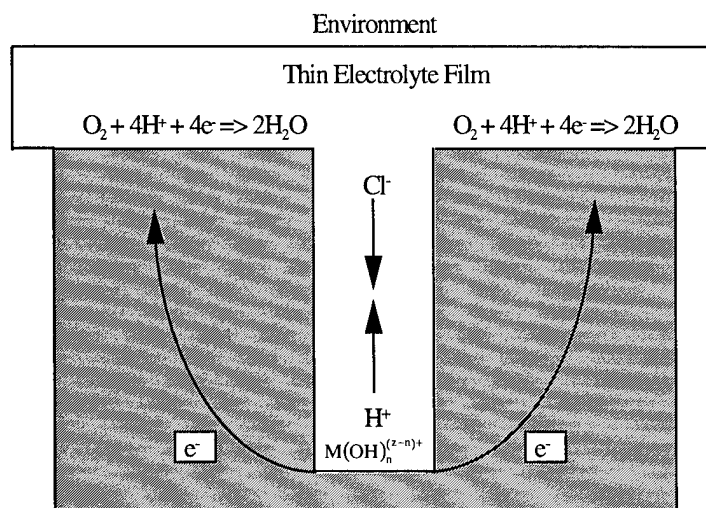
Figure 2. Schematic of Coupled Environment Pitting/Fracture Model Employed in the Deterministic Estimation of Pit and Crack Propagation Rates in Metals and Alloys Under Thin Electrolyte Films That Condense on a Surface.
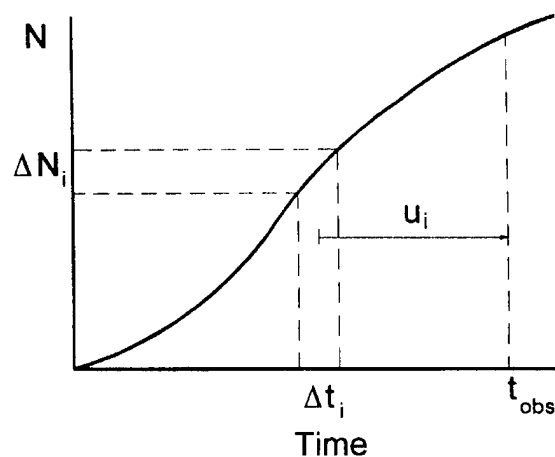
Figure 3. Schematic of Method for Calculating Damage Functions. u_i = Time for Growth of the ΔN_i Pits That Nucleate in Δt_i.
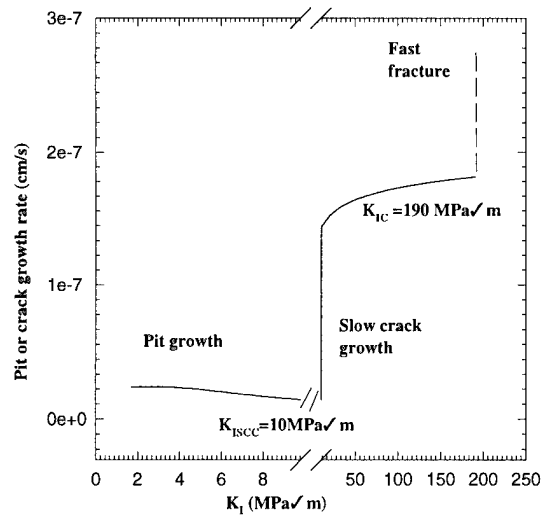
Figure 4. Stages of Development of a Pit Into a Crack Ultimately Resulting in Fast Fracture, Presented as a Plot of Growth Rate Versus Stress Intensity and Temperature in Comparison With Available Experimental Data [From References 1 and 2]. ([NaCl] = 1.0×10^{-3} mol/cm^3, [HCl] = 1.0×10^{-6} mol/cm^3, [O$_2$] = 1.0 ppm, σ = 3.0 x 10^2 MPa, h = 1.0×10^{-3} cm, a$_n$ = 5.0 x 10^{-5} cm, L$_n$ = 1.0 x 10^{-3} cm).
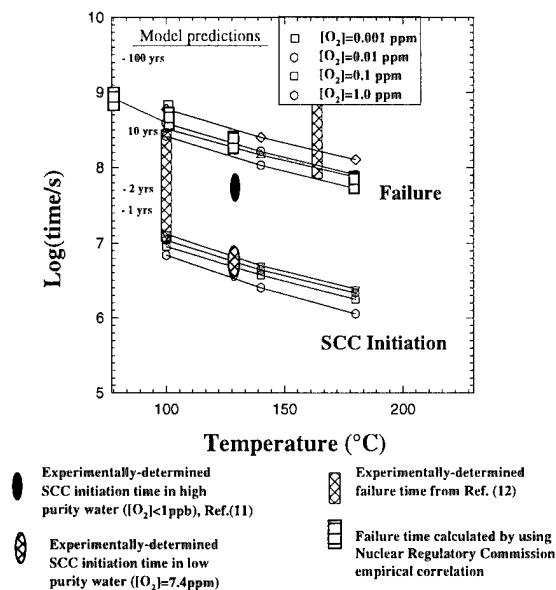
Figure 5. Calculated SCC Initiation and Total Failure Times as a Function of Oxygen Concentration and Temperature. ([NaCl] = 10^{-3} mol/cm^3, [HCl] = 10^{-5} mol/cm^3, σ = 3.0 x 10^2 MPa, h = 1.0×10^{-3} cm, a$_0$ = 5.0x10^{-5} cm, L$_0$ = 1.0x10^{-3} cm, K$_{ISCC}$ = 10 MPa m$^{1/2}$, K$_{IC}$ = 190MPa m$^{1/2}$). See Liu and Macdonald[22] for a Discussion of the Experimental Data.
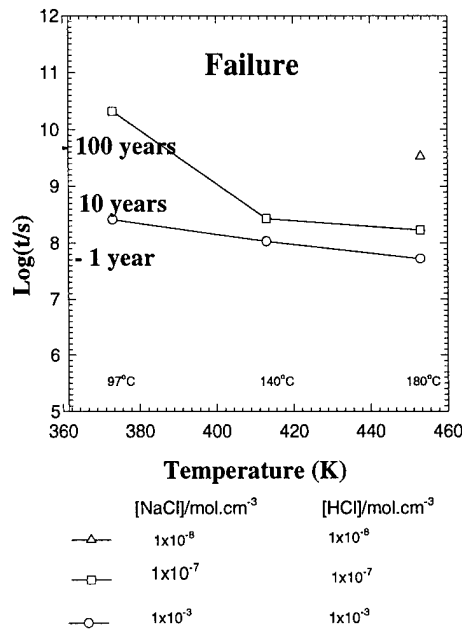
Figure 6. Calculated Failure ($K_I > K_{ISCC}$) Time for Low-Pressure Steam Turbine Disk as a Function of Temperature and Electrolyte Composition. ([O_2] = 1.0 ppm, σ = 3.0x10^2 MPa, h = 1.0x10^{-3} cm, a_0 = 5.0x10^{-5} cm, L_0 = 1.0x10^{-3} cm, K_{ISCC} = 10 MPa m$^{1/2}$, K_{IC} = 190MPa m$^{1/2}$).
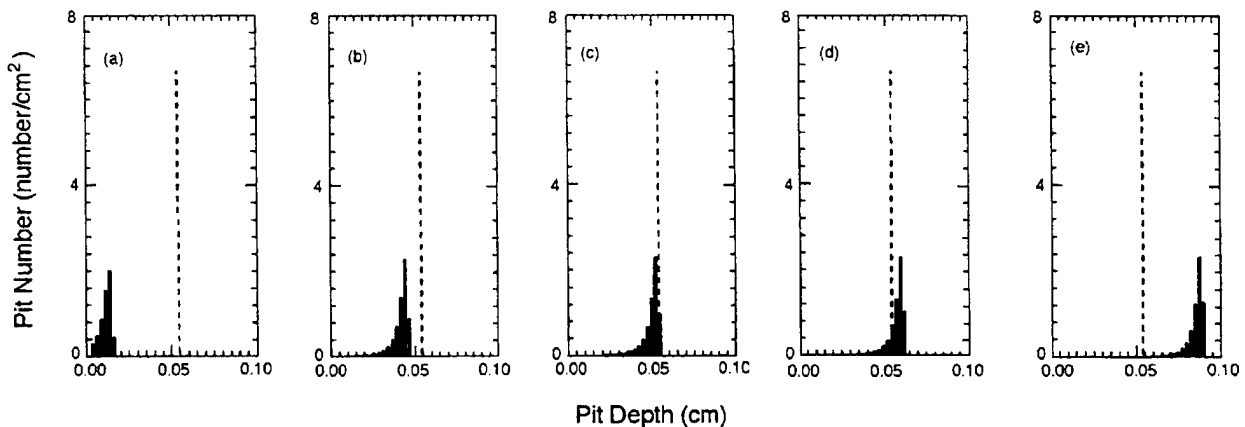
Figure 7. Calculated Pitting Damage Functions for Type 304L SS Heat Exchanger Tubes Under Condensing Conditions. ([Cl$^-$] = 26 ppm, Temperature = 77°C, P_{CO} = 2.60x10^{-5} atm (2.63x10^{-6} MPa), P_{CO_2} = 6.80x10^{-2} atm (6.89x10^{-3} MPa), P_{SO_2} = 9.37x10^{-9} atm (9.49x10^{-10} MPa), P_{SO_3} = 2.00x10^{-9} atm (2.03x10^{-10} MPa), P_{H_2S} = 1.20x10^{-4} atm (1.22x10^{-5} MPa), P_{NO} = 1.74x10^{-8} atm (1.76x10^{-9} MPa), P_{NO_2} = 2.67x10^{-8} atm (2.70x10^{-9} MPa), P_{O_2} = 1.00x10^{-4} atm (1.01x10^{-5} MPa), Pit Radius 1.00x10^{-4} cm, Initial Pit Depth 1.00x10^{-3} cm, Pit Counting Interval = 2.54x10^{-3} cm. (a) T_{obs} = 8.63x10^6 s; (b) T_{obs} = 2.52x10^7 s; (c) T_{obs} = 2.99x10^7 s; (d) T_{obs} = 3.46x10^7 s; (e) T_{obs} = 5.19x10^7 s; and Tube Thickness = 5.34x10^{-2}, as Indicated by the Dashed Line.

437
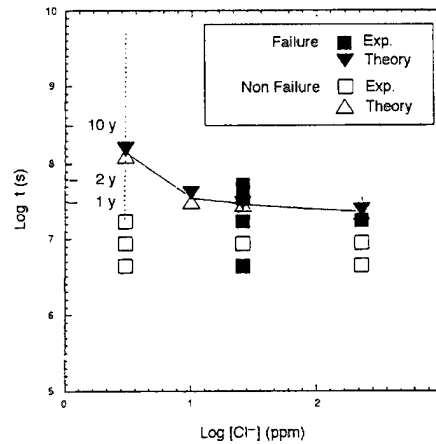
Figure 8. The Measured and Calculated Service Life for Type 304L SS Heat Exchanger Tubes as a Function of [Cl⁻]. Parameters are Identical to Those for Figure 7.
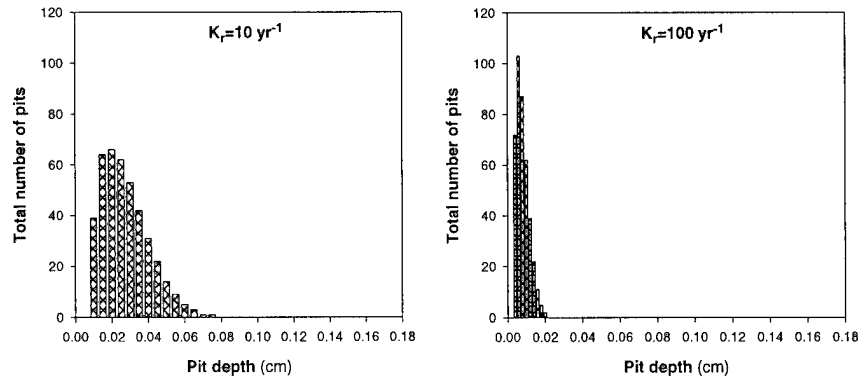
Figure 9. Differential Damage Functions for Carbon Steel in Oxygenated Pure Water (T = 150°C, pH = 5.82, $[O_2]$ = 7.5ppm, t_{obs} = 2yrs) as a Function of the Delayed Repassivation Rate Constants. Note that the Pit Depths Were Calculated Using an Empirical Correlation Between Pit Depth and Time for Pits Grown Under Identical Conditions.
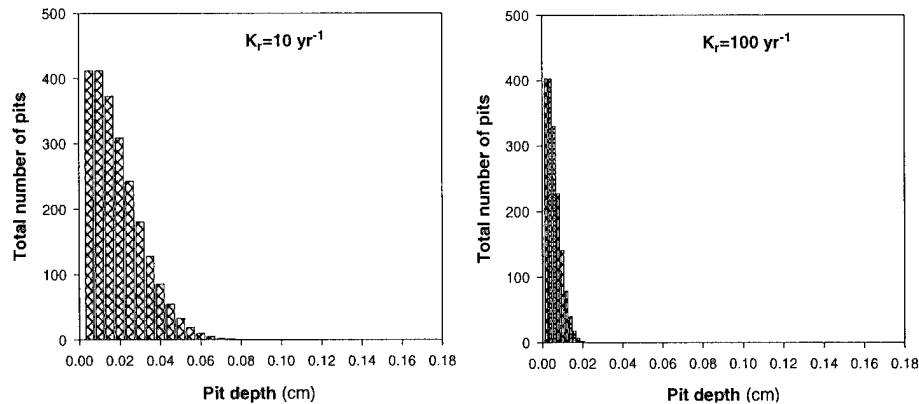
Figure 10. Integral Damage Functions for Carbon Steel in Oxygenated Pure Water (T = 150°C, Ph = 5.82, $[O_2]$ = 7.5ppm, t_{obs} = 2yrs) as a Function of the Delayed Repassivation Rate Constant.

438

INVESTIGATION OF FUSELAGE STRUCTURE SUBJECT TO WIDESPREAD FATIGUE DAMAGE

M. L. Gruber, K. E. Wilkins, and R. E. Worden
The Boeing Company
Seattle, WA

ABSTRACT

This paper presents work sponsored by the Federal Aviation Administration (FAA) under a contract titled "Investigation of Fuselage Structure Subject to Widespread Fatigue Damage." Two generic wide-body fuselage panels containing cracks in the upper rivet row of a lap joint were tested to obtain crack growth rate and residual strength data with and without the presence of simulated multiple site damage. Also, finite element models were used to predict the crack growth history of the lead cracks and the residual strength of the panels. In addition to the FAA contract results, this paper discusses independent work to evaluate available analysis methods and to develop an engineering analysis tool for predicting the effect of multiple site damage on residual strength.

INTRODUCTION

High replacement costs and competition have led airline operators to use their airplanes beyond the original design service objective. The result is an aging fleet with a higher probability of fatigue-initiated cracking and eventually widespread fatigue damage (WFD). WFD is defined as the simultaneous presence of cracks at multiple structural details that are of sufficient size and density whereby the structure no longer meets its damage tolerance requirements. A subset of WFD is multiple site damage (MSD), which is characterized by the simultaneous presence of fatigue cracks in the same structural element. Damage tolerance analysis methods that focus primarily on local damage may not be sufficient to account for the effects of WFD. It is possible that small undetected MSD in adjacent fastener holes might link together and increase the rate of damage growth in a lap joint. This scenario would reduce the opportunities to find the damage prior to failure. Furthermore, the residual strength may be impacted and the final critical damage size may be smaller in the presence of MSD. Finally, crack arrest devices such as tear straps may not be as effective as originally designed.

An increased understanding of MSD behavior would allow the aging fleet to be evaluated on a model-by-model basis once proven analytical methods are available. Modifications could be made to susceptible structure as required. For new configurations, an

understanding of the fundamental behavior of MSD would allow engineers to develop structural designs capable of containing MSD.

This paper includes recent work performed under the FAA contract titled "Investigation of Fuselage Structure Subject to Widespread Fatigue Damage" (ref. 1) and ongoing work at Boeing to investigate the behavior of airplane fuselage structure containing MSD.

WFD CONTRACT RESULTS

The primary program objective was to obtain data on airplane fuselage structure subject to MSD in an environment that reflects typical commercial jetliner manufacturing and operating conditions. The program involved both full-scale testing and analysis of pressurized stiffened panel structure. Testing was performed on two generic wide-body fuselage panels containing frame centered cracks in the outer skin of a lap joint along the upper row of rivets. Crack growth and residual strength were measured on panels with and without simulated MSD. Finite element models of the test panels containing skin cracks were analyzed. Stress intensity factors calculated from the finite element analyses were used to predict the residual strength of the panels and the crack growth rate of the lead crack. The results of these tasks are summarized in the following sections.

MATERIAL PROPERTY TESTS

Stress-strain, crack growth rate, and fracture toughness properties were developed for 0.063-inch-thick clad 2024-T3 aluminum using specimens fabricated from the same lot of material used to fabricate the large curved pressure panels. These properties were developed for the transverse material orientation, corresponding to the typical material orientation for hoop loading in a fuselage skin panel and used in the large curved pressure panel analysis. Four center-cracked tension M(t) panels were used to develop crack growth, R-curve, and toughness properties, while two tensile specimens were used to develop stress-strain data. The results are shown in table 1.

Table 1. 2024-T3 Transverse Material Properties.

Tensile Modulus (Msi)	Tensile Yield 0.2% (ksi)	Tensile Ultimate (ksi)	$K_{apparent}$ (ksi in$^{1/2}$
9.86	42.8	64.3	130

FULL-SCALE FUSELAGE PANEL TESTING

Two full-scale pressure panels with simulated MSD were tested in the wide-body pressure test fixture located in Tulalip, Washington. The test procedure consisted of inserting a 5-inch longitudinal sawcut in the lap joint upper rivet row, outer skin at the selected test location and pressure cycling until either test termination or the crack reached a length of two frame bays at which point a residual strength test was conducted. The crack was then repaired before proceeding to the next test location. Specific test details such as strain gage readings and dynamic crack extension observations can be found in reference 1.

Test Facility

The wide-body pressure test fixture shown in figure 1 has a 127-inch radius and is 20 feet long. The overall geometry of the fixture is consistent with typical fuselage design, having basic gages that are thicker than typical minimum gage fuselage structure to achieve realistic fixture stiffness yet provide adequate longevity. The end bulkheads are steel, one of which is fixed and the other on rollers to permit axial expansion during pressurization.

Wide-body fixture capabilities:
- 2 minutes/cycle with 40% void fill
- 1600 CFM (electric compressors)
- 300-channel data acquisition system
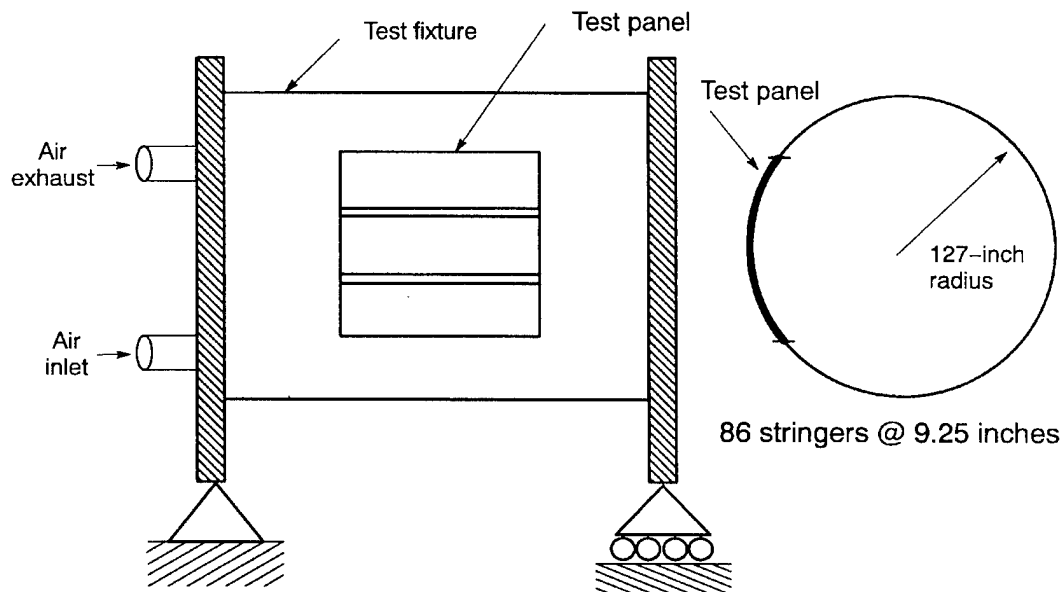
Figure 1. Wide-Body Pressure Test Fixture.

The test fixture has a rectangular cutout approximately 10 feet by 10 feet designed to accept a variety of test panels. The panels are attached to the fixture at the skin, frames, and stringers by a fusing arrangement to allow a panel to fail at loads below the elastic limit of the fixture components. The stringer and frame splices are designed to allow attachment fasteners to fail during a dynamic panel failure. The test panel skin is allowed to tear circumferentially along the perimeter fasteners with the help of a sharp notch introduced into the panel prior to its installation in the fixture. These features make it possible to conduct residual strength tests which result in test panel failure without extensive damage to the test fixture.

Compressed air is used as the pressurizing medium. Cyclic rates were approximately two minutes per cycle. Polystyrene blocks are placed within the fixture to reduce the required air volume. To reduce air leakage through the sawcut and thus improve cyclic rates, a thin internal rubber dam was installed after the sawcuts were made. The dam consisted of rubber sheet that was laid up against the skin.

Test Panel Configuration

Two identical curved wide-body generic panels (FAA 1 and FAA 2) were designed, fabricated, and assembled using standard Boeing practices. The panel design was similar to typical wide-body fuselage crown structure consisting of bonded tear straps and floating frames connected to hat section stringers via stringer clips. This is illustrated in figure 2. The skin panels are joined together along the longitudinal splices (lap joints) located at stringer 3 left and right. The lap joints are a typical three-row configuration assembled using 3/16-inch-diameter, 100 degrees countersunk head rivets and raying surface sealant. Circumferential tear straps are hot bonded to the skin at each frame station every 20 inches. The grain direction of the skin is oriented longitudinally unlike the hot bonded tear straps, which have their grain oriented circumferentially. The typical panel details such as fastener spacing, lap joint details, tear strap, frame, and stringer dimensions are found in reference 1. The tear strap dimensions are defined in terms of strap stiffening ratio: $R_s = A_{strap}/(B \times t_{skin})$. The frame cross-sectional area is not included in this area. The stiffening ratio for both test panels was: $R_s = 0.12$.

Materials and Fabrication

The skin material used to fabricate the pressure test panels was typical of that used in current production airplanes, as well as from the same lot of material as the flat panel tests previously discussed. The stringers and the frames were made from 7075 aluminum clad sheet with stringer clips machined from 7075-T6511 extrusion.
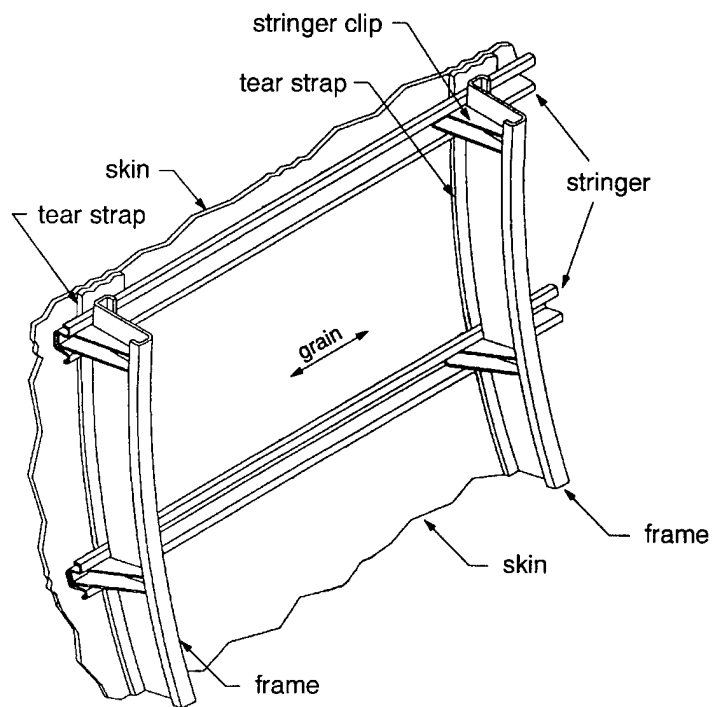
Structural Dimensions	
radius	127 inches
stringer spacing	9.25 inches
frame spacing	20.0 inches
skin thickness	0.063 inch
tear strap thickness	0.063 inch
tear strap width	2.4 inches
$R_s = A_{strap} / (B \times t_{skin})$ = 0.12	

Typical
Skin / Tear strap / Floating Frame
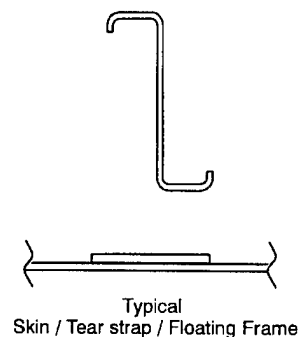
Figure 2. Structural Details of Panels FAA 1 and FAA 2.

Simulated MSD

Simulated MSD was introduced in the upper rivet row of three out of the four total lap joints. This was accomplished by installing sawcuts in the outer skin of the lap joints along the upper row of rivets. The sawcuts were oriented out of the fastener holes longitudinally in the horizontal plane by the use of a modified handsaw producing a 0.006- to 0.008-inch-wide cut. These sawcuts were introduced in the upper skin after the fastener holes had been drilled and countersunk to size, but prior to the application of the fey sealant and rivet installation. Figure 3 shows the MSD sawcut sizes and the four bay regions (80-inch sections) in which they were installed.

Test 1 of Panel FAA 1

Test 1 of panel FAA 1 was conducted on the lap joint in the four-bay region of 0.05-inch simulated MSD as shown in figure 4.

FAA 1

0.05 inch MSD

No MSD

FAA 2

0.15/0.10/0.05 inch MSD

Test 1

Initial Sawcut

Test 2

Sawcut width = 0.006 to 0.008 inch

Sawcut length (both sides)

0.063 inch
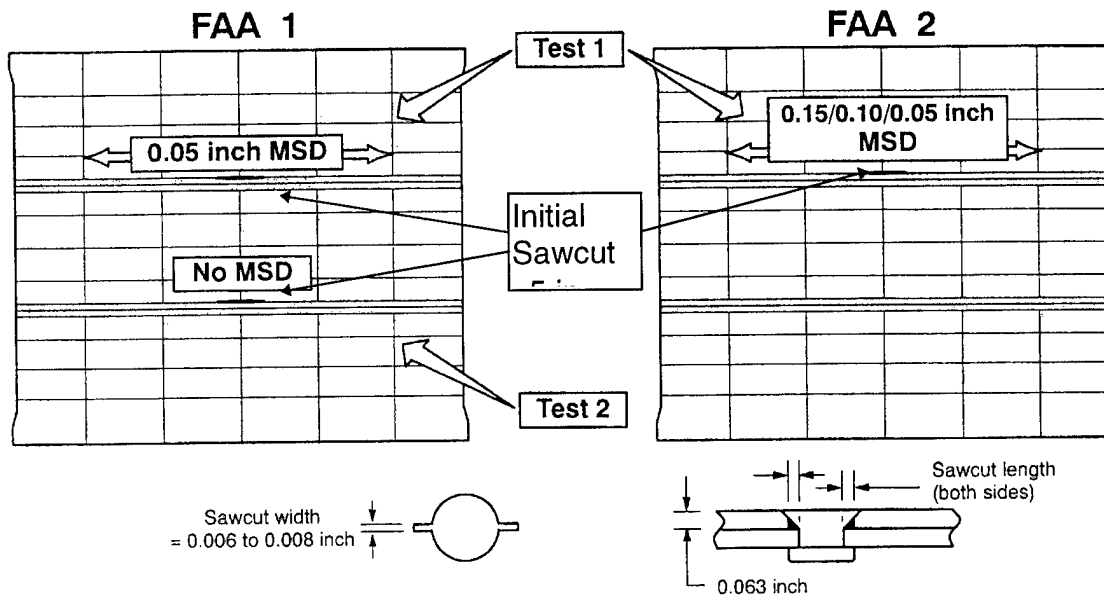
Figure 3. Simulated MSD Regions.

Frame Station

100   120   140

FAA 1-Test 1

Initial sawcut ≈ 5 in.

0.05 in MSD size   0.05 in MSD size

FAA 1-Test 2

No MSD   No MSD

FAA 2-Test 1

0.05 in   0.05 in   MSD size   0.05 in   0.05 in   MSD size   0.05 in   0.05 in

0.1 in   0.1 in   0.15 in   0.1 in   0.1 in   0.15 in   0.1 in   0.1 in
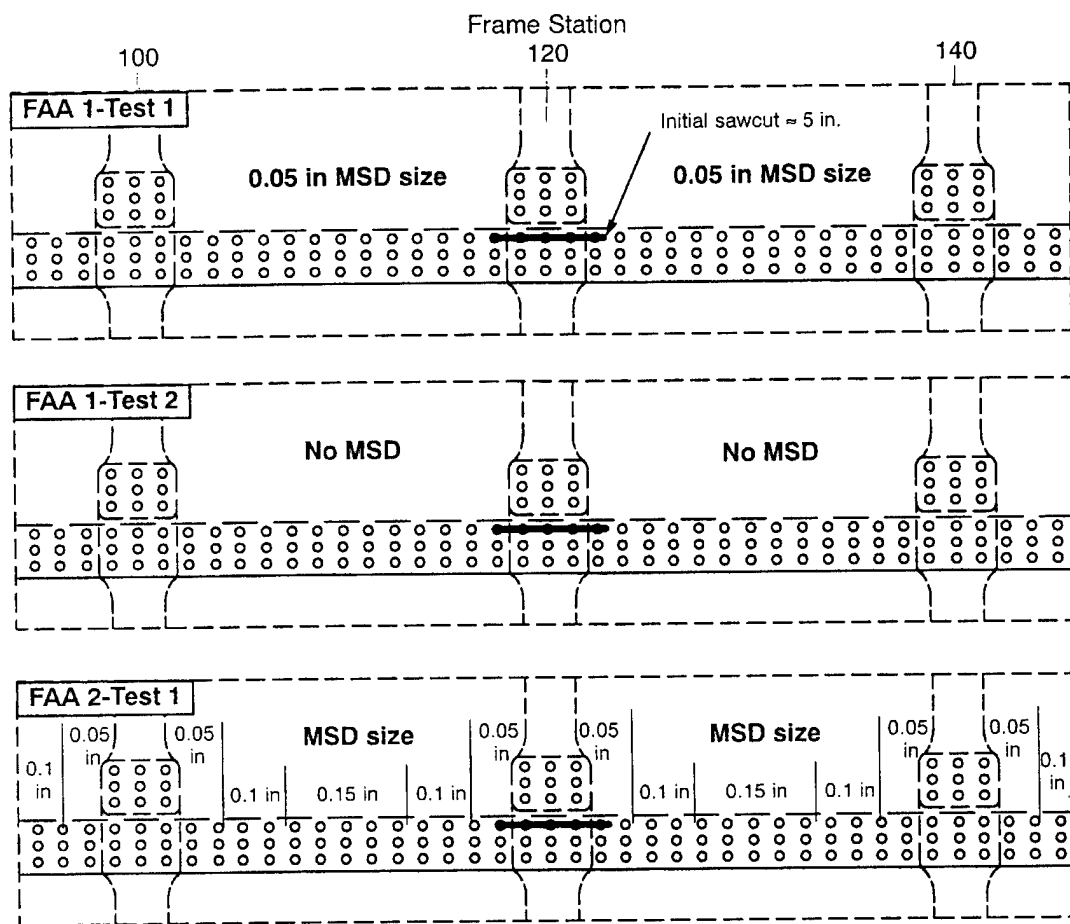
Figure 4. Initial Sawcut Installation and Simulated MSD Sizes.

444

A 5-inch sawcut was installed in the outer skin only, centered at frame station 120. The panel was pressure cycled at 8.6 psi. No crack initiations were visible after 281 pressure cycles. At that point the station 120 tear strap bridging the sawcut was cut. As cycling continued, the main crack steadily grew to approximately 6.5 inches, at which point the 0.05-inch MSD sawcuts one fastener ahead of the tips of the main crack had grown from under the rivets and had become visible.

The main crack extended dynamically at 1233 cycles after reaching a length of 17.2 inches and arrested at a length of 37.4 inches. The tear straps contained the dynamic crack, but visible cracks did develop in the fasteners common to the tear straps at the next adjacent frames, stations 100 and 140 respectively.

No residual strength test was conducted at this test location due to the potential destruction of the entire test panel prior to conducting Test 2 (the only non-MSD test in the program), which was intended to be used as the basis for measuring the influence of MSD on residual strength. The test location was repaired by applying a small external doubler over the crack.

Test 2 of Panel FAA 1

Test 2 of panel FAA 1 was conducted on the lap joint with no MSD, as shown in figure 4.

A 5-inch sawcut was then installed in the outer skin and tear strap centered on frame station 120. The panel was pressure cycled at 8.6 psi. After 1172 pressure cycles, no crack growth had been detected from the sawcut, and thus the sawcut was extended to 5.72 inches, terminating approximately 0.25 inch beyond a fastener hole at each end of the sawcut. As cycling continued the main crack steadily grew to a length of 36.91 inches.

The residual strength test of FAA 1-Test 2 consisted of increasing the internal pressure in small intervals until dynamic panel failure occurred. Prior to running the residual strength test the central frame at station 120 was severed. The crack length prior to pressurizing was 36.91 inches with the crack tips adjacent to the edges of the tear straps. As the pressure was increased the crack stably grew to a length of approximately 38.2 inches where, at a pressure of 9.4 psi, the crack ran dynamically to the ends of the panel, resulting in catastrophic failure. The configuration prior to failure is shown in figure 5.

Test 1 of Panel FAA 2

Test 1 of panel FAA-2 was conducted on the upper row of the lap joint in the four-bay region of variable size (0.05, 0.10 and 0.15 inch) simulated MSD, as shown in figure 4.
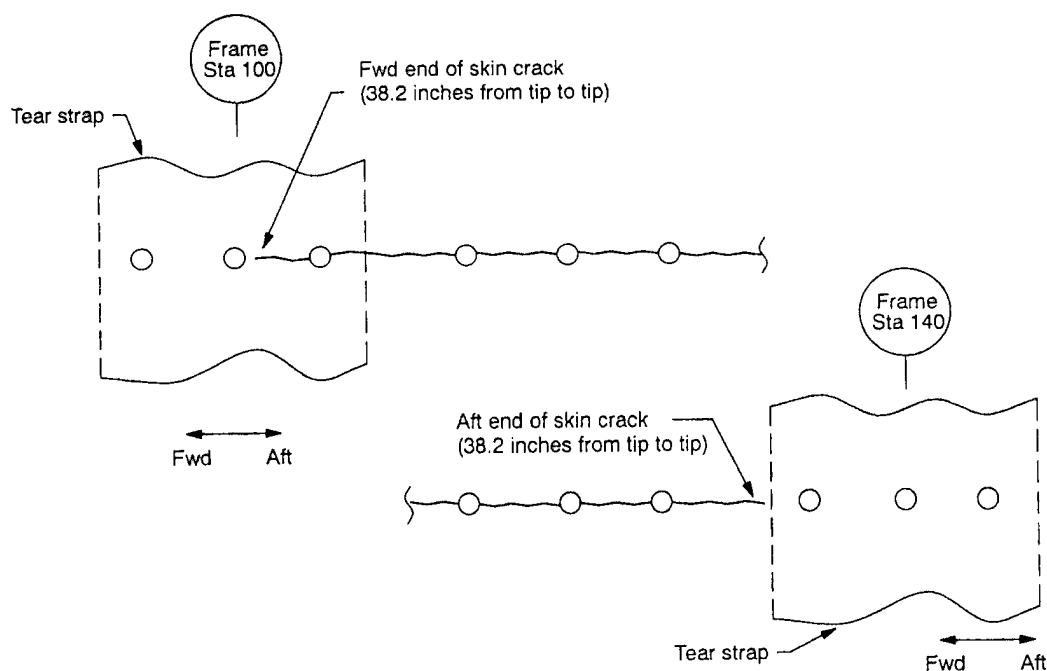
Figure 5. Crack Configuration Prior to Panel Failure (FAA 1-Test 2).

A 5-inch sawcut was installed in the outer skin and tear strap centered on frame station 120. The panel was pressure cycled initially at 8.6 psi. After 489 pressure cycles, 1.0 inch of visible crack extension was measured. As cycling continued the main crack steadily grew to 11.84 inches where the first 0.1-inch MSD sawcut grew and became visible ahead of the aft tip of the main crack. At this point the cyclic pressure was decreased from 8.6 to 7.0 psi in an attempt to reduce the risk of the crack dynamically running as demonstrated in FAA 1-Test 1. As cycling continued the main crack ran dynamically at a length of 15.29 inches and arrested after reaching a length of 35.72 inches.

The crack was then sawcut horizontally in order to develop the similar crack configuration as in FAA 1-Test 2. One more cycle was applied in order to sharpen the new sawcut, resulting in 1.88 inches of crack extension occurring at 8.0 psi. This made the tip-to-tip crack length 38.50 inches, which was 1.6 inches longer than the final crack length of the non-MSD test performed on FAA 1-Test 2. The crack extended under the tear strap region.

The residual strength test of FAA 2-Test 1 was conducted identically to the previously mentioned FAA 1-Test 2, increasing the pressure to failure after severing the central frame at station 120. The crack configuration prior to pressurization was 38.5 inches with the crack tips through the first fastener common to the tear straps. As the pressure was increased the crack stably grew to a length of approximately 41.7 inches where, at a pressure of 7.5 psi, the crack ran dynamically to the ends of the panel, resulting in catastrophic failure. The configuration prior to failure is shown in figure 6.
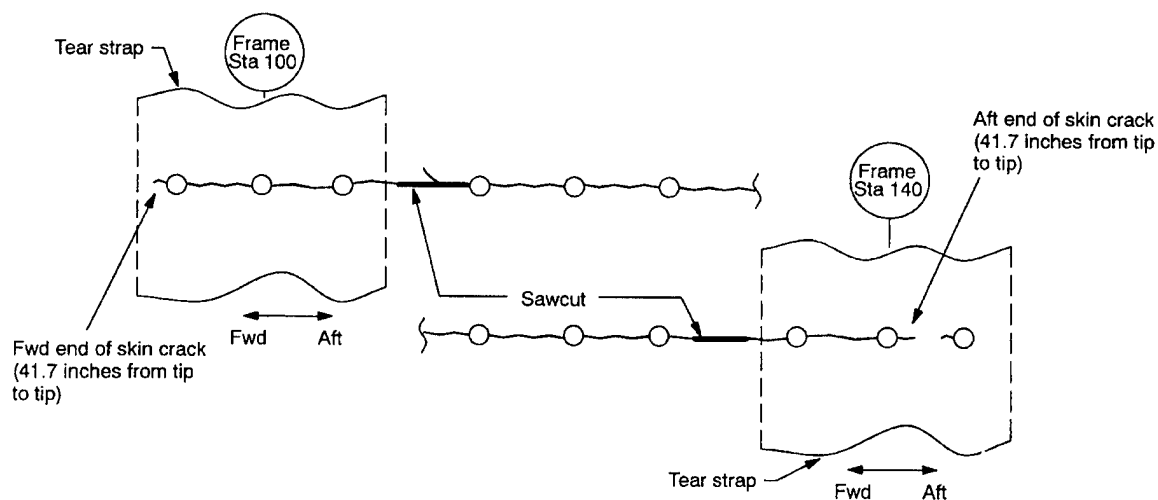
Figure 6. Crack Configuration Prior to Panel Failure (FAA 2-Test 1).

Curved Panel Testing Observations

The impact of the 0.05-inch MSD on the behavior of the test panels was most noticeable in terms of crack growth life and residual strength capability. Comparisons were made between the tests with MSD and without, producing the following conclusions:

- 2.5x reduction in crack growth life when comparing results from FAA 1-Test 1 with FAA 1-Test 2. Plots of these data are shown in figure 7.

- 20% reduction in residual strength when comparing results from FAA 1-Test 2 with FAA 2-Test 1.

In contrast to the test data presented in this paper, past Boeing pressure panel tests showed approximately a 10% reduction in residual strength due to 0.005-inch simulated MSD. The Boeing tests were run much the same way as the tests discussed in this paper: results from one test panel containing simulated MSD in the lap joint were compared with results from a similar panel without MSD.

PRESSURE PANEL FINITE ELEMENT MODEL DEVELOPMENT

This section discusses the development of finite element models to analyze the FAA test panels. Finite element analysis was used to predict strain gage stresses, crack growth life and residual strength. The models accounted for major structural effects on the lead crack, but did not include the effects of MSD. The stress distribution obtained from the analyses was used to predict the stresses at strain gage locations. Stress intensity factors were

447

calculated at different crack lengths and were used to predict crack growth and residual strength. The predictions were then compared with the test results. Only the crack growth and residual strength comparisons are discussed here; the reader is referred to reference 1 for a discussion of the comparison of predicted stresses with strain gage measurements.
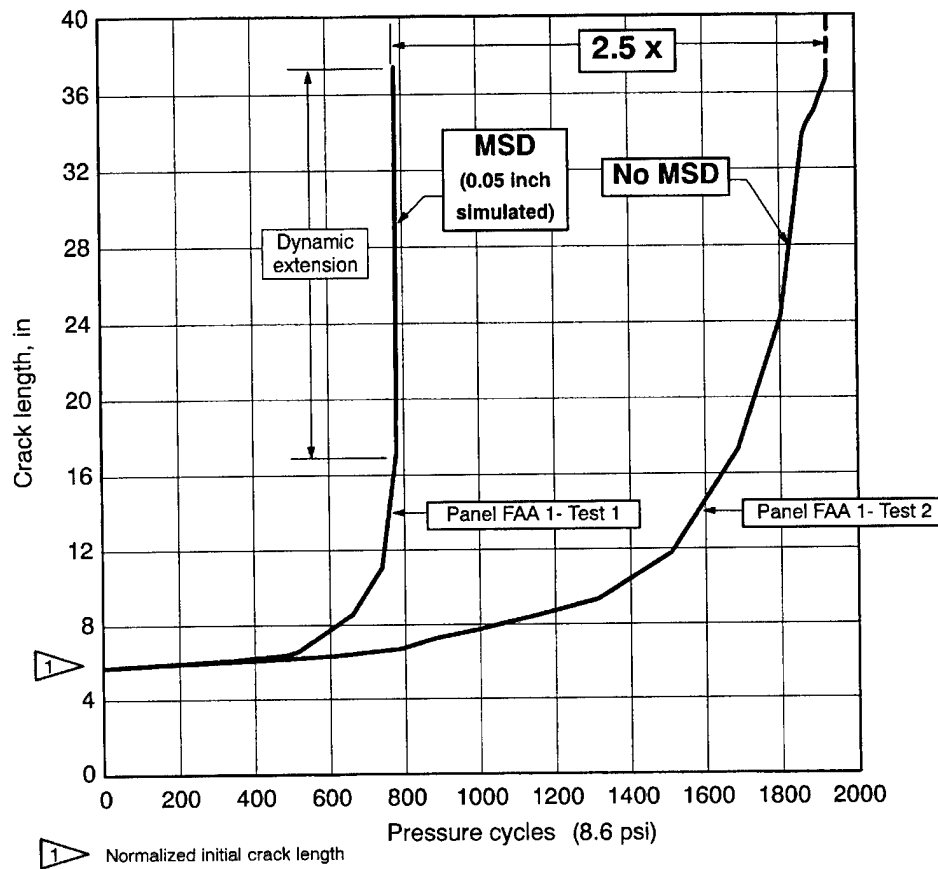
Figure 7. Crack Growth Comparison, MSD Versus Non-MSD.

For this study, a section of fuselage crown structure (i.e., the test panel) was modeled and boundary conditions for cylindrical symmetry were applied. The advantage to this strategy was that a model of the entire test fixture/test panel assembly was avoided, allowing a smaller, more detailed model of the test panel to be used. The disadvantage to this strategy was that the effect of the test fixture on the test panel was not modeled and is thus unknown.

The scope of the analysis was limited to modeling the major structure of the test panel, i.e., the skins, tear straps, stringers, and frames. Elements were included to model the load transfer at fasteners and stringer clips; however, local effects such as fastener holes and MSD cracks were not modeled.

The model was 15 stringer bays wide by three and one-half frame bays long. Only the six stringer bays nearest the lap joint were modeled in detail. The remainder of the model was a coarse mesh with rigidly connected structural elements. Extending the model beyond

448

six stringer bays was necessary to prevent spurious frame displacements when the model contained a severed frame as in the residual strength tests. Because the symmetrical boundary conditions imply that all damage is mirrored across the boundaries, significant interactions occur if the damage is too close to a boundary.

The skins and tear straps were modeled with eight-noded shell elements, and the stringers and frames were modeled with three-noded beam elements. Fastener elements were used at each rivet location to model the effect of load transfer, except along the crack where the fastener elements were removed from the model when the crack grew past them. Fastener elements were circular two-noded beam elements with a cross section radius equal to the radius of the rivet shank. Similarly, stringer clip elements were rectangular two-noded beam elements that made a simple connection between a frame node and a stringer node.

Geometric nonlinearity was accounted for in the ABAQUS analysis of the model. As well, material plasticity was accounted for in the residual strength analyses, where the central frame had been severed and significant plastic behavior was expected in the tear straps beneath the crack tips. In the model, the tear strap elements beneath the crack tips were given plastic material properties.

Figure 8 shows the displaced shape of the skin mesh of the finite element model for an intact test panel. Here the magnification factor on the displacements is high enough to see the detail of the skin bulging and the lap joint rotation. Figure 9 shows the displaced shape of the skin mesh containing a 30-inch crack. Here the bulging of the skin caused by the crack is much more significant than bulging caused by the stiffening structure.
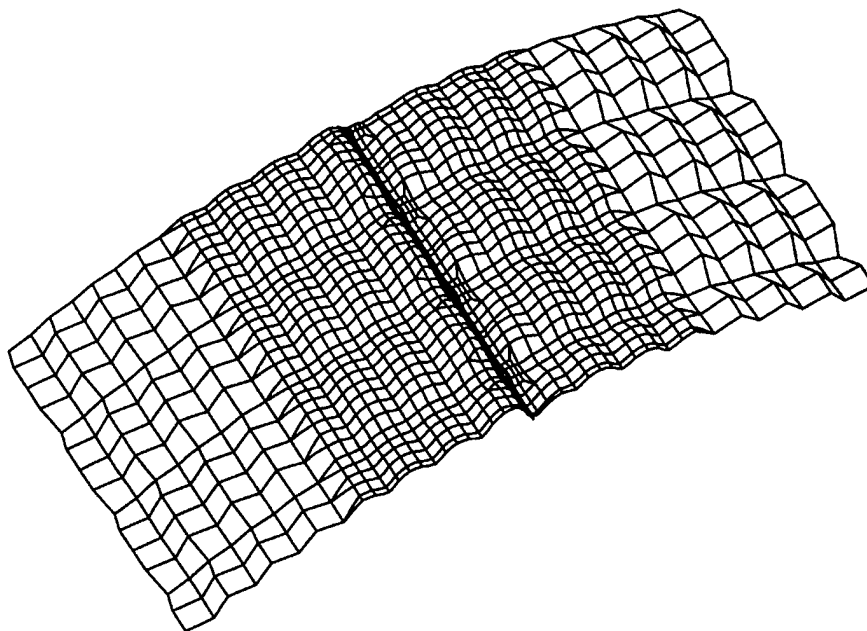
Figure 8. Displaced Intact Skin Mesh, Internal Pressure = 8.6 psi, Magnification Factor ≈ 100x.

449
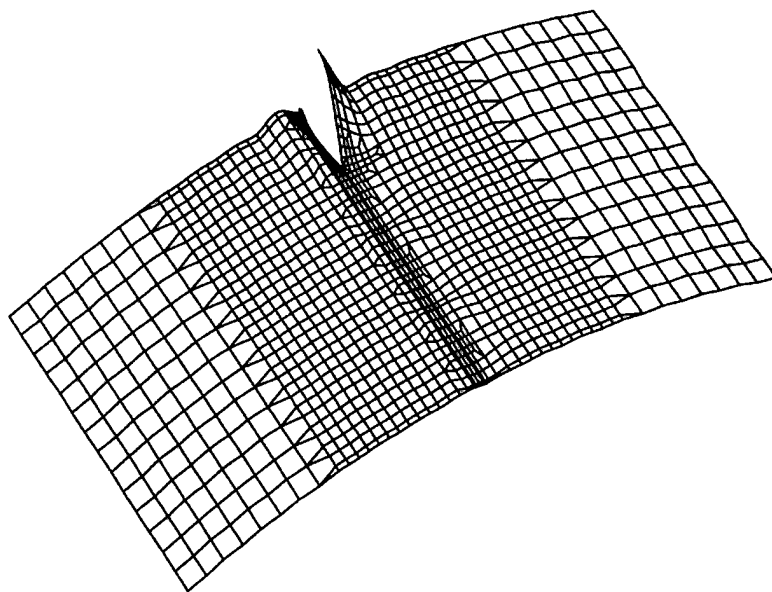
Figure 9. Displaced Skin Mesh Containing a 30-inch Crack, Internal Pressure = 8.6 psi, Magnification Factor ≈ 10x.

A total stress intensity factor that could be related to the strain energy release rate was used to calculate crack growth. Figure 10 contains a plot of the total stress intensity factors versus crack length. Crack growth predictions were then calculated using the K versus crack length curve and the crack growth rate data derived from the flat panel test results.
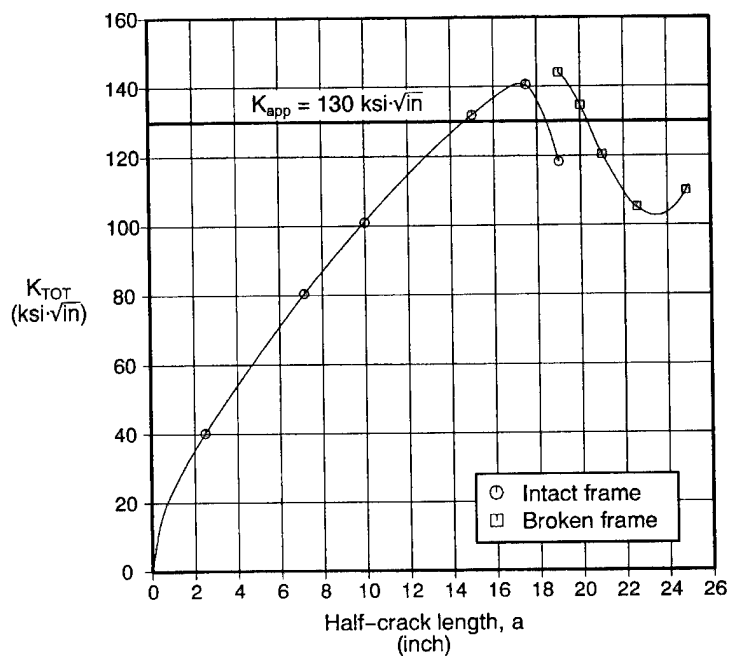
Figure 10. Stress-Intensity Factor Predictions at Operating Pressure.

450

Figure 11 shows a comparison of the finite element method (FEM) prediction vs. test results for crack growth along the lap joint with 0.05-inch MSD emanating from the rivet holes. In this case, the prediction was calculated so that at each rivet hole, the length of the lead crack was advanced forward by the diameter of the rivet shank plus the length of the MSD. Growth of the individual MSD cracks was not accounted for.
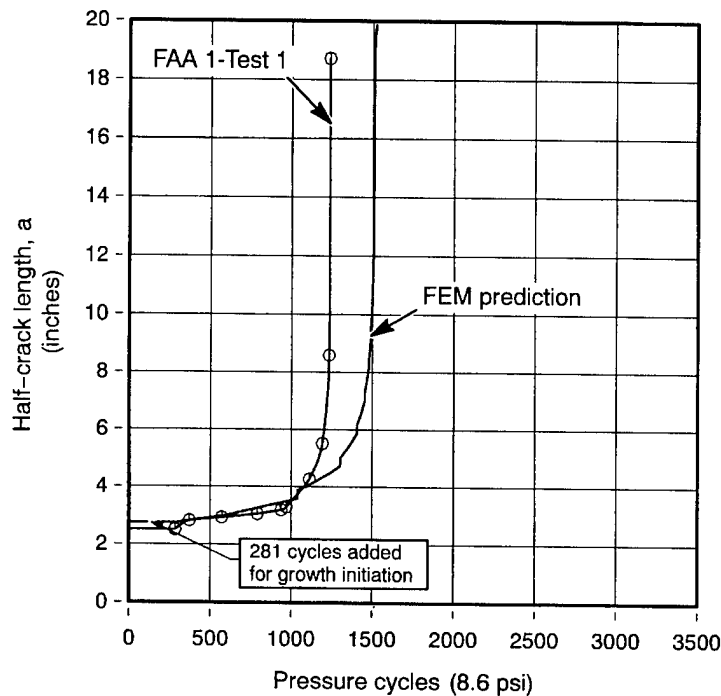
Figure 11. Crack Growth Predictions vs. Test Results for FAA 1-Test 1 (0.05-Inch MSD).

Figure 12 shows the crack growth comparison for the lap joint test without MSD. First the crack growth prediction was calculated from the K vs. crack length curve without accounting for the effect of the fastener holes. It was clear from the test that additional pressurization cycles were needed to initiate a new crack tip after the crack grew into a rivet hole. These additional cycles were estimated using an empirical equation which describes stop drilling test data:

$$N_{add} = \left[0.61 + \frac{f_a}{590ksi} \left(1 + 2\sqrt{\frac{a}{r_s}} \right) \right]^{-33} \tag{1}$$

where f_a is the membrane hoop stress at the rivet hole predicted by analysis, r_s is the radius of the rivet shank (3/32 inch), and a is the half-length of the crack to the outside edge of the rivet hole. N_{add} is the number of cycles needed for the crack to reinitiate on the outside edge of the rivet hole.

451
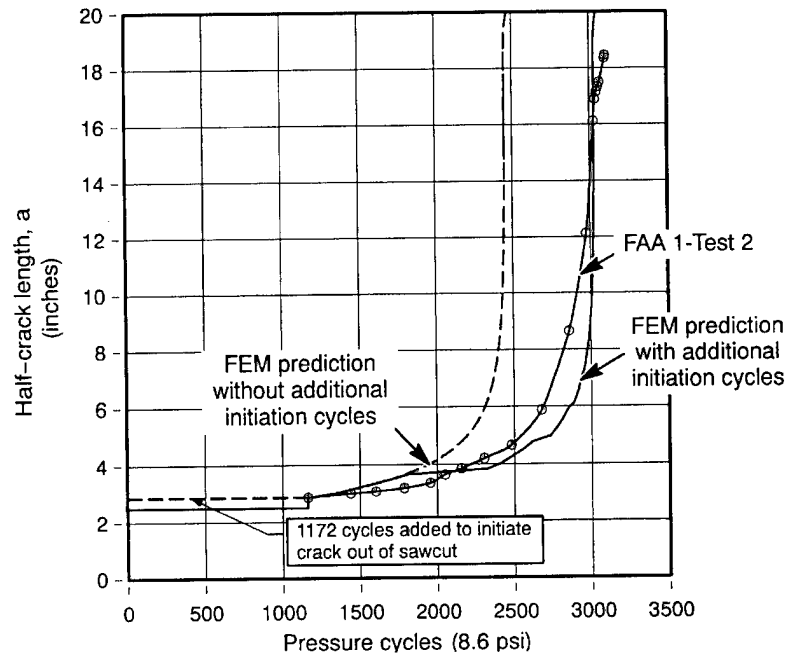
Figure 12. Crack Growth Predictions vs. Test Results for FAA 1-Test 2 (No MSD).

Figure 13 contains the crack growth comparison for the lap joint test with variable MSD. The method used here for calculating crack growth was the same as that for the case of 0.05 MSD shown in figure 11. Here the prediction does not match well with experimental results. Most likely, the larger-sized MSD in this test accelerated the crack growth.
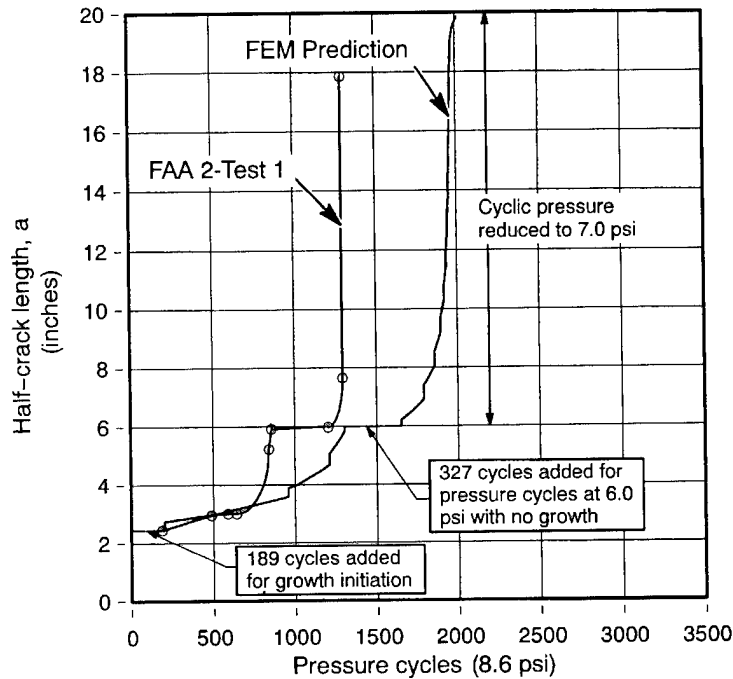
Figure 13. Crack Growth Predictions Versus Test Results for FAA 2-Test 1 (varied MSD).

452

In figure 14, an apparent fracture toughness of 130 ksi $\sqrt{\text{in}}$ was used to calculate a prediction of the maximum pressure vs. half-crack length for the intact frame residual strength case and for the severed central frame residual strength case using the stress intensity factor results shown in figure 10. The net section failure of the tear strap was predicted by calculating the average net stress for the tear strap across the upper rivet row for pressurizations of 7.2, 8.6 and 10.0 psi for varying crack lengths. Using a quadratic fit for the three pressurizations, a pressurization that caused the net tear strap average stress to equal the ultimate strength of the material (64 ksi) could be found for varying crack lengths. This curve indicates that as the crack extends, the tear strap is not able to support the additional load and fails, causing total panel failure.
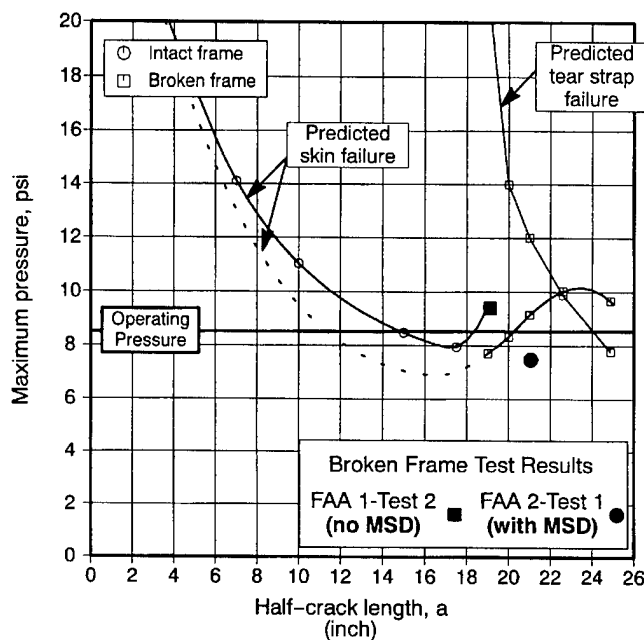
Figure 14. Residual Strength Test and Analysis Correlation.

The possibility that tear strap failure preceded dynamic skin crack growth was investigated further. Just prior to failure, the test panel without MSD contained a crack 38.2 inches long and failed at a pressure of 9.4 psi, and the test panel with MSD contained a crack 41.7 inches long and failed at a pressure of 7.5 psi, as shown in figure 14. For each of these cases, the finite element analyses predicted similar stresses in the ligament of the tear strap bridging the skin crack. Possibly, this ligament failed, causing complete tear strap failure and dynamic skin crack growth. However, this hypothesis cannot be verified from the test data because of the rapid sequence of events at final failure.

The modeling strategy chosen worked well for determining overall panel behavior. The crack growth predictions for the tests with no MSD and small MSD (0.05 inch) were relatively accurate, although the crack growth prediction for the test with variable MSD (up to 0.15 inch) failed to predict occurrences of fast crack growth. This is reasonable given that the analysis was for the lead crack only.

In cases where the effect of the fasteners was important, such as predicting residual strength, the present analysis did not produce good results. Further refinement using a global vs. local modeling strategy would be effective. Stringers, frames, and stringer clips could be modeled with shell elements. Fasteners could be modeled explicitly instead of treating them as load transfer points. This level of refinement would also allow the MSD at the fastener holes to be modeled. As well, a more refined theory could be used to predict residual strength than the apparent stress intensity factor approximation made here, such as plastic collapse of the ligaments between the lead crack tip and the MSD crack tips. Additional refinement of the tear straps would also allow a better prediction of tear strap failure.

RESIDUAL STRENGTH ANALYSIS WITH MSD

The following section summarizes work being done at Boeing to develop an engineering approach for determining the residual strength of structure containing MSD. This work has focused on using both test data and currently available analysis techniques to develop a practical method to be used in an airplane design environment.

Testing performed at Boeing on structure containing MSD has ranged from simple flat unstiffened panels to complex curved pressure panels. In addition to the data collected from Boeing tests, data have also been obtained from similar testing performed at the National Institute of Standards and Technology, NIST (ref. 2), and by Foster-Miller, Inc. (ref. 3). Collectively, these test data give a good representation of the effect of MSD on the behavior of the types of structure tested. This testing also provides data for use in evaluating and calibrating MSD link-up prediction methods.

Analysis methods for determining the stress at which the MSD cracks link up have been proposed by numerous researchers and include plastic zone interaction (ref. 4), R-curve (ref. 5), critical crack-tip opening angle, CTOA (ref. 6), and T* (ref. 7). The first two methods listed, plastic zone interaction and R-curve, are the most simple and are therefore more practical for design of airplane structure susceptible to MSD. The last two methods, CTOA and T*, are more accurate than the first two methods when the results presented in references 2, 6, and 7 are compared. The substantial time and computational capabilities required of performing CTOA and T* do not make them effective design tools; however, they are still of interest in evaluating the accuracy of the more simple link-up models and could preclude the need for extensive testing.

An effort has been made at Boeing to evaluate each of these analysis methods for predicting ligament and subsequent structural failure by comparing analysis results to test data generated both within and outside of Boeing. Because of time constraints, only the plastic zone interaction and R-curve methods have been investigated and are presented here. Figures 15 and 16 present a direct comparison of test results and the corresponding predicted link-up stresses obtained from both the plastic zone interaction (figure 15) and the R-curve method (figure 16). All these comparisons represent flat panels containing a lead crack along with adjacent MSD cracks.

454
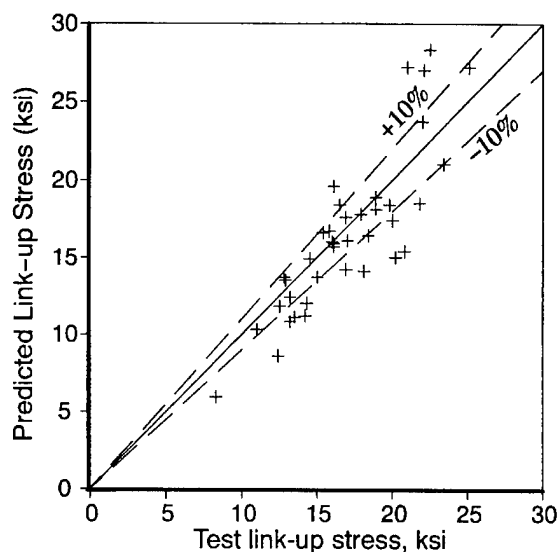
Figure 15. Predicted vs. Test Link-Up Stresses Using the Plastic Zone Interaction Method.
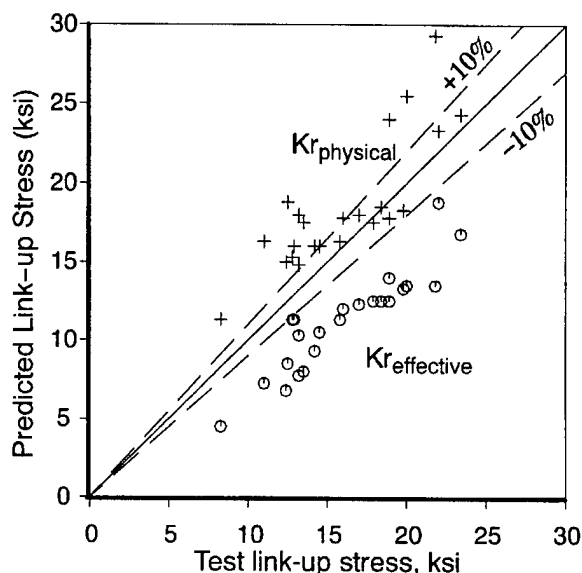
Figure 16. Predicted vs. Test Link-Up Stresses Using the R-Curve Method.

The results given in figure 15 for plastic zone interaction show that there can be significant error in predictions made using this method. Approximately half the data falls outside an accuracy of 10%, and in several cases the plastic zone interaction method gives link-up stresses that were larger than the failure stress for the panel with only a lead crack.

The R-curve results, shown in figure 16, were determined using both $Kr_{physical}$ and $Kr_{effective}$, where $Kr_{physical}$ is based on the physical crack length and $Kr_{effective}$ includes Irwin's plastic zone adjustment, r_y (ref. 5):

$$r_y = \frac{1}{2\pi}\left(\frac{K}{\sigma_y}\right)^2 \qquad (2)$$

where:

K = Stress-intensity factor
σ_y = Material yield stress

There is not as much data presented for the R-curve analysis as for the plastic zone interaction method because R-curve data were not available for all sets of panels tested. The R-curve results show that using $Kr_{physical}$ generally overpredicts the test results, while $Kr_{effective}$ generally underpredicts the test results. By modifying the plastic zone adjustment by a constant having a value less than 1.0, the predictions could be made to fall more in line with the test results.

455

In the course of performing predictions of MSD crack link-up, the test data were examined individually to determine if any trends or important parameters would be revealed. Figure 17 shows a plot of all test data gathered from Boeing and literature and includes flat panels without load transfer, flat panels with load transfer, curved pressure panels without stiffeners, and curved stiffened pressure panels. In this figure, the normalized failure stress of each panel containing MSD is plotted against the effective MSD crack length, $a_{msd\ effective}$, divided by the distance, d, which is measured between the lead crack and the first adjacent MSD crack. The effective MSD crack length, $a_{msd\ effective}$, was used as the dependent variable instead of the actual MSD length to improve the correlation between panels containing fasteners and those without fastener holes. The effective crack is calculated from the physical crack length using the following equation and geometry definition:

$$a_{msd\ effective} = \beta^2 \cdot L_{MSD}$$

where β is a correction factor that accounts for geometry, hole fill, and load transfer.
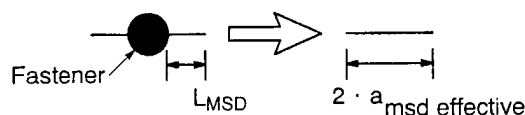
The failure stress of each panel containing MSD was normalized by dividing it by the corresponding failure stress of the panel without MSD assuming the same size lead crack. The failure stress without MSD for all the curved panels was obtained directly from test data. For some of the flat panel data, the failure stress without MSD was not available for the given lead crack, so it was determined using an R-curve analysis. Also, the failure stress of the panels containing MSD was taken as any point where the lead crack and adjacent MSD crack linked up. This procedure assumes that each panel contained multiple MSD cracks in front of the lead crack that had the same spacing as that between the lead crack and first adjacent MSD crack. Therefore, with this scenario, first link-up would lead to panel failure. For many of the panels tested, the spacing between the lead crack and the first adjacent MSD crack was not the same as the spacing between the remaining MSD cracks. Hence, the lead crack linked up several times with adjacent MSD cracks before final panel failure. Assuming equally spaced MSD cracks and using each link-up as a final failure stress allowed multiple data points to be generated from many of the panels that are shown in figure 17.

The two lines shown in figure 17 correspond to curve fits through the Boeing test data (solid line) and the data obtained from references 2 and 3 (dashed line). Two different lines were given because all the Boeing data come from tests performed on 0.063-inch-thick 2024-T3 clad aluminum material, while all the data obtained from literature were obtained from tests on both bare and clad 0.04-inch-thick 2024-T3 aluminum. The different results for the different skin thicknesses suggest that the effect of MSD may be different for each thickness and type of material. Also, some of the variability of the data shown in the plot may be caused by having to assume values for some test parameters that were not available.
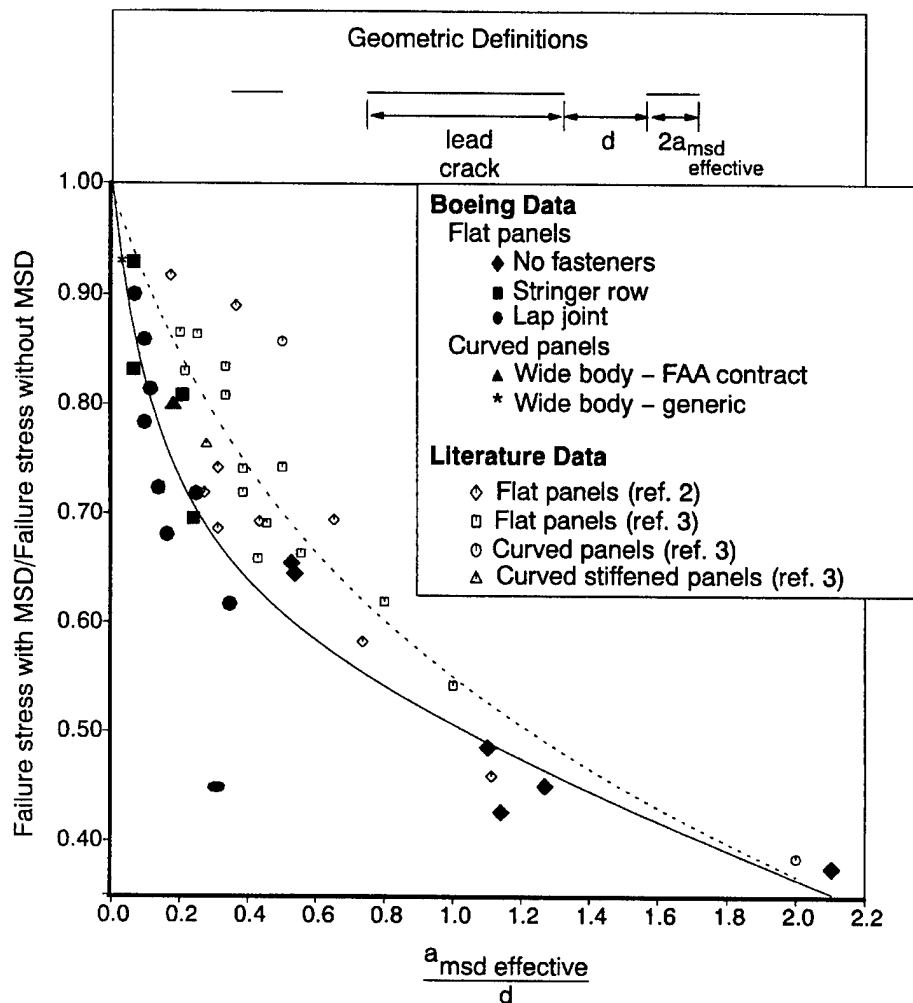
Figure 17. Comparison of MSD Test Data.

Regardless of the scatter observed in figure 17, there are definite trends in the results. As seen in the plot, the curves are very steep at low $a_{msd\ effective}/d$ ratios. Thus, small changes in the MSD size or the distance between cracks cause large differences in residual strength at these low values of $a_{msd\ effective}/d$. However, this sensitivity decreases as the MSD size increases or as d decreases. Also, the figure shows that the reduction in residual strength caused by MSD is not strongly dependent on the type of structure or the lead crack length. The data included in the plot account for flat unstiffened panels as well as built-up curved pressure panels with lead cracks ranging from 5 to 40 inches. This result shows that curves, similar to those presented in figure 17, could be developed from results obtained from relatively simple tests or analyses performed on flat panels. These curves would then be used as a design tool to determine the knockdown in residual strength for any built-up structure susceptible to a similar MSD scenario. This procedure removes the need to perform detailed MSD analyses on built-up structure.

457

CONCLUSIONS

Curved Pressure Panel Testing

- The crack growth rate of the lead crack in the lap joint was greater in the presence of simulated MSD. Without MSD the lead crack arrested in each fastener hole, and additional cycles were required to extend the crack out of the opposite side.

- For the floating frame panel geometry (no shear ties) and crack lengths tested in this program, the presence of 0.05-inch MSD in the lap joint upper rivet row reduced the residual strength of the panel by 20% compared to a panel containing no MSD.

- During the residual strength portion of the tests, the tear straps bridging the crack tips of the two-bay lead crack remained intact until the final failure load was reached. However, the test results are inconclusive as to whether tear strap failure led to dynamic extension of the lead crack.

Finite Element Analysis

- The predictions of skin and tear strap stresses and crack growth history with and without MSD are generally very accurate as shown in the test/analysis correlations. However, frame and stringer stresses could not be reliably predicted.

- The residual strength prediction using the R-curve and K_{app} methods show that, without MSD, the lap joint lead crack would not be expected to extend dynamically at the pressures and crack lengths observed in the tests.

- Examination of the stresses in the tear straps bridging the crack tips of the two-bay lead crack indicates that tear strap failure probably preceded lead crack instability for both the MSD and non-MSD cases.

MSD Analysis

- Predicting the residual strength of structure containing MSD using simple analysis methods such as plastic zone interaction and R-curve may not provide sufficient accuracy to be useful. However, more accurate methods such as CTOA and T* are too time- and resource-consuming to perform in a design environment.

- Comparing test results from various panel geometries shows that lead crack size and panel geometry do not have a big influence on the reduction in residual strength

caused by MSD. Therefore, tests and analyses can be performed on simple panel geometries to get an acceptable representation of the effect of MSD on the residual strength of built-up panels.

ACKNOWLEDGMENTS

The authors would like to acknowledge the graphics and publications support from Mr. W. J. Brewer and the Boeing Support Services. We would also like to acknowledge the leadership of Mr. Chris Mazur in performing work associated with the FAA contract. Finally, we would like to thank Dr. Roland deWit for providing additional information about the 90-inch-wide flat panel tests performed at NIST.

REFERENCES

1.   Gruber, M. L.; Mazur, C. J.; Wilkins, K. E.; and Worden, R. E.: Investigation of Fuselage Structure Subject to Widespread Fatigue Damage, FAA Technical Report, DOT/FAA/AR-95/47, February 1996.

2.   deWit, R.; Fields, R. J.; Low III, S. R.; Harne, D. E.; and Foecke, T.: Fracture Testing of Large-Scale Thin-Sheet Aluminum Alloy, FAA Technical Report, DOT/FAA/AR-95/11, February 1996.

3.   Thomson, D.; Hoadley, D.; and McHatton, J.: Load Tests of Flat and Curved Panels with Multiple Cracks, Foster-Miller Draft Final Report to the FAA Technical Center, September 1993.

4.   Broek, D.: The Effects of Multi-Site-Damage on the Arrest Capability of Aircraft Fuselage Structures, FractuREsearch TR9302, June 1993.

5.   Broek, D.: *Elementary Engineering Fracture Mechanics,* Martinus Nijhoff Publishers, Fourth Edition.

6.   Newman, Jr., J. C. and Dawicke, D. S.: Fracture Analysis of Stiffened Panels Under Biaxial Loading with Widespread Cracking, NASA TM 110197, November 1995.

7.   Wang, L.; Brust, F. W.; and Atluri, S. N.: The Elastic-Plastic Finite Element Alternating Method (EPFEAM) and the Prediction of Fracture under WFD Condition in Aircraft Structures, Part III - Computational Predictions of the NIST Multiple Site Damage Experimental Results, FAA Center of Excellence for Computational Modeling of Aircraft Structures, Georgia Institute of Technology, August 1995.

NUMERICAL INVESTIGATIONS INTO THE VIABILITY OF CRACK TIP OPENING DISPLACEMENT AS A FRACTURE PARAMETER FOR MIXED-MODE I/II TEARING OF THIN ALUMINUM SHEETS[1]

M. A. Sutton, Wenzhong Zhao, X. Deng
Department of Mechanical Engineering
University of South Carolina
Columbia, SC

D. S. Dawicke
Analytical Services and Materials, Inc.
Hampton, VA

J. C. Newman, Jr.
NASA Langley Research Center
Mechanics of Materials Branch
Hampton, VA

SUMMARY

Detailed two-dimensional finite element analyses of a mixed-mode I/II ARCAN test specimen machined from 2024-T3 aluminum have been performed to assess the viability of using a critical crack tip opening displacement (CTOD) criterion for prediction of the load-crack extension (P-Δa) response. Preliminary results for four levels of mode mixity indicate that (a) trends in the measured P-Δa behavior are accurately predicted throughout the crack growth process by the finite element analysis using experimentally determined mean CTOD values and (b) the predicted maximum load is within 7% of the measured value for all cases. Thus, the results indicate that use of a single parameter for prediction of crack growth in thin sheet materials under complex loading conditions is feasible.

INTRODUCTION

One of the objectives of aging aircraft research is to develop models of large-scale aeronautics structures that can accurately predict the residual strength of a damaged structure. In recent years, several researchers[1-6] have demonstrated conclusively that, under Mode I loading, a critical value for the crack tip opening angle (CTOA) exists in the region 0.5 to 1.5 mm behind the crack tip. Furthermore, use of CTOA in two-dimensional analyses

---

successfully predicts the measured P-Δa behavior for a variety of thin, ductile specimen geometries. Recently, Cordes et al.[7] used crack tip opening angle (CTOA) and the V_R curve approach in the ABAQUS numerical code to predict the fracture of compact tension (CT) and middle cracked tension (M(T)) specimens under Mode I loading. Their results indicated that CTOA was more accurate in predicting the P-Δa response than the V_R curve approach.

However, it is well known that cracks in aircraft fuselages undergo a combination of local loading conditions[8-10]. Recent modeling of aircraft fuselage structures[11] for fatigue crack growth using a nonlinear shell code with a maximum tangential stress theory along the midplane surface to predict the direction of crack growth has shown that the fatigue crack trajectory is reasonably predicted in the unreinforced skin region. However in the vicinity of structural stiffeners, where mixed-mode and deformation gradient conditions are more severe, predictions of observed crack trajectories are more difficult.

To assess the viability of extending the concept of CTOA to mixed-mode conditions, Amstutz et al.[12-13] developed a mixed-mode I/II test specimen that is an extension of the ARCAN[14] geometry used originally for composite specimens. By subjecting thin-sheet 2024-T3 aluminum specimens to a wide range of mode I/II conditions while measuring CTOD in the region between 0.5 and 1.5 mm behind the crack tip, they have shown that (a) a transition from Mode I to Mode II type fracture exists, (b) CTOD is reasonably constant for Δa $\geq$ 10 mm for all mode mixity values and is within the range measured for LT and TL specimens under pure mode I loading, and (c) the early stages of crack growth under mixed-mode loading show a transition towards a constant CTOD that is a function of the mode mixity. Due to the scatter in the observed CTOD, as well as recent observations indicating that there are significant through-thickness variations in CTOD even for thin specimens[15], the viability of a critical CTOD for prediction of the P-Δa response must be viewed as undetermined.

The enclosed work presents initial results from detailed two-dimensional finite element analyses of the mixed-mode I/II ARCAN test specimen and fixture[12,13], which have been performed to assess the viability of using a critical crack tip opening displacement (CTOD) criterion for prediction of the load-crack extension (P-Δa) response.

EXPERIMENTAL RESULTS

The ARCAN test fixture and test specimen, as well as the finite element method (FEM) mesh used to model the fixture and specimen, are shown in Figure 1. The test fixture was machined from precipitation hardened stainless steel and is nominally 12.7 mm thick. All specimens were machined from 2.4-mm-thick sheets of 2024-T3 aluminum and fatigue precracked using controlled load shedding to minimize the initial plastic zone size[12,13]; initial a/w values for all specimens were a/w = 0.167. Relevant properties for both materials are shown in Table 1. It is noted that, due to large rotations which occurred during crack

growth, the ARCAN test fixtures were remachined to increase the gap between the two fixtures so that they did not make contact during testing.

Table 1. Material Properties.

	Modulus of Elasticity E (GPa)	Poisson's Ratio ν	Yield Stress σ_y (MPa)
Stainless Steel	206.8	0.30	1722.5
2024-T3 aluminum	71.3	0.30	344.5

All tests were performed in displacement control to maximize the amount of stable crack growth. To measure CTOD, two-dimensional digital image correlation[15,16] was used. Each specimen was lightly sprayed with white enamel paint and lightly coated with Xerox toner powder to obtain a random, black and white pattern. Recalling that CTOD is defined as the magnitude of the relative crack tip opening displacement vector 1 mm behind the current crack tip, a high magnification of approximately 100 pixels/mm was used. Details of the experimental process are given in References 12 and 13.

For $\Phi = 0°$, $15°$, $45°$ and $90°$, Figure 2 presents the experimental data for CTOD-Δa. Table 2 presents the average value of the critical CTOD values, $CTOD_{avg}$, obtained from the CTOD-Δa data by averaging all CTOD measurements for Δa > 5 mm. It is noted that the standard deviation in the data is on the order of 0.01 mm, or approximately 10% of the average value, for all of the data. Furthermore, as noted by Amstutz et al[13], there is a 20% variation in $CTOA_{crit}$ (or CTOD at a fixed distance behind the crack tip) in 2024-T3 aluminum due to the effects of grain orientation; $CTOA_{crit}$ for a TL specimen is 20% lower than $CTOA_{crit}$ for an LT specimen). Given these complexities, results in Table 2 indicate that the variations in CTOD observed are well within the scatter band expected for this material.

Table 2. Experimental Average $CTOD_{avg}$ for All Loading Angles.

	$\Phi=0°$ (TL specimen)	$\Phi=15°$ (LT specimen)	$\Phi=45°$ (LT & TL specimen)	$\Phi=90°$ (LT specimen)
$CTOD_{avg}$ (mm)	0.079	0.084	0.097	0.097

To model the crack growth process, experimental data related to the crack growth direction throughout the stable crack growth process were required for each loading angle, Φ. The crack profiles were determined along the specimen centerline by mounting the fracture specimens in epoxy and polishing the specimen down to the centerplane. After polishing is completed, the specimen is placed in a scanner and digitized with a resolution of 0.127 mm and processed using digital image analysis software. The centerline crack profiles for $\Phi = 0°$, $15°$, $30°$, $45°$, $60°$, $75°$, and $90°$ have been obtained and these results are shown in Figure 3.

In this work, the crack profiles for $\Phi = 0^{\circ}$, 15°, 45°, and 90° have been used to develop FEM models for prediction of mixed-mode stable tearing. The following section outlines the FEM modeling process for these four cases. Additional results for the remaining crack profiles will be obtained in the near future.

FINITE ELEMENT MODEL

To determine whether the average CTOD can be used to predict the experimentally observed P-Δa response for the ARCAN specimen, finite element analyses of the ARCAN fixture and specimen geometry were initiated. The overall mesh which is used for both $\Phi = 0^{\circ}$ and 90° is shown in Figure 1; the meshes for other loading angles are the same except in the crack growth region. Figure 4 presents a close-up of the meshes in the crack growth regions for $\Phi = 0^{\circ}$, 15°, 45° and 90°; the 0° and 90° meshes are the same. In this work, the specimen and fixture were assumed to be connected without slip; hardened drill rod inserts were used in the gripping mechanism to minimize slip[12].

Three-noded, constant strain triangular elements were used exclusively in the FEM modeling. Plane stress conditions were enforced for all analyses. A refined mesh was used in the vicinity of the crack to improve the accuracy of the simulation; along the crack growth direction, there are eight rows of elements (4 above and 4 below the crack line) having an element size of approximately 0.50 mm (see Figure 4). To assess the importance of grip rotations on the specimen response, both large deformation analyses using the recently modified code ZIP2DL[17] and small deformation analyses using both ZIP2DL and ZIP2D[18] were performed. To simulate the observed stable crack growth process, the crack was constrained to follow the path observed experimentally for each loading angle, Φ, as shown in Figure 3. To predict the P-Δa response, each analysis was performed as follows. First, the displacement at the loading point was incrementally increased (and the applied load, P, computed) until the CTOD at approximately 0.50 mm behind the crack tip was equal to the measured $CTOD_{avg}$. Next, the crack tip node was released and equilibrium with a new crack length of a+Δa was iteratively computed; details of the numerical procedure used in the crack growth process for ZIP2DL are outlined in Reference 17. This process continued until the desired crack extension was obtained.

A comparison of the experimental and simulated P-Δa response for all Φ is given in Figure 5. Table 3 presents a comparison of the predicted maximum load (based on small deformation simulations) to the experimental maximum load for all Φ.

Table 3. Comparison for Predicted and Experimental Maximum Load for All Loading Angles, Φ.

	$\Phi=0°$ (TL specimen)	$\Phi=15°$ (LT specimen)	$\Phi=45°$ (LT & TL specimen)	$\Phi=90°$ (LT specimen)
Maximum Load from Simulation	18.8 kN	19.9 kN	18.2 kN	15.8 kN
Maximum Load from Experiment	18.8 kN	19.1 kN	17.0 kN	16.8 kN
Percent Difference	0%	+4%	+7%	-6%

DISCUSSION OF RESULTS

As shown in Figure 5, for all Φ, the trends in the experimental data are in very good agreement with the FEM predictions throughout the crack extension process. For $\Phi = 0°$, when $\Delta a > 10$ mm, large deformation analysis is required to accurately predict the experimental data. This is consistent with physical observations that grip rotation increases rapidly as the crack tip passes the centerline of the specimen. Interestingly, large deformation FEM analysis and small deformation FEM give nearly the same predictions when the applied loading is pure shear ($\Phi = 90°$). Relative to the maximum load, P_{max}, Table 3 indicates that (a) small-deformation FEM predictions were within 7% of the measured P_{max} for all cases and (b) the predictions are excellent on the average since the results are not weighted towards one side or the other. Given that there is a scatter of approximately 10% in the measured critical CTOD, it seems clear that the predictions of P-Δa during mixed-mode crack extension are quite good.

It is worth noting that this work studies the applicability of CTOD for prediction of extension of a crack along a known path under mixed-mode conditions; the work does not answer the question as to whether CTOD can be used to predict both the direction and onset of continued crack extension. Conceptually, such predictions using CTOD would require virtual crack kinking along arbitrary directions and crack tip remeshing, along with studies of how the FEM mesh size affects the predictions. However, due to the computational intensiveness associated with prediction of CTOD along arbitrary directions, this approach may be unfeasible due to increased time.

Another possibility would be a hybrid approach; use the FEM results in the crack tip region at the load corresponding to the measured $CTOD_{avg}$ to determine whether other parameters (e.g., mean stress (σ_{mean}), effective stress (σ_{eff}), stress intensity factors, J-integral, etc.) would be useful for predicting the direction of crack growth. Recent work by the authors using this approach and assuming small-scale yielding conditions with plane strain conditions up to the initiation of crack growth suggests that (a) $\sigma_{mean}/\sigma_{eff}$ and σ_{eff} appear to be

viable parameters for predicting the direction of crack growth under mixed-mode conditions and (b) the transition between Mode I type and Mode II type fracture can be reasonably predicted by use of critical values for $(\sigma_{mean}/\sigma_{eff})_{crit}$ [corresponding to Mode I type crack extension] and $(\sigma_{eff})_{crit}$ [corresponding to Mode I type crack growth].

ACKNOWLEDGMENTS

REFERENCES

1. Newman, J. C., Jr., Dawicke, D. S., and Bigelow, C. A.: "Finite Element Analyses and Fracture Simulation in Thin-Sheet Aluminum Alloys," Durability of Metal Aircraft Structures, S. Atluri, C. Harris, A. Hoggard, N. Miller, and S. Sampath, eds., 1992, pp. 167-186.

2. Bakuckas, J. G., Jr. and J. C. Newman, Jr., "Prediction of Stable Tearing of 2024-T3 Aluminum Alloy Using the Crack-Tip Opening Angle Approach, *NASA TM 109023*, 1993.

3. Dawicke, D. S., Sutton, M. A., and Amstutz, B. E.: "Stable Tearing of Thin Sheet 2024-T3 Aluminum Alloy in the L-T and T-L Orientations," *NASA TM 109131*, 1994.

4. Dawicke, D. S. and Sutton, M. A.: "CTOA and Crack-Tunneling Measurements in Thin Sheet 2024-T3 Aluminum Alloy," *Experimental Mechanics,* vol. 34, no. 4, 1994, pp. 357-368.

5. Dawicke, D. S., Sutton, M. A., Newman, J. C., Jr., and B. E. Amstutz: "Influence of Crack History on the Stable Tearing Behavior of a Thin-Sheet Material With Multiple Cracks," *NASA CR 3274*, 1994, pp. 193-213.

6. Han, G., Sutton, M. A., Chao, Y. J., and Lyons, J. S.: "A Study of Crack Blunting and Crack Growth in Thin SEC Specimens of 304 Stainless Steel by Computer Vision," *Engineering Fracture Mechanics*, vol. 52, no. 3, 1995, pp. 525-555.

7. Cordes, J., Chang, A. T., Nelson, N., and Kim, Y.: "Computational Predictive Methods for Fracture and Fatigue," *NASA CR 3274, Part 1*, 1994, pp. 175-192.

8.   Rankin, C. C. and Brogan, F. A.: "The Computational Structural Mechanics Testbed Structural Element Processor ES5: STAGS Shell Element," *NASA CR 4358* , 1991.

9.   Potyondy, D. O., Gray, L. J., and Ingraffea, A. R.: "Simulation of 3D Nonplanar Fatigue Crack Propagation in a Turbine Blade Root," *ASME-PVP-234*, 1992, pp. 31-42.

10.   Hui, C. Y. and Zehnder, A. T.: "A Theory for the Fracture of Thin Plates Subjected to Bending and Twisting Moments," *International Journal of Fracture*, vol. 61, 1993, pp. 211-229.

11.   Potyondy, D. O., Wawrzynek. P. A., and Ingraffea, A. R.: "Discrete Crack Growth Analysis Methodology for Through Cracks in Pressurized Fuselage Structures," *NASA CR 3274, Part 2*, 1994, pp. 193-213.

12.   Amstutz, B. E., Sutton, M. A., and Dawicke, D. S., and Newman, J. C., Jr.: "An Experimental Study of CTOD for Mode I/II Stable Crack Growth in Thin 2024-T3 Aluminum Specimens," *ASTM STP 1256*, 1996, pp. 256-272.

13.   Amstutz, B. E., Sutton, M. A., Dawicke, D. S., and Boone, M. L.: "Effects of Mixed Mode I/II Loading and Grain Orientation on Crack Initiation and Stable Tearing of 2024-T3 Aluminum," *ASTM STP 1296*.

14.   Arcan, M., Hashin, Z., and Voloshin, A.: "A Method to Produce Uniform Plane Stress States with Applications to Fiber-Reinforced Materials," *Experimental Mechanics*, vol. 18, 1978, pp. 141-146.

15.   Sutton, M. A., Bruck, H. A., Chae, T. L., and Turner, J. L.: "Experimental Investigations of Three-Dimensional Effects Near a Crack Tip Using Computer Vision," *International Journal of Fracture*, vol. 53, 1991, pp. 201-228.

16.   Sutton, M. A., Bruck, H. A., and McNeill, S. R.: "Determination of Deformations Using Digital Correlation with the Newton Raphson Method for Partial Differential Corrections," *Experimental Mechanics*, vol. 29, no. 3, 1989, pp. 261-267.

17.   Deng, X. and Newman, J. C., Jr.: "Implementation and Application of a Large-Rotation Finite Element Formulation in NASA Code ZIP2DL," Proceedings of the Symposium on Continued Airworthiness of Aircraft Structures, DOT/FAA/AR-97/2, June 1997.

18.   Newman, J. C., Jr., User Guide for ZIP2D, NASA Langley Research Center, Hampton, VA (modified 4/96).

Figure 1. ARCAN Fixture and Specimen with FEM Mesh.
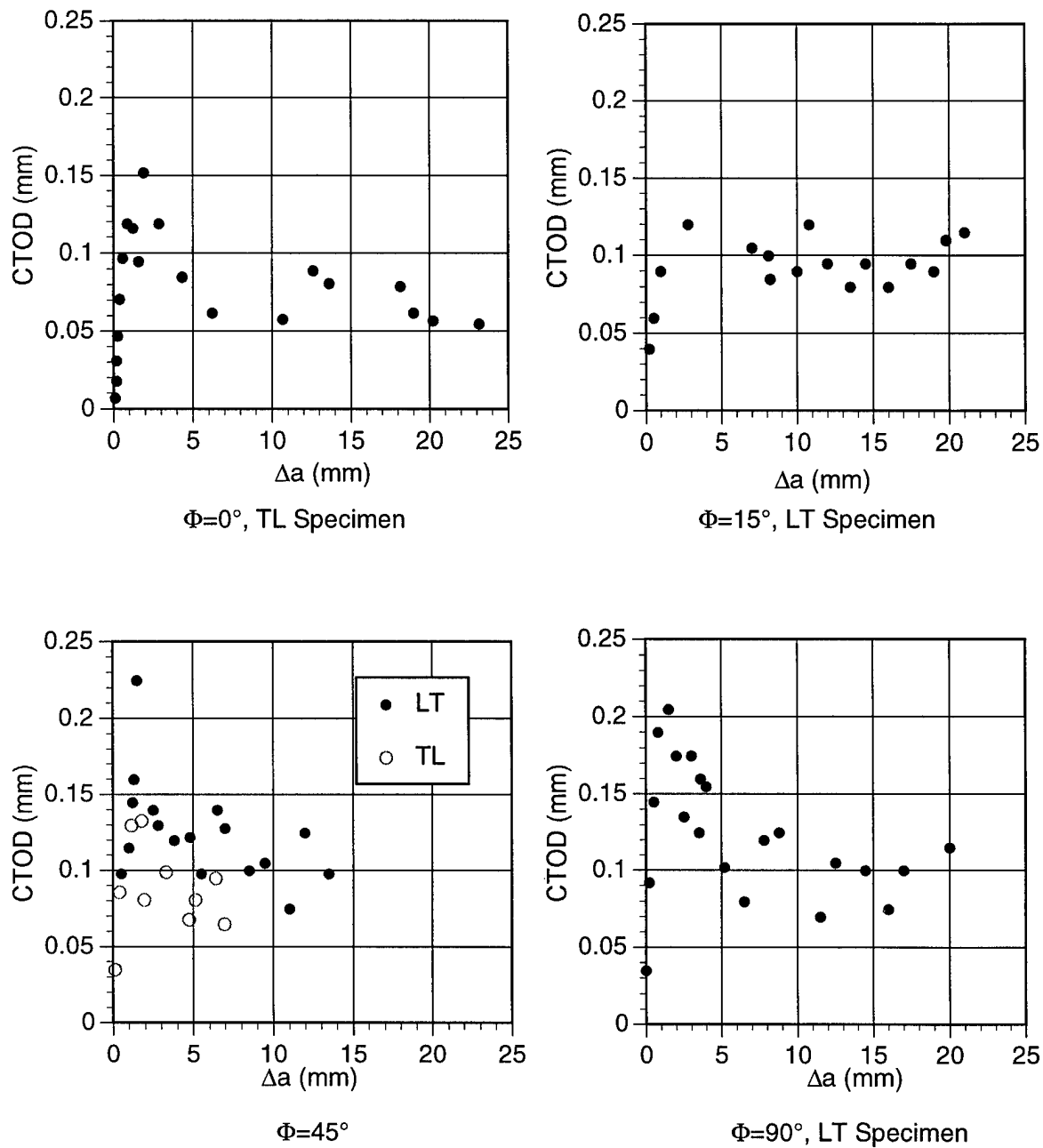
Figure 2. CTOD as a Function of Crack Extension for Various Loading Angles, Φ.

Consolidated Centerline Profiles

Crack Tip at 6.35mm

60°

45°

30°

15°

90°

0°

75°

y (mm)

x (mm)

Al 2024-T3 Specimen

Mode I Fatigue Precrack

Figure 3. Crack Growth Direction as a Function of Loading Angle, Φ.

$\Phi = 0^\circ$
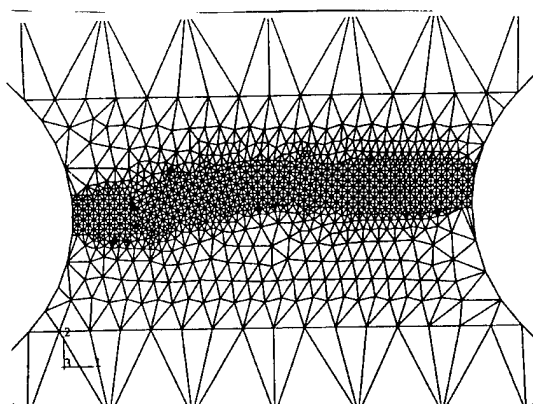
$\Phi = 15^\circ$
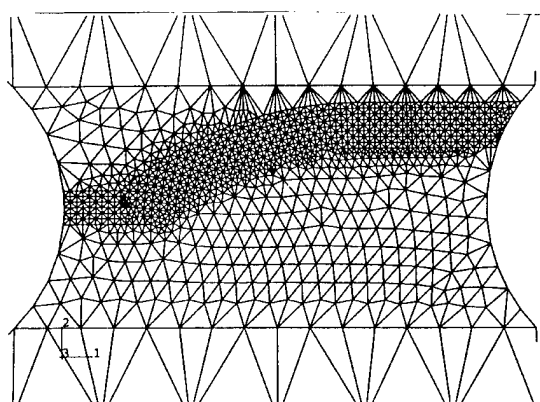
$\Phi = 45^\circ$
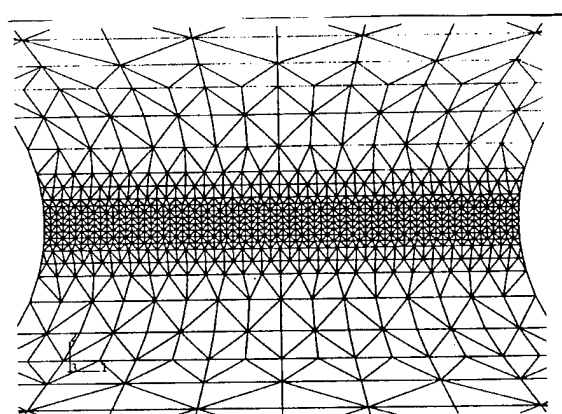
$\Phi = 90^\circ$

Figure 4. Refined FEM Meshes in Crack Growth Region.
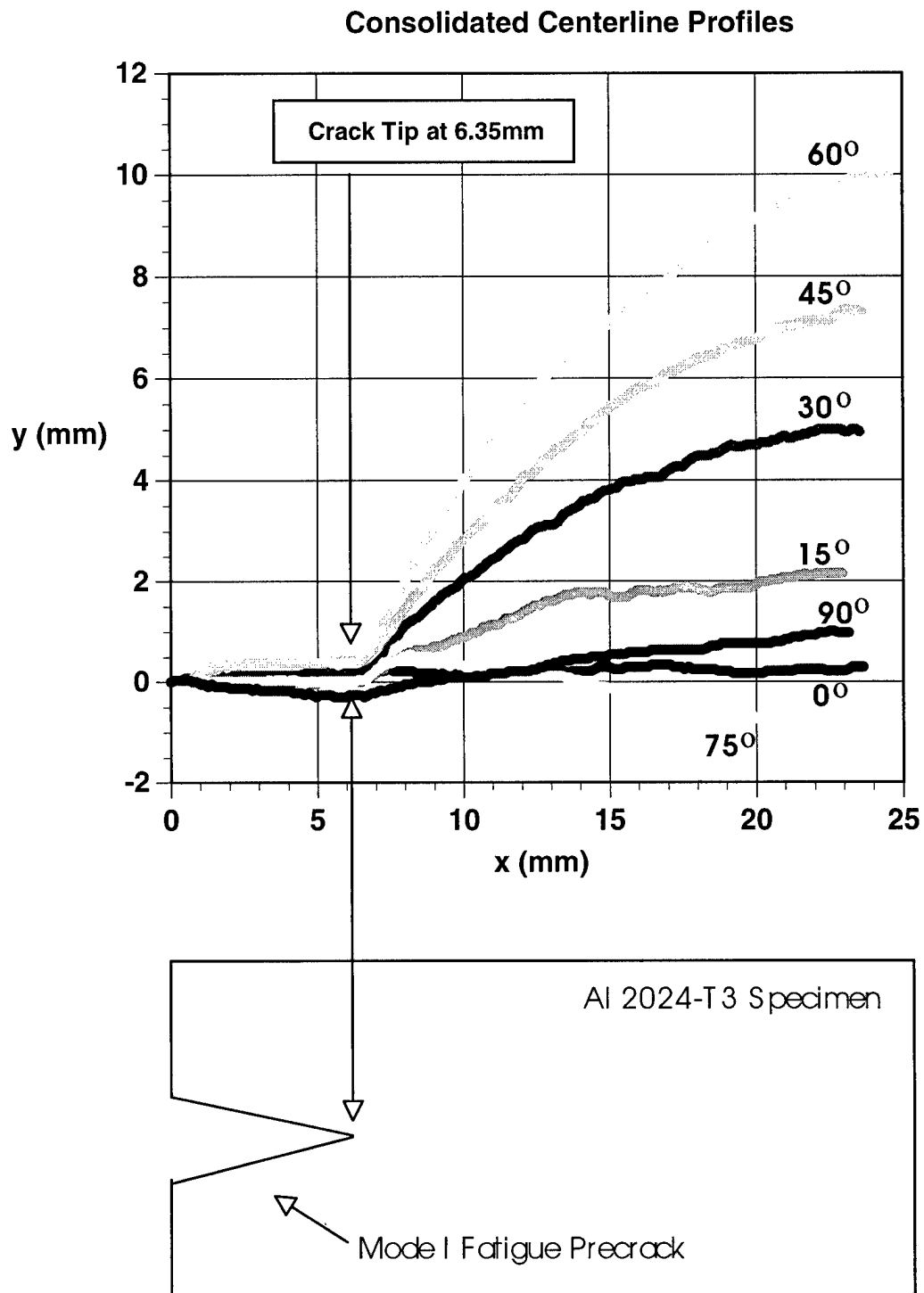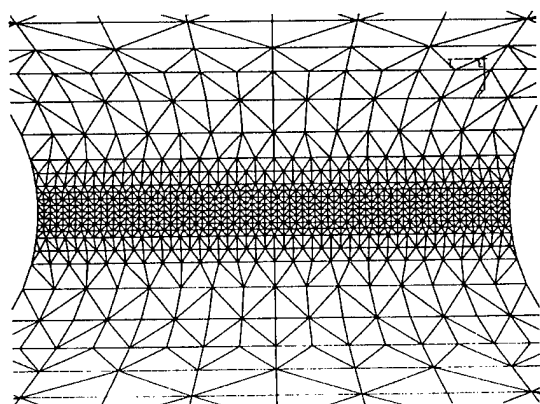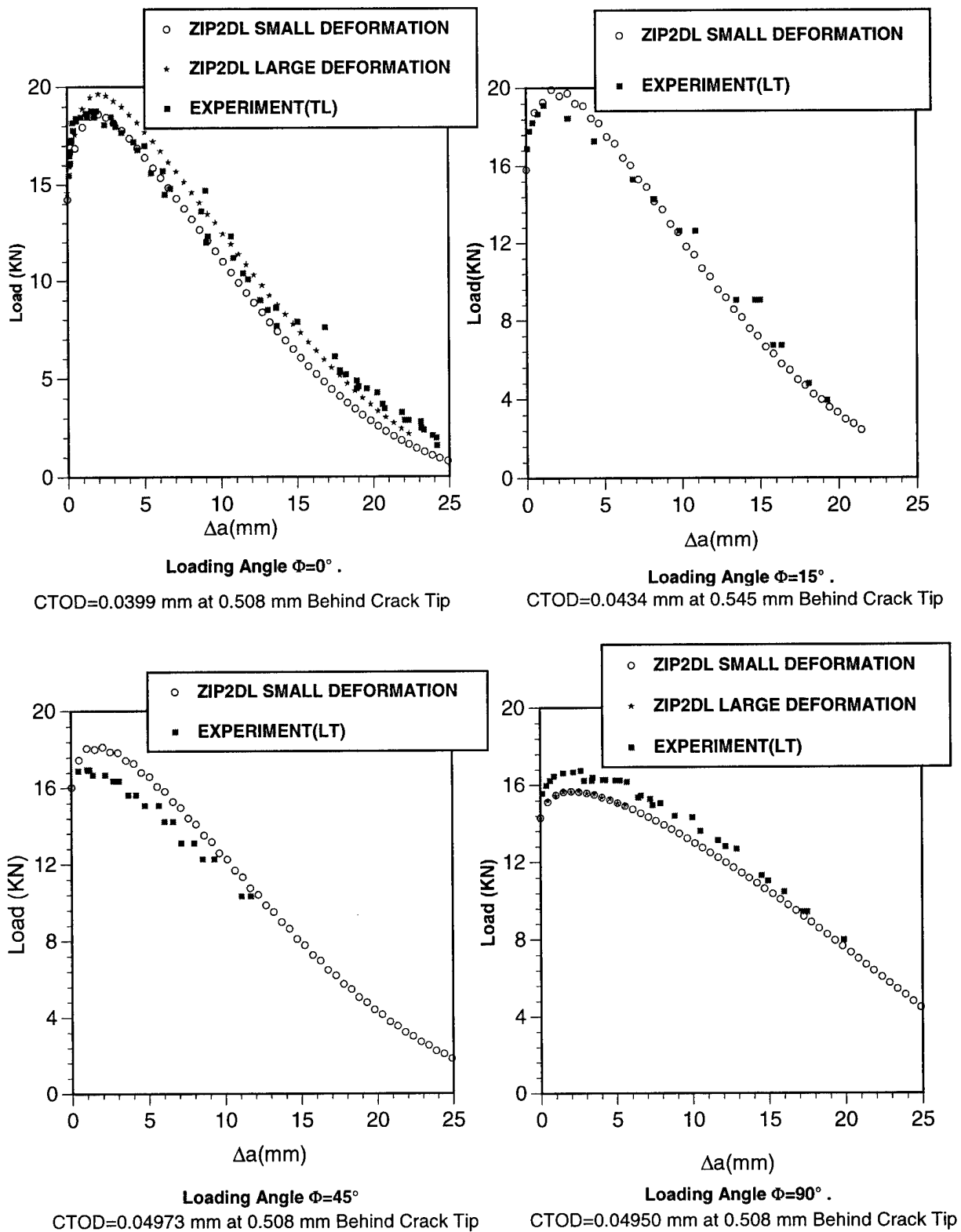
Figure 5. Load Versus Crack Extension for Various Loading Angles Φ.

472

A NUMERICAL STUDY OF THE INTERACTIONS BETWEEN MULTIPLE LONGITUDINAL CRACKS IN A FUSELAGE (MULTIPLE DISCRETE-SOURCE DAMAGES)

W. T. Chow, L. Wang, H. Kawai, and S. N. Atluri
FAA Center of Excellence for
Computational Modeling of Aircraft Structures
Georgia Institute of Technology, Atlanta, GA

SUMMARY

The purpose of this paper is to analyze the residual strength of a pressurized fuselage panel with multiple cracks in the longitudinal direction. Numerical studies based on the global-intermediate-local hierarchical process to model a full-scale fuselage panel have been carried out to understand the interactions of multiple cracks in a stiffened structure. These studies demonstrate the importance of performing an elastic-plastic analysis to obtain a conservative estimate of the residual strength of a fuselage panel. For the example of a two-bay longitudinal crack, the calculated residual strength based on the linear elastic assumption, on an average, is 30% higher than the solution based on the elastic-plastic assumption, and hence the linear elastic solution is anticonservative. In addition, the two-bay crack has been placed at three different locations to examine the effect that the crack location would have on the overall residual strength. It has been found that the residual strength of a two-bay crack existing on top of a stringer is significantly lower than the residual strength of a two-bay crack in a lap joint and that for a two-bay crack between two stringers. A study has been performed to examine the interaction between a two-bay crack and a single-bay crack separated by a frame section. The study found that the interaction between these two cracks is quite small until the crack tips of the two interacting cracks are about 2 inches apart. In addition, studies have also been carried out to understand the effect of multiple smaller cracks in front of a two-bay lead crack. The elastic-plastic analyses have shown that cracks with the size of only 1 inch can reduce the residual strength of the lead crack by half when these cracks are one-half inch apart. Furthermore, it has been found that when the same analyses are performed using the linear elastic assumption, the residual strength would be underestimated by a factor of two. Similar studies are also carried out to examine the effect of the interactions of multiple-site damage (MSD) cracks with the two-bay crack.

INTRODUCTION

For the past two decades, the damage tolerance requirement of a fuselage section has been set as the ability of the stiffened structure to contain a two-bay crack either in the longitudinal or circumferential direction from unstable crack propagation, as shown in

473

Figure 1. This requirement is to ensure the ability of the structure to sustain discrete-source damage induced by a foreign object. However, given that the cost of computing has declined by several orders of magnitude over the past decade, it is now economically feasible to perform numerical analysis of a full-scale pressurized fuselage panel to study not just a single two-bay crack but also the interactions of multiple cracks in a stiffened structures. Furthermore, it is also possible to include nonlinear features such as the elastic-plastic material behavior to accurately calculate the interactions of plastic zones. With the ability to model a full-scale fuselage panel, the effect of location of the two-bay crack can be studied.
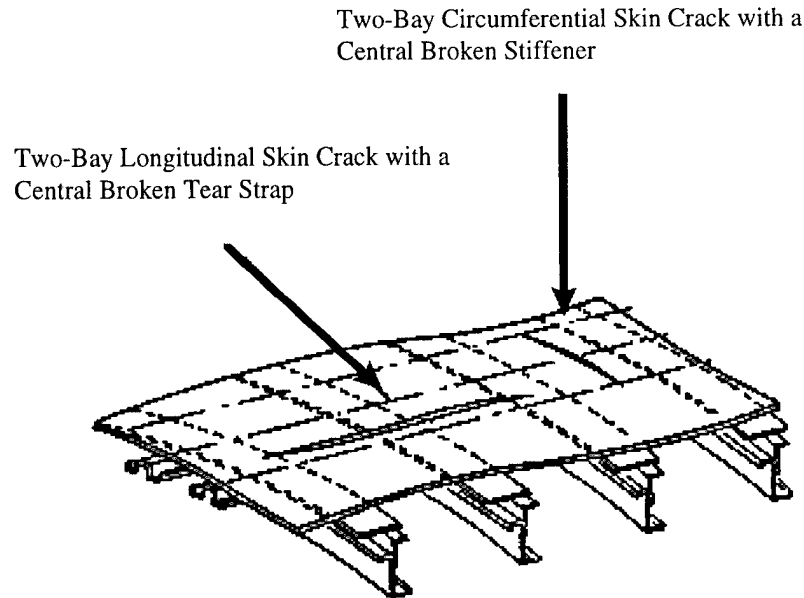
Figure 1. Damage Tolerance Requirement Based on Two-Bay Crack.

Due to the high replacement costs and the increased competition, many of the airplanes in the commercial fleet are used beyond their original design life objective. As a result of high cycles of repeated pressurization, MSD cracks begin to emanate from the rivet holes which may not be detectable. To ensure the structural airworthiness of these aging structures, this paper will study the interaction between these MSD cracks and a two-bay crack in order to determine if the residual strength of the fuselage panel is reduced below the required level. In addition, this paper will also study the interaction of multiple cracks to simulate discrete-source damage induced by fragments in the event of an engine disintegration.

PROBLEM DEFINITION

The fuselage shell panel under consideration is a typical wide-body commercial aircraft. It is stiffened along the longitudinal direction by stringers and in the circumferential direction by frames and tear straps. The tear strap at the center of the two-bay crack is

assumed to be broken. The skins, frames, stringer, and rivets are assumed to be made of aluminum while the tear strap is made of titanium. The overall dimensions of the fuselage are given in Figure 2. The critical stress intensity factor for the aluminum skin is given the value of 90 ksi√in. For elastic-plastic analysis, T* integral is used as the fracture criterion.

Fuselage Radius = 118.5″
Skin Thickness = 0.071″
Frame Spacing = 20″
Stiffener Spacing = 8″

0.025 Ti Tear Strap
Riveted to Skin

1.00″

3.50″
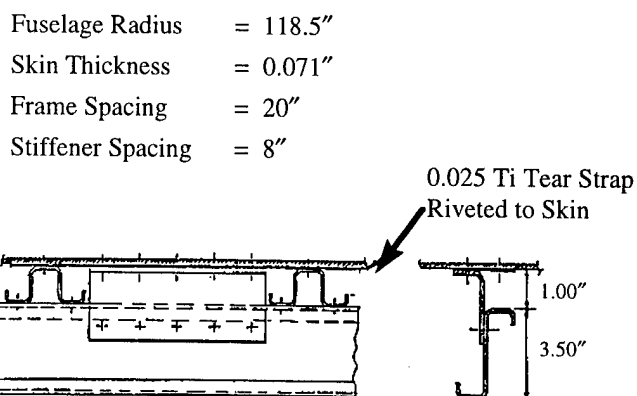
Figure 2. The Geometric Dimensions of the Fuselage Panel.

TWO-BAY CRACK IN THE LONGITUDINAL DIRECTION

In this study, the residual strength of the fuselage panel has been calculated as a function of the lead crack size. Figure 3 shows that the analysis based on the linear-elastic assumption would overestimate the critical pressure by about 30% when compared with the elastic-plastic solution. Therefore, the linear-elastic solution is significantly anti-conservative.

RESIDUAL STRENGTH CURVE
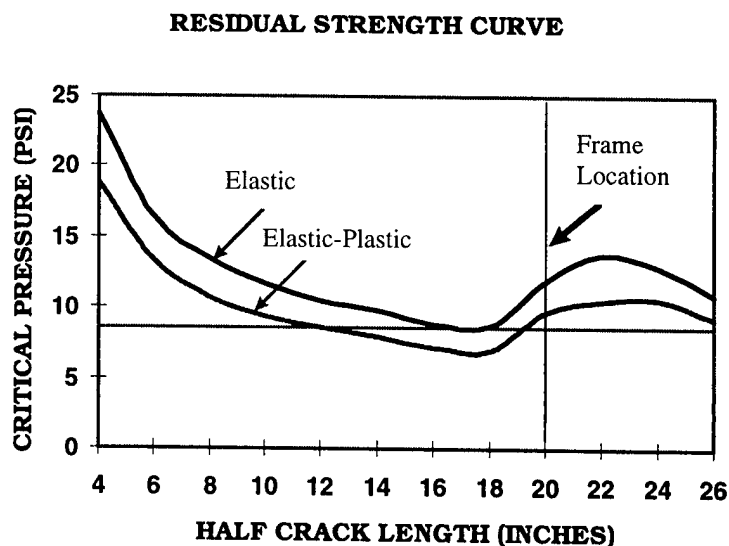
Figure 3. Residual Strength as a Function of Crack Size.

A two-bay crack has been placed at three different locations to examine the effect that the location of the two-bay crack would have on the overall residual strength curve as shown in Figure 4. In case I, the two-bay crack lies in the middle of two stringers; in case II, the two-bay crack lies in the row of fasteners on top of a stringer; and finally in case III, the two-bay crack lies on the top of the fastener row of the upper skin section of a lap joint. It has been found that the residual strength of a two-bay crack for case I is significantly higher than case II and case III as shown in Figure 5. Furthermore, assuming that the operating pressure on the fuselage is 8.6 psi, Figure 5 shows that a two-bay crack for case I would be arrested ahead of the frame while the two-bay crack for case II would not be arrested until the crack tip passes the frame location. The difference in the residual strength for these three locations can be attributed to the design of the frame structure. As can be seen from Figure 6, when the crack lies between two stringers, there is an additional frame clip which constrains the two-bay crack from opening. However, when the crack lies on the stringer or on the lap joint, there is no secondary frame to constrain the crack from opening.

CASE I:
Two-Bay Crack Between Stringers

CASE II:
Two-Bay Crack on the Stringer

CASE III:
Two-Bay Crack on the Lap Joint
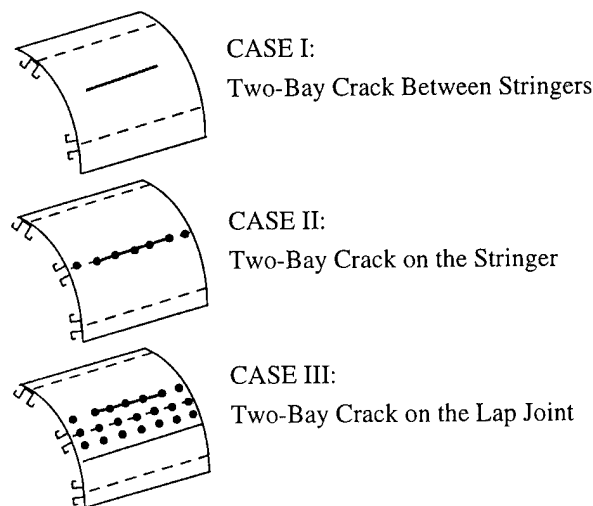
Figure 4. Locations of the Two-Bay Crack.

RESIDUAL STRENGTH CURVE
(ELASTIC-PLASTIC)
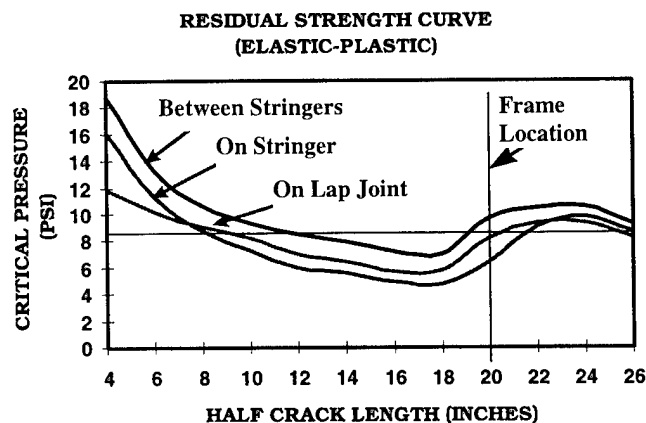
Figure 5. Residual Strength Curve for a Two-Bay Crack at Different Locations.

476
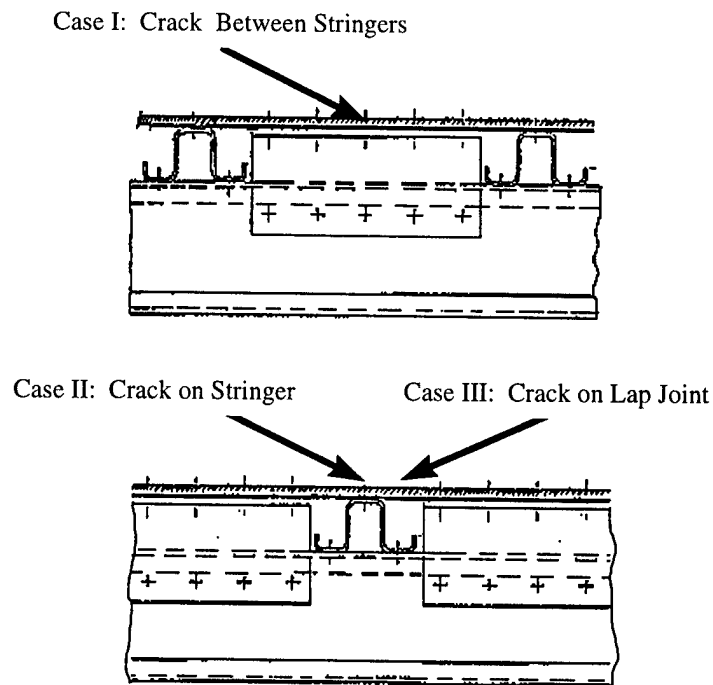
Figure 6. The Effect of Frame Design in the Residual Strength of a Two-Bay Crack.

INTERACTION OF MULTIPLE CRACKS

The first study concerns the interaction of a two-bay crack with a single-bay crack. Both of these cracks lie in the middle between two stringers. The center of the two-bay crack would lie on the frame while the center of the single-bay crack would lie in the middle of the bay. The sizes of these two cracks are varied such that both crack tips have an equal distance, d, to the frame position as shown in Figure 7. The result from Figure 7 shows little interaction between these two cracks when the distance between the two crack tips is more than 4 in. apart even though the size of the lead crack may be as large as 36 in. However, when these two crack tips are only 2 inches apart, the residual strength of the fuselage panel is reduced by more than 20%. The strong interaction between these two cracks can be attributed to the fact that the plastic zones for these two crack tips are interacting with each other.
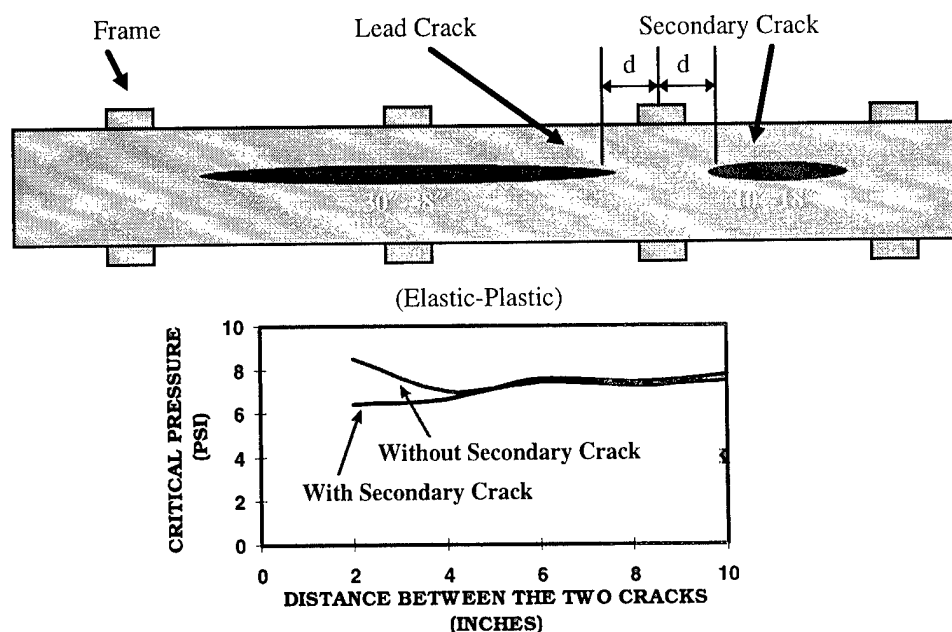
Figure 7. Interaction Between Two Large Cracks.

As shown in Figure 3, the maximum arresting capability of the stiffener occurs when the size of the two-bay crack exceeds the two frame interval. Therefore, to understand how a secondary crack can reduce the maximum arresting capability of the stiffener, the size of the lead crack in this example is chosen to exceed the two-frame interval by 4 in. In this example, the secondary crack is 2 in. ahead of the lead crack and the size of the secondary crack is varied from 2 to 8 inches, as shown in Figure 8. The result shows that the reduction of critical pressure in the presence of the lead crack varies linearly with the size of the secondary crack, from 10% to 30% (based on elastic-plastic analysis). Furthermore, the result also shows that the larger lead crack has more influence on the smaller secondary crack than the influence the smaller secondary crack would have on the lead crack. A comparison between linear elastic and elastic-plastic analysis shows that the linear-elastic solution would significantly underestimate the severity of the interaction between these two cracks.

In the next example, studies have been carried out to examine the extent of the reduction in residual strength due to three smaller cracks in front of the two-bay crack. The elastic-plastic analysis shows that the residual strength of the lead crack is not only influenced by the size of the smaller cracks but more importantly by the distance of these cracks from the lead crack as shown in Figure 9. Furthermore, it has been found that when the same analysis for the 1 in. cracks are performed using the linear-elastic assumption, the residual strength would be underestimated by a factor of two. Similar studies are also carried out to examine the effect of the interactions of MSD cracks with the two-bay crack. The result given in Figure 10 shows that the residual strength of the lead crack would be reduced by 10% when the size of the MSD cracks is 0.2 in. Again in Figure 10, the linear-elastic assumption greatly underestimates the interaction between the lead crack and the MSD cracks.

478
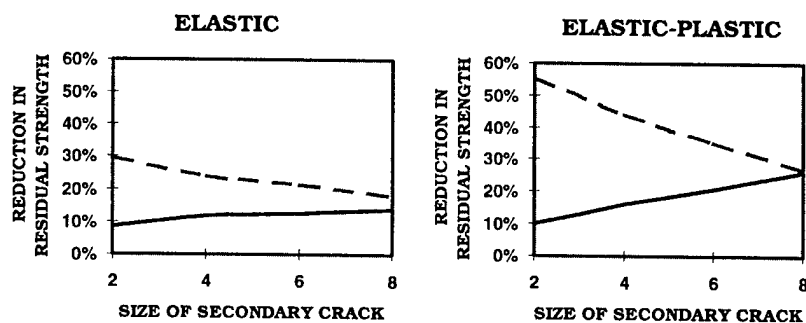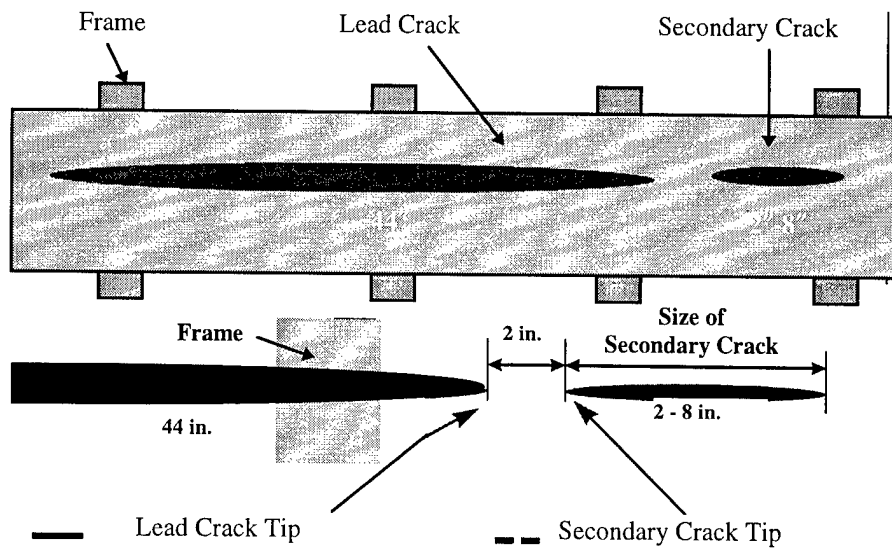
Figure 8. Interaction Between a Lead Crack and a Secondary Crack.
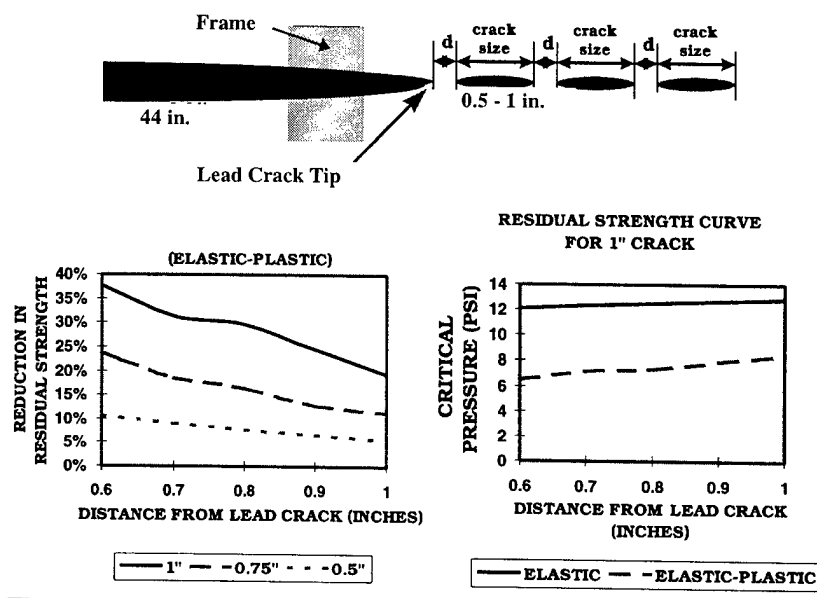
Figure 9. Interaction of a Lead Crack With Three Smaller Cracks.
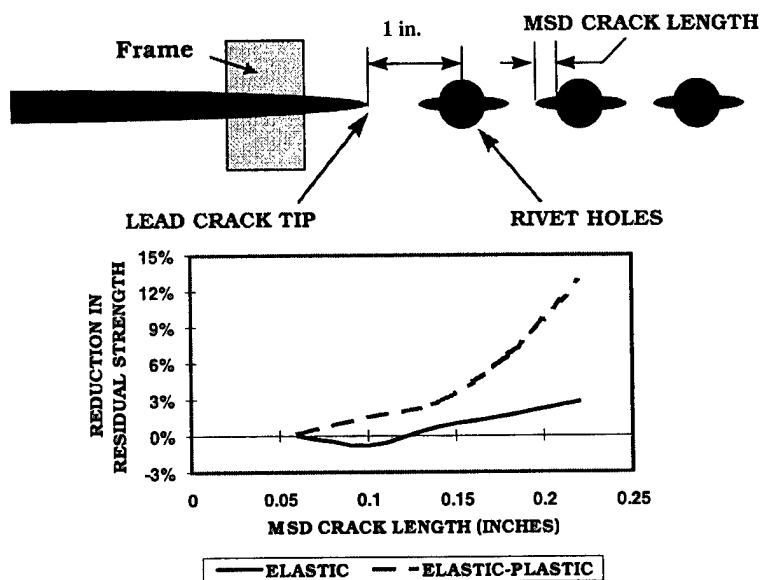
Figure 10. Interaction of a Lead Crack With MSD Cracks.

CONCLUSION

This research has found significant reduction in residual strength when elastic-plastic analysis is performed. Using the elastic-plastic assumption, the effects of the location of the two-bay crack on the residual strength has been studied. In addition, the interaction of multiple cracks including MSD cracks with a two-bay crack has been studied.

ACKNOWLEDGMENTS

ON-AIRCRAFT ANALYSIS OF F-14 AIRCRAFT WING BEARINGS USING ACOUSTIC EMISSION TECHNIQUES*

Donald J. Pointer, W. Drew Martin, and Adriano F. Almeida
Physical Acoustics Corporation
P.O. Box 3135
Princeton, NJ 08543

SUMMARY

Wing pivot bearings on several F-14 aircraft were tested in situ using acoustic emission (AE) before and after rework at the Naval Aviation Depot in Norfolk, VA. Acoustic emission data (mainly due to friction and binding) was recorded during the wing sweep operation while the aircraft were undergoing depot maintenance. The six-month project demonstrated that it is feasible to use AE for detecting friction signals and locating binding within the wing pivot bearings. The acoustic emission method was not only able to find which bearings were binding, but could also locate where the binding was taking place (on the bearing itself).

INTRODUCTION

The wing pivot bearings and the wing box found in variable swept wing designs are vital aircraft components since they must transfer complicated wing forces and moments to the fuselage. These intricate components are difficult to access and presently require the disassembly of the wing in order to service or replace. The limited access to the F-14 wing pivot joint hinders the safety-of-flight maintenance schedule and increases costs as well as maintenance time and total aircraft down time. The Navy's F-14 wing pivot bearings are currently being changed according to a time schedule or when wing sweeping causes excessive noise in the bearing. There are two problems with this method. First, the replacement of the bearing on a periodic schedule is costly, since not all bearings are faulty. Second, some wing pivot bearings fail before the scheduled replacement time. These faulty bearings on operating aircraft could bind, thus causing structural problems to the surrounding wing or box beam. If a failure of this type should occur, both the pilot and aircraft would be at risk.

The goal of the Phase I contract was to prove the feasibility of using acoustic emission techniques to determine bearing condition and locate problem bearings. The long term goals are stated below:

- To develop a nonintrusive, in situ method of inspection

- To obtain insight into the bearing's fitness for service through the wing sweep operation
- To develop a method that requires no disassembly of the aircraft
- To develop a low cost, rapid test technique that can be performed on regular intervals
- To develop a method that permits the scheduling of aircraft for depot maintenance on an empirical (as needed) basis

PROCEDURE

There are four wing pivot bearings per aircraft consisting of an upper and lower bearing for each wing. Figure 1 shows a cross section of the wing pivot bearing assembly from one side of the aircraft. The bearing consists of the "ball" portion and the "ring" portion where the inner and outer surfaces are the actual races. Access to the wing pivot bearings is gained by removing the necessary access panels surrounding the bearings.

Each bearing was instrumented with three sensors arranged in a triangle that surrounded the circular bearing. The wings were swept several times to their fore and aft positions while the AE data was processed and recorded to disk along with an output signal proportional to the position of the wing. This was done by feeding the voltage from the aircraft's on-board computer into the SPARTAN acoustic emission acquisition system. Three methods of data analysis were used to correlate the AE data with pivot bearing condition before and after rework. The first method was based on the overall amount of acoustic activity received. The second method was based on source location techniques using triangulation methods. The third method involved using pattern recognition techniques to discriminate between data from old and the newly replaced bearings.
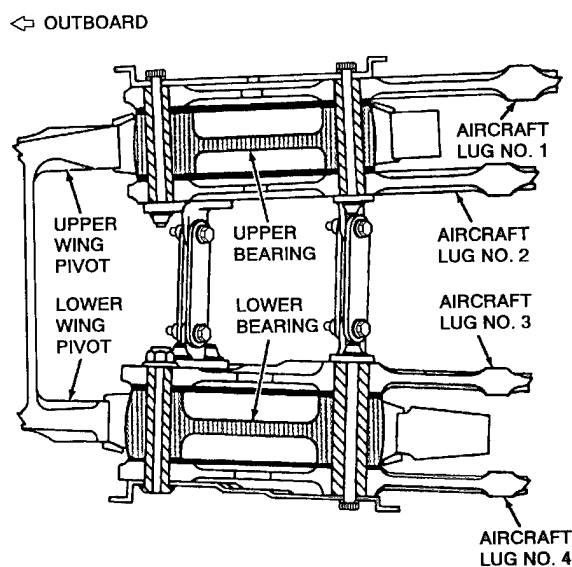
Figure 1. Cross Section of the Wing Pivot Bearing Assembly.

RESULTS

The overall reduction of acoustic emission data obtained after the wing bearing rework was on average 55%. Figure 2 is a typical plot of raw AE data (Hits) vs. Time (sec), with the wing sweep angle superimposed (before rework).
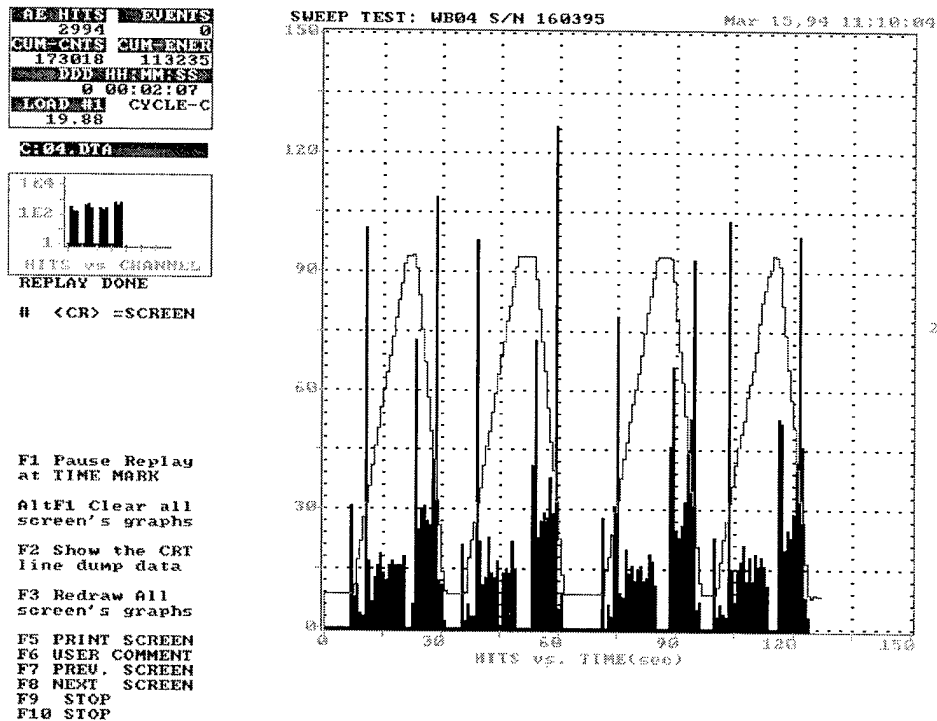
Figure 2. A Typical Plot of Raw AE Data (Hits) vs. Time (Sec), With the Wing Sweep Angle Superimposed (Before Rework).

The main point of interest in this figure is the repeatability between acoustic emission activity and wing sweep angle, that is, the bearing shows the same acoustic behavior during each wing sweep cycle. The raw data from the same bearing after rework is similar to Figure 2 with the exception of having about half as much activity.

The ability to locate acoustic emission sources within the wing pivot bearing proved to be the best indicator of severe binding. The severe binding problem is easily detected, since it produces high-amplitude signals that are very repeatable during the wing sweep operation. The 3-dimensional graph in Figure 3a indicates the location where the binding was taking place on the wing pivot bearing. Figure 3b shows the same bearing after rework.

LOWER BEARING - PORT SIDE
BEFORE REWORK

3a. Location Where the Binding Was Taking Place on the Wing Pivot Bearing.

LOWER BEARING - PORT SIDE
AFTER REWORK
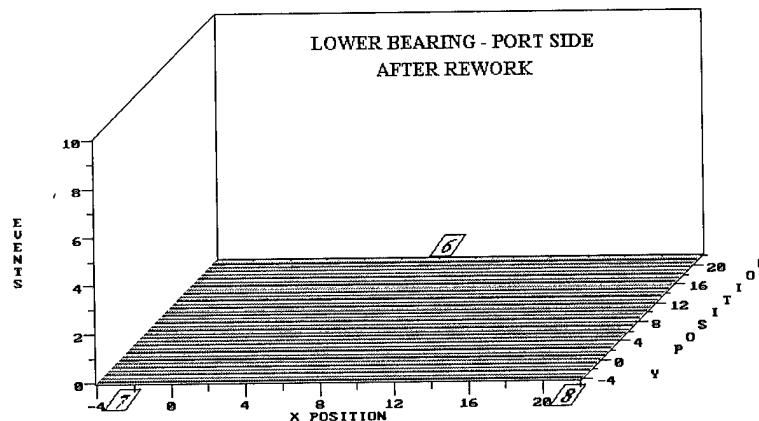
Figure 3b. Lower Bearing—Port Side After Rework.

Pattern recognition analysis was performed after the contract expired to ascertain if the amount of equipment could be reduced from three sensors per bearing to one. Through a statistical analysis of the five main signal features (counts, risetime, amplitude, duration, and energy) the data collected from a single bearing before and after rework was characterized and used to create a classifier for the application to all bearings. Figure 4a is a 2-D Fisher Pairwise projection which shows how the data collected before rework is separated using the classifier. Each "B" represents an acoustic hit which classified as baseline and each "F" represents hits classified as faults. Figure 4b shows how the data collected after rework is classified. Notice how many fewer hits are classified as faulty (F) after the bearing rework. The number of

signals classified as faulty for the before rework condition was 233. The number of signals that were classified as faulty for the after rework condition was 6. This shows that the classifier successfully distinguishes between "good" and "bad" bearings but also suggests that some minor binding is taking place in a reworked bearing. This condition will be explored further during additional work on this project. Also, this technique gives the indication that only one sensor per bearing is needed, thus saving weight and minimizing equipment requirements, however, the ability to locate binding on the bearing would be sacrificed.
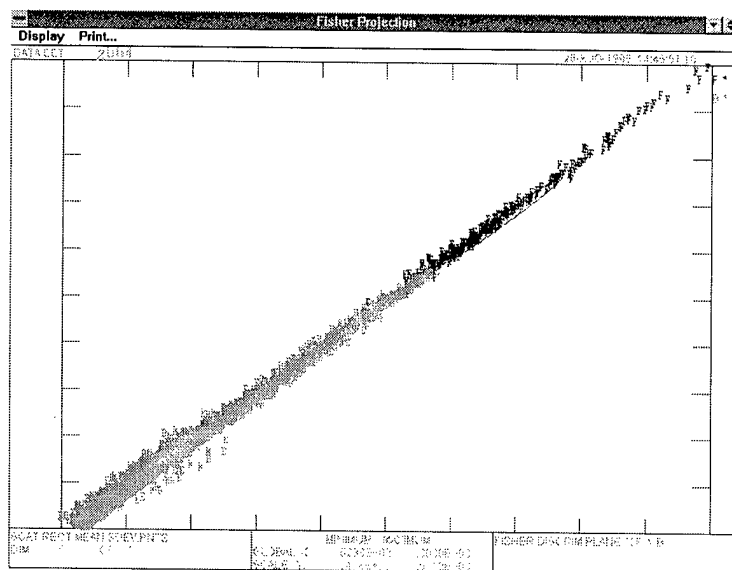
Figure 4a. Two-Dimensional Fisher Pairwise Projection Which Shows How the Data Collected Before Rework Is Separated Using the Classifier.
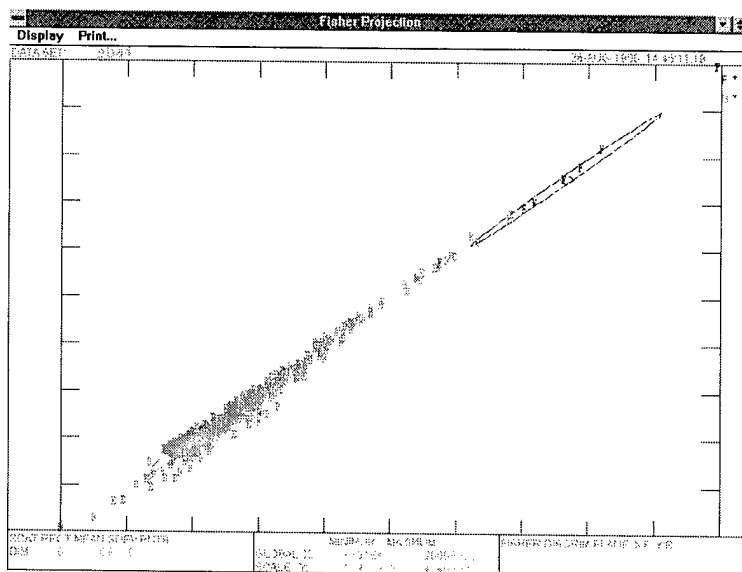
Figure 4b. Two-Dimensional Fisher Pairwise Projection Showing How the Data Collected After Rework Is Classified.

485

CONCLUSIONS

1.   The feasibility of using acoustic emission nondestructive testing methods has been established for the in situ inspection of Navy F-14 aircraft wing pivot bearings.

2.   There is a substantial reduction in the amount of acoustic emission activity after rework.

3.   Severe binding in two bearings was detected and located using the acoustic emission approach.

4.   The application of signal pattern recognition analysis techniques shows promise in reducing the amount of instrumentation and weight for an in-flight bearing monitor.

OPERATOR CONCERNS ABOUT WIDESPREAD FATIGUE DAMAGE AND HOW IT MAY BE HANDLED AND REGULATED IN THE COMMERCIAL ENVIRONMENT

David V. Finch
Consultant
Windsor, SL4 5ER, England

SUMMARY

The paper compares the theory and practice of aircraft structural maintenance and inspection in the current damage tolerant regime and how this may need to change in the presence of widespread fatigue damage. Aspects considered include the regulatory role, operator feedback, maintenance program development and whether widespread fatigue damage (WFD) means a return to safe life. Particular reference is made to the need for advice, support and training which is the principle professional interest of the author.

DEFINITIONS

Words and phrases printed in **bold italic type** are defined in Appendix C - Glossary. When subsequently used in the text these words and others having a specific meaning in aviation are printed in *italics*.

INTRODUCTION

Fail-safe and *damage tolerant* design together with inspections of appropriate frequency and focus have successfully safeguarded the structural integrity of public transport aircraft over the last 28 years. Models certified during this time and earlier have been subject to extensive structural analysis and testing leading to the specification of *directed inspections* searching for the initial indications of fatigue damage. Fatigue cracking in service, however, has frequently differed from that predicted by test or analysis [Ref. 1] and potentially catastrophic conditions have not always been found by scheduled inspection. In some instances *failure* has only been evident at a very advanced stage through malfunction or by chance observation.

Some of these failures have resulted from *multiple-site damage* (MSD) and *multiple element damage* (MED) [See Figure 1]. The Manufacturing and regulatory sectors of the industry have been aware of these phenomena for many years [Ref. 2] and of the limited

ability of the *fail-safe* features built into current designs to contain widely distributed cracking [Ref. 3].

Damage tolerance rules require consideration of damage at multiple sites [see FAR/JAR 25.571(b)] but *widespread fatigue damage* (WFD) reduces the probability that critical conditions will be found during routine work or will be revealed, prior to complete failure, by obvious and safe malfunction.

The potential immediacy of *WFD* is shown by the summary of service and fatigue test data for the 11 models overseen by the *Airworthiness Assurance Working Group (AAWG)* [see Appendix B]. Many other tests and inspections including the teardown of aircraft retired from service have been carried out to substantiate freedom from *WFD* but the table does indicate that some aircraft, those with the highest number of flight cycles relative to the service life objectives and full-scale fatigue test experience, are entering the phase where *WFD* may be present.

All the major manufacturers are evaluating their aircraft for *WFD* in the critical areas of the wing, empenage, and pressure fuselage i.a.w. guidelines provided through the Aviation Rulemaking Advisory Committee (ARAC) and the AAWG [Refs. 1 and 4]. Where *WFD* is forecast, more frequent and more intensive inspections, modifications, or life limits may be required. There may be additional criteria for repair and further constraints on maintenance program development.

Operators need to be aware that, for some of the oldest aircraft, the days of "Tolerance to Damage" and "Unlimited Life" may be numbered. This paper considers the contribution that airlines can make to the orderly and economic management of the *WFD* phenomena.

DAMAGE TOLERANT INSPECTION

Figure 2 shows how a structural item may be weakened by the combined effects of fatigue and other damage until final failure occurs at "F."

"M" is the minimum detectable flaw size
Ultimate strength is lost at "U."
At "L" the item can no longer support *Limit Load.*

To meet *damage tolerance* rules *failure* must be detected prior to "L." Area "MXL" represents a combination of defect size and time available for detection and may be regarded as the window for *damage tolerant* inspection.

To ensure adequate opportunity to detect deterioration *fail-safe* features, frames, stringers, and doublers are incorporated to arrest crack growth and to extend the inspection window. Compare MX_1L_1 and MX_2L_2 in Figure 3.

The inspection program that can then be applied is illustrated in Figure 4.

When a problem or potential problem has been identified, **Detail** or **Special Detail** inspections can be specified in which the **Inspector's** attention is *directed* very precisely to the subject feature. *Special detail* inspections may be used to find very small and inaccessible flaws but their area of search is limited and techniques must be tailored to the particular form of the potential defect. It is neither economic nor practical to survey the whole aircraft in this way.

General visual inspections cannot be expected to find small defects but serve to identify problems that, once known, may be more effectively controlled by *detail* or *special detail* inspections or **terminated** by modification.

In the figure the vertical distance between design strength and the horizontal bars representing the inspection levels indicates the minimum defect size that can be detected. The position and spacing of the vertical bars indicates the timing and frequency of inspection.

- Inspections which can detect deterioration before final failure are shown in solid black. The probability of damage detection increases with the vertical length of the solid bar.

- Inspections which are unlikely to find a defect because they are performed either too early or too late are shown by a shaded vertical bar.

If deterioration is not found by inspection then the *fail-safe* features of the design may well ensure that the structure continues to carry the applied loads until the condition becomes apparent during servicing or preflight checks or is revealed by malfunction, typically by fuel leaks from the wing or difficulty in pressurizing the fuselage.

The fact that serious structural defects have been found and, on occasion, continue to be found in this way on aircraft operated by some of the most sophisticated airlines in the world indicates that:

- *Damage tolerant* standards, as currently interpreted, are not over generous.

The fact, also, that these events now very rarely feature in the accident statistics shows:

- The importance of *Fail-safe*.

INSPECTION WITH WFD

Figure 5 illustrates the classic case of cracking in the longitudinal joints of a fuselage skin when *multiple site damage* is present and widespread:

- For both *detail* and *general* inspections the total crack length at detection is the sum of all the adjacent individual cracks; i.e., there can be a significant reduction in residual strength prior to detection.

- If *MSD* is sufficiently invasive, then, regardless of whether frames and doublers are intact, there is little to prevent the formation of a continuous multiple bay crack.

The effects are shown in Figure 6.

- The inspection window, if it still exists at all, is now much smaller than before. Cf. Figure 4.

- The possibility that catastrophic failure will be averted by evident damage prior to departure or by safe malfunction is greatly diminished. The *fail-safe* features are ineffective and deterioration through crack coalescence can be precipitously steep.

If Figure 6 comes close to representing the situation with *WFD* it would be difficult to claim that *damage tolerant* criteria per FAR/JAR 25.571 can be satisfied. The alternative is *safe life*.

SAFE LIFE

Figure 7 illustrates both the principle and the inherent weakness of the *safe life* philosophy.

Safe life attempts to control condition (strength) on the vertical scale by limiting life (flight cycles) along the horizontal scale and assumes a known relationship between these parameters.

Catherine Bigelow, speaking to the Sixth FAA-NASA International Conference on the Continued Airworthiness of Aircraft Structures [Ref. 5], listed 12 areas of uncertainty in the prediction of *WFD*.

Accidental damage incurred during manufacture or installation, a variable not specifically mentioned by Catherine, led to the failure of a Viscount wing spar over Western Australia after 8,090 flights [Ref. 6]. The approved *safe life* was 11,400 flights. Though the accident occurred nearly 28 years ago it still provides a classic illustration of the vulnerability of the *safe life* concept.

Testing and analytical techniques have improved immeasurably since 1968 and are still being developed. Some 28 of the papers presented at this Symposium are, by the author's estimation, concerned with fatigue life prediction or risk analysis.

- Is it now possible, by these methods alone, to resolve the uncertainties and to establish *safe* lives which will offer protection against *WFD* and also satisfy reasonable economic criteria?

- Do the manufacturers and regulatory authorities wish to take responsibility for setting inspection thresholds and/or life limits without the fullest possible reference to service experience?

- Do operators wish to participate in a managed approach to the identification of *WFD* and, if so, do they understand the task and are they prepared for it?

OPERATOR ATTITUDES

A problem in the past may have been that *damage tolerant* designs were too good. Serviceability was excellent, major incidents were few, complacency was not penalized, and it seemed that the aircraft structure could be left to look after itself.

In 1988 Boeing Maintenance Survey Teams which at that time had visited 44 operators over all five continents and witnessed major maintenance on 80 high-time aircraft, had to report that:

- Maintenance programs generally did not recognize the significance of aircraft age

- A few aircraft had improper modifications or repairs and some required extensive repairs for corrosion

- The condition of some aircraft reflected a reduction in operator's *engineering* and maintenance staffs [Ref. 7].

Contemporary comments by McDonnell Douglas support teams were broadly similar, adding that:

- Maintenance standards were generally below expectation, some below fail safe requirements [Ref. 4].

Have things changed in the post-Aloha world? Boeing and McDonnell Douglas report that it has. Both have continued their surveys and the total Boeing study now includes 97 operators and 190 aircraft. Both now comment to the effect that:

- Airlines are doing a better job in maintaining their aircraft and have an increased awareness of structural issues and sound maintenance practices.

Indeed, it would be remarkable if it were otherwise given all the aging aircraft activity of the past 8 years.

How can this awareness be sustained and enhanced to permit a successful managed approach to the problem of WFD - assuming that airlines do wish to participate in this activity?

DEVELOPMENT IN SERVICE

Figure 8 provides a further illustration of the current *damage tolerant* approach in which a minimum standard of structural strength is maintained directly by inspection.

A rising incidence of in-service defect findings will indicate the need for enhanced inspection or *termination* at some level "R" determined by the economic penalty or risk to *airworthiness* of continuing with inspection and repair. In a well managed program the operator will evaluate the data and use his judgment to initiate such action though the regulator may intervene on safety grounds.

The process had been likened to "Listening and responding to what the aircraft is telling you."

Though it eliminates many of the uncertainties associated with the control of *airworthiness* by *safe life, damage tolerant* inspection is crucially dependent on the standards of the operator and the performance of his inspection staff - with all their human and organizational frailties.

It is therefore appropriate to consider the role, status, and training of the *inspector* and the ethos of the organization in which he or she works.

INSPECTION

The inspection task may be expressed as: The examination of an item, assembly, or system for condition or functioning in conformity to a defined standard.

While this may be true for *directed inspections* aimed at well defined problems it is a gross oversimplification of the observations and judgments made by an *inspector* performing the more general inspections which are most likely to reveal new or unquantified defects.

Figure 9 illustrates the nature of the decisions that the *inspector* has to take [see also Figure 3]:

- Is *ultimate* strength or functional capability retained? (i.e., Conditions 1.→3. or Condition 4.)

- How rapid is the rate of deterioration and when must rectification be implemented?

- Does this represent a potentially hazardous condition which should be reported?

Inspectors generally understand and accept their responsibility for immediate *airworthiness* and perform this role conscientiously and well, taking appropriate account of operational demands and practical constraints. The task and responsibility reflect their experience and culture and it is to this end that training has been largely directed. They are less familiar with the more strategic role in which the aircraft may be regarded as a flying test article and they are part of a research team dedicated to extracting optimum performance.

Figure 10 illustrates how the system should work concentrating on the role of the *inspector* and the factors that shape his or her performance.

IDENTIFICATION OF WFD

Deficiencies in the system are relatively benign within the *damage tolerant* envelope. If an operator fails to recognize and evaluate a problem the inspection/maintenance program will not be as well tuned as it could be but *airworthiness* is not immediately at risk. For the reasons outlined in Section 3 the whole process is much more critical in the presence of *WFD* and a proper understanding of the operator's investigative role is essential if service experience is to be applied successfully to the determination of *WFD* maintenance policy.

The objective, illustrated in Figure 11, is:

- To position the *safe life* barrier as far, but no further, to the left than necessary to ensure that the risk "R" of catastrophic failure through *WFD* is extremely small.

- To determine what additional inspections "B" and/or other maintenance requirements are necessary to ensure safe operation prior to the imposition of a life limit.

The task of the *inspector* and the whole of the operator's research team is to **recognize** and **report** the **first indications** of *MSD/MED* and to **investigate** whether this is *widespread.*

Figure 1 provides an example of this task and the possible impact on a maintenance check.

The Figure shows cracks in three adjacent stringer end fittings. The aircraft could be repaired and returned to service simply by replacing the fittings but such *MED*, if *widespread*, could be potentially catastrophic.

Operator Action - Recognize the condition and report findings. Check other aircraft on maintenance and report on the condition of similar fittings, where accessible.

Possible Consequences - A *Telegraphic* AD to inspect fittings on all high-cycle aircraft. A *life limit* on fittings if integrity cannot be maintained by inspection.

A further example featuring *MSD* is given in the Repair Case Study (Appendix A).

INFORMATION, TRAINING AND TECHNICAL SUPPORT

It has been claimed that very few people in the industry understand the *WFD* condition [Ref. 3] and if this is the case there is a need for innovation and training at all levels to ensure commitment to, and proper implementation of, a participatory program as outlined in the previous section.

Advice is available to customers from the manufacturers. For example:

- Boeing offers structural integrity awareness material and training for engineers in repair design, provide integrated maintenance programs for aging aircraft, and also host structural conferences around the world.

- McDonnell Douglas offers aging aircraft program training to operators [Ref. 4].

Other opportunities include *Structures Task Group* (STG) meetings to which Lockheed Martin, for example, invites all L-1011 operators.

These initiatives are well supported but attendance is voluntary and the message does not necessarily reach to the executive level at which airline maintenance policy is determined or to those who work on the shop floor.

The recognition and assessment of structural deterioration is only one of many aspects in the requirements for the licensing and approval of aircraft *inspectors* and only one of many tasks that he or she may be required to undertake. The appropriate interpretation and action in the case of some findings may therefore be beyond the scope of the *inspector* and enter the realm of the structural *engineer*. It follows that a structural engineer should be available to advise and direct this activity, but it is the *inspector* who comes face to face with the aircraft and who must appreciate the need to alert the *engineer* to a potentially dangerous condition.

Some specific training for *inspectors* engaged in the maintenance of elderly aircraft, possibly in the form of a workshop in which experience can be shared, is therefore indicated.

Material for such workshops has been developed by the author, some of which is shown in the figures used to illustrate this paper.

Ad hoc attempts to develop and correlate inspection skills have also been made by some operators in the United States but such initiatives do not, as yet, form a part of any required training curriculum.

THE ROLE OF DIRECTIVES

Although the inflexibility of directives make them unsuited to the investigative work as described in the paragraphs on DEVELOPMENT IN SERVICE and IDENTIFICATION OF WFD directives do have a role:

- They ensure attention to known problems.

- They can raise awareness. The improved standards noted by McDonnell Douglas and Boeing can, in part, be attributed to the mandating of programs such as the corrosion prevention and control programs *(CPCP)*.

A proliferation of ADs can also encourage the perception that anything critical to *airworthiness* will be so covered. In discussing the regulation of aircraft structural maintenance programs, David Lotterer (ATA), playing devil's advocate, [Ref. 8] expressed this belief in the question:

> "If, from a business perspective, the FAA ACOs and the AD process will take care of your *airworthiness* issues, why do you need all those structures engineers at the airlines?"

Clearly, this approach is the very antithesis of that required for the identification and appropriate reporting of *MSD/MED* in service as discussed in this paper [See IDENTIFICATION OF WFD].

THE COMMERCIAL ENVIRONMENT

It would be unwise to assume that the favorable trends noted by Boeing and McDonnell Douglas will continue without some regulatory incentives. Avowals of "Safety is Paramount" notwithstanding, airlines and airline maintenance management will be driven, in

an increasingly competitive environment, by the most tangible of economic and legal criteria, i.e.,

- Budgets
- On time delivery
- Operational reliability
- Compliance with legislation

Maintenance will increasingly be contracted to facilities offering the lowest costs and the shortest, guaranteed delivery times. The quality of work may not be inferior but the economic imperatives and potential reduction in technical continuity are unlikely to be favorable to an understanding and the effective reporting of *WFD*.

Though highly resistant to accepting conservative *safe lives* or the early imposition of extensive and frequent special inspections [Ref. 9], operators may yet fail to fully embrace the participatory and investigative role and organizational commitment outlined in the paragraphs on IDENTIFICATION OF WFD and INFORMATION, TRAINING AND TECHNICAL SUPPORT unless this is supported by some legislation.

THE WAY AHEAD

The key to progress may lie in the words of John Chaplin, former Head of the CAA Airworthiness Division. Speaking at the Royal Aeronautical Society in London in 1980 he said:

"*Airworthiness* cannot be achieved by regulation (alone). Regulation can establish a framework within which all who are concerned with the design, construction, and operation of aircraft can work and can set boundaries of responsible behavior."

For the approval of organizations for structural work on aging aircraft it may be appropriate to require enhanced standards of management, organization, and technical oversight. For example:

- Production engineering staff to translate operating rules, Ads, and manufacturer's programs and bulletins into practical working instructions and control documents for use on the shop floor.

- Qualified technical or *engineering* staff who are familiar with the principles of structural *airworthiness* including the possible interaction of accidental, environmental, and fatigue damage, and who understand the requirements for corrosion control and the critical nature of *WFD*.

- Inspection and maintenance staff who have received general and model specific training in structural inspection practices and techniques, defect investigation and reporting, and have practical experience of structural inspection with an approved organization.

- Facilities, equipment, and resources necessary for the effective inspection of critical features of the aircraft structure.

- Effective reporting channels to the manufacturer and appropriate regulatory authority, functioning to their satisfaction.

- Maintenance contracts that provide for structural abnormalities to be effectively investigated, whether or not such work is originally scheduled.

- Quality oversight to ensure that the *airworthiness* intentions of these provisions are being achieved.

The above list is not exhaustive but does indicate the type of approach which may be effective in ensuring the proper detection, investigations, and reporting of *WFD* and other structural abnormalities of potential *airworthiness* concern.

Some may argue that all these good things are required and happen already. If that is true then we do not have a problem. If there are deficiencies, the authorities, manufacturers, and operators alike may wish to consider the case as outlined in this paper for some legal reinforcement to the three legged stool and to responsible behavior.

Such action would present no difficulty to many *engineering* and maintenance organizations as currently established. Others may have to upgrade if they wish to meet the criteria and to undertake structural work on aging airplanes.

CONCLUSIONS

1) Despite extensive fatigue testing, tear down evaluations, and the sophisticated analytical techniques now used by the manufacturers, service experience still provides the first and most reliable indication of many structural problems and potentially catastrophic failures.

2) *Widespread fatigue damage* significantly reduces the opportunity to safely detect damage by inspection or general alertness and the probability that a malfunction will be safe.

3) Operation to the threshold of the *WFD* regime demands a heightened awareness by maintenance and engineering managers of the principles underlying structural *airworthiness* and may require specific training for inspection and maintenance staff.

4) Additional maintenance approval requirements may be necessary for the safe operation and maintenance of aircraft susceptible to *WFD*.

REFERENCES

1. Hidano, Lance A. and Goranson, Ulf G.: Inspection Programs for Damage Tolerance—Meeting the Regulatory Challenge. Proceedings of the FAA-NASA Sixth International Conference on Continued Airworthiness of Aircraft Structures, DOT/FAA/AR-95/86, December 1995.

2. Maxwell, R. D. J.: RAE Farnborough, Fail Safe Philosophy: An Introduction to the Symposium. 7th. ICAF., London, TR73183, 1973.

3. Swift, Tom: WFD. Monitoring - Issues and Concerns, 5th. ICCAAS, Hamburg, DGLR-Bericht 93-02, 1993.

4. Billson, Margaret S.: Air Safety - Our Most Important Product as a Manufacturer. Proceedings of the FAA-NASA Sixth International Conference on Continued Airworthiness of Aircraft Structures, DOT/FAA/AR-95/86, December 1995.

5. Bigelow, Catherine A. and Tan, Paul W.: An Integrated Methodology for Assessing WFD in Aircraft Structures. Proceedings of the FAA-NASA Sixth International Conference on Continued Airworthiness of Aircraft Structures, DOT/FAA/AR-95/86, December 1995.

6. Viscount 720C VH-RMQ Mac Robertson Miller PTY Commonwealth of Australia Department of Civil Aviation Accident Investigation Report, Sept. 1969.

7. Boeing Aging Aircraft Conference - 1988. TE 41559 8-29-88.

8. Lotterer, David: Regulations Affecting Air Carrier Structural Inspection Programs. Proceedings of the FAA-NASA Sixth International Conference on Continued Airworthiness of Aircraft Structures, DOT/FAA/AR-95/86, December 1995.

9. McBride, Tony: Managed or Mandated Maintenance Programs—A Growing Concern. Proceedings of the FAA-NASA Sixth International Conference on Continued Airworthiness of Aircraft Structures, DOT/FAA/AR-95/86, December 1995.

10. Swift, Tom: Repairs to Damage Tolerant Aircraft. SIAA. Int. Symposium. FAA-AIR-90-01), Atlanta, 1990

Figure 12 shows an external patch repair of a fuselage skin for corrosion and cracking (D) along a stringer line.

Cracking which developed in the skin along the outer row of fasteners (Section AA) is hidden externally by the patch and internally by the stringer and could extend over a length (L) of more than two frame bays before it was detected by external inspection [Ref. 10].

Undetected cracking under the patch would also degrade the ability of the structure to survive adjacent foreign object damage. The repair does not meet *damage tolerant* criteria and would be classified as Category C - Temporary.

The scheme could be improved by extending the patch to line X. This moves the critical skin location to a line of new noncountersunk holes where crack initiation is less likely and cracking could be seen internally. The repair would have a longer life but would still be temporary.

A more immediate concern arises if the repair is applied to a very high-cycle aircraft. The cracking may result not from the corrosion but from *MSD* coalescence and other small undetected cracks may exist outside the boundaries of the proposed repair [See Figs. 1 and 6].

An appropriate operator action in this case would be:

- Recognize the possibility of *MSD*.

- Remove extra fasteners and check hole bores for cracks using a high frequency eddy-current probe.

- If no cracks are found, cold work hole bores to inhibit undetected damage and complete a temporary repair.

- If additional cracking is found report the condition.

Possible consequences of finding and reporting cracks are:

- On the subject aircraft, a much more extensive repair than originally proposed and possibly a skin change.

- An AD for *special detail* inspections at all skin attachment hole locations in the suspect area on all aircraft over the inspection threshold.

APPENDIX B—AIRCRAFT DATA

| Aircraft | Entered Service | Service Life Objective (cycles) | Active Aircraft | | | Test Sup. Life (cycles) (L) | Service Life/Test Ratio (R) |
			Number	Highest Cycles	Exceeding Service Life Objective Num/%		
B707 (1)	1958	20000	58	407000	43/74	25000	1.63
B727	1964	60000	1176	72900	15/1	85000	0.93
B737	1968	75000	2490	90100	20/1	75000	1.20
B747	1970	20000	888	32800	50/6	20000	1.64
DC8 (2)	1959	25000	303	47300	84/28	70200	0.67
DC 9	1965	40000	877	101100	715/82	102400	0.99
DC10-30	1971	30000	419	37700	3/1	30000	1.26
L1011 (3)	1972	36000	229	33800	0/0	26250	1.29
A300 (4)	1974	36000	137	35800	0/0	58000	0.62
BAC1-11	1964	55000	96	80700		57000	1.42
F28	1969	90000	119	90000			

Notes

(1)   Boeing Data - 30 Sept. 1955
(2)   McDonnell Douglas Data - 31 March 1966
(3)   Lockheed Data - 31 Dec. 1955.
(4)   Data for A300, BAC1 -11 and F28 from Flight International, 21 -27 Aug. 96 and other sources
(L)   Except where otherwise specified by the manufacturer, Test Supported Life = Full-scale fatigue test cycles on pressure fuselage x 1/2

(R)   A value of R greater than 1.0 indicates that the full scare tests may not offer assurance that WFD will not exist on the lead aircraft. Other tests and/or analysis may provide such assurance. Fatigue test specifications and procedures vary between aircraft models. Refer to manufacturer for further details.

APPENDIX C—GLOSSARY

The following definitions refer to the meaning of words and phrases as used in this paper. Other definitions may be found in other documentation.

Airworthiness - The ability of an airplane to complete a flight safely while operating anywhere within the fail-safe design envelope.

Airworthiness Assurance Working Group - A high-level industry steering committee formed to oversee the work of *Structures Task Groups* - Manufacturers' structural specialists, airline engineers, and regulatory authority representatives.

Damage Tolerance - The ability of structure to sustain anticipated loads in the presence of damage until such damage is detected by inspection or safe malfunction and repaired.

Directed Inspection - A scheduled inspection specified in the operator's maintenance program or in a service bulletin in which the attention of the inspector is directed to a particular item, component, assembly, or feature.

Engineering - That part of the organization staffed by professionally qualified engineers responsible for standards and procedures, the inspection schedule, inspection program development, specification of aircraft modifications, technical support to maintenance and design liaison with manufacturers, and the regulatory authority.

Failure - The inability of an item to perform within previously specified limits.

Fail-Safe

Design - A design which will permit continued operation of an airplane for a limited period after a failure in service.

Structure - The ability of damaged structure to withstand an infrequent high load.

Fatigue Damage

Multiple Element - The simultaneous cracking of multiple load path discrete elements working at similar stress levels.

Multiple Site - The presence of a number of adjacent small cracks that might coalesce to form a single long crack.

Widespread - The simultaneous presence of cracks at multiple structural details of such size and density that the structure will no longer meet Damage Tolerance requirements.

501

Inspection Levels *Maintenance Steering Group*

General Visual - A visual examination of an interior or exterior area, installation, or assembly to detect obvious damage, failure, or irregularity. This level of inspection is made under normally available lighting conditions such as daylight, hangar lighting, flashlight, or droplight and may require removal or opening of access panels or doors. Stands, ladders, or platforms may be required to gain proximity to the area being checked.

Detail - An intensive visual examination of a specific structural area, system, installation, or assembly to detect damage, failure, or irregularity. Available lighting is normally supplemented with a direct source of good lighting at an intensity deemed appropriate by the inspector. Aids such as mirrors, magnifying lenses, etc., may be used. Surface cleaning and elaborate access probes may be required.

Special Detail - An intensive examination of specific item(s), installation, or assembly to detect damage, failure, or irregularity. The examination is likely to make extensive use of specialized inspection techniques or equipment. Intricate cleaning and substantial access or disassembly procedures may be required.

Inspection Levels (Boeing and others)

Surveillance - A visual examination using adequate lighting and from a distance considered necessary to detect obvious unsatisfactory conditions in the subject area or item. Access procedures may be required to gain proximity. Surface cleaning may be required and inspection aids such as hand lenses and mirrors may be used where necessary.

Inspector - The person responsible for performing an inspection on an aircraft or component. Note: In the UK most inspections are performed by maintenance engineers or technicians who have the necessary authorization.

Maintenance Steering Group (MSG) logic - A decision process used to further the development of the initial maintenance programmer of public transport aircraft. Current edition is MSG.3. Rev 2.

Termination - The act of terminating the need for special inspections by modifying or replacing the subject item.

Figure 1. Examples of MSD and MED.

Figure 2. Damage Tolerance Inspection Window.

Figure 3. Extended Damage Tolerance Inspection Window With Fail-Safe Features.

Figure 4. Inspection Levels and Frequencies.

Figure 5. Detectable and Total Crack Lengths.

Figure 6. Inspection Opportunities With Widespread Fatigue Damage.
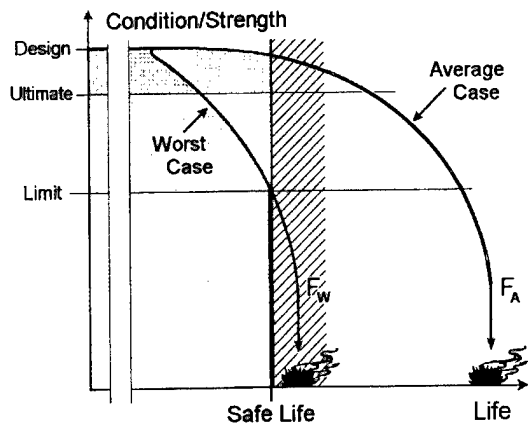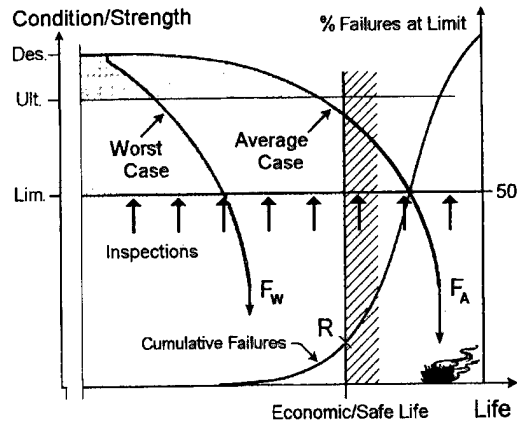
Figure 7. Airworthiness by Safe Life.

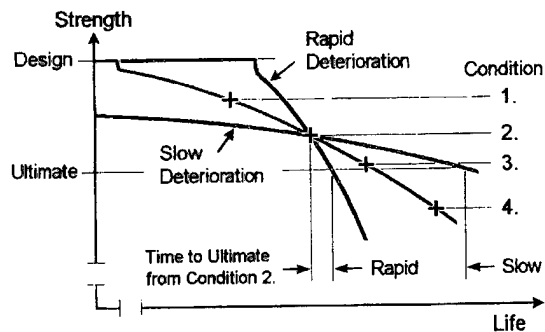Figure 8. Airworthiness by Inspection.

Figure 9. Assessment of Condition.
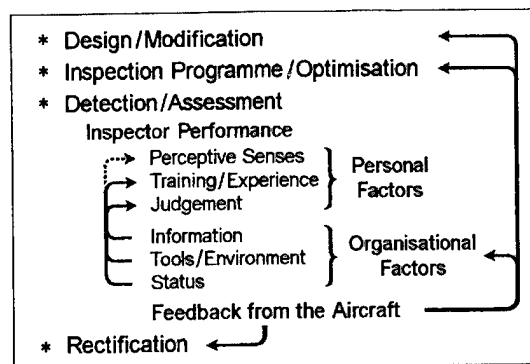

Figure 10. Inspector Role in Program Development.
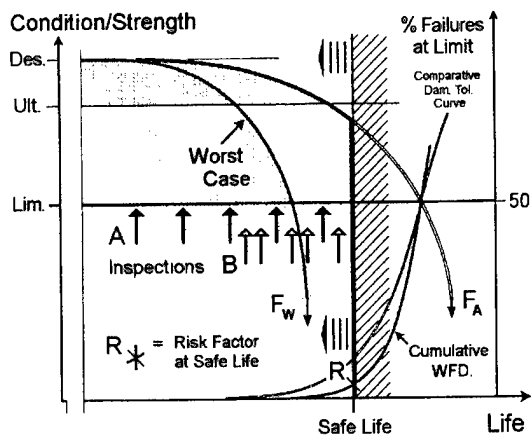

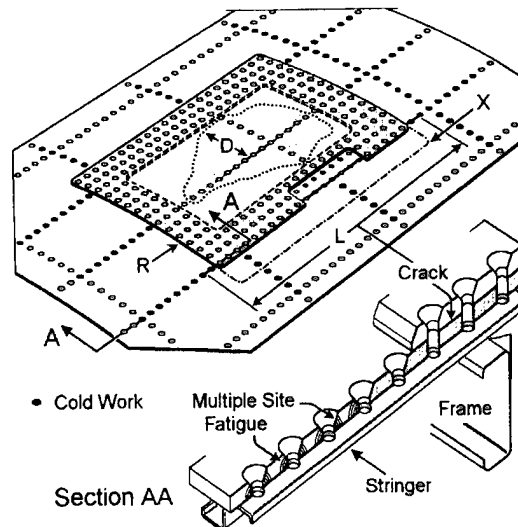Figure 11. Development of a WFD Program.

Figure 12. External Patch Repair of a Fuselage Skin.

504

PREDICTIONS OF STABLE GROWTH OF A LEAD CRACK AND MULTIPLE-SITE DAMAGE USING ELASTIC-PLASTIC FINITE ELEMENT METHOD (EPFEM) AND ELASTIC-PLASTIC FINITE ELEMENT ALTERNATING METHOD (EPFEAM)

L. Wang, F. W. Brust, and S. N. Atluri
FAA Center of Excellence for
Computational Modeling of Aircraft Structures
Georgia Institute of Technology
Atlanta, Georgia 30332-0356

SUMMARY

Damage tolerance analyses of an aging aircraft require numerical simulations of stable tearing of the skin of the aircraft. This paper presents a methodology for the analyses of multiple-site damage (MSD) in the presence of a lead crack, based on the T^*-integral fracture parameter and the finite element alternating method. In the proposed methodology, the T^*-resistance curve is obtained from the numerical simulations in the generation phase analyses of experiments of center-cracked panels containing single cracks. The computed T^*-resistance curve is then used in numerical predictions of stable tearing of the aircraft skin in the application phase analyses. To validate this methodology, generation phase analyses and application phase analyses are performed for the MSD tests performed at the National Institute of Standards and Technology (NIST). Numerical results show that a single T^*-resistance curve can be obtained from the tearing of center-cracked panels of different sizes, and the single T^*-resistance curve can be used to predict the stable tearing of the lead cracks and their linkup with MSD cracks in front of them. The predicted curves of load versus crack extension are in good agreement with the experimental measurements obtained at NIST. Through these numerical analyses and comparisons, this paper presents, for the first time, a truly validated energy based fracture criterion for the analysis of stable growth and linkup of multiple cracks in an MSD situation.

INTRODUCTION

Practical methods for predicting the residual strength of multiple-site damage (MSD) problems include the plastic zone method [1], the crack tip opening angle (CTOA) method [2], and the T^*-integral method [3, 4, 5, 6, 7]. As a simple engineering approach, the plastic zone method assumes that the main crack will link with the MSD crack ahead of it if their plastic zones overlap. The plastic zones are estimated using an elastic analogy such as an Irwin estimation. Since it is difficult to evaluate the effect of MSD cracks and the effect of plastic hardening within such a framework, significant errors can occur. Furthermore, when

the ligaments between the cracks are large enough to permit stable crack growth before linkups, as observed in the NIST tests, such a plastic-zone approach may not work. The CTOA method, which requires a rather detailed finite element analysis to apply, has been shown to be able to predict MSD failures [2]. However, CTOA is a geometric parameter and cannot be used under more general fracture conditions such as cyclic loading and rate-dependent fracture. As a promising and versatile fracture parameter, the T^*-integral is used in this study. Being an energy quantity, the T^*-integral is applicable under severe operating conditions of cyclic loading and rate-dependent fracture. Furthermore, it can be defined for cracks in any geometry (including a shell type fuselage structure) and when cracks bulge [8].

This paper presents elastic-plastic analyses of stable growth of a lead crack and MSD, using elastic-plastic finite element alternating method (EPFEAM). (A summary of the recent advances in finite element alternating method may be found in [9].) The analyses is performed based on the T^*-integral fracture parameter. The validation is made by comparing computational predictions of residual strength using these techniques to experimental data produced by The National Institute of Standards and Technology (NIST). One single set of material properties was used for all the predictions. Thus, the predictions provided here are true predictions, i.e., no fudging of either the experimental data or the analysis predictions were made to make the predictions look better.

PREDICTION METHODOLOGY

The well-accepted resistance curve methodology is used in conjunction with the elastic-plastic finite element alternating method (EPFEAM) and T^*-integral fracture parameter to carry out the computational predictions for the NIST MSD tests. There are two different types of analyses, i.e., the generation phase analysis and the application phase analysis, in the resistance curve method [10, 11]. In the generation phase analysis, information about material properties is generated. An experiment on a fracture specimen is analyzed. The values of a fracture mechanics parameter is computed for the fracture process. The computed curve of the fracture mechanics parameter versus the crack growth magnitude is the resistance curve, which is assumed to be a material property that governs the fracture process. Once the resistance curve is available, predictions can be made by forcing the fracture process to follow the resistance curve in the application phase analysis. The details are presented in the following.

The flow chart for a simulative analysis in the generation phase is shown in Figure 1. The test panel is first loaded to the crack initiation load. Then, the crack is extend by a small amount, while the load is changed simultaneously according to the load versus crack growth curve obtained in the experiment. After computing a fracture parameter (such as T^* or CTOA) for all the steps during the crack growth simulation, a resistance curve (fracture parameter versus crack growth) is obtained.

506

The generation phase analyses of test data to develop a resistance curve are usually performed when obtaining the curve directly from the test, which is time consuming, expensive, and impractical. It should be noted that both CTOA [2] and T^* [12] resistance curves can and have been obtained directly from experiments. But doing so is not necessary.

In a predictive analysis in the application phase, the crack extension is controlled by the T^*-resistance curve. A flow chart for the application phase is shown in Figure 2. It is assumed that 1) an increase in load (displacement) at the far field will increase the T^* value at the crack tip; 2) any crack extension will decrease the T^* value; and 3) the T^*-resistance curve does not decrease as the crack extends. Under these conditions, the simple predictive algorithm in Figure 2 can be used.

NIST MULTIPLE SITE DAMAGE EXPERIMENTS

Figures 3 and 4 summarize the series of tests carried out at NIST. More details on these tests can be found in [14]. The specimens were made of 2024-T3 aluminum, 90 inches wide, 150 inches high, 0.04 inch thick, with the lead crack located at the center of the panel. The definition parameters of MSD cracks, such as the MSD crack spacing, s_{MSD}, etc., are defined graphically in Figure 3. The MSD cracks were equally spaced. The specimens were symmetric about their horizontal and vertical centerlines.

The cracks were introduced by a series of saw cuts. The crack tips were made by the sharpest jeweler's saw available, having a tip radius of 0.003 inch. To simulate cracks emanating from rivet holes as occurs in an aircraft fuselage, the MSD cracks were cut from 0.22-inch holes that were drilled into the sheets before the saw cuts were made. Saw cuts can induce plastic deformations near the crack tips. However, this effect was not considered in this study. In addition, antibuckling guides were used in all tests, except for the MSD-6, so that the specimens did not buckle out of plane due to the small thickness. The test procedure consisted of pulling the specimen to fracture under displacement control. Both tips of the main crack did not grow at the same loads in the test due to imperfections in the symmetric condition. However, crack growth was only recorded at one crack tip.

Figure 4 provides a graphical representation of the crack growth behavior and MSD linkup results as observed from the tests. It is drawn to scale so that the main crack size, MSD crack size, and crack spacing can be directly observed. In Figure 4, the right side of the specimens is shown from the centerline of the center cracked panels (i.e., centerline of the main large crack) to the edge of the specimen. The half width is seen in Figure 4 to be 45 inches. The ligaments that failed simultaneously, as observed from the experimental results, are indicated with gray shading. The detailed experimental loads and crack growth response from these tests will be summarized in the next section during the discussion of comparisons between predictions and test results.

RESISTANCE CURVE CALCULATION—GENERATION PHASE

Generation phase analyses were performed on the two single-crack tests MSD-2 and MSD-3. The T^*-resistance curves were obtained from the generation phase analyses. The load versus crack growth data from NIST tests MSD-2 and MSD-3 are plotted in Figure 6. These data were fitted with curves to remove the scattering, as shown in Figure 6. Two generation phase analyses were performed for each of the two MSD tests. In the first analysis, the EPFEAM code was used. In the second analysis, a classical finite element analysis (FEA) was performed. For the classical finite element analysis, crack growth was modeled using a node release technique. For the EPFEAM analysis, new crack surface was created by erasing the crack closing traction using the analytical solution for an embedded crack in an infinite domain [9]. The plane stress assumption was used and eight-noded isoparametric elements were modeled. The material properties used for the analyses are given in Figure 5. The same material properties were also used for the predictive analyses described in the next section.

The calculated T^*-resistance curves from these generation phase analyses are illustrated in Figures 7 and 8 for cases MSD-2 and MSD-3, respectively. It is clearly seen that the computed T^* values are basically identical between the two methods, the EPFEAM and the classical FEA. This is a complete validation of the EPFEAM code since the numerical evaluation of T^* consists of integrating stress and strain (and their derivatives) type quantities at many locations along many paths surrounding the growing crack tip. Figures 7 and 8 illustrate the evaluation along six paths ranging in size from $\varepsilon = 0.087$ inch to $\varepsilon = 0.35$ inch. In addition, T^* was calculated along many other paths with identically good comparisons. The good agreement of computed T^* along many paths between the EPFEAM and classical FEA indicates that the full field solution using EPFEAM throughout the entire body is calculated accurately.

To compare the T^*-resistance curves obtained from different tests, Figure 9 places all of the results of Figures 7 and 8 on a single plot. It is seen that the T^*-resistance curves for the MSD-2, which had an initial crack size $2a = 8$ inches, and the T^*-resistance curves for the MSD-3, which had an initial crack size $2a = 20$ inches, are very close throughout the crack growth history. Ideally, the T^*-resistance curves for a given ε would be identical regardless of the crack size. The differences illustrated in Figure 9 are quite small, well within the scatter band of experimental error and the lot to lot material variability. Indeed, variations of the J-resistance curves from specimen to specimen (especially the initiation value, J_o) are quite significant. Thus, the obtained T^*-resistance curves can be viewed as a material property that governs the stable crack growth for aluminum 2024-T3.

The resistance curves for $\varepsilon = 0.087$ inch in Figure 9 were fitted with an equation as shown:

$$T^* = 0.706 - 0.0398\Delta a - 0.0697/(0.175 + \Delta a) \tag{1}$$

where the unit of T^* is (K lb/in) and the unit of Δa is inches. This curve represents an average of the resistance curves obtained from tests MSD-2 and MSD-3, and it was used for all other application phase analyses discussed throughout the rest of this paper. A discussion of the meaning for the different ε path size definitions and their physical significance can be found in [16].

PREDICTION OF STABLE CRACK GROWTH—APPLICATION PHASE

The first prediction shown here is for the single-crack test MSD-1. The analysis was forced to follow the T^*-resistance curve for $\varepsilon = 0.087$ inch obtained in the generation phase. Both the load and the crack growth were predicted from the displacement control analyses. Figure 10 shows the analysis prediction compared with the experimental data. As seen in Figure 10, both loads and crack growth predictions compare well with the experimental data.

The steps in Figure 10 are due to the nature of the predictive analysis. Consider a crack growth step. An increment of displacement is applied. When the driving force value T_D^* reaches the material resistance value T_R^* for the current crack size, the displacement is held constant while an increment of crack growth is permitted. If $T_D^* > T_R^*$, after the increment of growth, the crack must grow more. So again, the displacement is held constant and an increment of crack growth is modeled. As such, the horizontal steps in Figure 10 represent the amount of crack growth for a given displacement. Note also that during a growth step with the displacement held constant, the load, which is predicted, drops slightly. If $T_D^* < T_R^*$ after an increment of crack growth, the growth of the crack is stopped. Hence, an additional increment of displacement can be applied. This application phase predictive methodology is illustrated graphically in Figure 2. It is emphasized that the analyses in Figure 10, as well as all analyses shown in the next section (which presents the MSD analyses), provide predictions of both load and crack growth using only one T^*-resistance curve.

This fashion of predictive analyses allows the numerical test to follow the given T^*-resistance curve in an average sense. Small increments of displacements or crack growth are necessary in order to follow closely the T^*-resistance curve. At the expense of computational time, it is possible to design a more sophisticated algorithm to closely follow the T^*-resistance curve and to provide smoother predictions without steps in the predicted load versus crack-extension diagram.

The Foster-Miller [15] flat panel tests P1, P2, and P3 were also analyzed to provide additional verification of the predictive capability of the method and the obtained T^*-resistance curve (Eq. 1). These were tension tests of center-cracked panels, with initial crack size $2a = 4, 7, 11$ inches for tests P1, P2 and P3, respectively. They were also flat panels, 20 inches wide, 48 inches long, and 0.04 inch thick. They were much smaller than those used at NIST. Figure 11 compares the predictions for three tests with different initial crack sizes. Good comparison is observed. Note that the resistance curve used for these analyses was

obtained from the NIST material and not from the Foster-Miller material. The mechanical properties of the material were also assumed to be the same (Figure 5).

The application phase predictions for tests MSD-4 and MSD-5 are shown in Figures 12 and 13, respectively. In these figures (and all other similar figures shown subsequently) the abscissa represents crack growth and the ordinate represents load as predicted using the algorithm shown in Figure 2. The predicted results are for the right crack tip. In Figures 12 or 13, the point of zero crack extension corresponds to the initial position of the right tip of the main crack. The MSD cracks are drawn to scale in these figures so that the extension of the main crack, the MSD linkup points, and the corresponding simultaneous ligament failure predictions can be observed.

It is seen that the MSD-4 predictions (Figure 12) are excellent. Both the linkup loads, maximum loads, and crack growth predictions are almost identical with the experimental values. Figure 13 likewise shows good predictions for MSD-5 except that the failure load is predicted to be identical to the second and third linkup load. Experimentally, a slight increase in load was observed (after the third linkup) at about 4.5 inches of crack growth. However, these predictions are considered excellent given the many sources of statistical variability for these experiments. This variability includes: lot variability of material properties such as stress-strain response and T^*-resistance curves and slight errors in specimen fabrication which led to the experimentally observed crack growth rate differences between the left and right side crack tips, etc.

The application phase prediction for test MSD-7 is shown in Figure 14. This test had five MSD cracks ahead of both tips of the main crack. The crack spacing and crack sizes are illustrated in Figure 4 and at the top of Figure 14. As seen in Figure 4, all of the MSD cracks joined together after the second linkup (gray shaded regions in Figure 4). Excellent predictions of both linkup loads, linkup instability, and crack growth behavior are seen in Figure 14. Note that MSD-10 test data is also presented here. Having the same crack sizes, the MSD-7 and MSD-10 tests were identical. Some of the statistical variability in the results can be seen here with the test results for MSD-10 higher than those for MSD-7. The analyses for this case, as well as for MSD-8 and MSD-9 (discussed next), used a quarter model, i.e., only the right crack was modeled.

The application phase predictions for tests MSD-8 and MSD-9 are shown in Figures 15 and 16, respectively. The MSD spacing is illustrated at the bottom of these figures. Again, the initial position of the right main crack tip corresponds to the point of zero crack extension in Figures 15 and 16, with the MSD spacing ahead of the main crack. The initiation load prediction for MSD-8 (Figure 15) is quite good. The predicted load at first linkup is slightly higher than the test data. In addition, the predicted load at second linkup is higher than the test data. After the second linkup, the MSD cracks all linked together as shown in Figure 15 after about 2.5 inches of crack growth. This linkup instability was predicted by the EPFEAM model quite well.

Figure 16 illustrates the prediction for MSD-9. Note that the initial linkup led to a rapid crack jump (Figures 4 and 16). The rapid crack jump was also predicted by the model. The maximum load is somewhat underpredicted compared with the experimental results.

CONCLUSIONS

This paper presented the computational predictions and corresponding comparisons with test data developed at National Institute of Standards and Technology (NIST) on large panels with MSD. All eight unique tests in the NIST-90 test series were analyzed using the elastic-plastic finite element alternating method (EPFEAM). In addition, three tests performed by Foster-Miller were analyzed. Of the eight NIST tests, three were single crack tests and five had MSD cracks ahead of a main crack. The three Foster-Miller tests considered here were single-center crack panel tests. These predictions are simple to obtain with this newly developed methodology, and all predictions were made using the simple procedure without fudging of any results. Many of the predictions compared exactly with the experimental data, and at worst, a difference of 15% between analysis and experiment was obtained. These results are considered excellent given the material and test statistical variability.

ACKNOWLEDGMENTS

REFERENCES

1. Swift, T.: The Influence of Slow Stable Growth and Net Section Yielding on the Residual Strength of Stiffened Structure, *Presented to the 13th International Committee on Aeronautical Fatigue,* Pisa, Italy, May 1985.

2. Newman, J. C. Jr., Dawicke, D. S., Sutton, M. A., and Bigelow, C. A.: A Fracture Criterion for Widespread Cracking in Thin Sheet Aluminum Alloys, *Int. Committee on Aeronautical Fatigue,* 17th Symposium, 1993.

3.   Pyo, C. R., Okada, H., and Atluri, S. N.: An Elastic-Plastic Finite Element Alternating Method for Analyzing Widespread Fatigue Damage in Aircraft Structures, *FAA Center of Excellence Report by Georgia Institute of Technology,* November 1994.

4.   Pyo, C. R., Okada, H., and Atluri, S. N.: Residual Strength Prediction for Aircraft Panels With Multiple Site Damage, Using the "EPFEAM" for Stable Crack Growth Analysis, *Comput. Mech.* 16.3, June 1995, pp. 190-196

5.   Singh, R., Park, J. H., and Atluri, S. N.: Residual Life and Strength Estimates of Aircraft Structural Components with MSD/MED. *Proceedings of the FAA/NASA International Symposium on Advanced Structural Integrity Methods for Airframe Durability and Damage Tolerance,* C. E. Harris, (ed.), September 1994, pp. 771-784.

6.   Brust, F. W.: Numerical Modeling and Experiments of Creep Crack Growth Under Cyclic Loading, *ASTM STP 1256,* American Society for Testing and Materials, Philadelphia, PA, 1995.

7.   Brust, F. W.: Investigations of High Temperature Deformation and Crack Growth Under Variable Load Histories, *Int. J Solids Struct.,* 32 15, August 1995, pp. 2191-2218.

8.   Shenoy, V. B., Potyondy, D. O., and Atluri, S. N.: Methodology for Computing Nonlinear Fracture Parameters for a Bulging Crack in a Pressurized Aircraft Fuselage. *Computational Mechanics,* v. 14, n. 6, September 1994, pp. 529-548.

9.   Wang, L. and Atluri, S. N. (1996): *Recent Advances in the Alternating Method for Elastic and Inelastic Fracture Analyses* (to appear in Comput. Methods Appl. Mech. Engrg.)

10.   Kanninen, M. F.: A Critical Appraisal of Solution Techniques in Dynamic Fracture Mechanics, *Numerical Methods in Fracture Mechanics,* D. R. J. Owen and A. R. Luxmoore, (eds.), Pineridge Press, pp. 612-634, 1978.

11.   Kanninen, M. F. and Poplar, C. F.: *Advanced Fracture Mechanics,* Oxford University Press, New York, NY, 1985.

12.   Okada, H., Suzuki, Y., Ma, L., Lam, P. W., Pyo, C. R., Atluri, S. N., Kobayashi, A. S., and Tan, P. W.: Plane Stress Crack Growth and T^* Integral—An Experimental-Numerical Analysis, *The Proceedings of the ICES-95,* Hawaii, August 1995.

13.   Wang, L., Brust, F. W., and Atluri, S. N.: The Elastic-Plastic Finite Element Alternating Method (EPFEAM) and the Prediction of Fracture Under WFD Conditions in Aircraft Structures, Part III—Computational Predictions of the NIST Multiple Site Damage Experimental Results, (to appear in *Eng. Fract. Mech.,* 1996).

512

14.   deWit, R., Fields, R. J., Low, S. R., Harne, D. E., and Foecke, T.: Fracture Testing of Large-Scale Thin-Sheet Aluminum Alloy, NIST Report 5661, Prepared for FAA, May 1995.

15.   Broek, D.: The Effects of Multi-Site Damage on the Arrest Capability of Aircraft Fuselage Structures. *FractuResearch Technical Report* No. 9302, 1993.

16.   Brust, F. W.: The *T**-Integral: Definition and Use for Predicting Damage Accumulation and Fracture, *Contemporary Research in Engineering Science,* R. C. Batra (ed.), 1995, pp. 118-140.
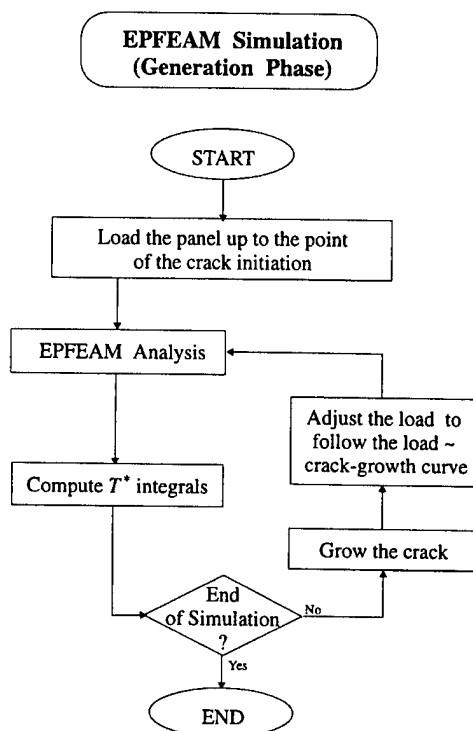
Figure 1. EPFEAM Crack Growth Simulation Based on an Experimental Load Versus Crack Extension Curve.
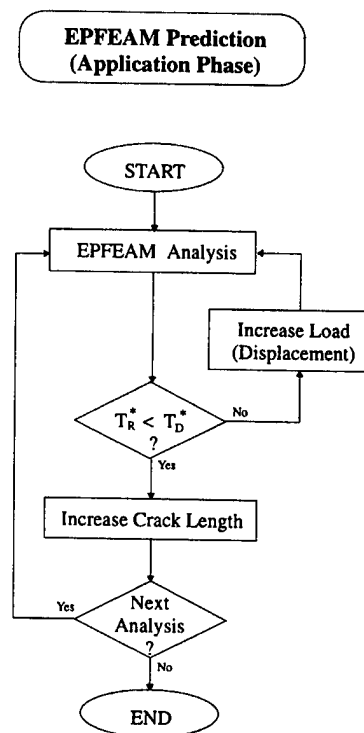
Figure 2. Predictive EPFEAM Crack Growth Algorithm Based on a *T** Fracture Criterion.

Figure 3. Test Matrix for NIST Tests.
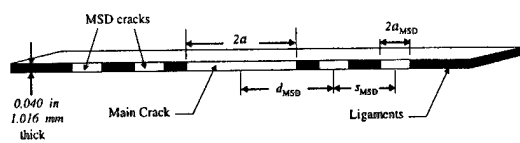
| Test | a (in) | MSD cracks | | | |
		d_{MSD} (in)	s_{MSD} (in)	$2a_{MSD}$ (in)	number per side
MSD-1	7.0				
MSD-2	4.0				
MSD-3	10.0				
MSD-4	7.0	7.5	1.0	0.4	3
MSD-5	2.8	3.5	1.5	0.6	3
MSD-6	10.0	(no anti-buckling guides)			
MSD-7	10.0	10.5	1.5	0.5	5
MSD-8	9.5	10.5	1.5	0.5	10
MSD-9	5.0	6.5	1.0	0.4	10
MSD-10[r]	10.0	10.5	1.5	0.5	5

[r] repeat of MSD-7
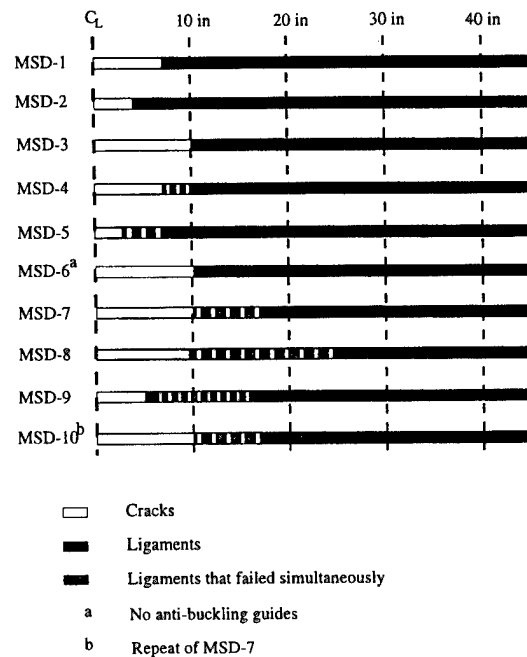
Figure 4. Experimental Results Illustrating the MSD Linkup Behavior for Each of the NIST-90 MSD Tests.
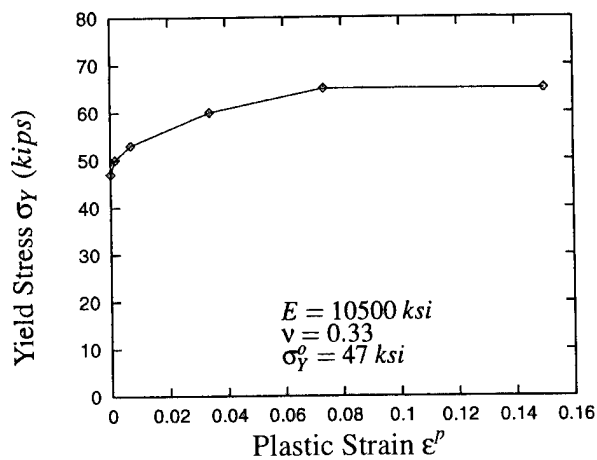
Figure 5. Elastic and Plastic Material Properties for Aluminum 2024-T3.
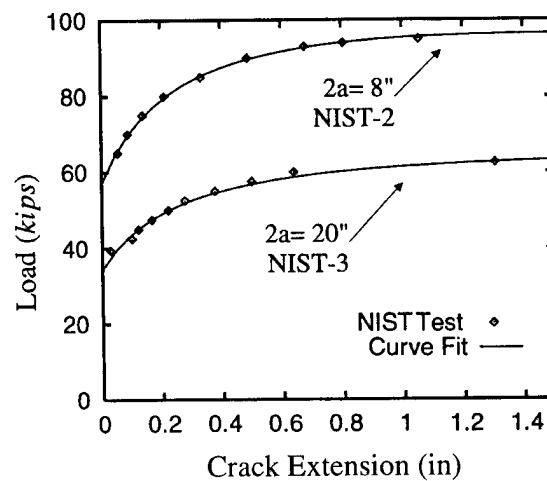
Figure 6. Experimental Data for NIST-90 MSD-2 and MSD-3.
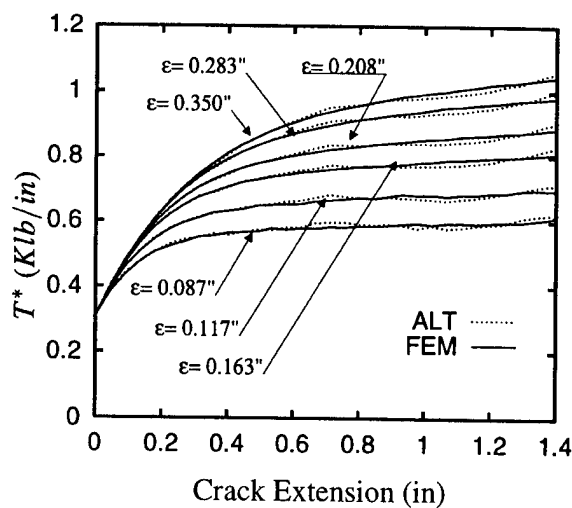
Figure 7. The T^* for NIST-90 MSD-2 Using EPFEAM and Classical FEM.
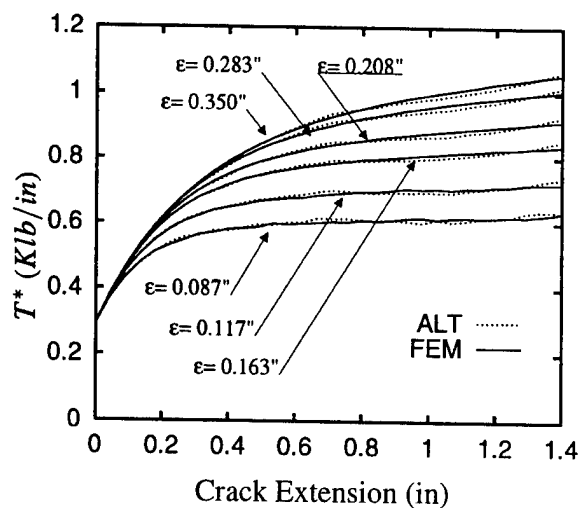
Figure 8. The T^* for NIST-90 MSD-3 Using EPFEAM and Classical FEM.
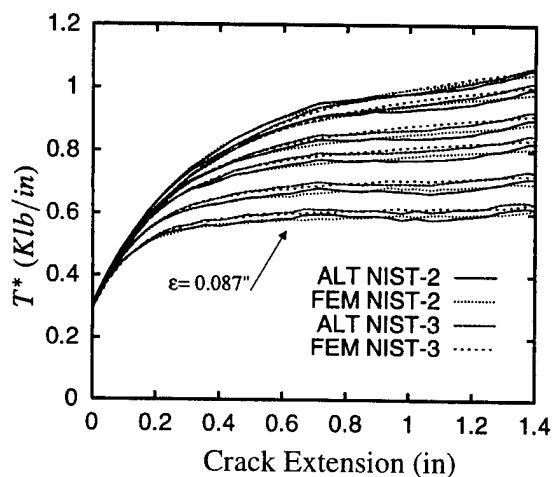
Figure 9. The T^* for NIST-90 MSD-2 and MSD-3 Using EPFEAM and Classical FEM.
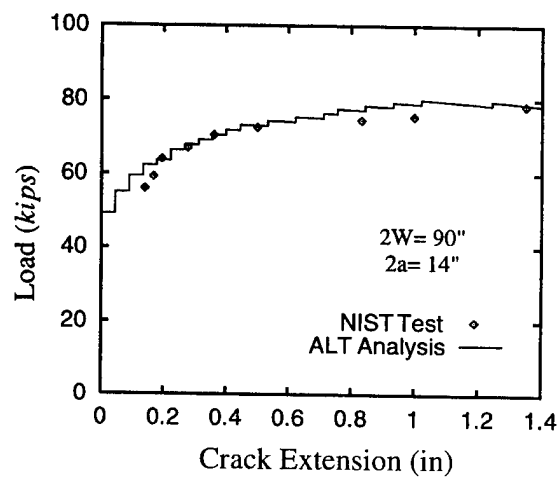
Figure 10. Load and Crack Growth Predictions for NIST-90 MSD-1 Compared With Experimental Results.

515
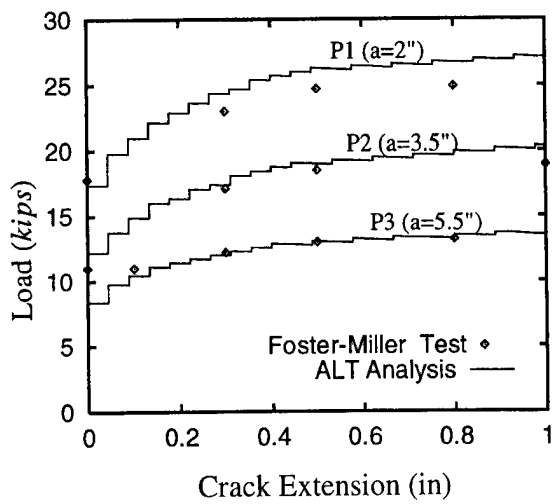
Figure 11. Load and Crack Growth Predictions for Foster-Miller Single Crack Panels P1, P2, and P3 Compared With Experimental Results.
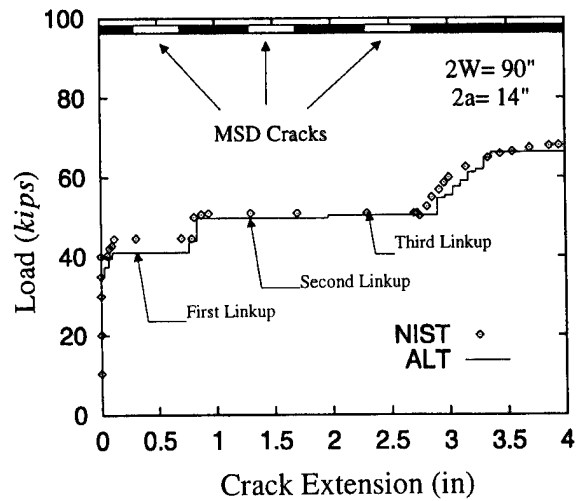
Figure 12. Load and Crack Growth Predictions for NIST-90 MSD-4 Compared With Experimental Results.
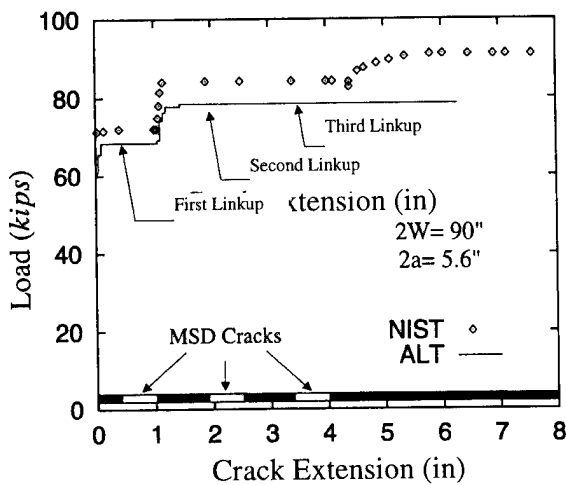
Figure 13. Load and Crack Growth Predictions for NIST-90 MSD-5 Compared With Experimental Results.
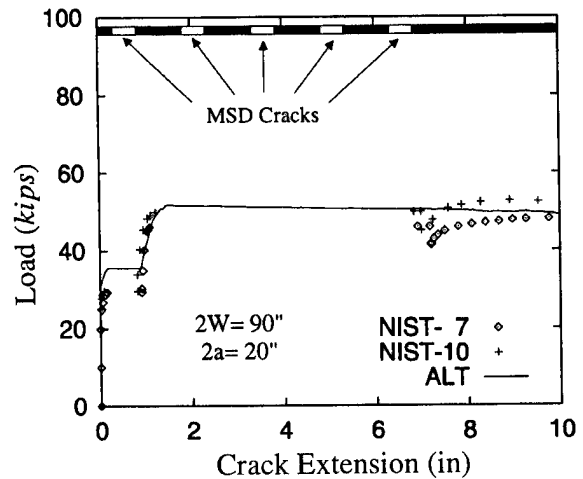
Figure 14. Load and Crack Growth Predictions for NIST-90 MSD-7 Compared With Experimental Results.
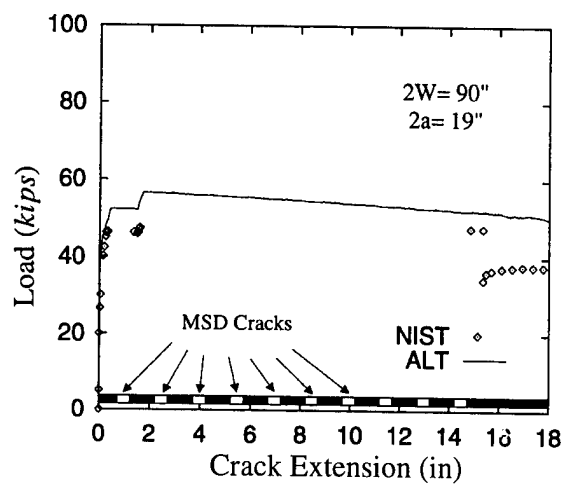
Figure 15. Load and Crack Growth Predictions for NIST-90 MSD-8 Compared With Experimental Results.
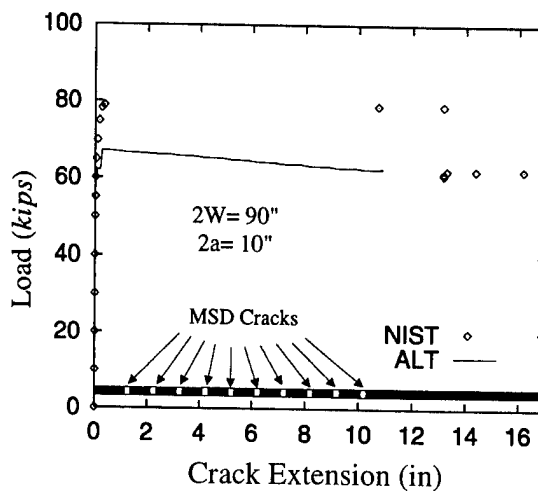
Figure 16. Load and Crack Growth Predictions for NIST-90 MSD-9 Compared With Experimental Results.

PREDICTIONS OF WIDESPREAD FATIGUE DAMAGE THRESHOLD

L. Wang, W. T. Chow, H. Kawai, and S. N. Atluri
FAA Center of Excellence for
Computational Modeling of Aircraft Structures
Georgia Institute of Technology
Atlanta, Georgia 30332-0356

SUMMARY

Commercial transport aircraft are required to operate under the concept of damage tolerance. This requires that aircraft fuselages and wings tolerate discrete source damages induced by foreign objects, such as impact damage due to engine disintegration. Due to the structural redundancy and the crack arrest capability, the current fleet of commercial aircraft were initially designed to have sufficient residual strength to sustain discrete source damage. However, fatigue damage during the life of an aircraft can significantly reduce the residual strength of an aging aircraft. Thus, it is important to predict the severity of the fatigue damage, since it can reduce the residual strength of an aging aircraft to below the damage-tolerant requirement. It is also important to estimate the remaining fatigue life of an aging aircraft so that inspection, maintenance, and repair can be scheduled before a catastrophic failure may occur. This paper presents a hierarchical approach for the numerical predictions of the widespread fatigue damage threshold and the remaining fatigue life of an aging aircraft. In this approach, the global load distribution is obtained using an finite element analysis with a coarse mesh, while the crack(s) is (are) modeled only to a level to determine the load flow redistribution due to its (their) presence. The crack tip parameters are obtained using the finite element alternating method at the local level. A detailed numerical study is presented to illustrate the typical characteristics of the widespread fatigue damage threshold for an aging aircraft.

INTRODUCTION

The fatigue damage due to the repetitive loading condition of pressurization is one of the major concerns among the civil aviation industry. There exists two different types of approach in dealing with the multiple-site fatigue damage problem. One of them is the Multiple-Site Damage Threshold (MSDT) approach, the other is the Widespread Fatigue Damage Threshold (WFDT) approach [1]. In the MSDT approach the severity of MSD is measured by the potential of linkup, while in the WFDT approach, it is indicated by the reduction of residual strength of the aircraft.

As shown in Figure l(a), the MSDT approach requires the study of fatigue growth and linkup of a number of small fatigue cracks. If the MSD cracks do not linkup during service inspections, it is considered safe. However, small MSD cracks may significantly reduce the residual strength of an aircraft in the presence of a lead crack, as illustrated in Figure l(b). For an aircraft designed to operate at a high level of working stress with a small amount of redundant residual strength, very small undetectable fatigue cracks can reduce the residual strength to below an acceptable level. On the other hand, aircraft with sufficient redundant residual strength can have enough residual strength in the presence of detectable fatigue cracks. Therefore, using the MSDT approach alone may lead to a false feeling of safety and the MSDT approach alone is not sufficient for the evaluation of the severity of multiple-site fatigue damage on an aircraft.

MSD Threshold   WFD Threshold

When Will These Fatigue
Cracks Link Up?

(a)

When Will The Panel Not Be Able
To Stop the Lead Crack?

(b)
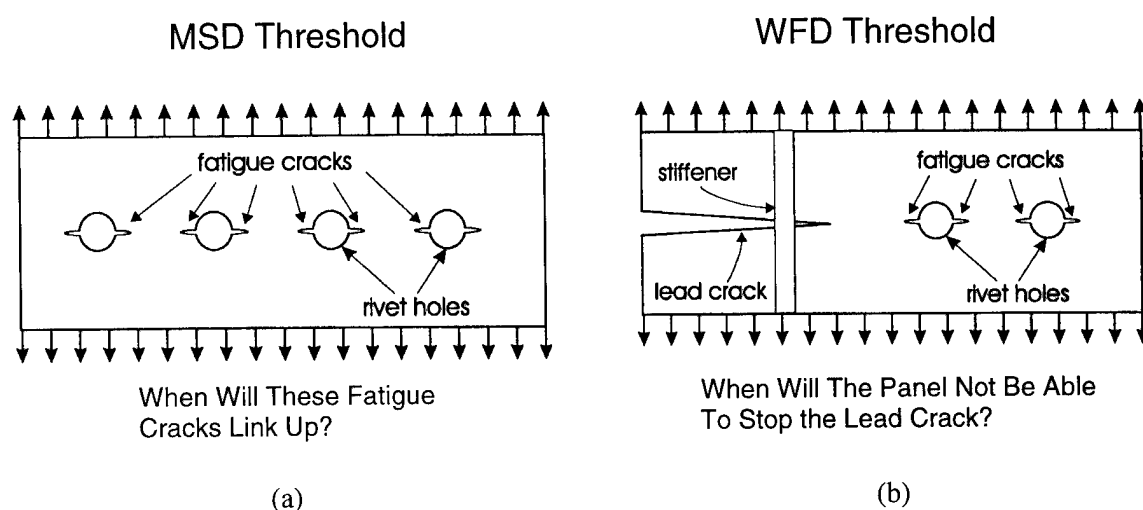
Figure 1. MSD Threshold Approach and WFD Threshold Approach.

Currently, the fleet of aging commercial aircraft in the U.S. is operating under the concept of damage tolerance [2], which requires an aircraft to have sufficient residual strength in the presence of damage in the principal structural elements during the interval of service inspections. Such damages include fatigue cracks, propagating between detectable and critical size, and discrete source damage induced by foreign objects such as fragments in the case of engine disintegration. Since fatigue damage can degrade the damage tolerance capability of an aircraft, evaluating the severity of fatigue cracks through the evaluation of the reduction in residual strength is very important in order to truly enforce the damage tolerance concept.

For practical interest, it is also important to predict the widespread fatigue damage (WFD) threshold, i.e., the number of loading cycles that will produce fatigue cracks such that the residual strength of the aircraft is reduced to below an acceptable level. With the knowledge of widespread fatigue damage threshold, aging aircraft operators can schedule service inspections economically without compromising safety requirements. This paper presents a methodology to predict the WFD threshold with numerical examples illustrating the typical characteristics of an aging aircraft.

EFFECTS OF MSD CRACKS ON RESIDUAL STRENGTH

To determine the critical MSD crack size that will reduce the residual strength of an aircraft fuselage below an acceptable level, we must perform residual strength analysis of the aircraft fuselage in the presence of a lead crack and MSD. Nonlinear material behavior must be considered in such a study. At the critical load, the plastic zone size ahead of the lead crack tip in a typical aircraft fuselage can be as large as more than a half inch to several inches. However, the typical rivet spacing is only about 1 inch. Therefore, the zone of plastic deformation ahead of the lead crack is not negligible when compared to the size of the MSD cracks and ligaments ahead of the lead crack. In an elastic fracture mechanics model, the deformation and stress are highly localized near the crack tip. Due to the plastic deformation, these stress must be redistributed along the ligaments to achieve static equilibrium, as suggested in an Irwin model for the estimation of plastic zone size. Such stress redistribution can significantly change the loading condition of the adjacent cracks in the MSD crack situation. On the other hand, the existence of MSD cracks limits the size of the ligaments on which the stress can be redistributed. Furthermore, the stress redistribution is much more complicated in the MSD situation due to the interaction between the MSD cracks and the lead crack. Therefore, a detailed elastic-plastic fracture analysis of the cracked panel is necessary.

Figure 2(a) shows a typical MSD situation, in which there is a single lead crack located at the center of the flat panel. There are two MSD cracks ahead of each of the lead crack tips. The length of the ligaments between adjacent cracks is 1 inch. The material is assumed to be aluminum 2024-T3. A piecewise linear flow curve is used for Al 2024-T3, as shown in Figure 2(b). The effect of MSD cracks on the residual strength of a cracked panel and the importance of elastic-plastic fracture mechanics approach can be seen in Figure 3.
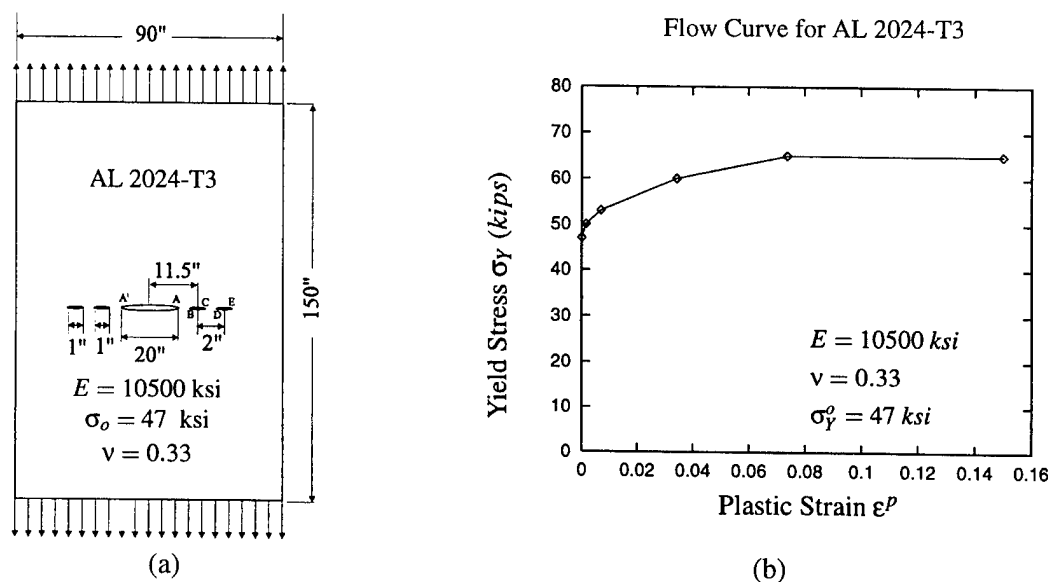
Figure 2. A Lead Crack and MSD in a Flat Sheet.

521

Figure 3 is the normalized residual strength plot for the panel shown in Figure 2(a). The residual strength is normalized with respect to the residual strength for the case where there is only a lead crack, obtained using linear elastic fracture mechanics (LEFM). It is seen that the LEFM approach overestimates the residual strength, compared to the elastic-plastic fracture mechanics (EPFM) approach. For the lead crack only case in this panel configuration, the amount of overestimation is very large. However, in the presence of MSD cracks, the LEFM approach can lead to significant error, especially if the panel is at a high stress level.
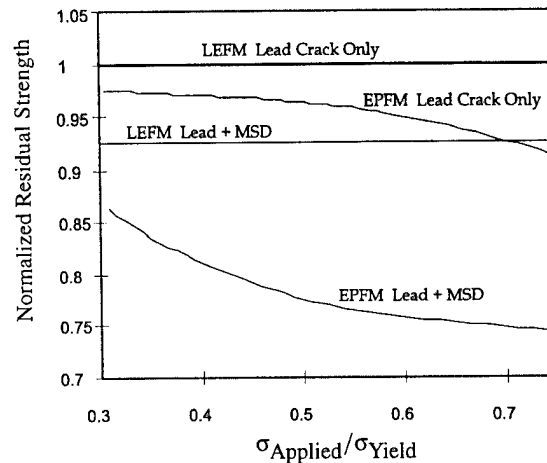
Figure 3. Normalized Residual Strength for the Lead Crack Only Using LEFM, the Lead Crack Only Using EPFM, the Lead Crack With MSD Using LEFM, and the Lead Crack With MSD Using EPFM.

RESIDUAL STRENGTH ANALYSES OF AIRCRAFT FUSELAGES

Global-intermediate-local hierarchical modeling is an efficient approach for the residual strength analyses of aircraft fuselages in the presence of a lead crack and MSD. Figure 4 graphically illustrates such a hierarchical approach. In a global analysis, linear elastic analyses of the global load flow in the aircraft fuselage are carried out using the ordinary finite element method. Stringers and frames are simplified as straight beams and curved beams. Skins are modeled using shell elements. Lead cracks are modeled explicitly. However, no mesh refinement around crack tips is necessary, since the purpose of the analysis is to obtain the load flow pattern, i.e., to obtain the boundary conditions for the more detailed intermediate model.

The intermediate model contains a smaller portion of the cracked fuselage, where stringers and frames are modeled in detail using shell elements. Each rivet is modeled individually using spring elements. The empirical formula suggested by Swift [3] is used to model the flexibility of rivets. Thus, the influence of the detailed structure on the membrane stress in the skin can be determined through this linear elastic intermediate analysis. Again,

the lead crack is modeled explicitly, but no mesh refinement around the crack tip is made in order to reduce the computational cost.

| Capture Global Load Flow | Structural Details Stringers, Frames, Rivets | Residual Strength Analysis Using EPFEAM |
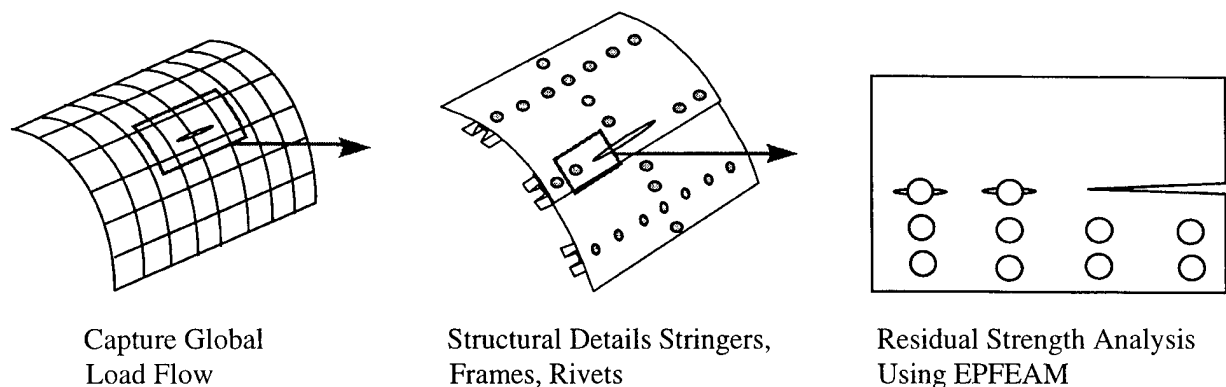
Figure 4. A Global-Intermediate-Local Hierarchical Approach for the Residual Strength Analysis of an Aircraft Fuselage.

A rectangular skin model is obtained from the intermediate analysis. In the local model the boundary loading conditions at the four edges and the rivet pin-loads on the rivet holes are obtained from the intermediate analysis. The skin-only local model is analyzed using Elastic-Plastic Alternating Method, where none of the cracks are modeled explicitly. Analytical solutions for an embedded crack in an infinite domain, subjected to arbitrary crack surface loadings, are used to capture the singular fields near the crack tips. More details about the Finite Element Alternating Method and its extension to the elastic-plastic analyses can be found in [4, 5, 6].

A typical residual strength plot obtained from such global-intermediate-local analyses is illustrated in Figure 5. In the analysis shown in Figure 5 we assume the aircraft fuselage has a radius of 118 inches. The longitudinal lead crack is located at a lap joint splice. We assume a broken center tear strip while the center frame remains intact. The skin thickness is 0.071 inch. The critical stress-intensity factor for the skin is taken as $K_{Ic} = 90$ ksi$\sqrt{in}$. Rivets are of radius 0.095 inch. The frame spacing is 20 inches, and the stringer spacing is 10 inches.

Figure 5 shows the critical cabin pressure P_{cr} versus the half crack length a of the lead crack. The critical pressure is defined as the cabin pressure at which the stress-intensity factor (or its equivalent elastic-plastic counter part, T^*, which is the same as J for stationary cracks) at the lead crack tip reaches the critical value. It is seen that the residual strength reaches a local maximum shortly after the lead crack penetrates the first crack arresting frame. In the numerical modeling, we assume that the crack arresting frame remains intact and the tear strip under the crack arresting frame is broken when the lead crack penetrates the crack arresting frame. The residual strength curve is obtained by computing the critical pressure for different sizes of the lead crack. Therefore, no stable tearing is considered. It is seen that the linear elastic analysis significantly overestimates the residual strength of the cracked fuselage.

523
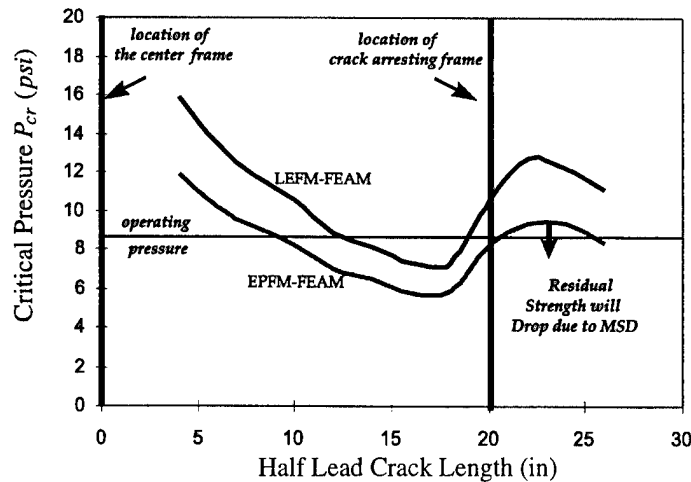
Figure 5. Residual Strength Curve for the Lead Crack Only Case.

The local maximum (see Figure 5) is above the operating pressure, which is assumed to be 8.4 *psi*. Therefore, if a large damage, due to link up of fatigue cracks or a foreign impact, is induced during the operation, the lead crack will be arrested around the local maximum at the operating pressure, provided that the damage extends to no more than two bays. However, MSD cracks ahead of the lead crack can bring down the local maximum to below the operating pressure. In such a case, the fuselage no longer has the required crack arresting capability. The aircraft with MSD can still operate with sufficient strength, provided no large damage is present in the fuselage. However, it becomes vulnerable to damage since it no longer has the capability to arrest a two-bay damage.

Figure 6 shows how the residual strength at the local maximum point decreases as the number and the size of fatigue cracks ahead of the lead crack tip increase. Here, we assume equal length fatigue cracks emanating from both sides of a rivet hole. The crack lengths are measured from the edges of rivet holes to the tips of fatigue cracks. The distance between the lead crack tip and the center of the first rivet hole is 1 inch. Three different MSD cases are presented. They correspond to fatigue cracks emanating from 1) the first rivet hole ahead of the lead crack tip, 2) the first three rivet holes ahead of the lead crack tip, and 3) the first five rivet holes ahead of the lead crack tip. From this analysis, we can find the critical size of fatigue cracks that will pose a WFD problem.

Figure 7 shows the reduction of residual strength for the MSD case in which there are only two equal length fatigue cracks emanating from the first rivet hole ahead of the lead crack tip, as indicated in the figure. The result obtained using the LEFM approach and the result obtained using EPFM approach are shown in the plot. It is seen that LEFM predicts a very small reduction in residual strength. LEFM overestimates the residual strength for the lead crack only case by a large amount, as shown in Figure 6. However, LEFM under-estimates the effect of MSD cracks as shown in Figure 7. Thus, using LEFM will lead to the

false impression that this structure is too strong to have WFD problems. Therefore, we conclude that EPFM approach is mandatory in the study of WFD problem.
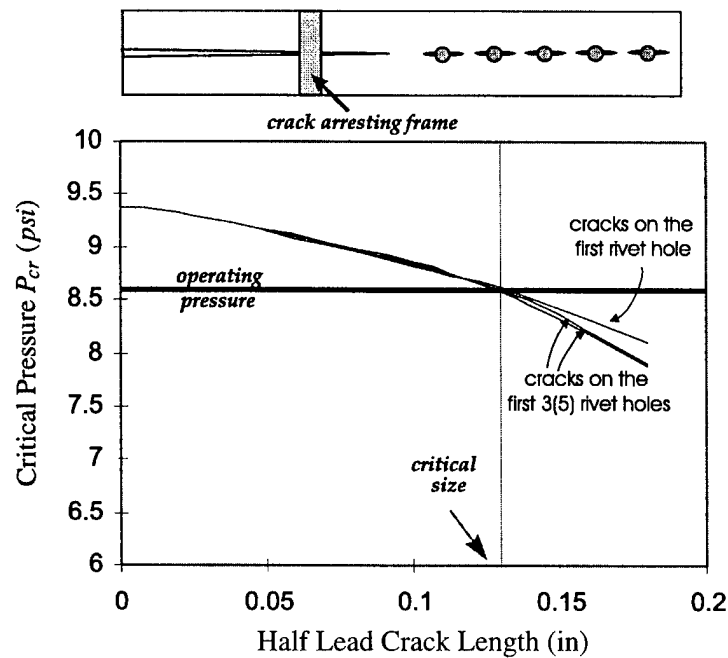
Figure 6. Residual Strength in the Presence of MSD Cracks.
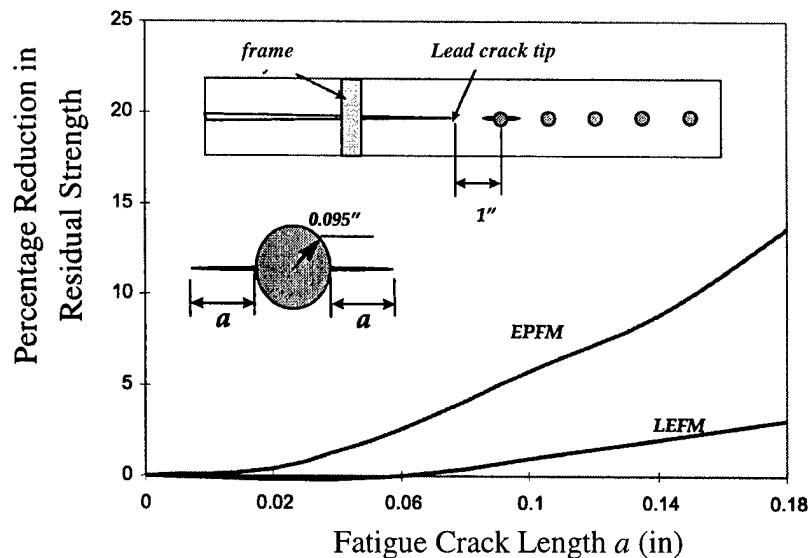
Figure 7. Reduction in Residual Strength for the Case of Fatigue Cracks Emanating From the First Rivet Hole Ahead of the Lead Crack Tip.

The reduction of residual strength also depends strongly on d_{MSD}, the distance between the lead crack tip and the center of the first rivet hole. The smaller d_{MSD}, the stronger the influence of MSD cracks. Figure 8 illustrates such effect. In practical

525

applications it is difficult to determine accurately and rationally the spacing d_{MSD}. From another point of view, the discrete source damage is random in nature. A probabilistic description seems to be more natural and a probabilistic analysis may be more suitable than a deterministic analysis.
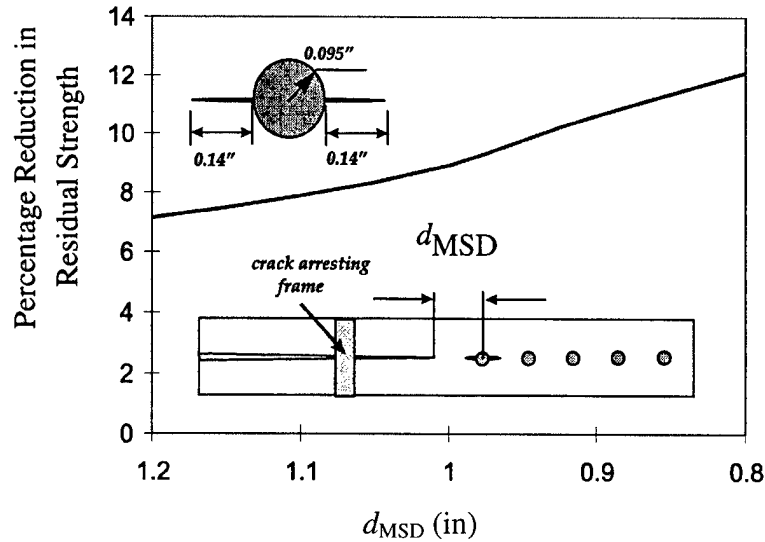
Figure 8. The Influence of d_{MSD}, the Distance Between the Lead Crack Tip and the Center of the First Rivet Hole, on the Reduction in Residual Strength.

FATIGUE CRACK GROWTH ANALYSES

After the analyses of the effect of MSD on the crack arresting capability of the aircraft fuselage panel, we can perform fatigue crack growth analyses to determine the WFD threshold. The hierarchical modeling strategy described in the previous section is also used for the fatigue analysis. The local fatigue analysis uses FEAM and LEFM. Figure 9 shows the results from a simple, straight forward fatigue analysis. Forman's crack growth equation [7] is used in the analysis. It is

$$\frac{da}{dN} = \frac{C(\Delta K)^n}{(1-R)K_c - \Delta K} \tag{1}$$

where ΔK is the stress-intensity factor range and R is the stress ratio in cyclic loading. The values of K_c, C, and n were given by Forman et al. [7] as the following:

$K_c = 83 \ ksi\sqrt{in}$
$C = 3 \times 10^{-4} \ kcyc \ ksi^{-2} \ in^{-2}$
$n = 3$

526
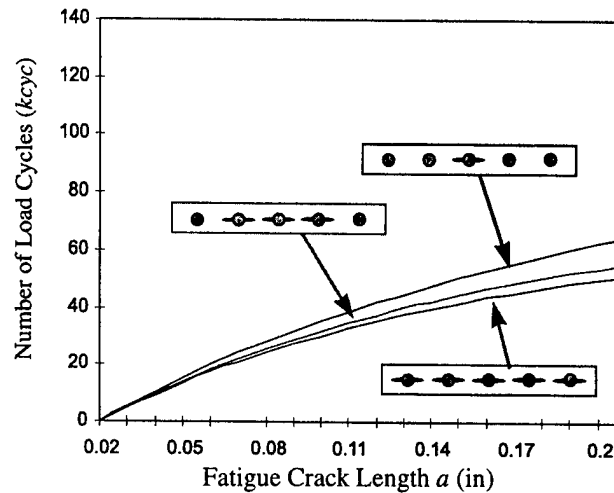
Figure 9. Fatigue Crack Growth Without Considering the Effect of Residual Stress.

However, the residual stress near rivet holes can change the fatigue life of these MSD cracks significantly. Residual stress due to misfitting, coldworking, rivet clamping forces, and fretting, etc., can all change the fatigue behavior. For illustration purpose, we demonstrate a case with the consideration of residual stress due to rivet misfitting and coldworking. More details of the effect due to coldworking and rivet misfitting may be found in [8].

Figure 10 shows the prediction of fatigue growth with the consideration of residual stress. It is seen that in the presence of residual stress the fatigue growth behavior changes significantly. When compared to the case where there is no residual stress, as seen in Figure 11, the small cracks grow faster and large cracks grow slower. Thus, the catch up phenomenon due to such residual stress, i.e., small fatigue cracks may grow faster to catch up to the size of large cracks, may be observed.
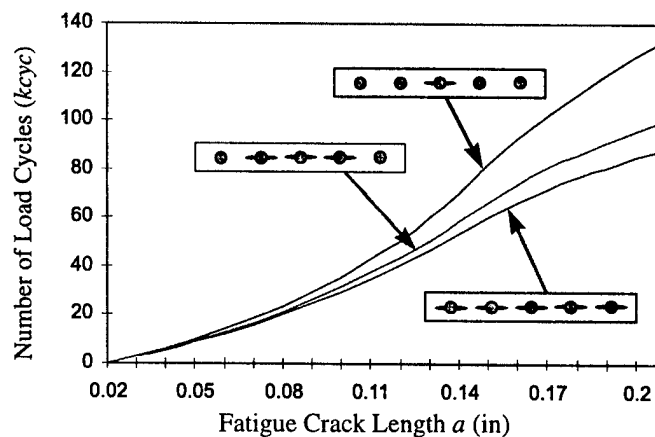
Figure 10. Fatigue Crack Growth Considering the Effect of Residual Stress.

527
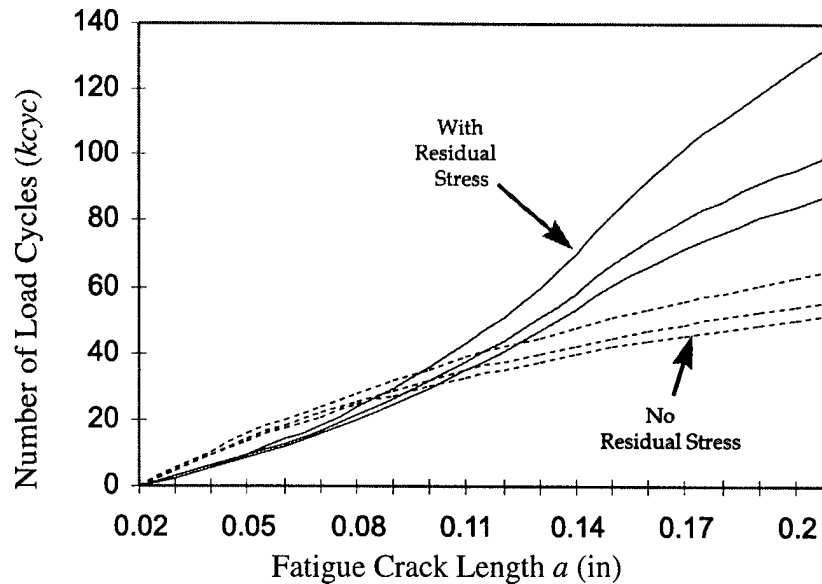
Figure 11. Fatigue Crack Growth With and Without the Effects of Residual Stress.

However, this analysis is based on a simplified residual stress model. In practice, misfitting and coldworking are displacement control processes. A more elaborated procedure may needed to evaluate the effect of misfitting and coldworking. Again, due to the random natural of residual stress, a probabilistic analysis as a follow up of the deterministic analysis may be necessary.

CONCLUSIONS

It is necessary to use WFDT approach to study the effect of MSD on the crack arresting capability of an aircraft fuselage in order to truly enforce the damage tolerance concept. With the knowledge of widespread fatigue damage threshold, operators of aging aircraft can schedule service inspections economically without compromising safety requirements and the aircraft designer can optimize aircraft designs for better tradeoff between production cost, operating cost, maintenance cost, and structural strength redundancy. Plasticity is very important in the residual strength analysis of not only the lead crack in the presence of MSD but also of the lead crack itself. Residual stresses, induced by rivet misfitting, coldworking, rivet clamping forces, fretting, etc., can significantly change the behavior of fatigue crack growth on an aircraft fuselage and WFD threshold. Since discrete source damages are random events and the magnitude of residual stresses have a large scatter, a probabilistic analysis as a follow-up of the present deterministic analysis may be necessary.

ACKNOWLEDGMENTS

REFERENCES

1.   Jeong, D. Y. and Tong, P.: Threshold of Multiple Site Damage in Aging Airplanes. *Structural Integrity in Aging Aircraft*, ASME-AD V.47, 1995, pp. 63-71.

2.   Swift, T.: Damage Tolerance Assessment of Commercial Airframes. *Fracture Problems in the Transportation Industry* ASCE, 1985, pp. 97-138.

3.   Swift, T.: Fracture Analysis of Stiffened Structure. *Damage Tolerance of Metallic Structures*, ASTM STP 842, 1984, pp. 69-107.

4.   Nikishkov, G. P. and Atluri, S. N.: Analytical-Numerical Alternating Method for Elastic-Plastic Analysis of Cracks. *Computational Mechanics*, v.13, no. 6, 1994. pp. 427-442.

5.   Wang, L. H. and Atluri, S. N.: Implementation of the Schwartz-Neumann Alternating Method for Collinear Multiple Cracks with Mixed Type of Boundary Conditions. *Computational Mechanics*, v. 16, no. 4, 1995, pp. 266-271.

6.   Wang, L. and Atluri, S. N. (1996): *Recent Advances in the Alternating Method for Elastic and Inelastic Fracture Analyses* (to appear in Comput. Methods Appl. Mech. Engrg.).

7.   Forman, R. G., Kearney, V. E., and Engle, R. M.: Numerical Analysis of Crack Propagation in Cyclic-Loaded Structures, J. *Basic Engg.* 89, 1967, pp. 459-464.

8.   Park, J. H. and Atluri, S. N.: Fatigue Growth of Multiple-Cracks Near a Row of Fastener Holes in a Fuselage Lap Joint, *Computational Mechanics*, v. 13 no. 3, 1993. pp. 189-203.

PROBABILITY AND STATISTICS MODELING OF CONSTITUENT PARTICLES AND CORROSION PITS AS A BASIS FOR MULTIPLE-SITE DAMAGE ANALYSIS[1]

N. R. Cawley, D. G. Harlow, and R. P. Wei
Department of Mechanical Engineering and Mechanics
Lehigh University
19 Memorial Drive West
Bethlehem, PA 18015-3085

SUMMARY

A probability model for the growth of corrosion pits in aluminum alloys in aqueous environments, in which the focus is the role of clustered particles, is suggested as a basis for estimating the distributions in size and location of fatigue cracks, as a function of time, for use in multiple-site damage (MSD) analyses. MSD is a condition in which multiple fatigue cracks occur within the same structural element, which is precipitated by pitting corrosion. The model replaces the practice of assuming the distributions for the size and location of MSD. Statistical distributions, estimated from experimental observations of 2024-T3 aluminum alloy, for the random size, density, and location of constituent particles are used as input for a mechanistically based probability model for severe corrosion pit growth. Pitting initiates at constituent particles, which are either anodic or cathodic relative to the matrix, and involves complex electrochemical processes. Local interactions between particles and the matrix enhance the growth rate. Spatial statistics models for cluster processes have been modified to characterize constituent particles, which are clustered randomly in size and shape.

INTRODUCTION

Multiple-site damage is a condition in which fatigue damage or cracks are at more than one site within the same structural element. MSD is of serious concern in terms of the integrity and safety of aging systems. In aging airplanes, for example, MSD may occur as a result of fatigue cracking at rivet holes along fuselage lap joints. Currently, statistical distributions for the size and location of MSD in aging airplanes are assumed. This procedure is unsatisfactory because of the absence of a rational basis for their selection and for estimating the time evolution of damage. A mechanistically based model for estimating the time evolution of these distributions of MSD, therefore, is needed and is discussed herein.

Pitting corrosion in aluminum alloys is recognized as an important precursor for the onset of fatigue crack growth, and it is influenced by the nature and distribution of the constituent particles in the alloys. Probability and statistical modeling of constituent particles and corrosion pits, coupled with fatigue growth analysis, therefore, provide a rational basis for MSD analyses. The primary thrust herein is to describe some the key features necessary for the development of a mechanistically based probility model for the growth of corrosion pits. The success of this approach is highly dependent on the accuracy of the mechanistic model for the corrosion process and on the proper identification of the random variables (*rvs*) that affect the process. The goal of this effort is to estimate the random pit size at an arbitrary time and location. Since fatigue cracks emanate from severe corrosion pits, the probability distribution for pit size at a specified location is a precursor to MSD analysis. A plausible mechanistic model is considered for the evolution of pitting corrosion and its probabilistic character. The model focuses on the growth of corrosion pits in an aluminum alloy in an aqueous environment. The main sources of variability in the model are from the mechanical and corrosion properties of the alloy and the electrochemical behavior induced by the environment. The significance of the variables is evaluated by using parameter values and assumed probability distributions which are typical in experimental observations.

DEVELOPMENT OF THE MODEL

The crucial aspect in mechanistically based probability modeling is the description of the damage process. The damage of interest is the growth of corrosion pits. The model is motivated by environmental effects on bare surfaces, e.g., the interior surface of rivet holes. Damage nucleates on bare surfaces as pits formed by localized galvanic corrosion near exposed constituent particles. As pits grow, neighboring particles are exposed and further contribute to growth. The process continues until a critical pit size is reached from which a small corrosion fatigue crack nucleates with high probability. Randomness in material properties and their sensitivity to the environment are represented explicitly. Because a detailed mechanistic model for pit growth is not developed fully, well-established empirical traits are incorporated. The corrosion pit size, as a function of the exposure time to the environment, is the key variable in this effort. The goal is to find the time dependent cumulative distribution function (*cdf*) for pit size. It is the *cdf* which accounts for scatter and which allows for identification, estimation, and prediction of reliability.

Constituent particles behave cathodically or anodically relative to the matrix. Corrosion pits formed by the dissolution of anodic particles terminate their growth, or are at least severely retarded, when the anodic particle is nearly dissolved [1]. Cathodic particles, however, promote dissolution of the adjacent matrix. Thus, cathodic particles are assumed to be critical for pit growth. The particles for 12 different square fields, 800 μm × 800 μm, were analyzed, principally by size and shape, to distinguish the cathodic particles.

Modeling the spatial statistics of particles is not easy [2, 3]; however, some of the properties can be obtained readily. Figure 1 shows a polished section of the rolling surface of

2024-T3 alloy before exposure to any environment. Cross sections of constituent particles, which have random size and shape, are manifest. Notice the particle clustering, where the predominant cluster pattern appears to be somewhat aligned, principally in the rolling direction. Clearly, a cluster may have a long dimension of several hundred μm. Particle clustering and alignment are attributed to processing. Geometrical properties of the particles and clusters, observed on polished sections, are measured from SEM micrographs. Thus, modeling the spatial statistics for particle clustering in the alloy is needed for predictions of the growth of corrosion.

Severe pitting is caused by interaction between the matrix and a cluster or clusters of subsurface particles, which form local galvanic cells to sustain dissolution. Figure 2 shows SEM micrographs of the cross section of pits formed from clusters of constituent particles. The inset shows the pits from the specimen surface. The larger pit is approximately 500 μm long, 70 μm wide at the surface, and 300 μm deep at this section. The overall shape reflects the planar distribution of constituent particles, which happen to be cathodic. An SEM microfractograph of a fatigue crack origin is shown in Figure 3. The crack originates at a pit displayed by the dark region at the center of the microfractograph. The features of the origin are identical to those of the deeper pit in Figure 2. The associated surface features of the fatigue origin, which are not shown, are also identical to those shown in the inset in Figure 2. These comparisons clearly link severe localized pitting to corrosion fatigue crack nucleation. Since particle clustering is critical, it must be modeled appropriately. Major damaged regions in the alloy can range from 50 to 150 μm in width and from 100 to 2,000 μm in length relative to the primary rolling direction [4]. The density of severe pits is approximately one pit/mm^2 [4].

The cluster size was estimated by the nearest neighbor *cdf*, which describes the minimum distance between each particle and its nearest neighbor, computed between centroids. The distances are fit quite well by a Weibull *cdf*, and the parameters, found by maximum likelihood, are as follows: shape parameter, $\hat{\alpha} = 1.80$ and scale parameter, $\hat{\beta} = 42.34 \mu m$. The scatter is 57%, and the mean is $\hat{\mu} = 37.65 \mu m$. The assumed clustering criterion is that two particles are clustered if their distance is less than the mean $\hat{\mu}$. Figure 4 is a spatial plot of the centroids of the cathodic particles on a polished section of the rolling surface of 2024-T3 alloy. The clusters are shown explicitly. A complete description of the cluster analysis is in [3]. Let N_c be the *rv* for the number of cathodic particles in a cluster. The estimated *cdf* for N_c is

$$\hat{p}_k = \text{Pr}\{N_c = k\} = 0.725k^{-2.41}; \quad k \geq 1. \tag{1}$$

The dilemma is that large clusters lead to the most severe damage, but yet, they are rare. For example, in the 7.68 mm^2 observed, only 8 clusters containing more than 9 particles were found of which three had 11, one had 12, one had 15, and one had 22 particles. For an improved estimate additional data are required.

Following [5, 6], it is assumed that pits grow at a constant volumetric rate dV/dt given by

$$dV/dt = \left(MI_{P_o}/nF\rho\right)\exp\left[-\left(\Delta H/RT\right)\right]]$$ (2)

where M is the molecular weight of the material, n is the valence, $F = 96514$ c/mol is Faraday's constant, ρ is the density, ΔH is the activation energy, $R = 8.314$ J/mol-K is the universal gas constant, T is the absolute temperature, and I_{P_O} is the pitting current coefficient. A mature corrosion pit is geometrically quite complex (Figure 2). As a first approximation, the shape is assumed to be half of a prolate spheroid. The orientation of a pit depends on the location on the aircraft. For example, the high-stress region of a rivet hole located on the fuselage is an S-T surface of the alloy. A severe pit emanating from such a location is modeled by a prolate spheroid in which the major axis represents the depth of the pit. The volume is

$$V = \left(2/3\right)\pi a b^2$$ (3)

where a and b are half the lengths of the major and minor axes, respectively. Alternatively, the high-stress region of a rivet hole located on a wing is the S-L surface of the alloy. A severe pit originating from this location should be approximated by a prolate spheroid in which the minor axis represents the depth. The volume of such a shape is similar to (3) except that the roles of the axes are reversed, i.e., a and b are one-half the lengths of the minor and major axes, respectively. Clearly, the location of a severe pit is essential for proper modeling. Herein, the analysis will be restricted to an application representative of the fuselage.

The time dependent behavior of the axes a and b in (3) is required for dV/dt. From observations, it is assumed that the aspect ratio ϕ_k is constant but dependent on the cathodic particle cluster size k. Thus,

$$b/a = \phi_k, \quad k \geq 0, \quad \phi_k \leq 1.$$ (4)

When $\phi_k = 1$, the pit growth is hemispherical, [6]. Since dV/dt is assumed to be constant, but dependent on the cluster size k, it is clear from (2) that the pitting current constant I_{P_O} likewise depends on k. Let a_0 be the initial pit radius, then meshing all of the appropriate equations yields the following:

$$\left(2/3\right)\pi\phi_k^2\left(a^3 - a_o^3\right) = \left(MI_{p_o}(k)/nF\rho\right)\exp\left[-\left(\Delta H/RT\right)\right]t,$$ (5)

Further details are available in [7].

SELECTION OF DETERMINISTIC AND RANDOM VARIABLES

The behavior of an aluminum alloy exposed to an aqueous environment is emphasized. Table 1 lists the deterministic values used in the computations. The temperatures are typical of operating temperatures, and ΔH of 30 kJ/mol is reasonable for aluminum alloys, [8, 9]. Estimation of the aspect ratio ϕ_k is problematic. A rough approximation was obtained by empirically estimating the ratio of the longest and shortest chords of a simple convex shape which circumscribes each cluster. The estimations are fairly good for clusters with less than six particles; however, for the remaining sizes, the data are too limited to be accurate. Since large clusters are most important for damage, the sample average is the only reasonable estimate for ϕ_k.

The cluster size N_c, which is directly related to the material composition, is assumed to be a *rv* with *cdf* given in (1). The initial pit size a_o, which is associated with the size of the cross section of the surface particle, and the pitting current coefficient Ip_o, which reflects the scatter in the electrochemical pit growth, are assumed to be *rvs*. Extensive experimental testing is needed to characterize each *rv*, and because the *cdfs* are unknown, the standard three parameter Weibull *cdf* is assumed for a_o and Ip_o, [7]. These approximations are intended to be typical, but they are not necessarily quantitatively accurate. Table 2 contains the assumed parameter values for the Weibull *cdfs*. The cluster size k and a_o are assumed to be independent, but Ip_o is definitely dependent on k because the electrochemical process depends on the interaction between the particles and the matrix. The assumed numerical values are acceptable for illustration purposes; however, for a specific physical application the identification and estimation of these parameters are very important. This is precisely where accurate and statistical modeling is required.

RESULTS AND DISCUSSION

The *cdf* for the pit size is a function of the underlying *rvs* given the cluster size k. Since it is assumed that the pit size V and depth a are related by (3) and (4), then the computation for the *cdf* for the pit depth $F(d; t)$ is required. Thus, $F(d; t)$ must be computed as an application of law of total probability, i.e.,

$$F(d;t) = \sum_{k \geq 1} \Pr\{a \leq d | N_c = k; t\} \Pr\{N_c = k\} = \sum_{k \geq 1} F_k(d;t) \Pr\{N_c = k\}, \qquad (6)$$

where $F_k(d; t)$ is the conditional *cdf* for the pit depth given a cluster size of k and where the distribution for N_c is given in (1). Given that $N_c = k$, the marginal *cdfs* for $Ip_o(k)$ and a_o are

used to find $F_k(d; t)$. To avoid excessive numerical difficulty, these conditional *cdfs* are estimated by Monte Carlo simulation, [7].

Figure 5 shows the conditional *cdfs* $F_k(x; t)$ for a time $t = 3$ *days* of exposure to the environment, given the cluster size $k = 2, 4, 6, 8$, and 10. The *cdfs* are spread over a broad range as k increases indicating that the variability increases as the cluster size increases. The variability is a reflection of the scatter associated with all of the *rvs*. The median pit depths range from 5.3 to 17.2 μm. The reason for the almost vertical lower tails is that there is a minimum pit depth associated with the assumed model. The minimum depth is quite sensitive to the cluster aspect ratio ϕ_k, temperature T, and the time t.

Figure 6 shows the conditional *cdfs* as a function of time when $t = 1, 2, 3, 4$, and 5 *days*, given a cluster size of $k = 22$. This corresponds to the largest experimentally observed cluster defined by the interparticle distance criterion. Since there was only one such observation, the statistical confidence is limited severely. Because the *cdfs* are essentially parallel, the variability is approximately the same for each *cdf*. Notice that the scatter is rather large. The median depths range from 11.5 to 19.8 μm.

One crucial aspect of mechanistically based probability modeling is the identification of the variables. This application highlights the need for good observations because the most needed information is the most difficult to obtain. Large clusters are the most probable sites for severe damage, but their density is very low, implying limited observations. The need for improved mechanistic descriptions for the pit growth is equally clear. Greater accuracy in modeling directly results in greater accuracy in reliability estimations.

An important application of this effort is the estimation of the frequency of MSD. A typical sheet of 1.6 *mm* thickness may contain many rivet holes with a diameter of about 5 *mm*. The high-stress region in each rivet hole is about 4 mm^2. Therefore, the probability of each rivet hole having at least one large cluster in the high-stress area is high. The probability density function (*pdf*) for the pit size, derived from (6), gives the frequency of pit depths. The *pdf* is used for estimating the probability of finding a pit of a given size in the high-stress area. Figure 7 shows an estimate of the *pdf* for the pit depth when $t = 3$ *days*. The bimodal behavior is apparent. The scatter is considerable, and the median of about 9 μm occurs at the peak of the dominant mode. Since the *pdf* is highly dependent on the preceding assumptions, Figure 7 is only illustrative. Nevertheless, the qualitative character is striking. There is a vast difference in the behavior of pits encompassing small clusters as opposed to those generated by larger clusters. As the time of exposure to the environment increases, the frequency of large pits also increases. Thus, the role of pit size and its *pdf* is a precursor for meaningful MSD assessment.

536

SUMMARY

A probability model has been developed for the growth of corrosion pits for aluminum alloys in aqueous environments. The focus has been the *cdf* for the size of the pit for a fixed time. This model assumes that the growth of corrosion pits can be approximated geometrically by prolate spheroids. The new feature of the modeling is the inclusion of particle interaction within clusters to enhance pit growth.

The probabilistic nature of the pit growth, as a function of the time of exposure to the environment, was assessed primarily as a function of particle cluster size. The effect of temperature was considered. The results are qualitatively consistent, and the trend of the calculations is in accord with typical observations. Also the need for this analysis in MSD assessment was discussed. This effort illustrates that mechanistic probability modeling is needed to adequately describe complex pit growth. It is apparent that better mechanistic understanding of corrosion pit growth and improved characterization of the key *rvs* is warranted.

REFERENCES

1. G. Chen, M. Gao, and R.P. Wei: Microconstituent-Induced Pitting Corrosion in Aluminum Alloy 2024-T3. *Corrosion* **52** (1996) 8-15.

2. D.G. Harlow, N.R. Cawley, and R.P. Wei: Spatial Statistics of Particles and Corrosion Pits in 2024-T3 Aluminum Alloy. *Proc. 15th Canadian Congress of Applied Mechanics*, B. Tabarrok and S. Dost, eds., Fleming Express Press Ltd., Victoria, B.C., vol 1 (1995) 116-117.

3. N.R. Cawley: Models for the Spatial Statistics of Constituent Particles and Corrosion Pits. Ph.D. Dissertation, Lehigh University, Bethlehem, PA, 1995.

4. G. Chen, C.-M. Liao, K.-C. Wan, M. Gao, and R.P. Wei: Pitting Corrosion and Fatigue Crack Nucleation. *Effects of the Environment on the Initiation of Crack Growth*, ASTM STP 1298, W.A. Van Der Sluys, R.S. Piascik, and R. Zawierucha, eds., 1997, to appear.

5. Y. Kondo: Prediction of Fatigue Crack Initiation Life Based on Pit Growth. *Corrosion* **45** (1989) 7-11.

6. D.G. Harlow and R.P. Wei: Probability Approach for Prediction of Corrosion and Corrosion Fatigue Life. *AIAA J.* **32** (1994) 2073-2079.

7. D.G. Harlow and R.P. Wei: Probability Modeling for the Growth of Corrosion Pits. *Structural Integrity in Aging Aircraft*, AD-Vol.47, C.I. Chang and C.T. Sun, eds., ASME, New York, (1995) 185-194.

8.	R.T. Foley: Localized Corrosion of Aluminum Alloys - A Review. *Corrosion* **42** (1986) 277-288.

9.	R.M. Burynski, G.-S. Chen, and R.P. Wei: Evolution of Pitting Corrosion in a 2024-T3 Alloy. *Structural Integrity in Aging Aircraft*, AD-Vol.47, C.I. Chang and C.T. Sun, eds., ASME, New York, (1995) 175-183.
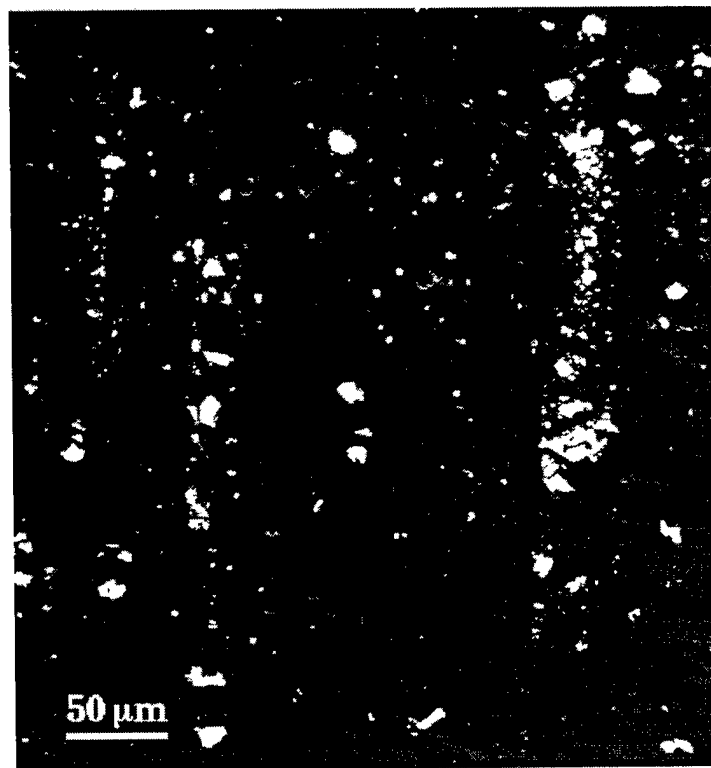
Figure 1. Polished Section of the Rolling Surface of 2024-T3 Aluminum Alloy Before Corrosion.
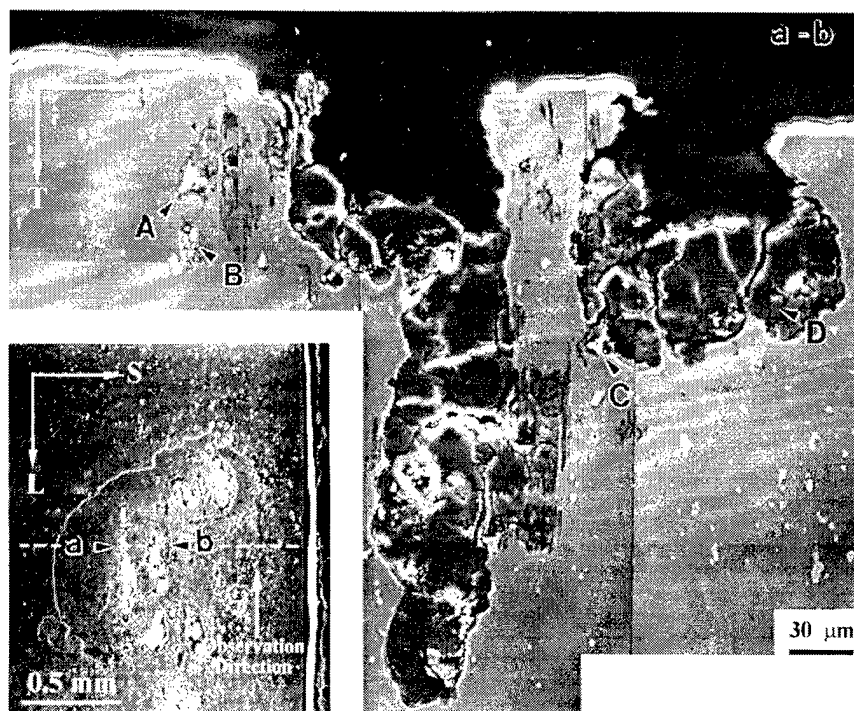
Figure 2. SEM Micrograph of the Cross Section of Severe Corrosion Pits in a 2024-T3 Alloy
(TS) Surface With an Inset Showing the Corresponding Surface Appearance of
the Pits.
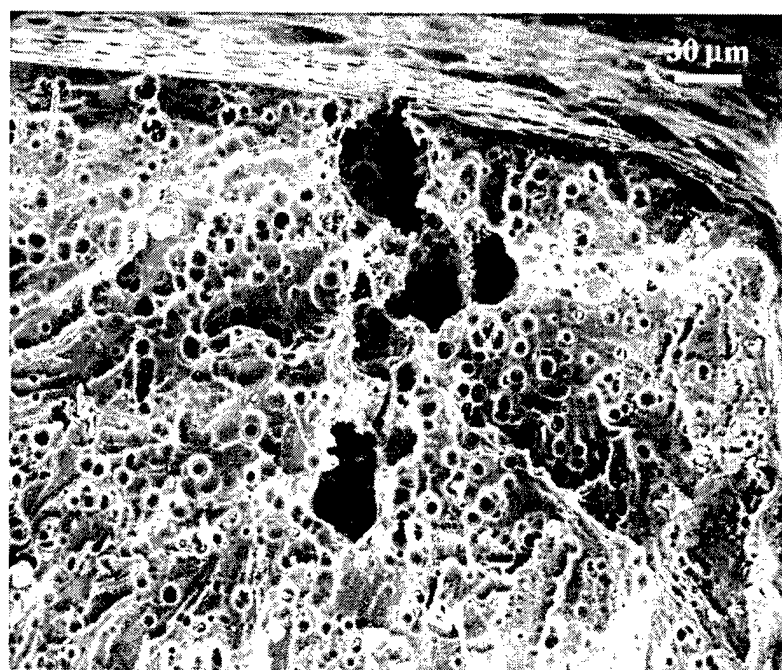
Figure 3. SEM Microfractograph of a Fatigue Fracture Surface of a 2024-T3 Alloy Showing a
Severe Corrosion Pit as the Crack Nucleus.
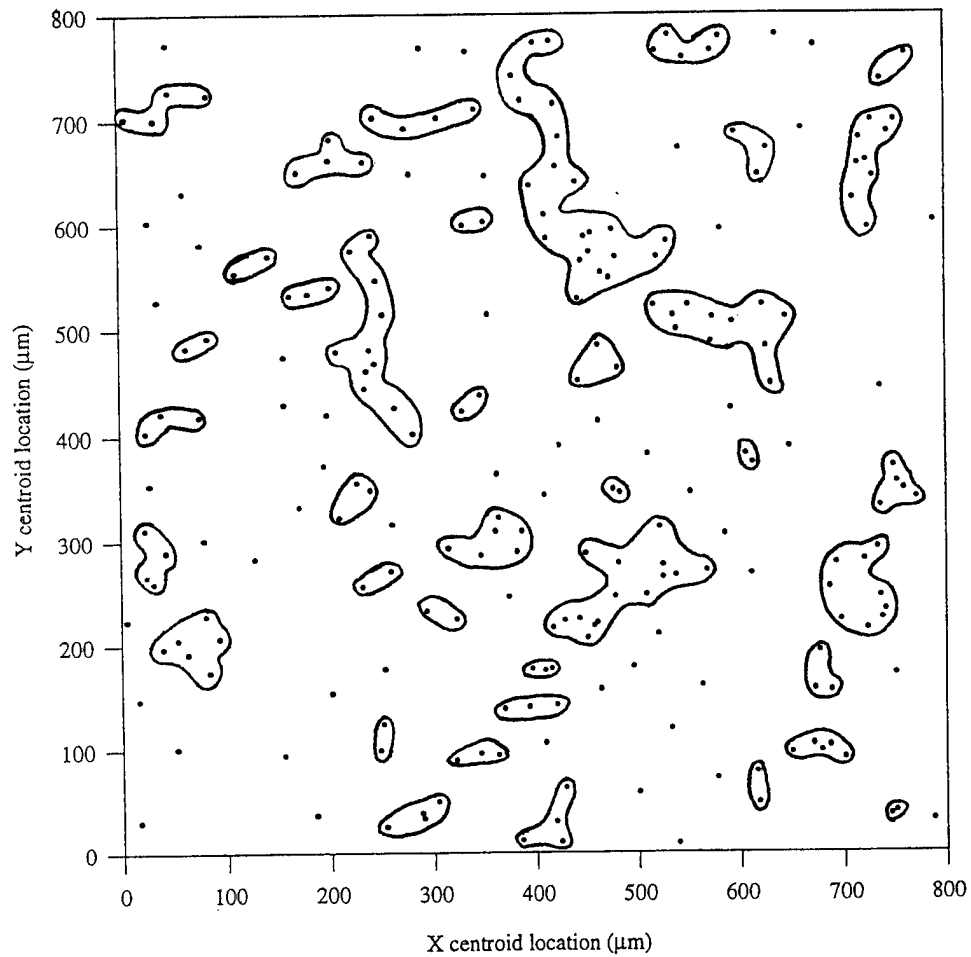
Figure 4. Spatial Plot of Cathodic Particles From a Polished Rolling Surface of a 2024-T3 Alloy Illustrating the Cluster Analysis Based on an Interparticle Distance Criterion.
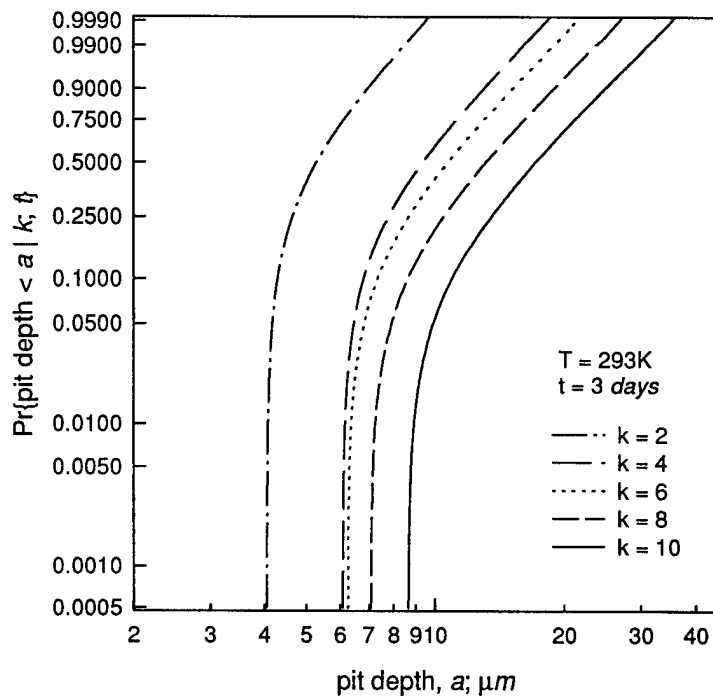
Figure 5. Conditional *cdfs* for Pit Depth When the Number of Particles per Cluster is $k = 2$, 4, 6, 8, and 10, Given an Exposure Time of 3 Days to the Environment at a Temperature of 293 K.
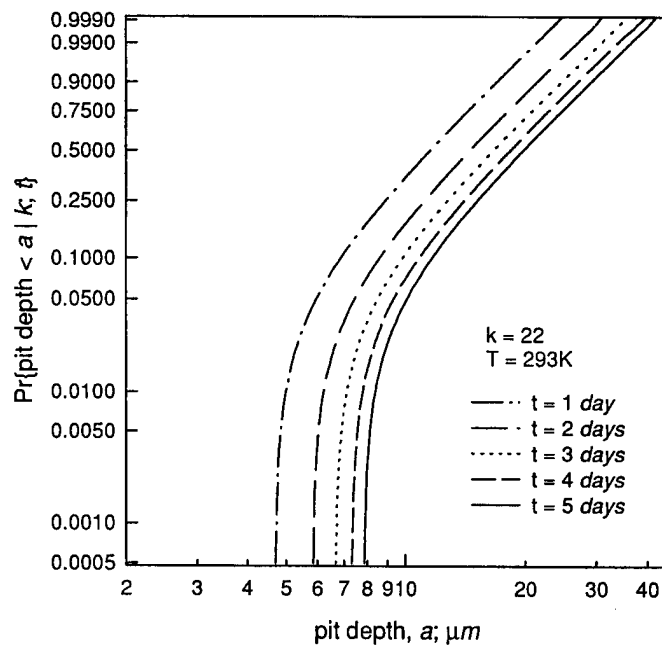
Figure 6. Conditional *cdfs* for Pit Depth When the Exposure Time is $t = 1, 2, 3, 4$, and 5 Days, Given a Temperature of 293 K and 22 Particles per Cluster.

541
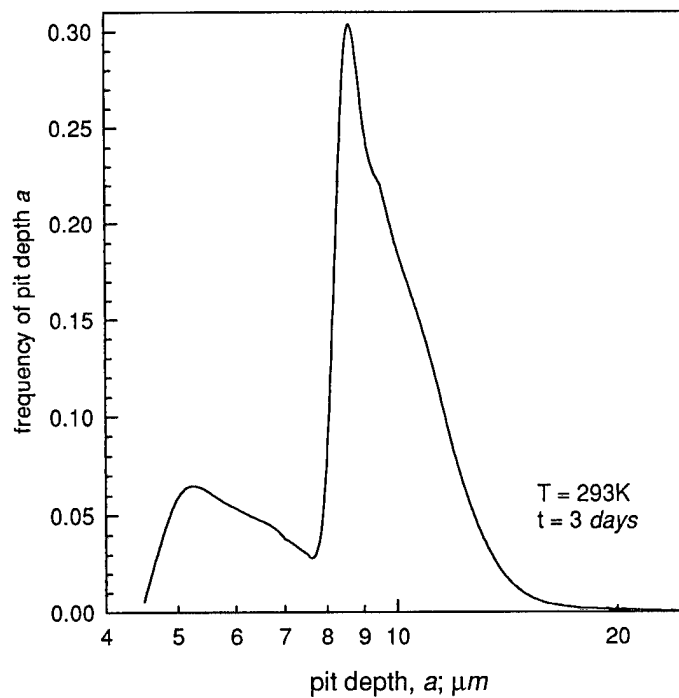
Figure 7. The Predicted *pdf* for the Pit Depth Given an Exposure Time of 3 Days to the Environment at a Temperature of 293 K.

Table 1. Deterministic Parameters Used in the Model for an Aluminum Alloy.

Parameter	Aluminum
Density ρ	2.7×10^6 (gm/m^3)
Molecular weight M	27
Valence n	3
Activation energy ΔH	30 (kJ/mol)
Temperature T	273, 293, 313 (K)

Table 2. Weibull Parameters Used in the Model for an Aluminum Alloy.

rvs	α	β	γ	μ
a_o (m)	12	5.0E-7	1.5E-6	1.98E-6
I_{Po} (c/sec)	1	$k \times 6.5$E-5	6.5E-5	$(k+1) \times 6.5$E-5

PROBABILITY-BASED COST-EFFECTIVE INSPECTION FREQUENCY FOR AGING TRANSPORT STRUCTURES

Victor Li, Ph.D., P.E.
Douglas Aircraft Company
McDonnell Douglas Corporation
Long Beach, California

SUMMARY

In the process of MD-80 supplemental inspection document (SID) development, an exploratory study focused on optimizing the inspection frequency for aircraft structures. An optimization scheme to determine the inspection frequency has been developed based on the expected cost of failure concept. The optimum inspection frequency is determined by minimizing the expected life-cycle costs while satisfying the constraints on specified airplane reliability. It has been shown that the optimum inspection frequency increases as the relative cost of inspection compared to the cost of failure becomes smaller, thus increasing the airplane reliability. The proposed approach can be an effective tool for inspection frequency determination.

INTRODUCTION

In response to the FAA Advisory Circular 91-56, "Supplemental Inspection Program for Large-Transport Categories Airplanes," and CAA Airworthiness Notice No. 89, "Continuing Structural Integrity of Transport Aeroplanes," Douglas Aircraft Company together with the effected operators initiated development of such programs on the DC-8, DC-9, DC-10, and MD-80 commercial transport aircraft. The objective of these programs was aimed to produce a supplemental inspection document (SID) for each aircraft. The DC-8 SID was published in January 1986, the DC-9 SID in June of 1986, the DC-10 SID in January of 1989, and the MD-80 SID is expected to be complete in 1997. The SID program emphasizes reevaluation of the structure known as principle structural elements (PSEs) for damage tolerance and the development of appropriate inspection programs to preclude failure of the PSEs. This evaluation is performed on the basis of current usage, service experience, and state-of-the-art durability and damage tolerance analysis and testing technologies. The results of this SID analysis are used to define a SID inspection program, which is then compared to the current maintenance inspection program, PSE by PSE. Supplemental inspections are scheduled only for those PSEs whose current maintenance programs are found to be inadequate by comparison to the established SID requirements.

DOUGLAS SID PROGRAM

The SID program basically consists of durability and damage tolerance analysis, inspection methods development, formulation of the inspection program, and documentation (Abelkis et al., 1985, Hagemaier et al., 1985, Ludas, 1993).

Durability and Damage Tolerance Analysis

Aircraft Usage Definition

The aircraft usage data for the SID programs are based on evaluation of the in-service utilization of the aircraft. A set of flight profiles are defined to identify the magnitude and variation through the flight of gross weight, payload, fuel, altitude, speed, distance, and any other information required to define the pertinent flight and ground parameters needed to develop the fatigue loads.

Stress Spectrum

A fatigue loads spectrum in terms of gross area stress is developed for each PSE to be analyzed, based on the flight usage profiles specified for the particular aircraft model series. The spectrum represents the following loading environments: flight loads (gust, maneuvers), landing impact, ground loads (taxi, take-off run, landing roll, etc.), ground-air-ground cycles (including fuselage pressurization and engine thrust), and other loading as appropriate. The resulting spectrum is a representative flight-by-flight, cycle-by-cycle random loading sequence that reflects the appropriate and significant elastic airplane dynamic response characteristics.

Selection of the Principal Structural Elements (PSE)

A PSE is that structure whose failure, if it remained undetected, could lead to the loss of the aircraft. Therefore, the selection of a PSE is based on the following considerations: (1) elements in tension or shear; (2) low static margin; (3) high stress concentration; (4) high load transfer; (5) high spectrum severity; (6) high stress in secondary members after primary member failure; (7) materials with high crack growth rates; (8) areas prone to accidental damage or corrosion; (9) component test results; (10) results of full-scale fatigue test; and (11) service experience.

The MD-80 aircraft was determined to have 42 PSEs from all portions of the aircraft.

Damage Tolerance Assessment

A damage tolerance evaluation is made of all the PSE's for the aircraft model. The evaluation includes a determination of the probable location and damage susceptibility (fatigue, accidental damage, corrosion) and is based on analysis supported by test data and service experience. The evaluation includes determining the crack growth time history and aircraft residual strength characteristics.

Linear elastic fracture mechanics are used to perform the damage tolerance analysis. This analysis method has been correlated with test data for both crack growth time histories and residual strength.

The crack growth time history is presented in terms of a characteristic crack dimension versus time in landings or flight hours. The crack growth curve is taken to be an average crack growth curve, because it is based on an average stress spectrum, average material crack growth rate data , and an average fracture toughness allowable.

The residual strength analysis determines the crack length at instability, a_{inst}, i.e., the crack length of the onset of rapid propagation due to limit load.

Nondestructive Inspection (NDI) Methods

A very important part of the SID program is selecting and evaluating state-of-the-art NDI methods applicable to each PSE, and determining a minimum detectable crack a_{det}, for each NDI method. For a given NDI method and PSE, a_{det} corresponds to a crack size with a 90% probability of detection.

Inspection Program

The SID inspection program was based on statistical-probabilistic concepts (Figure 1) of crack existence and detection as related to the fatigue life estimate and damage tolerance characteristics of each PSE and the applicable NDI methods. The current structural maintenance inspection program for each PSE is compared to the SID-established inspection program. If the current inspections equal or exceed the SID requirements for a given PSE, no supplemental inspections are required for that PSE. However, if the opposite is true, supplemental inspection in the form of more frequent inspections or better NDI methods, or both, must be scheduled while retaining all other aspects of the current structural maintenance program. Since the SID program emphasizes detection of cracking that has yet to occur in the fleet, its inspection program is a sampling program with emphasis on high-time aircraft.

Mean Life Estimate

The initial mean life estimate $\overline{N}_{a_{inst}}$, defined as the life to reach instability crack length, a_{inst}, is taken to be the design life or a newly demonstrated life, whichever is longer. This is the total life, which includes crack initiation and crack growth life to a_{inst}. Life is measured in terms of landings or flight hours, usually landings.

The design life for fail-safe structures has historically been defined by Douglas as the service life multiplied by a factor of two. For safe-life structures, the factor is three.

A newly demonstrated life may be based on re-evaluation of past analyses or tests, new tests, or service experience.

Fatigue Life Threshold

Fatigue life threshold defines the life when the SID program should be implemented. For a given PSE population, the fatigue life threshold N_{th} corresponds to a life when the probability of failure per flight reaches 10^{-9}. The meaning of 10^{-9} is that fatigue failure up to N_{th} is extremely improbable. This probability of failure, called failure rate (FR), is the product of the probability of having a crack length $a \geq a_{inst}$ during the N_{th} flight, given no previous failures, times the probability of equaling or exceeding the limit load per flight,

$$FR = [P(\Delta N_{th})_{a_{inst}}][P(^{LL}\!/_{FLT})] = 10^{-9} \tag{1}$$

The probability of encountering a 2.5g limit flight load per flight, $P(^{LL}\!/_{FLT})$, is taken to be 3.33×10^{-4} (Abelkis et al, 1985). This value is based on historical recorded service loads data.

Inspection Sampling Concept

The most direct application of damage tolerance and failure life threshold (N_{th}) concepts to define an inspection program is to inspect a given PSE when the aircraft reaches N_{th} and then to inspect it every $\Delta N_{di}\!/_2$ interval thereafter. ΔN_{di} is the time for a crack to grow from a_{det} to a_{inst}. In the next section, an alternative approach will be introduced to determine the inspection interval on the basis of a "cost of failure" concept.

Using a "fleet leader" sampling concept, consider inspecting n highest time aircraft before they reach N_{th} so that there is a 90% probability of having and detecting one or more cracks among these samples. Mathematically this statistical statement can be expressed as

$$p(c \geq 1) = 1 - \prod_{i=1}^{n}(1 - \Delta p_i P_2)(1 - \tilde{p}_i) = 0.9 \qquad (2)$$

where n = sample size

  c = number cracks

  Δp_i = probability of having a crack $a \geq a_{\text{det}}$ at life N_i

  P_2 = probability of detecting $a \geq a_{\text{det}}$ for a given NDI method

  $\tilde{p}_i$ = probability of detecting a crack $a \leq a_{inst}$ during normal maintenance

  N_i = the life when an operator i is expected to inspect the samples allocated to him. It is the mean life of Start and End dates for all samples of operator i in the sampling population.

If no cracks are found after inspection of n samples, a statement can be made that for a specified (90%) probability of having and detecting a crack the true N_{th}, $\overline{N}_{a_{inst}}$, and $\overline{N}_{a_{det}}$ are larger than the given estimates of N_{th}, $\overline{N}_{a_{inst}}$, and $\overline{N}_{a_{det}}$. Therefore, life estimates are advanced (Figure 2).

OPTIMUM INSPECTION FREQUENCY DESIGN

Cost of Failure

To effectively implement a SID program, identification inspection intervals are an important step to ensure the specified level of reliability. In this study, the concept of the cost of failure is used to formulate an optimization schedule for determining of the optimum inspection frequency for aircraft structures.

The objective function to be minimized is the expected life cycle cost while, at the same time, a prescribed level of reliability is maintained. The expected life-cycle cost $\overline{C}$ consists of the cost of inspection and the cost of failure of airplanes:

$$\overline{C} = n \sum_{i=1}^{Q}[M_i C_{I_i} + C_{f_i} P_f(M_i)] \qquad (3)$$

where

  M_i = total number of periodic inspections for the *ith* PSE in the design life, or a newly demonstrated life, whichever is longer

  n = total number of airplanes in a high-time sample

  Q = total number of PSEs in an airplane

C_{I_i} = cost of one inspection for the ith PSE, including the cost of repairs of the cracked components when fatigue cracks are detected during inspections

$P_f(M_i)$ = probability of failure of the ith PSE in the estimated mean life under M_i periodic inspections

C_{f_i} = cost of failure of the ith PSE, including the cost of PSE component replacement and revenue loss due to service interruptions, etc.

It is noted that the inspection and maintenance cost increase as M_i increases, but the cost of failure decreases since the probability of failure $P_f(M_i)$ decreases as the number of inspection M_i increase. A method for evaluating $P_f(M_i)$ will be introduced in the next section. It is noted that both the cost of inspection C_{I_i} and the probability of failure $P_f(M_i)$ depend on the quality of the inspections. For simplicity in this paper, it is assumed that a specific method of inspection is employed.

The probability of first failure of the *ith* PSE p_{f_i} in n high-time samples, which is related to $P_f(M_i)$, should be less than a prescribed level of failure probability $\bar{p}_{f_i}$.

$$p_{f_i} = 1 - \left[1 - P_f(M_i)\right]^n \le \bar{p}_{f_i}, \quad i=1,\ldots,Q \tag{4}$$

The constraints of Eq. 4 can then be written as

$$P_f(M_i) \le 1 - \left[1 - \bar{p}_{f_i}\right]^{1/n}, \quad i=1,\ldots,Q \tag{5}$$

The equivalent form of Eq. 3 is to minimize each PSE independently:

$$\overline{C}_i = n M_i C_{I_i} + n C_{f_i} P_f(M_i), \quad i=1,\ldots,Q \tag{6}$$

Define $\overline{C}_{r_i} = \overline{C}_i \big/ n C_{f_i}$, a nondimensional relative cost, and $\gamma_i = \dfrac{C_{I_i}}{C_{f_i}}$, then Eq. (6) can be expressed as

$$\overline{C}_{r_i} = \gamma_i M_i + P_f(M_i), \quad i=1,\ldots,Q \tag{7}$$

γ_i is the relative inspection cost compared to the cost of failure. It is an important parameter for the determination of the optimum inspection frequency M_i.

The optimum inspection frequency M_i ($i=1,...,Q$) is obtained by minimizing the relative cost $\overline{C}_{ri}$ given by Eq. 7, without violating the constraint of Eq. 5. Since $P_f(M_i)$ is a nonlinear function of M_i, the optimization is a nonlinear program problem.

Probability of Failure

As stated earlier, the SID programs consider the fatigue life and subsequent crack growth to reach a specified crack length to be a random variable represented by a log-normal distribution. The distribution function is the probability that the crack will reach a size a_{inst} before the service time N (Figure 3). Such a probability is equal to the probability that the crack size at service time N will exceed a_{inst} (Figure 4) (Manning & Yang, 1986). Hence,

$$F_{N(a_{inst})}(N) = P[N(a_{inst}) \le N] = P[a(N) \ge a_{inst}] = p(N, a_{inst}) \tag{8}$$

Assuming the total failure rate within an interval of inspection is denoted by K, then the probability of failure p_f in the time interval is (Yang & Trapp, 1974)

$$p_f = 1 - e^{-K} \tag{9}$$

Dividing the time period between N_{th} and $\overline{N}_{a_{inst}}$ into M periodic inspection interval (Figure 5) and denoting as ΔN and also letting $P_f(j)$ be the probability of failure within j service intervals $[N_{th}, N_{th} + j\Delta N]$, it is obvious that the probability of failure within the first inspection interval $P_f(1)$ is equal to

$$P_f(1) = 1 - e^{-\int_{N_{th}}^{N_{th}+\Delta N} p(N, a_{inst})P(LL/FLT)dN} \tag{10a}$$

The total failure rate in this inspection interval, denoted by K_1, follows from Eq. 8

$$K_1 = -\ln[1 - P_f(1)] \tag{10b}$$

The probability of failure in the first two inspection intervals $[N_{th}, N_{th} + 2\Delta N]$ can be written as

$$P_f(2) = F[a(1)]C_2^{(1)} + F^*[a(1)]V_2 \tag{11}$$

in which a(1) is the crack size at the first inspection time. $F[a(1)] = p(N_{th} + \Delta N, a_{\det})$ is the probability that this crack is detected at $(N_{th} + \Delta N)$ and $F^*[a(1)] = 1 - F[a(1)]$ is the probability of not detecting the crack at $(N_{th} + \Delta N)$. V_2 is the failure probability in $[N_{th}, N_{th} + 2\Delta N]$ under the condition that the crack is not detected at the first inspection. Hence,

$$V_2 = 1 - e^{-\int_{N_{th}}^{N_{th}+2\Delta N} p(N, a_{inst}) P(LL/FLT) dN} \tag{12}$$

The term $C_2^{(1)}$ denotes the failure probability in $[N_{th}, N_{th} + 2\Delta N]$ under the condition that the crack is detected at $(N_{th} + \Delta N)$:

$$C_2^{(1)} = 1 - e^{-K_1} \tag{13}$$

K_1 is the (renewal) total failure rate in $[N_{th} + \Delta N, N_{th} + 2\Delta N]$, which is the same as the failure rate for $P_f(1)$, because the crack is detected and the renewal process for the structure occurs after the first inspection.

The probability of failure in the first three inspection intervals $[N_{th}, N_{th} + 3\Delta N]$ can be written as:

$$P_f(3) = F[a(1)] C_3^{(1)} + F^*[a(1)] F[a(2)] C_3^{(2)} + F^*[a(1)] F^*[a(2)] V_3 \tag{14}$$

where $a(2)$ is the crack size at the second inspection time. The equation is self-explanatory, in which,

$$C_3^{(1)} = 1 - e^{-K_2} \tag{15a}$$

$$C_3^{(2)} = 1 - e^{-K_1} \tag{15b}$$

$$V_3 = 1 - e^{-\int_{N_{th}}^{N_{th}+3\Delta N} p(N, a_{inst}) P(LL/FLT) dN} \tag{15c}$$

where K_2 is the total renewal failure rate in $[N_{th} + \Delta N, N_{th} + 3\Delta N]$, which is the same as the total failure rate for $P_f(2)$:

$$K_2 = -\ln[1 - P_f(2)] \tag{16}$$

550

In a similar fashion, the general solution for the probability of failure within j service interval $[N_{th}, N_{th} + j\Delta N]$ can be obtained recursively as follows:

$$P_f(j) = F[a(1)]C_j^{(1)} + \left\{ \prod_{k=1}^{j-1} F^*[a(k)] \right\} V_j + \delta_{j-3} \sum_{k=2}^{j-1} \left\{ \prod_{m=1}^{k-1} F^*[a(m)] \right\} F[a(k)]C_j^{(k)} \quad (17a)$$

$$V_j = 1 - e^{-\int_{N_{th}}^{N_{th} + j\Delta N} p(N, a_{inst}) P(LL/FLT) dN} \quad (17b)$$

$$C_j^{(k)} = 1 - e^{-K_{j-k}} \quad (17c)$$

$$K_k = -\ln[1 - P_f(k)], \quad k=1,....,j-1 \quad (17d)$$

where $\delta_{j-3} = 1$ if $j-3 \geq 0$ and $\delta_{j-3} = 0$ otherwise.

NUMERICAL EXAMPLE

A typical PSE is used here to demonstrate the approach proposed in this paper. The crack growth time history based on stress spectrum is first evaluated. The residual strength analysis is furnished to obtain instability crack length, $a_{inst} = 0.65$ inch. The detectable mean crack length, a_{det}, is determined to be 0.125 inch under the assumption that eddy current inspection method is used. The design life of the PSE is assumed to be 100,000 landings, and its corresponding fatigue life distribution follows a log-normal distribution with $\overline{N}_{a_{inst}} = 100,000$ landings and a standard deviation of 0.24 (for steel) (Abelkis et al., 1985). The fatigue life threshold of this PSE is obtained as $N_{th} = 33,000$ landings. For simplicity, assume n=1 and Q=1 in this analysis. Figure 6 shows the variation of relative cost $\overline{C}_r$ with the number of inspections under a given relative cost factor γ. The optimum number of inspections during the design life are 8, 12, and 17 for $\gamma = 10^{-2}$, 10^{-3}, and 10^{-4} respectively, with the corresponding probability of the PSE's failure 1.53×10^{-2}, 2.3×10^{-3}, and 7.58×10^{-4}.

A general characteristic observed from this example is that the smaller the value of γ, the higher the optimum number of inspections, M. This characteristic is consistent with our intuition, because the smaller the inspection cost is compared to the cost of failure, the more frequently inspection can be afforded hence effecting a higher fleet reliability.

In the optimization process, it is not necessary to estimate the absolute value of both the cost of inspection C_I and the cost of failure C_f. All one has to estimate is γ, i.e., the

relative importance of C_I to C_f. For instance, if the replacement cost of a PSE is very high, or if its failure has serious consequences, such as loss of airplanes and lives, γ will be very small and hence the optimum inspection frequency M is higher. Thus higher reliability of the airplanes fleet is achieved.

CONCLUSIONS

An optimization scheme for the inspection frequency has been formulated on the basis of the expected cost of failure concept. The optimum inspection frequency is determined by minimizing the expected life-cycle cost while satisfying the constraints on specified airplane reliability. It has been shown that the optimum inspection frequency increases as the relative cost of inspection compared to the cost of failure becomes smaller, thus increasing the airplane reliability more significantly. The proposed approach can be an effective tool for designing inspection program where cost effectiveness is the major concern.

ACKNOWLEDGMENTS

REFERENCES

Abelkis, P. R., Harmon, M. B., and Warren, D. S.: Use of Durability and Damage Tolerance Concepts in the Development of Transport Aircraft Continuing Integrity Program, *International Committee on Aeronautical Fatigue*, Pisa, Italy, May 22-24, 1985.

Hagemaier, D. et al.: Supplemental Inspection of Aging Aircraft, *1985 Air Transport Association Nondestructive Testing Forum*, Miami, Florida, Sept. 1985.

Ludas, K.: Influence of Aging Aircraft Programs on the MD-11 Damage Tolerance Certification Process, *International Committee on Aeronautical Fatigue*, Stockholm, Sweden, June 7-11, 1993.

Manning, S. D. and Yang, J. N.: Advanced Durability Analysis, Vol. I - Analytical Methods, AFWAL-TR-98-3017, 1986.

Yang, J. N. and Trapp, W. J.: Reliability Analysis of Aircraft Structures Under Random Loading and Periodic Inspection, *AIAA Journal*, Vol. 12, Dec. 1974.
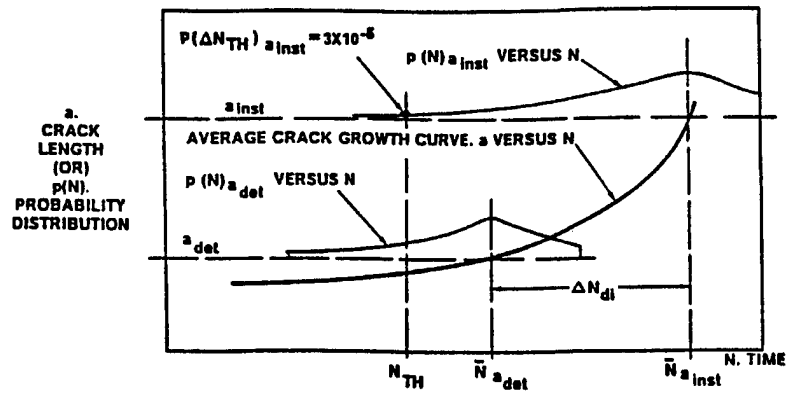
Figure 1. SID Inspection Program Basic Concept.
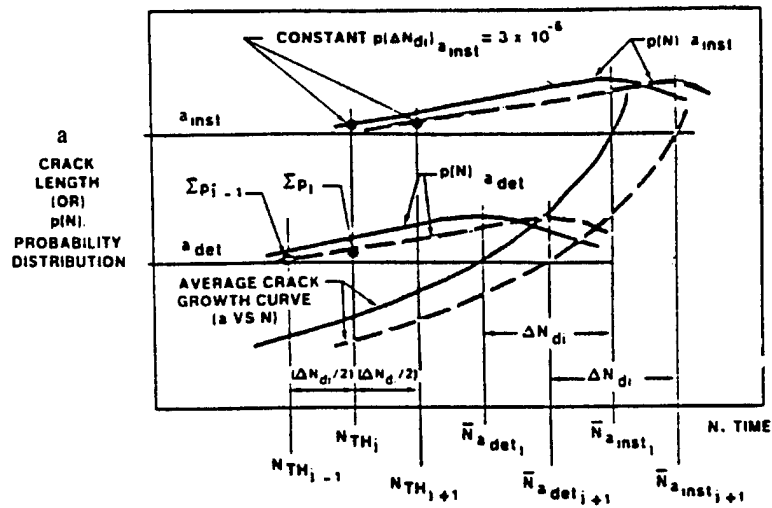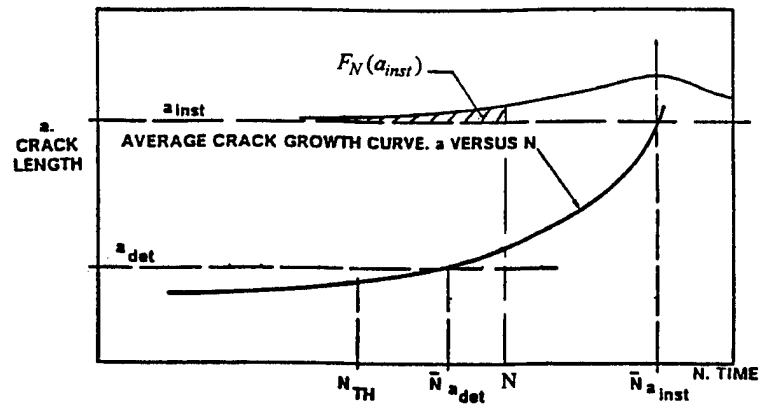

Figure 2. Inspection Sampling Concept.

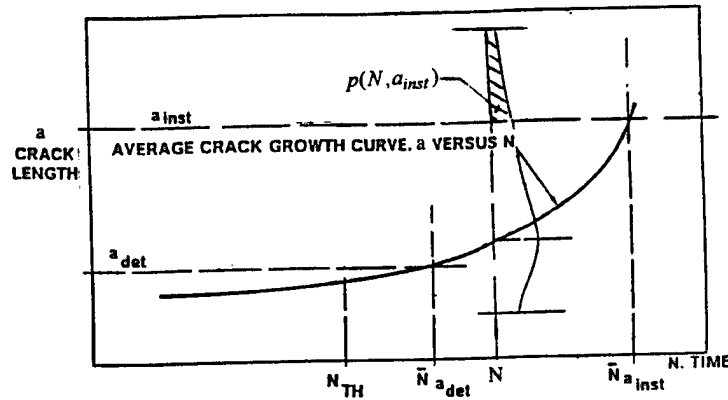Figure 3. Cumulative Distribution of Fatigue Life.

553

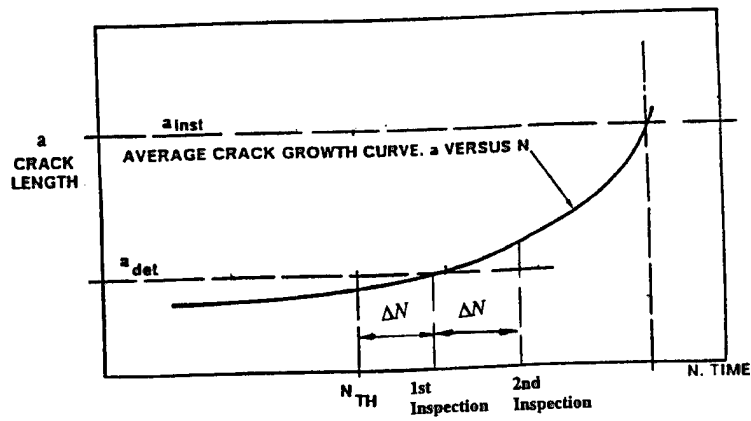Figure 4. Probability of Crack Exceedance.
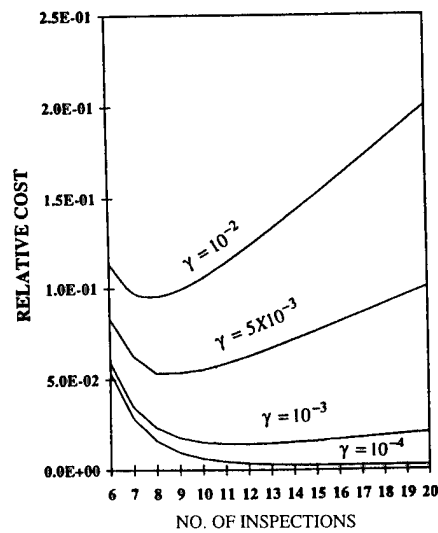

Figure 5. Periodic Inspection.

Figure 6. Relative Cost C_r Versus Number of Inspection.

RESIDUAL STRENGTH PREDICTIONS USING A CRACK TIP OPENING ANGLE CRITERION[1]

D. S. Dawicke
Analytical Services and Materials, Inc.
Hampton, VA 23666

SUMMARY

The fracture behavior of 0.09-inch-thick 2024-T3 aluminum alloy was investigated. Fracture tests were conducted on 1.2-, 3.0-, 12.0-, and 24.0-inch-wide M(T) specimens and 6.0-inch C(T) specimens. The critical CTOA criterion was used in two- and three-dimensional elastic-plastic finite element simulations and predictions. The three-dimensional finite element analysis required a single parameter to predict the fracture behavior (crack tip opening angle (CTOA) = 5.25°). The two-dimensional finite element analysis required a plane strain core height of 0.06 inch in addition to a CTOA of 5.25°. The three-dimensional and two-dimensional finite element predictions were within 4% and 5% of the experimental measurements, respectively.

INTRODUCTION

The NASA Aircraft Structural Integrity Program [1] is developing analysis tools and investigating fracture criteria for applications on the aging commercial aircraft fleet. The fuselage structure of these aircraft contain wide, thin aluminum components and require a fracture methodology to predict residual strength. Several fracture mechanics parameters have been proposed to characterize stable crack growth: crack tip strain [2], energy release rate [3], the J-integral [4], average crack opening angle (COA) [5], crack tip opening displacement (CTOD) [6-8], and crack tip opening angle (CTOA) [9,10].

The prediction of residual strength for large aircraft components requires a fracture criterion that ascertains the material behavior from small laboratory coupons and predicts the behavior of the larger structures. The critical CTOA criteria has been shown to successfully predict the fracture behavior in a wide range of crack configurations for thin-sheet (0.09 inch) aluminum alloys [11, 12]. This criteria assumes that stable crack growth will occur when an angle made by a point (at a fixed distance behind the crack tip) on the upper surface of a crack, the crack tip and a point (again at a fixed distance behind the crack tip) on the lower surface reaches a critical angle. This CTOA is a mild function of the distance behind the crack tip where the angle is measured and a distance of 0.04 inch has been used for consistency between experimental measurements and analyses [11].

The objective of this study was to evaluate the effectiveness of the CTOA criterion on 0.09-inch-thick 2024-T3. Fracture tests were conducted on middle crack tension, M(T), specimens ranging in width from 1.2 to 24.0 inches and 6.0-inch-wide compact tension specimens, C(T). CTOA measurements were made using an optical microscope [13]. Two-dimensional and three-dimensional, elastic-plastic finite element simulations were performed for all experiments and predictions were made for M(T) specimens as wide as 60 inches.

EXPERIMENTAL PROCEDURE

Fracture tests were conducted on M(T) and C(T) specimens machined from 0.09-inch-thick 2024-T3 aluminum alloy sheet. M(T) specimens were tested at a crack length to width ratio of $2a/W = 1/3$ for widths of 1.2, 3.0, 12.0, and 24.0 inches. The 6.0-inch-wide C(T) tests had a crack length to width ratio of $a/W = 0.4$. Critical CTOA measurements were made using an optical method.

Each specimen was fatigue precracked at a stress level that resulted in a stress intensity factor range of $\Delta K = 7$ ksi $\sqrt{inch}$. The tests were conducted under displacement control and measurements of load, crack extension, and critical CTOA were made. The critical CTOA was measured using an optical surface technique [13] that used a long focal length microscope to capture images of the crack tip while the crack was growing. For each image, the surface CTOA was measured 5-10 times at distances of between 0.02 to 0.06 inch behind the crack tip. The measurements for each image were averaged to give a measurement of the CTOA at a distance of 0.04 inches behind the crack tip.

FINITE ELEMENT ANALYSES

The elastic-plastic finite element codes ZIP2D [14] and ZIP3D [15] used the critical CTOA criterion to simulate fracture. The critical CTOA was always evaluated at a distance of 0.04 inch behind the crack tip. Convergence studies were conducted to ensure that the crack tip element was small enough, and for the three-dimensional analysis, that a sufficient number of elements were used to model the through-thickness behavior. The elastic-plastic stress-strain curve used in the finite element analyses is given in Table 1.

Three-Dimensional Analyses

The three-dimensional analyses used 8-noded brick elements to model the crack geometries. Symmetry conditions required that only a quarter of the C(T) specimens and an eighth of the M(T) specimens were needed to be modeled. The mesh sizes used in this study are summarized in Table 2. The critical CTOA was evaluated at the middle of the specimen, 0.04 inch behind the crack front.

Two convergence studies were conducted to determine the minimum element size along the crack plane and the number of elements required to model the thickness. First, two M(T) meshes were created with crack-plane element sizes of 0.04 and 0.02 inch (the former required that the CTOA be analyzed at the first node behind the crack tip and the latter required it to be analyzed at the second node behind the crack tip). Both meshes modeled the half thickness with a single layer of elements. The two analyses produced nearly the same applied load at failure, indicating that convergence was achieved. Thus, the 0.04 inch element size (with CTOA evaluated at the first node behind the crack tip) was chosen for the three-dimensional analyses.

For the second convergence study, the half thickness was modeled with one, two, and three elements. The failure load of the two-layer model was slightly larger than the one-layer model and was nearly the same as the three-layer model, as shown in Figure 1. This indicates that convergence was achieved with two or more layers, thus, the half thickness was modeled with two-layers for all of the three-dimensional analyses.

Two-Dimensional Analyses

The two-dimensional analysis used 3-noded constant strain triangular elements. Symmetry conditions required that only a quarter of the M(T) specimens and half of the C(T) specimens were needed to be modeled. The mesh sizes used in this study are summarized in Table 3. The critical CTOA was evaluated 0.04 inch behind the crack tip.

Four meshes were developed with crack tip element sizes of 0.04, 0.02, 0.01 and 0.005 inch (evaluating the critical CTOA an the 1st, 2nd, 4th, and 8th node behind the crack tip, respectively) for M(T) specimen widths of 1.2, 3.0, 6.0, 12.0, and 24.0 inches. For each mesh, an elastic-plastic finite element analysis was conducted under plane stress conditions and a critical CTOA of 5.25° was used to simulate the fracture behavior. The critical stresses from the analyses are shown in Figure 2. The smaller specimens required smaller element sizes to achieve convergence, while the 12.0- and 24.0-inch-wide specimen exhibited very little influence of mesh size. To balance the convergence requirements of the smaller specimens and the computer resources required to analyze the larger specimens, the two-dimensional meshes used in this study all had the 0.02 inch crack tip elements.

The finite element analyses were conducted for plane strain and plane stress conditions and using a plane strain core. The plane strain core analyses forced a core of elements along the crack plane to be under plane strain conditions while the rest of the specimen was under plane stress conditions, as illustrated in Figure 3. The plane strain core was intended to approximate the three-dimensional constraint that develops at the crack tip [16]. The height of the plane strain core (PSC) generally increases with specimen thickness and was obtained through comparison with three-dimensional analyses.

RESULTS AND DISCUSSION

Fracture tests were conducted on the 0.09-inch-thick 2024-T3 aluminum alloy in both M(T) and C(T) configurations. An optical technique was used to measure the critical CTOA at the surface. Two- and three-dimensional, elastic-plastic finite element analyses were conducted to simulate the fracture experiments.

Critical CTOA Measurements

The surface CTOA measurements were made during fracture testing of the 3.0-, 12.0-, and 24.0-inch-wide M(T) and 6.0-inch-wide C(T) specimens, as shown in Figures 4a and 4b [15, 17]. The trends of the surface CTOA values indicate that: (1) initially the CTOA was high and decreased during a transient period, (2) after a small amount of stable crack growth, the CTOA oscillated about a constant value, (3) the scatter in the measurements was as about ±1°, (4) the CTOA behavior of the different sized M(T) specimens and the C(T) specimen were identical, and (5) the average CTOA for all of the measurements after the transient region was about 5.5°.

Finite Element Analyses

Three-dimensional, elastic-plastic finite element analyses were conducted for each fracture test. Fracture simulations were performed for C(T) specimens ranging in width from 2.0 to 8.0 inches. The critical CTOA required for the analysis to match the critical load of the 6.0 inch C(T) fracture test was 5.25°, as shown in Figure 5. This CTOA value was then used to predict the fracture behavior of the 1.2- to 24.0-inch-wide M(T) tests, as shown in Figure 6. The M(T) finite element predictions were all within 4% of the experimental measurements. The critical CTOA of 5.25° was within the scatter band and slightly below the mean of the experimental surface measurements.

The critical CTOA (5.25°) determined by the three-dimensional finite element analyses was used to predict fracture in two-dimensional analyses. Plane stress and plane strain analyses were conducted for both the C(T) and M(T) fracture tests, as shown in Figures 7 and 8 respectively. Neither plane stress nor plane strain analyses were able to predict the experimental measurements. The plane strain predictions overpredicted the critical stress of the smaller specimens and underpredicted the larger specimens. The plane stress predictions were reversed from the plane strain, underpredicting the critical stress of the smaller specimens and overpredicting the larger specimens. The difference between the plane stress and plane strain predictions were greatest for the large specimens, diverging as specimen size increased. Two- and three-dimensional finite element predictions were performed for M(T) specimens up to 60.0 inches wide. For the 60.0-inch-wide M(T), the plane stress analysis

overpredicted and the plane strain analysis underpredicted the three-dimensional critical stress by 13% and 38%, respectively.

The plane strain core concept was used to approximate the through-thickness constraint in a two-dimensional finite element analysis. A plane strain core height of PSC = 0.06 inch was determined to best fit the experimental measurements, as shown by the dashed line in Figures 7 and 8. The two-dimensional predictions using the plane strain core were within 3% of the experimental measurements from the M(T) fracture tests and about 5% below the measured critical stress of the 6.0-inch-wide C(T) test. The C(T) predictions were consistently about 5% below the three-dimensional fracture predictions for specimen widths ranging from 2.0 to 8.0 inches.

CONCLUDING REMARKS

The fracture behavior of 0.09-inch-thick, 2024-T3 aluminum alloy was investigated. Fracture tests were conducted on 1.2-, 3.0-, 12.0-, and 24.0-inch-wide M(T) specimens and 6.0-inch C(T) specimens. The critical CTOA criteria was used in two- and three-dimensional elastic-plastic finite element simulations and predictions. The three-dimensional finite element analysis required a single parameter to predict the fracture behavior (CTOA = 5.25°). The two-dimensional finite element analysis required a plane strain core height of 0.06 inch. The results from this study indicate:

1. The three-dimensional finite element analyses required a critical CTOA of 5.25° to simulate the fracture behavior of the 6.0-inch-wide C(T) specimens. This angle was within the scatter band and slightly below the mean of the experimental surface measurements.

2. The critical CTOA required to match the 6.0-inch-wide C(T) was used to predict the fracture behavior of the M(T) specimens. These predictions were within 4% of the experimental measurements for specimens ranging in width from 1.2 to 24.0 inches.

3. The two-dimensional plane strain and plane stress analyses were as much as 10% different from the experimental measurements and did not follow the trends of the measurements. Furthermore, the three-dimensional analysis indicates that plane stress and plane strain predictions would become worse as the specimen size increases.

4. A plane strain core height of PSC = 0.06 inch was required for the two-dimensional analyses to match the measured fracture behavior and the three-dimensional fracture predictions for large specimen sizes. These predictions were within 5% of the experimental measurements.

ACKNOWLEDGMENTS

REFERENCES

1. Harris, C. E., "NASA Aircraft Structural Integrity Program," NASA TM-102637, April 1990.

2. Orowan, E., "Fracture and Strength of Solids," Report of Progress in Physics, Physical Society of London, Vol. 12, pp. 185-233, 1949.

3. Broberg, K. B., "On Stable Crack Growth," Journal of the Mechanics and Physics of Solids, Vol. 23, 1975, pp. 215-237.

4. Rice, J. R., "A Path Independent Integral and the Approximate Analysis of Strain Concentration by Notches and Cracks," ASME Journal of Applied Mechanics, Vol. 35, 1968, pp. 368-379.

5. Kanninen, M. F., "The Analysis of Stable Crack Growth in Type 304 Stainless Steel," in Proceedings of the International Conference of Fracture, pp. 1759-1768 (1980).

6. Wells, A. A., "Unstable Crack Propagation in Metals: Cleavage and Fast Fracture," in Proceedings of the Cranfield Crack Propagation Symposium, Vol. 1, 1961, pp. 210-230.

7. Wells, A. A., "Application of Fracture Mechanics at and Beyond General Yielding," British Welding Journal, Vol. 11, 1961, pp. 563-570.

8. Wells, A. A., "Notched Bar Tests, Fracture Mechanics and Brittle Strengths of Welded Structures," British Welding Journal, Vol. 12, 1963, pp. 2-13.

9. Anderson, H., "Finite Element Representation of Stable Crack Growth," Journal of Mechanics and Physics of Solids, Vol. 21, 1973, pp. 337-356.

10. de Koning, A. U., "A Contribution to the Analysis of Quasi Static Crack Growth in Steel Materials," in Fracture 1977, Proceedings of the 4th International Conference on Fracture, Vol. 3, pp. 25-31.

11. Dawicke, D. S., Newman, J. C., Jr., Sutton, M. A., and Amstutz, B. E., "Influence of Crack History on the Stable Tearing Behavior of a Thin-Sheet Material with Multiple Cracks," NASA Conference Publication 3274, pp. 193-212, September 1994.

12. Newman, J. C., Jr. and Dawicke, D. S., "Fracture Analysis of Stiffened Panels Under Biaxial Loading with Widespread Cracking," AGARD-CP-568, pp. 3-1 - 3-16, December 1995.

13. Dawicke, D. S. and Sutton, M. A., "Crack Tip Opening Angle Measurements and Crack Tunneling Under Stable Tearing in a Thin Sheet 2024-T3 Aluminum Alloy, NASA-CR 191523, September 1993.

14. Newman, J. C., Jr., "Finite-Element Analyses of Fatigue Crack Propagation-- Including the Effects of Crack Closure," Ph.D. Thesis, Virginia Polytechnic Institute and State University, Blacksburg, VA, May 1974.

15. Shivakumar, K. N. and Newman, J. C., Jr., "ZIP3D - An Elastic and Elastic-Plastic Finite-Element Analysis Program for Cracked Bodies," NASA TM-102753, 1990.

16. Hom, C. L. and McMeeking, R. M., "Large Crack Tip Opening in Thin, Elastic-Plastic Sheets," International Journal of Fracture, Vol. 45, pp. 103-122, 1980.

17. Sutton, M. A., Dawicke, D. S., and Newman, J. C., Jr., "Orientation Effects on the Measurement and Analysis of Critical CTOA in an Aluminum Alloy Sheet," Fracture Mechanics: 26th Volume, ASTM STP 1256, W. G. Reuter, J. H. Underwood, and J. C. Newman, Jr., Eds., American Society for Testing and Materials, Philadelphia, 1995.

Table 1. Elastic-Plastic Stress-Strain Curve.

Stress (ksi)	Strain	
0.0	0.0	
50.0	0.00483	E = 10350 ksi
56.5	0.015	
62.5	0.04	$\mu = 0.3$
68.5	0.1	
71.0	0.16	
71.0	0.2	

Table 2. Three-Dimensional Finite Element Mesh Sizes.

M(T) Specimens		C(T) Specimens	
Width	Number of Nodes	Width	Number of Nodes
1.2	513	2.0	1596
3.0	1224	4.0	2454
6.0	2008	6.0	3900
12.0	4692	8.0	6261
24.0	5887		
60.0	8656		

Table 3. Two-Dimensional Finite Element Mesh Sizes.

M(T) Specimens		C(T) Specimens	
Width	Number of Nodes	Width	Number of Nodes
1.2	344	2.0	858
3.0	702	4.0	1865
6.0	2432	6.0	2332
12.0	3026	8.0	3249
24.0	5010		
60.0	7322		
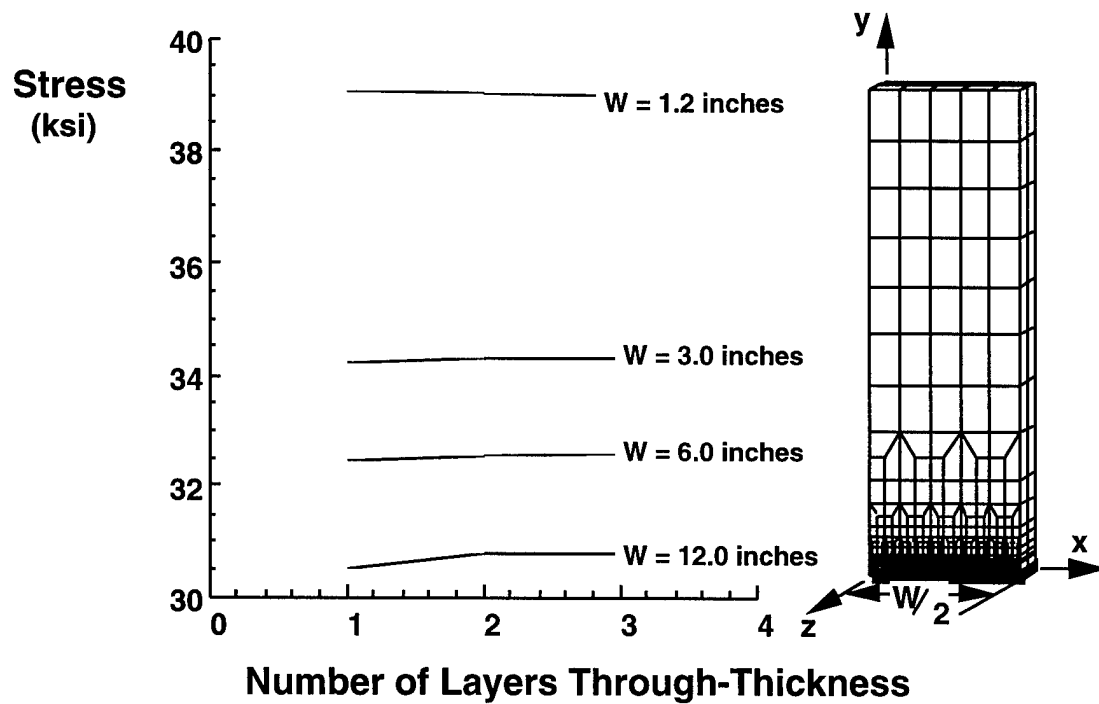
Figure 1. Three-Dimensional Finite Element Analysis Through-Thickness Convergence Study.
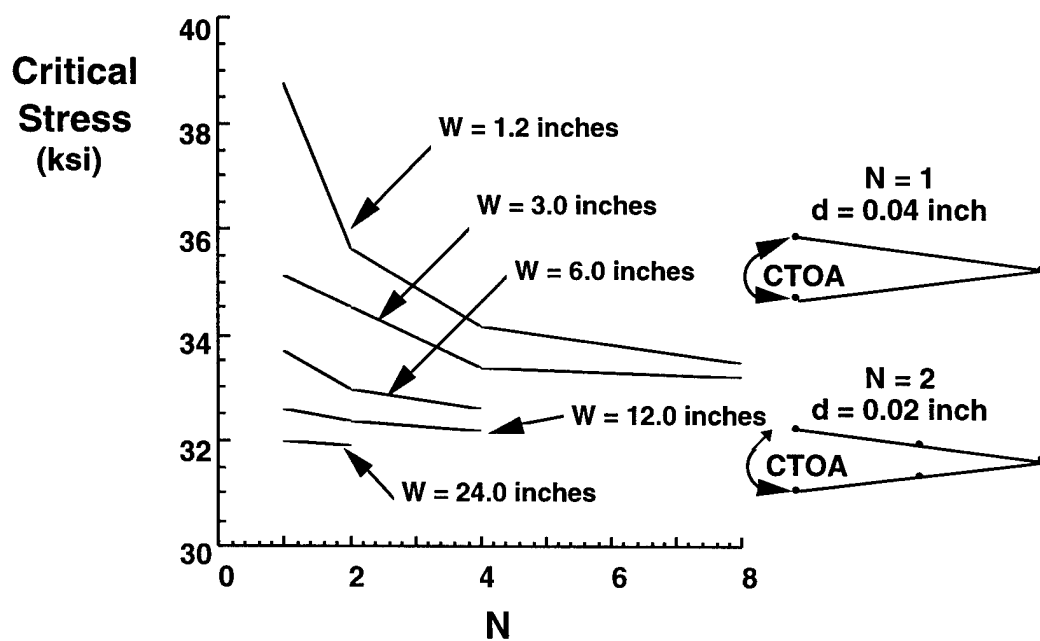
Figure 2. Convergence Study for the Two-Dimensional Finite Element Analyses.
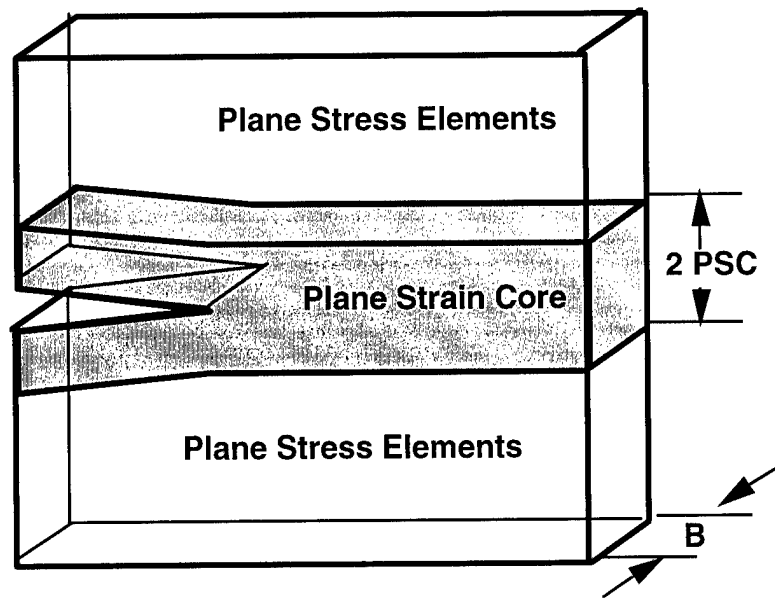
Figure 3. Illustration of the Plane Strain Core Concept.

a. Full Crack Extension Range

b. Expanded Crack Extension Range
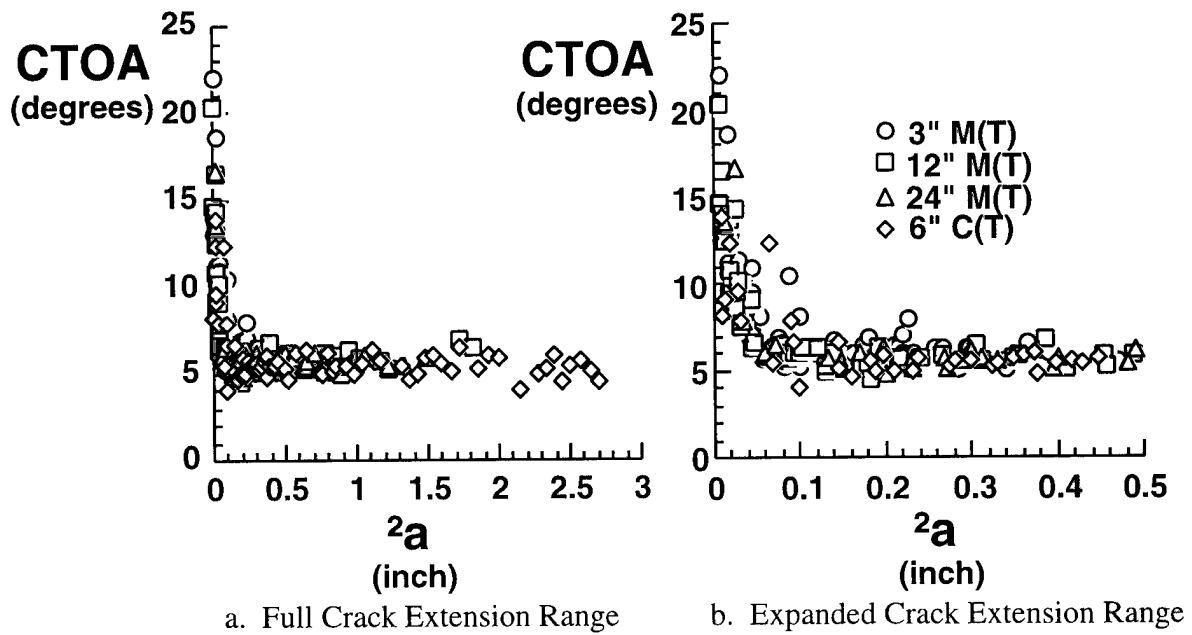
Figure 4. Surface CTOA Measurements for 2024-T3 Aluminum Alloy Fracture Tests.
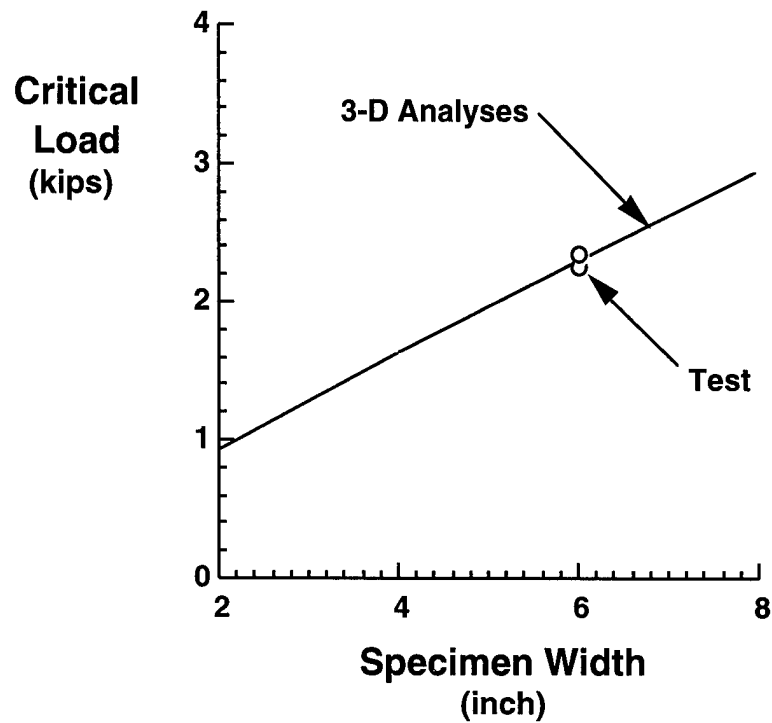
Figure 5. Critical Load Measured in the C(T) Fracture Tests and the Three-Dimensional
Finite Element Simulations.
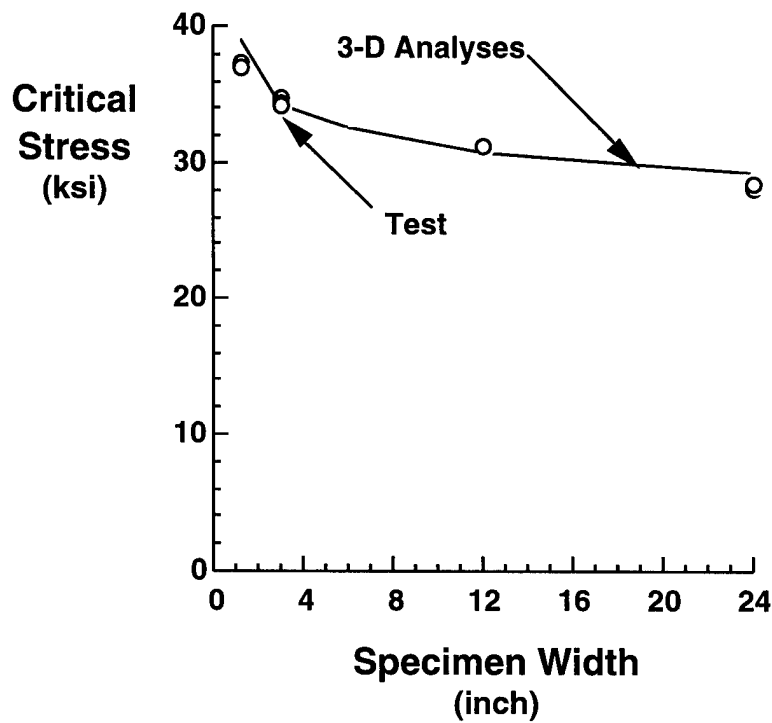
Figure 6. Critical Stress Measured in the M(T) Fracture Tests and the Three-Dimensional
Finite Element Predictions.
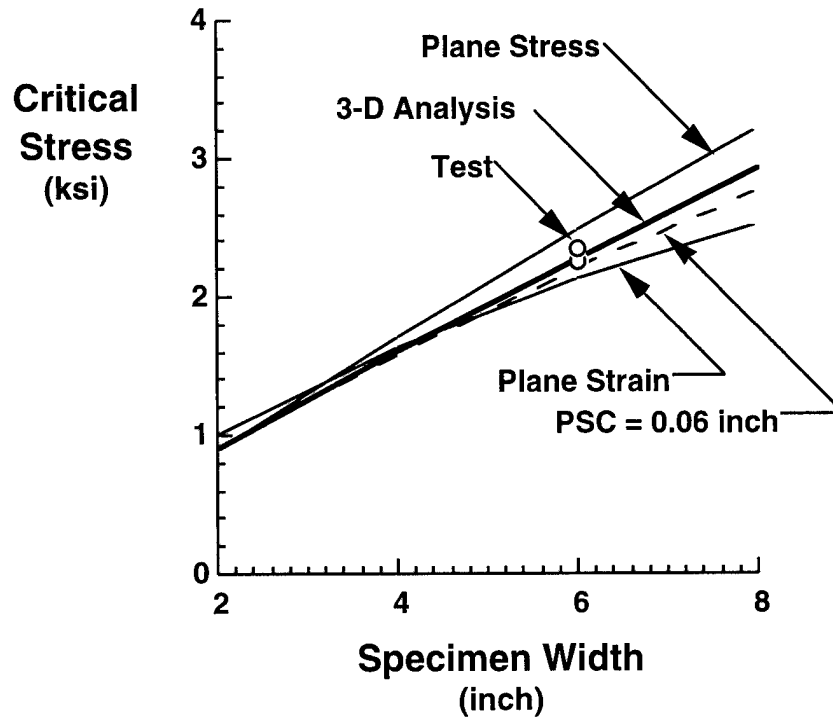
Figure 7. Critical Load Measured in the C(T) Fracture Tests, the Three-Dimensional Finite Element Simulations, and the Two-Dimensional Finite Element Predictions.

Figure 8. Critical Stress Measured in the M(T) Fracture Tests, the Three-Dimensional Finite Element Predictions, and the Two-Dimensional Finite Element Predictions.

A REVIEW OF ROTORCRAFT STRUCTURAL INTEGRITY/ AIRWORTHINESS APPROACHES AND ISSUES

Dr. Daniel P. Schrage
Center of Excellence in Rotorcraft Technology (CERT)
Codirector, Aerospace Systems Design Laboratory (ASDL)
School of Aerospace Engineering
Georgia Institute of Technology
Atlanta, GA 30332-0150

ABSTRACT

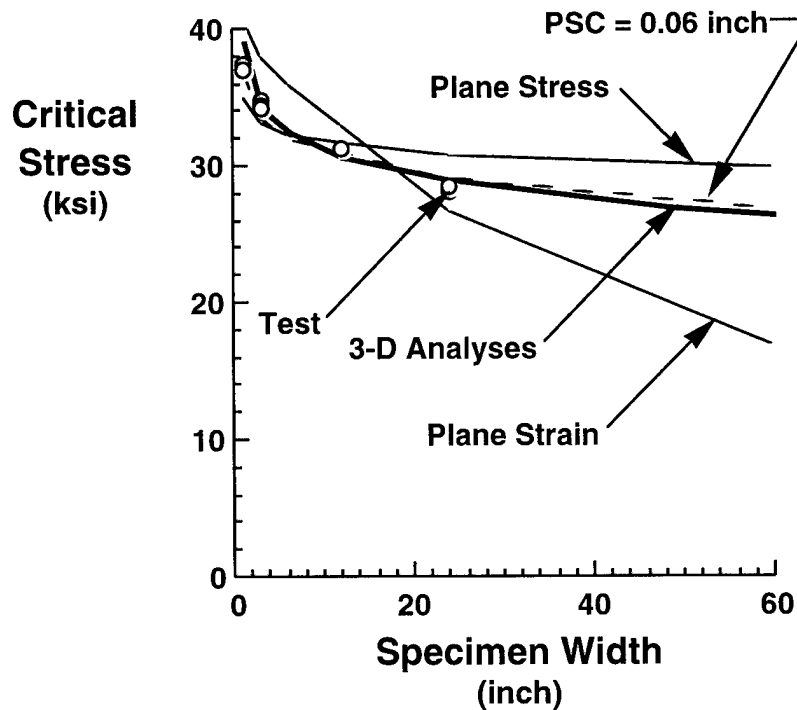Rotorcraft are versatile machines that perform a variety of civil and military missions, thereby making fleet usage often difficult to track. Because the rotor system(s) and other dynamic components are sized and designed principally on oscillatory loads, fatigue analysis and component tests form a substantial part and cost of a development program. While the fixed-wing community has moved from a safe-life (1950s) to fail-safe (1960s) to damage tolerant (1970s) structural design philosophy for the entire aircraft, many rotorcraft dynamic component lives are still calculated using a safe-life design approach. This conservative approach is principally due to the uncertainty in rotor loads prediction in both the low- and high-speed flight regime. The fact that rotorcraft have virtually six degrees of freedom maneuverability capability in low speed provides incomparable agility (to fixed-wing aircraft), but complicates flight envelope definition and provides an extremely complex multidisciplinary environment and unique interactions with the environment (terrain, earth boundary layer turbulence, wake induced from obstacles, etc.). In the relatively high-speed flight regime (-120 to 180 knots for helicopters) the aerodynamic load gradient across the main rotor disk transcends the entire subsonic, and a substantial portion of the transonic, regime (mach number 0 to 0.95). Stalling on the retreating blade side of the main rotor disk and compressibility on the advancing blade side produces extreme complications for rotor loads prediction. Military helicopters in the past have included ballistic damage tolerant and fail-safe design approaches, and new military rotorcraft developments, the V-22 Tilt Rotor Aircraft (Osprey) and the RAH-66 Conventional Helicopter (Comanche), are taking more of an overall damage tolerant and fail-safe approach. However, a piecemeal structural design philosophy is still being used for most rotorcraft and active research, although at a low level, has been ongoing to move to a more integrated structural design philosophy. Army, Air Force, Navy, the National Aeronautics and Space Administration (NASA), and the Federal Aviation Administration (FAA) have all had small efforts without any coordinated, sustained effort. The Army has had several false starts at initiating a Helicopter Structural Integrity Program (HSIP). The Air Force has supported efforts to apply the fixed wing damage tolerance approach (ASIP) to its special operations helicopters. The Navy has developed a structural monitoring system based on the regime recognition concept for fatigue tracking of individual dynamic components. NASA has continued a low level effort to develop fracture

mechanics databases for metals and composites. The FAA has developed a low-level Research Project Description entitled: Rotorcraft Structural Integrity and Safety Issues. With the recent establishment of the National Rotorcraft Technology Center (NRTC), involving industry, government, and universities, perhaps a more collaborated sustained effort can occur. An NRTC initiative in Health Usage Monitoring Systems (HUMS), involving all four major rotorcraft manufacturers, is underway. This presentation will review some of the rotorcraft structural integrity/airworthiness approaches and issues.

INTRODUCTION

While rotorcraft are extremely versatile machines and have a variety of civil and military applications, they are extremely complex machines to design, analyze, build and certificate. The multidisciplinary complexity of rotorcraft is illustrated in Figure 1. In low-speed flight the vortices shed from each blade interact with the next blade and the rotor wake below the rotor interacts with the airframe and the surrounding environment. In high-speed flight, the differential velocities seen across the rotor disk by the advancing and retreating blades cut across the subsonic flow regime and deep into transonic flow. The faster the helicopter goes the more the retreating blade is stalled, as the velocity differential between forward flight and rotor rotational speed approaches zero and causes it to operate at higher and higher local blade angles of attack. This flow environment is further illustrated in Figure 2 and shows that the tip of the retreating blade is stalled and that further inboard reverse flow (trailing edge to leading edge) is encountered. On the contrary, the advancing blade is operating at very small local angles of attack (even negative) and the tip is experiencing extreme compressibility effects with a resultant drag rise. To keep the rotor from rolling to the left (due to the asymmetric lift distribution) most of the lift on the advancing side cannot be used and the working section of a rotor in forward flight is mostly the forward and aft sections.
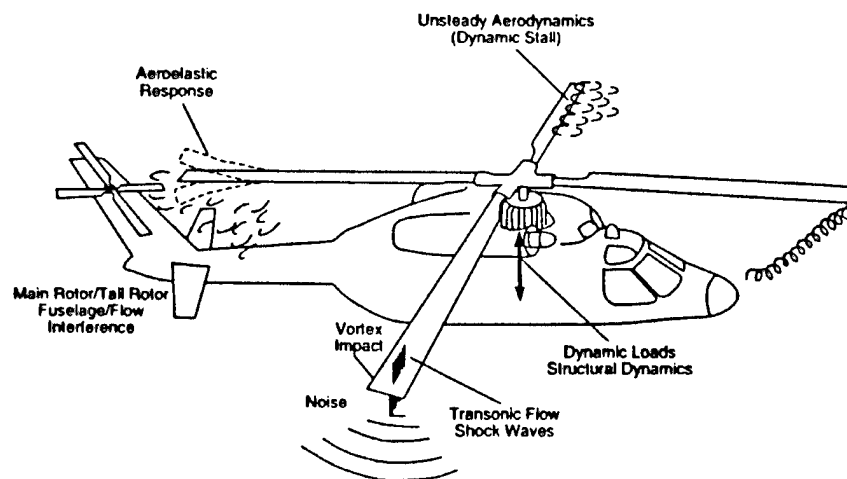
Figure 1. Rotorcraft Multidisciplinary Complexity.
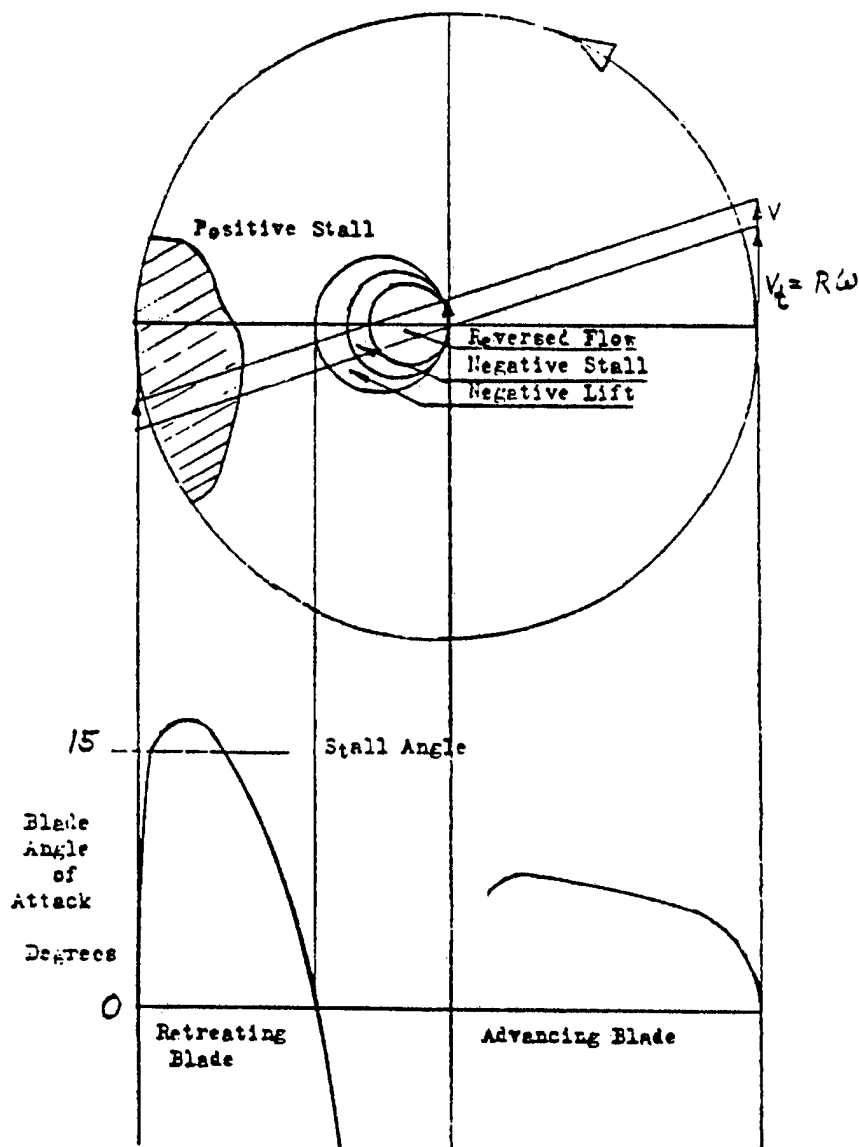
Figure 2. The Flow Environment.

Rotorcraft have properly been called "aeroelastic machines" and this is illustrated by the interdisciplinary interactions for the main lifting rotor in Figure 3. In addition to the complex aerodynamics discussed in the preceding paragraph substantial dynamics (both structural and kinematic) are also involved. Structural dynamics, associated with high-aspect ratio blades coupled with a complex drive system and a relative soft fuselage (due to cutouts for doors, etc.), are strongly coupled with the complex aerodynamics. Transformations between rotating and dynamic components and the fact that the flight controls are directly coupled in both the stationary and rotating environment provide substantial kinematics complexity. All of this complexity is illustrated by a number of feedback loops in Figure 3.
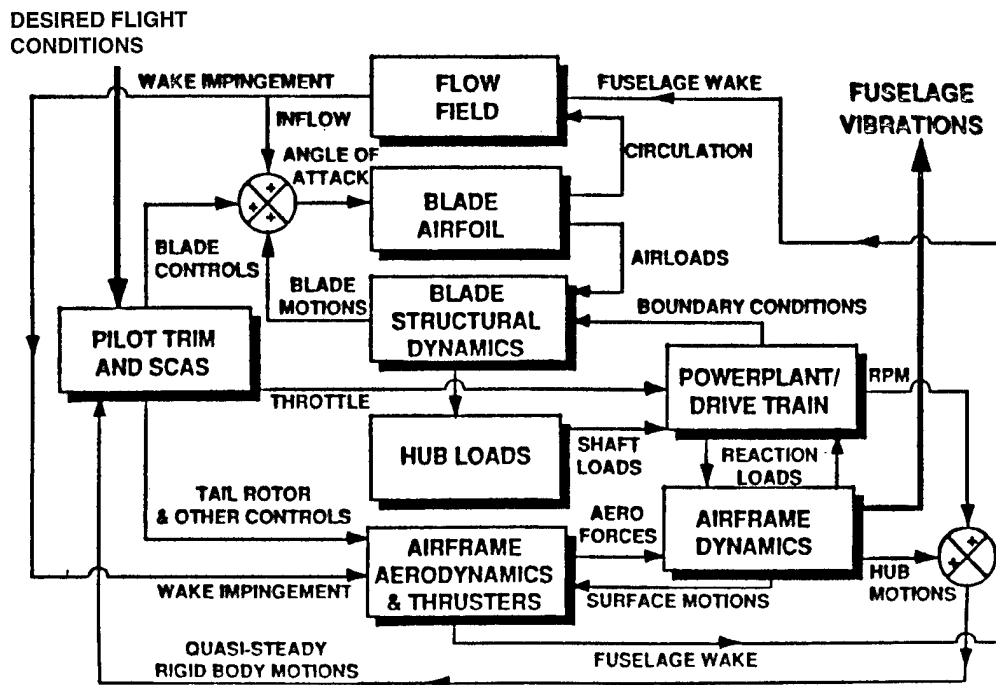
Figure 3. Rotorcraft Interdisciplinary Interactions for Main Lifting Rotor.

For all the complexity that rotorcraft entail, they are truly elegant machines in that they provide six degrees of freedom control in hover, low-speed flight (all directions), and forward flight with only two devices (lifting rotor and engine) and are the most agile machines, in terms of turning rate, as illustrated in Figure 4. The ability to turn 80 degrees per second without altitude loss is remarkable, but readily realized in most rotorcraft in low-speed flight.
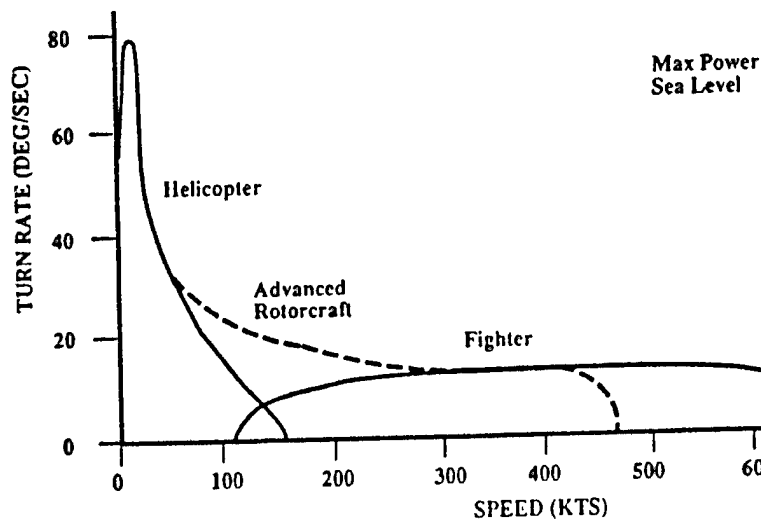
Figure 4. Rotorcraft are Agile Machines in Terms of Turning Rate.

STRUCTURAL DESIGN PHILOSOPHIES

While a safe life structural design philosophy has served the helicopter industry well during its early years of development, there has been a continuing interest since the mid 1970s in trying to replace it with a less conservative, more affordable approach based on damage-tolerant and/or fail-safe approaches. Following the major Army helicopter development programs of the 1970s (UTTAS- UH-60 Black Hawk; AAH- AH-64 Apache), the American Helicopter Society (AHS) hosted a Specialists' Meeting on Helicopter Fatigue Methodology [1]. A highlight of this Meeting was the presentation of the manufacturers' (U.S. and Europe) fatigue methodology based on a calculated fatigue life of a hypothetical helicopter component. Using various treatments of the same basic data, the seven companies calculated fatigue lives for the same component (a pitch link) with variations from a low of 745 hours to a life in excess of 1,000,000 hours. While all predicted lives could be considered conservative, the sensitivity of calculated fatigue life to minute variations in critical values of the parameters indicated that any arbitrarily selected schedule or technique may produce a highly erroneous estimate of fatigue life. Subsequent to this Specialists Meeting the Structures and Materials Panel of the Advisory Group for Aerospace Research and Development (AGARD) published a Helicopter Fatigue Design Guide [2] and a follow-up AHS Helicopter Fatigue Specialists' Meeting was held in 1984 [3].

Following these meetings, the Army pushed for a statistical approach and developed Aeronautical Design Standard (ADS)-29: Structural Design Criteria For Rotary Wing Aircraft [4], which specified combined minimum fatigue strength, severe loads, and severe usage with Miner's cumulative damage theory to compute fatigue lives with a remote probability of failure. The objective of the Army was to quantify this remote probability of failure with the goal of achieving a one in a million failure which means a reliability of 0.999999 (six nines). Later in the 1980s the Army tried to initiate an Army Helicopter Structural Integrity Program (HSIP) [5]. Rationale for this initiative was that then current rotorcraft design and development specifications were outdated and required extensive revision to keep pace with emerging technologies. It recommended that the Army establish overall statistical reliability as a design goal, since it was felt that a statistically based design requirement is compatible with any chosen design methodology, and it would provide the Army with a means to establish, evaluate, and substantiate structural integrity. An alternative to either safe-life or damage-tolerant design was proposed as the total life approach, which was intended to marry the two concepts. The proposed total life methodology is illustrated in Figure 5 and was developed for metallic structures. It was intended to encompass both the time to crack initiation size and the time to propagate the crack to failure. The requirements for crack initiation would guarantee durability while the requirement for crack growth would imply a damage-tolerant design. The time to crack initiation could be determined by a local strain-life approach which bounds the fatigue life for each selected maximum load value. The local strain-life approach would mimic a safe-life design by utilizing a strain-life curve and a cumulative damage algorithm such as the Palmgren-Miner rule. For the crack propagation portion of the total life approach, the crack growth for metallic structure can be

predicted by various models relating crack growth rates and the stress intensity factors [5]. While the total life approach was proposed it has not been developed or implemented.
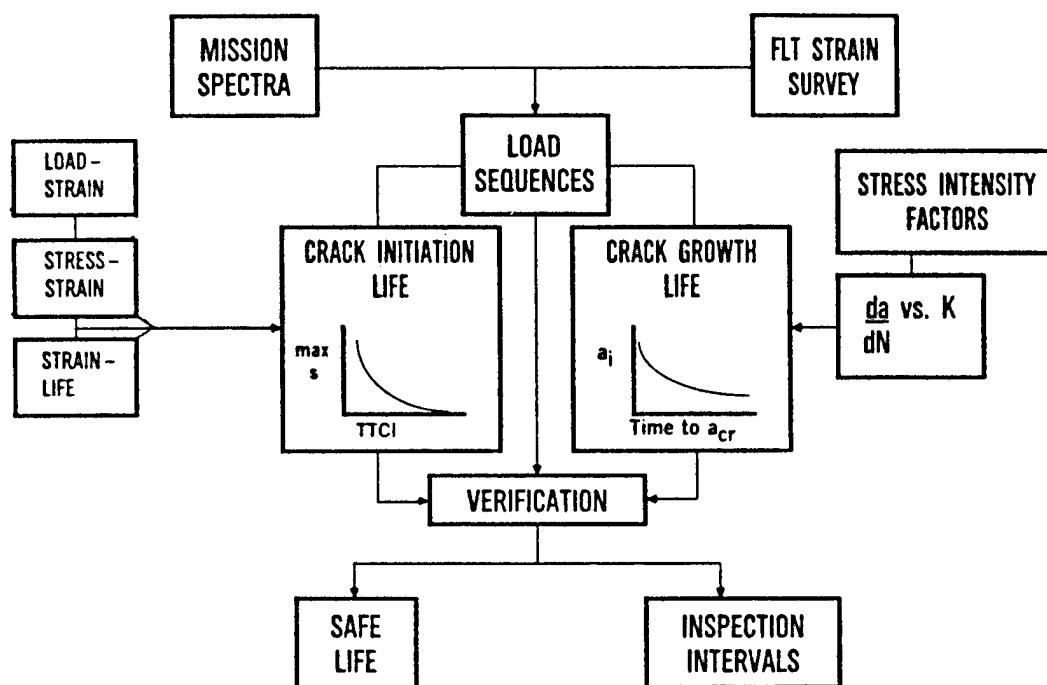
Figure 5. Flow Diagram of the Total Life Methodology.

While the Air Force has contracted with Sikorsky Aircraft and the Georgia Tech Research Institute(GTRI) to evaluate the practicality of using the Air Force's Aircraft Structural Integrity Program (ASIP) damage-tolerant approach for its special operations helicopters (H-53 and H-60), no firm conclusions have been drawn that can be applied in general or on new development programs. The Navy has developed a structural usage monitoring system based on the regime recognition concept for fatigue tracking of individual dynamic components with the objectives of maximizing the safety, reliability, and readiness of the fleet in an environment of limited defense resources [6]. The first Structural Data Recording Set (SDRS) was installed in the AH-IW Cobra fleet in February 1993. Fifty aircraft were equipped with SDRS and a total 3,400 flight hours of usage were required. Conclusions drawn from this Navy effort [6] were:

1. Helicopter component fatigue strength, usage, and component flight loads in each regime can be modeled with a three-parameter Weibull distribution.

2. The incremental joint probability density function of a component failure due to three independent variables (usage, load, and strength) can be numerically computed using Weibull distribution parameters and the expression of cumulative probability density function.

572

3.	The reliability associated with each life can be accurately determined. The contribution of usage, load, and strength to six nines reliability can be identified.

4.	The reliability associated with a life is a function of the approach with which it is determined. The differences in methodology could result in as much as two nines difference in reliability prediction.

5.	Additional work in evaluating each of the variables is necessary if an acceptable reliability methodology is to be developed.

The FAA's position is that damage-tolerant design is the only practical way to decrease the number of accidents involving fatigue failures in civilian aircraft [7]. The FAA has also noted that if damage tolerance is only 50 percent effective, then the fatal fatigue accident rate would be reduced by one-half. In 1995 the FAA started a Research Project Initiative (RPI) - Rotorcraft Structural Integrity and Safety Issues [8]. This RPI was composed of six tasks with the following industry sponsors:

1.	*Rotorcraft Health Usage Monitoring Systems (HUMS) Operational Development* - Bell Helicopter Textron, Inc. and Petroleum Helicopters, Inc.

2.	*Teetering Rotor System Aircraft* - Robinson Helicopter

3.	*Damage Tolerance Database and Application Methodology* - To be determined (TBD)

4.	*Guidance Material for Replacing Existing Parts with Advanced Material Parts* - TBD

5.	*Fly-By-Wire Certification Requirements* - TBD

6.	*Crash Protection Airbag Application to Light Helicopters* - Simula/Sikorsky Aircraft

Results from the first task were reported by Bell Helicopter Textron at the 52nd AHS Annual Forum in Washington, DC [9]. Usage data, collected on a Bell Model 412 helicopter that was equipped with a commercially available HUMS and operated by Petroleum Helicopters Inc. (PHI) under an independent flight trial program, was used to evaluate two usage monitoring techniques, flight condition recognition (FCR) and flight load synthesis (FLS). For the selected components that were analyzed, the results of the evaluation indicated a potential for extending retirement lives. This was due to the damage accumulation rate for the FCR and FLS techniques being slower ("slow clock") than the current method of using actual flight hours as the basis for retirement times. Based on the mission flown for this aircraft, which is transporting workcrews to offshore oil platforms, the flight hours charged against retirement times could be reduced by 50 percent or greater. Thus the operator would gain a considerable payback in reduced maintenance costs due to extension of retirement intervals [9].

The use of HUMS on rotorcraft is seen as an excellent opportunity to improve safety while at the same time save on operations and support costs. HUMS activities for rotorcraft are taking place around the world. In Britain the Civil Aeronautics Authority (CAA) has sponsored trials to prove the technology. North Sea helicopter operators are equipping fleets with HUMS and working groups have been active since 1986. Military applications for HUMS are also proceeding in the U.S. Navy and Army, and in the UK Ministry of Defense (MOD). The National Rotorcraft Technology Center (NRTC) in the U.S. is also supporting a cost-shared HUMS Project with the Rotorcraft Industry Technology Association (RITA), which is made up of the four major U.S. rotorcraft companies. Also, an array of suppliers are offering HUMS and HUMS-related capabilities.

CONCLUSIONS

Ensuring rotorcraft structural integrity/airworthiness is extremely complex and not always appreciated, due to the relatively low static load flight envelope (~3g's) for helicopters, i.e., V-N diagram. However, the capability of rotorcraft to provide six degrees of maneuvering freedom in low-speed flight make them the most agile (in terms of turning rate) of aircraft. This capability also makes defining flight envelopes, both steady and transient, extremely difficult due to the aero-servoelastic complications of the problem. Structural design philosophies for rotorcraft have evolved at a much slower rate than for fixed-wing aircraft, largely due to the inability to accurately predict the oscillatory loads and to track crack growth in a high cycle environment. The utility of rotorcraft and their usage in a variety of environments also make tracking fleet usage and crack detection and growth extremely difficult. Therefore, no single structural design philosophy, such as damage tolerance, has been accepted. There are low-level efforts in industry and government to move toward an integrated structural design philosophy/methodology, but no unified approach. One particular promising technology for rotorcraft structural integrity and airworthiness is Health Usage Monitoring Systems (HUMS) which will allow the individual tracking of usage, provided it proves to be cost effective.

REFERENCES

1. Borgman, D. C. and Schrage, D. P.: "Synopsis of Specialists' Meeting On Helicopter Fatigue Methodology," AGARD Conference Proceedings No. 297: HELICOPTER FATIGUE LIFE ASSESSMENT, 1981.

2. AGARD Helicopter Fatigue Design Guide, 1993.

3. AHS Midwest Region Helicopter Fatigue Specialists' Meeting, St. Louis, MO, October 16-18, 1984.

4. Structural Design Criteria For Rotary Wing Aircraft, Aeronautical Design Standard (ADS) - 29, United States Army Aviation Systems Command. St. Louis, MO, September 1986.

5. Spigel, B.: "Foundations of an Army Helicopter Structural Integrity Program," AHS National Specialists' Meeting on Advanced Rotorcraft Structures, Williamsburg, VA, October 25-27, 1988.

6. Moon, S., Menon, D., and Barndt, G.: "Fatigue Life Reliability Based On Measured Usage, Flight Loads and Fatigue Strength Variations," Proceedings of the 52nd Annual Forum of the AHS, Washington, DC, June 4-6, 1996.

7. Weaver, R. T.: "Damage Tolerance and Civil Helicopter Design," AHS Specialists' Meeting on Fatigue Methodology, St. Louis, MO, October 1984.

8. Federal Aviation Administration (FAA) Research Project Initiative (RPI) - Rotorcraft Structural Integrity and Safety Issues, January 1995.

9. Dickson, W. and Cronkhite, J. D.: "Usage and Structural Life Monitoring with HUMS," Proceedings of the 52nd Annual Forum of the AHS, Washington, DC, June 4-6, 1996.

RIVET BEARING LOAD CONSIDERATIONS IN THE DESIGN OF MECHANICAL REPAIRS FOR AGING AIRCRAFT[1]

Hemant Chickermane and Hae Chang Gea
Department of Mechanical and Aerospace Engineering
Rutgers, The State University of New Jersey
Piscataway, NJ 08855

INTRODUCTION

Mechanical repairs of aging repairs need to be designed to restore the structure to its original or better structural integrity. Poor repairs give rise to a nonuniform distribution of forces across the doubler patch. The original details for service loadings may be changed and thereby adversely effect the fatigue life of the aircraft structure. Due to the load transfer between aircraft skin and the repair doubler, fastener holes are subjected to bearing stresses. High stress concentrations at the rivet holes in the skin could lead to crack initiation and multisite damage, which could be catastrophic. While the rivets themselves are subject to shear failure, it has been found that bearing failure at fastener joints predominates.

In the past a methodology was developed to generate designs for mechanical repairs based on an energy criterion. This procedure determines optimal locations for rivets on the doubler patch in a manner that minimizes the deformations in the structural system comprising the aircraft skin, doubler patch, and rivets. Repair designs were generated for a variety of repair configurations for different shapes of doublers and regions of rivet placement. One concern that needs to be addressed is the possibility of localized high-stress regions in the vicinity of the rivets. In this work, the computation of bearing loads and their incorporation into the repair design problem has been investigated. Emphasis is placed on generating repairs with greater stiffness without subjecting rivets to excessively large loads.

BACKGROUND

At present, the main criterion for the design of mechanical repairs is static strength. Swift [1] proposed one of the earliest models for aircraft repairs. It is a one-dimensional model in which the skin and doubler are represented by axial rods and rivets by shear rods. An implicit assumption of this model is that load transfers in fasteners are uniform. However, a two-dimensional model is necessary to account for biaxial stresses and for greater accuracy in calculation of load transfers. The researchers at Battelle (see Rice, et. al [2]) extended the Swift model to two dimensions using spring-like discrete members connecting

---

the fasteners in both principal axes with axial and shear stiffness terms. This was implemented in the form of an analysis code called SKINFIX.

Since most of the research in the field of aircraft repairs deals with analysis of repairs, the design of repairs depend on the skill and experience of the engineer. Therefore, Chickermane and Gea [3] proposed a systematic design methodology which integrates the analysis of the repair with the redesign capability obtained by formulating it as an optimization problem. A three-dimensional model has been used to analyze the repair. Aircraft skin and doubler are modeled by quadrilateral thin-shell elements and rivets by rigid linear springs in three directions. The effect of a central crack in the skin is simulated by subjecting the skin to in plane loads, perpendicular to the direction of the crack.

MAIN COMPONENTS OF THE METHODOLOGY

Formulation of an Optimization Problem

The objective of the repair design procedure is to locate the rivets on the doubler patch in a way that minimizes the structural deformation. Since deformation is a local phenomenon, the location of the maximum displacement may vary from one design to another leading to a discontinuous objective function. To avoid this problem, a global measure of deformation of the structure in terms of the strain energy has been used. Therefore, the objective function is the mean compliance of the structure which is twice the strain energy. The strategy employed here is to constrain the bearing stresses in aircraft skin and doubler by ensuring that the maximum bearing loads stay within limits. This would also ensure a more uniform distribution of rivet loads. An upper limit is also placed on the number of rivets permitted.

Every rivet is modeled by rigid springs in three directions. The spring acting in the direction of the external loading is responsible for the shear resistance of the rivet. The shear force acting on the rivet is equal to the force exerted by the rivet on the doubler and skin is the bearing load. Therefore, rivet bearing loads are calculated in the direction of the applied skin loads. For a particular rivet i, bearing load transferred in direction j is

$$F_{ij} = k_{ij}(u_{1ij} - u_{2ij}) \tag{1}$$

where u_{1ij} and u_{2ij} are the doubler and skin displacements at the point of attachment respectively and k_{ij} is the rivet stiffness. Rivets having the maximum bearing loads are targeted and appropriate limits are placed on them based on results obtained from previous designs. The bearing load constraints are then introduced into the optimization problem as constraints.

The problem is defined as

Minimize   Mean compliance of the system
Subject to   Constraint on the number of rivets used
Constraints on maximum bearing loads

Modeling of the Rivets

A microstructure-based model proposed by Gea [4] has been utilized to model the rivets. The rivets are made of a composite material which consists of spherical micro-inclusions embedded in solid material (referred to as the matrix). The choice of spherical inclusions in an isotropic matrix ensures that the shape and orientation of the inclusion do not enter the problem formulation. The derivation of the density function is based on the work by Weng [5]. This method provides a means for redistributing the rivets during the optimization process, as the density of the rivet can be varied on a continuous scale from 0 to 1. The density (strength) of the rivets ρ_i are the design variables in the repair problem. The rivets in the initial design can be imagined to be made of porous material and are therefore weak.

Design Sensitivity Analysis

The design sensitivity analysis is to evaluate the effect of any rivet l on the load F_{ij} transferred by rivet i in the direction j,

$$\frac{\partial F_{ij}}{\partial x_l} = \frac{\partial k_{ij}}{\partial x_l}(u_{1ij} - u_{2ij}) + k_{ij}(\frac{\partial u_{1ij}}{\partial x_l} - \frac{\partial u_{2ij}}{\partial x_l}) \tag{2}$$

where

$$\frac{\partial k_{ij}}{\partial x_l} = 0 \text{ if } i \neq l \tag{3}$$

The static equilibrium of the system is expressed by

$$[K]\begin{bmatrix} u_1 \\ u_2 \end{bmatrix} = [F] \tag{4}$$

Differentiating with respect to x_l and rearranging

$$\begin{bmatrix} \dfrac{\partial u_1}{\partial x_l} \\ \dfrac{\partial u_2}{\partial x_l} \end{bmatrix} = -[K]^{-1}\frac{\partial [K]}{\partial x_l}\begin{bmatrix} u_1 \\ u_2 \end{bmatrix} \tag{5}$$

To extract the sensitivities of u_1 and u_2 corresponding to a particular bearing load F_{ij}, the above expression is premultiplied by a matrix with unit vectors in both rows. This is equivalent to applying unit loads at the nodes under consideration. The global stiffness matrix $[K]$ contains the contributions of skin, doubler and rivets, so $[K]$ is a function of rivet densities only. Therefore

$$\frac{\partial [K]}{\partial x_l} \begin{bmatrix} u_1 \\ u_2 \end{bmatrix} = \frac{\partial f(x_i)}{\partial x_l} k_0^e \begin{bmatrix} I & -I \\ -I & I \end{bmatrix} \begin{bmatrix} u_1^e \\ u_2^e \end{bmatrix} \tag{6}$$

$\begin{bmatrix} u_1^e \\ u_2^e \end{bmatrix}$ is the nodal displacement vector for rivet l and k_0^e is the rivet stiffness coefficient. Substituting this into Equation (5)

$$\begin{bmatrix} \dfrac{\partial u_1}{\partial x_l} \\ \dfrac{\partial u_2}{\partial x_l} \end{bmatrix} = -\frac{\partial f(x_i)}{\partial x_l} k_0^e \begin{bmatrix} (\lambda_{11}^{ij\,T} - \lambda_{11}^{ij\,T})(u_1^e - u_2^e) \\ (\lambda_{21}^{ij\,T} - \lambda_{22}^{ij\,T})(u_1^e - u_2^e) \end{bmatrix} \tag{7}$$

where λ_{11}^{ij} and λ_{12}^{ij} are doubler and skin displacements due to a unit dummy load on the doubler, and λ_{21}^{ij} and λ_{22}^{ij} are doubler and skin displacements due to a unit dummy load on the skin. For any general loading condition, the mean compliance of the system is

$$l = [F]^T \cdot \begin{bmatrix} u_1^e \\ u_2^e \end{bmatrix} \tag{8}$$

The expression for the sensitivity of the mean compliance can be shown to be

$$\frac{\partial l}{\partial x_l} = -\frac{\partial f(x_i)}{\partial x_l} k_0^e (u_1^e - u_2^e) \cdot (u_1^e - u_2^e) \tag{9}$$

Use of Local Function Approximations

Function evaluations (FE analyses) required for the optimization process are expensive. Therefore, function approximations are used to formulate an approximate problem. The Generalized Convex Approximation (GCA) method proposed by Chickermane and Gea [6] is used to formulate and solve the optimization problem. Function values and first order sensitivity information from the current and previous design are utilized to generate the approximation. These convex, separable subproblems are solved iteratively using mathematical programming to obtain the next design.

COMPUTATIONAL RESULTS: 3D REPAIR CONFIGURATION

In this example, the aircraft skin and doubler patch are modeled as curved shell structures as shown in Fig. 2. The aircraft skin is stiffened by frames running parallel to the edges. The repair is performed in a region enclosed by the frames. The upper limit on rivets was 14 in this case. The final design without the incorporation of rivet bearing load constraints is seen in Fig. 4. An upper limit for rivet bearing loads is chosen 20% less than that observed in this design. When this is incorporated into the problem, the optimal rivet placement is as shown in Fig. 5. From the iteration history in Fig. 6, it is noticed that at the start of the optimization of the bearing loads is below the upper limits. As the objective function (mean compliance) is reduced, the bearing loads increase and reach the upper limit. A more uniform rivet bearing load is obtained as the difference between the maximum and minimum bearing loads is decreased.

CONCLUSIONS

This paper presents a method for the incorporation of rivet bearing load constraints into a methodology for the design of optimal aircraft repairs. The overall stiffness of the structure is not compromised due to the decrease in the bearing loads. It is observed that the difference between the maximum and minimum bearing loads is reduced and more rivets are closer to the upper bearing load limit. This leads to a more uniform load distribution in the skin and doubler and minimizes the possibility of localized high stress regions.

REFERENCES

1.   Swift, T.: Repairs to Damage Tolerant Aircraft. Technical Report FAA-AIR-90-01, International Symposium on Structural Integrity of Aging Airplanes, Atlanta, Georgia, 1990.

2.   Rice, R., Francini, R., and Rosenfeld, S.: Effects of Repair on Structural Integrity. Technical Report DOT/FAA/CT-93/79, FAA Technical Center, 1993.

3.   Chickermane, H. and Gea, H.: Topology Optimization of Mechanical Repairs for Aging Aircraft. Computational Mechanics '95 : Proceedings of the International Conference on Computational Engineering Science, Vol. 2, pp. 2171-2176.

4.   Gea, H.: Topology Optimization: A New Micro-Structure Based Design Domain Method. Advances in Design Automation 1994, Vol. 2, pp. 283-290.

5.   Weng, G.: Some Elastic Properties of Reinforced Solids, With Special Reference to Isotropic Ones Containing Isotropic Inclusions. International Journal of Engineering Science, Vol. 22, 1994, pp. 845-856.

6.   Chickermane, H. and Gea, H.: A New Local Function Approximation Method for Structural Optimization Problems. International Journal for Numerical Methods in Engineering., Vol. 39, 1996, pp. 829-846.
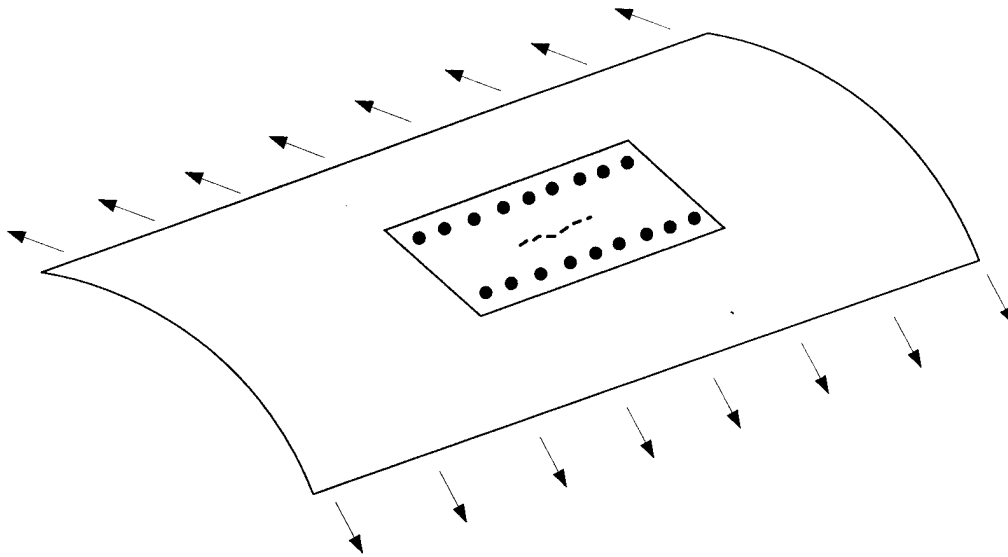
Figure 1. Mechanical Repair: Doubler Patch Riveted to Aircraft Skin.
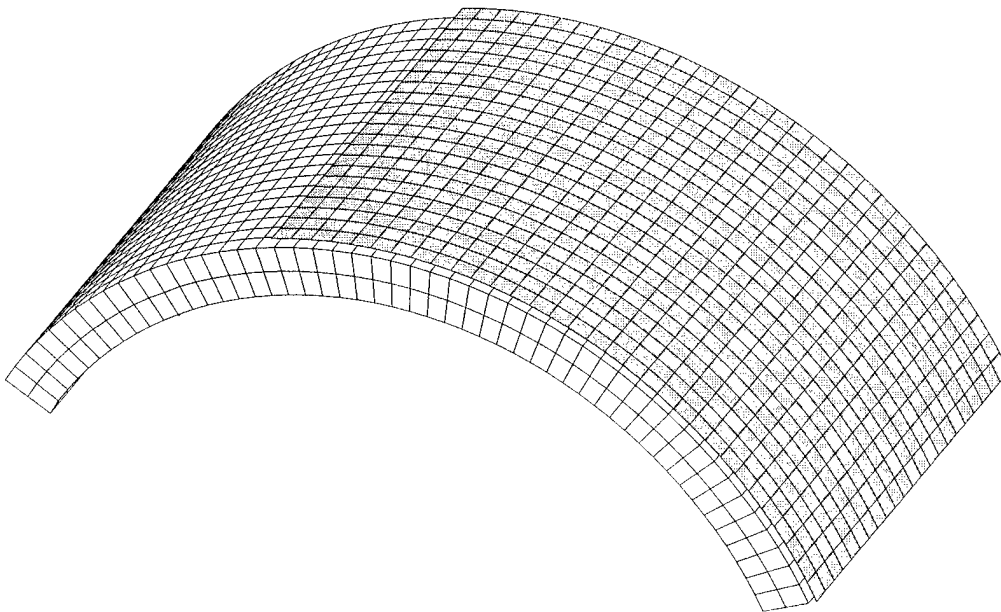

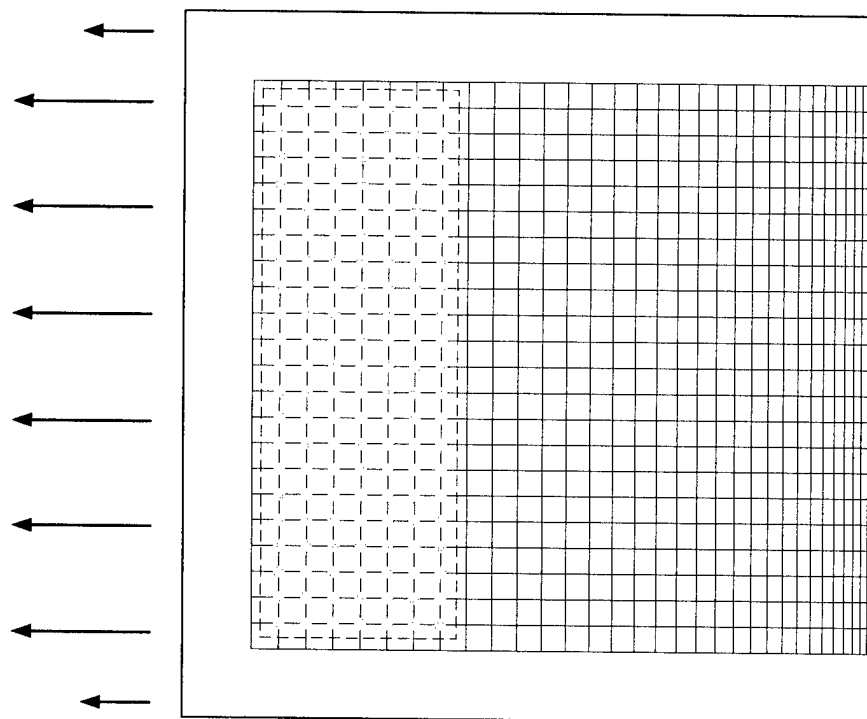Figure 2. Doubler Location on the Skin.
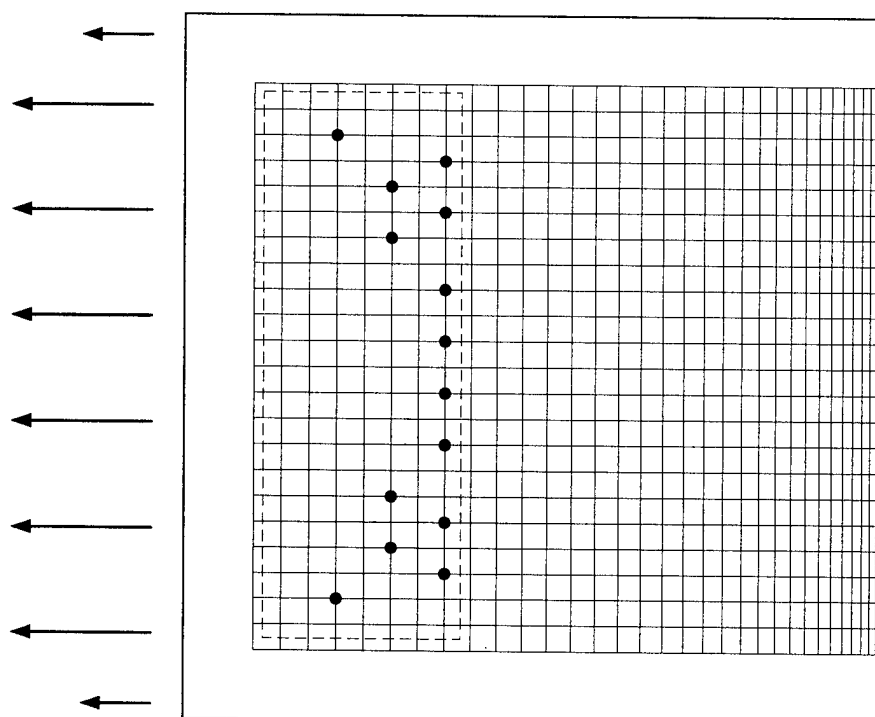
Figure 3. Initial Design.

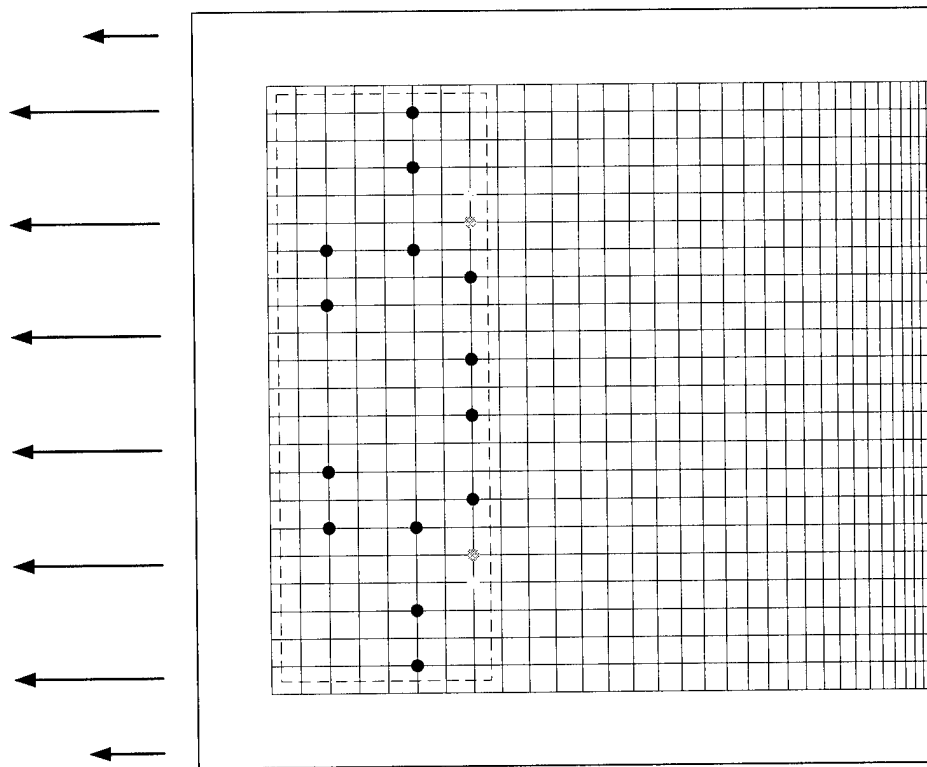Figure 4. Final Design Without Bearing Load Constraints.

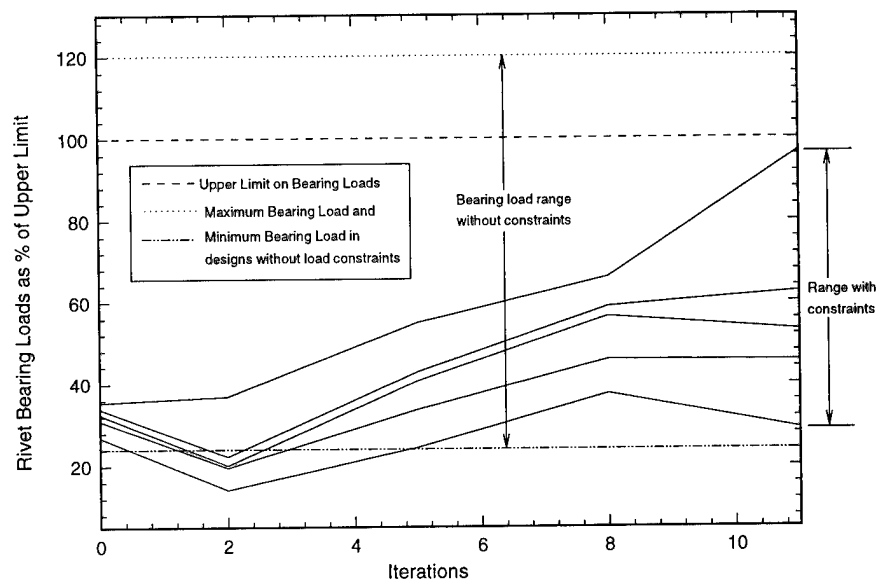Figure 5. Final Design With Rivet Bearing Load Constraints.

Figure 6. Iteration History of Bearing Load Constraints.

THE ROLE OF FRETTING CRACK NUCLEATION IN THE ONSET OF WIDESPREAD FATIGUE DAMAGE: ANALYSIS AND EXPERIMENTS[*]

Matthew P. Szolwinski, G. Harish,
Pamela A. McVeigh, and Thomas N. Farris
School of Aeronautics & Astronautics
Purdue University
West Lafayette, Indiana

SUMMARY

The localized contact stresses, strains, and surface microslip induced by fretting at fastener, hole, or joint interfaces serve to accelerate the nucleation of widespread fatigue damage (WFD) when compared to the sole action of the global structural loads. Analytical, numerical, and experimental approaches are integrated to predict the nucleation of cracks under the fretting contact stresses. Multiaxial fatigue theory, uniaxial strain-life material data, and finite element analysis are combined to predict the nucleation of cracks by fretting contact in a reduced experimental model of an aircraft joint. The finite element method (FEM) is combined with multiaxial fatigue theory to predict lives of actual aircraft joints.

INTRODUCTION

Fretting, the damage process that manifests itself when nominally clamped surfaces are subjected to oscillatory loads or external vibrations, is not a recently discovered malady. In fact, damage from fretting contact was reported as early as 1911 by researchers carrying out fatigue tests of steel who discovered "red rust...due to the varying stress between the test-specimen and its holder" (fretting corrosion) (ref. 1). Those interested in the design and maintenance of both fixed- and rotary-wing aircraft after World War II gave concurrent acute attention to the role fretting plays in the degradation of the airframe structure and mechanical components (ref. 2). In spite of its importance, very little work analyzing the nucleation of cracks under the influence of fretting contact has been available. Instead, researchers have focused primarily on either reporting the effect of fretting on the reduction in total fatigue life or analyzing the effect of the fretting contact on surface cracks.
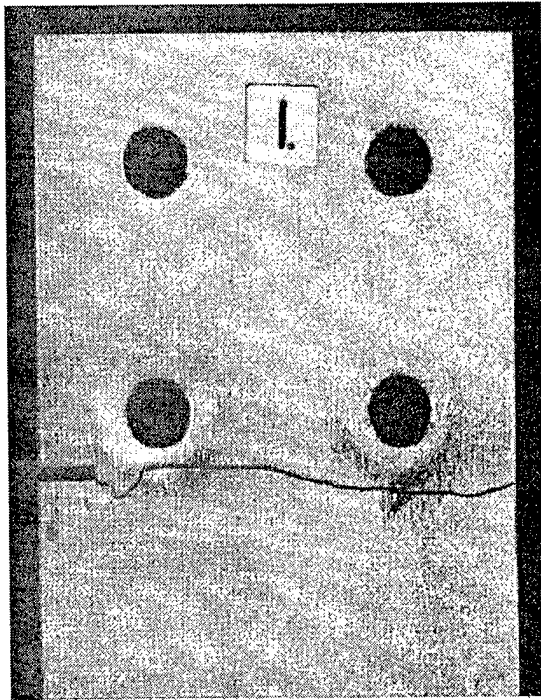

Figure 1. Fatigue Failure of a Lap Splice Attributed to Fretting (Ref. 3).

The current objective is to understand the ability of fretting to initiate and accelerate widespread fatigue damage (WFD) in airframe joints. Both periodic teardown inspections and laboratory simulations of common riveted aircraft lap splice joints have revealed evidence of fretting crack nucleation near the rivet-skin interface and at the faying surfaces of riveted joints, as shown in Figure 1. (refs. 3, 4). To ascertain accurately a more complete understanding of the effect of fretting and, possibly fretting corrosion, on the onset of widespread fatigue damage in aging airframes, the highly localized microslip distribution and contact stresses related to the fretting action present in these structural members must be considered in detail.

This paper describes research efforts in two related areas: (1) understanding the mechanics of fretting fatigue crack nucleation, with particular emphasis on the development of predictive capability rooted in a blend of analytical and experimental methodologies and (2) accurate finite element modeling of a typical lap splice joint that incorporates the intimate localized contact between both the fastener and hole and faying surfaces of the sheets. Blending the results from these endeavors has led to the current phase of research: assessing the effects of rivet installation on fretting fatigue crack nucleation in aircraft joints. The following highlights achievements and ongoing work in each of these areas to elucidate the development of this current research objective.

PREDICTION OF FRETTING FATIGUE CRACK NUCLEATION

The synergistic competition among the wear, fatigue, and corrosive phenomena associated with fretting contact is driven by the highly localized microslip distribution and contact stresses that vary nonproportionally with any bulk or global loading. Development of an understanding of the mechanics of fretting fatigue crack nucleation requires the careful characterization of the cyclic stresses, strains, and displacements associated with fretting. This effort is made complicated by many effects, including the fact that the local coefficient of friction changes during the life of the fretting surfaces.

586

Analytical and Numerical Models for Cyclic Fretting Contact Stress Field

An analytical model of the surface tractions and stresses associated with the two-dimensional fretting problem was proposed independently by both Cattaneo (ref. 5) and Mindlin (ref. 6) in 1938 and 1949, respectively. Assuming Hertzian contact of isotropic, elastic cylinders subjected to a monotonic tangential loading and a Coulomb law of sliding friction on a localized basis, a condition of "stick" or no relative motion between the contact surfaces in a central stick zone can be imposed, as illustrated in Figure 2. In the stick zone, the local shear traction, $q(x)$, is less than the local frictional force, $\mu p(x)$, while in the regions of slip, $|q(x)| = \mu p(x)$.
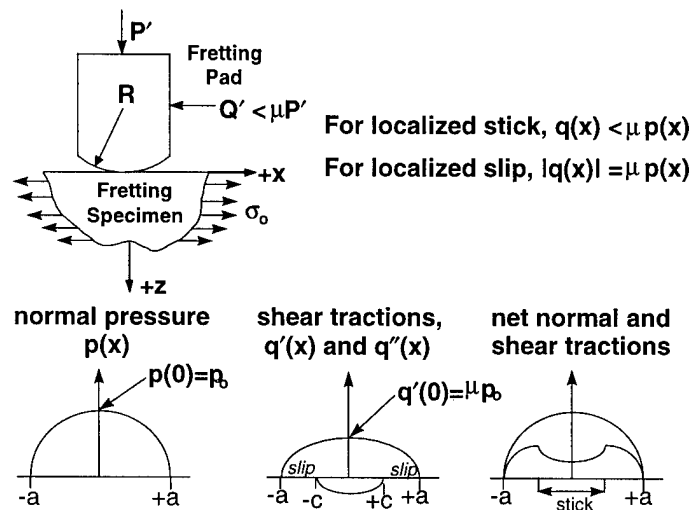

For localized stick, $q(x) < \mu\, p(x)$

For localized slip, $|q(x)| = \mu\, p(x)$

normal pressure
$p(x)$

shear tractions,
$q'(x)$ and $q''(x)$

net normal and
shear tractions

Figure 2. A Schematic of the Surface Tractions Associated With Fretting.

Closed-form solutions for the stresses, strains, and surface displacements associated with given normal and tangential loads (P and Q) and coefficient of friction in the slip zones (μ) are available (ref. 7). The bulk tension shown in Figure 2 leads to a nonsymmetric stick zone (ref. 8). Results from a wide range of loading parameters point toward the source of crack nucleation due to fretting: a sharp tensile peak in the tangential stress, σ_{xx}, at the edge of the contact zone, $x = +a$ (see Figure 3). The analytical expression for the component of σ_{xx} due to the fretting alone reduces conveniently to (ref. 9)

$$(\sigma_{xx})_{\text{fretting}} = 2p_o\sqrt{\mu Q/P} \tag{1}$$

where p_o is the maximum Hertzian pressure and μ is the coefficient of friction in the slip zones. The effect of the applied bulk stress component in the x-direction (σ_o) can be approximated by superposing it with $(\sigma_{xx})_{\text{fretting}}$, as shown in Figure 3. Thus for contact pressures in the ranges of 25 to 30 ksi, bulk stresses on the order of 12 to 14 ksi, and nominal

values of $Q/P = 0.3$ and $\mu = 0.6$, the fretting contact provides a stress concentration $[(\sigma_{xx})_{total}/(\sigma_o)]$ between approximately 2.5 and 2.8.
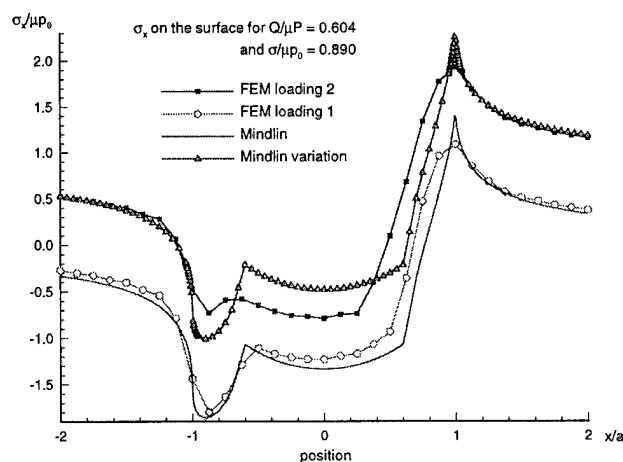
Figure 3. Tangential Stress, σ_{xx}, Along the Contact Surface. FEM Loading 1 and the Mindlin Cases Involve no Bulk Stress While FEM Loading 2 and the Mindlin Variation Cases Incorporate the Bulk Stress σ_o. For the Given Set of Conditions $(Q/\mu P)$ and $(\sigma_o/\mu p_o)$, no Reversal of Microslip at the Contact Surface Occurs.

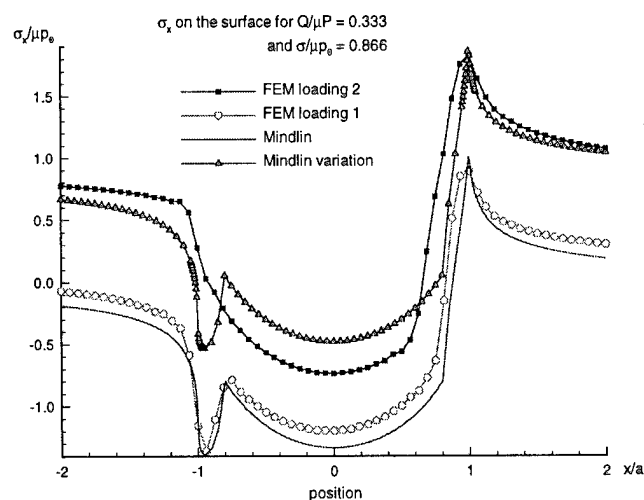Figure 4. Tangential Stress, σ_{xx}, Along the Contact Surface for a Case of Reversed Slip. Again, FEM Loading 1 and the Mindlin Cases Involve no Bulk Stress While FEM Loading 2 and the Mindlin Variation Cases Incorporate the Bulk Stress σ_o. Note That Even While the Mindlin Solutions Do Not Account for the Slip Reversal, the Predicted Values of σ_{xx} at the Trailing Edge $(x/a = +1)$ Agree Well With the FEM Values.

As the ratio of the tangential load to normal load, *Q/P,* changes with an oscillatory tangential load, the cyclic stresses and strains are nonproportional in nature, leading to a state of multiaxial fatigue at all points. Any attempt to predict nucleation of fatigue cracks due to the influence of fretting must account for this fact. Based on the hypothesis that the peak in tensile stress at the trailing edge (*x/a* = +1) of contact drives the observed nucleation of fretting cracks perpendicular to the contact surface (ref. 10), Szolwinski and Farris (ref. 7) attempted to correlate published experimental observations of fretting fatigue crack failures with predictions made with multiaxial fatigue theory based on principal planes (ref. 11), uniaxial strain-life constants, and the aforementioned fretting contact elastic stress analysis. The relationship between reversals to nucleation (defined as a crack of length 1 mm) and the product of strain amplitude and maximum stress during a complete loading cycle normal to the principal plane (the plane of the nucleated crack) is

$$\Gamma = \sigma_{max}(\Delta\varepsilon/2) = [(\sigma_f')^2/E](2N_f)^{2b} + \varepsilon_f'(2N_f)^{b+c} \tag{4}$$

This is the familiar uniaxial strain-life Smith-Watson-Topper equation with uniaxial fatigue constants that has been shown to hold for cases of multiaxial fatigue (ref. 11). The expression, coupled with the two-dimensional stress analysis, identifies the location and orientation of the critical plane of crack nucleation as the trailing edge of contact perpendicular to the contact surface, respectively, agreeing with published observations (ref. 10).

The experimental setup presented in Figure 5 has been constructed at Purdue University to generate and monitor precisely the requisite loads necessary for fretting fatigue for verification of the postulated multiaxial fatigue predictive model. The fretting test fixture, designed around a 22-kip servo-hydraulic load frame, induces fretting between a cylindrical pad and flat specimen, a geometrical configuration identical to the one assumed in the analytical and FEM models. The fixture and associated data acquisition hardware and software (the details of which are presented elsewhere (ref. 12)) allow for complete control over the variables necessary to characterize the contact stress field: (1) *Q/P,* (2) σ_o, (3) p_o, and (4) 2*a,* the width of the contact zone.

Aluminum 2024-T351 specimens and cylindrical pads have been used in the tests. Each specimen is run to fracture for a given maximum Hertzian contact pressure and amplitudes of bulk stress and *Q/P.* By measuring these quantities and having determined the steady-state coefficient of friction in the slip zones to be $\mu = 0.6$ (ref. 12), a prediction can be made for the number of cycles required to nucleate a crack of 1 mm in the specimens. A propagation life for each test is estimated by assuming a thumbnail crack of 1 mm depth is grown through the specimen by the bulk stress using a Paris-law approach. It has been calculated that this propagation phase occurs in the latter 25%-40% of total cycles to failure. Figure 6 displays fretting data both generated at Purdue and published data (ref. 10) for which the requisite loads and experimental parameters were known. To this end, the nucleation life

for each experiment has been plotted as the number of cycles to failure minus the estimated propagation life.
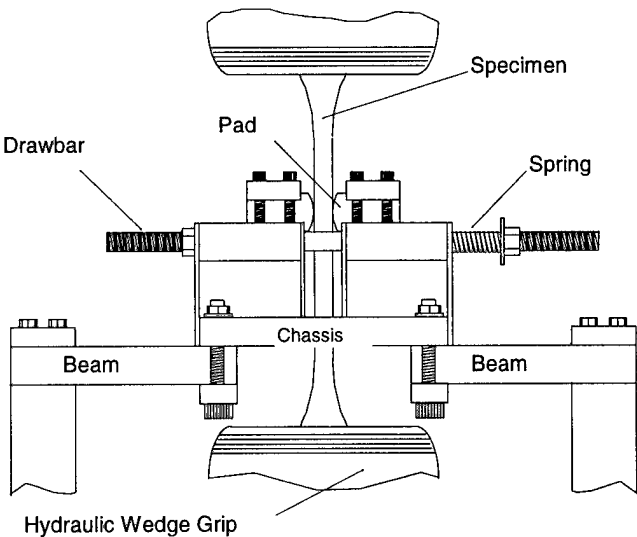

Figure 5. Experimental Setup Used in the Fretting Fatigue Crack Nucleation Studies at Purdue University.
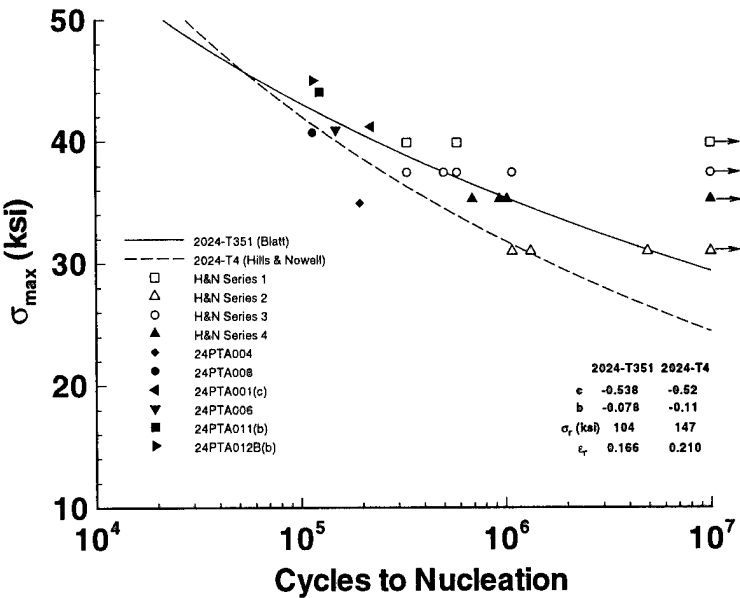

Figure 6. Comparison Between Nucleation Lives as Predicted by the Multiaxial Fatigue-Based Approach and Experimental Observations. For the Series of Tests Conducted at Purdue, the Steady-State Coefficient of Friction in the Slip Zones Was Determined To Be $\mu = 0.60$.

590

For the sake of comparison, two theoretical curves are plotted along with the experimental data. The first, for 2024-T351, uses strain-life constants generated by Blatt (ref. 13). The material in the published study was only identified as a 4% copper (by weight) aluminum alloy. As a result, a second curve using strain-life constants for 2024-T4 alloy is also plotted on the graph (ref. 14). While it appears from even a cursory review of the data that the multiaxial fatigue-based theory is able to accurately predict fretting fatigue crack nucleation, a statistically designed set of tests is currently underway to provide further support to this claim.

MODELING OF JOINT CONFIGURATIONS WITH APPLICATIONS TO FRETTING FATIGUE

With the confidence in the capability to predict fretting crack nucleation from contact stresses and strains, the next logical step is to quantify the stresses and strains present in common joint configurations. Such an effort has been undertaken using finite element modeling with the expressed goal of verifying the presence of interfacial tractions and contact stresses indicative of fretting in lap splice joints.

Two separate finite element models of a skin panel with an infinite row of rivets are formulated using plane-strain quadrilateral elements and three-dimensional shell elements, respectively. Material properties of 2024-T3 aluminum were assumed for each component. The calculations are performed using ANSYS™, a finite element software package provided to Purdue University on an academic license by Swanson Analysis, Inc. Each model consists of a typical cell composed of one half rivet and the portion of the skin around it. A complete lap joint may be thought of as being built up with these cells. Symmetry conditions are imposed on both the top and bottom of the model to simulate the presence of the infinite row of rivets. The presence of multiple rivet rows is accounted for by the elastic supports (on one side for the 2D model and on either side—one for each shell—for the shell model). By varying the stiffness of these elastic supports, the amount of load being transferred through the rivet can be controlled. To simulate global loading, a uniform tensile traction is applied on the remaining free edge or edges, with the rivet fixed at its center to prevent rigid body motion. Note that the applied global loading causes partial loss of contact between the rivet and plate as no shrink effect due to rivet bucking is included in the present analysis.

The three-dimensional model is represented schematically in Figure 7. This model incorporates contact elements along the rivet-skin interface as well as on the interface between the two plates, which are modeled as shells. For reasons of consistency, the rivets are also modeled as shells. Constraint conditions are imposed to force the two rivet shells to act as one body. The stiffnesses of the interface elements between the plates are calculated by assuming that the plates deform like rods under the action of an axial load provided by transverse pressure applied to the plates. With this approach, the effect of clamping the rivet head can be studied through application of axisymmetric pressure on an annular area around the rivet shells (ref. 15). The pressure is assumed to fall to zero on both sides of this annulus

in order to ensure a continuous profile. Note, though, there is no transverse shear stress capability in the current model.
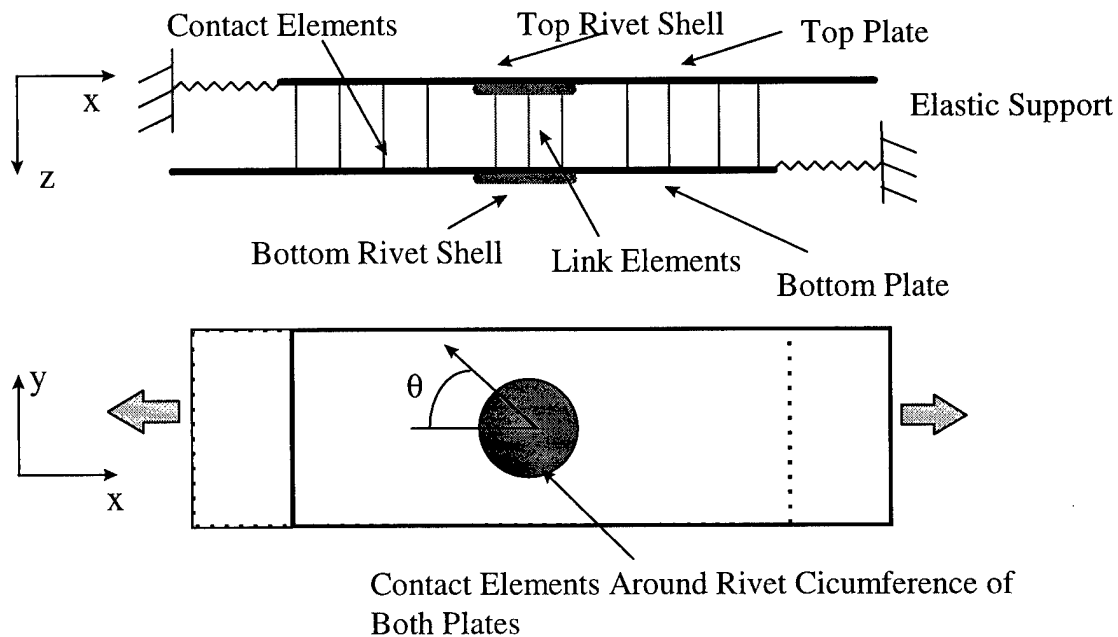

Figure 7. Schematic of Shell Model.

With integration of this clamping pressure into the three-dimensional shell model, it is found that interfacial friction at the faying surfaces accounts for some of the load transfer through the joint; hence, load transfer through the rivet is less than the overall load transfer through the rivet assembly. This division of load transfer is also observed upon unloading and subsequent reloading, as the stress distribution is nearly identical to the one present after the initial loading. This result may be explained by examining the manner in which the load is being transferred. With the initial loading, the plate-plate contact is initially stuck and the interfacial friction force transmits the load. Thus, the rivet does not experience any loading until the plates attempt to move into contact with it. However, this contact will only commence when the plate-plate interface begins to slip nearly globally at the faying surfaces. Only after this point will the rivet begin to take up the bulk of the additional load. Similarly, when the load is released, the rivet will begin to unload only when the plates begin to move in the opposite direction. This requires reversed slip (slip in the direction opposite to slip due to the initial loading) to occur in the plate-plate interface. Finally, when reloading occurs, the slip again has to reverse before the rivet takes up any more load. Thus, the fraction of the contact area in slip at any given time looks similar to the schematic given in Figure 8. Such a stick-slip action indicative of fretting leads to high localized contact stresses both at the faying surfaces and the rivet-skin interface.

Also, an increase in rivet head clamping results in a higher interfacial frictional force between the two plates causing a state of stress highly favorable to crack nucleation, especially as the interface is a hidden surface. This stress, combined with high slip
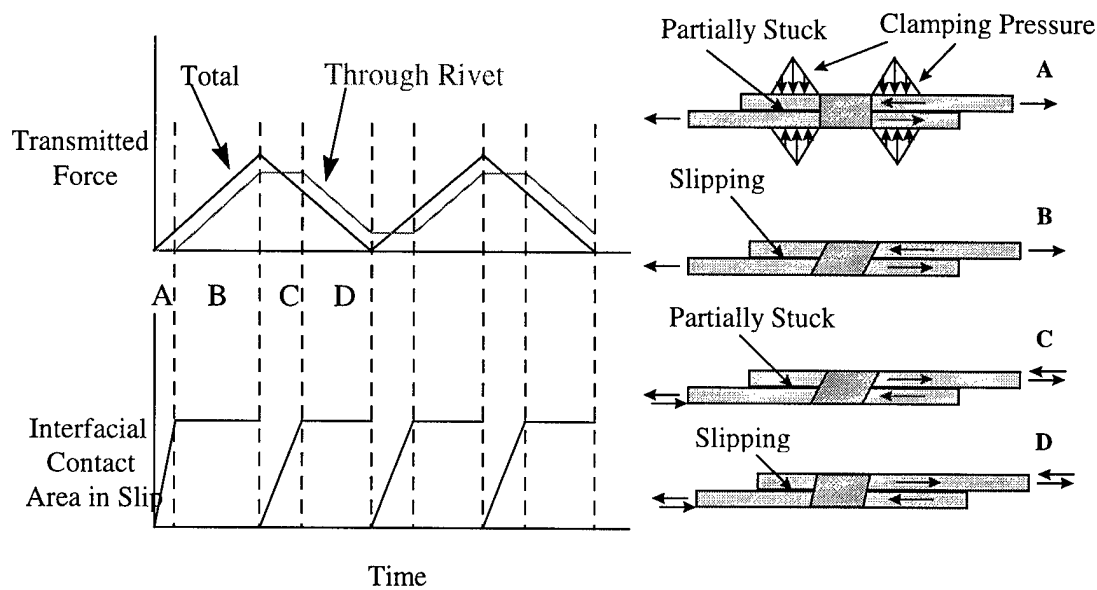
Figure 8. Schematic of Load Transfer Mechanisms.

amplitudes, can cause the influence of interfacial friction is to increase load transfer ratio, but at a lower maximum extensive wear and fatigue damage to the surfaces. For a given value of elastic support stiffness, tangential stress. The penalty lies in extending the zone of fretting damage.

The contact between the fastener and plate spans roughly half the interface, centered around $\theta = 0°$. This is in good agreement with the results published by Narayana and Dayananda (ref.16). The stress results are expressed in the form of stress distribution around the fastener hole for a given longitudinal transverse ratio and coefficient of friction. The normal pressure, p, the shear traction on the plate at the interface, q, and the tangential stress around the fastener hole, σ_h, are plotted as functions of the angular coordinate θ in Figure 9.

From these results, it can be concluded that the contact between the fastener and plate can be approximated by the analytical tractions derived for the Mindlin case. This conclusion is supported by the distinct "fretting-like" stick-slip behavior in the contact, the nominally-Hertzian pressure distribution and the shear traction that follows the pressure distribution, in the slip region where $q(\theta) = \mu p(\theta)$. In the stick region, q decreases slowly as θ approaches zero. The region of slip is dependent on the coefficient of friction, varying from 15° to 60° of arc as the coefficient of friction increases from 0.2 to 0.7. The tangential stress (or hoop stress, σ_h) shows a tensile peak at the edge of contact ($\theta = 0°$), similar to the results presented earlier in Figure 3. This stress then decays away from the edge of contact. In general, increases in the coefficient of friction result in a decrease in the maximum value of normal pressure and an increase in the maximum tangential stress. The tangential stress peak coupled with the stick-slip behavior must be included in any analysis of nucleation of cracks at and around fastener holes.
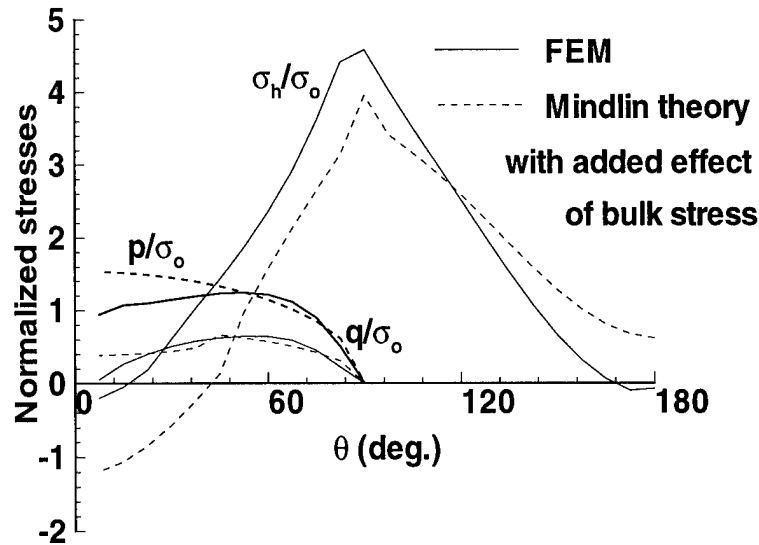
593

Figure 9. Normalized Contact Stresses at Fastener Hole at the Mid-Plane of the Top Plate. The Applied Clamping Force is 75 lb., and 40% of Applied Load is Transferred Through the Rivet Assembly. The Assumed Coefficient of Friction at the Fastener-Skin Interface is $\mu = 0.5$.

Results from this model also provide insight into load transfer ratio and rivet spacing. As the stiffness of the elastic support is varied, the load taken up by the rivet changes accordingly. In the model, the resistive stiffness is the series sum of two springs with stiffnesses equal to that of the support and the region of the panel aft of the rivet. Thus, in order to reduce the rivet load, rivet spacing must be decreased in conjunction with an increase in the number of rivets.

The origin of the tractions at the plate-fastener interface can be identified as the combination of stress concentrations due to the fastener hole and the plate-fastener contact. The stress concentration solution is determined by solving the same model without the fastener but with all other boundary conditions intact and superposing contact stresses as determined by Mindlin theory, assuming a contact area and slip zone size as given by the full model. The tangential stress is calculated as the sum of the Mindlin solution stress and the stress due to the effect of the stress concentration provided by the hole.

Close to the trailing edge of contact, which is the primary point of interest, the values predicted by the analytical approach theory are quite reasonable when compared to the FEM results. The 3D model results also compares well to the 2D results (ref. 17) which is expected as the mid-plane results are basically devoid of bending stresses. It is also important to note that the stick-slip condition is evaluated on basis of nodal forces and not stresses. Hence only mid-plane values can be expected to conform strictly to Coulomb friction theory.

As shown, the use of finite element modeling of a typical joint configuration to predict and analyze probable zones of fretting is a useful approach. It may be the only way to understand the behavior of the rivet-skin contact subjected to complex loadings in the presence of cracks which may have been nucleated by fretting. This type of analysis is of particular significance for design of rivet size and spacing and the implications of rivet installation procedures in the context of widespread fatigue damage.

CONCLUSION

The combination of appropriate stresses and multiaxial fatigue theory allows the prediction of fretting crack nucleation in a two-dimensional experimental approximation of the rivet-skin interface. As the three-dimensional fastener-skin interfacial stress state calculated by finite element analysis is similar to that of the experiment, it is believed that the onset of widespread fatigue damage at the fastener-skin interface can be predicted. Further experimental and analytical work, particularly in the area of the stresses induced during the rivet installation process, is required to predict fretting at the faying surfaces of lap joints.

REFERENCES

1.   Eden, E. M; Rose, W. N.; and Cunningham, F. L.: The Endurance of Metals. *Proceedings of the Institution of Mechanical Engineers*, part 3, 1911, pp. 839-924.

2.   Rahm, A. E. and Wurster, H. J.: Fretting Corrosion in Aircraft and Aircraft Accessories. *Lubrication Engineering*, vol. 7, February 1951, pp. 22-40.

3.   Harris, W. J.: *Metallic Fatigue.* Pergamon, 1961.

4.   Müller, R. P. G.: An Experimental and Analytical Investigation on the Fatigue Behavior of Fuselage Riveted Lap Joints. Ph.D. thesis. Delft University of Technology, The Netherlands, 1995.

5.   Cattaneo, C.: Sul Contatto di Due Corpi Elastici: Distribuzione Locale Degli Sforze. *Rendiconti dell' Accademia nazionale dei Lincei*, vol. 27, 1938, pp. 342-348, pp. 434-436, pp. 474-478.

6.   Mindlin, R. D.: Compliance of Elastic Bodies in Contact. *Journal of Applied Mechanics*, vol. 16, 1949, pp. 259-268.

7.   Szolwinski, M. P. and Farris, T. N.: Mechanics of Fretting Fatigue Crack Formation. *Wear*, 1996, in press.

8.   McVeigh, P. A. and Farris, T. N.: Finite Element Analysis of Fretting Stresses. *Journal of Tribology*, 1996, in press

9. Hills, D. A.; Nowell, D.; and Sackfield, A.: Surface Fatigue Considerations in Fretting. *Interface Dynamics*, eds. Dowson, D.; Taylor, C. M.; Godet, M.; and Berthe, D., Elsevier, 1988, pp. 35-40.

10. Hills, D. A.; Nowell, D.; and O'Connor, J. J.: On the Mechanics of Fretting Fatigue. *Wear*, 1988, vol. 125, pp. 129-156.

11. Socie, D.: Critical Plane Approaches for Multiaxial Fatigue Damage Assessment. *Advances in Multiaxial Fatigue*, ASTM STP 1191, 1993, pp. 7-36.

12. Szolwinski, M. P.; Harish, G.; and Farris, T. N.: Experimental Observation of the Effect of Contact Parameters on Fretting Fatigue Crack Nucleation. *Proceedings of the 1995 USAF Structural Integrity Program Conference*, San Antonio, 1995.

13. Blatt, P. A.: Evaluation of Fatigue Crack Initiation Behavior of an Experimental Ternary Aluminum-Lithium Alloy. M. S. thesis, Purdue University, West Lafayette, 1990.

14. Hertzberg, R. W.: *Deformation and Fracture Mechanics of Engineering Materials*. Wiley, 1976.

15. Reithmaier, L.: *Standard Aircraft Handbook*. 4th ed., Tab Books, 1986.

16. Narayana, K. B. and Dayananda, T. S.: Cracks Emanating from Pin-Loaded Joints. *Egg. Fracture Mechanics*, vol. 47, 1994, pp. 29-38.

17. Farris, T. N.; Grandt, A. F., Jr.; Harish, G.; and Wang, H. L.: Analysis of Widespread Fatigue Damage in Structural Joints. *Proceedings of 41st International SAMPE Symposium and Exhibition*, Anaheim, 1996.

THE ROLE OF NEW-TECHNOLOGY NONDESTRUCTIVE INSPECTION TECHNIQUES

A. Quincy Howard
Boeing Commercial Airplane Group
Seattle, WA 98124

SUMMARY

There has been a large nondestructive inspection (NDI) research and development effort directed toward the use of new technology. Many of the techniques developed are wide-area techniques designed to help decrease the time and human factor difficulties involved with existing techniques. Although many of the existing service bulletin (SB) inspections may not benefit by these new-technology techniques, the increased use of advanced composite materials provides an excellent opportunity for these techniques to be utilized. This paper describes where these new-technology techniques might be used, both in existing and future applications.

INTRODUCTION

Commercial airplanes are designed to be damage tolerant, that is, able to sustain regulatory loads in the presence of damage until the damage is detected through inspection or malfunction and repaired. Corrosion and fatigue are such types of damage that can occur to an airplane. It is the goal of an Original Equipment Manufacturer (OEM) to design airplanes to be resistant to corrosion and fatigue and to develop maintenance programs that provide opportunities to identify damage before the airplane's residual strength is impaired.

This residual strength requirement is one of the primary concerns in selecting an inspection method. The goal of inspection is not necessarily to ensure that there is absolutely no damage, but to ensure that the residual strength of the structural member is not compromised.

LAP JOINT INSPECTIONS

The inspection requirements for the B727, B737, and B747 model lap joints have been the focus of much attention. Service Bulletin 737-53A1039 addresses the longitudinal lap joints of the B737. The requirements of this service bulletin are similar to those for the B727 and B747 airplanes. In this service bulletin, visual inspection is the method used to identify the presence of corrosion. The service bulletin requires that if there are visual signs

of corrosion, these areas must be inspected with low-frequency eddy current to determine the amount of material loss. (The B727 equivalent service bulletin requires the entire skin panel be inspected for material loss.) Eddy-current inspection is the current NDI method of choice because the equipment is relatively inexpensive and portable, and the method is able to estimate material loss.

Many new-technology NDI techniques have been investigated for the lap joint disbond/corrosion problem. Since there is such a large amount of lap splice area, these service bulletins appear to be good candidates for these techniques. Many of these techniques are able to detect the presence of disbonding or corrosion, but at this time, they are unable to quantify the amount of material loss. If these methods were to be used currently, they would only be replacing a visual inspection, as the eddy-current inspection would still be required to estimate the amount of remaining material.

It is also important to note that the lap joint corrosion problem is applicable to a limited number of airplanes. The service bulletin requirements for corrosion inspections are only applicable to line numbers 1 to 849 for the B727, 1 to 291 for the B737, and 1 to 200 for the B747. After these line numbers, the lap joints, as well as all airplanes built thereafter, were assembled with sealant between the skin panels. This lap joint configuration has not experienced a corrosion problem. The number of applicable airplanes is becoming smaller as some airplanes are modified and others retired due to age.

NDI FOR CORROSION

Corrosion problems occur in more areas than just lap joints. Because of the increasing problem with corrosion as airplanes age, the Corrosion Prevention and Control Program (CPCP) was developed by industry. The CPCP is mandated by the FAA for all model airplanes, and it requires operators to perform repeat visual inspections on all airplane structure at designated intervals. The fact that all airplane models are affected and that large areas of each airplane are inspected would lead some to believe that new-technology inspection techniques could be a big help to CPCP inspections. One must look at the program as a whole, however, to see why visual inspection was chosen.

There are several different parts to CPCP implementation. Along with the visual inspection task are tasks of reapplying any damaged protective finishes, clearing drain paths, applying corrosion inhibiting compounds, and drying insulation blankets. All of these steps must be performed even if there is no corrosion found, and therefore, internal access must be gained. Since access must be gained, it makes sense to perform a visual inspection rather than use a new-technology inspection technique.

Many service bulletins allow the option of external inspection using an NDI technique or internal visual inspection. The existence of the CPCP may influence which inspection option an operator chooses. For instance, if a service bulletin inspection is to be carried out, a visual inspection can be performed during the CPCP inspection with no

additional time for gaining access, and many times, with no additional time for inspection (i.e., the same area is being looked at with the same level of inspection). If an operator has a choice of a visual inspection with an interval equal to or greater than the CPCP interval or an external NDI technique, it might make sense to perform the visual inspection, since access will already have been gained for the CPCP inspection.

Visual inspection, however, is not always the best inspection method for corrosion detection. Recent advances in the use of ultrasonics to detect and measure corrosion in second-layer structure has made this new-technology technique very useful. Although not a wide-area technique, it has been shown to save many hours over existing visual inspections [1]. The use of this technique does require that the structure being inspected be sealed at the faying surfaces.

Other advanced technology techniques, such as D-sight [2], infrared thermography [3], and Magneto-Optic Imaging [4], are able to find areas of corrosion. At this time, however, they are unable to estimate the amount of material loss. These techniques may still be useful to supplement visual inspections for detecting hidden corrosion.

SERVICE BULLETIN INSPECTIONS

Much of the NDI research and development effort has been directed toward service bulletin applications, such as lap joint inspections. Much of the research has been directed toward so-called wide-area techniques to help decrease the time and human factors difficulties involved in these inspections. A study was done recently to identify how many Boeing service bulletins could be applicable to wide-area techniques for corrosion and disbond detection. The selection of these service bulletins did not mean that a wide-area technique should be used or was necessarily beneficial, only that it was possible that one could be used.

Six B727, six B737, and four B747 service bulletins were selected as candidates for possible wide-area inspection applications. These numbers are reduced if the wide-area technique cannot measure the amount of material loss caused by corrosion. As discussed previously, if the technique is not capable of doing this, it simply replaces an external visual inspection and may not be of any benefit.

Table 1 shows the B727 service bulletins selected, the current inspection method, and the amount of time estimated to accomplish the inspection. No time estimates are given for the eddy-current inspections for corrosion, because the amount of time depends on the area requiring inspection and how much corrosion is present. Again, the listing of these bulletins does not mean that a wide-area technique would be beneficial, but rather that a wide-area technique could be of possible benefit.

Table 1. B727 Service Bulletins Selected.

Service Bulletin	Area	Current Method (SB time estimates)	Approximate Material Thickness
727-53-0072	Longitudinal Lap Joints	Longitudinal flap eddy current (LFEC) for material loss (N/A)	0.04″ - 0.14″
727-53-0082	Upper Body Tear Straps	Ultrasonic testing (UT) for disbonds (16 hours - Group 1, 8 hours - Group 2)	0.04″ - 0.065″ skin/ 0.063″ doubler
727-53-0084	Circumferential Doublers	LFEC for material loss (100 hours)	0.04″ skin/ 0.02″ doubler
727-53-0109	Circumferential Doublers	LFEC for material loss (N/A)	0.04″ skin/ 0.02″ doubler
727-53-0144	Forward Lower Body Skin Panel	Visual for corrosion (8 hours)	0.04″ skin/var. doublers
727-53-0159	Aft Lower Body Skin Panel	Visual/LFEC for corrosion (128 hours access + 8 hours inspection)	0.05″ -0.07″ skin/ 0.045 doublers

Figure 1 illustrates the number of airplanes affected by the service bulletins selected. Two of these bulletins are affected by the mandatory modification program, which requires that the service bulletin modifications be performed at or before 20 years of service, eliminating the inspections. As of June 1996, only line numbers 1205 to 1216 are left with less than 20 years of service. The remaining four service bulletin modifications have to be carried out on or before the airplanes reach 60,000 flight cycles.
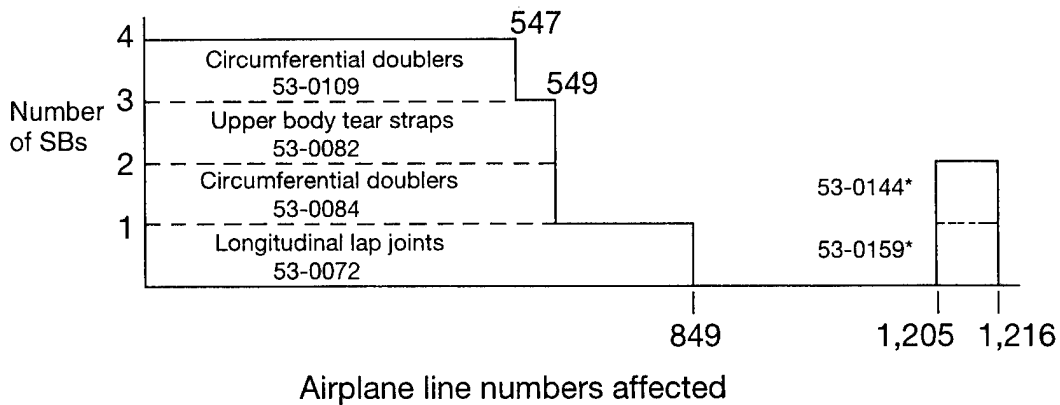
*20-year mandatory modification—as of 6/96 only L/Ns 1205 to 1216 remaining

Figure 1. B727 Service Bulletins Line Numbers.

Table 2 lists the six B737 service bulletins selected. Service Bulletin 53-1179 currently calls out a one-time internal visual inspection for disbonding of the tear straps. It is estimated that this inspection takes 136 hours, plus time for gaining and restoring access. The service bulletin allows an external ultrasonic bond inspection as an option that is estimated to take 12 hours to perform.

Table 2. B737 Service Bulletins Selected

Service Bulletin	Area	Current Method (SB time estimates)	Approximate Material Thickness
737-53A1039	Longitudinal Lap Joints	LFEC for corrosion (N/A)	0.036″ skin/ doublers
737-53-1065	Aft Fuselage Skin Panel	UT for disbonds (4 to 6 hours)	0.036″ skin/ doublers
737-53-1076	Circumferential Joints	Visual for corrosion (24 hours), UT for disbonds—L/N 1-219 (80 hours)	0.036″ skin/ doublers
737-53-1078	Window Belt	LFEC for corrosion—L/N 1-519 (N/A), UT for disbonds (4 hours)	0.036″ skin/ doublers
737-53-1179	Fuselage Tear Straps	Visual for disbonds (136 hours plus access) UT for disbonds (12 hours)	0.036″ skin/ doublers
737-55-1022	Elevator Rear Spar	UT for disbonds (3 hours)	0.012″ skin/ doublers

Figure 2 illustrates the number of airplanes affected by the B737 service bulletins selected. It can be seen that the one-time inspection called out in Service Bulletin 53-1179 affects over 2000 airplanes. An operator with a large B737 fleet could save a large amount of time if a wide-area technique could be used.
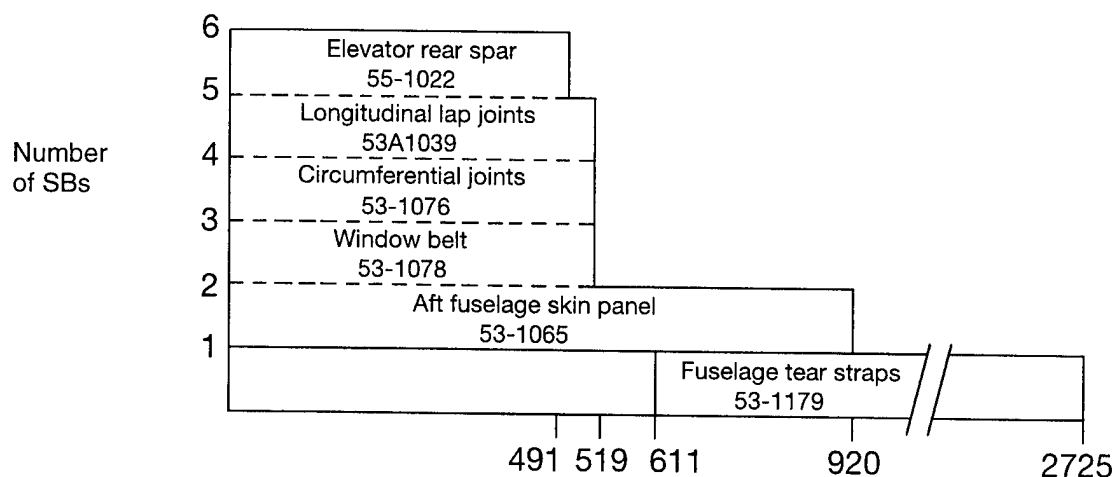

Figure 2. B737 Service Bulletin Line Numbers

Table 3 lists the four B747 service bulletins selected. A very large time savings could be achieved by a wide-area technique for Service Bulletin 53A2279. The service bulletin estimates 72 hours for inspecting non-Special Performance (SP) airplanes (36 hours for SPs) using ultrasonic inspection.

Table 3. B747 Service Bulletins Selected.

Service Bulletin	Area	Current Method (SB time estimates)	Approximate Material Thickness
747-53A2279	Upper Skin Tear Strap	UT for disbonds (72 hours - Group 1, 36 hours - Group 2)	0.062″ - 0.094″ skin/ 0.063″ - 0.071doubler
747-53-2307	Longitudinal Lap Joints	LFEC for material loss (N/A)	0.062″ - 0.250″
747-55-2017	Outboard (OB) Elevator Trailing Edge (TE) Wedge	RT for water in honeycomb (12 hours)	0.03″ fiberglass
747-57-2261	Inboard Fixed TE Panel	RT (16 hours) or Infrared (IR) (1hour) for water UT for disbond (32 hours)	0.047″ 0.066″ fiberglass

Figure 3 shows the number of airplanes affected by the B747 service bulletins selected. After line number 349 there is only one applicable service bulletin. This bulletin, for the wing inboard fixed trailing edge panel, requires inspections for delamination and water ingression. The inspection for water ingression only has to be carried out once if there is no water present. The ultrasonic inspection for disbonding, however, has to be repeated every 1200 flight cycles until the panel is replaced.
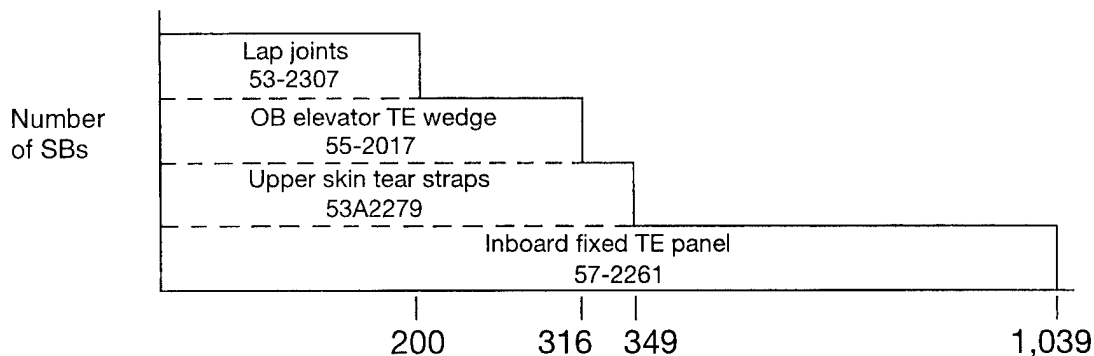

Figure 3. B747 Service Bulletin Line Numbers.

COMPOSITE INSPECTION

Service Bulletin 747-57-2261 for the inboard fixed trailing edge panel is an example of where wide-area, new-technology inspection techniques are being used. The early revisions of the service bulletin required the use of radiography to detect water. The service bulletin also called out the use of ultrasonic bond testing to detect delamination between the panel skin and core. The latest release of the service bulletin includes an option to use infrared thermography in place of radiography to detect water. This newer technology inspection techniques have many advantages over conventional radiography. Approval has

also been given for the use of laser shearography in place of the bond test procedure called out in the service bulletin. This service bulletin is a good example of the great potential for new-technology inspection techniques.

The increased use of advanced composite materials provides a great opportunity for new-technology NDI techniques to be used. The introduction of the B737-300, B757, and B767 airplanes in the 1980s created a demand for new NDI techniques to inspect the advanced composite materials. Although there are a few composite parts, such as the B757 and B767 rudder and elevators, that require ultrasonic inspection for delamination, the primary inspection method is visual for evidence of damage, such as damage from impact or lightening strike. NDI techniques are then used to assess the damage and inspect the ensuing repair. Damage assessment is usually performed with a tap test or ultrasonic inspection, and it is relatively straightforward. The use of ultrasonics for composite repair inspection, however, has proven to be difficult, and some of the new-technology techniques may offer advantages, such as simplified interpretation of results.

Although existing techniques are currently meeting the needs of composite inspection, there is a potential for improvements with new-technology techniques. Already, infrared thermography has been shown to be an excellent replacement for radiographic detection of water and ice in honeycomb. Thermography has been shown to save time, with equivalent results, without the radiation hazard [5]. The need for advanced inspection techniques will also increase as airplanes like the B777, with composite primary structure, grow older.

CONCLUSIONS

New-technology inspection techniques offer a big potential in the airplane industry. It is important, however, that the techniques fit into the overall picture of damage tolerance. In some cases, the technique that can find the smallest defect may not be the technique of choice.

The detection of hidden corrosion is a concern on older model airplanes. Visual inspection has been used as the primary means of detecting hidden corrosion in such areas as lap joints. Visual inpsection is also the method used in the FAA-mandated Corrosion Prevention and Control Program for all model airplanes. For almost all Boeing commercial airplane applications, visual inspection for corrosion is more than adequate to meet the inspection requirements.

A detailed study of existing service bulletins for the B727, B737, and B747 showed that there are some applications for wide-area, new-technology techniques. Many of these potential applications require that the new techniques be able to estimate the amount of corrosion material loss before it can effectively replace the existing eddy-current technique. There is a possible large time savings for one B737 and one B747 service bulletin currently calling out ultrasonic bond inspection.

The expanded use of advanced composite materials provides the greatest opportunity to maximize the benefit from new-technology techniques. Although existing methods are capable of performing these inspections, research and development into newer and more advanced techniques is an important part of improving the overall inspection process.

The Boeing Company will continue to research new-technology techniques and try to identify new applications. We will also continue to monitor the research into these techniques being done throughout the industry, and we will encourage the advancement of NDI technology.

REFERENCES

1. Komsky, I. N. et al.: An Ultrasonic Technique to Detect Corrosion in DC-9 Wing Box From Concept to Field Application, *Materials Evaluation*, Vol. 53, No. 7, July 1995, pp. 848-852.

2. Komorowski, J. P. et al.: Double Pass Retroreflection for Corrosion Detection in Aircraft Structures, *Materials Evaluation*, Vol. 54, No. 1, January 1996, pp. 80-86.

3. Favro, L. D. et al.: Thermal Wave Imaging of Aircraft Structures, *Review of Progress in Quantitative NDE*, Vol. 14, pp. 461-466, Edited by D. O. Thompson and D. E. Chimenti, Plenum Press, New York, 1995.

4. Fitzpatrick, G. I. et al.: Magneto-Optic/Eddy-Current Imaging of Subsurface Corrosion and Fatigue Cracks in Aging Aircraft, *Review of Progress in Quantitative NDE*, Vol. 15, pp. 1159-1166, Edited by D. O. Thompson and D. E. Chimenti, Plenum Press, New York, 1996.

5. Thompson, J. G.: Thermography for Honeycomb Panel Inspection, *Review of Progress in Quantitative Nondestructive Evaluation*, Vol. 15B, Plenum Press, New York, 1996, pp. 1271-1274.

SIMULATION OF STABLE TEARING AND RESIDUAL STRENGTH PREDICTION WITH APPLICATIONS TO AIRCRAFT FUSELAGES

Chuin-Shan Chen, Paul A. Wawrzynek, and Anthony R. Ingraffea
Cornell University Fracture Group
31 Rhodes Hall
Ithaca, NY 14853

SUMMARY

The FRANC3D/STAGS software system is developed to model curvilinear crack growth in aircraft fuselages. Simulations of fatigue crack growth have been reported previously [1, 2]. This paper presents an enhancement to model stable tearing for residual strength prediction. A tearing simulation along a crack path that captures the material nonlinearities inherent at the crack tip is performed. The CTOA (Crack Tip Opening Angle) is used as a crack growth criterion to characterize the fracture process under conditions of large-scale yielding. Numerical simulations of a middle crack tension specimen were performed. Results of predicted residual strength from FRANC3D/STAGS agree closely with experimental measurements, but the relative difference between them increases as the width of the panel increases. A better agreement is achieved by including plane strain effects around the crack tip.

Stable tearing simulations of a pressurized fuselage panel, representative of a typical narrow-body aircraft, were performed using the predicted crack path obtained from the fatigue crack growth simulation. A simple extrapolation of the maximum tangential stress theory to materials with orthotropic toughness is used as the directional criterion for the fatigue crack growth simulation. Cracks are allowed to grow arbitrarily as a part of the simulation. Predicted trajectories agree well with measurements from a full-scale pressurized panel test. Residual strength with the initial crack located in various positions in the fuselage panel is predicted. Results show that a difference in the initial crack location could have significant effect on the residual strength prediction.

INTRODUCTION

The FRANC3D (FRacture ANalysis Code for 3D Solids and Shells) program has been developed for simulating curvilinear crack growth in aircraft structures [1, 2]. It supports simulation of both curvilinear discrete crack propagation in stiffened thin-shell structures and nonplanar discrete crack propagation in solid structures. It can be used to represent the crack geometry in a fuselage and to simulate crack interaction with various structural elements. The stresses and displacements needed to calculate the relevant fracture

parameters are provided by the STAGS (**ST**ructural **A**nalysis of **G**eneral **S**hells) program [3]. This innovative numerical strategy, combining the geometric modeling and curvilinear crack growth simulation in FRANC3D, with the shell finite element analysis of STAGS, allows one to simulate fatigue and fracture in aircraft fuselages.

In ductile material states, slow stable tearing can precede rapid fracture when yielding is extensive. A number of different fracture criteria including crack tip stress or strain, crack tip opening displacement or angle, crack tip force, energy release rate, J-integral, and the tearing modulus have been proposed to characterize this fracture process under conditions of large-scale yielding. Of these, the crack tip opening angle (CTOA) or the crack tip opening displacement (CTOD) at a specified distance from the crack tip was shown to be suitable for modeling ductile fracture in thin aluminum sheet [4-6]. In the present work, the CTOA criterion developed by Newman *et al.* [7-9] is used as the fracture criterion to characterize stable crack growth in aluminum fuselage structures. Elastic-plastic finite element analysis based on incremental flow theory with a small strain assumption is used to capture material nonlinearity [10]. A nodal force relaxation technique is used to simulate the stable crack growth [3].

In the first part of the paper, a middle crack tension specimen M(T) is modeled. Results of predicted residual strength by FRANC3D/STAGS are compared with experimental measurements [11]. An engineering approach utilizing the concept of a "plane strain" core [9] to capture the three-dimensional behavior near the tip of the crack in a thin shell is proposed.

In the second part of the paper, a stable tearing simulation of a cracked fuselage is performed on a predefined but arbitrary curvilinear crack path. The tearing path is determined from a fatigue crack simulation with the crack grown in an anisotropic medium. An appropriate length of the crack is then "closed" to predict residual strength assuming stable tearing. Effects of the various locations of the initial crack in the fuselage panel on residual strength prediction are investigated.

RESIDUAL STRENGTH PREDICTION: MIDDLE CRACK TENSION SPECIMEN, M(T)

The objective of this study is to verify the applicability of FRANC3D/STAGS to predict residual strength of cracked shell structures. The M(T) test specimen configuration and the simulation model are shown in Figure 1. In the simulation, displacements are applied uniformly in a vertical direction, and the applied stresses are obtained by averaging total forces from all nodes on the displaced edge, divided by the product of width and thickness. A piecewise linear representation is used for the uniaxial stress-strain curve for 2024-T3 aluminum (Figure 2). The critical CTOA is 6 degrees, measured 0.04" behind the crack tip. STAGS five-noded elements are used to transition from locally refined zones around the crack tip to a coarse mesh away from the crack. The finite element mesh model for the 12" wide panel is shown in Figure 3.
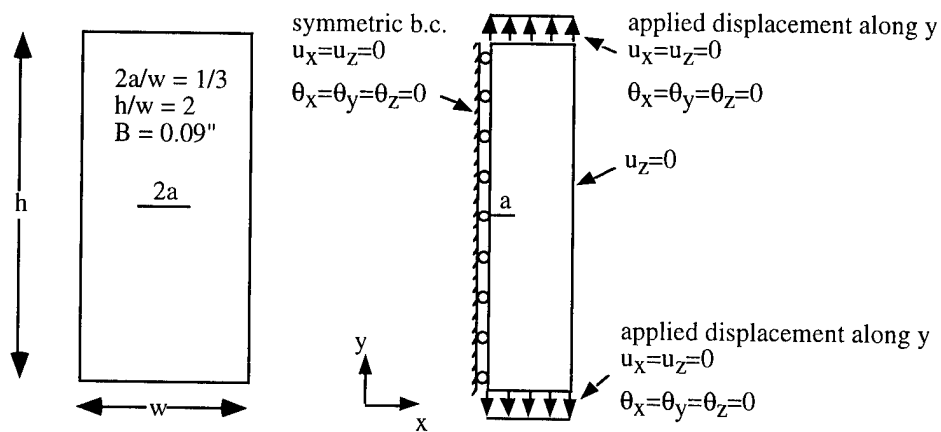
Figure 1. The M(T) Test Specimen Configuration and the Simulation Model.
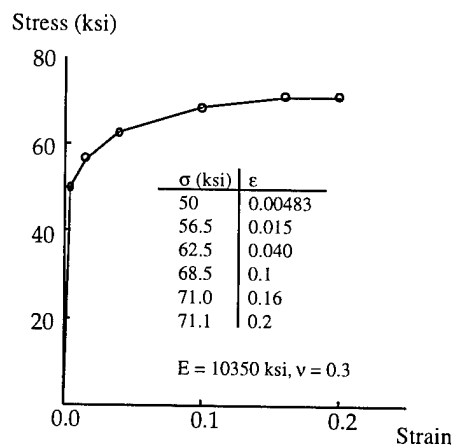

σ (ksi)	ε
50	0.00483
56.5	0.015
62.5	0.040
68.5	0.1
71.0	0.16
71.1	0.2

E = 10350 ksi, ν = 0.3

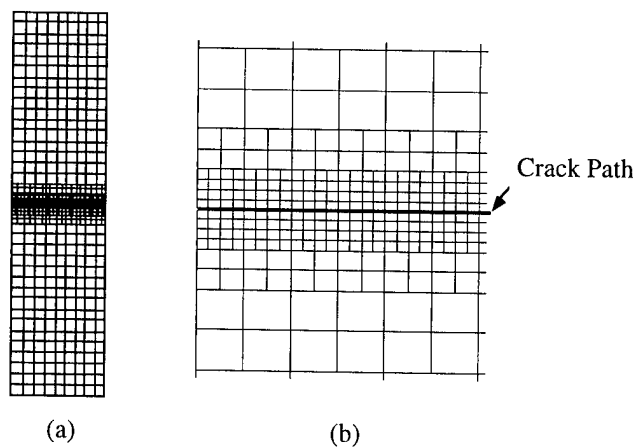Figure 2. Piecewise Linear Representation of the Uniaxial Stress-Strain Curve for 2024-T3 Aluminum.

(a)   (b)

Figure 3. (a) Finite Element Mesh for 12" Wide M(T) Specimen and (b) Detail Along Crack Path.

Plasticity information was obtained during the course of the simulation. Figure 4 depicts the plastic zone of the 12" panel for the cases with 0.2", 0.32", and 0.36" half crack extension. The shape and location of the plastic zone related to the crack tip varies as the crack grows. During the nodal release step, the plastic zone behind the crack tip unloads to an elastic state (but with residual stresses), while the portion of the zone ahead of the tip expands. In effect, the plastic zone moves with the crack tip as expected, leaving the appropriate plastic wake. The plastic zone size continues to expand until it reaches the boundary of the M(T) test specimen.

$\Delta a = 0.2"$ $\Delta a = 0.32"$ $\Delta a = 0.36"$
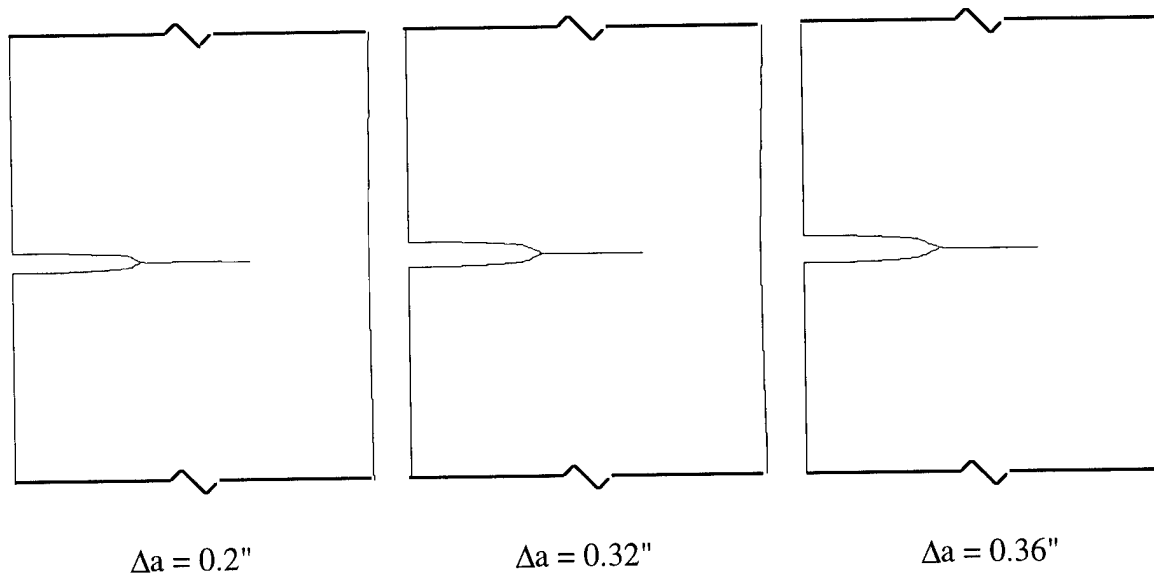
Figure 4. The Predicted Plastic Zone of the 12" Panel for the Cases With 0.2", 0.32", and 0.36" Half Crack Extension.

Figure 5 plots the applied stress vs. half crack extension for the 12" panel and predicted results obtained from FRANC3D/STAGS are compared with experimental measurements [11]*. The peak stress obtained from the applied stress-crack extension curve is the residual strength of the cracked panel. For the 12" panel, residual strength is approximately equal to the applied load when net section plasticity is reached (Figure 4, Δa = 0.36"). For the 24" panel, the predicted residual strength is slightly higher than the loading corresponding to net section plasticity. This may be due to the strain hardening effects of the material.

Table 1 compares predicted residual strength for various panel widths with experimental measurements. As the width of the panel increases, the relative difference between experimental measurements and numerical prediction increases. Similar behavior was reported by Newman et al. [9]. They observed better correlation by including a "plane strain core" at the crack tip. For the present work, similar effects are incorporated into the simulation and are discussed in detail below.

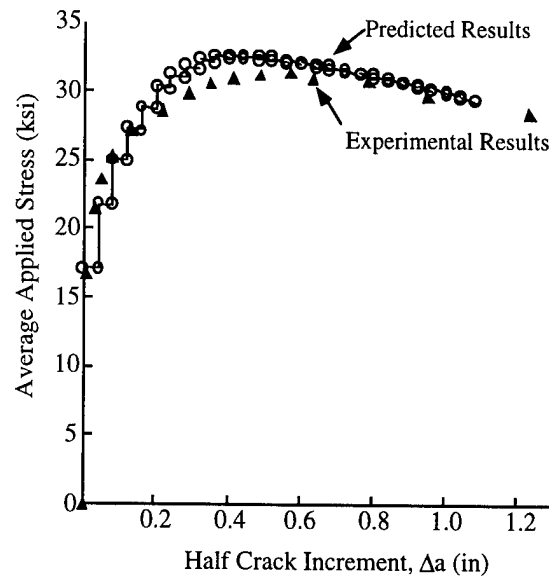* The scatter of the experimental data is about ± 1 %.

Figure 5. The Applied Stress Versus Half Crack Extension for the 12" Panel.

Table 1. Residual Strength Prediction of M(T) test by FRANC3D/STAGS.

Width (w)	Initial Crack (2a)	Experimental	Predicted	% Difference
1.5"	0.5"	37.3 ksi	37.6 ksi	+0.8 %
3"	1"	34.5 ksi	34.9 ksi	+1.2 %
12"	4"	31.3 ksi	32.6 ksi	+4.1 %
24"	8"	28.4 ksi	32.3 ksi	+13.7 %

An Engineering Approach to Account for Plane Strain Core Effects

Thin-shell finite elements behave essentially in plane stress. However, due to the finite thickness of the panel, the behavior near the tip of the crack is three-dimensional in nature, and higher stress triaxiality can build up leading to a plane strain constraint at the crack tip [12]. No analytical solution was found to incorporate this effect into the shell finite element analysis. Instead, an engineering approach that "adjusts" the initial yield stress, σ_y, in shell elements based on the HRR fields [13, 14] is proposed.

Based on the relationship between J-integral and the crack opening displacement derived from the HRR fields, one has [15]

$$\delta_t = d_n \frac{J}{\sigma_y} \qquad (1)$$

609

in which the crack tip opening displacement, δ_t, is defined as the opening distance between the intercept of two $45°$ lines, drawn from the tip to the deformed profile. Dependence of the coefficient d_n upon the strain hardening exponent and the initial yield strain for plane stress and plane strain conditions was determined by Shih [15]. For the material used in this example, d_n is about 0.74 for plane stress and 0.55 for plane strain. By assuming that J and δ_t remain constant during the crack growth simulation, one can obtain an equivalent initial yield stress, $\overline{\sigma}_y$, for the plane strain condition. The modified uniaxial stress-strain curve that accounts for plane strain effects is plotted in Figure 6.
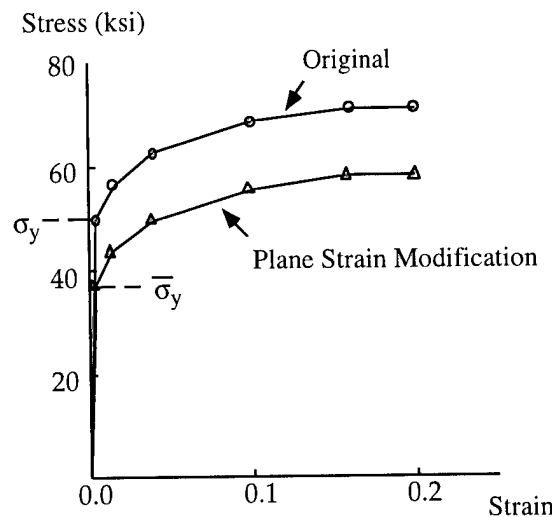

Figure 6. The Uniaxial Stress-Strain Relationship for the Original Material and the Material With Plane Strain Modification.

Due to the introduction of $\overline{\sigma}_y$, a mixed plastic zone is developed and a small, artificial elastic zone between the original and plane strain material is observed (Figure 7). A series of numerical simulations was performed with a core of plane strain shell elements around the crack. Table 2 compares predicted residual strength for various panel widths, with various plane strain core heights embedded, to experimental measurements. With the introduction of a lower initial yielding stress for the plane strain material, the predicted results decrease as the height of the plane strain core increases, and a better agreement with experimental measurements is achieved for the 12" and 24" panels. However, the validity of this ad-hoc approach to general applications other than the M(T) specimen is not clear. To investigate effects of the behavior near the crack tip on residual strength prediction, a fully three-dimensional analysis with a large strain formulation is needed in the future. Thus, only the regular shell finite element analysis will be used in the prediction of the residual strength of cracked fuselages discussed next.
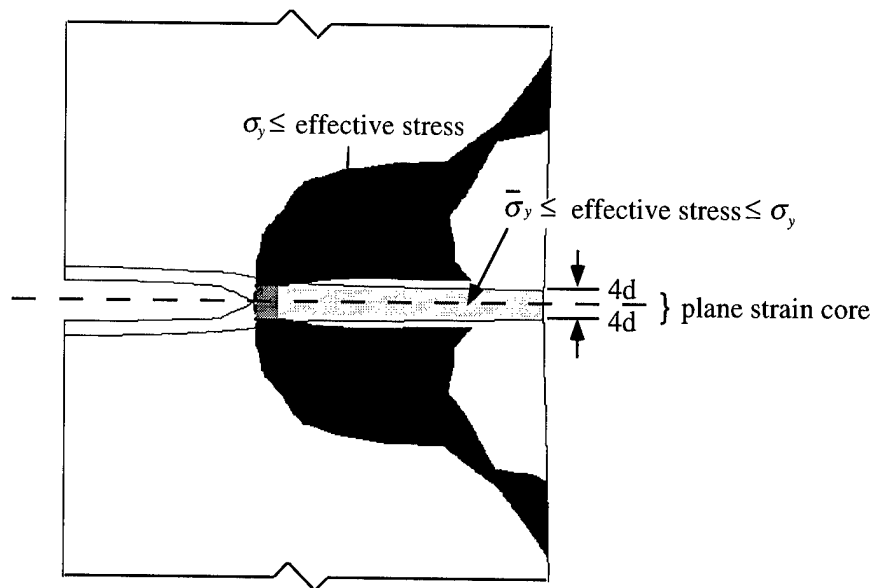
610

Figure 7. A Predicted Mixed Plastic Zone of the 12" Panel (Da = 0.44" and Plane Strain Core Height = 2 x 4d).

Table 2. Residual Strength Prediction of M(T) test by FRANC3D/STAGS Considering "Plane Strain Core" Effects.

Panel Width (w)	Plane Strain Core Height (d = 0.04")	Experimental	Predicted	% Difference
3"	2 x d	34.5 ksi	32.5 ksi	-2.9 %
12"	2 x d	31.3 ksi	32.4 ksi	+3.5 %
	2 x 2d		32.0 ksi	+2.2 %
	2 x 4d		31.5 ksi	+0.6 %
24"	2 x 4d	28.4 ksi	31.6 ksi	+11.2 %
	2 x 8d		30.9 ksi	+8.8 %

RESIDUAL STRENGTH PREDICTION OF AN AIRCRAFT FUSELAGE

In this section, FRANC3D/STAGS is used to predict the residual strength of a pressurized fuselage panel that is representative of a typical narrow-body aircraft. The panel, comprised of skin, frames, stringers, tear straps, and shear clips, is illustrated in Figure 8. Detailed dimensions, structure component idealizations, and the hierarchical modeling strategy are reported by Potyondy et al. [1, 2]. The FRANC3D geometric model (Figure 9a) represents a 2x2 bay panel with an initial saw cut along an edge of a stringer in the skin of the panel, and the corresponding initial mesh model is shown in Figure 9b.
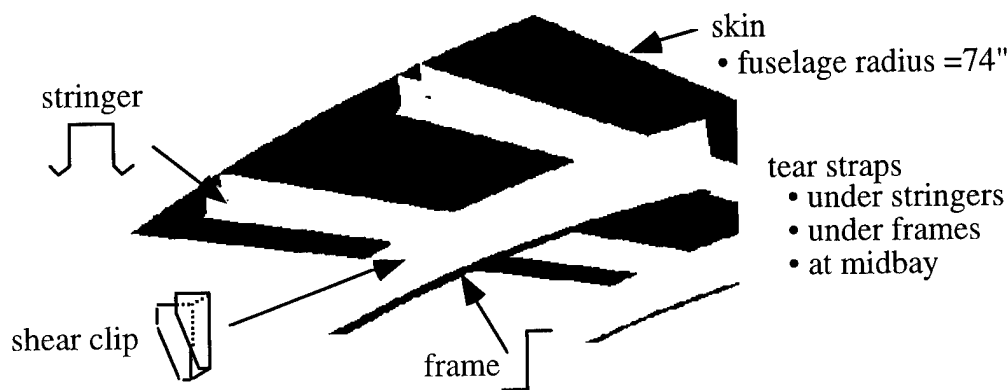
Figure 8. The Structural Components of a Typical Narrow-Body Aircraft Fuselage.
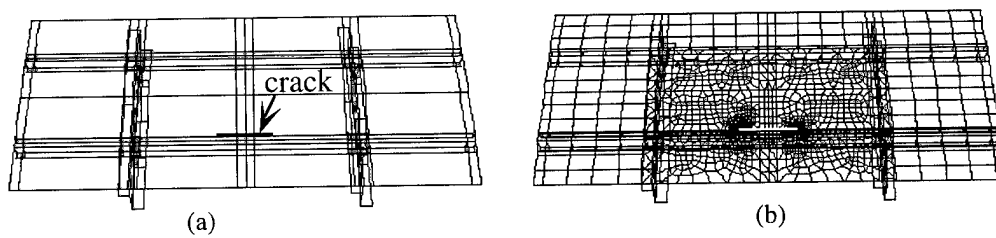

Figure 9. (a) The FRANC3D Geometric Model, and (b) the Mesh Model With an Initial Crack Along an Edge of a Stringer in the Skin of the Panel.

A geometrically nonlinear elastic analysis of fatigue crack growth is performed first. An appropriate length of crack is then "closed" to perform a tearing simulation that includes both geometric and material nonlinear effects. The possible trajectory change due to stable tearing is neglected, and the transition from fatigue to tearing is assumed to occur abruptly and the plasticity history prior to tearing is ignored for this analysis.

Crack Trajectory Prediction

Crack trajectories are predicted based on fatigue crack growth simulation. A set of four stress intensity factors (k_1, k_2, K_I, K_{II}) proposed by Hui and Zehnder [16] accounts for both the in-plane membrane loading (K_I, K_{II}) and the out-of-plane bending loading (k_1, k_2) experienced by a crack in a fuselage structure. For each crack growth simulation cycle, the equilibrium state with fully applied loading is obtained from a geometrically nonlinear shell analysis. Stress intensity factors are computed using the modified crack closure integral method [17].

Depending on the material's rolling direction, the apparent toughness along circumferential and longitudinal directions may be different. For 2024-T3 aluminum, the direction perpendicular to the rolling direction could have a 5% to 20% higher toughness than that of the rolling direction. For the panel tested, the rolling direction was longitudinal; thus, the cracks growing from the initial saw cut are experiencing T-L crack growth. In general, crack propagation in an anisotropic medium is considerably more complicated than the isotropic case [18]. In the present work, a simple extrapolation of the maximum tangential stress theory to materials with orthotropic toughness proposed by Buczek and Herakovich [19] is used. The tangential stress is normalized with respect to the directional strength of the material and crack propagation is assumed to be in the direction of maximum normalized stress, such that

$$Max\left\{\frac{\sigma_{\theta\theta}(K_I, K_{II})}{R(\theta)}\right\} = (\frac{\sigma_{\theta\theta}}{R})_{critical}, \text{ at } \theta = \theta_c \qquad (2)$$

where $R(q)$ is a strength parameter characterizing the material fracture resistance, $\sigma_{\theta\theta}$ is the tangential stress, and θ_c is the angle of impending crack propagation. The fracture resistance is characterized simply as an ellipse based on fracture toughness for propagation along T and L directions. The theory is for fracture propagation so its applicability to fatigue crack growth is not clear. The initial propagation angle away from the stringer/tear strap for the orthotropic case, with 20% higher toughness in the T than in the L direction of propagation, differs by 16.5° compared to the isotropic case (Figure 10).
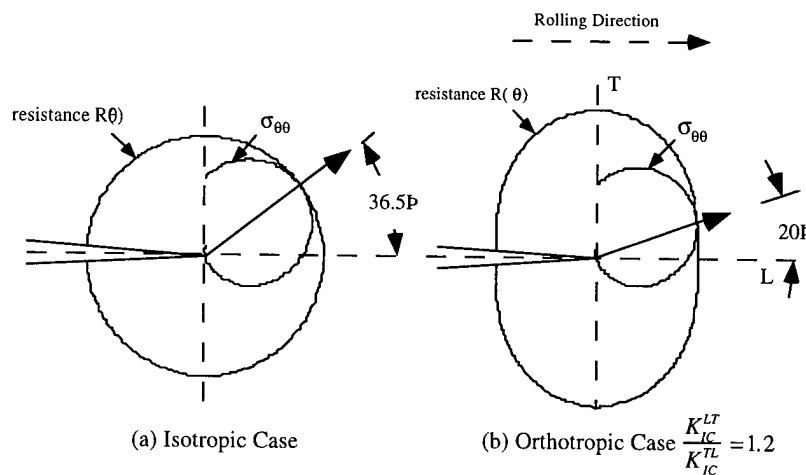

Figure 10. The Predicted Initial Propagation Angles Away From the Stringer/Tear Strap for the (a) Isotropic and (b) Orthotropic Cases.

The crack is grown in 1-inch increments at each crack tip. The predicted results are compared with a full-scale pressurized panel test [20] with an initial saw cut just above the stringer/tear strap (Figure 11). Good agreement between the predicted results and the experimental measurements is obtained.
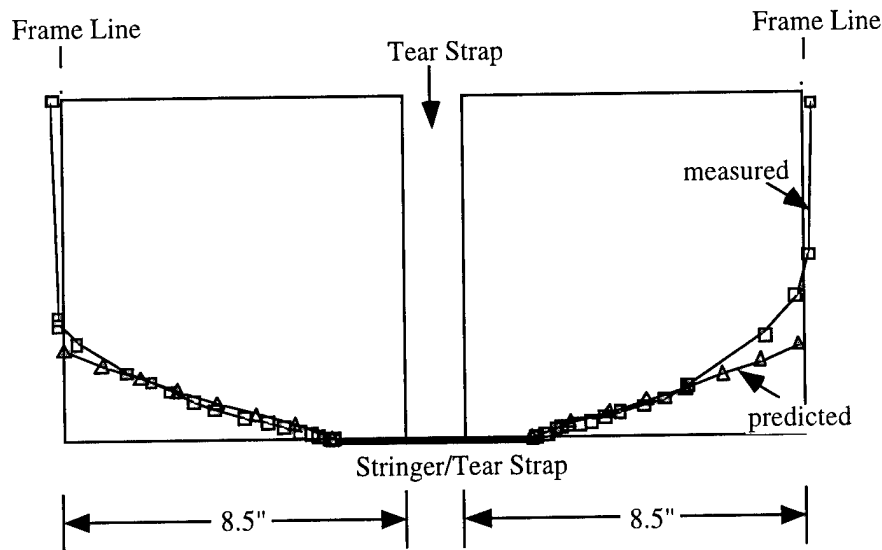
Figure 11. Comparison Between Computed and Measured Crack Trajectories. The Triangle and Box Denote the Crack Tip Location From Prediction and Experimental Measurements.

Numerical simulations of fatigue crack growth were performed for three different locations of the initial crack: along the stringer/tear strap, slightly away from the stringer (0.45" above the stringer), and at a quarter of the distance between stringers. Predicted crack trajectories are plotted in Figure 12. The last inch of crack growth increment at each end will be used as the tearing path in the following simulation.
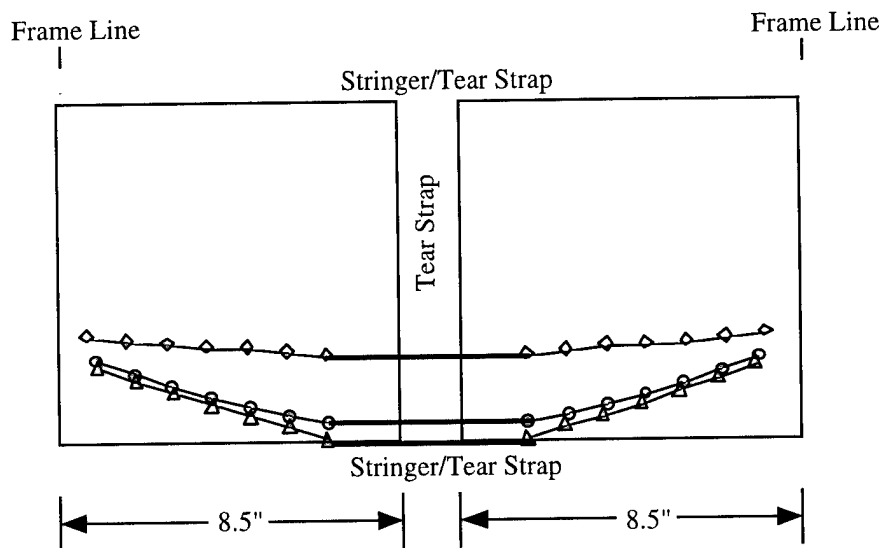

Figure 12. Comparison Among Computed Crack Trajectories. The Triangle, Circle, and Diamond Denote the Crack Tip Location From Prediction With Initial Crack Located Along the Stringer, 0.45" Above the Stringer, and at a Quarter of the Distance Between Stringers.

614

Stable tearing simulation was performed for cases with three different initial crack positions. Predefined crack paths shown in Figure 12 obtained from the fatigue crack growth simulation are used to predict residual strength assuming stable tearing. The last inch of fatigue crack growth is "closed" to perform the tearing simulation. A critical CTOA of 5.1 degrees, measured 0.04" behind the crack tip and assumed to be the same along the T and L directions, is used. The finite element mesh is created by the all-quadrilateral element mesh generator [21] with a template inserted along the tearing path (Figure 13).

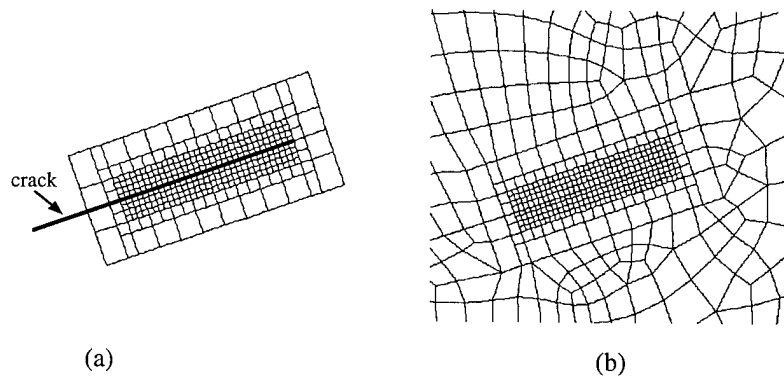
(a)   (b)

Figure 13. (a) A Template Inserted Along the Tearing Path and (b) the Final Mesh Generated By the all-Quadrilateral Element Meshing Algorithm.

Figure 14 plots the applied pressure vs. half crack extension curve of the left crack tip for each case. Results of predicted residual strength based on an asymptotic value of curve fitting are 9, 9, and 11 psi for cases with initial crack located along the stringer, 0.45" above the stringer, and at a quarter of the distance between stringers, respectively. By comparing the first and second cases with the third, a 22 % difference in the residual strength prediction due to the initial crack location was found.
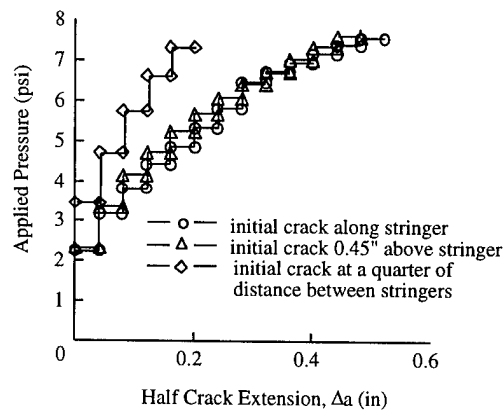

Figure 14. The Applied Pressure Versus Half Crack Extension Curves for the Cases With the Initial Crack Located Along the Stringer/Tear Strap, 0.45" Above the Stringer, and at a Quarter of Distance Between Stringers.

CONCLUDING REMARKS

An enhancement of the FRANC3D/STAGS software system with respect to stable tearing simulation for residual strength prediction is presented. For tearing simulations of a middle crack tension specimen, the predicted residual strength from FRANC3D/STAGS agrees closely with that from the test. However, the relative difference between experimental measurements and the prediction increases as the width of the panels increases. An engineering approach for shell finite element analysis by utilizing the concept of "plane strain" core to capture the three-dimensional behavior near the tip of the crack is proposed. A better agreement with experimental measurements is obtained. However, the validity of this heuristic approach to general applications other than the M(T) specimen is not clear. To further investigate effects of the crack tip field on residual strength prediction, a fully three-dimensional analysis with a large strain formulation is needed in the future.

Stable tearing simulation of a pressurized fuselage panel, representative of a typical narrow-body aircraft, is performed using the predicted crack path obtained from the fatigue crack growth simulation. The skin is assumed to have 20% higher toughness in the direction perpendicular to the rolling direction than in the rolling direction. The fatigue crack growth direction criterion based on a simple extrapolation of the maximum tangential stress theory to materials with orthotropic toughness is used. Predicted crack growth trajectories agree well with the measurements from a full-scale pressurized panel test. Residual strength with the initial crack located in various positions in the fuselage panel is investigated. Results showed that a difference in the initial crack location could have significant effects on the residual strength prediction. In the present study, we (a) neglect the possible trajectory change due to stable tearing, assume (b) that the transition from fatigue to tearing occurs abruptly, and (c) that the plasticity history before the tearing simulation can be ignored. Each of these might have significant effects on residual strength prediction and should be investigated in the future.

An innovative numerical strategy in simulating fatigue and fracture of an aircraft fuselage has been developed. The close coupling of FRANC3D/STAGS, by combining the geometric modeling and curvilinear crack growth simulation in FRANC3D with the shell finite element analysis of STAGS, seeks not only to represent and analyze the problems faithfully but also efficiently.

ACKNOWLEDGMENTS

REFERENCES

1. Potyondy, D. O.: A Software Framework for Simulating Curvilinear Crack Growth in Pressurized Thin Shells, Ph.D. Thesis, *School of Civil and Environmental Engineering*, Cornell University, Ithaca, NY, 1993.

2. Potyondy, D. O., Wawrzynek, P. A., and Ingraffea, A. R.: Discrete Crack Growth Analysis Methodology for Through Cracks in Pressurized Fuselage Structures. *International Journal for Numerical Methods in Engineering*, vol. 38, no. 10, 1995, pp. 1611-1633.

3. Brogan, F. A., Rankin, C. C., and Cabiness, H. D.: *STAGS User Manual Version 2.0*, 1994, Lockheed Palo Alto Research Laboratory, Palo Alto, CA.

4. Dawicke, D. S., Sutton, M. A., Newman Jr., J. C., and Bigelow C. A.: Measurement and Analysis of Critical CTOA for an Aluminum Alloy Sheet, *NASA TM-109024*, 1993.

5. Dawicke, D. S., and Sutton, M. A.: Crack-Tip-Opening Angle Measurement and Crack Tunneling under Stable Tearing in Thin Sheet 2024-T3 Aluminum Alloy, *NASA CR-191523*, 1993.

6. Newman, J. C., Jr., Bigelow, C. A., and Dawicke, D. S.: Finite-Element Analyses and Fracture Simulation in Thin-Sheet Aluminum Alloy, in *Durability of Metal Aircraft Structures, Proceedings of the International Workshop on Structural Integrity of Aging Airplanes*, 1992, Atlanta Technology Publications, Atlanta, GA.

7. Newman, J. C., Jr.: An Elastic-Plastic Finite Element Analysis of Crack Initiation, Stable Crack Growth, and Instability, in *Fracture Mechanics: Fifteen Symposium, ASTM STP 833*, 1984.

8. Newman, J. C., Jr., Booth, B. C., and Shivakumar, K. N.: An Elastic-Plastic Finite-Element Analysis of the J-Resistance Curve Using a CTOD Criterion, in *Fracture Mechanics: Eighteen Symposium, ASTM STP 945*, 1988, Philadelphia.

9. Newman, J. C., Jr., Dawicke, D. S., Sutton, M. A., and Bigelow, C. A.: A Fracture Criterion for Widespread Cracking in Thin-Sheet Aluminum Alloys, in *Proc. of the 17th Symposium of the International Committee on Aeronautical Fatigue*, 1993, Stockholm, Sweden.

10. Zienkiewicz, O. C., and Taylor, R. L.: The Finite Element Method. 4th Ed. Vol. 2, McGraw-Hill Book Company, New York, 1991.

11. Dawicke, D. S.: *Personal Communication*, 1996.

12. Hom, C. L. and McMeeking, R. M.: Large Crack Tip Opening in Thin Elastic-Plastic Sheets. *International Journal of Fracture*, Vol. 45, 1990, pp. 103-122.

13. Hutchinson, J. W.: Singular Behavior at the End of a Tensile Crack in a Hardening Material. *J. Mech. Phys. Solids*, Vol. 16, 1968, pp. 13-31.

14. Rice, J. R. and Rosengren, G. F.: Plane Strain Deformation near a Crack Tip in a Power-Law Hardening Material. *J. Mech. Phys. Solids*, Vol. 16, 1968, pp. 1-12.

15. Shih, C. F.: Relationships Between the J-Integral and the Crack Opening Displacement for Stationary and Extending Cracks. *J. Mech. Phys. Solids*, Vol. 29, No. 4, 1981, pp. 305-326.

16. Hui, C. Y. and Zehnder, A. T.: A Theory for the Fracture of Thin Plates Subjected to Bending and Twisting Moments. *International Journal of Fracture*, Vol. 61, 1993, pp. 211-229.

17. Viz, M. J., Potyondy, D. O., Zehnder, A. T., Rankin, C. C., and Riks, E.: Computation of Membrane and Bending Stress Intensity Factors for Thin, Cracked Plates. *International Journal of Fracture*, Vol. 72, 1995, pp. 21-38.

18. Boone, T. J., Wawrzynek, P. A., and Ingraffea, A. R.: Finite Element Modeling of Fracture Propagation in Orthotropic Materials. *Engineering Fracture Mechanics*, Vol. 26, No. 2, 1987, pp. 185-201.

19. Buczek, M. B., and Herakovich C. T.: A Normal Stress Criterion for Crack Extension Direction in Orthotropic Composite Materials. *J. Compos. Mater.*, Vol. 19, 1985, pp. 544-553.

20. Miller, M., Kaelber, K. N., and Worden, R. E.: Finite Element Analysis of Pressure Vessel Panels, in Durability of Metal Aircraft Structures: *Proc. of International Workshop on Structural Integrity of Aging Airplanes*, 1992, Atlanta Technology Publications, Atlanta, GA.

21. Potyondy, D. O., Wawrzynek, P. A., and Ingraffea, A. R.: An Algorithm to Generate Quadrilateral or Triangular Element Surface Meshes in Arbitrary Domains With Applications to Crack Propagation. *International Journal for Numerical Methods in Engineering*, vol. 38, 1995, pp. 2677-2701.

A STUDY OF CIRCUMFERENTIAL CRACKS IN THE PRESENCE OF MULTIPLE-SITE DAMAGE IN AN AIRCRAFT FUSELAGE

L. Wang, W. T. Chow, H. Kawai,
J. Zhang, and S. N. Atluri
FAA Center of Excellence for
Computational Modeling of Aircraft Structures
Georgia Institute of Technology
Atlanta, Georgia 30332-0356

SUMMARY

Much research has been devoted to the studies of the cracks in the fuselage skin lap joints. However, circumferential cracks, which can be critical, have received little attention. Although the axial skin stress due to internal pressure is smaller than the hoop stress in the skin, the axial stress in the skin can be higher than that in the hoop direction due to bending in the fuselage. This paper presents a detailed study of circumferential cracks in the fuselage using a hierarchical approach. The effect of multiple-site damage MSD on the residual strength is presented together with the residual strength diagrams.

INTRODUCTION

Recent studies [1, 2, 3] suggest that widespread fatigue damage can significantly reduce the residual strength capability of an aircraft fuselage. Much research has been devoted to the studies of cracks in the fuselage lap joints. However, circumferential cracks may result in more serious consequences if their growth cannot be arrested by the stiffened structure of an aircraft fuselage. Circumferential cracks received less attention due to the fact
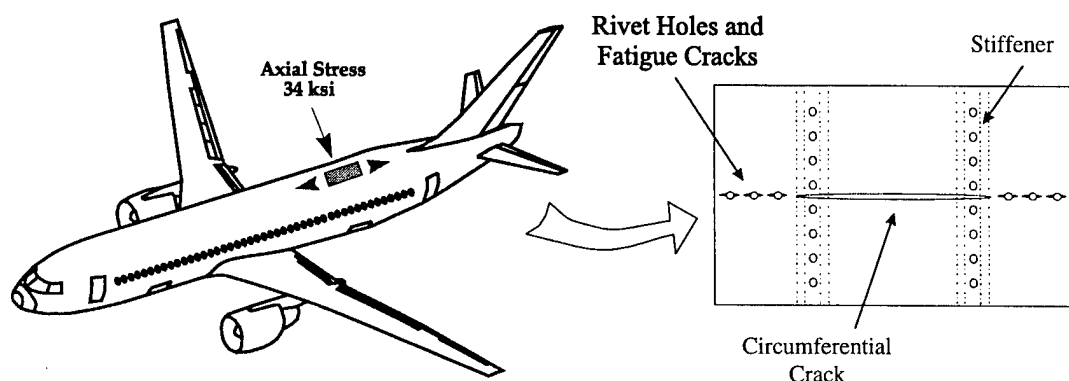

Figure 1. A Critical Location on the Aircraft Fuselage for Circumferential Damage.

that the axial stress due to pressurization is smaller than the hoop stress caused by pressurization. However, the axial skin stress at certain locations on the aircraft fuselage, as illustrated in Figure 1, can be higher than the hoop stress, due to the fuselage down bending and the cabin pressure. The axial stress can be as high as 34 ksi (see [2]), which is about 70% of the initial yield stress. (The initial yield stress of Al 2024-T3 is 47 ksi.) Since the panel works at such a high level of gross stress, even a small stress concentration factor can lead to yielding. Therefore, extensive plastic deformation can be expected in the presence of a lead crack, and nonlinear material behavior becomes very important in the study of residual strength in such a case.

RESIDUAL STRENGTH ANALYSIS

A global-intermediate-local modeling strategy was used to perform the detailed analyses of circumferential cracks. The effort to automate the procedure of global-intermediate-local analysis of an aircraft fuselage reported in [5] makes the analyses much easier. The crack configuration in Figure 2 is chosen because there was a component test [4] carried out in such a configuration. At the time of the test, it was considered to be the most critical situation for a circumferential crack.
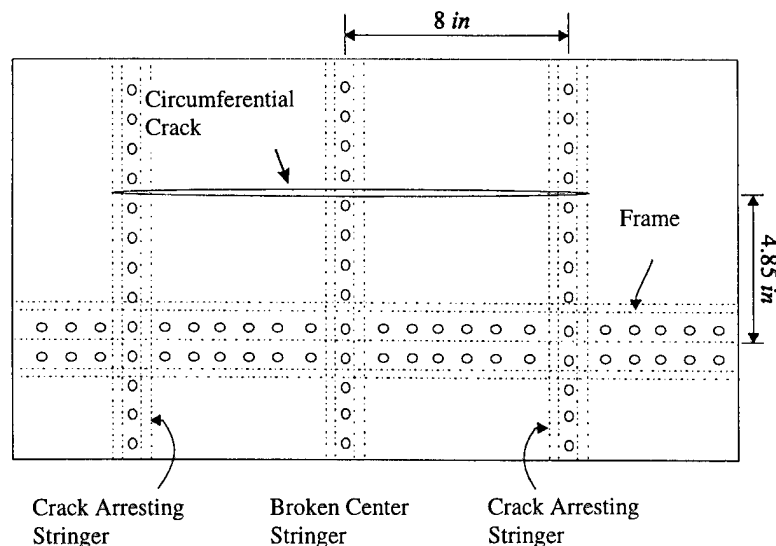

Figure 2. The Location of the Circumferential Crack in the Component Test.

The following is a brief description of the panel under consideration. More details may be found in [4]. The skin is Al 2024-T3 and 0.071 in. thick. Stringer spacing is 8 in. The cross-sectional area of each stringer is 0.5471 in. In the test, the panel failed at the gross stress of 39.7 ksi, with the half-crack length equal to 9.88 inches. The fracture toughness of the skin material is 198 ksi, as suggested by Swift in [2].

Figure 3 shows the residual strength curves obtained using a linear elastic fracture mechanics (LEFM) approach and using an elastic-plastic fracture mechanics (EPFM) approach. When the computed residual strength is compared to the load at the test failure, it is seen that the LEFM prediction overestimates the residual strength of the panel by a large amount. However, the EPFM approach only slightly underestimated the residual strength of the panel. Here, the residual strength curve is obtained by computing the failure load at different crack sizes. Therefore, the effect of stable tearing of the skin is not considered. In the test a static loading was applied on the panel to force the crack to grow from a half-crack length of 7.38 in. to the final failure. Due to the plastic hardening, the panel can take a slightly higher load than the load at the crack initiation. Therefore, the load at crack initiation will be slightly smaller than the failure load observed in the test. Thus, we consider the prediction obtained by the EPFM approach to be very good.
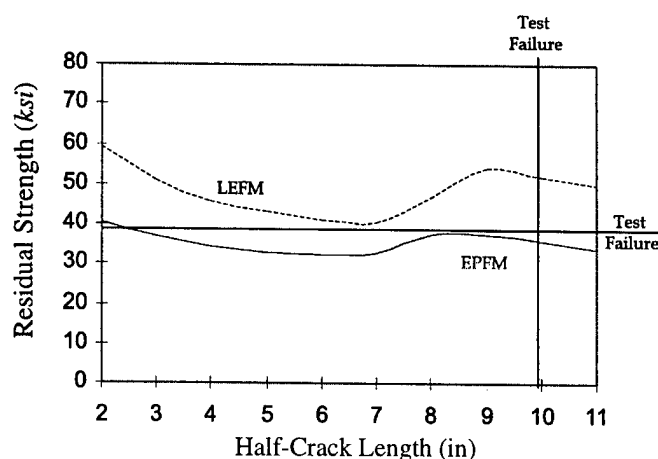

Figure 3. Residual Strength Curve for the Circumferential Crack.

Figure 4 shows the equivalent plastic strain contour plots for cracks of different sizes at the critical loads. It is seen that the plastic zones are very large, with a radius of more than 5 in. The plastic deformations around the rivet holes can also be recognized by the small dark zones near the location of the rivet holes. As the crack size increases, the center broken stringer takes less load. This is indicated by the disappearing of plastic deformations near the rivet holes located at the center stringer. More and more load is transferred onto the crack arresting stringers as the crack size increases, as indicated by the plastic deformations near the rivet holes at the crack arresting stringers. As the crack tips approach the crack arresting stringer, the plastic deformations around the crack tips are restricted by the stringers. However, right after the crack tips penetrate the crack arresting stringers, as seen in the contour plot of Figure 4(g) (a = 8 in), the size of plastic deformation reaches the maximum. At this point, the residual strength curve reaches a local maximum point (see Figure 3) and the crack arresting stringers are behind the crack tips.
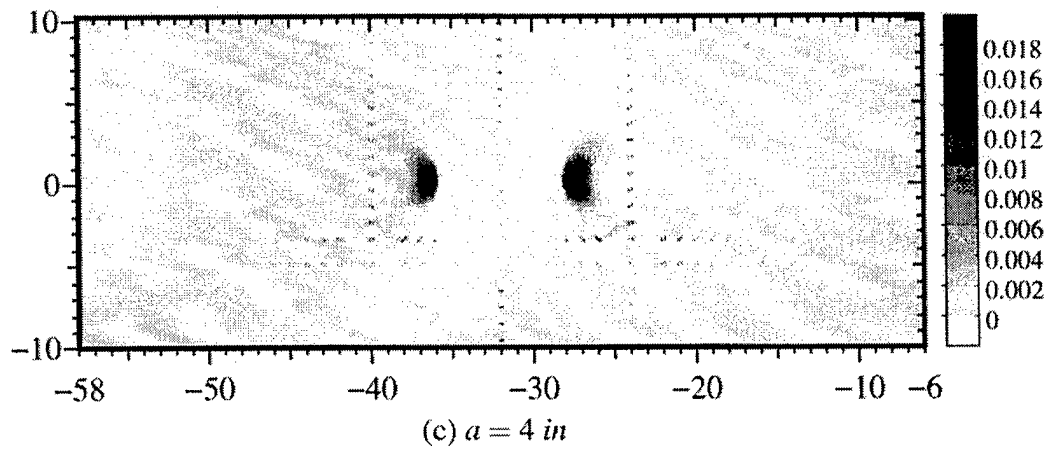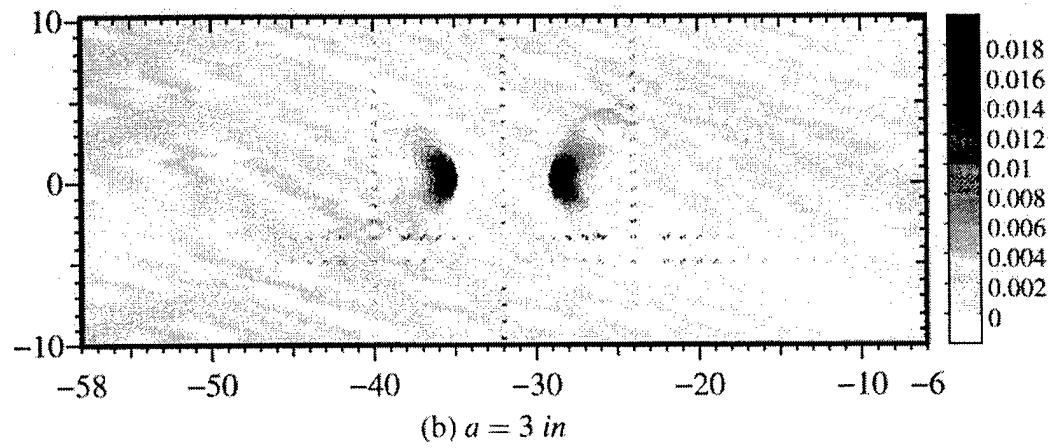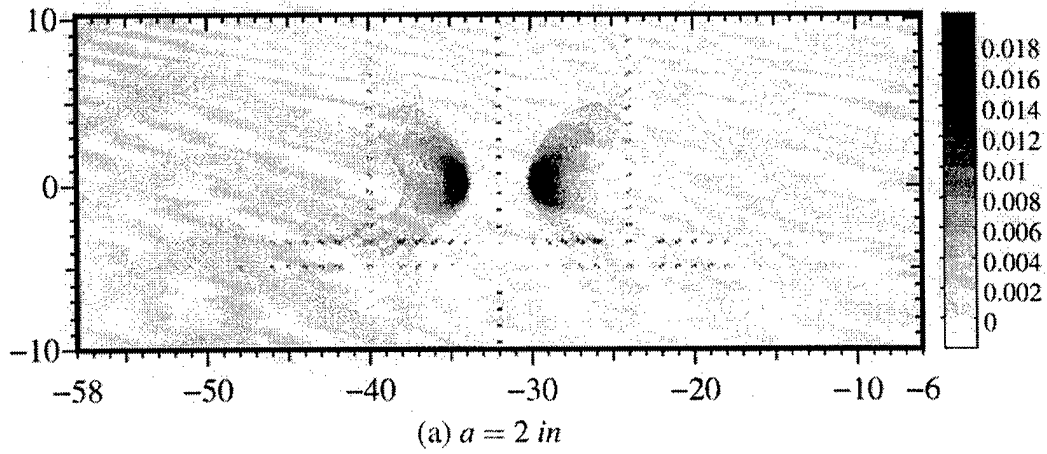
Figure 4. Equivalent Plastic Strain Contour Plot for Lead Cracks of Different Half Lengths.
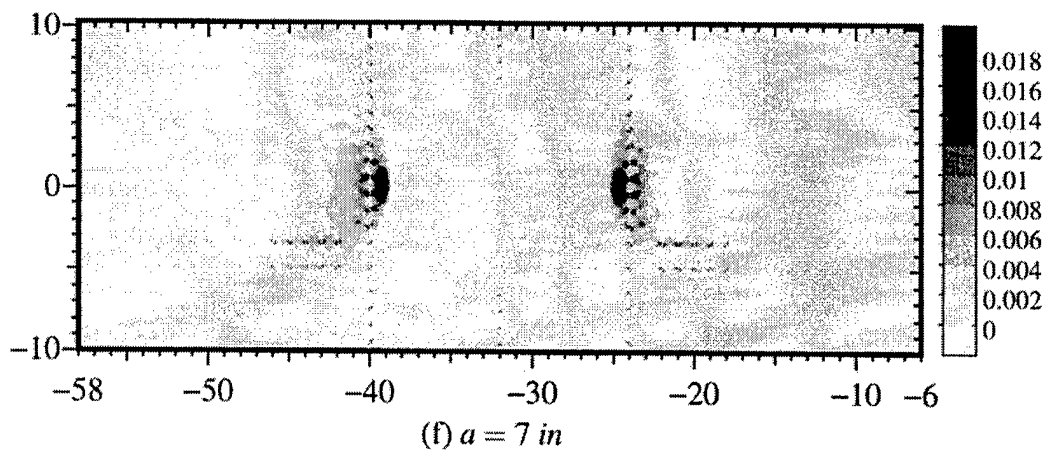
(d) $a = 5$ in

(e) $a = 6$ in

(f) $a = 7$ in

Figure 4. Equivalent Plastic Strain Contour Plot for Lead Cracks of Different Half Lengths (Continued).
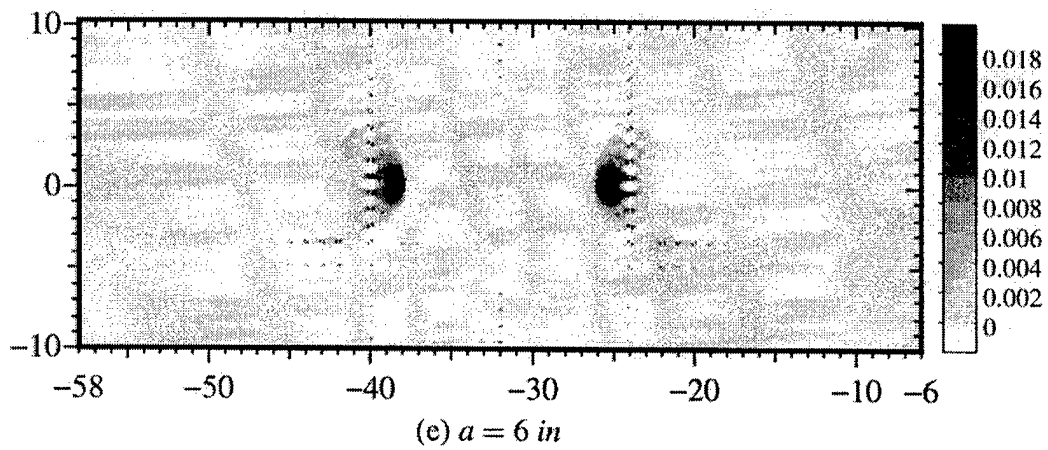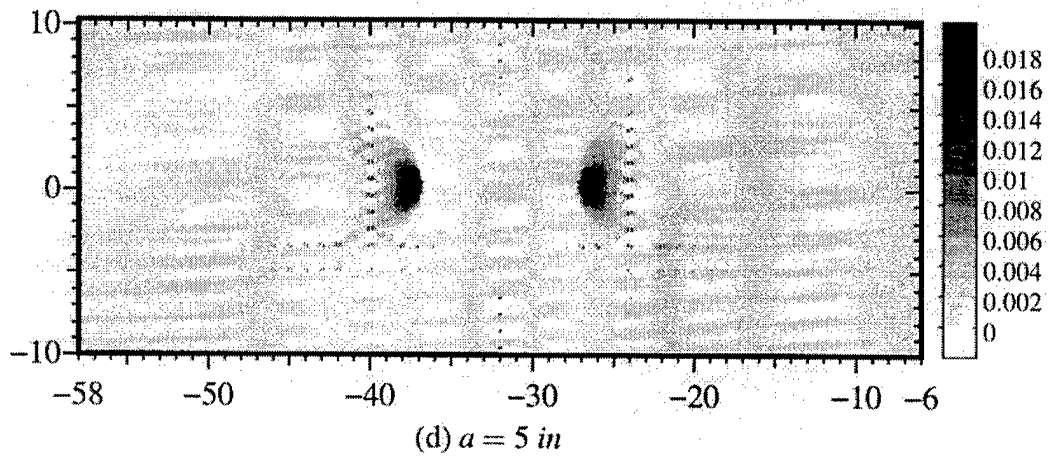
623

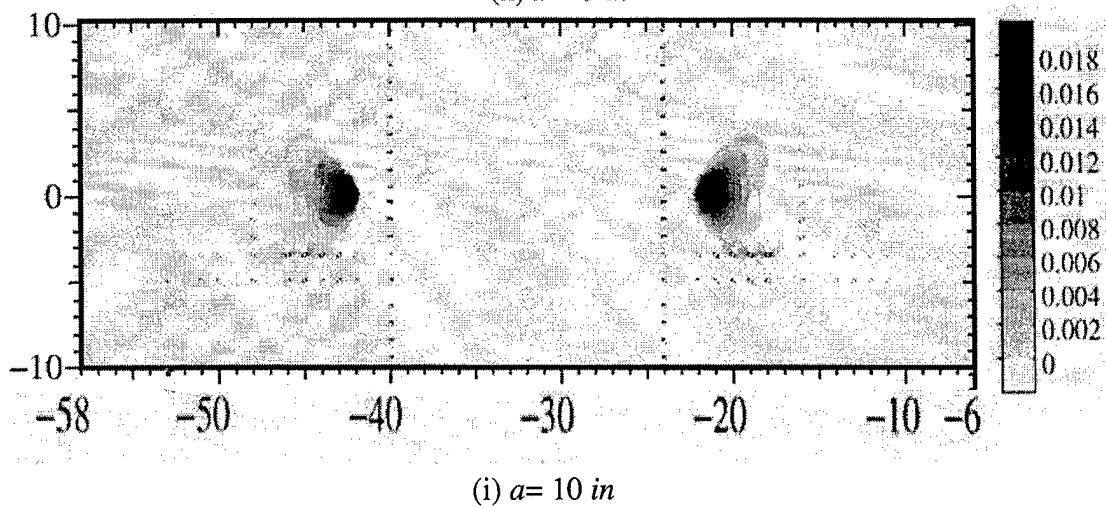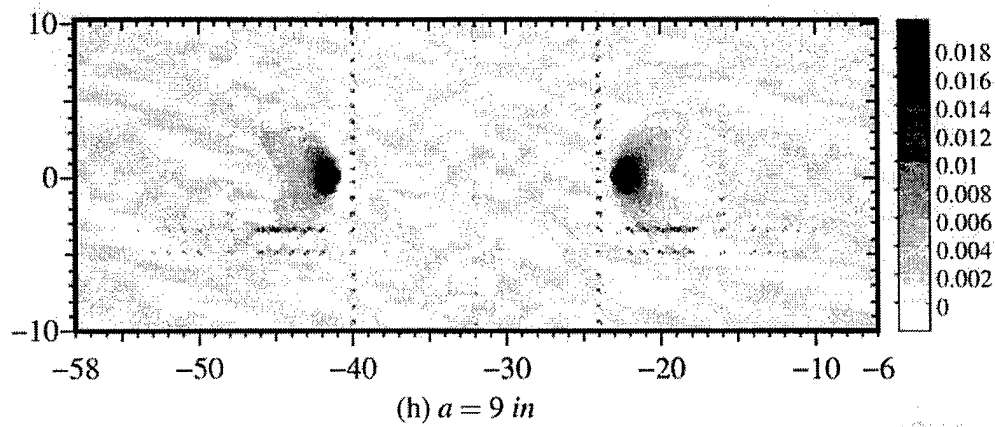(g) *a* = 8 *in*

(h) *a* = 9 *in*

(i) *a*= 10 *in*
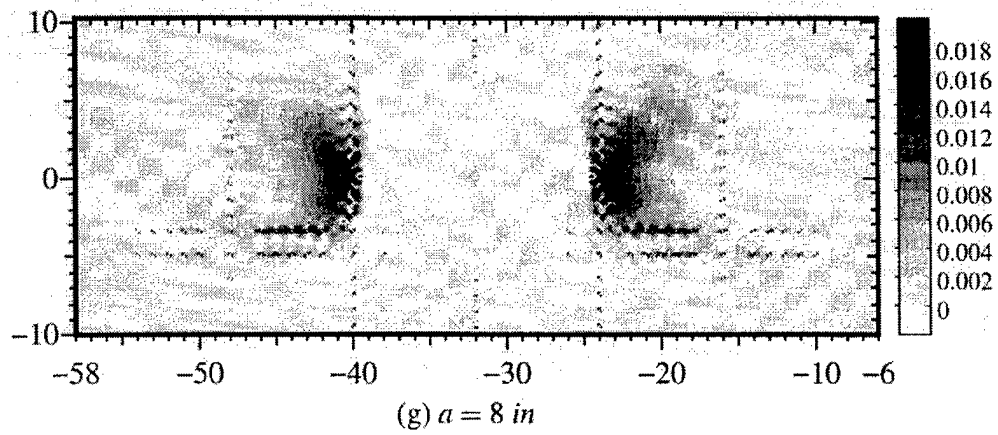
Figure 4. Equivalent Plastic Strain Contour Plot for Lead Cracks of Different Half Lengths.
(Continued).
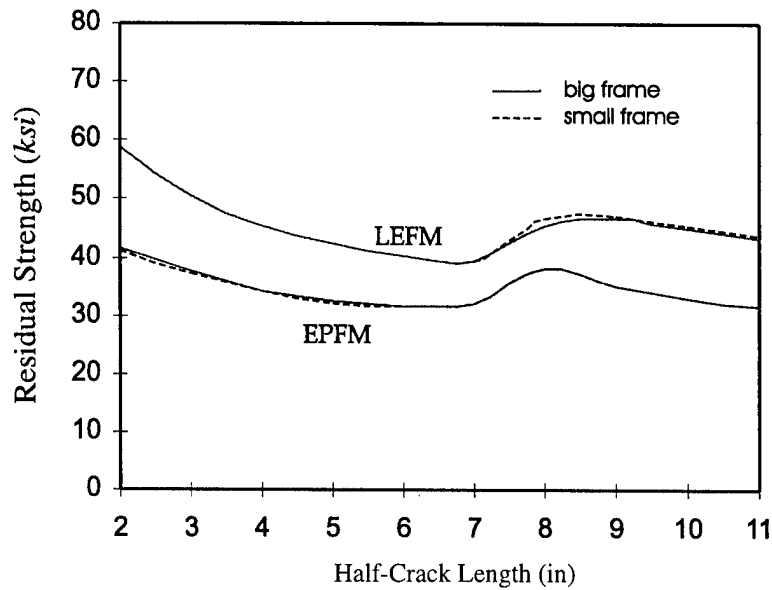
Figure 5. The Residual Strength Curves for the Circumferentially Cracked Panel With Frames of Different Sizes.
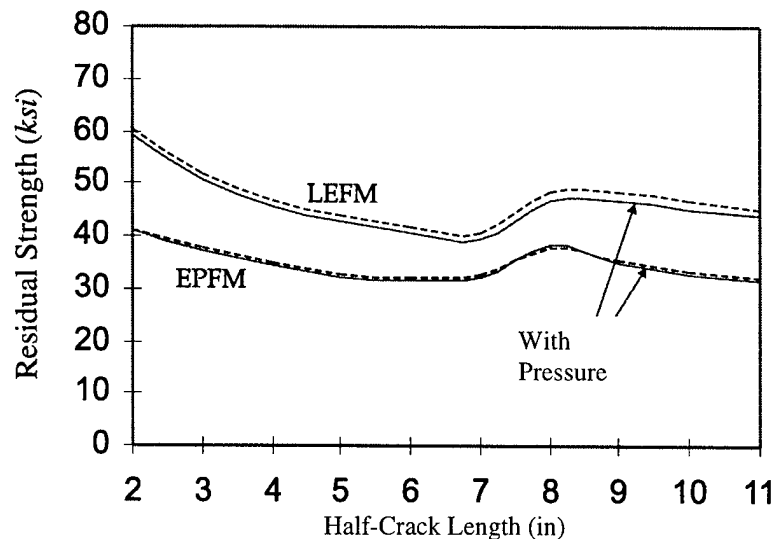
Figure 6. The Residual Strength Curves for the Circumferentially Cracked Panel With and Without Cabin Pressure.

The plastic deformations are nearly symmetric about the crack plane for all crack sizes, though they are disturbed near the location of the frame (located below the crack in the contour plots). This indicates that the effect of the frame is not significant. Figure 5 shows the residual strength curves for the circumferentially cracked panel with frames of different sizes. In this analysis, we doubled the size of the frame to study the effect of the frame. It is

625

seen that that the size of the frame makes almost no difference. In a real structure, the skin of the fuselage will buckle in the presence of a large crack. A frame near the crack can act as an antibuckling guide. In this hierarchical analysis, no buckling was allowed. Therefore, the antibuckling effect of the frame is not studied in this paper.

Figure 6 shows the effect of pressurization in which we compute the residual strength for the case where there is only axial loading and the case where there are both axial loading and hoop direction loading (due to pressurization). Since the pressurization changes mainly the hoop stress, which does not affect mode I loading of the circumferential crack, little difference in residual strength curves is observed in both the linear elastic fracture analysis and the elastic-plastic fracture analysis.

In the test, it was observed that the panel failure was precipitated by rivet failure in the crack arresting stringers. Since the rivets on the crack arresting stringers transfer the load from the skin to the stringers, the nonlinear behavior of the rivets can have a considerable effect on the crack arresting capability of the panel. To study this effect, we use the empirical flexibility curve [2] to model the nonlinear effect of the rivets on the residual strength of the panel. The empirical flexibility curve is shown in Figure 7. This flexibility curve in Figure 7 was obtained from an experiment in which a riveted joint was loaded until the rivet failed. Therefore, this flexibility curve includes the actual plastic deformation of the skin. The effect of nonlinear behavior of rivets can be seen in Figure 8. Due to the yielding of rivets, less load is transferred into the stringer from the skin. This decreases the residual strength of the cracked panel. The reduction is observed in both the LEFM analysis and EPFM analysis. However, the influence of the nonlinear behavior of rivets is smaller in the EPFM analysis, since the yielding of skin around rivet holes was modeled in the EPFM analysis.
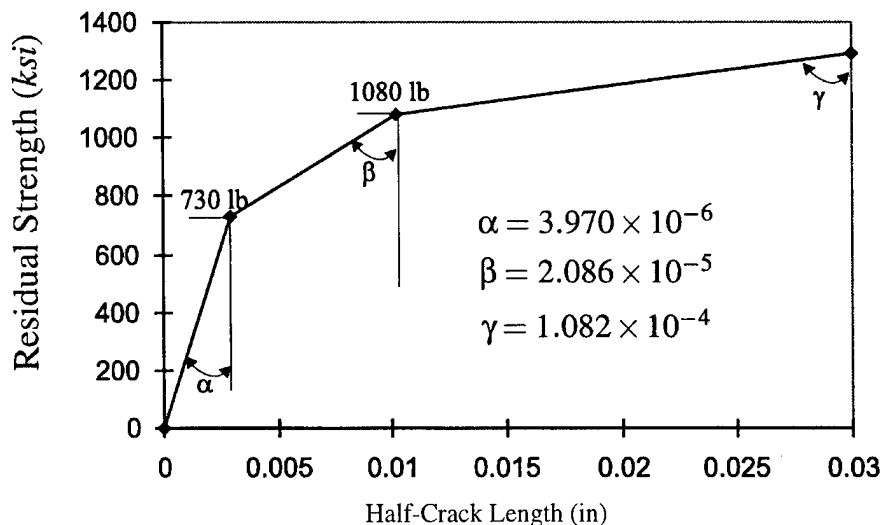

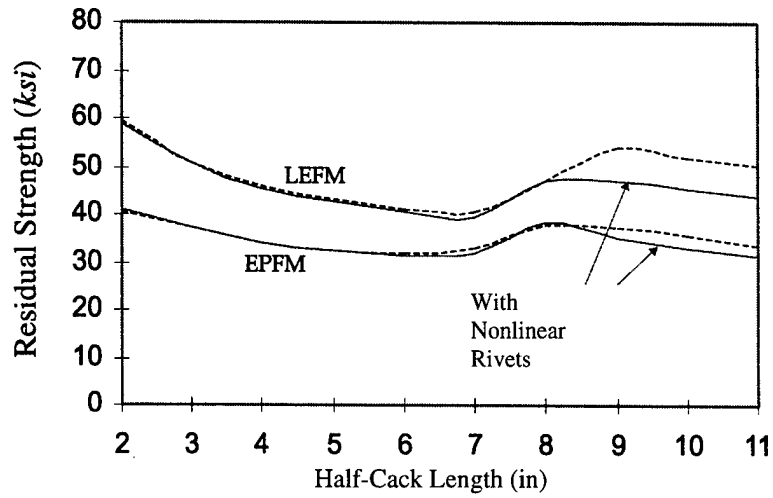Figure 7. Nonlinear Rivet Flexibility Curve.

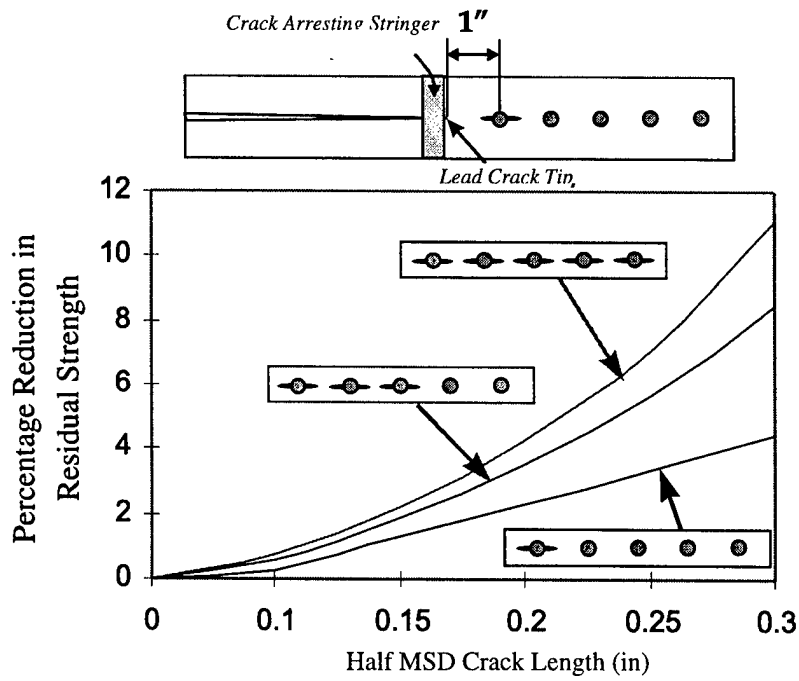Figure 8. Effect of the Nonlinear Behavior of the Rivets.

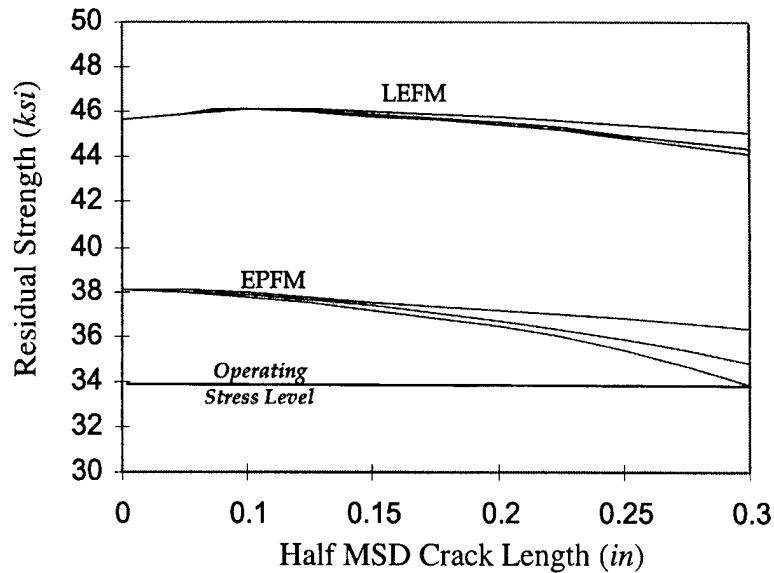Figure 9. Percentage Reduction in Residual Strength Due to MSD Cracks.

Figure 10. Residual Strength in the Presence of MSD Cracks and a Lead Crack With a Half-Crack Length of 8 Inches.

Multiple-site fatigue damages can reduce the residual strength of an aircraft fuselage in the presence of a large circumferential crack. Figure 9 shows the percentage reduction in residual strength for the case where the lead crack tips just penetrated the crack arresting stringers, and the distance between the first MSD and the tip of the lead crack is 1 inch. Three different cases were analyzed corresponding to 1) there is one MSD crack ahead of the lead crack tip, 2) there are three MSD cracks ahead of the lead crack tip, and 3) there are five MSD cracks ahead of the lead crack tip. Figure 10 shows how the residual strength decreases as the size and the number of MSD cracks increase. The more MSD cracks, the larger the reduction in residual strength. Although the fatigue damages can significantly reduce the residual strength of the panel, this panel will not degrade sufficiently to lose the capability to arrest a two-bay circumferential crack at the operating stress level (assumed to be 34 ksi) until the MSD cracks are of significant length. This can be seen in Figure 10.

CONCLUSIONS

A circumferential crack at a critical location with high axial stress was analyzed. Very large plastic zones were observed with a radius of more than 5 inches at the critical loads. Plastic deformation near rivet holes was also very significant. The yielding and failure of the rivets on the crack arresting stringers decreased the crack arresting capability of a circumferentially cracked fuselage; a similar result was observed for multiple-site damages in the skin of the fuselage. Since the linear elastic fracture mechanics approach significantly overestimated the residual strength of a cracked panel and underestimated the influence of MSD, the elastic-plastic fracture mechanics approach is mandatory for the study of residual strength of a circumferential crack at critical locations.

628

ACKNOWLEDGMENTS

REFERENCES

1. Jeong, D. Y.; Tong, P.: Threshold of Multiple Site Damage in Aging Airplanes. *Structural Integrity in Aging Aircraft*, ASME-AD Vol. 47, 1995, pp. 63-71.

2. Swift, T.: Effect of MSD on Large Damage Residual Strength. *Contemporary Research in Engineering Science*, R. C. Batra (ed.), 1995, pp. 516-539.

3. Wang, L.; Chow, W. T.; Kawai, H.; Atluri, S. N.; Predictions of Widespread Fatigue Damage Threshold. *Proceedings of the FAA-NASA Symposium on Continued Airworthiness of Aircraft Structures*, DOT/FAA/AR-97/2, 1997.

4. Swift, T.: Fracture Analysis of stiffened structure. *Damage Tolerance of Metallic Structures*, ASTM STP 842, 1984, pp. 69-107.

5. Chow, W. T.; Kawai, H.; Wang, L.; Atluri, S. N.; Automated Analyses of Widespread Fatigue Damage and Residual Strength Analysis. *Proceedings of the FAA-NASA Symposium on Continued Airworthiness of Aircraft Structures*, DOT/FAA/AR-97/2, 1997.

6. Nikishkov, G. P.; Atluri, S. N.: Analytical-Numerical Alternating Method for Elastic-Plastic Analysis of Cracks. *Computational Mechanics*, Vol. 13, No. 6, 1994. pp. 427-442.

7. Wang, L. H.; Atluri, S. N.: Implementation of the Schwartz-Neumann alternating method for collinear multiple cracks with mixed type of boundary conditions. *Computational Mechanics*, Vol. 16, No. 4, 1995, pp. 266-271.

8. Wang, L. H.; Atluri, S. N. (1996): *Recent Advances in the Alternating method for Elastic and Inelastic Fracture Analyses* (to appear in Comput. Methods Appl. Mech. Engrg.)

A STUDY OF FATIGUE CRACK GENERATION AND GROWTH IN RIVETED ALCLAD 2024-T3 SPECIMENS

Z. M. Connor, M. E. Fine, and B. Moran
Northwestern University
Department of Materials Science
Evanston, Illinois 60208

SUMMARY

Initiation and propagation of fatigue cracks at rivets in Alclad 2024-T3 specimens were investigated microscopically. Fatigue tests were performed on five identical specimens. Each specimen was assembled from two pieces of Alclad 2024-T3 sheet material using three 2017T4 aluminum alloy rivets. One piece of the sheet material had three countersunk rivet holes and the mating sheet had three straight holes. The specimens were loaded in uniaxial tension with a maximum load of 4.0 kN and an R ratio of 0.1. The number of cycles until a crack approximately 2 mm in length was seen in the plate near the rivet head was defined as N_i. The average N_i was 310,000 cycles with a standard deviation of 80,000 cycles. A surface rumpling consisting of plastic deformation and microcracks is observed adjacent to the rivet head prior to emergence of a propagating crack. Both circumferential and radial microcracks are seen. Using a 40 times magnification microscope, the propagating cracks were 0.5 to 1.7 mm long when first observed. In many specimens, such cracks did not grow significantly for many cycles after first observed. The time period between when surface rumpling is first observed and the end of the slow crack growth may provide a window of opportunity for early crack detection. This is a useful method for preparing specimens for nondestructive evaluation (NDE) calibration.

INTRODUCTION

Prior to investigating fatigue crack initiation and propagation in riveted joints, uniaxially loaded specimens of Alclad 2024 T3 aluminum alloy with countersunk rivet holes were investigated microscopically. A significant variation was observed in the cycles to initiation of a detectable crack under closely controlled conditions that were intended to be identical. The holes were made with a computer controlled machine tool and the maximum and minimum loads in the fatigue cycle were constant. The fatigue cracks initiated as microcracks in the blunt knife edges of the countersunk rivet holes and then extended as Mode I cracks [1-3]. This present paper reports the results on lap joint specimens consisting of two panels fastened with three rivets aligned in the stress direction and loaded in uniaxial tension.

The load transfer conditions for riveted lap joint specimens are very different from unriveted specimens with a rivet hole. The load is concentrated at the rivets with load by-pass occurring in the panels so that the outer rows of rivets carry the largest load. In addition, even if the load axis is along the center line of the riveted panels, there is a bending moment exerted on the outer rivets and these are the rivets where failure is expected. Other factors, such as the amount of clearance or interference in the fit of the rivet in the hole and friction between the two sheets, also affect the load transfer conditions for a riveted lap joint specimen [4, 5]. In addition, residual stresses are present in riveted joints. In specimens of the same design as those used in this study, the residual stresses were found to be compressive in the rivet and tensile in the sheet at low riveting forces, but at higher riveting forces, such as used in the present study, the stresses in the sheet became compressive [6]. Such compressive stresses are expected to increase the initiation time and reduce the crack propagation rate. Schijve has shown that S-N curves are approximately the same for lap joints and asymmetric butt joints of 2024-T3 Alclad material [4].

The initiation and propagation of fatigue cracks in the riveted specimens were investigated microscopically as a function of fatigue cycles. This work concentrates on crack initiation and short crack formation and growth. The first indication of cracking is surface rumpling due to plastic deformation and microcracking in the metal adjacent to the rivet. Then a short radial crack emerges after many cycles. It's initial growth rate is very slow. A statistical study of the crack initiation and growth is given. The rumpling and short crack precursor period afford a window of opportunity for early crack detection by NDE.

One of the objectives of this research was to prepare specimens with characteristic cracks for NDE studies and calibration. Often pseudo-cracks are prepared for this purpose by electro-discharge machining (EDM). Actual cracks are preferable. As discussed in this paper, riveting a precracked specimen into a panel may change the crack characteristics such as the crack opening. Specimens with in-situ cracks are available and have been supplied to others.[1]

SPECIMEN PREPARATION

Lap joint specimens were prepared consisting of two pieces of Alclad 2024-T3 aluminum alloy sheets, one piece with countersunk rivet holes and the mating piece with straight holes, as shown in Figure 1. The sheet material was 1.02 mm thick including a layer of 1050 aluminum alloy cladding 0.05 mm thick on each side. The countersunk rivet holes had a 100° included angle and a maximum diameter of 6.35 mm as specified by Boeing Company 737 Structural Repair Standard (1970) [7]. The rivet holes were drilled and countersunk using a computer controlled machining center [8]. The rivets were 3.97 mm diameter and were made of 2017-T4 aluminum alloy (Boeing Part No. BACR15CE5D4). Typical flushness requirements for rivets are +0.10 to -0.000 mm [9]. This gives a blunt knife edge of 0.20 mm, which is 20 percent of the thickness of the sheet. In the specimens

used for this study, the countersink was machined to a depth that would give a blunt knife edge of 0.20 ± 0.01 mm (Figure 2).
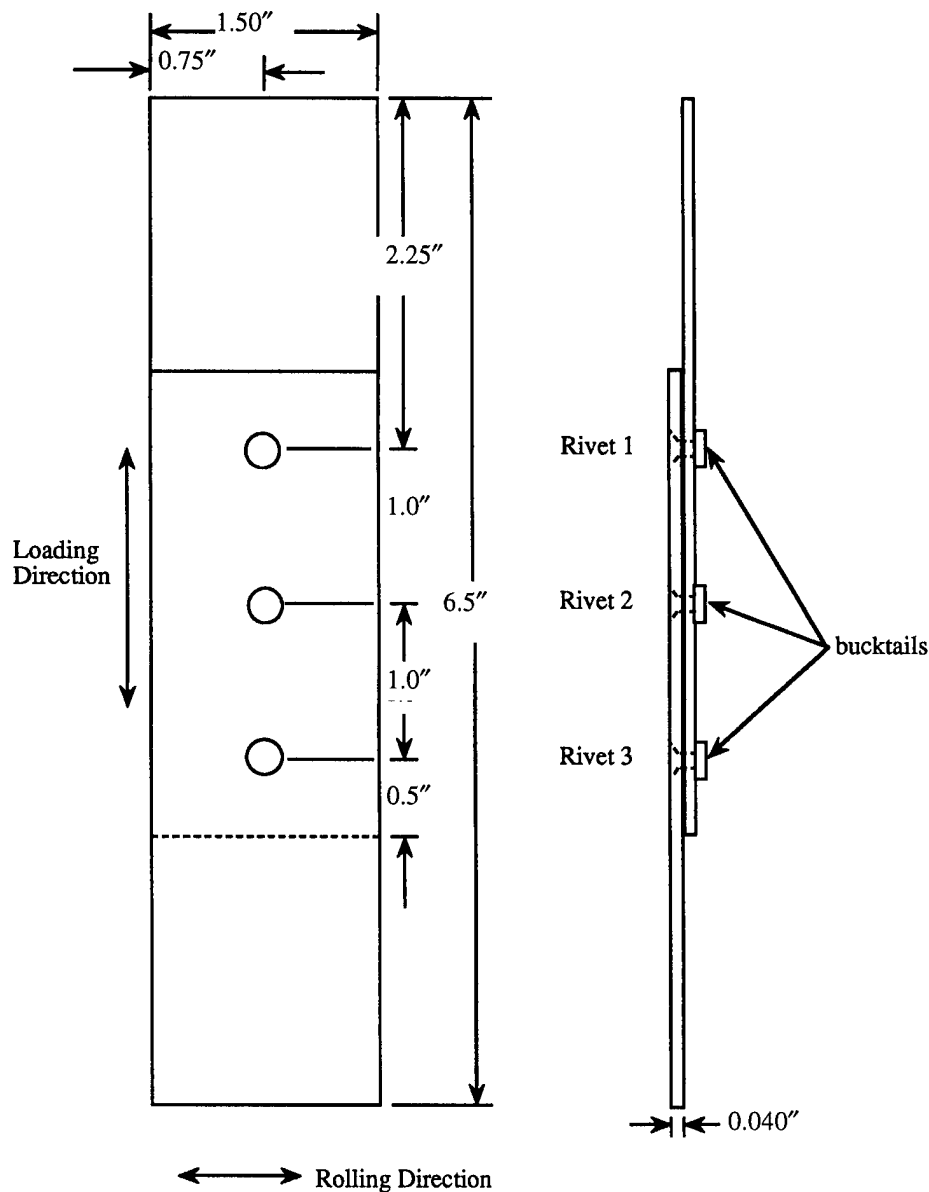
Panel Material: Alclad 2024T3
Rivet Material: 2017T4
Bucktail Dia: 0.241"±0.002"

Figure 1. Riveted Lap Joint Specimen. A Top Panel has Countersunk Rivet Holes, and a Bottom Panel has Straight Drilled Holes and are Riveted With Flush Head Rivets.
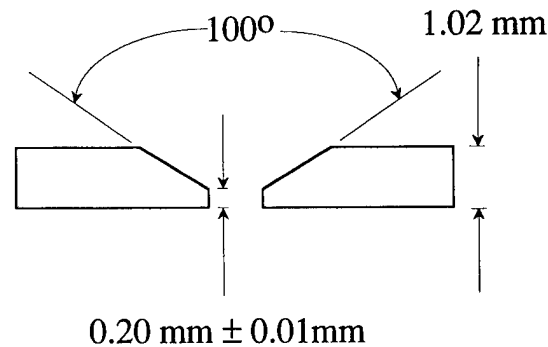
633

Figure 2. Section View of Sheet With Countersunk Hole.

The panels were riveted together on a manually operated hydraulic press where the rivets were compressed between two flat plates at a constant load of five tons for the three rivet specimens. This load gave bucktail diameters of 6.12 ± 0.05 mm as called for in the Boeing specification [7].

EXPERIMENTAL PROCEDURE

An MTS servohydraulic uniaxial fatigue testing machine with a rating of 100 kN was used to perform the experiments. The three-rivet lap joint specimens were loaded in uniaxial tension with an R ratio of 0.1 and a maximum load of 4.0 kN resulting in a nominal stress of 52 MPa. Shims were used in the grips so that the load axis was along the initial center line of the specimen. A saw-tooth wave with a frequency of 5 Hz was applied with a function generator and fine tuned with the use of a digital recording oscilloscope. A positive R-ratio was selected to prevent damage to the crack surface from crack closure.

Cracks were viewed at a magnification of 40x with an optical microscope mounted on an X-Y micrometer stage which was used to measure the crack length from the edge of the rivet head. In general, two propagating cracks formed, one on each side of the rivet. Definitions of individual crack length, a, and end-to-end crack length, c, are given in Figure 3.
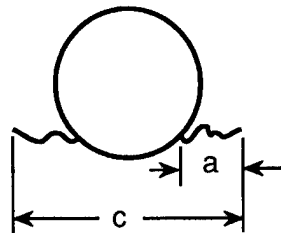

Figure 3. Drawing of Top Panel Surface With Rivet Head Defining a and c.

RESULTS AND DISCUSSION

Since one way to make cracked riveted specimens for NDE that are more realistic than those made using EDM notches is to rivet specimens that are already cracked, an experiment was performed to determine if riveting will change the crack opening of a pre-existing crack. An unriveted panel containing a countersunk hole was fatigued until a crack appeared that extended beyond the countersunk area of the specimen. Fiducial lines were then drawn on both sides of the crack. This specimen was then riveted with increasing pressure and micrographs were taken after each increase in pressure. After compressing the rivets under four tons of pressure, there was no apparent change in the fiducial line separation. This gave an average bucktail diameter of 5.89 mm; however, the Boeing specification requires a bucktail diameter of 6.12 ± 0.05 mm [7]. After compressing the rivets under five tons of pressure, an average bucktail diameter of 6.12 mm was obtained and the separation of the fiducial lines was 0.01 ± 0.005 mm greater than initially. Thus, an actual crack produced by fatiguing an already riveted panel may be different than one produced by riveting a panel with a pre-existing crack. Furthermore, as shown in the present work, the crack initiation process and the location of the macroscopic crack are much different for a countersunk rivet hole and a specimen containing a rivet [1, 2, 3].

Rivet 3   Rivet 2   Rivet 1

Figure 4. Side View Drawing of Lap Joint Specimen Illustrating Asymmetric Loading and Specimen Bending.

As shown in Figure 4, the lap joint specimen gives rise to bending due to the asymmetric loading; the loads being transferred through the upper and lower plates are offset. A detailed stress analysis of the riveted specimen would be required to determine the contribution of bending to the stress concentrations at the rivets. Alternatively, it may be possible to use a simple mechanics of materials approach such as that suggested by Schijve [4]. Because of this bending moment, rivets 1 and 3 (Figure 1) experience a larger load than Rivet 2. Due to load bypass, the plates are most heavily loaded at Rivet 3 in the top plate and Rivet 1 in the bottom plate. Because the top plate rivet holes are countersunk, crack initiation can be expected at rivet 3 in the top plate.

Initially, circumferential and radial microcracks occurred in the panel at this rivet and later a dominant radial crack was formed as depicted in Figure 5. A rumpled region was seen that consisted of slip steps and microcracks. The microcracks were approximately 100 to 200 microns in length when the rumpled region was first observed. The dominant radial cracks in the plates were at an angle which was not normal to the loading direction. The radial cracks became normal to the load direction on growth. This indicates combined tensile and shear mode fracture occurred until the crack propagation became normal to the loading direction. Typical microcracks are shown in the photomicrograph in Figure 6. Rumpling was first noticed at 175,000 cycles. This photomicrograph was taken at 215,000 cycles. A portion of the rivet head is seen in the upper left corner. The machining marks (large radius) are very

superficial. A typical radial crack is shown in the photomicrograph in Figure 7. The radial crack forms at the lower edge of the rumpled region. Ultrasonic C-scan imaging of one specimen containing microcracks and two specimens containing radial cracks revealed projected images of the cracks.[2]
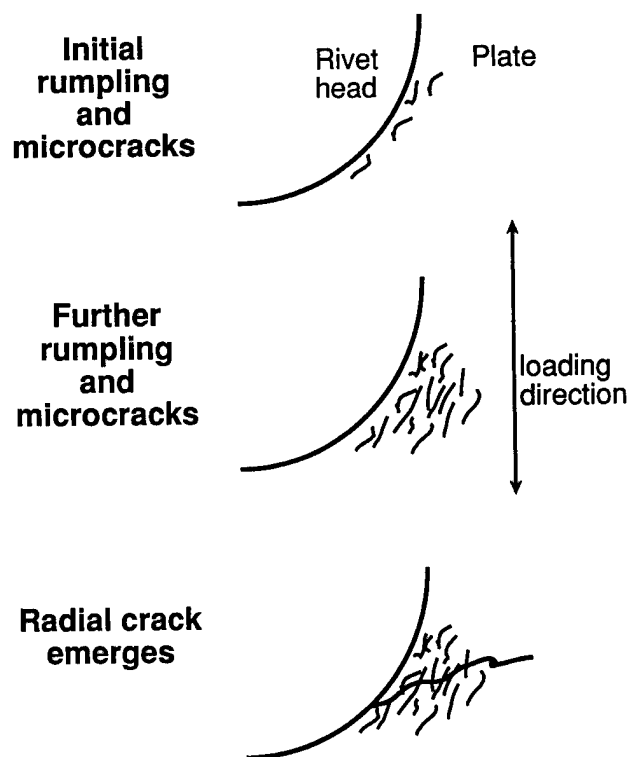
Figure 5. Sketch Depicting Microcracks and Propagating Radial Crack Adjacent to Rivet Head.

Several specimens were disassembled by grinding off the bucktail and carefully removing the rivet and all showed evidence of fretting as seen by black particles which were present. One specimen was disassembled before a radial crack was seen in the region of the plate adjacent to the rivet head. After disassembly, microcracks were observed on the back side of the panel which had countersunk rivet holes. These microcracks are shown in the photomicrographs in Figure 8a and 8b. Both circumferential and radial microcracks were observed. These microcracks did not originate at the knife edge.

Figure 6. Photomicrograph of Microcracks Adjacent to Rivet Head Prior to the Emergence of a Propagating Radial Crack.

Figure 7. Photomicrograph of Propagating Radial Crack Emerging From Microcracks.

Figure 8a. Photomicrograph of Back Surface of Panel With Countersunk Rivet Holes Showing Microcracks.

Figure 8b. Same Area at a Higher Magnification.

The results of crack growth measurements for five specimens are plotted as a vs. N in Figure 9. There is a wide variation in the number of cycles until the first propagating radial crack is seen. It occurs on one side of the specimen and then later occurs on the o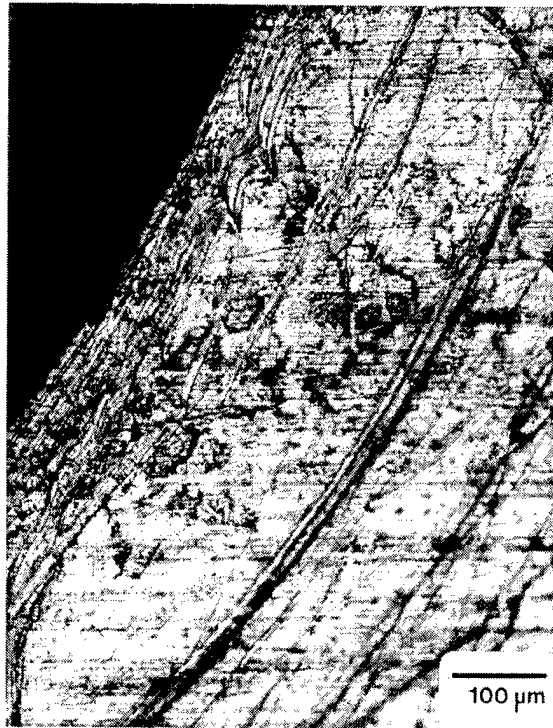ther side of the specimen. Its length when first seen was in the range of 0.5 to 1.7 mm. The number of cycles between the first observation of rumpling and the first propagating radial crack is somewhere in the neighborhood of 20,000 to 80,000 cycles; however, further data is necessary to determine this more accurately. Observations were made every 10,000 cycles.

Typical crack growth data for the first radial crack seen is exhibited in Figure 10 on an expanded scale for three specimens. There is an interval of approximately 20,000 to 60,000 cycles during which crack growth is slow and an opportunity exists for early crack detection. This occurs when the length of a, as defined in Figure 4, is less than about 3 mm. When a is equal to 3 mm, the crack is 12 mm from the edge of the specimen and any edge effect should be minimal. Figure 11 which is a plot of a vs. $N_{total} - N_{2\,mm}$ shows that the number of cycles between a crack of approximately 2 mm and 7 mm in length is 20,000 to 105,000 cycles, a difference of 85,000 cycles. Defining N_i as the number of cycles until a 2 mm radial crack had grown past the rivet head, it is observed that most of the lifetime is in this stage. N_i in the five specimens varied from 200,000 cycles to 450,000 cycles, a variation of 250,000 cycles. The average value of N_i was 310,000 cycles. Thus the variation in the number of cycles for crack initiation is much greater than the variation in the number of cycles for crack growth [4].
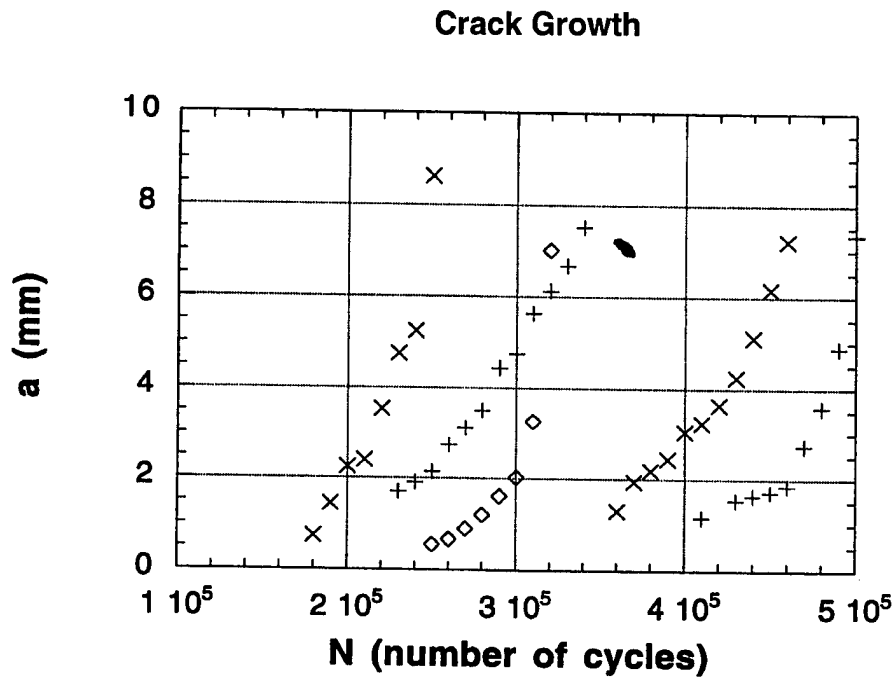
Crack Growth

Figure 9. Crack Growth Data for Five Specimens. Note Wide Variation Among Specimens in the Number of Cycles Until a Dominant Crack is First Observed.
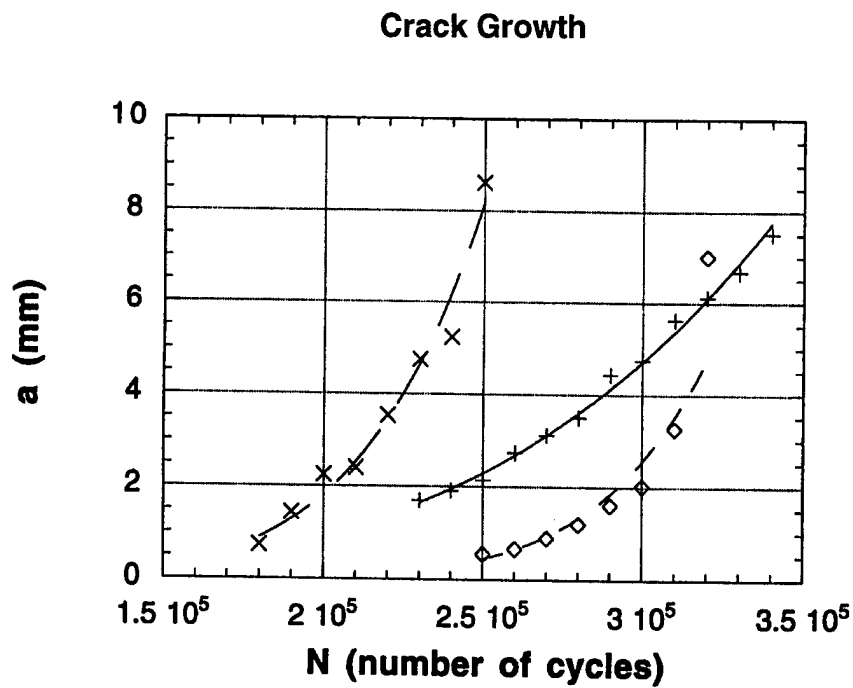
Crack Growth

Figure 10. Crack Growth Data of First Three Specimens in Figure 9 on an Expanded Scale to Better Show Initial Crack Growth.
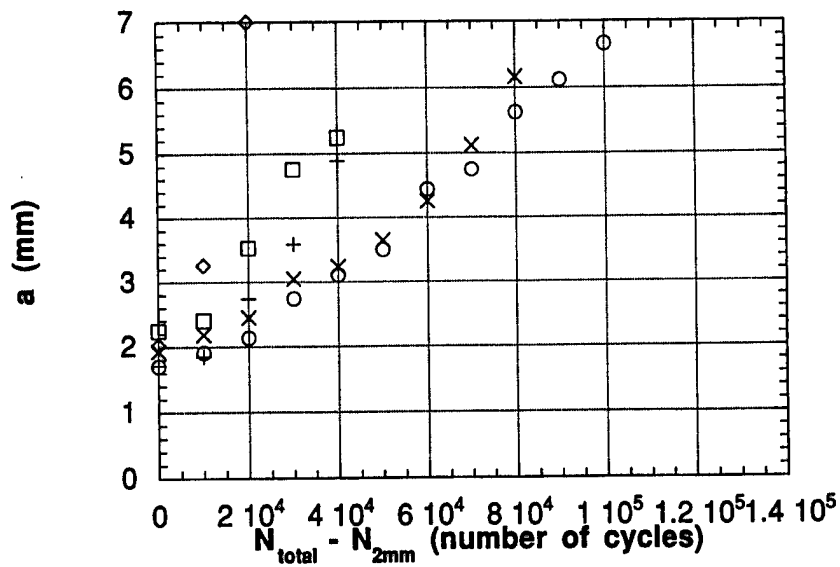
Figure 11. Crack Growth After Initiation, a vs. N_{total}-N_{2mm}. A Variation of 85,000 Cycles for Growth of an Approximate 2-mm Crack to 7 mm in Length Is Observed. Most of the Variation in the Total Cycles to 7 mm Is in the Number of Cycles for Crack Initiation.

Total Crack (c)
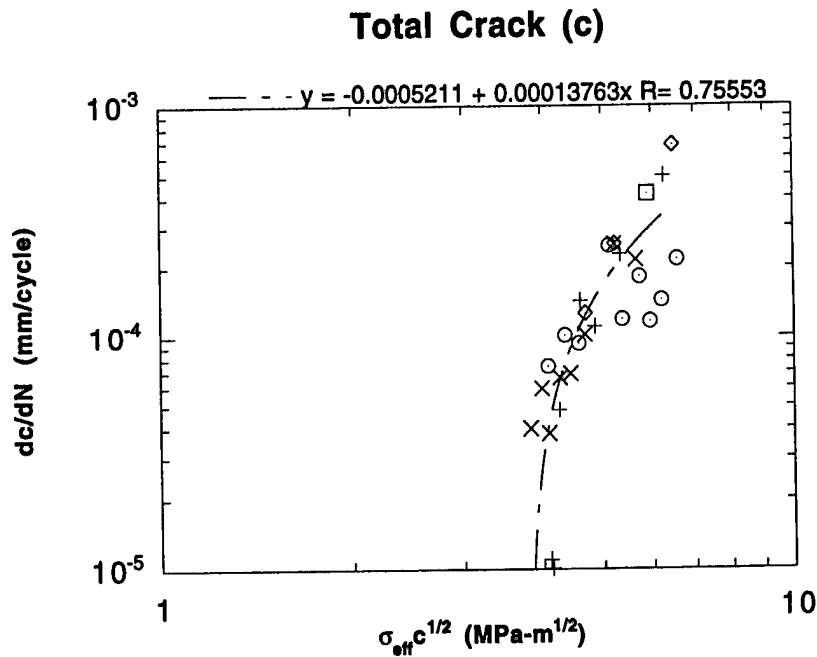
Figure 12. Plot Showing Crack Growth Rate of End-To-End Crack on Both Sides of the Rivet as a Function of the Effective Stress Times Square Root of End-To-End Crack Length, c.

It is customary to plot the crack growth rate, dc/dN, vs. ΔK. Since ΔK cannot be calculated at this time, dc/dN was plotted vs. $\sigma_{eff}c^{1/2}$. The effective stress, σ_{eff}, is defined as the maximum applied load divided by the total cross-sectional area, including the rivets. Such a plot for the five specimens is shown in Figure 12. dc/dN was determined from the crack growth such as plotted in Figure 9. In several specimens, a near threshold region of slow crack growth was observed. Later a power law (Paris type behavior) is suggested. Region III (unstable crack growth) occurs much later in the life of the specimen than plotted in the figure.

CONCLUSIONS

A method was developed for producing in situ cracked riveted specimens for NDE examination. A threshold value for $\sigma_{eff}c^{1/2}$ is suggested. Surface rumpling and microcracks are a precursor to a propagating crack. A first estimate of the number of cycles between the observance of the microcracks and the observance of a propagating crack is in the neighborhood of 40,000 cycles. A window of opportunity exists for early detection of fatigue cracks as crack growth is slow for a major portion of the fatigue life.

ACKNOWLEDGMENTS

REFERENCES

1. Fadragas, M. I., Fine, M. E., and Moran, B.: <u>Statistical Investigation of Fatigue Crack Initiation and Growth Around Chamfered Rivet Holes in Alclad 2024 T3 as Affected by Corrosion.</u>

2. Fine, M. E., Kung, C. Y., Fadragas, M. I., and Achenbach, J. D.: "Fatigue Crack Initiation and Microcrack Propagation Data Base in Precipitation Hardened Aluminum Alloys," *Durability of Metal Aircraft Structures*, <u>Proceedings of the International Workshop on Structural Integrity of Aging Airplanes</u>, edited by S. N. Atluri, C. E. Harris, A. Hoggard, N. Miller, and S. G. Sampath (Atlanta Technology Publications, Georgia, 1992), pp. 2-27.

3. Fadragas, M. I., "Tensile Fatigue Crack Initiation and Growth Database for Chamfered Rivet Holes in Alclad 2024-T3 Aluminum Alloy," Masters of Science Thesis, Northwestern University, Evanston, IL, 1993.

4. Schijve, J.: "Multi-Site-Damage Fatigue of Riveted Joints," *Durability of Metal Aircraft Structures*, Proceedings of the International Workshop on Structural Integrity of Aging Airplanes, edited by S. N. Atluri, C. E. Harris, A. Hoggard, N. Miller, and S. G. Sampath, Atlanta Technology Publications, Georgia, 1992, pp. 2-27.

5. Jones, R., Rees, D., and Kaye, R.: "Stress Analysis of Fuselage Lap Joints," *Durability of Metal Aircraft Structures*, Proceedings of the International Workshop on Structural Integrity of Aging Airplanes, edited by S. N. Atluri, C. E. Harris, A. Hoggard, N. Miller, and S. G. Sampath, Atlanta Technology Publications, Georgia, 1992, pp. 2-27.

6. Fitzgerald, T. J. and Cohen, J. B.: "Residual Stresses in and Around Rivets in Clad Aluminum Alloy Plates," *Materials Science and Engineering*, A188, 1994, pp. 51-58.

7. Boeing Company 737 Structural Repair Standard (1970)

8. Boeing Part Standard, BACR15CE RIVET, 100° Shear Head, Boeing Co., 22 Jul. 87.

9. Installation, Inspection, and Removal Methods for Aerolock 905, 906, 907, and 908 Rivets, H. D. Little Co., 10 Sept. 90.

T*$_\varepsilon$ INTEGRALS FOR CURVED CRACK GROWTH[*]

P. W. Lam and A. S. Kobayashi
University of Washington
Seattle, WA 98195-2600

H. Okada and S. N. Atluri
Georgia Institute of Technology
Atlanta, GA 30332-0356

P. W. Tan
Federal Aviation Administration
William J. Hughes Technical Center
Atlantic City International Airport, NJ 08405

SUMMARY

T*$_\varepsilon$ integral values associated with a stable, curved crack growth in biaxially loaded, fatigued precracked, 2024-T3 single edge notched (SEN) specimens, which were loaded in a combined modes I and II loading, were determined. These SEN specimens mimicked the flapping of a failed lap slice of a pressurized airplane fuselage. Most specimens were outfitted with a tear strap, which was either bonded, bonded and riveted, or integrally machined in the specimen. The crack curved upon propagation due to the imposed mode II crack tip deformation and either penetrated or curved again upon hitting the tear strap. T*$_{1\varepsilon}$ integral was identical to that of mode I crack extension while T*$_{2\varepsilon}$ vanished. In general, the crack curved in the direction of maximum principal strain.

INTRODUCTION

When a pre-existing axial crack in a lap slice of a pressurized fuselage extends under critical load, the flap generated by the one-sided bulging will tend to tear away from the lap joint. The mechanism of this flap generation was attributed to the imposed mode II stress intensity factor, K_{II}, induced by the characteristic one-sided bulging peculiar to a lap splice joint failure and results in an abrupt crack kinking away from the axial direction. This crack kinking was analyzed in detail by Kosai, et al. [1-3] using linear elastic fracture mechanics despite the presence of considerable large-scale plastic yielding. This plastic yielding is often

compounded by the presence of multisite damage (MSD) which links up with the main axial crack through plastic collapse [4]. After kinking, the crack normally propagates diagonally until it approaches a tear strap or a frame after which it most likely will kink again and propagate circumferentially until the driving force, i.e., fuselage pressure, has been exhausted. Again, the numerical analyses of Kosai, et al. [1 - 3] exhibited considerable plastic yielding during the propagation phase of the kinked crack. The above brief review shows that while linear elastic fracture mechanics (LEFM) techniques can be used effectively, particularly in an industrial setting, to predict crack kinking in a lap joint and at a crack arrestor, the fracture mechanic-based prediction technique can be improved by incorporating the plasticity effect in the analysis.

This paper presents our initial effort toward the development of an elastic-plastic crack curving criterion. T^*_ε integral, which has been used successfully by the authors and their colleagues in analyzing mode I, stable and dynamic ductile crack growth [5 - 7], will be used in assessing crack curving in the presence of large-scale yielding.

THEORETICAL BACKGROUND

T^*_ε is a path dependent integral based on incremental theory of plasticity where the integration contour expands together with the extending crack [8,9]. By confining the integration contour, Γ_ε, to the very vicinity of a traction-free crack and by using the stress and strain fields generated by the incremental theory of plasticity, Okada and Atluri [10] have shown that T^*_ε can be computed by the current T^*_ε without the need to sum ΔT^*_ε for each incremental crack extension. Moreover, the trailing portion of the contour integral can be ignored since the resultant surface tractions acting on such near-crack contours vanish. This nearness, ε, is set to the thickness of the specimen in order to guarantee a state of plane stress along the integration contour, Γ_ε [11].

Without the contour integration involving the unloaded region, the contour integral ahead of the crack tip can be evaluated by using the deformation theory of plasticity since this frontal region is dominated by the loading process. Thus the experimentally impractical procedure of evaluating ΔT^*_ε is avoided and T^*_ε was determined directly from the measured displacement field surrounding a partial contour near and in front of the crack tip. This is fortunate since the state of stress based on the incremental theory of plasticity cannot be readily computed from the measured displacement and strain fields in the trailing crack wake region. The T^*_ε for this near field Γ_ε represents the energy flux into a strip parallel to the crack as shown also by Memhard, et al. [12].

For a straight crack, which is subjected to a mixed modes I and II crack tip deformation, as is the case of the initial phase of a lap joint failure, the two modes of the $T^*_{k\varepsilon}$ for self-similar straight crack propagation are

$$T^*_{k\varepsilon} = \int_{\Gamma_\varepsilon} [\, W\, n_k - \sigma_{ij}\, n_i\, u_{i,k}\,]\, d\Gamma \tag{1}$$

where $k = 1$ and 2 represent the crack tip deformation of modes I and II, respectively, and i, j = 1, 2. For mode I, $T^*_{k\varepsilon}$ vanishes in the trailing crack wake since $n_1 = 0$ and $\sigma_{12} \approx \sigma_{22} \approx 0$ very close to the traction-free crack. For mode II, only the W term contributes to $T^*_{k\varepsilon}$ along the crack wake.

For a curved crack, the energy flux into an elongated curved contour will require the evaluation of $T^*_{k\varepsilon}$ along the entire contour, including the crack wake region, as well as an additional term which accounts for the rotation of the curved crack. Thus for a curved crack, a locally self-similar crack field, as shown in Fig. 1, where $T^*_{k\varepsilon}$, as represented by Eq. 1, is evaluated along a near-crack contour, Γ_ε, which surrounds only the frontal region of the growing crack tip and does not extend back to the original crack tip location.

EXPERIMENTAL ANALYSIS

Biaxial SEN Specimen

The mode II crack tip deformation generated by the unsymmetric flap opening along the lap joint in a rupturing pressurized fuselage was simulated by an in-plane shear loading along a single edge crack. Figure 2 show the basic configuration of the biaxial fracture specimen which is similar in design with that used by Kosai, et al. [13]. The x- and y-direction loads, P_x and P_y, were applied through pin-loaded heavy steel grips. P_y simulates the hoop stress of the fuselage and the load parallel to the crack, i.e., the x-direction load, P_x, simulates the unsymmetric axial stress generated by the opening flap. This axial stress was identified as the dominant force which caused crack curving in a pressurized fuselage [1 - 3]. The upper load, P_{x1}, which is twice the lower load, P_{x2}, simulated the unequal axial load imposed by the one-sided flapping of the fuselage skin as the crack propagated axially along a fuselage lap joint. The specimen was fatigue precracked under uniaxial cyclic loading. A tear strap was either epoxy bonded, bonded and riveted at spacing 12.5 mm apart, or integrally machined onto the specimen at the far edge.

Test Procedure

The test section of the specimen was covered with a crossed Moiré diffraction grating of 40 lines/mm over a region of 50 x 50 mm. This coarse Moiré grating was necessary due to the large-scale plastic yielding, which resulted in Moiré fringe patterns too dense to resolve by the traditional high-density grating. The grating was transferred onto the highly polished specimen surface by contact printing a master grating on to a relatively thick photo-resist coating which was deposited onto the specimen surface [14]. The deep cross-grooved, photoresist coating and the exposed, highly reflective specimen surface constituted a diffraction grating which withstood the large straining in the crack tip region. The specimen was illuminated by a four-beam Moiré interferometer for sequential recording of the two Moiré interferometry fringe patterns, which correspond to the two orthogonal displacement fields and which, unlike the traditional Moiré interferometry, could be viewed from any angular orientation [15].

The specimen was loaded in a biaxial testing machine with fixed grip loading conditions, Δ_x and Δy. The test protocol consisted of gradually increasing Δ_x and Δ_y while recording the Moiré fringe patterns associated with curved crack growth. The unsymmetric x-direction load at the left tab of the biaxial fracture specimen was generated by a simple mechanical lever system at the side of the cruciform specimen which provided a fixed upper-to-lower load ratio of $P_{x1}/P_{x2}= 2$. The two time-varying loads, i.e., P_x and P_y, were measured with two load cells and the imposed fixed grip loading, Δ_x and Δ_y, were measured by linear variable transducers.

RESULTS

Twenty-four biaxial test specimens were fabricated without or with tear straps and these results are being evaluated. We report in this paper the results obtained in one specimen with a bonded tear strap. Figure 3 shows the Moiré fringe patterns corresponding to the u- and v-displacements, respectively, in the biaxial test specimen with a curving crack path. Here the u- and v-fields refer to the displacements parallel and perpendicular to the crack, respectively.

Figure 4 shows the curved crack which for analysis purpose is represented by segments of straight cracks. Also shown is the frontal portion of the Γ_ε contour of $\varepsilon = 0.8$ mm (specimen thickness) in front of the extended curved crack.

Figure 5 shows the $T^*_{k\varepsilon}$, which were determined by evaluating the contour integral of Eq. 1, along the frontal portion of Γ_ε at the seven crack tip locations of the curved crack. The numerical procedure described in Reference 10 were used to deduce $T^*_{k\varepsilon}$ from the u- and v-displacement fields obtained from the corresponding seven sets of Moiré fringe patterns. The

$T^*_{1\varepsilon}$ here is the same steady-state value of about 140 MPa-mm for the T^*_{ε} associated with self-similar crack extension in the SEN and CN specimens [5,6]. $T^*_{2\varepsilon}$, on the other hand, is nearly zero throughout the entire curved crack extension. These results suggest that $T^*_{1\varepsilon}$ is the necessary driving force for locally self-similar crack growth and that the crack curves in the direction of vanishing $T^*_{2\varepsilon}$ which is the elastic-plastic counterpart of the vanishing elastic K_{II} criterion [16,17]. Also shown are the corresponding J_1 and J_2 integrals evaluated along a closed square contour with $\varepsilon = 0.8$ mm. Unlike the vanishing $T^*_{2\varepsilon}$, J_2 is a fluctuating quantity and J_1 decreased with curved crack extension.

Figure 6 shows the experimentally determined crack tip opening displacement (CTOD) and the crack tip sliding displacement (CTSD) which are defined as the displacements 1 mm from the crack tip. Both the CTOD and CTSD reach constant values through crack extension despite the varying instantaneous crack curvature or the crack kinking angle with crack extension. These results suggest that crack curving is insensitive to the magnitude of CTSD. The crack tip opening angle (CTOA) computed from the CTOD is shown in Fig. 7. Unlike the pure mode I crack extension data [5, 6], the CTOA reaches a lower maximum value of 7° after a $\Delta a = 4$ mm as shown in Fig. 7 and a slightly lower steady state value of 4.8°.

Figure 8 shows contour maps of maximum strains, which were obtained directly from the measured u- and v-displacements, for two crack extensions. Also shown are increments of the curved crack path. The remarkable coincidence between the maximum strain contours and the curved crack paths suggests that the maximum strain criterion could be a plausible crack curving criterion for ductile fracture.

CONCLUSIONS

1. An experimental procedure for determining $T^*_{k\varepsilon}$ for a curving crack is presented.

2. Variations in $T^*_{k\varepsilon}$ with stable curved crack growth in biaxially loaded 2024-T3 aluminum SEN specimen suggest that while $T^*_{1\varepsilon}$ could be the driving force for locally self-similar curved crack extension , the crack curves in a direction of vanishing $T^*_{2\varepsilon}$.

3. The direction of crack propagation appears to coincide with the direction of maximum principal strain.

REFERENCES

1. Kosai, M. and Kobayashi, A. S.: "Axial Crack Propagation and Arrest in Pressurized Fuselage," *Structural Integrity of Aging Airplanes*, eds. Atluri, S. N., Sampath, S. G., and Tong, P., Springer-Verlag, pp. 225-239, 1991.

2. Kosai, M., Kobayashi, A. S., and Raumulu, M.: "Tear Straps in Airplane Fuselage," *Durability of Metal Aircraft Structures*, eds. Atluri, S. N., Harris, C. E., Hoggard, A., Miller, N., and Sampath, S. G., Atlanta Technology Publications, pp. 443-457, 1992.

3. Kosai, M., Shimamoto, A., Yu, C. T., Kobayashi, A. S., and Tan, P. W.: "Axial Crack Propagation and Arrest in Pressurized Fuselage - An Experimental-Numerical Analysis," to be published in *International Journal of Applied Finite Element and Computer Aided Engineering*.

4. Broek, D., Jeong, D. Y., and Thomson, D.: Testing and Analysis of Flat and Curved Panels with Multiple Cracks. *FAA/NASA International Symposium on Advanced Structural Integrity Methods for Airframe Durability and Damage Tolerance*, Harris, C. E., ed., Conference Publication 3274 Part II, NASA Langley Research Center, pp. 85-98, September 1994.

5. Omori, Y., Okada, H., Ma, L., Atluri, S. N, Kobayashi, A. S., and Tan, P. W.: Further Studies on T*$_\varepsilon$ Integral Under Plane Stress Crack Growth. Localized Damage, IV, *Computer-Aided Assessment on Control*, H. Nishitani, et al. eds. Computational Mechanics Publication, pp. 511-517, 1996.

6. Omoti, Y., Ma, L., Okada, H., Atluri, S. N., and Kobayashi, A. S.: T*$_\varepsilon$-Integral Analysis of Fracture Specimens. *Proceedings of the 1996 Joint Engineering Systems Design and Analysis Conference*, A. Lagarde and M. Raous, eds., ASME, pp. 89-94, 1996

7. Lee, J., Kokaly, M. T., and Kobayashi, A. S.: Dynamic Ductile Fracture of Aluminum SEN Specimens - An Experimental -Numerical Analysis. To be published in Proceedings of the International Conference on Fracture, Sydney, May 1997.

8. Stonesifer, R. C. and Atluri, S. N.: On a Study of the (ΔT) and C* Integrals for Fracture Analysis Under Non-Steady Creep. *Engineering Fracture Mechanics*, 16, pp. 769-782, 1982.

9. Brust, F. W., Nishioka, T., Atluri, S. N., and Nakagaki, M.: Further Studies on Elastic-Plastic Stable Fracture Utilizing T* Integral. *Engineering Fracture Mechanics*, 22, pp. 1079-1103, 1985.

10. Okada, H. and Atluri, S. N.: T $*_\varepsilon$ Integral Evaluation From Experimental Displacement Field for a Plate With Stably Propagating Crack: Development of Calculation Procedure and Implication of T$*_\varepsilon$. To be submitted.

11. Narasimhan, R. and Rosaries, A. J.: Three-Dimensional Effects Near a Crack Tip in a Ductile Three-Point Bend Specimen. *ASME Journal of Applied Mechanics*, 57, pp. 607-617, 1990.

12. Memhard, D., Brock, W., and Fricke, S.: Characterization Ductile Tearing Resistance by Energy Dissipation Rate. *Fatigue, Fracture of Engineering Materials and Strictures*, 16, 10, pp. 1109-1124, 1993.

13. Kosai, M., Shimamoto, S., Yu, C.-T., Kobayashi, A. S., and Tan, P. W.: A Biaxial Test Specimen for Crack Arrest Studies. To be published in *Experimental Mechanics*.

14. Ifju, P. and Post, D.: Zero-Thickness Specimen Gratings for Moiré Interferometry. *Experimental Techniques,* 15, pp. 45-47, 1991.

15. Wang, F. X., May, G. B., and Kobayashi, A. S.: Low-Spatial Frequency Steep Geometric Grating for Use in Moiré Interferometry. *Optical Engineering*, 33, pp. 1125-1131, 1994.

16. Cotterell, B. and Rice, J. R.: Slightly Curved or Kinked Cracks. *International Journal of Fracture*, 10, pp. 155-169, 1980.

17. Sumi, Y., Nemat-Nasser, S., and Keer, L. M.: On Crack Path Stability in a Finite Body. *Engineering Fracture Mechanics*, 22, pp. 759-771, 1985.
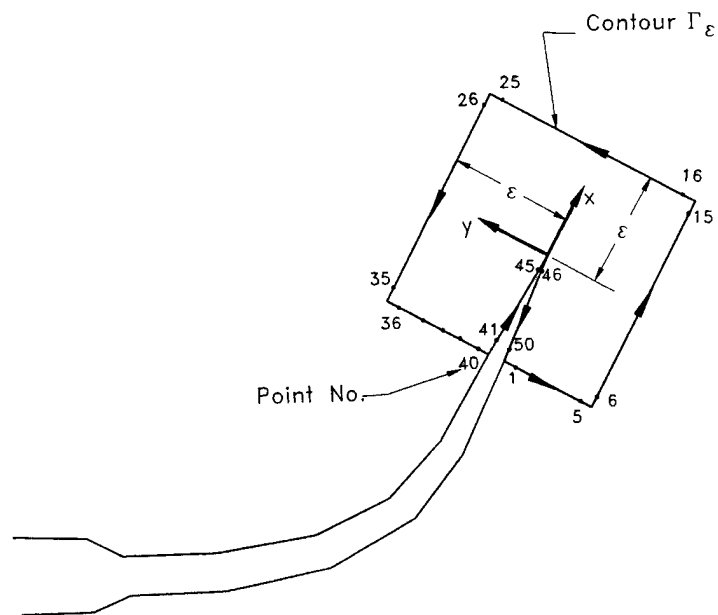
Figure 1. Curved Crack With a Locally Elongating Path.
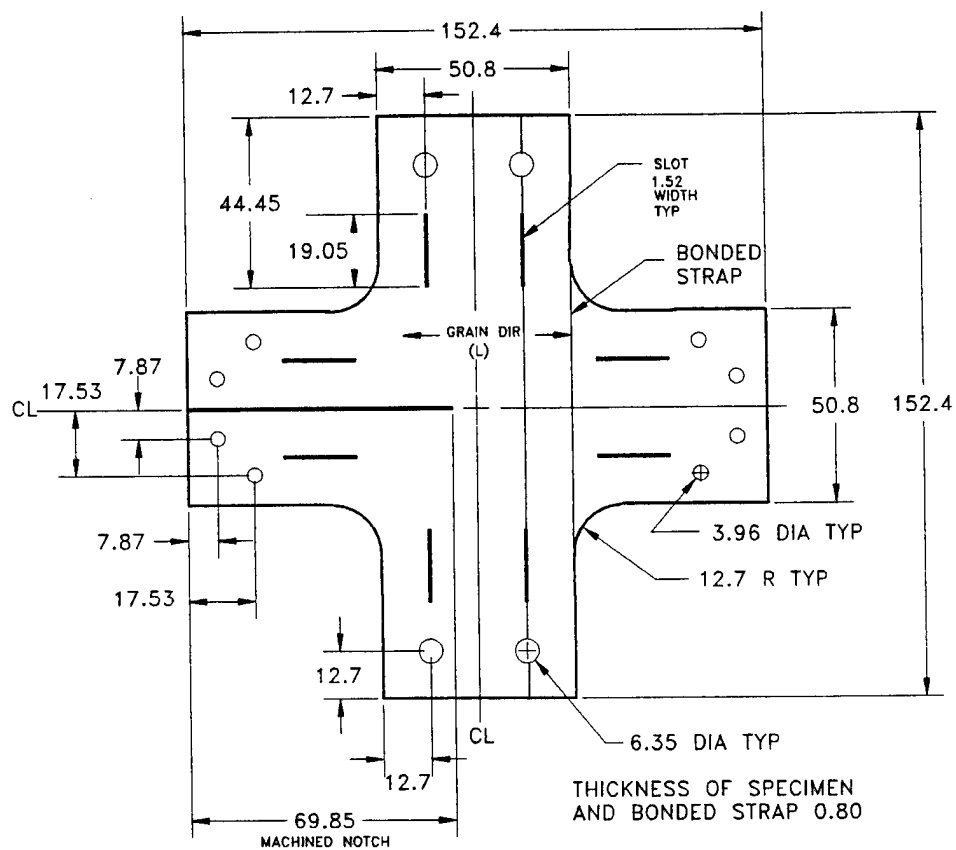
Figure 2. Biaxially Loaded SEN Specimen.

650

(a) u-field (b) v-field
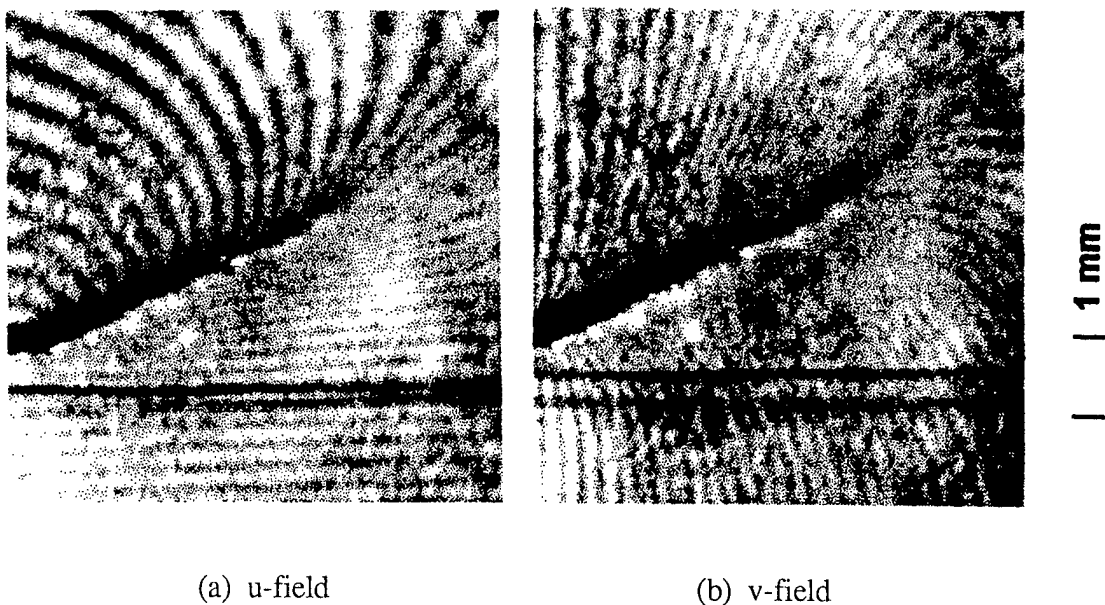
Figure 3. Moiré Fringe Patterns of a Biaxially Loaded 2024-T3 Aluminum SEN Specimen.

Figure 4. Curve Crack Path in a Biaxially Loaded Aluminum SEN Specimen.

651

Figure 5. T*$_{k\epsilon}$ Variation With Crack Extension.

Figure 6. CTOD and CTSD Variation With Curved Crack Extension.

Figure 7. CTOA Variation With Crack Extension.

(a) $\Delta a = 3.44$ mm

(b) $\Delta a = 8.23$ mm

Figure 8. Maximum Strain Contours for Two Crack Extensions.

USE OF NEURAL NETWORKS FOR
AVIATION SAFETY RISK ASSESSMENT[1]

Huan-Jyh Shyur, Ph.D. Candidate
James T. Luxhøj, Ph.D.
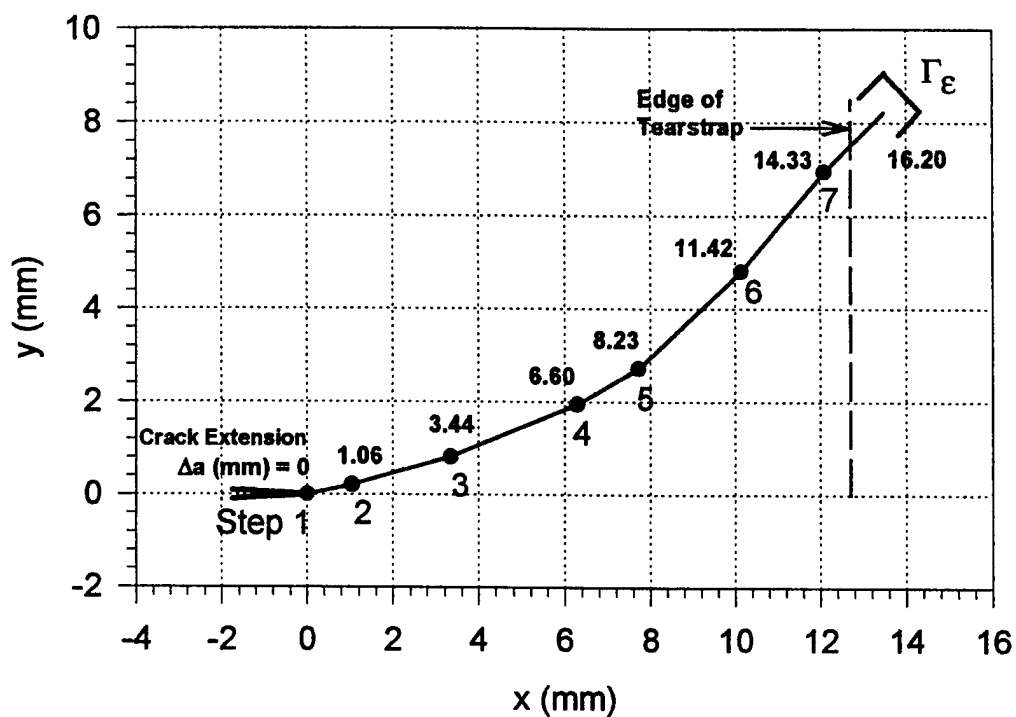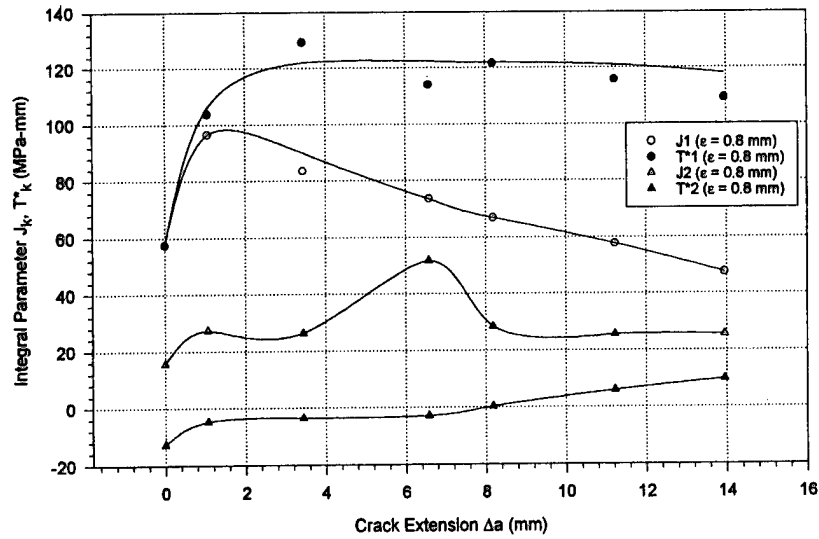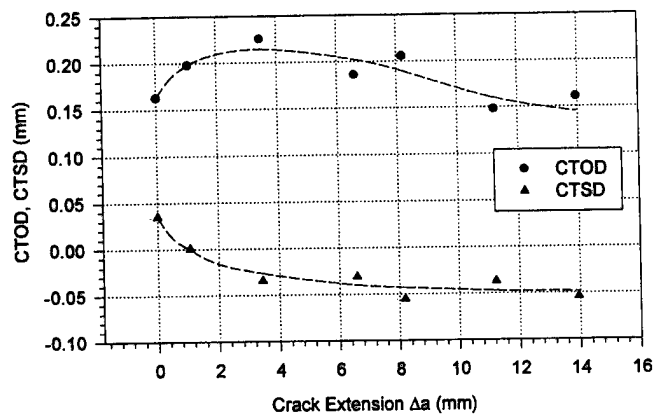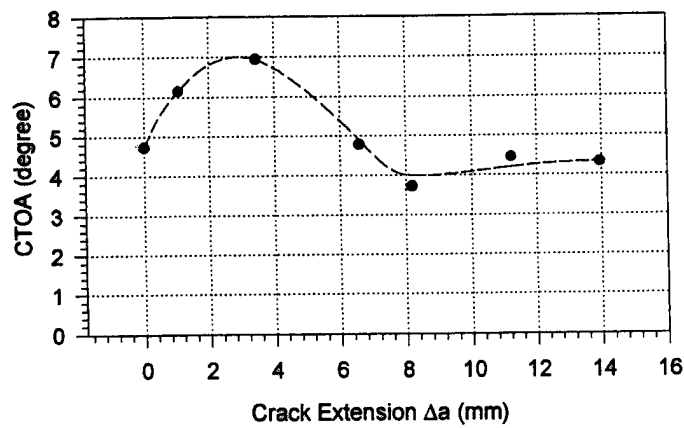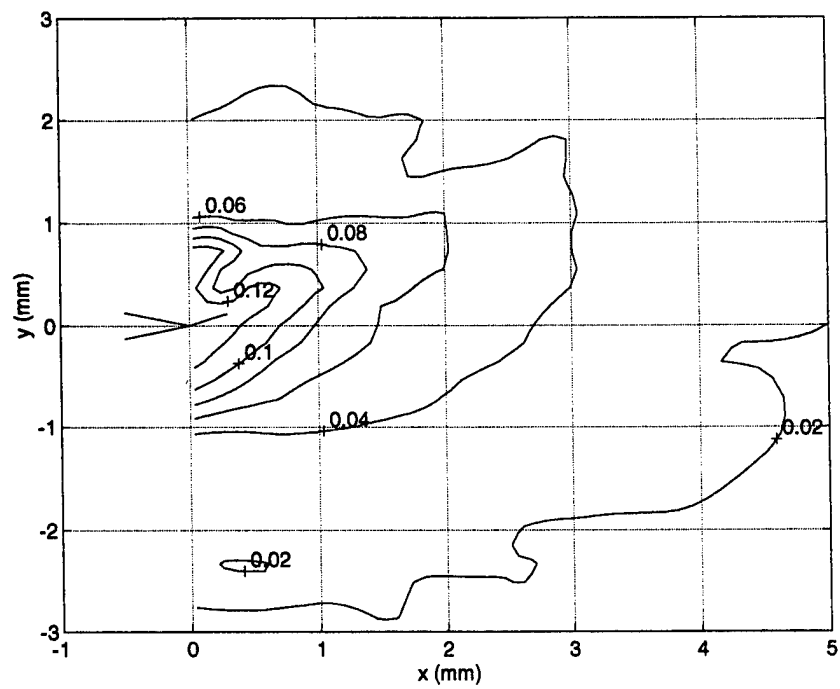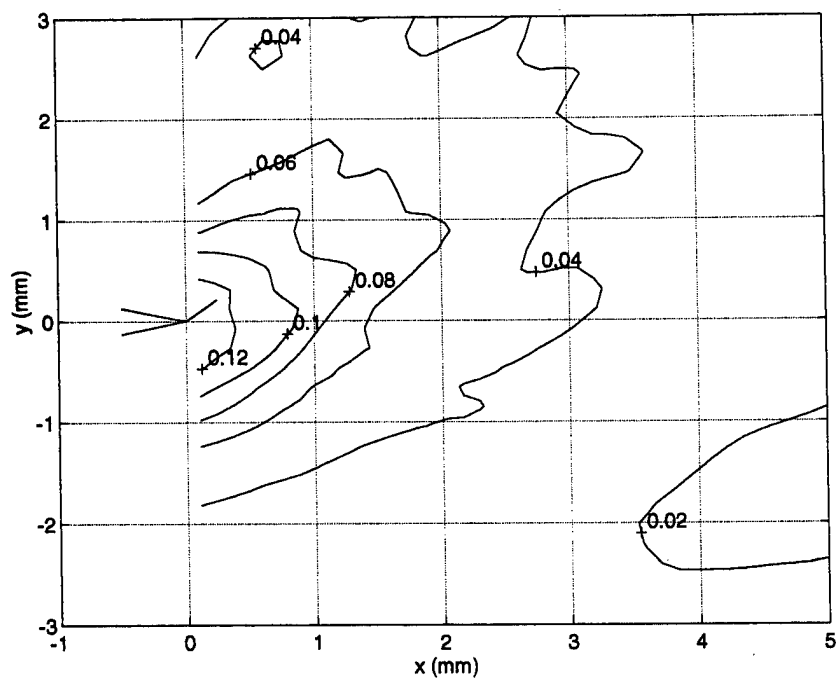Department of Industrial Engineering
Rutgers University

Trefor P. Williams, Ph.D.
Department of Civil Engineering
Rutgers University

SUMMARY

The Event Rate represents the frequency of aviation events (i.e., all accidents, incidents, and occurrences) as reported in the National Program Tracking and Reporting Subsystem (NPTRS). This research focuses on forecasting the number of incidents, along with the aggregate Event Rate, with the motivation being that advanced warning and knowledge of the number and trending of potential incidents could lead to enhanced risk assessment and proactive aircraft operator safety measures to prevent serious accidents.

Neural network models are developed to forecast the number of potential incidents and total Event Rate for aircraft operators with both large and small fleet sizes. The contribution of Service Difficulty Reports (SDRs) to the forecasting capability of the neural network is also examined. The SDR database contains data related to the identification of abnormal, potentially unsafe conditions in aircraft or aircraft components/equipment. Research results support the use of a Probabilistic Neural Network (PNN) to classify such inputs as the fleet size, number of SDRs/fleet size, and proportion of unfavorable operations surveillance inspections into four output classes for the number of potential aircraft incidents and total events.

INTRODUCTION

The Safety Performance Analysis System (SPAS) is a Federal Aviation Administration (FAA) initiative to develop an integrated decision support system to assist safety inspectors with surveillance activities (refs. 1, 2). Currently under phase 2

---

development, SPAS is novel to the FAA in that it attempts to integrate safety information related not only to the aircraft, but to aircraft operators, agencies, and personnel. There are a number of performance measures defined in SPAS for comparing the performance of any operator (i.e., airline) to another operator or to national norms with respect to airworthiness, operations, maintenance, equipment, training, reporting, procedures, management, finances, among others (ref. 3).

One of the SPAS performance measures, the Event Rate (ref. 3), represents the frequency of events (i.e., all accidents, incidents, and occurrences) as recorded in the National Program Tracking and Reporting Subsystem (NPTRS). The calculated value is the total number of these events for a 1-month period divided by the aircraft operator's fleet size for that same period. The value is normalized by fleet size to consider that an operator's exposure to events depends on the number of aircraft in its fleet.

An aircraft accident is defined as an event associated with the operation of an aircraft that results in death or serious injury and causes substantial damage to the aircraft (ref. 4). An incident is defined as an event, other than an accident, associated with the operation of an aircraft that affects or could affect the safety of operations (ref. 4). For example, near mid-air collisions, minor damage to an aircraft, and emergency evacuations are classified as incidents. The term occurrence does not have a strict definition, but is used to represent an event category that is neither an accident nor an incident. As an example, an occurrence could be an anomalous reading on a gauge that led to the plane taxiing back from the runway. If the anomalous reading could not be reproduced by the maintenance crew, then this event would most likely be classified as an occurrence. Although there are guidelines offered to FAA safety inspectors in conducting their investigations, in some cases, the classification of an event as either an accident, incident, or occurrence is subject to inspector judgment and experience.

If risk is considered to be exposure to possible loss or injury, then advanced warning and knowledge of the number and trending of potential aircraft incidents could lead to enhanced risk assessment and to proactive operator safety measures to prevent more serious accidents. Neural network models are developed to forecast the number of potential incidents for aircraft operators with both large and small fleet sizes for the next 3-month period. The contribution of the Service Difficulty Reporting (SDR) database that contains data related to the identification of abnormal, potentially unsafe condition in aircraft or aircraft components and equipment is particularly assessed.

NEURAL NETWORK MODELING

Emanating from research in artificial intelligence (AI) (McCulloch and Pitts (ref. 5)); Hopfield (refs. 6, 7), neural network (NN) attempt to simulate the functioning of human biological neurons. Neural networks have been particularly useful in pattern recognition problems that involve capturing and learning complex underlying (but consistent) trends in

data. Neural networks are highly nonlinear, and in some cases, are capable of producing better approximations than multiple regression which produces a linear approximation (Simpson, ref. 8; Wasserman, ref. 9). Neural network learning supports incremental updating and is easier to embed in an intelligent decision system since batch processing is not required. While neural networks offer an alternative to regression that will learn functional relationships among variables to predict an outcome measure, neural network outcomes lack a simple interpretation of results. For instance, the modeling technique does not provide objective criteria to decide what set of predictors is more important for the prediction. Neural networks may also suffer from overfitting of the data and lack of prediction generality. The limitations of neural networks with respect to outliers, multicollinearity, and other problems inherent in real world data have received scant attention.

Generally, backpropagation neural networks are the most commonly used neural network architectures. These neural networks are especially good for pattern recognition. In neural network modeling, the R^2 value compares the accuracy of the model to the accuracy of a trivial benchmark model where the prediction is simply the mean of all the sample patterns. A perfect fit would result in an R^2 value of 1, a very good fit near 1, and a poor fit near 0. If the neural network model predictions are worse than one could predict by just using the mean of the sample case outputs, the R^2 will be 0. Although not precisely interpreted in the same manner as the R^2 value in regression modeling, nevertheless, the R^2 value from neural network modeling may be used as an approximation when comparing model adequacy to a multiple regression model.

The neural network models in this research were developed on an IBM-PC compatible computer using the NeuroShell 2 (ref. 10) computer program. This program requires Microsoft Windows, a minimum of 4 Mb of RAM, and at least a 386 microprocessor. The NeuroShell 2 program enables the implementation of a variety of NN architectures.

This research attempts to classify inputs corresponding to airline and aircraft inspection data into some predefined output categories for the number of incidents or accidents. As such, a Probabilistic Neural Network (PNN) is used since it is a supervised neural network that trains quickly on sparse data sets and separates data into a specified number of output categories (Specht, refs. 11, 12). PNN networks are three-layer networks where the training patterns are presented to the input layer and the output layer has one neuron for each possible category. Training a PNN is very fast because it requires that each pattern be presented to the network only once during training. In the process of training, the PNN clusters patterns by producing activations in the output layer. The value of the activations correspond to the probability density function estimate for that category. The highest output represents the most probable category. It was thought that the use of a PNN is this study could be helpful in wrinkling the SDR data and facilitate the classification of potential incidents or accidents based upon an input profile of airline data.

With NeuroShell 2 a feature termed NET-PERFECT is used to prevent overfitting of the data. With the PNNs, NET-PERFECT determines the smoothing factor for the optimum network that minimizes outputs of incorrect classifications or maximizes the number of

657

correct classifications. The success of PNNs depends upon the smoothing factor which requires a trial-and-error search. In the next section, PNNs to forecast the number of potential incidents and total events for airlines are developed.

NEURAL NETWORK MODELS FOR AVIATION SAFETY RISK ASSESSMENT

The CMAS research team was provided a sample of SPAS data by the FAA William J. Hughes Technical Center (FAATC) in Atlantic City, NJ, for four different performance measures for ten different aircraft operators. For confidentiality, the names of the air carriers (i.e., operators) were masked as Carrier 1, Carrier 2, etc. The original data set consisted of inspection records of a 66 month period from October 1989 to March 1995. In addition to the Event Rate as defined previously, the other three performance measures were the following:

Performance Measure Description

Operations Records

General assessment of the results from all operations records surveillances performed on an air operator. Represents the percentage of unfavorable operations records related findings for a given 1-month period smoothed.

Operations Surveillance Results

Assessment of the results from all operations surveillances performed on an air operator. Represents the percentage of unfavorable operations surveillance records for a given 1-month period smoothed.

SDR Compliance

Assessment of an air operator's compliance with the regulations for reporting mechanical failures. Represents the number of Service Difficulty Reports (SDRs) submitted by an operator over a 6-month period.

Detailed definitions with sample calculations for the above performance measures are provided in (ref. 6). Table 1 displays representative data. The specific performance measure of *Operations Records* is not used in this research, since the *Operations Surveillance Results* measure is broader and provides a more general assessment of airlines and aircraft by considering personnel, manuals, records/reports, facilities, equipment, maintenance, and management, among others.

Table 1. Sample of SPAS Data (for one carrier).

Date	No. of SDRs	Fleet Size	Total # of Operations Surveillance Inspections	Actual # of Unfavorable Operations Surveillances	Total # of Operations Records	Actual # of Unfavorable Operations Records	Number of Incidents	Number of Occurrences	Number of Accidents
10/31/89	46	488	265	9	44	5	0	0	0
11/30/89	112	493	223	4	60	6	1	2	0
12/31/89	62	500	251	8	65	6	2	0	1
01/31/90	74	502	322	16	91	4	4	0	3
02/28/90	57	506	275	12	67	2	0	0	1
03/31/90	46	514	332	10	85	1	3	0	0
04/30/90	62	516	313	7	65	1	0	0	0
05/31/90	59	520	351	14	73	4	0	1	0
06/30/90	71	524	319	10	80	7	2	2	0
07/31/90	81	527	346	14	44	1	2	2	0
08/31/90	60	532	322	6	126	7	1	0	0
09/30/90	88	541	375	8	69	2	0	0	0
10/31/90	98	547	256	17	70	3	1	1	0
11/30/90	75	555	245	6	67	4	1	5	0
12/31/90	76	552	238	14	106	8	3	6	0

To provide a means for checking the NN predictions against existing data, the data were subdivided into two different sets. The first set was used to build the prediction model and the second set was used to evaluate the prediction model's performance on new, unfit data. Such an approach is useful for testing prediction model generality (Pindyck and Rubinfeld, ref. 13). This approach is used in neural network modeling to create a training set of data to build the model and a production set of data to evaluate model performance on new data. These terms are used in the paper to distinguish between the two data sets.

We were subsequently advised by the FAA William J. Hughes Technical Center staff to not use data prior to June 1992 due to the discovery of data reporting errors. Thus, the NN models are constructed and evaluated with data from June 1992 - March 1995. After some sensitivity analyses on using fleet size to group the data, it was decided to partition the data into two groups. The first group contains operators where the fleet size is greater than or equal to 200 airplanes (i.e., 192 data records), and the second group had operators with a fleet size less than 200 airplanes (i.e., 128 data records). For the first data group (i.e., large carriers), the mean number of incidents is 1.212 and the standard deviation is 1.088. The mean number of events for the first group is 2.788 and the standard deviation is 1.398. For the second data group (i.e., small carriers), the median was used rather than the mean due to the smaller number of observations in the sample size. The median number of incidents is 0.9667 and the upper fourth number is 1.664 and the upper eighth number is 2.270. The median number of events in this group is 2.505 and the upper fourth number is 3.420 and the upper eighth number is 4.234.

Due to the time shifting of the data to create output variables and the data reporting errors prior to June 1992, note that only 320 of the original 660 records are used in the modeling procedure. It is important to note that the distinction between large and small airlines based upon using the number of 200 aircraft is determined graphically and does not represent an official FAA classification.

A Probabilistic Neural Network (PNN) architecture is used to classify the input patterns into one of four different output classes for the potential number of incidents.

The notation used is defined as follows:

FLEET SIZE fleet size at the beginning of period t
SDR/fs(t)   # of SDRs / fleet size (per month) at the beginning of period t
P(t)   the percentage of unfavorable inspections at the beginning of period t
      (based on *Operations Surveillance Results*)

For both the large and small carriers, four classes of outputs are created. However, the classification scheme varies for each carrier grouping as displayed in Figure 1. Note that for small carriers, the median rather than the mean is used to create the first class due to the small number of observations for incidents or events that are found in this data grouping.

Figure 1. A Probabilistic Neural Network (PNN) Model.
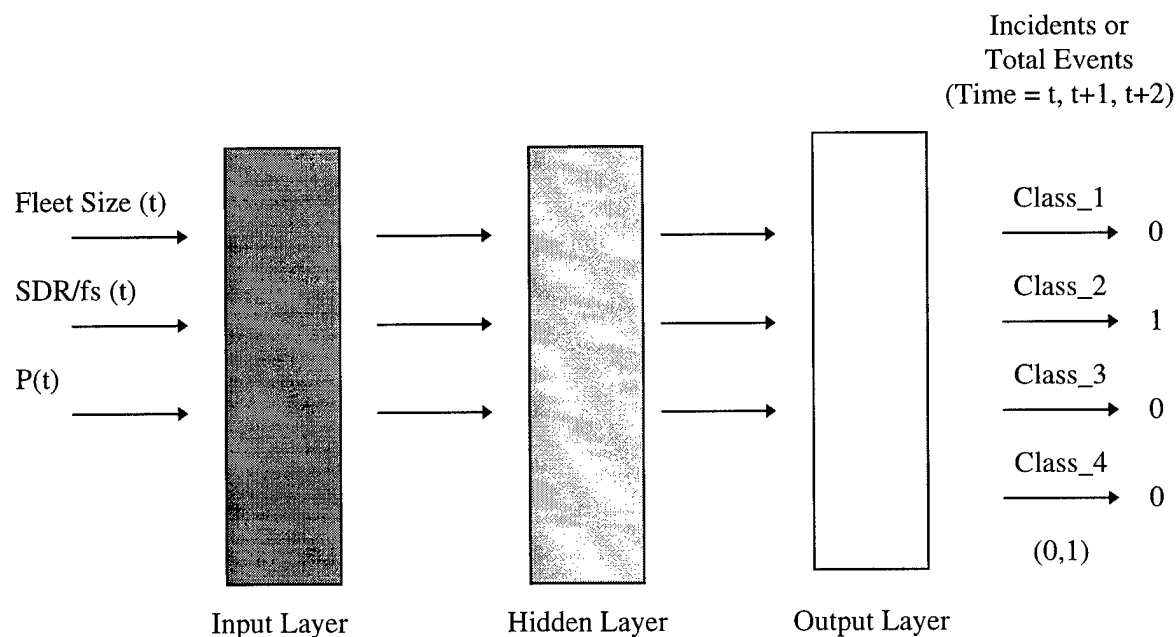
Figure 2 displays the PNN with its inputs of fleet size, SDRs/fleet size, and P and the four output classes. The model forecasts the number of potential incidents or events for each of the four classes for time periods t, t+1, and t+2. Consistent with the SPAS paradigm, these numbers represent the proportion of potential incidents per 100 aircraft for a 3-month period.
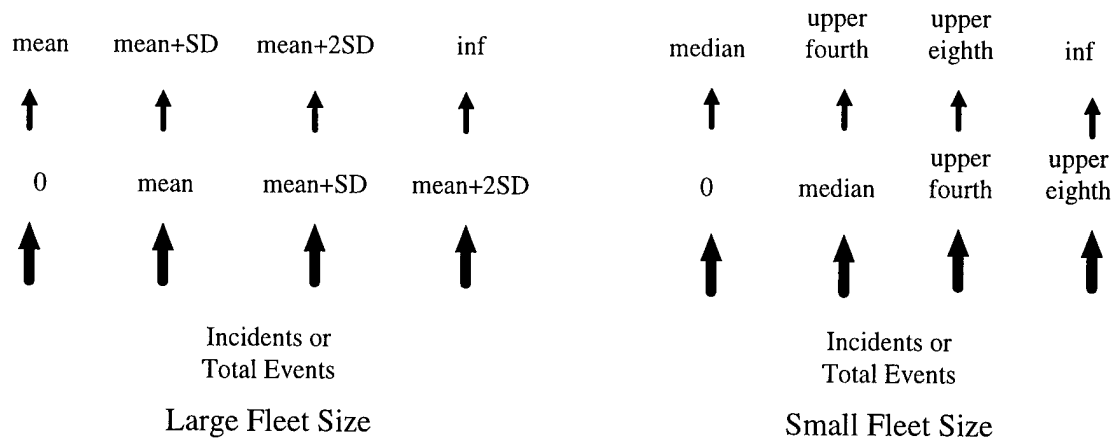
mean   mean+SD   mean+2SD   inf   median   upper fourth   upper eighth   inf

↑   ↑   ↑   ↑   ↑   ↑   ↑   ↑

0   mean   mean+SD   mean+2SD   0   median   upper fourth   upper eighth

↑   ↑   ↑   ↑   ↑   ↑   ↑   ↑

Incidents or   Incidents or
Total Events   Total Events

Large Fleet Size   Small Fleet Size

Figure 2. PNN Output Classification Scheme.

SENSITIVITY ANALYSIS

A number of variations of the basic PNN model presented in Figure 2 are evaluated by changing the combination and number of input variables used. Table 2 summarizes four different PNN models for operators with a fleet size greater than 200 aircraft. The percentages of correct classifications for the number of potential incidents or events for both the training and production patterns are also reported.

Table 2. PNN Models for Carriers With Large Fleet Size (≥ 200 aircraft).

Model #	Models	Training Pattern		Production Pattern	
		Corr.	Incorr.	Corr.	Incorr.
1	f.s SDR/f.s. ⇒ Classified Incidents P S.F. = 0.015 (3:180:4)	161 89.44%	19	10 83.33%	2
2	f.s ⇒ Classified Incidents P S.F. = 0.015 (2:180:4)	131 72.78%	49	8 66.67%	4
3	f.s SDR/f.s. ⇒ Classified Events P S.F. = 0.012 (3:180:4)	165 91.67%	15	10 83.33%	2
4	f.s ⇒ Classified Events P S.F. = 0.012 (2:180:4)	147 81.67%	33	8 66.67%	4

With Model 1, all the inputs are used. The PNN has 3 inputs, 180 hidden nodes, and 4 outputs (hence the notation 3:180:4 given in parentheses). One hundred and eighty training and 12 production patterns are used. The smoothing factor (S.F.) is 0.015. This PNN correctly classifies 161 input patterns (i.e., 89.44%) into the correct output category for the number of potential incidents. Nineteen patterns are incorrectly classified. When the model is evaluated on new, unfit data (i.e., the production data), the PNN correctly classifies 10 of the 12 patterns (i.e., 83.33%). The favorable performance of the PNN on the production set suggests that a model with the ability to generalize has been identified.

In Model 2, the input variable of SDR/f.s. is removed. The classification accuracy percentage decreases to 72.78% on the training data. The performance of the PNN on the production data is severely degraded, as the classification accuracy rate decreases to 66.67%. This observation suggests that SDR/f.s. is an important input to the model.

In Models 3-4, the output is the aggregate number of Events. Note that the classification accuracy rate is 91.67% in Model 3 for the training data. In Model 4, the input SDR/f.s. is removed and the classification accuracy rate decreases to 81.67% on the training data and to 66.67% on the production data. This again suggests that the input of SDR/f.s. is an important variable for the PNN.

Table 3 exhibits neural network models for aircraft operators with a fleet size less than 200 airplanes. Four PNNs are presented with their corresponding input and output variables, smoothing factors, and classification accuracy rates for both training and production patterns. In general, classification performance is enhanced by including the input of SDR/f.s. to the PNN.

Table 3. PNN Models for Carriers With Small Fleet Size (< 200 Aircraft).

| Model # | Models | Training Pattern | | Production Pattern | |
		Corr.	Incorr.	Corr.	Incorr.
1	f.s SDR/f.s. ⇒ Classified Incidents P S.F. = 0.01 (3:180:4)	103 87.29%	15	9 90.00%	1
2	f.s ⇒ Classified Incidents P S.F. = 0.01 (2:180:4)	97 82.20%	21	8 80.00%	2
3	f.s SDR/f.s. ⇒ Classified Events P S.F. = 0.005 (3:180:4)	106 89.83%	12	10 100%	0
4	f.s ⇒ Classified Events P S.F. = 0.007 (2:180:4)	102 86.44%	16	9 90.00%	1

It is acknowledged that there are small sample sizes for the production data in the cases of large and small carriers that make it difficult to assess model generality. These models will be updated as new data become available. Nevertheless, the research results from using a PNN to assess aviation safety risk appear promising.

CONCLUSIONS

The forecasting of the number of potential aircraft incidents is a complex problem and is receiving increased attention by the FAA due to the dramatic growth in domestic air traffic. This research investigated the use of artificial neural networks to detect complex, underlying patterns in safety inspection reporting and to use this information to forecast the number of potential incidents for aircraft operators. In addition, the contribution of the Service Difficulty Reporting (SDR) database to improving the forecasting capability of the neural network was examined.

A Probabilistic Neural Network (PNN) was found to be highly suitable for classifying inputs such as the fleet size, number of SDRs/fleet size, and proportion of unfavorable operations surveillance inspections into four output classes for the number of potential incidents. In particular, the inclusion of the number of SDRs/fleet size for both large and small airlines improved the general forecasting capability of the PNNs on new, unfit data. A different number of output classes for large versus small airlines should be examined in future research.

It must be noted that any data reporting errors will affect the neural network classification performance. It is recommended that the FAA continue to verify the quality and integrity of both primary and secondary data sources for SPAS.

The ability to anticipate the number of potential incidents will enable the FAA to promptly recognize adverse trends and to heighten inspection activities. Additional focused surveillance by the inspectors may lead to preemptive maintenance actions by the airlines and to enhanced air traffic safety.

ACKNOWLEDGMENT

REFERENCES

1. Safety Performance Analysis Subsystem, "Functional Description Document," U.S. Department of Transportation, Volpe National Transportation Systems Center, Cambridge, MA, March 1992.

2. Safety Performance Analysis Subsystem, "Prototype Concept Document," U.S. Department of Transportation, Volpe National Transportation Systems Center, Cambridge, MA, April 1992.

3. Safety Performance Analysis System, "SPAS Performance Measure Definitions (Version 1.0)," U.S. Department of Transportation, Volpe National Transportation Systems Center, Cambridge, MA, October 1995.

4. The Federal Aviation Administration Airworthiness Inspector's Handbook, FAA Order 8300.10, Volume 2, Department of Transportation, September 1989.

5. McCulloch, W. S. and Pitts, W., "A Logical Calculus of Ideas Immanent in Nervous Activity," Bulletin of Mathematical Biophysics, Vol. 5, 1943, pp. 115-133.

6. Hopfield, J. J., "Neurons With Graded Response Have Collective Computational Properties Like Those of Two-State Neurons," Proceedings of the National Academy of Science, Vol. 81, 1984, pp. 3088-3092.

7. Hopfield, J. J., "Neural Networks and Physical Systems With Emergent Collective Abilities," Proceedings of the National Academy of Science, Vol. 79, 1982, pp. 2554-2558.

8. Simpson, P., Artificial Neural Systems, Pergamon Press, New York, NY, 1990.

9. Wasserman, P., Neural Computing: Theory and Practice, Van Nostrand Reinhold, New York, NY, 1989.

10. NeuroShell 2, Ward Systems Group, Inc., Frederick, MD, 1993.

11. Specht, D., "Probabilistic Neural Networks for Classification, Mapping, or Associative Memory," Proceedings of the IEEE International Conference on Neural Networks, Vol. 1, 1988, pp. 525-532.

12. Specht, D., "Probabilistic Neural Networks," Neural Networks, Vol. 3, 1990, pp. 109-118.

13. Pindyck, R. S. and Rubinfield, D. L., Econometric Models and Economic Forecasts, McGraw-Hill, New York, NY, 1991.

WIDESPREAD FATIGUE DAMAGE THRESHOLD ESTIMATES

I. C. Whittaker and H. C. Chen
Boeing Commercial Airplane Group
Seattle, Washington

ABSTRACT

This paper describes a simple analytical tool for the use by structures engineers to predict the operational age at which a fleet of airplanes would start to experience more than the isolated incident of fatigue cracking. This operational age is often referred to as a fatigue threshold and is usually measured in flights. The analysis approach follows the traditional practice used for fatigue design by applying a "reduction-factor" to individual structural component average life estimate (central tendency fatigue performance) to determine the fatigue threshold. The two-parameter Weibull distribution with assumed shape parameters is used to develop the procedure for use by structures engineers. The procedure is facilitated by a nomograph which is entered with the number of structural components in the population and on exiting the reduction-factor is obtained. The structures engineer must identify certain targets such as the limits on the number of fatigued components and the number details within any single component. Several examples of application of this test/service statistics based method to estimation of widespread fatigue damage threshold are provided.

INTRODUCTION

The likelihood of the occurrence of fatigue damage in an airplane structure increases with the number of flights the airplane experiences. Commercial airplanes are generally designed with an intended minimum design service objective during which the probability of fatigue cracking is expected to be low and if cracks do occur they will be in isolation and grow independently. Airplanes are frequently utilized beyond their original design service objective in the current commercial airline industry. This makes damage tolerant structures together with competent fatigue damage inspection programs essential elements to ensure continuous airworthiness for aging airplanes throughout their operational lives until economics dictate their retirement from service.

Multiple cracks may occur and become interactively dependent as they grow in an aging airplane. Existing damage tolerance programs for aging fleets such as the supplemental structural inspection program only address damage at multiple sites or elements, whose damage extent is restricted to a *local* structural area or detail and no significant damage exists beyond this area. Since the Aloha 737 accident in 1988, much of the focus has been on widespread fatigue damage (WFD) (Figure 1). WFD has been characterized by the

simultaneous presence of cracks at multiple structural areas and details (multiple site damage (MSD) and multiple element damage (MED)) that are of sufficient size and density whereby the structure may no longer meet its damage tolerance requirement. The presence of WFD can accelerate the loss of residual strength as shown in Figure 2, and results in a shorter damage detection period. An airplane structure that is WFD susceptible usually consists of a number of similar structural details subjected to similar stress levels. A typical example of widespread fatigue damage is at a fuselage skin lap joint where simultaneous cracking at fastener holes along several adjacent bays may reduce its damage tolerance below the regulatory level before the cracks are readily detectable. Other WFD-susceptible structures may include fuselage frames, tear straps, circumferential splices, wing chordwise splices, etc.

- Maximum allowable damage shown
- Damage connection up to this size is tolerated
- No significant damage beyond this region
- All MSD or MED within this area is local and already accounted for in damage tolerance analysis

- Widespread similar details
- Similar stresses
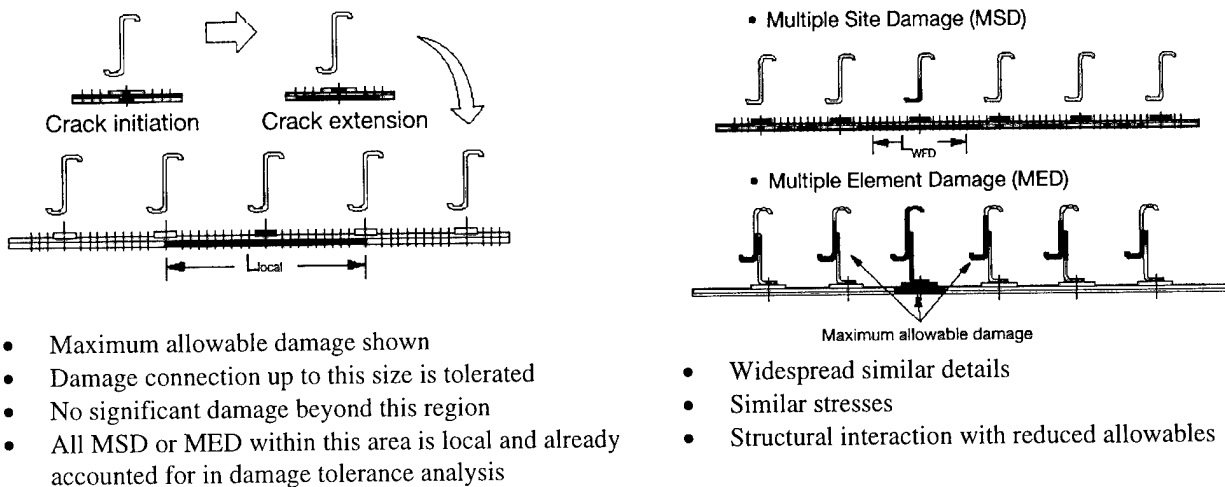- Structural interaction with reduced allowables

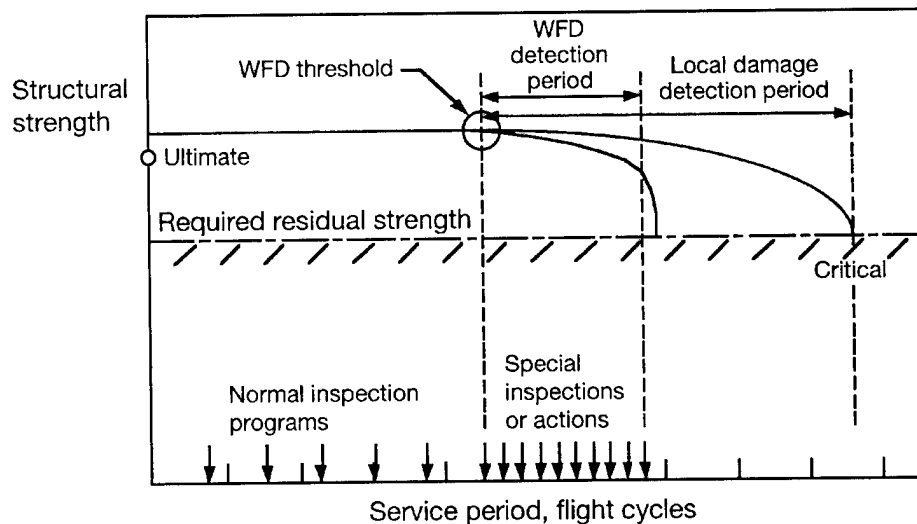Figure 1. Example of Local and Widespread Fatigue Damage.

Figure 2. Comparison of Damage Detection Opportunities, Local vs. Widespread Fatigue Damage.

Industry guidelines for the evaluation of widespread fatigue damage have been proposed by the Airworthiness Assurance Working Group (AAWG) (Reference 1). Boeing Commercial Airplane Group (BCAG) has initiated WFD evaluations on Boeing's aging airplane models using these guidelines. As shown in Figure 3, a multistage evaluation process is recommended in these guidelines. In this paper only the "estimate of WFD occurrence" will be addressed. As suggested in the guidelines, this may involve evaluations of WFD size, extent, and its occurrence time, with incorporation of test and in-service fleet experiences.
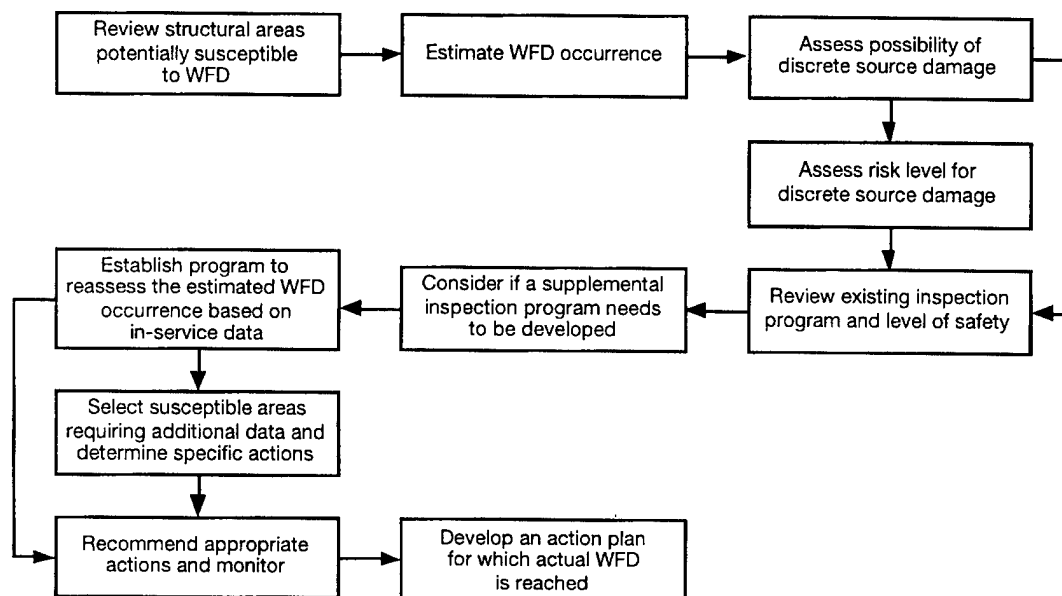

Figure 3. WFD Evaluation Process.

A WFD threshold can be viewed as an airplane operational life in flights at which the damages in multiple structural details could start to interact and result in an accelerated loss of residual strength (Figure 2). At this threshold, special fatigue inspection/modification programs may be needed in addition to other existing programs in order to provide sufficient damage detection opportunities before an occurrence of link-up of discrete detail damage. In some cases when the WFD-susceptible structure is also susceptible to discrete source damage, this threshold may become a WFD onset which is at a certain safety margin before the occurrence of widespread fatigue damage. The WFD onset indicates the time when some structural modifications become necessary to prevent the occurrence of widespread fatigue damage in a fleet.

Significant research effort has been made in developing methods for predicting WFD thresholds. A number of computational tools have been developed for this purpose and are fracture mechanics based (References 2 and 3). A typical fracture-mechanics based method often starts with assumed initial flaws including their sizes and locations. Crack growth analysis for small cracks is then carried out until the moment when some of the cracks start to interact, thus constituting a WFD threshold. To predict the WFD onset, continued crack

growth analysis with a consideration of crack interactions and residual strength analysis for determining the occurrence of widespread fatigue damage is often needed. It should be noted, however, the uncertainties associated with initial flaws, loads, and the stochastic nature of crack growth and residual strength can make these methods become unnecessarily complicated to achieve meaningful results.

This paper describes a simple analytical tool for use by structures engineers to predict WFD thresholds. It incorporates test and service experiences and simple statistical models in such a way that all the uncertainties are systematically taken into account and the resulting WFD threshold can be estimated at any reliability level. The analysis approach follows the traditional practice used for fatigue design by applying a reduction factor to the structure's central tendency fatigue performance (average life) to determine the fatigue threshold. In this approach the factor is dependent on population (i.e., at-risk fleet) size and the interdependent relationship between structural components and structural details within the component(s). This relationship was developed from Boeing's extensive test and airplane service databases.

In the following, BCAG's experience in widespread fatigue damage from service and test experiences is described. Emphasis is on the extent of cracking, i.e., number of assumed initiated small cracks, that determines the criteria for WFD threshold. It is followed by an explanation of the proposed approach to predicting WFD threshold and the use of nomographs in carrying out the prediction. Finally, a few examples are discussed to illustrate the application and effectiveness of the approach.

Fleet Service and Test Experience in WFD

For over four decades, the airplane industry has been using full-scale fatigue tests, panel tests, and data from inspections of in-service jet transports to validate the design concepts and identify appropriate preventive maintenance actions for the fleets. In early years, all the full-scale tests and uses of service data were aimed at validating the fail-safe concept that involves only local damage at multiple sites, e.g., a fuselage fail-safe capability for cracks up to one or two bays. Since the late 1980s, BCAG has conducted a series of full-scale fatigue tests and panel tests to address widespread fatigue damage issues. The primary goal was to investigate the damage extent that might lead to widespread fatigue damage. A detailed description of these tests and their findings can be found in Reference 4. More recently, under an FAA contract BCAG conducted full-scale panel tests to investigate the effect of MSD in a lap joint on the residual strength of a simulated wide-body fuselage (Reference 5). Also, a full-scale fatigue test of a retired B727 fuselage has just been completed. Very detailed cracking information has been recorded and data reduction is currently being undertaken for WFD analysis.

Over the years, as more high-time airplanes remain in service more data from in-service airplanes have become available for developing WFD criteria for aging airplanes. Most of the service data have been from the Boeing Significant Item Reporting System (SIRS) to which most discrepancies found by operators were reported. Other service data

came from service bulletins (SB), fleet survey programs in which engineers went out to the operators to inspect high-time airplanes, and teardown inspections of retired service airplane structures. The data from these various sources showed mixed cracking scenarios. For example, the cracking along a lap joint was in some cases dominated by local damage at multiple rivet holes in one or two frame bays, whereas in other cases by uniformly distributed cracks across several frame bays, i.e., a prelude of widespread fatigue damage. Since local damage at multiple sites has already been accounted for in the existing damage tolerance methods, only those cases with uniform damage were selected for data reduction in determining the criteria for WFD threshold.

Reviews of available test and service data by BCAG have led to a preliminary concept of choosing criteria for WFD threshold. The damage extent in terms of a percentage of cracking among the structural details per airplane or component seems to provide a simple and logical criterion for WFD threshold. For example, a 10 percent cracking of small cracks in rivet holes along a lap joint might be a suitable threshold for a special WFD inspection program for lap joints, whereas a smaller percentage of cracking might be appropriate for wing chordwise splices. The WFD threshold can also be estimated at a selected reliability level. For example, it can be estimated as to when the first lap joint develops 10 percent cracking in a fleet of at-risk lap joints, or when two lap joints in the fleet develop 10 percent cracking. Such simple criteria also enable a continuing use of a reduction factor, which is similarly applied in fatigue design.

As more test and service data are evolving and most of the development remains ongoing, change or refinement of WFD threshold selections is likely to happen. The methodology described below is therefore expected to go through a process of continuous improvement.

Prediction of Fatigue Threshold

BCAG has a well developed structural fatigue prediction capability that has been tested and refined by extensive full-scale testing and decades of operational fleet data. Structural design philosophy is focused on the early, i.e., extreme, event and consequently fatigue design criteria are in place which reflect this philosophy. For example, the statistical model used is Weibull, one of the family of extreme value distributions, instead of the log-normal distribution which is in more common use in the aviation industry.

There was considerable activity within Boeing during the late 1960s and early 1970s to ascertain the Weibull parameters that could model airplane structural fatigue (References 6 and 7). The studies resulted in selection of the two-parameter Weibull

669

$$F(x) = 1 - \exp\left[-\left(\frac{x}{\beta}\right)^{\alpha}\right]$$

$F(x)$ = cumulative probability function
x = flight cycles
α = shape parameter
β = scale parameter or characteristic fatigue life

with selected shape parameters and this model is built into the "Design for Durability" system used by all BCAG structural designers and analysts. This system has been discussed previously (References 8 and 9). It should be noted that fleet data are monitored for lessons learned, to analyze early fatigue incidents when necessary, and to develop and document the demonstrated fatigue ratings of the structures. This activity has been ongoing for very many years resulting in design standards (Figure 4) reflecting lessons learned from a large maintained database, and high confidence in the correlation between fatigue analysis prediction and service demonstrated performance.
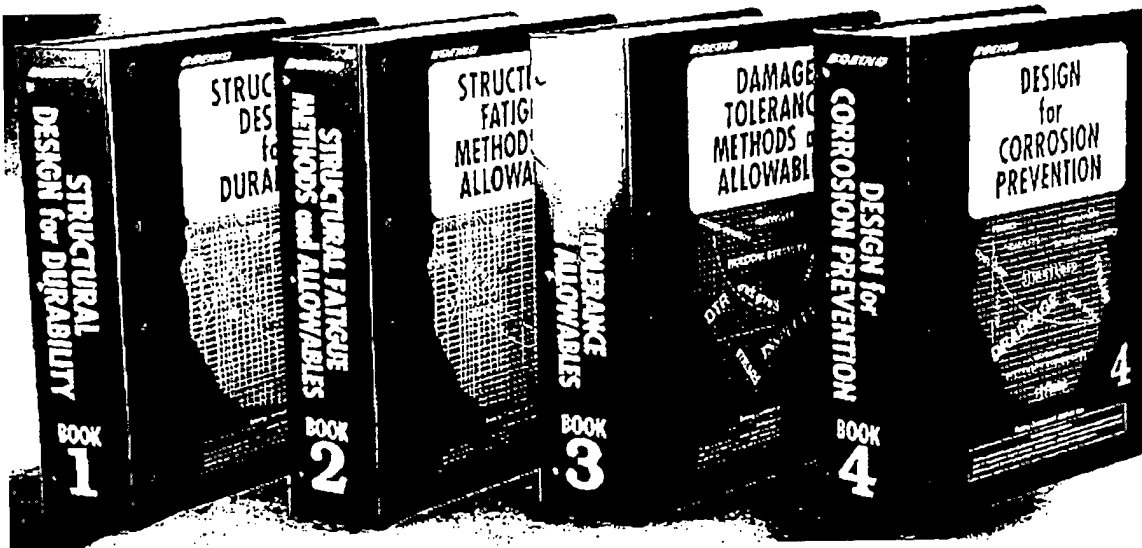
Figure 4. Boeing Durability and Damage Tolerance Technology Standards.

Given this background it is believed that a similar designer/analyst-oriented procedure could be used for predicting thresholds for WFD. Currently BCAG structural design criteria specify that any structural component must equal or exceed a specific level of reliability for the duration defined by the minimum Design Service Objective. These levels of reliability range from high to very high depending upon the criticality of the component. The concept of widespread fatigue damage may add another dimension, namely a consideration of order statistics. When designing for reliability today, BCAG designers/analysts must select from a menu of fatigue reliability factors that are appropriate for their structural applications. These factors are Weibull based in order to provide sufficiently high levels of reliability in the fleet without the need to address fleet size, i.e., reliability in terms of percent, e.g., 99 percent. However, in the case of WFD consideration may have to be given to the 1st, or 2nd, or ith event in a fleet of n structures. This would force unfamiliar scenarios on designers/analysts

such as the number of fatigue events within any single component, or within n components per airplane, or m airplanes in the fleet.

The Weibull parameters characterizing structural fatigue were already known, verified, and used over the past 30 years. It was therefore logical to expand on the current fatigue reliability factor design procedure to include a WFD threshold factor which considers i events in samples of size n. A nomograph was selected as the medium to present the WFD threshold factor. This was done to provide the designer/analyst with a visual aid (Figure 5) to the interactive relationships between i fatigue events and n sample size whether it be details per component or components per airplane or airplane per fleet. The initial nomograph was developed for application to fuselage structures, i.e., predominantly pressure-loaded structural details such as fuselage lap joints, circumferential splices, and frames (Figures 6 through 8). The underlying assumption for the nomograph is based on the observation that airplane-to-airplane variation in fatigue is greater than component-to-component variation within the same airplane. Therefore, the graph was developed using the inverse Weibull function and a series of Weibull shape parameters as follows.

Reduction Factor: $$\left(\frac{\beta_{POP}}{\beta_i}\right)_{STR} \approx \left[-\ln(1 - F_{STR}(x_i))\right]^{-1/\alpha_{STR}}$$

in which the subscript STR represents structural detail, structural component, or airplane. For each structural category,

β_{POP} = population characteristic life to specified damage for STR
β_i = characteristic life to ith occurrence of damaged STR in a sample of n STRs
x_i = expected life to ith occurrence of damaged STR in a sample of n STRs
$F_{STR}(x_i)$ = probability of damage for an STR at x_i flights

$\approx i/(n + 0.5)$

α_{STR} = shape parameter for STR

$\approx$ 8.0 for rivet holes in a lap joint
6.0 for lap joints in an airplane
5.0 for airplanes in a fleet

These parameters are not expected to be universally good for all structural details, and will likely need refinement. The resulting WFD threshold factor S_{WSF} for this particular case is calculated as

$$S_{WSF} = \left(\frac{\beta_{POP}}{\beta_i}\right)_{RIVET} \left(\frac{\beta_{POP}}{\beta_j}\right)_{LAP} \left(\frac{\beta_{POP}}{\beta_k}\right)_{AIRPLANE}$$
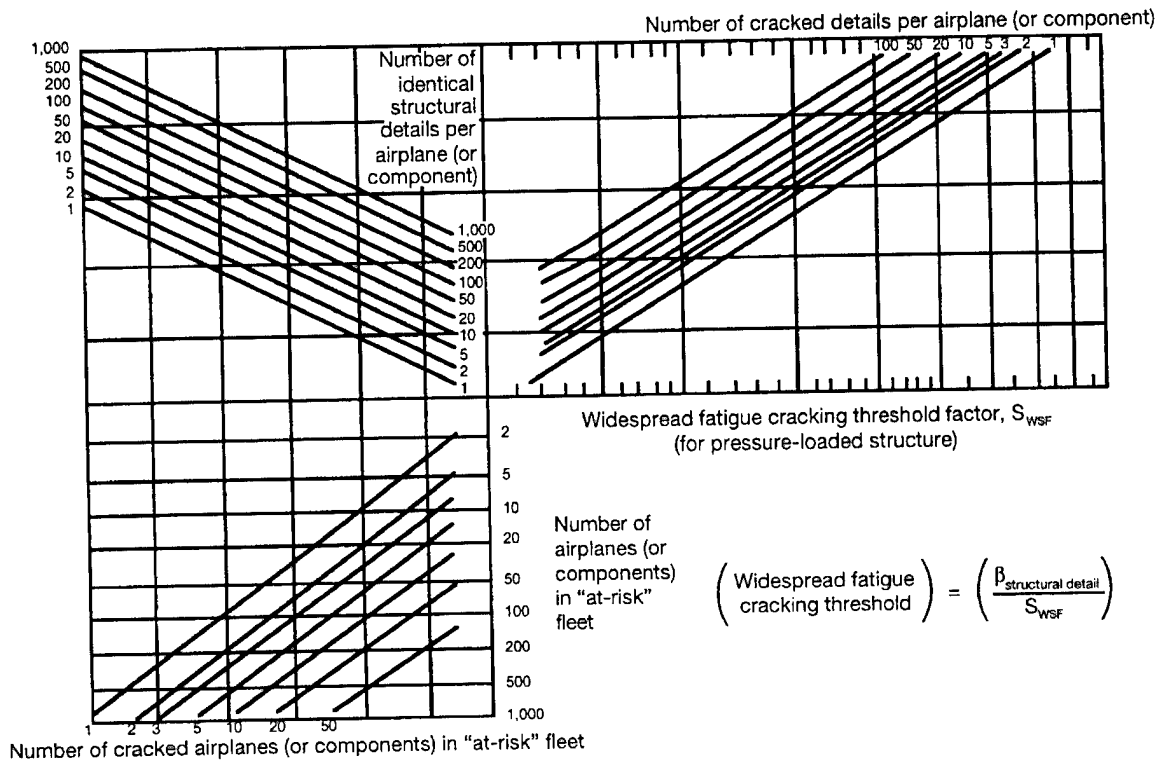
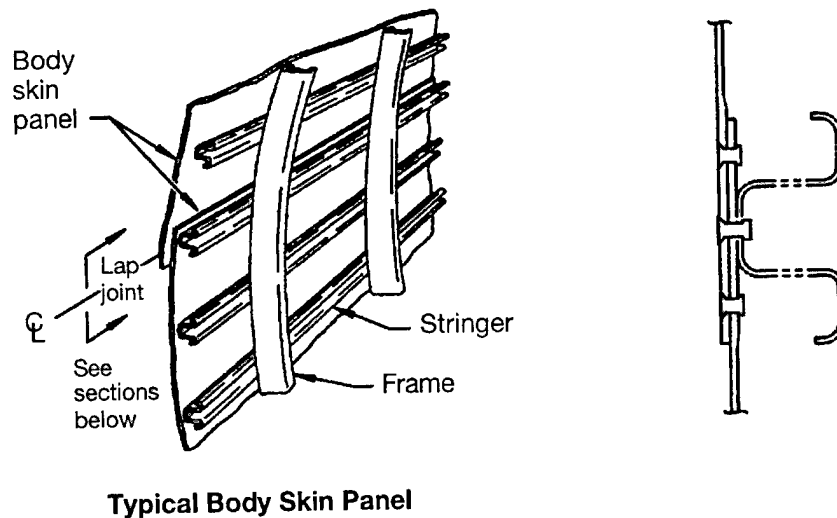Figure 5. Nomograph for Estimating WFD Threshold Factor for Pressurized Structures.

Typical Body Skin Panel

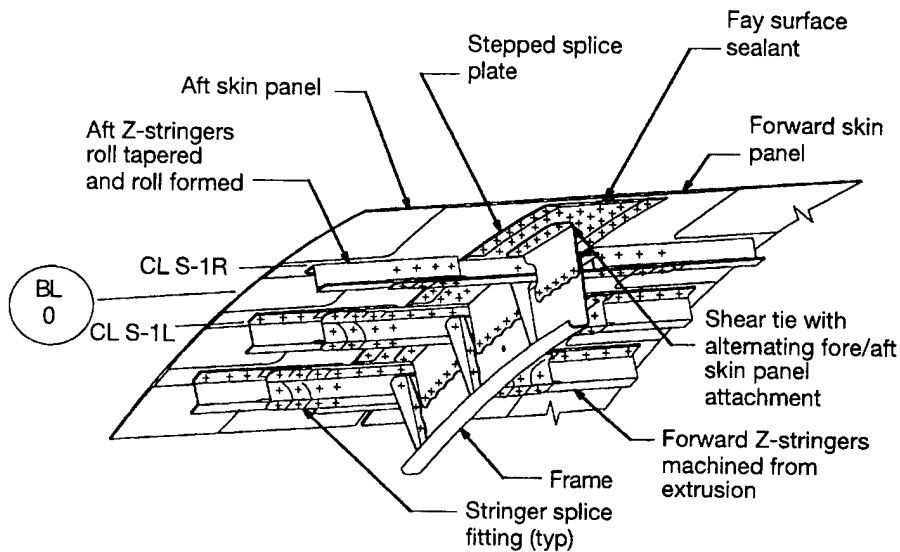Figure 6. Typical Body Skin Lap Joint—Longitudinal.

672

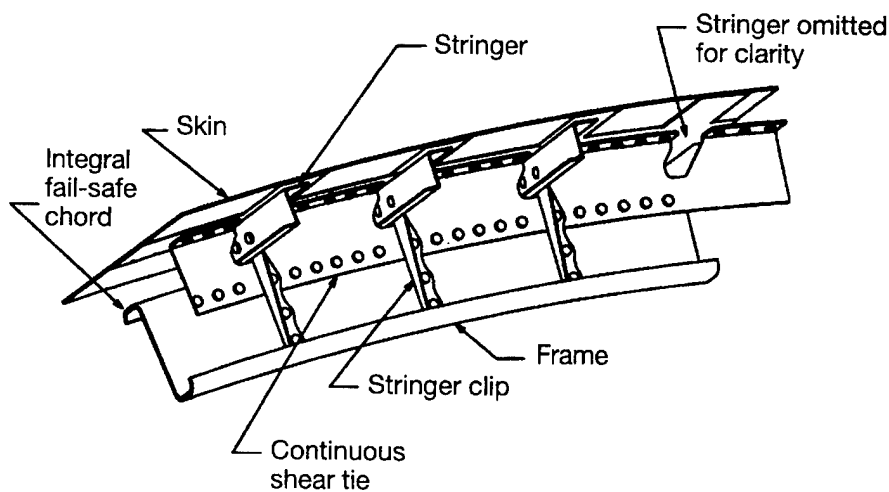Figure 7. Circumferential Splice—Skin and Stringer.

Figure 8. Frame With Shear Ties.

Analysts supporting the standard- and wide-body airplane programs have been evaluating this threshold factor to ascertain the level of correlation between predictions based on the nomograph and observed fleet history. Some difficulties were encountered due to a lack of consensus on what damage extent constituted WFD. As seen from Figure 5 the analyst must make certain decisions regarding sample size at risk of fatigue cracking and the WFD limit in terms of number of cracks, in order to enter and exit the graph. Nevertheless, a few examples were completed and predictions were found to be encouraging although somewhat more conservative than intended; see example below.

A more extensive evaluation is presently underway and results, when available, will be used to refine the WFD threshold factor as necessary. It is also anticipated that more than a single nomograph will be required to cover all primary structural details.

EXAMPLES

Some examples are presented below for illustrative purposes. All specific details have been omitted in this paper as the procedure is still in development.

The initial examples are on fuselage lap joints.

Example 1 is based on a fleet of 323 airplanes with 6 identical lap joints per airplane and 380 equally critical rivet connections per lap joint. It was assumed that the WFD threshold was consistent with small cracks initiated at 10%, i.e., 38, of the rivet holes in a lap. Figure 9 is a plot comparing the cracking history predicted via the factors from the nomograph against the service history as reported by the airplane operators. It is noted that the correlation at the first event is very close, but from there on the prediction becomes increasingly conservative.

Example 2 is based on a fleet of 154 airplanes with 8 identical lap joints per airplane and 220 equally critical rivet connections per lap joint. As in the previous example, the WFD threshold was assumed to occur when 10% of the rivet holes in a lap contain small cracks. Figure 10 is a plot similar to that shown in the first example, and as before, it is clear that the predictions are more conservative than desired.

Example 3 is based on a fleet of 83 airplanes with 8 identical lap joints per airplane and 300 equally critical rivet connections per lap joint. All WFD assumptions remained unchanged from the two previous examples. In this example good correlation was obtained between prediction and service history; see Figure 11.

In all these examples, the analysts were required to determine the characteristic, i.e., central tendency, life to fatigue crack initiation in a specific lap joint. This characteristic life is then divided by the appropriate WFD threshold factor S_{WSF} to obtain the predicted life to the ith fatigue event. As stated earlier, BCAG has collected over several decades, a large database which is incorporated into design standards, Figure 4, and provided to every structural designer/analyst. It is to Book 1 of these design standards that the analyst refers in order to obtain information on lap joints and their expected performance. It is an easy step from there for the analyst to estimate the characteristic life to initiation of a small fatigue crack(s) in any particular lap joint such as those addressed in the previous examples. Specifically, the analyst finds a lap joint in the design standard that is similar to the lap joint being investigated. A fatigue rating is obtained from Durability Design Technology Standards, see Figure 12, and this rating is modified as necessary to match the specific detail

of the lap joint being investigated. The modification factors are supplied in the Durability Analysis Technology Standards of the BCAG design standards (Figure 13). Once the modified rating is obtained, the analyst determines the characteristic fatigue life of the investigated lap joint by using the appropriate combination of S-N curve and reliability factor provided in the same analysis standard (Figure 14).
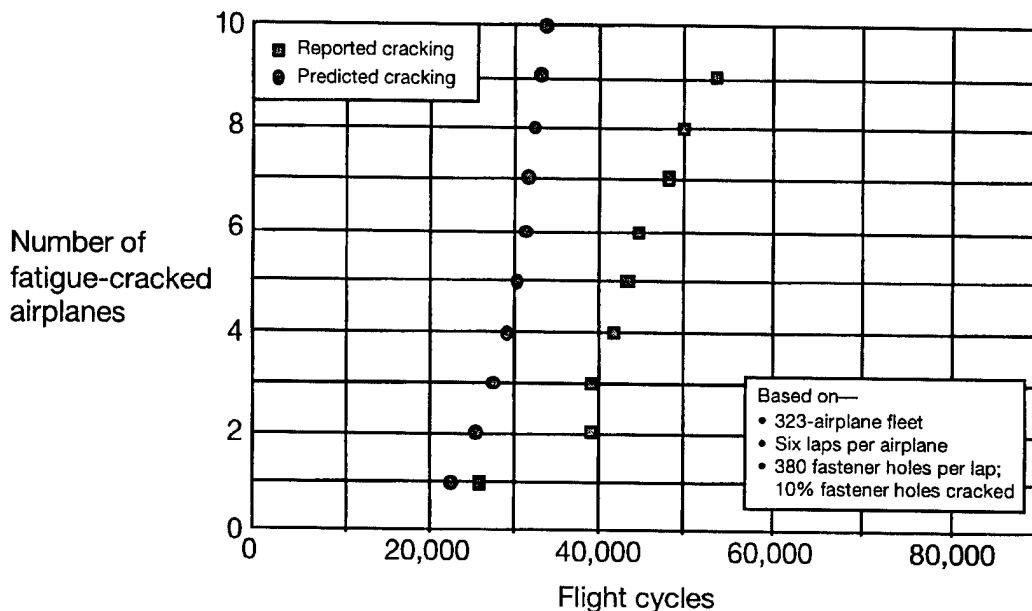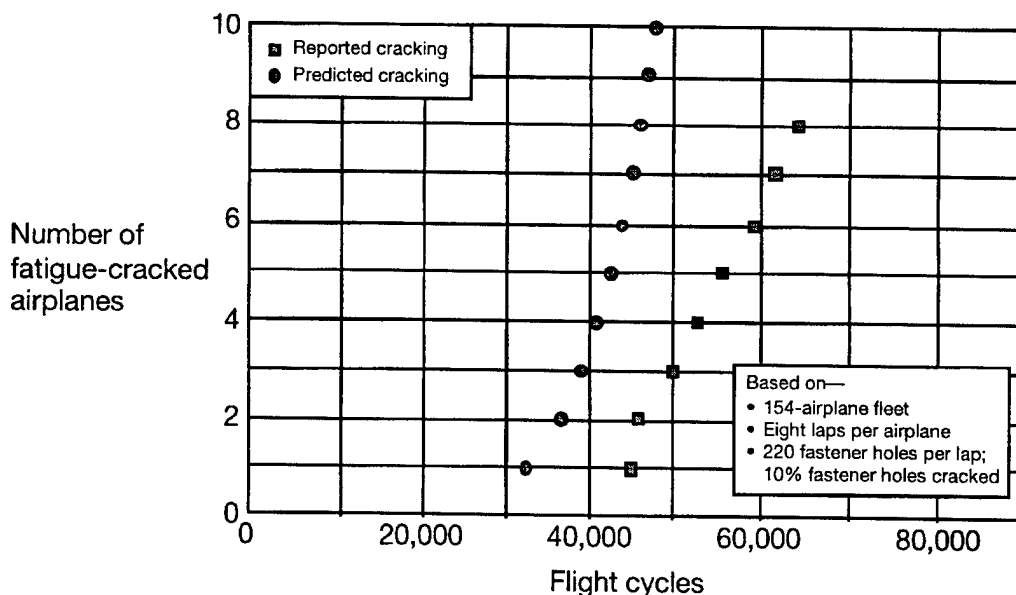

Figure 9. Comparison of Predicted and Actual Cracking Histories for Example 1 Problem.

Figure 10. Comparison of Predicted and Actual Cracking Histories for Example 2 Problem.
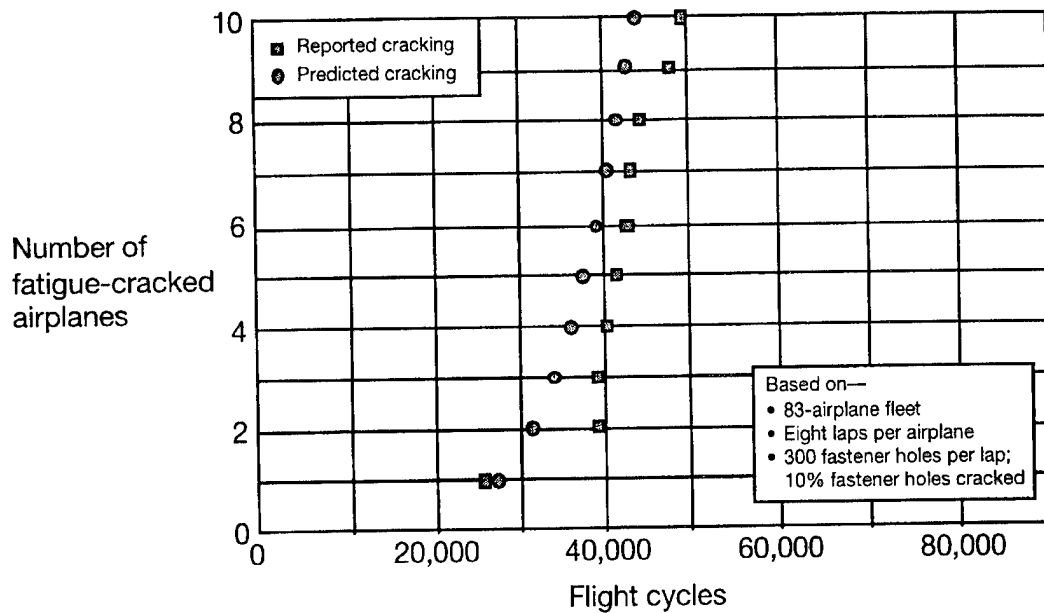
675

Figure 11. Comparison of Predicted and Actual Cracking Histories for Example Problem 3.
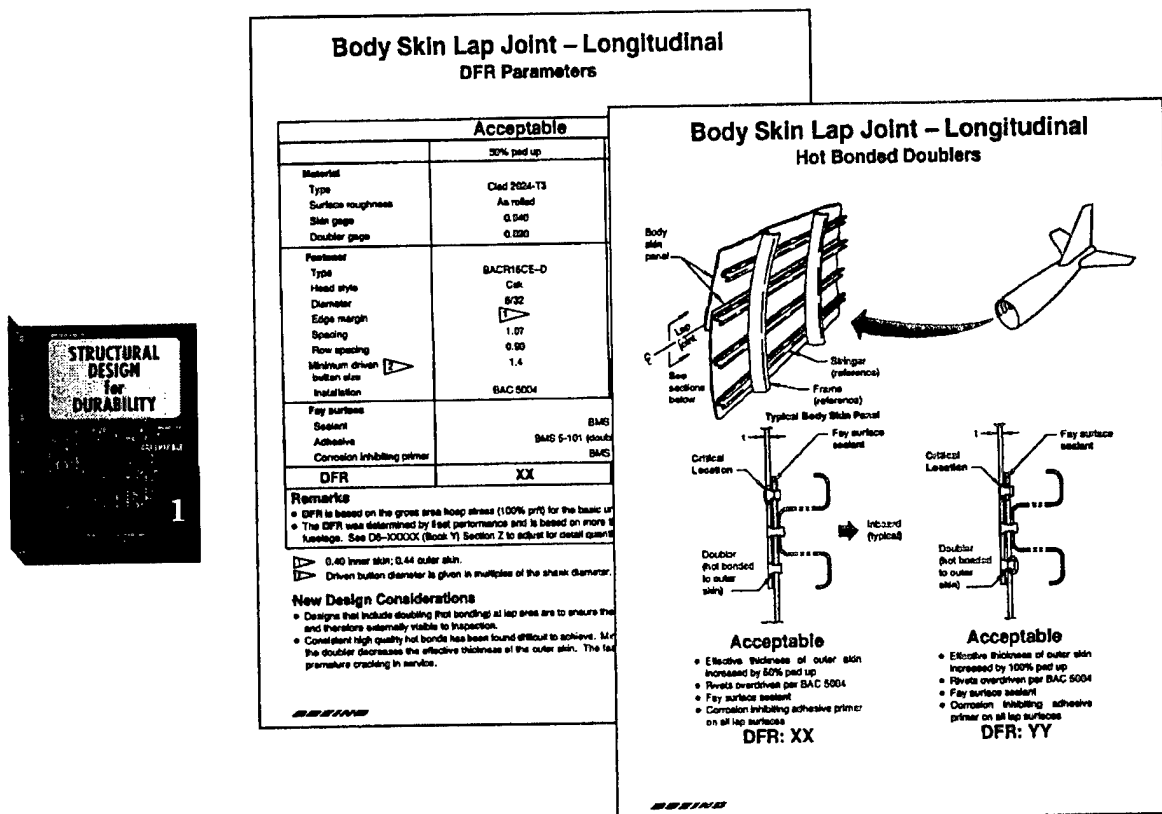

Figure 12. Design for Durability of the BCAG Design Standards Maintains a Library of Fatigue Ratings for Airplane Structures.
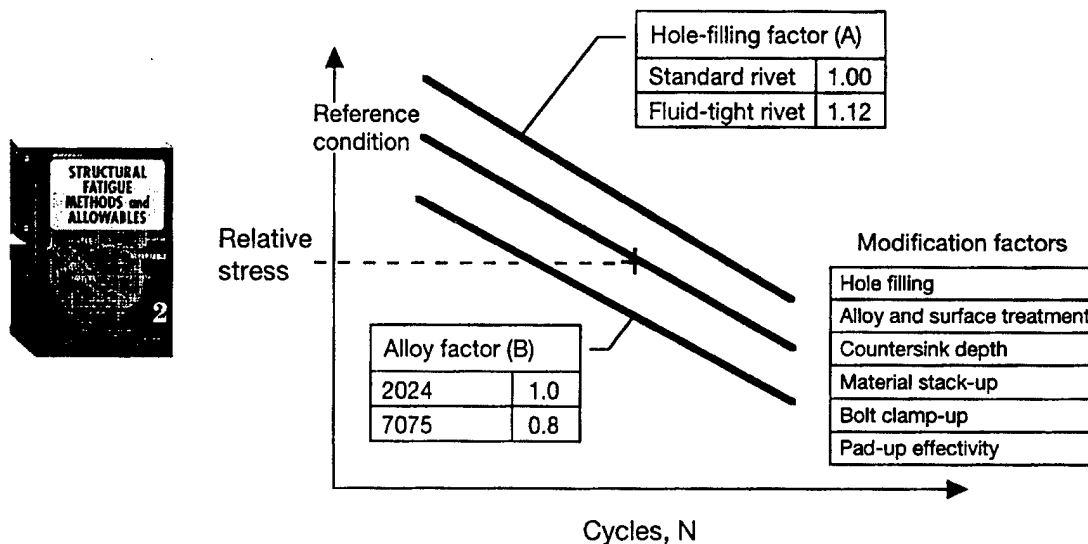
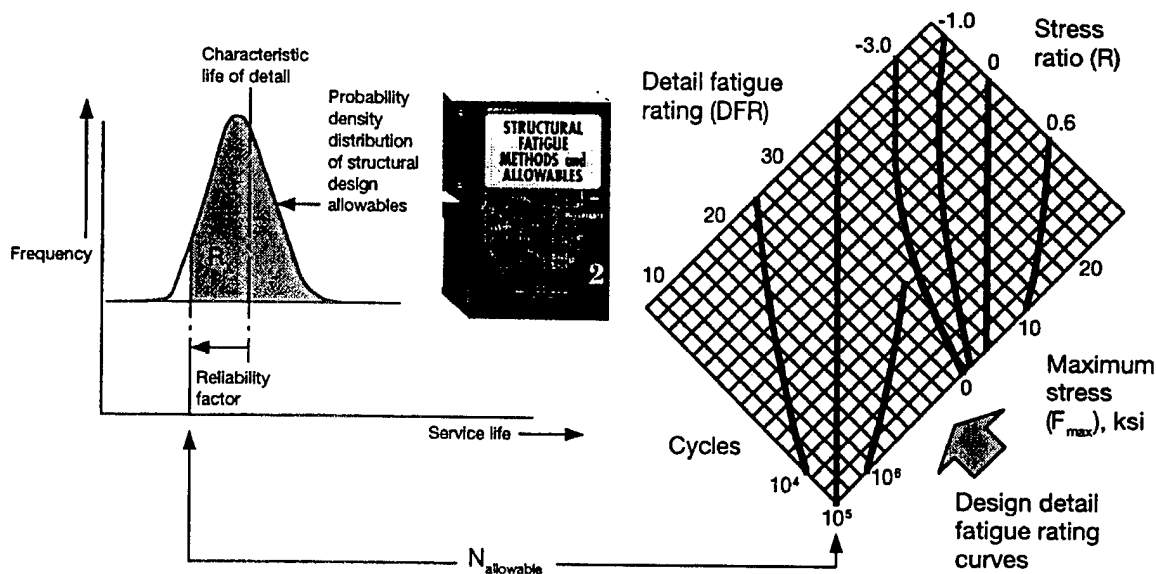**Figure 13. Fatigue Rating Modification Factors.**

Figure 14. Estimation of Characteristic Life from Fatigue Rating via Fatigue Design Elements.

Several other examples have been undertaken by program personnel and are at different stages of completion. To date all feedback indicates the proposed S_{WSF} factor provides conservative estimates relative to service history; however, data are insufficient to proceed with refinement of the procedure. A nomograph for gust critical structure, e.g., wings, has also been developed and provided to airplane program personnel for evaluation, but there has been no feedback at this time.

SUMMARY

In summary, a fatigue-based procedure for estimating thresholds for WFD allows BCAG to utilize its extensive historic fatigue database and proven fatigue analysis methods. The WFD procedure in question continues with the industry-wide approach, namely the use of the "scatter factor" concept, except in this application it requires the designer/analyst to consider variables associated with population size to determine the factor. The relationship of these variables with the threshold factor has been presented in the form of a nomograph to help the designer/analyst visualize the impact of the population variables. A few test cases have been completed to date and the predictions relative to fleet data have been encouraging. It was intended and anticipated that predictions would be somewhat conservative relative to fleet history. However, in some examples the level of conservatism was higher than expected, indicating some "tweaking" of the WFD factor is desirable. Additional examples are still being evaluated and when completed the threshold factor may need refining, and there could be a possible requirement for a family of factors representing different types of structural details.

ACKNOWLEDGMENTS

REFERENCES

1. *A Report of the AAWG on Structural Fatigue Evaluation for Aging Airplanes,* October 1993.

2. Bigelow C. A. and P. W. Tan: "An Integrated Methodology for Assessing Widespread Fatigue Damage in Aircraft Structures," Proc. FAA-NASA 6th Int'l. Conf. on the Continued Airworthiness Aircraft Structures, Atlantic City, New Jersey, June 27-28, 1995, pp. 121-138.

3. Harris, C. E.; Starnes, Jr., J. H.; and Newman, Jr., J. C.: "Development of Advanced Structural Analysis Methodologies for Predicting Widespread Fatigue Damage in Aircraft Structures," Proc. FAA-NASA 6th Int'l. Conf. on the Continued Airworthiness Aircraft Structures, Atlantic City, New Jersey, June 27-28, 1995, pp. 139-164.

4. Maclin, J. R.: "Performance of Fuselage Pressure Structure," 3rd Int'l. Conf. on Aging Aircraft and Structural Airworthiness, Washington, DC, November 19-21, 1991.

5. Gruber, M. L.; Mazur, C. J.; Wilkins, K. E.; and Worden, R. E.: "Investigation of Fuselage Structure Subject to Widespread Fatigue Damage," FAA Technical Report, DOT/FAA/AR-95/47, February 1996.

6. Whittaker, I. C. and Besuner, P. M.: "A Reliability Analysis Approach to Fatigue Life Variability of Aircraft Structures," Air Force Materials Laboratory Technical Report AFML-TR-69-65, April 1969.

7. Whittaker, I. C.: "Development of Titanium and Steel Fatigue Variability Model for Application of Reliability Analysis Approach to Aircraft Structures," Air Force Materials Laboratory Technical Report AFML-TR-72-236, October 1972.

8. Goranson, U. G.; Hall, J.; Maclin, J. R.; Watanabe, R. T.: "Long Life Damage Tolerant Jet Transport Structures," ASTM Symposium on Design of Fatigue and Fracture Resistant Structures, November 10-11, 1980.

9. Whittaker, I. C.; Miller, M.; Goranson, U. G.: "Durability and Damage Tolerance Evaluations of Jet Transport Structures," Proc. 5th Int'l. Conf. on Structural Safety and Reliability (ICOSSAR), August 7-11, 1989.